

# 科研基本和业绩条件 佐证材料

姓名：黄忠凯



与原件相符





## 关于国家自然科学基金资助项目批准及有关事项的通知

黄忠凯 先生/女士：

根据《国家自然科学基金条例》的规定和专家评审意见，国家自然科学基金委员会（以下简称自然科学基金委）决定批准资助您的申请项目。项目批准号：

11947205，项目名称：耗散可调多量子比特的量子电动力学系统的非平衡态动力学，直接费用：18.00万元，项目起止年月：2020年01月至2020年12月，有关项目的评审意见及修改意见附后。

请尽早登录科学基金网络信息系统（<https://isisn.nsfc.gov.cn>），获取《国家自然科学基金资助项目计划书》（以下简称计划书）并按要求填写。计划书电子文件通过科学基金网络信息系统（<https://isisn.nsfc.gov.cn>）上传，由依托单位确认后，自然科学基金委进行审核；打印为计划书纸质版（一式两份，双面打印）由依托单位审核并加盖单位公章后报送至自然科学基金委项目材料接收工作组。

自然科学基金委接收依托单位提交计划书电子版截止时间为**2020年01月03日16点前**，提交计划书电子修改版截止时间为**2020年01月10日16点前**；计划书纸质版于计划书电子版通过自然科学基金委审核后另行打印（建议双面打印），自然科学基金委接收计划书纸质版截止时间为**2020年01月17日16点前**。

请按照依托单位规定时间，及时将计划书电子版和纸质版先后提交依托单位进行确认审核。对于有修改意见的项目，请按修改意见及时调整计划书相关内容；如对修改意见有异议，须在计划书电子版报送截止日期前提出。计划书电子文件和纸质文件内容应当保证一致。

未说明理由且逾期不报计划书者，视为自动放弃接受资助。

附件：项目评审意见及修改意见



国家自然科学基金委员会  
数理科学部

2019年12月13日

与原件相符

附件：项目评审意见及修改意见表

项目批准号	11947205	项目负责人	黄忠凯	申请代码1	A05
项目名称	耗散可调多量子比特的量子电动力学系统的非平衡态动力学				
资助类别	专项项目	亚类说明	研究项目		
附注说明	理论物理专款研究项目				
依托单位	长江师范学院				
直接费用	18.00 万元	起止年月	2020年01月 至 2020年12月		
<p>通讯评审意见：</p> <p>&lt;1&gt;该项目拟采用以multi-D2波函数为试探波函数的变分法作为研究方法，分析多量子比特耦合的QED设置的量子态在周围环境中的动力学演化，探究环境对相干态的耗散作用。该项目将使用外加电磁场，研究多比特量子态QED装置的功能。申请人已在JCP、Phys. Rev. A等国际杂志上发表多篇研究论文，有很好的研究基础。建议予以资助。</p> <p>&lt;2&gt;申请人拟采用multi-D2变分波函数研究多量子比特耦合的系统在周围环境中的动力学演化，并探究环境对相干态的耗散作用。申请人在相关领域有多篇论文在包括PRA等期刊上发表，研究基础较强。拟开展的研究在理论和实际应用上都有一定的价值，建议优先资助。</p> <p>&lt;3&gt;量子开放系统涉及到诸多领域的内容，该申请项目完成基于申请人良好的研究经验积累，涉及的内容更深刻，申请书逻辑清晰，将来产生的研究结果具有创新性。</p>					
<p>修改意见：</p> <p style="text-align: right;">数理科学部</p> <p style="text-align: right;">2019年12月13日</p>					

## 国家自然科学基金 资助项目准予结题通知

黄忠凯 同志：

您承担的国家自然科学基金项目：（耗散可调多量子比特的量子电动力学系统的非平衡态动力学），批准号：（11947205）按有关规定已审核完毕，准予结题。

与本项目资助有关的后续成果，请您继续及时报送。

祝您在研究工作中取得更好的成绩！



与原件相符







项目批准号	11947205
申请代码	A05
归口管理部门	
依托单位代码	40810008A0113-0187



11947205 1011366

# 国家自然科学基金委员会 资助项目计划书

资助类别： 专项项目

亚类说明： 研究项目

附注说明： 理论物理专款研究项目

项目名称： 耗散可调多量子比特的量子电动力学系统的非平衡态动力学

直接费用： 18万元 执行年限： 2020.01-2020.12

负责人： 黄忠凯

通讯地址： 中国重庆市涪陵区聚贤大道16号

邮政编码： 408100 电 话： 023-72790088

电子邮件： 20190011@yznu.edu.cn

依托单位： 长江师范学院

联系人： 李言栋 电 话： 023-72790088

填表日期： 2019年12月13日



国家自然科学基金委员会制

*(Handwritten signature)*

Version: 1.011.366  
与原件相符



## 国家自然科学基金委员会资助项目计划书填报说明

- 一、项目负责人收到《关于国家自然科学基金资助项目批准及有关事项的通知》（以下简称《批准通知》）后，请认真阅读本填报说明，参照国家自然科学基金相关项目管理办法及《国家自然科学基金资助项目资金管理办法》（请查阅国家自然科学基金委员会官方网站首页“政策法规”栏目），按《批准通知》的要求认真填写和提交《国家自然科学基金委员会资助项目计划书》（以下简称《计划书》）。
- 二、填写《计划书》时要求科学严谨、实事求是、表述清晰、准确。《计划书》经国家自然科学基金委员会相关项目管理部门审核批准后，将作为项目研究计划执行和检查、验收的依据。
- 三、《计划书》各部分填写要求如下：
  - （一）简表：由系统自动生成。
  - （二）摘要及关键词：各类获资助项目都必须填写中、英文摘要及关键词。
  - （三）项目组主要成员：计划书中列出姓名的项目组主要成员由系统自动生成，与申请书原成员保持一致，不可随意调整。如果批准通知中“项目评审意见及修改意见表”中“对研究方案的修改意见”栏目有调整项目组成员相关要求的，待项目开始执行后，按照项目成员变更程序另行办理。
  - （四）资金预算表：根据批准资助的直接费用，按照《国家自然科学基金项目预算表编制说明》填报资金预算表和预算说明书。国家重大科研仪器研制项目、重大项目还应按照预算评审后批复的直接费用各科目金额填报资金预算表、预算说明书及相应的预算明细表。
  - （五）正文：
    1. 面上项目、青年科学基金项目、地区科学基金项目：如果《批准通知》中没有修改要求的，只需选择“研究内容和研究目标按照申请书执行”即可；如果《批准通知》中“项目评审意见及修改意见表”中“对研究方案的修改意见”栏目明确要求调整研究期限和研究内容等的，须选择“根据研究方案修改意见更改”并填报相关修改内容。
    2. 重点项目、重点国际（地区）合作研究项目、重大项目、国家重大科研仪器研制项目：须选择“根据研究方案修改意见更改”，根据《批准通知》的要求填写研究（研制）内容，不得自行降低、更改研究目标（或仪器研制的技术性能与主要技术指标以及验收技术指标）或缩减研究（研制）内容。此外，还要突出以下几点：
      - （1）研究的难点和在实施过程中可能遇到的问题（或仪器研制风险），拟采用的研究（研制）方案和技术路线；
      - （2）项目主要参与者分工，合作研究单位之间的关系与分工，重大项目还需说明课题之间的关联；
      - （3）详细的年度研究（研制）计划。



3. 国家杰出青年科学基金、优秀青年科学基金和海外及港澳学者合作研究基金项目：须选择“根据研究方案修改意见更改”，按下列提纲撰写：
  - (1) 研究方向；
  - (2) 结合国内外研究现状，说明研究工作的学术思想和科学意义（限两个页面）；
  - (3) 研究内容、研究方案及预期目标（限两个页面）；
  - (4) 年度研究计划；
  - (5) 研究队伍的组成情况。
4. 国家自然科学基金基础科学中心项目：须选择“根据研究方案修改意见更改”，应当根据评审委员会和现场考察专家组的意见和建议，进一步完善并细化研究计划，作为评估和验收的依据。按下列提纲撰写：
  - (1) 五年拟开展的研究工作（包括主要研究方向、关键科学问题与研究内容）；
  - (2) 研究方案（包括骨干成员之间的分工及合作方式、学科交叉融合研究计划等）；
  - (3) 年度研究计划；
  - (4) 五年预期目标和可能取得的重大突破等；
  - (5) 研究队伍的组成情况。
5. 对于其他类型项目，参照面上项目的方式进行选择和填写。





简表

项目负责人信息	姓 名	黄忠凯	性 别	男	出生年月	1988年09月	民 族	汉族
	学 位	博士			职称	博士后		
	是否在站博士后	是		电子邮件	20190011@yznu.edu.cn			
	电 话	023-72790088		个人网页				
	工 作 单 位	长江师范学院						
	所 在 院 系 所	无机特种功能材料重庆市重点实验室						
依托单位信息	名 称	长江师范学院					代码	40810008A0113
	联 系 人	李言栋		电子邮件	kjc1931@163.com			
	电 话	023-72790088		网站地址	http://www.yznu.cn			
合作单位信息	单 位 名 称							
项目基本信息	项 目 名 称	耗散可调多量子比特的量子电动力学系统的非平衡态动力学						
	资 助 类 别	专项项目			亚 类 说 明	研究项目		
	附 注 说 明	理论物理专款研究项目						
	申 请 代 码	A05:物理学II						
	基 地 类 别							
	执 行 年 限	2020.01-2020.12						
	直 接 费 用	18万元						





## 项目摘要

## 中文摘要:

通过对波函数进行制备、操作和测量,量子计算的基本物理过程可以得到实现。为了保证量子计算所涉及的物理过程能准确进行,参与量子计算的体系必须能在足够长的时间内保持良好的相干性。因此,量子比特系统与周围环境相互作用引起的耗散不能被忽略。为了量子逻辑门操作的更好实现,外加场可以用于操控多量子比特的状态。在本项目中,申请人首先将构建多量子比特的量子电动力学体系,并考虑环境的影响,进而构造出相应的开放量子系统。其次,将利用Dirac-Frenkel含时变分原理和multi-D2试探波函数,在无外场和有外场的条件下模拟波函数的含时演化。第三,通过对变分参数的仔细测试,保证计算的精确度。第四,依据计算得出的波函数,合理分析相干态和可观测量的演化。最后,根据计算结果的分析,为设计具有易操控的、能保持长时相干态的量子电动力学装置提供更加有效的理论支持。

## Abstract:

The basic physical processes of quantum computing can be achieved by preparing, manipulating, and measuring wave functions. In order to ensure that the physical processes involved in quantum computing can be performed accurately, systems involved in quantum computing must be able to maintain good coherence for long enough. Therefore, the dissipation caused by the interaction of the qubit system with the surrounding environment cannot be ignored. In order to achieve a better implementation of quantum logic gate operations, the applied field can participate in manipulating the state of multiple qubits. In this project, the applicant will firstly construct a multi-qubit quantum electrodynamic system, consider the influence of the environment on the qubits, and then build an open quantum system including the multi-qubit system and the coupled environment. Secondly, Dirac-Frenkel time-variational principle and the multi-D2 trial wave function will be employed to simulate the time-dependent evolution of the wave function in the absence and presence of an external field. Thirdly, via careful tests in the variational parameters, the accuracy of the calculation will be guaranteed, so that the dissipation caused by the surrounding environment to the quantum state of the system can be accurately treated. Fourthly, the evolution of coherent states and observables of interest will be analyzed based on the calculated wave function. At last, analysis of calculated results will provide more effective theoretical support for designing a quantum electrodynamic device with easy control and long-term coherent state.

**关键词(用分号分开):** 耗散; 可调制; 量子比特; 量子电动力学系统; 非平衡态动力学

**Keywords(用分号分开):** dissipative; tunnable; qubit; quantum electrodynamics; nonequilibrium dynamics



项目组主要成员

编号	姓名	出生年月	性别	职称	学位	单位名称	电话	证件号码	项目分工	每年工 作时间 (月)
1	黄忠凯	1988.09	男	博士后	博士	长江师范学院	023-72790088	411202198809043070	项目负责人	12
总人数				高级	中级	初级		博士后	博士生	硕士生
1								1		



## 国家自然科学基金项目直接费用预算表（定额补助）

项目批准号：11947205

项目负责人：黄忠凯

金额单位：万元

序号	科目名称	金额
1	项目直接费用合计	18.0000
2	1、设备费	9.0000
3	(1)设备购置费	8.0000
4	(2)设备试制费	1.0000
5	(3)设备升级改造与租赁费	0.0000
6	2、材料费	0.0000
7	3、测试化验加工费	2.0000
8	4、燃料动力费	0.0000
9	5、差旅/会议/国际合作与交流费	1.8000
10	6、出版/文献/信息传播/知识产权事务费	2.0000
11	7、劳务费	1.2000
12	8、专家咨询费	2.0000
13	9、其他支出	0.00



## 预算说明书（定额补助）

（请按照《国家自然科学基金项目预算表编制说明》等的有关要求，对各项支出的主要用途和测算理由，以及合作研究外援资金、单价 $\geq 10$ 万元的设备费等内容进行必要说明。）

### 设备费：

本项目主要通过multi-D2变分动力学方法和并行数值计算开展研究，依托单位已有昆泰塔式服务器及个人PC设备，但不能满足研究需求，需要购买小型服务器设备2台，目前4通路小型服务器设备的市场价格约为4万元/台；并且需要对计算软件进行升级和维护，约需要1万元；合计约为9万元。

### 测试化验加工费：

根据多量子比特情况下的计算任务，需要进行一些必要的并行计算，租赁超算中心计算机并行50核机时费2万元。

### 差旅/会议/国际合作与交流费：

项目组成员预计前往北京、上海、杭州等地进行学术交流等研究活动。每次出差时间约4天，平均每人每天住宿费0.032万元，伙食及交通补助0.018万元计算，往返交通费每人每次按0.1万元计算，项目执行期内预计出差4人次，差旅费总计为1.2万元。

### 出版/文献/信息传播/知识产权事务费：

预计发表论文2篇，平均每篇1万元，共2万元。

### 劳务费：

课题组拟聘用科研助理1人，负责资料整理、财务、科研画图、校稿等相关事务，项目期间工作约10月，每月发放劳务费0.1元，计1.2万元。

### 专家咨询费：

计划请量子开放系统领域的知名专家对研究思路、方法、技术进行访谈或者通讯咨询。每人每次按0.2万元计算，预计10人次，约计2万元。

项目负责人签字：

科研部门公章：

财务部门公章：



## 报告正文

研究内容和研究目标按照申请书执行。





## 国家自然科学基金资助项目签批审核表

<p>我接受国家自然科学基金的资助，将按照申请书、项目批准意见和计划书负责实施本项目（批准号：11947205），严格遵守国家自然科学基金委员会关于资助项目管理、财务等各项规定，切实保证研究工作时间，认真开展研究工作，按时报送有关材料，及时报告重大情况变动，对资助项目发表的论著和取得的研究成果按规定进行标注。</p> <p>项目负责人（签章）： 年 月 日</p>		<p>我单位同意承担上述国家自然科学基金项目，将保证项目负责人及其研究队伍的稳定和研究项目实施所需的条件，严格遵守国家自然科学基金委员会有关资助项目管理、财务等各项规定，并督促实施。</p> <p>依托单位（公章） 年 月 日</p>					
本栏目由基金委填写	<p>科学处审查意见：</p>						
	<p>建议年度拨款计划（本栏目为自动生成，单位：万元）：</p>						
	年度	总额	第一年	第二年	第三年	第四年	第五年
	金额						
本栏目主要用于重大项目等	<p>科学部审查意见：</p> <p>负责人（签章）： 年 月 日</p>						
	<p>相关局室审核意见：</p> <p>负责人（签章）： 年 月 日</p>						
	<p>委领导审批意见：</p> <p>委领导（签章）： 年 月 日</p>						



# 中国博士后科学基金资助证书

Certificate of China Postdoctoral Science Foundation Grant

西南大学

博士后研究人员

黄忠凯

(全国博管办编号为 228742 )，获得第 66 批中国博士后科学基金面上资助 二 等资助，资助编号为 2019M663877XB。

特颁此证。



与原件相符

中国博士后科学基金会

2019 年 11 月 15 日

证书查验请登录中国博士后科学基金会网站





## 第66批面上资助“西部地区博士后人才资助计划”拟资助人员名单

序号	省份	设站单位名称	姓名	博士后编号	一级学科	资助等级	资助金额
1	内蒙古	包商银行	马宝林	223352	应用经济学	2等	50000
2	内蒙古	内蒙古大学	谢鹏	218933	化学	2等	80000
3	内蒙古	内蒙古工业大学	陈歌	231045	力学	2等	80000
4	广西	广西博世科环保科技股份有限公司	刘杨	215947	环境科学与工程	2等	80000
5	广西	广西大学	刘艳艳	220379	生物学	2等	80000
6	广西	广西贺州市桂东电子科技有限公司	潘斯宁	229684	材料科学与工程	2等	80000
7	广西	广西交通投资集团有限公司	闫强	220513	交通运输工程	2等	80000
8	广西	广西师范大学	蒙显鹏	229833	中国语言文学	2等	50000
9	广西	广西新发展交通集团有限公司	邵羽	221403	土木工程	2等	80000
10	广西	广西医科大学	牛志杰	223364	临床医学	2等	80000
11	广西	广西医科大学	钟鉴宏	226967	临床医学	2等	80000
12	重庆市	西南大学	黄忠凯	228742	物理学	2等	80000
13	重庆市	西南大学	丁智	229854	地理学	2等	80000
14	重庆市	西南大学	梅秀鹏	222892	作物学	2等	80000
15	重庆市	西南大学	刘华伟	209838	畜牧学	2等	80000
16	重庆市	西南大学	唐宜轩	231944	药理学	2等	80000
17	重庆市	西南大学	刘颖	231217	心理学	2等	50000
18	重庆市	西南大学	汤斯惟	236710	艺术学	2等	50000
19	重庆市	西南大学	孙吟霖	234117	农林经济管理	2等	50000
20	重庆市	西南政法大学	廖呈钱	224212	法学	2等	50000
21	重庆市	西南政法大学	王琦	205993	工商管理	2等	50000
22	重庆市	招商局重庆交通科研设计院	吴庆良	225819	土木工程	2等	80000
23	重庆市	重庆长安汽车股份有限公司	李捷	230026	动力工程及工程热物理	2等	80000
24	重庆市	重庆交通大学	崔晓璐	228752	机械工程	2等	80000
25	重庆市	重庆交通大学	邱珍锋	228512	水利工程	2等	80000
26	重庆市	重庆医科大学	钟毅欣	239303	临床医学	2等	80000
27	重庆市	重庆医科大学	杜燕娥	222267	临床医学	2等	80000
28	重庆市	重庆医科大学附属口腔医院	高翔	231215	口腔医学	2等	80000
29	四川省	成都中医药大学	王绪	239289	生物医学工程	2等	80000
30	四川省	四川省社会科学院	范水兰	232273	法学	2等	50000
31	四川省	四川师范大学	张力波	223334	哲学	2等	50000
32	四川省	西南交通大学	段青松	226507	力学	2等	80000
33	四川省	西南交通大学	张蒙祺	235892	机械工程	2等	80000
34	四川省	西南交通大学	易彩	239523	机械工程	2等	80000
35	四川省	西南交通大学	全欣	228289	信息与通信工程	2等	80000
36	四川省	西南交通大学	姚超凡	228760	土木工程	2等	80000
37	四川省	西南科技大学	袁文	225043	药理学	2等	80000
38	四川省	中国地质调查局成都地质调查中心	侯乾	219171	地质学	2等	80000
39	四川省	中国工程物理研究院	万舜	238279	材料科学与工程	2等	80000
40	四川省	中航工业成都飞机工业(集团)有限责任公司	罗维	227007	纺织科学与工程	2等	80000
41	贵州省	贵州大学	尹存宏	236818	材料科学与工程	2等	80000
42	贵州省	贵州大学	刘海	238673	计算机科学与技术	2等	80000
43	贵州省	贵州省社会科学院	朱静洁	234705	法学	2等	50000
44	贵州省	贵州省社会科学院	潘文富	240284	工商管理	2等	50000
45	云南省	昆明理工大学	黄太红	210699	材料科学与工程	2等	80000
46	云南省	昆明理工大学	王飞	240348	环境科学与工程	2等	80000
47	云南省	云南师范大学	Anna-Marie Klumt	207354	地理学	2等	80000
48	西藏	西藏天路股份有限公司	张泽宇	236880	机械工程	2等	80000
49	陕西省	长安大学	陈鹏	239632	信息与通信工程	2等	80000
50	陕西省	长安大学	刘喜	231023	土木工程	2等	80000
51	陕西省	长安大学	秦朝刚	232589	土木工程	2等	80000
52	陕西省	长安大学	史文海	240682	水利工程	2等	80000
53	陕西省	长安大学	黄何鑫	239608	地质资源与地质工程	2等	80000
54	陕西省	陕西科技大学	杨将	237014	数学	2等	80000
55	陕西省	陕西科技大学	张跃宏	239540	林业工程	2等	80000
56	陕西省	陕西科技大学	李菡	211956	中药学	2等	80000
57	陕西省	陕西师范大学	邓晨晖	221375	地理学	2等	80000
58	陕西省	陕西师范大学	刘焕才	235302	地理学	2等	80000
59	陕西省	陕西师范大学	王政革	211676	心理学	2等	50000
60	陕西省	西安电子科技大学	陈改革	229883	机械工程	2等	80000
61	陕西省	西安电子科技大学	唐宁	236064	仪器科学与技术	2等	80000



62	陕西省	西安电子科技大学	赵天龙	231470	材料科学与工程	2等	80000
63	陕西省	西安电子科技大学	杨 谦	217175	电子科学与技术	2等	80000
64	陕西省	西安电子科技大学	苏浩楠	225338	电子科学与技术	2等	80000
65	陕西省	西安电子科技大学	卢 阳	219195	电子科学与技术	2等	80000
66	陕西省	西安电子科技大学	张明阳	211021	控制科学与工程	2等	80000
67	陕西省	西安建筑科技大学	邢相栋	229073	冶金工程	2等	80000
68	陕西省	西安建筑科技大学	蒋维乐	205935	建筑学	2等	80000
69	陕西省	西安建筑科技大学	乔汝佳	236181	土木工程	2等	80000
70	陕西省	西安建筑科技大学	梁添寿	238769	土木工程	2等	80000
71	陕西省	西安科技大学	黄荣宾	220380	矿业工程	2等	80000
72	陕西省	西安科技大学	双海清	219745	矿业工程	2等	80000
73	陕西省	西安理工大学	彭 磊	223295	环境科学与工程	2等	80000
74	陕西省	西安理工大学	翟兆阳	230440	机械工程	2等	80000
75	陕西省	西安理工大学	张燕飞	239709	机械工程	2等	80000
76	陕西省	西安理工大学	陈 丹	233539	材料科学与工程	2等	80000
77	陕西省	西安理工大学	张 月	208426	电子科学与技术	2等	80000
78	陕西省	西安理工大学	薛海斌	225671	土木工程	2等	80000
79	陕西省	西安理工大学	石涵予	238656	应用经济学	2等	50000
80	陕西省	西北大学	李嘉辰	237999	化学	2等	80000
81	陕西省	西北大学	张 雳	228678	化学	2等	80000
82	陕西省	西北大学	刘玉霞	223162	生物学	2等	80000
83	陕西省	西北大学	李 珂	215968	电子科学与技术	2等	80000
84	陕西省	西北大学	车俊岭	206491	电子科学与技术	2等	80000
85	陕西省	西北大学	李小亚	240481	信息与通信工程	2等	80000
86	陕西省	西北大学	申世红	230663	化学工程与技术	2等	80000
87	陕西省	西北大学	柯尊斌	239837	中国语言文学	2等	50000
88	陕西省	西北大学	冯 颖	216845	工商管理	2等	50000
89	陕西省	西北政法大学	刘学文	239714	法学	2等	50000
90	陕西省	西北政法大学	李 锐	232061	法学	2等	50000
91	甘肃省	兰州交通大学	李 伟	224677	测绘科学与技术	2等	80000
92	甘肃省	兰州交通大学	何 毅	225583	测绘科学与技术	2等	80000
93	甘肃省	西北永新涂料有限公司	张安杰	227289	化学	2等	80000
94	青海省	青海省地质调查院	任海东	214783	地质学	2等	80000
95	宁夏	宁夏大学	曹兴华	230031	民族学	2等	50000
96	新疆	乌鲁木齐正大畜牧有限公司	赵玉强	238668	畜牧学	2等	80000
97	新疆	新疆维吾尔自治区人民医院	李奇凤	215417	基础医学	2等	80000
98	新疆	新疆医科大学	丁 路	227662	临床医学	2等	80000
99	新疆	新疆医科大学	李 榕	215160	临床医学	2等	80000
100	新疆	新疆油田公司	杨智峰	229203	地质资源与地质工程	2等	80000

立项编号： cstc2020jcyj-msxmX0003

重庆市自然科学基金面上项目任务书

项目名称	电路 QED 量子模拟器中受外场调控的 Holstein 模型的极化子动力学的研究
承担单位	长江师范学院
项目负责人	黄忠凯
通讯地址	重庆市涪陵区聚贤大道 16 号
联系电话	15292291686
起止年限	2020-07-01 至 2023-06-30

重庆市科学技术局  
二〇二〇年六月制



与原件相符

## 填写说明

- 1、本任务书由重庆市科委、项目承担单位共同签订，甲方为重庆市科委，乙方为项目承担单位。
- 2、本任务书是项目经费拨付和结题的依据。任务书的内容根据《基础研究与前沿探索项目（重庆市自然科学基金）项目申报书》自动生成。
- 3、立项编号由项目管理系统统一分配。

## 一、考核指标

### (一) 考核指标概述

- 1) 设计用于模拟标准 Holstein 模型的 QED 量子模拟装置, 研究基于标准 Holstein 模型的 QED 装置的量子比特的动态特性, 揭示热库对其相干态的耗散作用, 为设计具有长时相干态的 QED 装置提供有效的理论依据;
- 2) 分析复杂外场下的基于 Holstein 模型的 QED 装置的量子态的动态特性, 通过外场变化对相应装置中的量子比特进行操控, 为外场控制的量子逻辑门操作的实验探索提供理论上的支撑;
- 3) 使用以 multi-D2 波函数为试探波函数的含时变分法处理模拟器中量子态的含时演化, 通过映射得出相应参数下的极化子动力学, 分析基于标准 Holstein 模型和受到外场调控的 Holstein 模型在多参数空间的极化子运动规律;
- 4) 发表 3 篇以上高水平论文, 培养多名学生参与研究。

### (二) 考核指标及验收依据

时间阶段	工作内容	拟解决的关键问题	考核指标
2021 年 1 月-2021 年 12 月	设计用于模拟标准 Holstein 模型的 QED 量子模拟器, 用含时变分法计算模拟器哈密顿量中量子态的动力学, 通过映射得到 Holstein 模型中极化子的动力学	模拟器中微波谐振器对量子比特的影响以及被模拟的 Holstein 模型中声子对电荷载流子运动的作用	形成研究成果发表期刊论文。参加学术会议一次, 并开展学术交流和两次。
2022 年 1 月-2022 年 12 月	结合上一年研究基础, 设计基于复杂外场调控下的 Holstein 模型的 QED 装置, 构造相应的哈密顿量, 用含时变分法计算得到受外场操控的极化子的动力学	在模拟器平台上, 被模拟的 Holstein 模型中外场对电荷载流子运动的作用	形成研究成果发表期刊论文。参加学术会议一次, 并开展学术交流两次
2023 年 1 月-2023 年 12 月	结合前两年研究基础, 通过改变外场类型对 Holstein 量子比特的状态进行调制	多参数区间的极化子动力学, 特别是过渡区间的长时间动力学演化	形成研究成果并发表期刊论文。参加学术会议两次, 开展学术交流, 介绍项目研究进展并推广研究成果。



二、项目组成员

姓名	证件号码	性别	学历	职称	专业	工作单位	联系电话	项目中的分工	每年工作时间(月)	签字
黄忠凯 (负责人)	411202198809043070	男	博士研究生	中级	材料科学与工程	长江师范学院	15292291686	项目思路、理论推导、计算、论文撰写、交流推广	10	
李佶彪	620102197906187218	男	博士研究生	中级	材料科学与工程	长江师范学院	17783324571	项目研讨、理论计算、论文撰写	3	

### 三、项目经费

甲方为乙方提供本项目研究经费0万元，在签约后一次拨付；乙方自筹或匹配经费不少于10.0万元。

#### 四、相关责任

1、甲方在项目执行过程中不得无故撤销或终止项目。

2、乙方及专项牵头单位在项目实施过程中应建立相应的规章制度，加强安全管理，确保人员及设备安全，对科研安全负全部责任。项目执行过程中应严格遵守重庆市科技局科技计划项目管理的各项规定并承担相应权责，按约定保证项目实施所需的人力、物力、财力，督促项目负责人和本单位项目管理部门按重庆市科技局的规定及时报送有关报表和材料并按期结题。

3、乙方及专项牵头单位要严格按照《关于进一步完善我市财政科研项目资金管理等政策的实施意见》（渝委办发〔2017〕31号）的要求，对项目资金单独设帐，严格按照预算专款专用，严禁挤占挪用项目经费、超预算范围开支的行为，严禁违反规定自行调整项目经费预算，严禁编制虚假预算套取项目经费，严禁项目结题后不及时进行财务结算、长期挂账报销费用，严禁提供虚假配套承诺或不及时足额提供配套资金。乙方及专项牵头单位在项目执行过程中，必须接受甲方对经费使用及项目进度的监督和检查，并按甲方要求及时提供年度计划执行情况报告，逾期不报，甲方有权暂停资助。

4、乙方在项目执行过程中，项目任务书中签订内容、人员和完成时间原则上不作变更；如因某种原因需对计划任务书内容作调整，应向市科技局提交书面申请，并经市科技局批准后签订修改（补充）任务书。专项牵头单位在项目执行过程中，依据签订的协议内容，对乙方实行监管，项目实施情况需及时向甲方报告。

5、乙方及专项牵头单位在项目执行过程中，如遇重大变化（如：与任务书研究内容有出入、技术措施或某些条件不落实等）致使计划无法执行，应主动及时要求中止任务或延长结题时间。对要求中止任务的，应视不同情况，部分或全部退还所拨经费；对要求延期结题的，延期结题时间不能超过一年，超出一年后结题的，视为总结结题，按照《重庆市科研项目管理办法》中规定，终止负责人三年项目申报资格。如乙方及专项牵头单位没有提出中止任务的要求，甲方根据调查情况有权提出终止任务的处理意见，有权延期或停止资助，甚至收回项目全部经费，并减少乙方申报数量；情节严重的，取消申报资格，直至追究法律责任。

6、乙方应在本计划任务书规定的完成时间前2个月向甲方提出结题申请，并根据甲方要求完成项目结题验收有关事宜。约束性指标未全部完成或选择性指标完成率未达85%的项目不能验收结题；结题验收未通过的，按《重庆市科研项目管理办法》中



有关规定追究乙方及专项牵头单位责任。结题验收通过后,该项目才能作为正式完成。

7、乙方及专项牵头单位应建立健全促进科研诚信、科技行为廉洁的规章制度,组织开展廉洁自律宣传教育,监督并认真查处本单位在科研过程中出现的违规违纪行为。乙方及专项牵头单位不得在有关人员职称、简历以及研究基础等方面提供虚假信息,不得在项目实施中抄袭、剽窃他人科研成果,不得捏造或篡改科研数据,不得在涉及人体的研究中违反知情同意、保护隐私等规定,不得违反实验动物保护规范等。


8、乙方及专项牵头单位不得向甲方工作人员行贿;不得报销应由甲方工作人员个人支付的任何费用;不得为甲方工作人员购置或提供通讯工具、交通工具、高档办公用品等贵重物品。乙方及专项牵头单位在项目立项和实施过程中贿赂甲方工作人员,或者为其报销应由个人支付的费用、购买贵重物品等,被纪检监察机关或司法机关查证属实的,甲方有权终止项目实施并追缴拨付的全部科研经费;若甲方工作人员主动向纪检监察机关上缴乙方及专项牵头单位提供的贿赂或者贵重物品,甲方同样有权终止项目实施并追缴拨付的全部科研经费。

9、乙方及专项牵头单位发现甲方工作人员在科技管理工作中有索贿、暗箱操作等违反廉政建设规定的行为,应及时向科技纪工委举报并积极协助查处工作。

其他约定:

责任约定签订的约定书、合同协议及签订的其他相关约定以附件形式上传

## 五、任务书签订各方

甲方：重庆市科技局代表： 基础研究处 处长  (签章)

项目管理人 陈恒 (签章)



月 日

乙方：项目第一承担单位负责人 蔡家林 (签章)

项目负责人 黄忠凯 (签章)

帐户名： 长江师范学院

帐号： 31620101040009181

开户银行： 中国农业银行重庆涪陵城区支行

(单位签章)

二〇 年 月 日

# 重庆市教育委员会科学技术研究项目

## 合 同 书

项目下达方（甲方）：重庆市教委

合 同 编 号：KJQN202201421

项目承担方（乙方）：长江师范学院

合同签订地点：重庆市教委

为保证重庆市教委科学技术研究项目的顺利实施和完成，依据《中华人民共和国民法典》，

经甲乙双方协商，订立如下合同：

### 一、项目基本情况

项目负责人：黄忠凯

项目名称：旋转石墨烯/六角氮化硼的电子结构

项目组成员：黄忠凯 薄茂林

合作单位：无

项目起止时间：从 2022-10-01 至 2025-09-30



与原件相符

## 二、项目主要研究内容

本项目应完成的主要研究内容如下：

在本项目中，我们将通过第一性原理研究石墨烯/六角氮化硼体系，探究由莫里条纹诱导的周期性电势对石墨烯层的影响。

需要特别提出的是，由于六角氮化硼和石墨烯的晶格常数存在晶格差  $\delta \approx 1.8\%$ ，六角氮化硼与石墨烯实际产生的莫里超晶格与双层石墨烯的略有不同，其形成的莫里超晶格的晶格常数可由下式描述：

$$\lambda = \frac{(1 + \delta)a}{\sqrt{2(1 + \delta)(1 - \cos(\phi)) + \delta^2}}$$

其中  $a$  为石墨烯的晶格常数， $\delta$  为石墨烯和六角氮化硼原胞的晶格差， $\phi$  为六角氮化硼相对于石墨烯的转角。在转角和失配同时存在时，石墨烯/六角氮化硼的系统尺寸会非常大（零转角时的原子数上万），超晶格内部会出现分布不均匀的内部应力，层间电荷的转移也是不均匀的，甚至在小转角时会出现次级狄拉克锥。本项目将通过研究不同转角的稳定结构和电子结构特征，深入理解其中的物理机制，为旋转石墨烯/六角氮化硼异质体系的应用提供理论基础。

本项目将包括以下两个层面的研究内容：

- 1) 筛选出旋转角和晶格失配共同存在时的稳定结构。首先是研究理想晶格失配和不同旋转角下存在的超晶格，其次是通过弛豫理想超胞，得到能量最小和受力最小的稳定结构。
- 2) 稳定结构下的电子结构。我们将讨论整体对称性破缺和莫里条纹中的局部堆积次序的共同作用。分析弱的层间范德瓦尔斯相互作用的影响，考虑六角氮化硼层对石墨烯的机械支撑作用之外对石墨烯电子结构的调制，分析层间电荷转移、电荷再分布和能带移动。

具体研究内容和研究目标按照申请书执行。



### 三、预期成果和考核指标

与申报书预期成果和考核指标一致

### 四、项目经费：

本项目经费总计4 万元，大写：人民币肆万元整，其中：

- 1 甲方资助经费 0 万元，大写：人民币零元整
- 2 乙方自筹经费 4 万元，大写：人民币肆万元整
- 3 其他经费 0 万元，大写：人民币零元整

### 五、甲方的权利和义务：

- 1、甲方在本合同签字生效后及时按合同规定核拨经费。
- 2、甲方有权依据《重庆市教委科学技术研究计划项目管理办法》，在项目执行过程中检查监督研究进展和经费开支情况，要求乙方按甲方规定及时提供项目进展报告、结题总结报告和经费决算报告等全套资料。
- 3、甲方有权要求乙方及时转化本项目研究成果。
- 4、若乙方违反本合同规定，造成本项目不能正常实施和完成时，甲方根据调查情况有权提出终止合同的处理意见，有权延期或停止资助，甚至收回项目全部经费。情节严重的，甲方有权取消项目负责人申报资格，直至追究法律责任。

### 六、乙方的权利和义务：

- 1、乙方有权按照本合同的规定获得甲方项目拨款。经费拨付后，乙方要严格按照国家、教育部有关规定以及合同约定，组织科研人员合理使用项目经费，加强对科研经费的管理，完善经费支出、报销审核监督制度。
- 2、乙方须依据本合同规定和《重庆市教委科学技术研究计划项目管理办法》，提供配套研究经费及相关条件，保证项目的顺利实施和按期完成。乙方应接受甲方的检查和监督，及时报送有关项目研究进展报告、结题总结报告和经费决算报告等全套资料。项目成果请标注“重庆市教委科学技术研究项目(KJ\*\*\*\*\*)资助”，英文“Supported by the Science and Technology Research Program of Chongqing Municipal Education Commission (Grant No. KJ\*\*\*\*\*)”。在项目完成后，按甲方要求进行结题验收。
- 3、乙方应鼓励项目负责人使用本项目成果以技术转让、技术入股和联合生产等方式实施有偿转化，成果转化收益分配比例按照国家、重庆市有关政策执行。
- 4、乙方在项目执行过程中，本合同签订的内容、考核指标、人员和完成时间原则上不作变更，如需对合同书内容进行调整，应向甲方提交书面申请，并经甲方批准后签订修改(补充)任务书。
- 5、乙方在项目执行过程中，如遇重大变化致使项目无法继续实施，应主动及时要求终止任务或延长结题时间。对要求终止任务的，视情况，部分或全部退还所拨经费；对要求延期结题的，延期结题时间不能超过一年，超出一年的，暂停项目负责人三年本项目申报资格。
- 6、乙方应建立健全科研诚信体系、科研行为廉洁的规章制度，监督并认真查处本单位在科研过程中出现的违规违纪行为。

### 七、项目技术保密：

凡属技术保密的项目和内容，甲乙双方均有义务执行国家有关保密规定。在需要公开发表研究内容和用于国际合作、交流时，必须先送市技术保密管理部门审查批准。

### 八、本合同自签字之日起生效。本合同由市教委科技处负责解释。

甲 方：市教委 单位公章（合同专用章）（签章）



日

乙 方：法人代表：\_\_\_\_\_（签章）

项目负责人：\_\_\_\_\_（签字）

账户名：\_\_\_\_\_

开户银行：\_\_\_\_\_

帐号：\_\_\_\_\_

已在线审核

单位(签章)

年 月 日

合作单位：法人代表：\_\_\_\_\_（签章）

负责人：\_\_\_\_\_（签字）

单位（签章）

年 月 日

# 重庆市教育委员会科学技术研究项目

## 合 同 书

项目下达方（甲方）：重庆市教委

合 同 编 号：KJQN202401422

项目承担方（乙方）：长江师范学院

合同签订地点：重庆市教委

为保证重庆市教委科学技术研究项目的顺利实施和完成，依据《中华人民共和国民法典》，

经甲乙双方协商，订立如下合同：

### 一、项目基本情况

项目负责人：黄忠凯

项目名称：受到非局域系统-环境耦合影响的布洛赫-齐纳振荡的研究

项目组成员：杨姿依

合作单位：无

项目起止时间：从 2024-10-01 至 2027-10-01

与原件相符





## 二、项目主要研究内容

本项目应完成的主要研究内容如下：

本项目将运用变分求解方法，研究受外加线性势场调控的双周期势场中的激发子模型在环境作用下的量子态演化行为，探究环境对布洛赫-齐纳振荡的耗效应。重点是研究包含非局域系统-环境耦合的系统-环境相互作用的影响。外加线性势场会在周期性体系中引起布洛赫振荡。双周期势场的基本单元，由两个能量不等的势阱组成。这种能量差异导致了显示的能带分裂现象，上下能带之间存在一个  $2\delta$  的带隙，为齐纳隧穿提供了条件。双周期势场对应的超晶格结构，最小周期单元的长度为  $2d$ 。相邻格点由于势场的不同而具有不同的能量结构，激发子可以通过耦合强度  $J$  在相邻格点之间转移。需要说明的是，如果相邻格点的势场相同，超晶格势场将退化为单周期势场，对应的能带结构中不存在带隙，也就无法发生齐纳隧穿现象。然而，外加线性势场仍然能够引起布洛赫振荡。

在实际情况下，任何量子系统都无法完全隔离环境的影响。对于布洛赫-齐纳振荡的实现装置而言，环境效应也是一个不可忽视的因素。实验中已经观察到，在冷原子光晶格中，原子的能级会受到环境的影响而发生改变，而波导阵列的性能也会受到环境的干扰。因此，本项目的重点将是研究系统与环境的局域耦合效应，以及非局域耦合对布洛赫-齐纳振荡的耗散影响。

本项目将包括以下两个层面的研究内容：

1) 构建并分析总哈密顿量，其中包括系统哈密顿量、环境哈密顿量和系统-环境耦合哈密顿量这三个部分。环境将通过二次量子化的谐振子模型来描述。系统-环境耦合哈密顿量包含局域耦合和非局域耦合两部分。基于所得到的哈密顿量，我们研究在若系统-环境耦合的情况下布洛赫-齐纳振荡的行为。

2) 探究不同系统-环境耦合类型与布洛赫-齐纳振荡构型的关系，揭示非局域耦合对布洛赫振荡演化的调控规律，为耦合调控的实现打下基础。

具体研究内容和研究目标按照申请书执行。



**三、预期成果和考核指标**

与申报书预期成果和考核指标一致

**四、项目经费：**

本项目经费总计4 万元，大写：人民币肆万元整，其中：

- 1 甲方资助经费 0 万元，大写：人民币零元整
- 2 乙方自筹经费 0 万元，大写：人民币零元整
- 3 其他经费 4 万元，大写：人民币肆万元整

**五、甲方的权利和义务：**

- 1、甲方在本合同签字生效后及时按合同规定核拨经费。
- 2、甲方有权依据《重庆市教委科学技术研究计划项目管理办法》，在项目执行过程中检查监督研究进展和经费开支情况，要求乙方按甲方规定及时提供项目进展报告、结题总结报告和经费决算报告等全套资料。
- 3、甲方有权要求乙方及时转化本项目研究成果。
- 4、若乙方违反本合同规定，造成本项目不能正常实施和完成时，甲方根据调查情况有权提出终止合同的处理意见，有权延期或停止资助，甚至收回项目全部经费。情节严重的，甲方有权取消项目负责人申报资格，直至追究法律责任。

**六、乙方的权利和义务：**

- 1、乙方有权按照本合同的规定获得甲方项目拨款。经费拨付后，乙方要严格按照国家、教育部有关规定以及合同约定，组织科研人员合理使用项目经费，加强对科研经费的管理，完善经费支出、报销审核监督制度。
- 2、乙方须依据本合同规定和《重庆市教委科学技术研究计划项目管理办法》，提供配套研究经费及相关条件，保证项目的顺利实施和按期完成。乙方应接受甲方的检查和监督，及时报送有关项目研究进展报告、结题总结报告和经费决算报告等全套资料。项目成果请标注“重庆市教委科学技术研究项目(KJ\*\*\*\*\*)资助”，英文“Supported by the Science and Technology Research Program of Chongqing Municipal Education Commission (Grant No. KJ\*\*\*\*\*)”。在项目完成后，按甲方要求进行结题验收。
- 3、乙方应鼓励项目负责人使用本项目成果以技术转让、技术入股和联合生产等方式实施有偿转化，成果转化收益分配比例按照国家、重庆市有关政策执行。
- 4、乙方在项目执行过程中，本合同签订的内容、考核指标、人员和完成时间原则上不作变更，如需对合同书内容进行调整，应向甲方提交书面申请，并经甲方批准后签订修改(补充)任务书。
- 5、乙方在项目执行过程中，如遇重大变化致使项目无法继续实施，应主动及时要求终止任务或延长结题时间。对要求终止任务的，视情况，部分或全部退还所拨经费；对要求延期结题的，延期结题时间不能超过一年，超出一年的，暂停项目负责人三年本项目申报资格。
- 6、乙方应建立健全科研诚信体系、科研行为廉洁的规章制度，监督并认真查处本单位在科研过程中出现的违规违纪行为。

**七、项目技术保密：**

凡属技术保密的项目和内容，甲乙双方均有义务执行国家有关保密规定。在需要公开发表研究内容和用于国际合作、交流时，必须先送市技术保密管理部门审查批准。

**八、本合同自签字之日起生效。本合同由市教委科技处负责解释。**

甲 方：市教委 单位公章（合同专用章签章）



日

乙 方：法人代表：\_\_\_\_\_（签章）

项目负责人：\_\_\_\_\_（签字）

账户名：\_\_\_\_\_

开户银行：\_\_\_\_\_

帐号：\_\_\_\_\_

已在线审核

单位(签章)

年 月 日

合作单位：法人代表：\_\_\_\_\_（签章）

负责人：\_\_\_\_\_（签字）

单位（签章）

年 月 日





与原件相符

根据《关于印发重庆市博士后创新人才支持计划的通知》(渝人社发〔2017〕65号)、《重庆市人力资源和社会保障局办公室<关于开展2019年重庆市“博士后创新人才支持计划”等项目申报工作的通知>》(渝人社办〔2019〕213号)和《重庆市人力资源和社会保障局办公室<关于开展2019年设站单位招收海外全职博士后科研资助等项目申报工作的通知>》(渝人社办〔2019〕213号)要求,经组织专家评选,拟资助博士后创新导师工作室等5个项目157人,现予以公示,接受社会监督。

公示时间:2019年11月15日至11月21日

来信地址:重庆市人力资源和社会保障局1号楼5楼1512室(渝北区春华大道99号)

邮政编码:401120

联系电话:袁杰,88152120,86868884(传真)

博士后创新导师工作室拟设立名单			
(按姓氏笔画排序)			
序号	姓 名	单 位	
1	卞修武	陆军军医大学	
2	王智彪	重庆医科大学	
3	叶丽林	陆军军医大学	
4	付子堂	西南政法大学	
5	李晓辉	陆军军医大学	
6	张贤明	重庆工商大学	
7	周建庭	重庆交通大学	
8	夏庆友	西南大学	
9	谢 鹏	重庆医科大学	
10	潘 洵	西南大学	
博士后研究项目特别资助拟资助人员名单			
(同一类别按姓氏笔画排序)			
序号	姓 名	单 位	资助类别
1	王国华	陆军军医大学	一等
2	邱珍锋	重庆交通大学	一等
3	邹 卓	西南大学	一等
4	张曦木	重庆医科大学	一等
5	赵 谦	西南政法大学	一等
6	于建强	重庆大学	二等
7	王 民	招商局重庆交通科研设计院有限公司	二等
8	牛俊天	重庆大学	二等
9	左钱飞	陆军军医大学	二等

10	刘海潮	西南政法大学	二等
11	杨 嫻	西南政法大学	二等
12	张 宇	重庆大学	二等
13	陈里里	重庆市勘测院	二等
14	林 黎	重庆工商大学	二等
15	周 莹	西南大学	二等
16	周成芳	陆军军医大学	二等
17	周艳涛	西南大学	二等
18	胡翠美	陆军军医大学	二等
19	高 翔	重庆医科大学	二等
20	唐宜轩	西南大学	二等
21	黄忠凯	长江师范学院	二等
22	董兴有	市人民医院	二等
23	谢贝贝	重庆大学	二等
24	廖 希	重庆金美通信有限责任公司	二等
25	薛艳华	重庆大学	二等
26	王 英	重庆两江药物研发中心有限公司	三等
27	王艳磊	市地质矿产勘查开发局	三等
28	王晓松	陆军军医大学	三等
29	尹 俊	中国电子科技集团公司第二十四研究所	三等
30	邓 睿	西南政法大学	三等
31	刘宪庆	重庆交通大学	三等
32	汤斯惟	西南大学	三等
33	许 杰	重庆医科大学	三等
34	孙江洲	西南大学	三等
35	孙晗霖	西南大学	三等
36	李 刚	陆军军医大学	三等
37	李 敏	中国兵器工业第五九研究所	三等
38	李成海	重庆医科大学	三等
39	李俊杰	重庆医科大学	三等
40	李 准	重庆机场集团	三等
41	李海玉	市公共卫生医疗救治中心	三等
42	肖作林	市气象局	三等
43	吴庆庆	重庆医科大学	三等
44	何素婷	西南大学	三等
45	余大亮	重庆三峡学院	三等
46	张小梅	陆军军医大学	三等
47	张林	西南大学	三等
48	张瑞杰	重庆交通大学	三等
49	陈大鹏	西南政法大学	三等
50	陈永利	重庆山外山血液净化技术股份有限公司	三等
51	陈兆玮	林同棧国际工程咨询(中国)有限公司	三等
52	罗士琰	西南大学	三等
53	罗 钢	西南政法大学	三等
54	周 磊	市社科院	三等
55	郑绪昌	重庆大学	三等
56	孟子群	西南政法大学	三等
57	赵方莹	西南大学	三等
58	战东升	西南政法大学	三等
59	钟守琴	西南大学	三等
60	姜灿中	西南大学	三等



61	聂绪强	陆军军医大学	三等
62	徐玉梭	市科学技术研究院	三等
63	郭文涛	西南政法大学	三等
64	涂义亮	招商局重庆交通科研设计院有限公司	三等
65	崔洪涛	市中医院	三等
66	崔晓璐	市轨道交通（集团）有限公司	三等
67	彭 烨	重庆工商大学科技开发总公司	三等
68	韩佳丽	西南政法大学	三等
69	程 呈	重庆大学	三等
70	廖呈钱	西南政法大学	三等
71	翟二猛	西南大学	三等
72	熊 锋	重庆山外山血液净化技术股份有限公司	三等

## 全职博士后出站留（来）渝拟资助人员名单

(按姓氏笔画排序)

序号	姓名	单位	
1	于 洋	重庆交通大学	
2	万 宇	重庆交通大学	
3	马先睿	西南大学	
4	王义涛	重庆医科大学	
5	王 训	西南大学	
6	王成祥	重庆师范大学	
7	王 岩	重庆医科大学	
8	王海军	西南大学	
9	方小梅	西南大学	
10	田 荣	中国科学院重庆绿色智能研究院	
11	史 君	西南大学	
12	付 平	重庆师范大学	
13	白文钦	市农业科学院	
14	刘太行	重庆医科大学	
15	刘非拉	重庆理工大学	
16	刘 炜	重庆科技学院	
17	李千音	重庆医科大学	
18	李星怡	重庆大学	
19	李修磊	重庆交通大学	
20	杨 玲	西南政法大学	
21	杨 柳	长江师范学院	
22	连成杰	重庆医科大学	
23	吴庆跃	重庆银行	
24	何将福	重庆大学	
25	余 璐	西南大学	
26	沈关望	西南大学	
27	宋一弘	重庆渝富资产经营管理集团有限公司	
28	宋一清	西南大学	
29	张玉龙	重庆师范大学	
30	张 青	西南大学	
31	张铭凯	西南大学	
32	陈红生	重庆大学	
33	陈志伟	重庆医科大学	
34	陈 林	重庆师范大学	
35	陈 廉	西南政法大学	

36	陈静影	中国科学院重庆绿色智能研究院	
37	范家铭	重庆医科大学	
38	范 辉	重庆医科大学	
39	周 杨	重庆医科大学	
40	赵 敏	重庆医科大学	
41	胡二峰	重庆大学	
42	钟邦超	重庆师范大学	
43	贾 凌	西南大学	
44	晏清皓	西南大学	
45	晏 慧	重庆科技学院	
46	徐 晨	西南政法大学	
47	翁凌飞	重庆大学	
48	谈 娟	西南大学	
49	常 鹏	西南大学	
50	曾伟南	市人民医院	
51	谢云霞	重庆工商大学	
52	解巧利	重庆大学	
53	谭建桃	重庆师范大学	
54	谭 端	西南大学	
55	魏丽娟	西南大学	
56	魏 杰	西南大学	
中国(重庆)新加坡博士后国际培养交流计划拟资助人员名单			

## (按姓氏笔画排序)

序号	姓名	单位	
1	刘晓英	工商大学	
2	刘培基	重庆大学	
3	李泓涟	重庆大学	
4	吴风艳	重庆大学	
5	张 瀚	重庆大学	
6	赵 勇	重庆大学	

## 博士后国际学术交流计划拟资助人员名单

## (按姓氏笔画排序)

序号	姓名	单位	
1	MORVE ROSHAN KHALIL	西南大学	
2	丁勇杰	交通大学	
3	代祥光	三峡学院	
4	毕 闯	长安集团	
5	刘俊利	陆军军医大学	
6	李 杨	西南政法大学	
7	李冠楠	西南大学	
8	陈石磊	陆军军医大学	
9	邵 峰	西南大学	
10	唐万燕	重庆市肿瘤研究所	
11	曾伟南	市人民医院	
12	翟二猛	西南大学	

项目汇总表

报表条件:

起始日期:2020年01月

截止日期:2022年01月

项目信息: (0108)人事处/(010830015)耗散布洛赫-齐纳振荡的非平衡态动力学

科目编号	科目名称	年初余额	借方发生	贷方发生	当前余额
30010101	事业基金	0.00	0.00	0.00	-99,339.41
900204	专项、科研分配	0.00	0.00	100,000.00	100,000.00
7201010102-3021807	项目支出-教学材料	0.00	19,044.00	0.00	0.00
7201010102-3022601	项目支出-单位	0.00	4,000.00	0.00	0.00
7201010102-3023904	项目支出-过路过桥费	0.00	255.30	0.00	0.00
7201020102-3020701	项目支出-邮寄费	0.00	210.00	0.00	0.00
7201020102-3020702	项目支出-电话费	0.00	499.00	0.00	0.00
7201020102-3021802	项目支出-实验耗材	0.00	71,591.11	0.00	0.00
7201020102-3022601	项目支出-单位	0.00	572.00	0.00	0.00
7201020102-3023902	项目支出-燃料费	0.00	3,168.00	0.00	0.00
项目期末余额		0.00	0.00	0.00	660.59

打印日期:2022/1/10



Handwritten signature in black ink.

与原件相符



# 科技检索报告

项目名称：黄忠凯发表的论文在《SCI》数据库的收录情况

委托人：长江师范学院

委托日期：2025 年 11 月 12 日

查新机构（盖章）：教育部科技查新工作站 (L02)

重庆大学科技查新站

完成日期：2025 年 11 月 12 日



教育部科技发展中心

二〇一三年制

与原件相符



项目名称	黄忠凯发表的论文在《SCI》数据库收录情况					
查新机构	名称	教育部科技查新工作站(L02) 重庆大学科技查新站				
	通信地址	重庆大学			邮政编码	400044
	负责人	黄娟	电话	023-65106364	传真	023-65105224
	联系人	黄晓玲	电话	023-65106364		
	电子信箱	973184324@qq.com				
<b>一、检索要求：</b> 署名长江师范学院黄忠凯发表的论文在《SCI》中的收录情况						
<b>二、文献检索范围</b> 《SCI-Expanded》 Science Citation Index Expanded                      2017 年～2025 年						
<b>三、检索结果：</b> 根据用户委托，针对检索要求，通过数据库，对黄忠凯发表的论文在《SCI》数据库中的收录引用情况进行检索，结论如下： 黄忠凯发表的论文被《SCI》数据库收录 10 篇，10 篇为第一作者。 论文的详细信息见附件。						
教育部科技查新工作站(L02) 重庆大学科技查新站 2025 年 11 月 12 日						

## 一、所发论文期刊中科院升级版分区如下

序号	题名	刊名	ISSN	Review	Open Access	年份
1	Single-Atom Cobalt-Doped 2D Graphene: Electronic Design for Multifunctional Applications in Environmental Remediation and Energy Storage	INORGANICS		否	是	2025
	类别	学科			分区	TOP 期刊
	大类分区	化学			3 区	否
	小类分区	CHEMISTRY, INORGANIC & NUCLEAR 无机化学与核化学			3 区	-
2	Single electron transistor based on twisted bilayer graphene quantum dots	JOURNAL OF PHYSICS D-APPLIED PHYSICS	0022-3727	否	否	2025
	类别	学科			分区	TOP 期刊
	大类分区	物理与天体物理			3 区	否
	小类分区	PHYSICS, APPLIED 物理：应用			3 区	-
3	Detecting Air Pollutant Molecules Using Tube-Shaped Single Electron Transistor	MOLECULES		否	是	2021
	类别	学科			分区	TOP 期刊
	大类分区	化学			3 区	否
	小类分区	BIOCHEMISTRY & MOLECULAR BIOLOGY 生化与分子生物学			3 区	-
		CHEMISTRY, MULTIDISCIPLINARY 化学：综合			3 区	-
4	Polaron dynamics of Bloch-Zener oscillations in an extended Holstein model	NEW JOURNAL OF PHYSICS	1367-2630	否	是	2021
	类别	学科			分区	TOP 期刊
	大类分区	物理与天体物理			2 区	否
	小类分区	PHYSICS, MULTIDISCIPLINARY 物理：综合			2 区	-
5	Dissipative dynamics in a tunable Rabi dimer with periodic harmonic driving	JOURNAL OF CHEMICAL PHYSICS	0021-9606	否	否	2019
	类别	学科			分区	TOP 期刊
	大类分区	化学			2 区	是

	小类分区	CHEMISTRY, PHYSICAL 物理化学			3 区	-
		PHYSICS, ATOMIC, MOLECULAR & CHEMICAL 物理：原子、分子和化学物理			3 区	-
6	Transient Dynamics of Super Bloch Oscillations of a 1D Holstein Polaron under the Influence of an External AC Electric Field	ANNALEN DER PHYSIK	0003-3804			2019（基础版）
	类别	学科			分区	TOP 期刊
	大类分区	物理			2 区	否
	小类分区	PHYSICS, MULTIDISCIPLINARY 物理：综合			2 区	-
7	Dynamics of dissipative Landau-Zener transitions	PHYSICAL REVIEW A	2469-9926			2018（基础版）
	类别	学科			分区	TOP 期刊
	大类分区	物理			2 区	是
	小类分区	OPTICS 光学			2 区	-
		PHYSICS, ATOMIC, MOLECULAR & CHEMICAL 物理：原子、分子和化学物理			3 区	-
8	Polaron dynamics with off-diagonal coupling: beyond the Ehrenfest approximation	PHYSICAL CHEMISTRY CHEMICAL PHYSICS	1463-9076			2017（基础版）
	类别	学科			分区	TOP 期刊
	大类分区	化学			2 区	是
	小类分区	CHEMISTRY, PHYSICAL 物理化学			3 区	-
		PHYSICS, ATOMIC, MOLECULAR & CHEMICAL 物理：原子、分子和化学物理			2 区	-
9	Effect of Off-Diagonal Exciton-Phonon Coupling on Intramolecular Singlet Fission	JOURNAL OF PHYSICAL CHEMISTRY LETTERS	1948-7185			2017（基础版）
	类别	学科			分区	TOP 期刊
	大类分区	化学			1 区	是
	小类分区	CHEMISTRY, PHYSICAL 物理化学			2 区	-
		MATERIALS SCIENCE, MULTIDISCIPLINARY 材料科学：综合			1 区	-



10		NANOSCIENCE & NANOTECHNOLOGY 纳米科技			2 区	-
		PHYSICS, ATOMIC, MOLECULAR & CHEMICAL 物理：原子、分子和化学物理			1 区	-
	Transient dynamics of a one-dimensional Holstein polaron under the influence of an external electric field	ANNALEN DER PHYSIK	0003-3804			2017（基础版）
	类别	学科			分区	TOP 期刊
	大类分区	物理			2 区	否
	小类分区	PHYSICS, MULTIDISCIPLINARY 物理：综合			2 区	-

## 二、SCI 检索结果

### 第 1 条，共 10 条

**文献标题:** Single-Atom Cobalt-Doped 2D Graphene: Electronic Design for Multifunctional Applications in Environmental Remediation and Energy Storage

**作者:** Huang, ZK (Huang, Zhongkai); Zhang, Y (Zhang, Yue); Li, CJ (Li, Chunjiang); Deng, L (Deng, Liang); Song, B (Song, Bo); Bo, ML (Bo, Maolin); Yao, C (Yao, Chuang); Lu, HL (Lu, Haolin); Long, GK (Long, Guankui)

**文献类型:** Article

**来源出版物:** INORGANICS **出版年:** SEP 24 2025 **卷:** 13 **期:** 10 **文献号:** 312 **DOI:** 10.3390/inorganics13100312

**Web of Science 核心库的“被引频次”:** 0

**被引频次合计:** 0

**引用的参考文献数:** 56

**摘要:** Through atomic-scale characterization of a single cobalt atom anchored in a pyridinic N3 vacancy of graphene (Co-N3-gra), this study computationally explores three interconnected functionalities mediated by cobalt's electronic configuration. Quantum-confined molecular prototypes extend prior bulk models, achieving a competitive catalytic activity for CO oxidation via Langmuir-Hinshelwood pathways with a 0.85 eV barrier. These molecular prototypes' discrete energy states facilitate single-electron transistor operation, enabling sensitive detection of NO, NO2, SO2, and CO2 through adsorption-induced conductance modulation. When applied to lithium-sulfur batteries using periodic Co-N3-gra, cobalt sites enhance polysulfide conversion kinetics and suppress the shuttle effect, with the Li2S2 → Li2S step identified as the rate-limiting process. Density functional simulations provide atomic-scale physicochemical characterization of Co-N3-gra, revealing how defect engineering in 2D materials modulates electronic structures for multifunctional applications.

**入藏号:** WOS:001601627600001

**语言:** English

**作者关键词:** 2D material defects; electronic structure engineering; environmental gas sensors; lithium-sulfur batteries; structure-property relationships

**KeyWords Plus:** CATALYTIC-OXIDATION; OXIDE CLUSTERS; CO; BATTERIES; HYDROFORMYLATION; MECHANISM; OPPORTUNITIES; TEMPERATURE; ADSORPTION; CARBONYL

**作者地址:** [Huang, Zhongkai; Zhang, Yue; Li, Chunjiang; Deng, Liang; Song, Bo; Bo, Maolin; Yao, Chuang] Yangtze Normal Univ, Key Lab Extraordinary Bond Engr & Adv Mat Technol, Chongqing 408100, Peoples R China

[Lu, Haolin; Long, Guankui] Nankai Univ, Natl Inst Adv Mat, Renewable Energy Convers & Storage Ctr, Sch Mat Sci & Engr, Tianjin 300350, Peoples R China

**通讯作者地址:** [Huang, Zhongkai] (corresponding author), Yangtze Normal Univ, Key Lab Extraordinary Bond Engr & Adv Mat Technol, Chongqing 408100, Peoples R China

[Long, Guankui] (corresponding author), Nankai Univ, Natl Inst Adv Mat, Renewable Energy Convers & Storage Ctr, Sch Mat Sci & Engr, Tianjin 300350, Peoples R China



电子邮件地址:  
zhongkaihuang@yznu.edu.cn;yuezhang0922@163.com;lichunjiang2004@163.com;dengliangacademic@163.com;songboacademic@163.com;bmlwd@yznu.edu.cn;yaochuang@yznu.cn;1713638@mail.nankai.edu.cn;longgk09@nankai.edu.cn  
Affiliation: ["Yangtze Normal University","Nankai University"]  
作者识别号:

作者	Web of Science ResearcherID	ORCID 号
Yao, Chuang	HPG-8802-2023	
huang, zhongkai	JSK-6419-2023	
Bo, Maolin	LUW-7890-2024	
Lu, Haolin	JAN-4479-2023	
Long, Guankui	JXL-2865-2024	

出版商: MDPI  
出版商地址: MDPI AG, Grosspeteranlage 5, CH-4052 BASEL, SWITZERLAND  
Web of Science Index: Science Citation Index Expanded (SCI-EXPANDED)  
Web of Science 类别: Chemistry, Inorganic & Nuclear  
研究方向: Chemistry  
IDS 号: 9AJ2V  
eISSN: 2304-6740  
ISO 来源出版物缩写: INORGANICS  
来源出版物页码计数: 19  
基金资助机构和授权号

基金资助机构	授权号
Fuling District guiding scientific research project	['FLKJ.2024BAG5130']
Science and Technology Research project of Chongqing Education Commission	['KJQN202201421', 'KJQN202401422']

基金资助正文: This research was funded by the Science and Technology Research project of Chongqing Education Commission under No. KJQN202201421 and KJQN202401422, and the Fuling District guiding scientific research project under No. FLKJ.2024BAG5130.  
ESI 高被引论文: N  
ESI 热点论文: N  
输出日期: 2025 年 11 月 12 日

第 2 条, 共 10 条

文献标题: Single electron transistor based on twisted bilayer graphene quantum dots  
作者: Huang, ZK (Huang, Zhongkai);He, YP (He, Yuping);Cao, J (Cao, Jing);Li, QQ (Li, Qianqian);Li, C (Li, Chen);Li, GC (Li, Guichuan);Bo, ML (Bo, Maolin);Yao, C (Yao, Chuang)  
文献类型: Article  
来源出版物: JOURNAL OF PHYSICS D-APPLIED PHYSICS 出版年: MAR 15 2024 卷: 57 期:11 文献号:115104 DOI: 10.1088/1361-6463/ad1351  
Web of Science 核心库的“被引频次”: 0  
被引频次合计: 0  
使用次数 (最近 180 天): 2  
使用次数 (2013 年至今): 29  
引用的参考文献数: 40

摘要: Electrical properties of twisted bilayer graphene exhibit angle-dependent characteristics, sparking a thriving development in the field of twistrionics. However, the application of quantum dots (QDs) made of twisted bilayer graphene in single-electron transistors (SETs) remains largely unexplored so far. We here investigate the electronic properties of twisted bilayer graphene QDs (TBG QDs) within a SET configuration. We compare the performance of conventional and double-gated SET structures and find that the double-gated configuration provides enhanced control over the electronic properties of TBG QDs. We analyze the influence of rotation angles on the charge stability diagrams and observe that the linear and quadratic gate-island coupling strengths generally decrease as the rotation angle decreases. Furthermore, we quantify the effect of QD size on the charge stability

diagrams and find that the size of the diamond-shaped regions decreases as the TBG QD size increases. Results presented herein may help pave the way for realization and application of TBG QDs based SET.

入藏号: WOS:001126412900001

语言: English

作者关键词: single electron transistor; twisted bilayer graphene; quantum dots

作者地址: [Huang, Zhongkai; He, Yuping; Cao, Jing; Li, Qianqian; Li, Chen; Li, Guichuan; Bo, Maolin; Yao, Chuang] Yangtze Normal Univ, Key Lab Extraordinary Bond Engn & Adv Mat Technol, Chongqing 408100, Peoples R China

通讯作者地址: [Huang, Zhongkai] (corresponding author), Yangtze Normal Univ, Key Lab Extraordinary Bond Engn & Adv Mat Technol, Chongqing 408100, Peoples R China

电子邮件地址: zhongkaihuang@yznu.edu.cn

Affiliation: ["Yangtze Normal University"]

作者识别号:

作者	Web of Science ResearcherID	ORCID 号
Bo, Maolin	LUW-7890-2024	
Yao, Chuang	HPG-8802-2023	0000-0002-6673-8388
HUANG, ZHONGKAI		0000-0002-4062-0402
QIANQIAN, LI	AFP-3195-2022	
huang, zhongkai	JSK-6419-2023	

出版商: IOP Publishing Ltd

出版商地址: TEMPLE CIRCUS, TEMPLE WAY, BRISTOL BS1 6BE, ENGLAND

Web of Science Index: Science Citation Index Expanded (SCI-EXPANDED)

Web of Science 类别: Physics, Applied

研究方向: Physics

IDS 号: CP3P1

ISSN: 0022-3727

eISSN: 1361-6463

ISO 来源出版物缩写: J PHYS D APPL PHYS

来源出版物页码计数: 9

基金资助机构和授权号

基金资助机构	授权号
National Natural Science Foundation of China <a href="http://dx.doi.org/10.13039/501100001809">http://dx.doi.org/10.13039/501100001809</a>	['11947205']
Natural Science Foundation of China	['cstc2020jcyj-msxmX0003']
Natural Science Foundation of Chongqing	['KJQN202201421']
Science and Technology Research project of Chongqing Education Commission	['JG2019234']
Educational Reform Project Fund of Yangtze Normal University	

基金资助正文: Supported by the Natural Science Foundation of China under Grant No. 11947205, by the Natural Science Foundation of Chongqing Under No. cstc2020jcyj-msxmX0003, Science and Technology Research project of Chongqing Education Commission Under No. KJQN202201421, and Educational Reform Project Fund of Yangtze Normal University (No. JG2019234).

ESI 高被引论文: N

ESI 热点论文: N

输出日期: 2025 年 11 月 12 日

### 第 3 条, 共 10 条

文献标题: Detecting Air Pollutant Molecules Using Tube-Shaped Single Electron Transistor

作者: Huang, ZK (Huang, Zhongkai);Peng, XY (Peng, Xiangyang);Peng, C (Peng, Cheng);Huang, J (Huang, Jin);Bo, ML (Bo, Maolin);Yao, C (Yao, Chuang);Li, JB (Li, Jibiao)

文献类型: Article

来源出版物: MOLECULES 出版年: DEC 2021 卷: 26 期: 23 文献号: 7098 DOI: 10.3390/molecules26237098

Web of Science 核心库的“被引频次”: 0

被引频次合计: 0

使用次数 (最近 180 天): 1

使用次数 (2013 年至今): 19

引用的参考文献数: 48

**摘要:** An air pollution detector is proposed based on a tube-shaped single-electron transistor (SET) sensor. By monitoring the flow control component of the detector, each air pollutant molecule can be placed at the center of a SET nanopore and is treated as an island of the SET device in the same framework. Electron transport in the SET was incoherent, and the performances of the SET were sensitive at the single molecule level. Employing first-principles calculations, electronic features of an air pollutant molecule within a tube-shaped SET environment were found to be independent of the molecule rotational orientations with respect to axis of symmetry, unlike the electronic features in a conventional SET environment. Charge stability diagrams of the island molecules were demonstrated to be distinct for each molecule, and thus they can serve as electronic fingerprints for detection. Using the same setup, quantification of the air pollutant can be realized at room temperature as well. The results presented herein may help provide guidance for the identification and quantification of various types of air pollutants at the molecular level by treating the molecule as the island of the SET component in the proposed detector.

入藏号: WOS:000734545500001

PubMed ID: 34885680

语言: English

**作者关键词:** tube-shaped single electron transistors; incoherent transport; air pollutant molecule; first-principle calculations; identification and quantification

**KeyWords Plus:** CO

**作者地址:** [Huang, Zhongkai; Huang, Jin] Southwest Univ, Sch Chem & Chem Engrg, Chongqing Key Lab Soft Matter Mat Chem & Funct Mf, Chongqing 400715, Peoples R China

[Huang, Zhongkai; Peng, Cheng] Yangtze Normal Univ, Key Lab Inorgan Special Funct Mat Chongqing, Chongqing 408100, Peoples R China

[Peng, Xiangyang] Xiangtan Univ, Hunan Key Lab Micronano Energy Mat & Devices, Xiangtan 411105, Peoples R China

[Bo, Maolin; Yao, Chuang; Li, Jibiao] Yangtze Normal Univ, Key Lab Extraordinary Bond Engrg & Adv Mat Technol, Chongqing 408100, Peoples R China

**通讯作者地址:** [Huang, Jin] (corresponding author), Southwest Univ, Sch Chem & Chem Engrg, Chongqing Key Lab Soft Matter Mat Chem & Funct Mf, Chongqing 400715, Peoples R China

[Peng, Cheng] (corresponding author), Yangtze Normal Univ, Key Lab Inorgan Special Funct Mat Chongqing, Chongqing 408100, Peoples R China

[Peng, Xiangyang] (corresponding author), Xiangtan Univ, Hunan Key Lab Micronano Energy Mat & Devices, Xiangtan 411105, Peoples R China

**电子邮件地址:** xiangyang\_peng@xtu.edu.cn; 20090008@yznu.edu.cn

**Affiliation:** ["Southwest University - China", "Yangtze Normal University", "Xiangtan University", "Yangtze Normal University"]

**作者识别号:**

作者	Web of Science ResearcherID	ORCID 号
Bo, Maolin		0000-0003-1173-8919
Li, Jibiao		0000-0002-1948-6675
Yao, Chuang	HPG-8802-2023	0000-0002-6673-8388
Peng, Xiangyang		0000-0001-8561-0382
HUANG, ZHONGKAI		0000-0002-4062-0402
Huang, Jin		0000-0003-0648-2525
Bo, Maolin	LUW-7890-2024	
Li, Jibiao	GLS-7259-2022	
huang, zhongkai	JSK-6419-2023	

**出版商:** MDPI**出版商地址:** MDPI AG, Grosspeteranlage 5, CH-4052 BASEL, SWITZERLAND



**Web of Science Index:** Science Citation Index Expanded (SCI-EXPANDED)  
**Web of Science 类别:** Biochemistry & Molecular Biology; Chemistry, Multidisciplinary  
**研究方向:** Biochemistry & Molecular Biology; Chemistry  
**IDS 号:** XU8ZI  
**eISSN:** 1420-3049  
**ISO 来源出版物缩写:** MOLECULES  
**来源出版物页码计数:** 20  
**基金资助机构和授权号**

基金资助机构	授权号
China Postdoctoral Science Foundation	['2019M663877XB']

**基金资助正文:**  
**ESI 高被引论文:** N  
**ESI 热点论文:** N  
**输出日期:** 2025 年 11 月 12 日

**第 4 条, 共 10 条**

**文献标题:** Polaron dynamics of Bloch-Zener oscillations in an extended Holstein model  
**作者:** Huang, ZK (Huang, Zhongkai); Somoza, AD (Somoza, Alejandro D.); Peng, C (Peng, Cheng); Huang, J (Huang, Jin); Bo, ML (Bo, Maolin); Yao, C (Yao, Chuang); Li, JBA (Li, JiBiao); Long, GK (Long, Guankui)  
**文献类型:** Article  
**来源出版物:** NEW JOURNAL OF PHYSICS 出版年: DEC 2021 卷: 23 期: 12 文献号: 123020  
**DOI:** 10.1088/1367-2630/ac3ac7  
**Web of Science 核心库的“被引频次”:** 3  
**被引频次合计:** 3  
**使用次数 (2013 年至今):** 21  
**引用的参考文献数:** 72

**摘要:** Recent developments in qubit engineering make circuit quantum electrodynamics devices promising candidates for the study of Bloch oscillations (BOs) and Landau-Zener (LZ) transitions. In this work, a hybrid circuit chain with alternating site energies under external electric fields is employed to study Bloch-Zener oscillations (BZO), i.e. coherent superpositions of BOs and LZ transitions. We couple each of the tunable qubits in the chain to dispersionless optical phonons and build an extended Holstein polaron model with the purpose of investigating vibronic effects in the BZOs. We employ an extension of the Davydov ansatz in combination with the Dirac-Frenkel time-dependent variational principle to simulate the dynamics of the qubit chain under the influence of high-frequency quantum harmonic oscillators. Band gaps emerge due to energy differences in site energies at alternating qubit sites, and are shown to play key roles in tuning band structures and time periodic reconstructions of the wave patterns. In the absence of qubit-phonon interactions, the qubits undergo either standard BZOs or breathing modes, depending on whether the initial wave packet is formed by a broad or narrow Gaussian wave packet, respectively. The BZOs can get localized in space if the band gaps are sufficiently large. In the presence of qubit-phonon coupling, the periodic behavior of BZOs can be washed out and undergo dynamic localization. The influence of an ohmic bath on the dynamics of BZOs is investigated by means of a Markovian master equation approach. Finally, we calculate the von Neumann entropy as a measure of the entanglement between qubits and phonons.

**入藏号:** WOS:000729598600001

**语言:** English

**作者关键词:** Bloch-Zener oscillations; phonons effect; open quantum system

**KeyWords Plus:** ELECTRONS; TRANSITIONS; LATTICES; MOTION; LADDER; STATE

**作者地址:** [Huang, Zhongkai; Peng, Cheng] Yangtze Normal Univ, Key Lab Inorgan Special Funct Mat Chongqing, Chongqing 408100, Peoples R China

[Huang, Zhongkai; Huang, Jin] Southwest Univ, Sch Chem & Chem Engr, Chongqing Key Lab Soft Matter Mat Chem & Funct, Chongqing 400715, Peoples R China

[Huang, Zhongkai] Chongqing Univ, Dept Phys, Chongqing 401330, Peoples R China

[Somoza, Alejandro D.] German Aerosp Ctr DLR, D-70569 Stuttgart, Germany

[Bo, Maolin; Yao, Chuang; Li, JiBiao] Yangtze Normal Univ, Key Lab Extraordinary Bond Engr & Adv Mat Technol, Chongqing 408100, Peoples R China

[Long, Guankui] Nankai Univ, Sch Mat Sci & Engn, Tianjin 300071, Peoples R China  
通讯作者地址: [Huang, Zhongkai; Peng, Cheng] (corresponding author), Yangtze Normal Univ, Key Lab Inorgan Special Funct Mat Chongqing, Chongqing 408100, Peoples R China  
[Huang, Zhongkai; Huang, Jin] (corresponding author), Southwest Univ, Sch Chem & Chem Engn, Chongqing Key Lab Soft Matter Mat Chem & Funct, Chongqing 400715, Peoples R China  
[Huang, Zhongkai] (corresponding author), Chongqing Univ, Dept Phys, Chongqing 401330, Peoples R China  
电子邮件地址:  
zhongkaihuang@yznu.edu.cn;;20090008@yznu.edu.cn;huangjin2015@swu.edu.cn  
Affiliation: ["Yangtze Normal University", "Southwest University - China", "Chongqing University", "Helmholtz Association; German Aerospace Centre (DLR)", "Yangtze Normal University", "Nankai University"]  
作者识别号:

作者	Web of Science ResearcherID	ORCID 号
Bo, Maolin	LUW-7890-2024	
Li, Jibiao		0000-0002-1948-6675
Long, Guankui	JXL-2865-2024	
huang, zhongkai	JSK-6419-2023	
Yao, Chuang	HPG-8802-2023	0000-0002-6673-8388
Somoza, Alejandro		0000-0002-4973-8052
Li, Jibiao	GLS-7259-2022	
HUANG, ZHONGKAI		0000-0002-4062-0402

出版商: IOP Publishing Ltd  
出版商地址: TEMPLE CIRCUS, TEMPLE WAY, BRISTOL BS1 6BE, ENGLAND  
Web of Science Index: Science Citation Index Expanded (SCI-EXPANDED)  
Web of Science 类别: Physics, Multidisciplinary  
研究方向: Physics  
IDS 号: XN6FN  
ISSN: 1367-2630  
ISO 来源出版物缩写: NEW J PHYS  
来源出版物页码计数: 19  
基金资助机构和授权号

基金资助机构	授权号
Natural Science Foundation of China	['11947205', '12047564']
Fundamental Research Funds for the Central Universities	['2020CDJQY-Z003']
Natural Science Foundation of Chongqing	['cstc2020jcyj-msxmX0003', '298']
China Postdoctoral Science Foundation	['2019M663877XB']

基金资助正文: This work was supported in part by the Natural Science Foundation of China under Grant Nos. 11947205 and 12047564, by the Fundamental Research Funds for the Central Universities under Grant No. 2020CDJQY-Z003, by the Natural Science Foundation of Chongqing under No.cstc2020jcyj-msxmX0003, Yu Ren She [2019] No. 298, and by China Postdoctoral Science Foundation under Grant No. 2019M663877XB.

ESI 高被引论文: N  
ESI 热点论文: N  
输出日期: 2025 年 11 月 12 日

第 5 条, 共 10 条  
文献标题: Dissipative dynamics in a tunable Rabi dimer with periodic harmonic driving  
作者: Huang, ZK (Huang, Zhongkai);Zheng, FL (Zheng, Fulu);Zhang, YY (Zhang, Yuyu);Wei, YD (Wei, Yadong);Zhao, Y (Zhao, Yang)  
文献类型: Article



来源出版物: JOURNAL OF CHEMICAL PHYSICS 出版年: MAY 14 2019 卷: 150 期: 18 文献号: 184116 DOI: 10.1063/1.5096071

Web of Science 核心库的“被引频次”: 13

被引频次合计: 13

使用次数 (最近 180 天): 2

使用次数 (2013 年至今): 20

引用的参考文献数: 54

**摘要:** Recent progress on qubit manipulation allows application of periodic driving signals on qubits. In this study, a harmonic driving field is added to a Rabi dimer to engineer photon and qubit dynamics in a circuit quantum electrodynamics device. To model environmental effects, qubits in the Rabi dimer are coupled to a phonon bath with a sub-Ohmic spectral density. A nonperturbative treatment, the Dirac-Frenkel time-dependent variational principle together with the multiple Davydov D-2 ansatz, is employed to explore the dynamical behavior of the tunable Rabi dimer. In the absence of the phonon bath, the amplitude damping of the photon number oscillation is greatly suppressed by the driving field, and photons can be created, thanks to the resonance between the periodic driving field and the photon frequency. In the presence of the phonon bath, one can still change the photon numbers in two resonators and indirectly alter the photon imbalance in the Rabi dimer by directly varying the driving signal in one qubit. It is shown that qubit states can be manipulated directly by the harmonic driving. The environment is found to strengthen the interqubit asymmetry induced by the external driving, opening up a new venue to engineer the qubit states.

入藏号: WOS:000470154100046

PubMed ID: 31091928

语言: English

**KeyWords Plus:** MAPPING POLARON STRUCTURE; ENERGY-BAND THEORY; QUANTUM; SPECTROSCOPY; SYSTEMS

**作者地址:** [Huang, Zhongkai; Zheng, Fulu; Zhao, Yang] Nanyang Technol Univ, Div Mat Sci, Singapore 639798, Singapore

[Huang, Zhongkai] Yangtze Normal Univ, Coll Mat Sci & Engr, Chongqing 408100, Peoples R China

[Zheng, Fulu; Wei, Yadong] Shenzhen Univ, Sch Phys & Energy, Shenzhen 518060, Peoples R China

[Zhang, Yuyu] Chongqing Univ, Dept Phys, Chongqing 404100, Peoples R China

**通讯作者地址:** [Zhao, Yang] (corresponding author), Nanyang Technol Univ, Div Mat Sci, Singapore 639798, Singapore

**电子邮件地址:** YZhao@ntu.edu.sg

**Affiliation:** ["Nanyang Technological University", "Yangtze Normal University", "Shenzhen University", "Chongqing University"]

**作者识别号:**

作者	Web of Science ResearcherID	ORCID 号
wei, yadong		0000-0001-8565-5695
huang, zhongkai	JSK-6419-2023	
Zheng, Fulu	HJI-2794-2023	
Zheng, Fulu		0000-0003-3439-1575
Zhao, Yang	D-1014-2009	0000-0002-7916-8687
yu-yu, zhang	HGB-7747-2022	
HUANG, ZHONGKAI		0000-0002-4062-0402

**出版商:** AMER INST PHYSICS

**出版商地址:** 1305 WALT WHITMAN RD, STE 300, MELVILLE, NY 11747-4501 USA

**Web of Science Index:** Science Citation Index Expanded (SCI-EXPANDED)

**Web of Science 类别:** Chemistry, Physical; Physics, Atomic, Molecular & Chemical

**研究方向:** Chemistry; Physics

**IDS 号:** IB3FT

**ISSN:** 0021-9606

**eISSN:** 1089-7690

**ISO 来源出版物缩写:** J CHEM PHYS

**来源出版物页码计数:** 12

**基金资助机构和授权号**

基金资助机构	授权号
--------	-----



Singapore National Research Foundation through the Competitive Research Programme (CRP)	['NRF-CRP5-2009-04']
Singapore Ministry of Education Academic Research Fund Tier 1	['RG106/15', 'RG102/17', 'RG190/18']

**基金资助正文:** The authors thank Cao Xiufeng for useful discussion. Support from the Singapore National Research Foundation through the Competitive Research Programme (CRP) under Project No. NRF-CRP5-2009-04 and from the Singapore Ministry of Education Academic Research Fund Tier 1 (Grant Nos. RG106/15, RG102/17, and RG190/18) is gratefully acknowledged.

**ESI 高被引论文:** N

**ESI 热点论文:** N

**输出日期:** 2025 年 11 月 12 日

**第 6 条, 共 10 条**

**文献标题:** Transient Dynamics of Super Bloch Oscillations of a 1D Holstein Polaron under the Influence of an External AC Electric Field

**作者:** Huang, Z (Huang, Zhongkai);Hoshina, M (Hoshina, Masayuki);Ishihara, H (Ishihara, Hajime);Zhao, Y (Zhao, Yang)

**文献类型:** Article

**来源出版物:** ANNALEN DER PHYSIK **出版年:** JAN 2019 **卷:** 531 **期:** 1 **文献号:** 1800303 **DOI:** 10.1002/andp.201800303

**Web of Science 核心库的“被引频次”:** 10

**被引频次合计:** 17

**使用次数 (2013 年至今):** 10

**引用的参考文献数:** 82

**摘要:** Theoretical formalism for DC-field polaron dynamics is extended to the dynamics of a 1D Holstein polaron in an external AC electric field using multiple Davydov trial states. Effects of carrier-phonon coupling on detuned and resonant scenarios are investigated for both phase and nonzero phase. For slightly off-resonant or detuned cases, a beat between the usual Bloch oscillations and an AC driving force results in super Bloch oscillations, that is, rescaled Bloch oscillations in both the spatial and the temporal dimension. Super Bloch oscillations are damped by carrier-phonon coupling. For resonant cases, if the carrier is created on two nearest-neighboring sites, the carrier wave packet spreads with small-amplitude oscillations. Adding carrier-phonon coupling localizes the carrier wave packet. If an initial broad Gaussian wave packet is adopted, the centroid of the carrier wave packet moves with a certain velocity and with its shape unchanged. Adding carrier-phonon coupling broadens the carrier wave packet and slows down the carrier movement. Our findings may help provide guiding principles on how to manipulate the dynamics of the super Bloch oscillations of carriers in semiconductor superlattice and optical lattices by modifying DC and AC field strengths, AC phases, and detuning parameters.

**入藏号:** WOS:000455239200008

**语言:** English

**作者关键词:** carrier-phonon coupling; Davydov Ansatz; polaron dynamics; super Bloch oscillations

**KeyWords Plus:** STARK-LADDER; WAVE-FUNCTIONS; LOCALIZATION; TEMPERATURE; SIMULATION; SOLITONS; SYSTEM; DC

**作者地址:** [Huang, Zhongkai] Yangtze Normal Univ, Coll Mech & Elect Engn, Chongqing 408100, Peoples R China

[Huang, Zhongkai; Hoshina, Masayuki; Zhao, Yang] Nanyang Technol Univ, Div Mat Sci, Singapore 639798, Singapore

[Hoshina, Masayuki; Ishihara, Hajime] Osaka Prefecture Univ, Dept Phys & Elect, Naka Ku, 1-1 Gakuen Cho, Sakai, Osaka 5998531, Japan

[Ishihara, Hajime] Osaka Univ, Div Frontier Mat Sci, 1-3 Machikaneyama Cho, Toyonaka, Osaka 5608531, Japan

**通讯作者地址:** [Zhao, Yang] (corresponding author), Nanyang Technol Univ, Div Mat Sci, Singapore 639798, Singapore

**电子邮件地址:** YZhao@ntu.edu.sg

**Affiliation:** ["Yangtze Normal University", "Nanyang Technological University", "Osaka Metropolitan

University", "University of Osaka"]

作者识别号:

作者	Web of Science ResearcherID	ORCID 号
huang, zhongkai	JSK-6419-2023	
HUANG, ZHONGKAI		0000-0002-4062-0402
Zhao, Yang	D-1014-2009	0000-0002-7916-8687

出版商: WILEY-VCH VERLAG GMBH

出版商地址: POSTFACH 101161, 69451 WEINHEIM, GERMANY

Web of Science Index: Science Citation Index Expanded (SCI-EXPANDED)

Web of Science 类别: Physics, Multidisciplinary

研究方向: Physics

IDS 号: HG8GW

ISSN: 0003-3804

eISSN: 1521-3889

ISO 来源出版物缩写: ANN PHYS-BERLIN

来源出版物页码计数: 11

基金资助机构和授权号

基金资助机构	授权号
Singapore National Research Foundation through the Competitive Research Programme	['NRF-CRP5-2009-04']
Singapore Ministry of Education Academic Research Funds	['RG106/15', 'RG102/17']

基金资助正文: Support from the Singapore National Research Foundation through the Competitive Research Programme (Project No. NRF-CRP5-2009-04) and the Singapore Ministry of Education Academic Research Funds (Grant Nos. RG106/15 and RG102/17) is gratefully acknowledged.

ESI 高被引论文: N

ESI 热点论文: N

输出日期: 2025 年 11 月 12 日

第 7 条, 共 10 条

文献标题: Dynamics of dissipative Landau-Zener transitions

作者: Huang, ZK (Huang, Zhongkai); Zhao, Y (Zhao, Yang)

文献类型: Article

来源出版物: PHYSICAL REVIEW A 出版年: JAN 3 2018 卷: 97 期:1 文献号:013803 DOI: 10.1103/PhysRevA.97.013803

Web of Science 核心库的“被引频次”: 35

被引频次合计: 35

使用次数 (2013 年至今): 32

引用的参考文献数: 65

摘要: A nonperturbative treatment, the Dirac-Frenkel time-dependent variation is employed to examine dynamics of the Landau-Zener model with both diagonal and off-diagonal qubit-bath coupling using the multiple Davydov trial states. It is shown that steady-state transition probabilities agree with analytical predictions at long times. Landau-Zener dynamics at intermediate times is little affected by diagonal coupling, and is found to be determined by off-diagonal coupling and tunneling between two diabatic states. We investigate effects of bath spectral densities, coupling strengths, and interaction angles on Landau-Zener dynamics. Thanks to the multiple Davydov trial states, detailed boson dynamics can also be analyzed in Landau-Zener transitions. The results presented here may help provide guiding principles to manipulate the Landau-Zener transitions in circuit QED architectures by tuning off-diagonal coupling and tunneling strength.

入藏号: WOS:000419097100010

语言: English

KeyWords Plus: MATTER

作者地址: [Huang, Zhongkai; Zhao, Yang] Nanyang Technol Univ, Div Mat Sci, Singapore 639798,



Singapore

通讯作者地址: [Zhao, Yang] (corresponding author), Nanyang Technol Univ, Div Mat Sci, Singapore 639798, Singapore

电子邮件地址: yzhao@ntu.edu.sg

Affiliation: ["Nanyang Technological University"]

作者识别号:

作者	Web of Science ResearcherID	ORCID 号
huang, zhongkai	JSK-6419-2023	
Zhao, Yang	D-1014-2009	
HUANG, ZHONGKAI		0000-0002-4062-0402

出版商: AMER PHYSICAL SOC

出版商地址: ONE PHYSICS ELLIPSE, COLLEGE PK, MD 20740-3844 USA

Web of Science Index: Science Citation Index Expanded (SCI-EXPANDED)

Web of Science 类别: Optics; Physics, Atomic, Molecular & Chemical

研究方向: Optics; Physics

IDS 号: FR5HI

ISSN: 2469-9926

eISSN: 2469-9934

ISO 来源出版物缩写: PHYS REV A

来源出版物页码计数: 10

基金资助机构和授权号

基金资助机构	授权号
Singapore National Research Foundation through the Competitive Research Programme (CRP)	['NRF-CRP5-2009-04']
Singapore Ministry of Education Academic Research Fund Tier 1	['RG106/15']

基金资助正文: The authors would like to thank Qinghu Chen, Nengji Zhou, Kewei Sun, and Lipeng Chen for useful discussion. Support from the Singapore National Research Foundation through the Competitive Research Programme (CRP) under Project No. NRF-CRP5-2009-04 and from the Singapore Ministry of Education Academic Research Fund Tier 1 (Grant No. RG106/15) is gratefully acknowledged.

ESI 高被引论文: N

ESI 热点论文: N

输出日期: 2025 年 11 月 12 日

#### 第 8 条, 共 10 条

文献标题: Polaron dynamics with off-diagonal coupling: beyond the Ehrenfest approximation

作者: Huang, ZK (Huang, Zhongkai); Wang, L (Wang, Lu); Wu, CQ (Wu, Changqin); Chen, LP (Chen, Lipeng); Grossmann, F (Grossmann, Frank); Zhao, Y (Zhao, Yang)

文献类型: Article

来源出版物: PHYSICAL CHEMISTRY CHEMICAL PHYSICS 出版年: JAN 14 2017 卷: 19

期: 2 页: 1655-1668 DOI: 10.1039/c6cp07107d

Web of Science 核心库的“被引频次”: 42

被引频次合计: 43

使用次数 (2013 年至今): 27

引用的参考文献数: 53

摘要: Treated traditionally by the Ehrenfest approximation, the dynamics of a one-dimensional molecular crystal model with off-diagonal exciton-phonon coupling is investigated in this work using the Dirac-Frenkel time-dependent variational principle with the multi-D2 Ansatz. It is shown that the Ehrenfest method is equivalent to our variational method with the single D2 Ansatz, and with the multi-D2 Ansatz, the accuracy of our simulated dynamics is significantly enhanced in comparison with the semi-classical Ehrenfest dynamics. The multi-D2 Ansatz is able to capture numerically accurate exciton momentum probability and help clarify the relation between the exciton momentum redistribution and the exciton energy relaxation. The results demonstrate that the exciton momentum



distributions in the steady state are determined by a combination of the transfer integral and the off-diagonal coupling strength, independent of the excitonic initial conditions. We also probe the effect of the transfer integral and the off-diagonal coupling on exciton transport in both real and reciprocal space representations. Finally, the variational method with importance sampling is employed to investigate temperature effects on exciton transport using the multi-D2 Ansatz, and it is demonstrated that the variational approach is valid in both low and high temperature regimes.

入藏号: WOS:000392399400078

PubMed ID: 27995258

语言: English

**KeyWords Plus:** CONDUCTING-POLYMER NANOTUBES; TEMPERATURE-DEPENDENCE; MOLECULAR-CRYSTALS; DAVYDOV SOLITON; QUANTUM; SUPERCAPACITORS; POLYACETYLENE; SYSTEM; STATES; FILMS

**作者地址:** [Huang, Zhongkai; Wang, Lu; Chen, Lipeng; Zhao, Yang] Nanyang Technol Univ, Div Mat Sci, Singapore, Singapore

[Wang, Lu] Zhejiang Univ, Dept Phys, Hangzhou 310027, Peoples R China

[Wu, Changqin] Fudan Univ, State Key Lab Surface Phys, Shanghai 200433, Peoples R China

[Wu, Changqin] Fudan Univ, Dept Phys, Shanghai 200433, Peoples R China

[Grossmann, Frank] Tech Univ Dresden, Inst Theoret Phys, D-01062 Dresden, Germany

**通讯作者地址:** [Zhao, Yang] (corresponding author), Nanyang Technol Univ, Div Mat Sci, Singapore, Singapore

**电子邮件地址:** yzhao@ntu.edu.sg

**Affiliation:** ["Nanyang Technological University", "Zhejiang University", "Fudan University", "Fudan University", "Technische Universitat Dresden"]

**作者识别号:**

作者	Web of Science ResearcherID	ORCID 号
Grossmann, Frank	A-1114-2012	
HUANG, ZHONGKAI		0000-0002-4062-0402
huang, zhongkai	JSK-6419-2023	
Zhao, Yang	D-1014-2009	
CHEN, LIPENG	AAW-7490-2020	

**出版商:** ROYAL SOC CHEMISTRY

**出版商地址:** THOMAS GRAHAM HOUSE, SCIENCE PARK, MILTON RD, CAMBRIDGE CB4 0WF, CAMBS, ENGLAND

**Web of Science Index:** Science Citation Index Expanded (SCI-EXPANDED)

**Web of Science 类别:** Chemistry, Physical; Physics, Atomic, Molecular & Chemical

**研究方向:** Chemistry; Physics

**IDS 号:** EI3OB

**ISSN:** 1463-9076

**eISSN:** 1463-9084

**ISO 来源出版物缩写:** PHYS CHEM CHEM PHYS

**来源出版物页码计数:** 14

**基金资助机构和授权号**

基金资助机构	授权号
Singapore National Research Foundation through the Competitive Research Programme (CRP)	['NRF-CRP5-2009-04']

**基金资助正文:** We thank Yuta Fujihashi and Zheng Fulu for helpful discussion. Support from the Singapore National Research Foundation through the Competitive Research Programme (CRP) under Project No. NRF-CRP5-2009-04 is gratefully acknowledged.

**ESI 高被引论文:** N

**ESI 热点论文:** N

**输出日期:** 2025 年 11 月 12 日

**第 9 条, 共 10 条**

**文献标题:** Effect of Off-Diagonal Exciton-Phonon Coupling on Intramolecular Singlet Fission

**作者:** Huang, ZK (Huang, Zhongkai);Fujihashi, Y (Fujihashi, Yuta);Zhao, Y (Zhao, Yang)

文献类型: Article

来源出版物: JOURNAL OF PHYSICAL CHEMISTRY LETTERS 出版年: JUL 20 2017 卷: 8  
期: 14 页: 3306-3312 DOI: 10.1021/acs.jpclett.7b01247

Web of Science 核心库的“被引频次”: 34

被引频次合计: 34

使用次数 (2013 年至今): 44

引用的参考文献数: 72

**摘要:** Intramolecular singlet fission (iSF) materials provide remarkable advantages in terms of tunable electronic structures, and quantum chemistry studies have indicated strong electronic coupling modulation by high frequency phonon modes. In this work, we formulate a microscopic model of iSF with simultaneous diagonal and off-diagonal coupling to high-frequency modes. A nonperturbative treatment, the Dirac-Frenkel time-dependent variational approach is adopted using the multiple Davydov trial states. It is shown that both diagonal and off-diagonal coupling can aid efficient singlet fission if excitonic coupling is weak, and fission is only facilitated by diagonal coupling if excitonic coupling is strong. In the presence of off-diagonal coupling, it is found that high frequency modes create additional fission channels for rapid iSF. Results presented here may help provide guiding principles for design of efficient singlet fission materials by directly tuning singlet triplet interstate coupling.

入藏号: WOS:000406358000023

PubMed ID: 28673087

语言: English

**KeyWords Plus:** CHARGE-TRANSFER STATES; MAPPING POLARON STRUCTURE; ENERGY-BAND THEORY; ELECTRONIC-STRUCTURE; THIN-FILMS; DYNAMICS; MECHANISM; TETRACENE; PENTACENE; COHERENT

作者地址: [Huang, Zhongkai; Fujihashi, Yuta; Zhao, Yang] Nanyang Technol Univ, Div Mat Sci, Singapore 639798, Singapore

通讯作者地址: [Zhao, Yang] (corresponding author), Nanyang Technol Univ, Div Mat Sci, Singapore 639798, Singapore

电子邮件地址: YZhao@ntu.edu.sg

Affiliation: ["Nanyang Technological University"]

作者识别号:

作者	Web of Science ResearcherID	ORCID 号
Zhao, Yang	D-1014-2009	0000-0002-7916-8687
HUANG, ZHONGKAI		0000-0002-4062-0402
Fujihashi, Yuta	KYQ-8676-2024	0000-0002-2201-269X
huang, zhongkai	JSK-6419-2023	

出版商: AMER CHEMICAL SOC

出版商地址: 1155 16TH ST, NW, WASHINGTON, DC 20036 USA

Web of Science Index: Science Citation Index Expanded (SCI-EXPANDED)

Web of Science 类别: Chemistry, Physical; Nanoscience & Nanotechnology; Materials Science, Multidisciplinary; Physics, Atomic, Molecular & Chemical

研究方向: Chemistry; Science & Technology - Other Topics; Materials Science; Physics

IDS 号: FB7ZH

ISSN: 1948-7185

ISO 来源出版物缩写: J PHYS CHEM LETT

来源出版物页码计数: 7

基金资助机构和授权号

基金资助机构	授权号
Singapore National Research Foundation through the Competitive Research Programme (CRP)	['NRF-CRP5-2009-04']

**基金资助正文:** Support from the Singapore National Research Foundation through the Competitive Research Programme (CRP) under Project No. NRF-CRP5-2009-04 is gratefully acknowledged.

ESI 高被引论文: N

ESI 热点论文: N

输出日期: 2025 年 11 月 12 日

第 10 条, 共 10 条

文献标题: Transient dynamics of a one-dimensional Holstein polaron under the influence of an external electric field

作者: Huang, ZK (Huang, Zhongkai);Chen, LP (Chen, Lipeng);Zhou, NJ (Zhou, Nengji);Zhao, Y (Zhao, Yang)

文献类型: Article

来源出版物: ANNALEN DER PHYSIK 出版年: MAY 2017 卷: 529 期:5 文献号:1600367 DOI: 10.1002/andp.201600367

Web of Science 核心库的“被引频次”: 28

被引频次合计: 33

使用次数 (2013 年至今): 15

引用的参考文献数: 84

摘要: Following the Dirac-Frenkel time-dependent variational principle, transient dynamics of a one-dimensional Holstein polaron with diagonal and off-diagonal exciton-phonon coupling in an external electric field is studied by employing the multi-D(2)Ansatz, also known as a superposition of the usual Davydov D-2 trial states. Resultant polaron dynamics has significantly enhanced accuracy, and is in perfect agreement with that derived from the hierarchy equations of motion method. Starting from an initial broad wave packet, the exciton undergoes typical Bloch oscillations. Adding weak exciton-phonon coupling leads to a broadened exciton wave packet and a reduced current amplitude. Using a narrow wave packet as the initial state, the bare exciton oscillates in a symmetric breathing mode, but the symmetry is easily broken by weak coupling to phonons, resulting in a non-zero exciton current. For both scenarios, temporal periodicity is unchanged by exciton-phonon coupling. In particular, at variance with the case of an infinite linear chain, no steady state is found in a finite-sized ring within the anti-adiabatic regime. For strong diagonal coupling, the multi-D2Ansatz is found to be highly accurate, and the phonon confinement gives rise to exciton localization and decay of the Bloch oscillations.

入藏号: WOS:000400596300005

语言: English

作者关键词: Bloch oscillations; polaron dynamics; Davydov Ansatz; exciton-phonon coupling; electric field

KeyWords Plus: OPTICAL BLOCH OSCILLATIONS; WANNIER-STARK LADDERS; SOLITONS; MOTION; LOCALIZATION; TRANSPORT; PHONONS; SYSTEM; STATES

作者地址: [Huang, Zhongkai; Chen, Lipeng; Zhou, Nengji; Zhao, Yang] Nanyang Technol Univ, Div Mat Sci, Singapore 639798, Singapore

通讯作者地址: [Zhao, Yang] (corresponding author), Nanyang Technol Univ, Div Mat Sci, Singapore 639798, Singapore

电子邮件地址: YZhao@ntu.edu.sg

Affiliation: ["Nanyang Technological University"]

作者识别号:

作者	Web of Science ResearcherID	ORCID 号
Zhao, Yang	D-1014-2009	
huang, zhongkai	JSK-6419-2023	
HUANG, ZHONGKAI		0000-0002-4062-0402
CHEN, LIPENG	AAW-7490-2020	

出版商: WILEY-VCH VERLAG GMBH

出版商地址: POSTFACH 101161, 69451 WEINHEIM, GERMANY

Web of Science Index: Science Citation Index Expanded (SCI-EXPANDED)

Web of Science 类别: Physics, Multidisciplinary

研究方向: Physics

IDS 号: ET9AG

ISSN: 0003-3804

eISSN: 1521-3889

ISO 来源出版物缩写: ANN PHYS-BERLIN

来源出版物页码计数: 12



**基金资助机构和授权号**

基金资助机构	授权号
Singapore National Research Foundation through the Competitive Research Programme (CRP)	['NRF-CRP5-2009-04']

**基金资助正文:** Support from the Singapore National Research Foundation through the Competitive Research Programme (CRP) under Project No. NRF-CRP5-2009-04 is gratefully acknowledged.

**ESI 高被引论文:** N

**ESI 热点论文:** N

**输出日期:** 2025 年 11 月 12 日



# 科技检索报告

项目名称：黄忠凯发表的论文在《SCI》数据库的收录情况

委托人：长江师范学院

委托日期：2023 年 09 月 12 日

查新机构（盖章）：教育部科技查新工作站（L02）

重庆大学科技查新站

与原件相符

完成日期：2023 年 09 月 12 日



教育部科技发展中心

二〇一三年制

项目名称	黄忠凯发表的论文在《SCI》数据库收录情况					
查新机构	名称	教育部科技查新工作站(L02) 重庆大学科技查新站				
	通信地址	重庆大学			邮政编码	400044
	负责人	黄娟	电话	023-65106364	传真	023-65105224
	联系人	蔡佳	电话	023-65106364		
	电子信箱	984100324@qq.com				
<p>一、检索要求： 署名长江师范学院黄忠凯发表的论文在《SCI》中的收录情况</p> <p>二、文献检索范围 《SCI-Expanded》 Science Citation Index Expanded      2023 年~2023 年</p> <p>三、检索结果： 根据用户委托，针对检索要求，通过数据库，对黄忠凯发表的论文在《SCI》数据库中的收录引用情况进行检索，结论如下： 黄忠凯发表的论文被《SCI》数据库收录 1 篇，为第一兼通讯作者。 论文的详细信息见附件。</p> <p style="text-align: right;">检索人员（签字）： 教育部科技查新工作站(L02) 重庆大学科技查新站 2023 年 09 月 12 日</p>						



## 一、所发论文期刊 JCR 分区如下

序号	篇名	刊名	影响因子
1	Dynamics of Bloch-Zener Oscillations with Tuning Gap	ANNALEN DER PHYSIK	2.4(2022)
	类别		分区
	PHYSICS, MULTIDISCIPLINARY (SCIE)		Q3

## 二、所发论文期刊中科院分区如下

序号	题名	刊名	ISSN	Review	Open Access	年份
1	Dynamics of Bloch-Zener Oscillations with Tuning Gap	ANNALEN DER PHYSIK	0003-3804	否	否	2022
	类别	学科			分区	TOP 期刊
	大类分区	物理与天体物理			3 区	否
	小类分区	PHYSICS, MULTIDISCIPLINARY 物理: 综合			3 区	-

## 三、SCI 检索结果

## 第 1 条, 共 1 条

文献标题: Dynamics of Bloch-Zener Oscillations with Tuning Gap

作者: Huang, ZK (Huang, Zhongkai); Bo, M (Bo, Maolin); Yao, C (Yao, Chuang)

文献类型: Article

来源出版物: ANNALEN DER PHYSIK 出版年: JUN 2023 卷: 535 期: 6 DOI:

10.1002/andp.202300101 提前访问日期: MAY 2023

Web of Science 核心库的“被引频次”: 0

被引频次合计: 0

入藏号: WOS:000982374000001

作者地址: [Huang, Zhongkai; Bo, Maolin; Yao, Chuang] Yangtze Normal Univ, Key Lab Inorgan Special Funct Mat Chongqing, Chongqing 408100, Peoples R China

通讯作者地址: [Huang, Zhongkai] (corresponding author), Yangtze Normal Univ, Key Lab Inorgan Special Funct Mat Chongqing, Chongqing 408100, Peoples R China

电子邮件地址: zhongkaihuang@yznu.edu.cn

Affiliation: ["Yangtze Normal University"]

Web of Science Index: Science Citation Index Expanded (SCI-EXPANDED)

IDS 号: I5ST9

ISSN: 0003-3804

eISSN: 1521-3889

来源出版物页码计数: 11

基金资助机构和授权号

基金资助机构	授权号
Natural Science Foundation of China	['11947205']
Natural Science Foundation of Chongqing	['cstc2020jcyj-msxm0003']
Science and Technology Research project of Chongqing Education Commission	['KJQN202201421']

基金资助正文: Acknowledgements This work was supported in part by the Natural Science Foundation of China under Grant No. 11947205, and by the Natural Science Foundation of Chongqing under No. cstc2020jcyj-msxm0003, and the Science and Technology Research project of Chongqing Education Commission under No. KJQN202201421.





## Article

# Single-Atom Cobalt-Doped 2D Graphene: Electronic Design for Multifunctional Applications in Environmental Remediation and Energy Storage

Zhongkai Huang <sup>1,\*</sup>, Yue Zhang <sup>1</sup>, Chunjiang Li <sup>1</sup>, Liang Deng <sup>1</sup>, Bo Song <sup>1</sup>, Maolin Bo <sup>1</sup>, Chuang Yao <sup>1</sup>, Haolin Lu <sup>2</sup> and Guankui Long <sup>2,\*</sup>

<sup>1</sup> Key Laboratory of Extraordinary Bond Engineering and Advanced Materials Technology of Chongqing, Yangtze Normal University, Chongqing 408100, China; yuezhang0922@163.com (Y.Z.); lichunjiang2004@163.com (C.L.); dengliangacademic@163.com (L.D.); songboacademic@163.com (B.S.); bmlwd@yznu.edu.cn (M.B.); yaochuang@yznu.cn (C.Y.)

<sup>2</sup> Renewable Energy Conversion and Storage Center (RECAST), National Institute for Advanced Materials, School of Materials Science and Engineering, Nankai University, Tianjin 300350, China; 1713638@mail.nankai.edu.cn

\* Correspondence: zhongkaihuang@yznu.edu.cn (Z.H.); longgk09@nankai.edu.cn (G.L.)

## Abstract

Through atomic-scale characterization of a single cobalt atom anchored in a pyridinic N<sub>3</sub> vacancy of graphene (Co-N<sub>3</sub>-gra), this study computationally explores three interconnected functionalities mediated by cobalt's electronic configuration. Quantum-confined molecular prototypes extend prior bulk models, achieving a competitive catalytic activity for CO oxidation via Langmuir–Hinshelwood pathways with a 0.85 eV barrier. These molecular prototypes' discrete energy states facilitate single-electron transistor operation, enabling sensitive detection of NO, NO<sub>2</sub>, SO<sub>2</sub>, and CO<sub>2</sub> through adsorption-induced conductance modulation. When applied to lithium–sulfur batteries using periodic Co-N<sub>3</sub>-gra, cobalt sites enhance polysulfide conversion kinetics and suppress the shuttle effect, with the Li<sub>2</sub>S<sub>2</sub> → Li<sub>2</sub>S step identified as the rate-limiting process. Density functional simulations provide atomic-scale physicochemical characterization of Co-N<sub>3</sub>-gra, revealing how defect engineering in 2D materials modulates electronic structures for multifunctional applications.

**Keywords:** 2D material defects; electronic structure engineering; environmental gas sensors; lithium–sulfur batteries; structure–property relationships



Academic Editors: Martina Vrankić and Melita Menelaou

Received: 12 August 2025

Revised: 9 September 2025

Accepted: 22 September 2025

Published: 24 September 2025

**Citation:** Huang, Z.; Zhang, Y.; Li, C.; Deng, L.; Song, B.; Bo, M.; Yao, C.; Lu, H.; Long, G. Single-Atom Cobalt-Doped 2D Graphene: Electronic Design for Multifunctional Applications in Environmental Remediation and Energy Storage. *Inorganics* **2025**, *13*, 312. <https://doi.org/10.3390/inorganics13100312>

**Copyright:** © 2025 by the authors. Licensee MDPI, Basel, Switzerland. This article is an open access article distributed under the terms and conditions of the Creative Commons Attribution (CC BY) license (<https://creativecommons.org/licenses/by/4.0/>).

## 1. Introduction

The concept of single-atom catalysis has emerged as a powerful strategy for achieving high activity and selectivity [1]. Leveraging its unique electronic configuration and tunable coordination chemistry, single-atom cobalt (Co) [2] emerges as a versatile platform spanning heterogeneous catalysis to quantum electronics. Beyond catalytic carbon oxide (CO) oxidation [3], Co sites exhibit non-sequential electron transport in single-electron transistors (SETs) [4], while analogous charge modulation enables molecular sensing [5,6] and energy storage catalysis [7]. This multifunctionality positions cobalt as a key building block for integrated environmental and energy technologies.

The exceptional activity of atomic Co catalysts originates from tunable coordination environments that optimize adsorption/desorption kinetics—critical for applications like pollutant degradation [8,9]. While Co-based systems show broad catalytic versatility (e.g., hydroformylation [10–14], and C–H activation [15–18]), their efficacy in gaseous pollutant



elimination remains underexplored. In 2016, Zhang et al. pioneered single Co atoms in pyridinic N<sub>3</sub> graphene (Co-N<sub>3</sub>-gra), demonstrating efficient CO oxidation via Langmuir–Hinshelwood pathways with a 0.86 eV barrier [19].

However, two fundamental questions arise from this work [19]: How do quantum confinement effects in nanoscale Co-N<sub>3</sub>-gra flakes modify electronic structures and catalytic behavior? Can the charge transfer mechanisms governing catalysis enable other functionalities like sensing and energy storage? Addressing these gaps requires multiscale computational probes bridging discrete and periodic systems.

The discrete energy states of quantum-confined flakes provide an ideal platform for SETs. When configured with Co-based islands [20,21], SETs resolve single-electron charging effects through Coulomb blockade phenomena—including quantized charge states and stability diamonds—that fingerprint molecular energy landscapes [22,23]. This approach offers direct electrical readouts of electronic states complementary to spectroscopic methods.

Molecular adsorption at Co sites enables environmental monitoring, particularly for bioactive gases (NO/NO<sub>2</sub>) [24,25] and pollutants (CO<sub>2</sub>/SO<sub>2</sub>) [26]. Crucially, adsorption-induced conductance shifts in SETs directly correlate with charge redistribution during catalytic activation. For instance, NO<sub>2</sub> adsorption triggers electron transfer analogous to O<sub>2</sub> activation in CO oxidation, establishing SETs as *in situ* probes of catalytic behavior.

In energy storage, lithium–sulfur (Li-S) batteries face challenges from polysulfide shuttling [27,28]. Recent advances highlight the promise of two-dimensional (2D) layered nitrogenous carbon-based material for suppressing the polysulfide shuttle effect in Li-S batteries [29]. Unlike prior nanoparticle approaches [7,30,31], we pioneer periodic Co-N<sub>3</sub>-gra for Li-S systems—retaining identical coordination while enabling electrode-scale simulations. Co-based catalysts enhance polysulfide conversion [32–34] and improve conductivity [7,32,35,36], directly translating electronic insights from flakes to practical interfaces.

Through density functional theory (DFT), this work implements a three-tier strategy: revisiting CO oxidation on a quantum-confined Co-N<sub>3</sub>-gra molecular prototype to probe size effects, employing SETs to quantify charge states and adsorption behavior, and applying these insights to Li-S catalysis via periodic Co-N<sub>3</sub>-gra models. Rather than treating these applications in isolation, this work seeks to demonstrate a unified design principle: the electronic structure of the atomically dispersed cobalt site serves as a universal ‘control knob’ for diverse functionalities. Section 3 details computational methods, with results progressing systematically from catalysis (Section 2.1) to SET characterization (Section 2.2), molecular sensing (Section 2.3), and Li-S battery applications (Section 2.4). Section 4 summarizes how charge redistribution unifies functionality across systems.

## 2. Results and Discussion

### 2.1. Catalytic Design for Environmental Remediation

In this section, the catalytic effect of the single Co atom embedded in pyridinic nitrogen vacancy sites in graphene molecular prototype (Co-N<sub>3</sub>-gra molecular prototype) on CO is investigated for the first time, as far as we know. As shown in Equations (1) and (2), CO can be oxidized in two reactions:



The catalytic oxidation of CO (Equation (1)) was investigated through two well-established pathways: the Eley–Rideal (ER) and LH mechanisms [37]. In the ER pathway, CO molecules from the gas phase react directly with pre-adsorbed oxygen molecules on the



cobalt site, forming a carbonate-like intermediate that undergoes subsequent dissociation. By contrast, the LH mechanism initiates with co-adsorbed CO and O<sub>2</sub> species that undergo intramolecular rearrangement before decomposing through a peroxide-like intermediate. Following CO<sub>2</sub> desorption, the residual atomic oxygen on the cobalt center retains catalytic activity, enabling continuous oxidation cycles through Equation (2) with minimal energy penalty.

The reaction adsorption energy is calculated using the following formula:

$$E_{\text{ads}} = E_{\text{total}} - E_{\text{adsorbate}} - E_{\text{cluster}} \quad (3)$$

where  $E_{\text{ads}}$ ,  $E_{\text{total}}$ ,  $E_{\text{adsorbate}}$ ,  $E_{\text{cluster}}$  denote the energies adsorbed on the Co atoms, total energy of combined cluster-and-adsorbate complex, the energy of the isolated adsorbate, and the energy of the isolated cluster model itself (e.g., the CoC<sub>9</sub>N<sub>3</sub>H<sub>9</sub> molecular prototype), respectively. Note that  $E_{\text{cluster}}$  represents the entire supported active site, not just the single metal atom.

The energy barriers mentioned above were evaluated at zero Kelvin (0 K). However, to account for the effects of temperature, the free-energy changes ( $\Delta G$ ) of the processes need to be corrected, resulting in the adjusted energy barriers  $E'_{\text{bar}}$ . The adjusted energy barriers can be calculated using the equation  $\Delta G = \Delta H - T\Delta S$ , where  $\Delta H$  the change in enthalpy,  $T$  is the room temperature (298.15 K), and  $\Delta S$  is the change in entropy. Given that  $\Delta H = \Delta U - P\Delta V$ ,  $\Delta U = \Delta E_{\text{tot}} + \Delta E_{\text{vib}} + \Delta E_{\text{trans}} + \Delta E_{\text{rot}}$  and  $\Delta S = \Delta S_{\text{vib}} + \Delta S_{\text{trans}} + \Delta S_{\text{rot}}$ , where  $\Delta U$  is the change in internal energy,  $\Delta E_{\text{tot}}$  is the change in total electronic energy obtained from DFT calculations, and the subscripts vib, trans, and rot represent the vibrational, translational, and rotational components, respectively.

In the CO oxidation process, the ER mechanism is followed. As described in previous studies [19,38], this process consists of multiple steps and involves various intermediate products. Every reaction step is characterized by a different transition state, such as the transition state in step 1 of Equation (1) labeled as TS1 in Figure 1a, and that in step 2 of Equation (1) noted by TS2 in Figure 1b. In the initial step (Figure 1a), the reaction begins with physically adsorbed CO molecules, which gradually approach the O<sub>2</sub> molecules on the Co surface. During the transition from the initial state (IS) to the TS, the O-O bond elongates from 1.39 Å to 2.67 Å, requiring an energy barrier of 0.91 eV to be overcome. Subsequently, the system enters an intermediate state (MS), forming a carbonate-like structure, which is accompanied by the cleavage of one O-O bond and the formation of two C-O bonds.

As shown in Figure 1b, the reaction proceeds further. From the MS to the TS2, an energy barrier of 1.48 eV needs to be overcome, ultimately leading to the formation of a CO<sub>2</sub> molecule. Adsorption energy of -0.269 eV is consistent with typical van der Waals interactions, confirming the physical nature of the binding in the final state (FS). It is worth noting that the energy of the MS is 0.96 eV lower than that of the FS, making MS more stable. From a thermodynamic perspective, this stability hinders the spontaneous desorption of the generated CO<sub>2</sub> molecule, which is consistent with the results of other related studies [19]. Thus, the quite big barriers of CO<sub>3</sub> formation and dissociation indicate that the CO oxidation on Co-N3-gra molecular prototype via the ER mechanism is difficult.

In the LH mechanism, when transitioning from IS to MS, an energy barrier of 1.21 eV needs to be overcome. When FS is formed, the O-O bond is stretched from 1.521 Å to 1.968 Å. Subsequently, CO<sub>2</sub> begins to dissociate. After overcoming an energy barrier of 0.28 eV, the O-O bond is broken, forming TS2 where the distance between C and Co is 2.408 Å, as shown in Figure 2. After that, the C-Co bond breaks, and CO<sub>2</sub> is successfully dissociated, generating FS where the distance between C and Co is 4.258 Å. The energy released in the entire process is 0.21 eV. Comparative analysis between ER and LH mechanisms reveals distinct energetic landscapes for these routes; the LH pathway demonstrates superior

kinetics due to its lower activation barrier of 0.85 eV after temperature corrections and energy-favorable dissociation between formed  $\text{CO}_2$  and the Co- $\text{N}_3$ -gra molecular prototype. This calculated barrier is competitive with experimental values reported for noble metal catalysts, such as Pt-based systems (1.0 eV) [39].

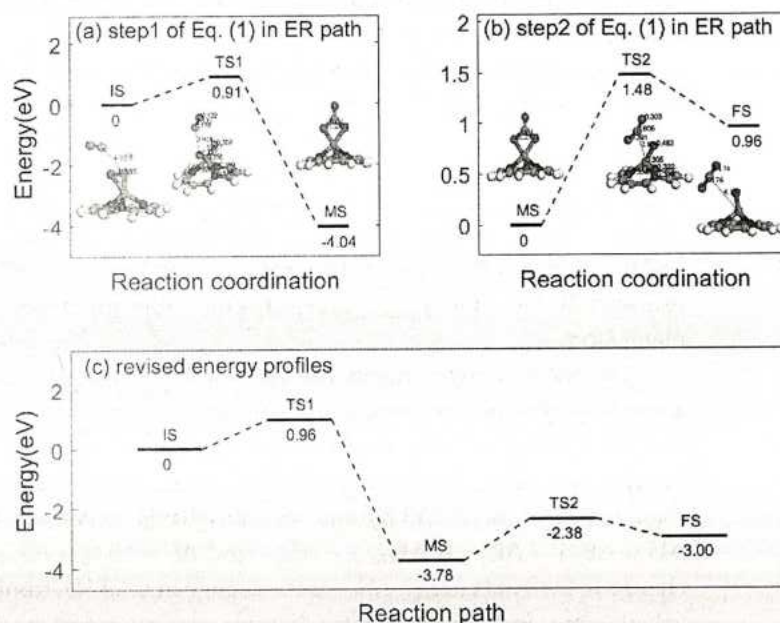


**Figure 1.** Catalytic reaction's energy profiles for CO oxidation over Co-3-gra molecular prototype with the ER mechanism. (a) Initial step of Equation (1) transitions from IS to MS via TS1. (b) Second step of Equation (1) moves from MS to FS via TS2. (c) Revised energy profile including temperature corrections: Red, gray, deep blue, light blue, and white color balls in the figures represent oxygen, carbon, nitrogen, cobalt, and hydrogen atoms, respectively.

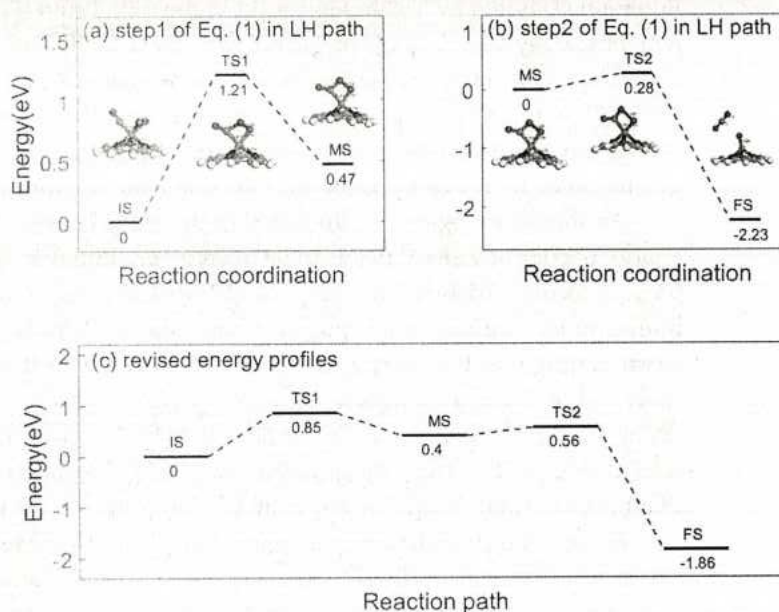


**Figure 2.** Catalytic reaction's energy profiles for catalytic CO oxidation over Co-3-gra molecular prototype with the LH mechanism. (a) Initial step of Equation (1) transitions from IS to MS via TS1. (b) Second step of Equation (1) moves from MS to FS via TS2. (c) Revised energy profile including temperature corrections.



Following Equation (1) discussed above, there is an oxygen ion remaining on the Co atom. In the reaction described by Equation (2), an oxygen ion on the Co surface reacts with another CO molecule to form CO<sub>2</sub>, with an energy barrier of 0.50 eV to be overcome (Figure 3a). The transition state in step 1 of Equation (2) is given by TS in Figure 3. This step releases an energy of 1.65 eV, which is significantly higher than the physisorption energy of CO<sub>2</sub> in the final state (FS) at 0.006 eV, indicating that the desorption of CO<sub>2</sub> is feasible [19]. Additionally, the validity of Equation (2) is supported by the reaction pathway in Equation (2) that starts with oxygen atoms [40].

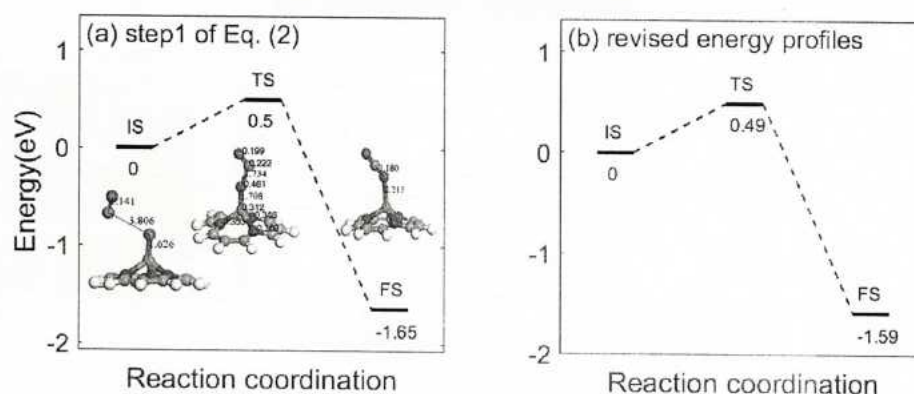


**Figure 3.** (a) Catalytic reaction's energy profiles for Equation (2) advances from IS to FS through TS. (b) Revised energy profile including temperature corrections.

The reaction paths following Equation (1) with LH mechanism and Equation (2) are thermally favorable, compared with those with ER mechanism. Partial density of states (PDOS) analysis for the LH mechanism and Equation (2) is given in Appendix A.1. It is also shown that inclusion of van der Waals interactions via DFT-D method does not alter the overall trends or conclusions of the active reaction pathways (LH and Equation (2)), as given in Appendix A.2. Reaction time for Figures 2a,b and 3a at room temperature is estimated by the following equation:

$$\tau = \nu^{-1} \exp\left(\frac{E_{\text{bar}}}{k_B T}\right) \quad (4)$$

where  $\nu$  is in order of  $10^{12}$  Hz, and  $k_B$  is the Boltzmann constant. For Figures 2a,b and 3a, we can obtain  $\tau_1 = 2.33 \times 10^{-2}$  s,  $\tau_2 = 2.9 \times 10^{-3}$  s, and  $\tau_3 = 1.92 \times 10^{-4}$  s, respectively. Therefore, the adsorption of oxygen ions by Co exhibits fast reaction kinetics for CO oxidation, indicating rapid kinetics for oxygen-ion-mediated oxidation.

## 2.2. Single-Electron Phenomena in Defective 2D Graphene

In this study, the potential applications of Co atom-doped graphene in SETs were explored through theoretical simulations and calculations. Figure 4a depicts a schematic diagram of the SET device. A single Co atom-embedded pyridinic nitrogen-doped graphene molecular prototype is placed between two electrodes and serves as the central island for controlling the horizontal electron transport. The gate electrode is located below the central island, and the electron-transport characteristics are controlled by adjusting the gate voltage to achieve precise regulation of the electrical properties of the device [41,42].

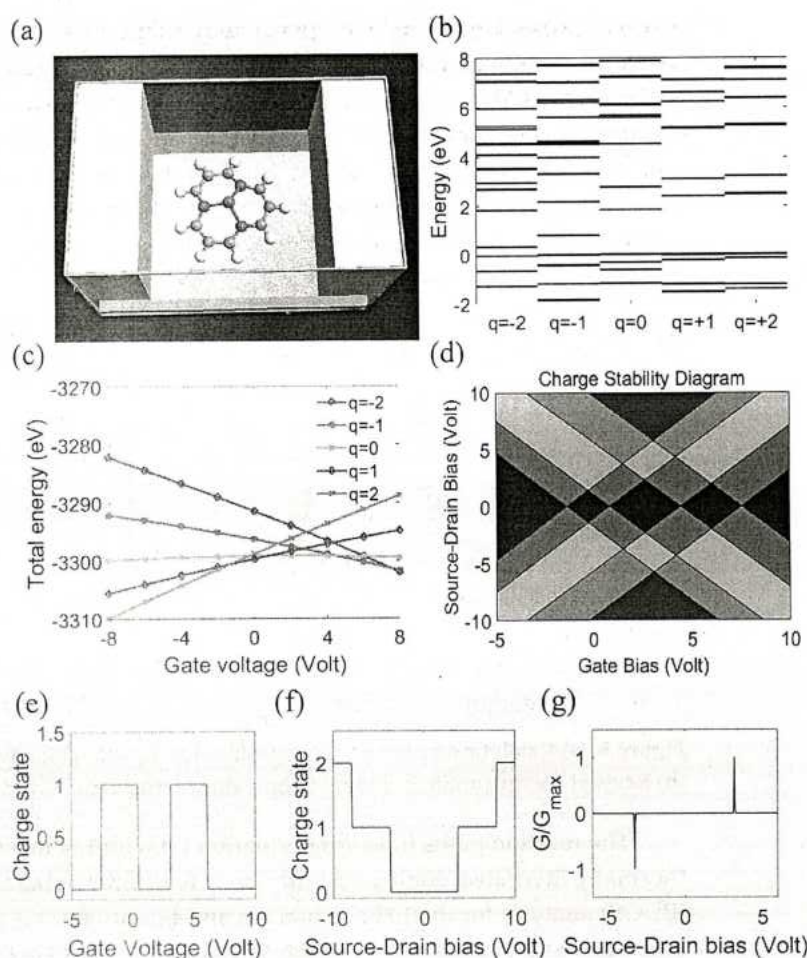


**Figure 4.** (a) The scheme of SET configuration with an island of a Co-N<sub>3</sub>-gra molecular prototype, (b) the energy distribution across different charge states, (c) the influence of gate voltage on energy, and (d) voltage-dependent charge stability diagram for the Co-N<sub>3</sub>-gra molecular prototype; the color scheme of dark blue, blue, green, orange, and red indicates the number of charge states of 0, 1, 2, 3, and 4, respectively. (e,f) Responses of charge states to gate voltage at fixed source-drain bias of 2.5 V, and its counterpart with fixed gate bias of −3.8 V, respectively, and (g) conductance under varying source-drain biases with fixed gate voltage of 0 V.

Figure 4b shows the energy distribution of Co atoms in different charge states. PDOS analysis for the neutral charge state is given in Appendix A.1. It can be seen that as the charge state changes from  $q = -2$  to  $q = +2$ , the energy levels exhibit obvious quantization characteristics. In particular, when the charge states are  $q = +1$  and  $q = +2$ , the energy levels are densely distributed near zero energy, indicating that these states are the most stable and most likely to be occupied under normal conditions. However, the energy levels for  $q = -2$ ,  $q = -1$ ,  $q = 0$ , and  $q = +1$  are relatively sparse and far from the zero-energy level, suggesting that these states have higher energies and are less likely to be occupied under normal conditions. This discrete energy-level distribution enables Co atoms to exhibit single-electron charging behavior during the charge transfer process.

Figure 4c further shows the relationship between the total energy of Co atoms in the SET and the gate voltage. The total energy is a large negative value due to the sum of the energies of all electrons and nuclei in the system. The physically relevant information is the relative change in energy with gate voltage. As the gate voltage changes, the total energy under different charge states exhibits non-linear changes, which are closely related to the capacitive characteristics of the system. To gain additional insights into how total



energy varies with gate voltage and to explore the electronic properties of various central island configurations, we performed DFT calculations and fitted the results to a quadratic function:  $E(q, V_g) = E_0 + qW + \alpha qV_g + \beta (eV_g)^2$  [32,41,42]. Here,  $E(q, V_g)$  is the total energy of the SET with charge state  $q$  and gate voltage  $V_g$ .  $E_0$  is a constant energy term,  $qW$  represents stored energy (a value of 5.28 eV is used to simulate gold electrodes), and  $\alpha qV_g$  describes the linear coupling between the island and gate electrode. For Co, the parameters are  $\alpha = 0.6477$  and  $\beta = -0.0054$ .

Figure 4d illustrates the charge stability diagram of the Co-based SET. With the source-drain bias voltage fixed, as the gate voltage is scanned, a series of periodic peaks can be observed, indicating that electrons are either added to or removed from the central island. These peaks form characteristic diamond-shaped regions in the  $V_g - V_{sd}$  plane, constituting the charge stability diagram. The existence of these regions demonstrates the stability of the Co-based SET in different charge states [5], providing visual evidence for the charge control of the SET.

To better observe the performance of the SET, Figure 4e shows the variation of the charge state of the Co-N<sub>3</sub>-gra molecular prototype with the gate bias under a fixed source-drain voltage of 2.5 volts, indicating that within a specific range of gate voltages, the Co-N<sub>3</sub>-gra molecular prototype can stably maintain a single-charge state. Figure 4f presents the changes in the charge states under different source-drain biases at a fixed gate bias of  $-3.8$  V. Figure 4g shows the variation of the maximum conductance of the Co-N<sub>3</sub>-gra molecular prototype under different source-drain biases, and the Co-N<sub>3</sub>-gra molecular prototype exhibits two conductance changes in the range from  $-5$  V to  $5$  V.

The quantized charge states and gate-tunable energy levels reveal the discrete electronic structure of Co sites. This enables precise probing of electron transfer processes—a capability we leverage to investigate catalytic interactions with bioactive gases.

### 2.3. Catalytic Design for Environmental Remediation

In this part, building on the electronic state mapping of Co sites (Section 2.2), we employ SETs to detect bioactive gases through adsorption-induced conductance changes. As a highly sensitive device, the SET can detect the charge of a single electron, giving it a unique advantage in molecular adsorption detection.

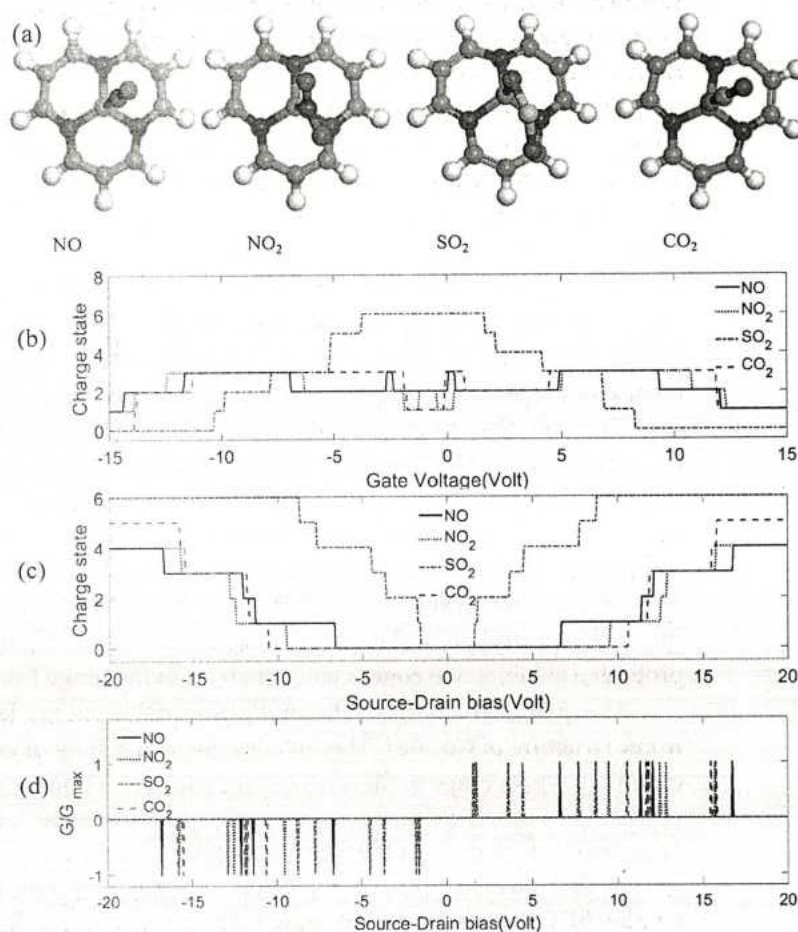
Figure 5a illustrates the binding models of NO, NO<sub>2</sub>, SO<sub>2</sub>, and CO<sub>2</sub> gas molecules with Co atoms. The adsorption structures formed between different gas molecules and Co atoms are distinct. The Co complexes can be regarded as islands within the SET configuration. PDOS analysis for the four Co complexes is given in Appendix A.1, reflecting the crucial role of Co-N<sub>3</sub> center in molecule absorption. The selectivity between gas molecules is quantified with adsorption energies and charge transfer values in Appendix B.1. Due to the different interactions between the molecules and the SET, it is possible to evaluate their sensitivity to the adsorption of gas molecules.

Figure 5b shows the relationship between the charge states of different gas molecules in the SET as a function of gate voltage. It can be observed that the charge states of NO<sub>2</sub> and CO<sub>2</sub> molecules undergo significant changes at lower voltages as the gate voltage increases, while NO and SO<sub>2</sub> molecules require higher voltages to cause changes in their charge states. This indicates that NO<sub>2</sub> and CO<sub>2</sub> molecules have stronger interactions with cobalt atoms, which can more easily lead to electron transfer within the SET.

Figure 5c further demonstrates the changes in charge states of various gas molecules under different source-drain biases. The results show that SO<sub>2</sub> can achieve charge state transitions at smaller source-drain biases, while NO, SO<sub>2</sub>, and CO<sub>2</sub> molecules require larger biases, consequently. Figure 5d shows the variation of normalized conductance of different



gas molecules in a SET with the source-drain bias, featuring distinct conductance peaks corresponding to specific air pollutants.



**Figure 5.** (a) Molecules of NO, NO<sub>2</sub>, SO<sub>2</sub>, and CO<sub>2</sub> adsorb onto the Co-N<sub>3</sub>-gra molecular prototype. (b) Impact of gate voltage on charge state at fixed source-drain bias of −15 V. (c) Effect of source-drain voltage on charge state at fixed gate bias of 0 V. (d) Influence of source-drain voltage on conductivity at fixed gate bias of 0 V.

It is important to note that this study focuses on the fundamental charge transfer-based sensing mechanism. Translating this principle into a practical device would necessitate addressing several engineering challenges, including the fabrication of large-scale, uniform arrays of Co-N<sub>3</sub> sites, the minimization of 1/f noise and charge noise in graphene-based SETs at room temperature, and ensuring long-term stability against oxidation and poisoning. Nonetheless, quantifying the intrinsic electronic response, as done here, is a critical first step for identifying promising material candidates for next-generation sensors.

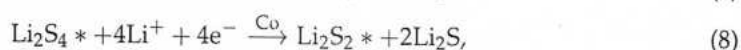
Co-N<sub>3</sub>-gra can also be used to detect more complex molecules containing hydrocarbon radicals such as methanol, ethanol, butanol, etc., which are extremely important for many practical applications [43–45]. A detailed study can be found in Appendix B.2. The unique structural and electrical response characteristics of Co atoms' adsorption to different air pollutant molecules provide a theoretical basis for the development of highly sensitive air pollutant molecule detection devices based on Co atoms.

#### 2.4. Stepwise Polysulfide Conversion Catalyzed by Atomic Cobalt Centers

Effective suppression of the polysulfide shuttle effect in Li-S batteries necessitates strong anchoring of lithium polysulfides (LiPSs). During discharge, sulfur undergoes stepwise re-

duction through adsorbed intermediates:  $S_8^* \rightarrow Li_2S_8^* \rightarrow Li_2S_6^* \rightarrow Li_2S_4^* \rightarrow Li_2S_2^* \rightarrow Li_2S^*$  where asterisks denote binding at Co-N<sub>3</sub>-gra catalytic sites (Figure 6). PDOS analysis for  $Li_2S^*$  represents the key of Co-N<sub>3</sub> center in anchoring of the LiPs, as given in Appendix A.1. This cascade serves as an ideal model system for probing how atomically dispersed Co catalysts control reaction kinetics and thermodynamics in multielectron transfer processes.

The overall discharge process involves the reduction of adsorbed sulfur:  $S_8 + 16Li^+ + 16e^- \rightarrow 8Li_2S$ , which encompasses multiple elementary steps with associated intermediates [46]. To resolve the catalytic function of atomic Co sites, we decompose this process into five concerted reactions:



where each step occurs at the Co-N<sub>3</sub> active sites.

To gain deeper mechanistic insights into polysulfide conversion catalyzed by Co-N<sub>3</sub>-gra, we systematically evaluated the Gibbs free-energy landscape for the sulfur reduction pathway. The computational hydrogen electrode approach [47] was employed to determine the free-energy change ( $\Delta G$ ) for each elementary step according to

$$\Delta G = \Delta E + \Delta ZPE - T\Delta S. \quad (10)$$

In this expression,  $\Delta E$  represents the reaction energy computed via DFT,  $\Delta ZPE$  accounts for zero-point energy (ZPE) variations,  $\Delta S$  corresponds to entropy adjustments, and  $T$  denotes the absolute temperature. Thermodynamically favorable processes exhibit negative  $\Delta G$  values (exergonic), whereas positive  $\Delta G$  indicates endergonic reactions requiring energy input. As demonstrated in Figure 7, all five lithium polysulfide formation reactions maintain negative free-energy values throughout the 0–500 K temperature range, confirming their spontaneous character under battery operating conditions.

Under typical battery operating conditions (ambient temperature, 293 K), the free-energy profile for sulfur reduction on Co-N<sub>3</sub>-gra reveals critical insights (Figure 8). The initial  $S_8^* \rightarrow Li_2S_8^*$  conversion exhibits the most negative  $\Delta G$  (−1.82 eV), confirming its exothermic and spontaneous nature. Analysis of the complete reaction pathway identifies the  $Li_2S_2^* \rightarrow Li_2S^*$  transition as kinetically limiting, with a substantial positive barrier of 3.52 eV—significantly higher than other elementary steps. This kinetic bottleneck originates from the solid–solid restructuring required for  $Li_2S_2$  to  $Li_2S$  conversion, whereas preceding transitions involve more facile phase changes, including  $S_8^* \rightarrow Li_2S_4^*$  as a dissolution-mediated solid-to-liquid transition,  $Li_2S_4^* \rightarrow Li_2S_2^*$  as a liquid-to-solid precipitation, and  $Li_2S_2$  to  $Li_2S$  as a solid–solid crystal transformation. Such phase-dependent barriers align with experimental reports of nucleation-limited kinetics in sulfur cathodes [48]. This barrier value is higher than barriers reported for other cobalt-based catalysts (e.g., 1.38 eV on Co(111) [49]), suggesting our Co-N<sub>3</sub> site needs further optimization. Future catalyst design should therefore focus on optimizing Co-S bonding interactions through coordination engineering to facilitate this critical solid-state conversion.



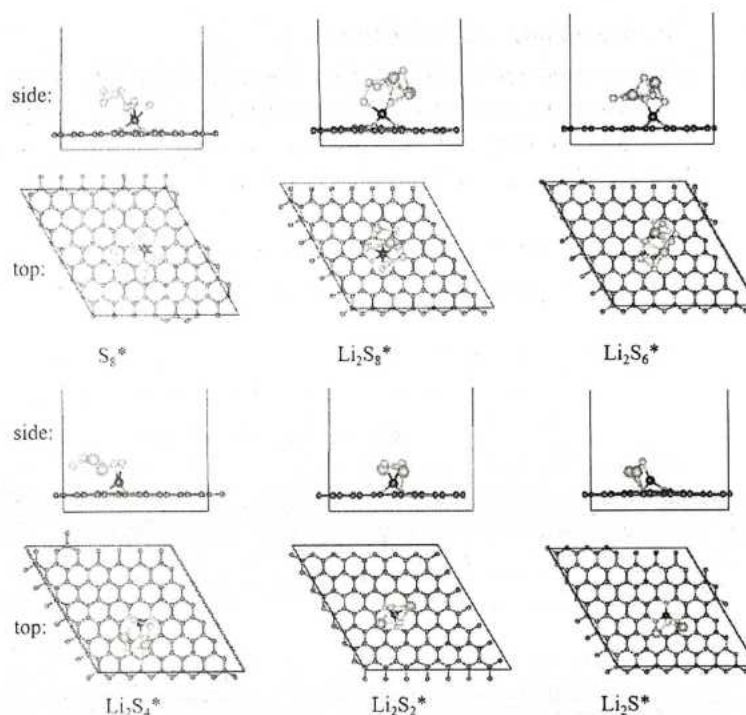


**Figure 6.** Side and top views of optimized geometrical configurations of sulfur species on Co-N<sub>3</sub>-gra surfaces. Brown, blue, green, and yellow color balls represent carbon, cobalt, lithium, and sulfur atoms, respectively.

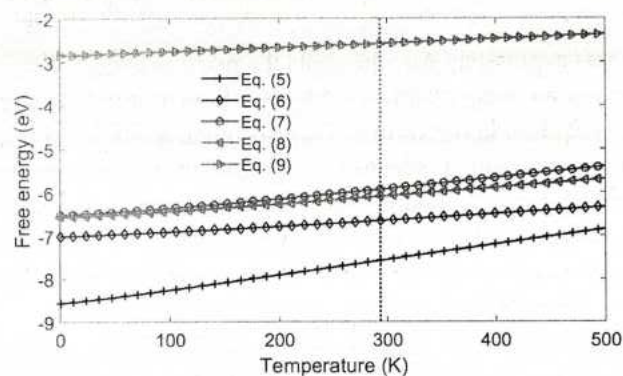


**Figure 7.** The Gibbs free-energy profile for Equations (5)–(9) from 0 to 500 K. The dotted vertical line marks the temperature of 293 K.

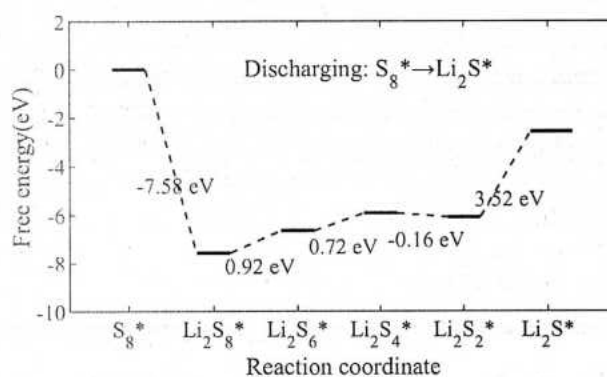


**Figure 8.** The Gibbs free-energy profile of LiPS species on the surface of Co-CN<sub>3</sub>-gra in the LiPS reduction process at the temperature of 293K.



### 3. Materials and Methods

In the study of properties and catalytic applications of Co atom-doped graphene, spin-unrestricted DFT is employed. The computational setup was designed to ensure both accuracy and efficiency for the diverse systems studied, ranging from molecular clusters to periodic surfaces and transport devices.

#### 3.1. Model Systems and Computation Details

In the work, two distinct types of models were utilized, depending on the application.

##### 3.1.1. Molecular Cluster Models (for CO Oxidation, SET, and Molecular Sensing)

The active site was modeled using a  $\text{CoC}_9\text{N}_3\text{H}_9$  molecular cluster (as shown in Figures 1–5), representing a single cobalt atom anchored in a pyridinic  $\text{N}_3$  vacancy within a finite graphene molecular prototype. This cluster size was carefully chosen to balance computational efficiency with the accurate representation of the electronic structure of the Co- $\text{N}_3$  center. For CO oxidation and gas adsorption energy calculations, computations were performed in the DMol3 module without periodic boundary conditions. This approach is standard for modeling isolated molecular reactions and is in agreement with conventional first-principles studies of Co-based absorption and catalysis [50,51]. For SET simulations, the  $\text{CoC}_9\text{N}_3\text{H}_9$  molecule served as the central island. Neumann boundary conditions were adopted, following established first-principles modeling practices for molecular-scale electronic devices [41]. Simulations were conducted using QuantumATK software 2019, combining DFT with the non-equilibrium Green's function (NEGF) formalism. The DFT-NEGF method was used to investigate the charging energies in SETs, while self-consistent-charge DFT was employed to study the electronic properties of the Co atoms' structures [32,52], ensuring model stability and the accurate capture of discrete energy levels and Coulomb blockade effects.

##### 3.1.2. Periodic Model (for Li-S Battery Applications)

A periodic model was constructed using a  $7 \times 7$  graphene supercell (in-plane lattice parameter of 2.46 Å) with a single Co- $\text{N}_3$  center. A vacuum layer of 15 Å was added along the z-direction to decouple the periodic slabs and prevent any spurious interactions between them, which is sufficient for convergence of the electronic structure.

#### 3.2. Exchange-Correlation Functional and Basis Set

The Perdew–Burke–Ernzerhof (PBE) functional within the generalized gradient approximation (GGA) was employed for all calculations. While this functional possibly underestimates absolute reaction barriers, it provides a well-established and computationally efficient framework for describing catalytic reaction mechanisms [19], adsorption energetics, and electronic structures in carbon-based materials and transition-metal complexes, and its use is consistent with previous computational studies of cobalt-based catalysts [50,51]. The double numerical plus polarization (DNP) basis set was used throughout this work. The DNP basis set is the default in the DMol3 module, offering good accuracy in describing both the localized d-orbitals of the cobalt atom and the delocalized  $\pi$ -system of the graphene substrate. Grimme's DFT-D method was used to account for dispersion interactions. Core electrons were treated with DFT semi-core pseudopotentials (DSPPs) to account for relativistic effects [6,53–55].

#### 3.3. Convergence Parameters and Transition State Search

During the calculations, the energy convergence tolerance was set to  $5 \times 10^{-7}$  Hartree, the maximum force to 0.005 Hartree/Å, and the displacement to 0.05 Å, to ensure the precision of the calculations. To determine the minimum energy path for the CO oxidation

reaction, the linear synchronous transit/quadratic synchronous transit (LST/QST) methods were utilized [56]. The vibrational frequencies were calculated to obtain the zero-point energy (ZPE) and thermal corrections to the Gibbs free energy.

#### 4. Conclusions

This computational study demonstrates that the multifunctionality of single-atom cobalt-doped graphene stems from a common root: the tunable electronic structure of the Co-N<sub>3</sub> active site. The ability of this site to undergo charge redistribution enables it to facilitate catalytic cycles, alter conductance in SETs for sensing, and enhance reaction kinetics in batteries. Our key findings reveal that in catalytic applications, Co-N<sub>3</sub>-gra molecular prototypes drive efficient CO oxidation via LH pathways, with the rate-limiting step exhibiting a 0.85 eV barrier. The coordination environment critically tunes reaction energetics, as shown in the contrasting mechanisms between ER and LH pathways. For electronic and sensing applications, quantum confinement in nanoscale molecular prototypes creates discrete energy states that enable precise SET operation. When configured as Coulomb islands, these systems detect adsorption events through characteristic conductance shifts—particularly for environmentally relevant gases like NO, NO<sub>2</sub>, SO<sub>2</sub>, and CO<sub>2</sub>. In energy storage, periodic Co-N<sub>3</sub>-gra models significantly mitigate the polysulfide shuttle effect in Li-S batteries. Our work identifies the Li<sub>2</sub>S<sub>2</sub> → Li<sub>2</sub>S conversion as the rate-limiting step and quantifies its challenging barrier, providing a key metric for future catalyst design. This work demonstrates that the electronic structure of a single Co-N<sub>3</sub> active site serves as a unified platform for multifunctional applications. We elucidate the mechanism by which charge redistribution at this specific site simultaneously governs its catalytic, sensing, and energy storage functionalities.

**Author Contributions:** Conceptualization, Z.H. and G.L.; methodology, Z.H. and L.D.; software, M.B. and C.Y.; validation, Y.Z., C.L. and L.D.; formal analysis, Z.H., L.D. and G.L.; investigation, Z.H., Y.Z., C.L., L.D., B.S. and H.L.; resources, G.L.; data curation, Y.Z., C.L., L.D. and B.S.; writing—original draft preparation, Y.Z.; writing—review and editing, Z.H.; visualization, Z.H., Y.Z. and C.L.; supervision, G.L.; project administration, Z.H. and G.L.; funding acquisition, Z.H. All authors have read and agreed to the published version of the manuscript.

**Funding:** This research was funded by the Science and Technology Research project of Chongqing Education Commission under No. KJQN202201421 and KJQN202401422, and the Fuling District guiding scientific research project under No. FLKJ.2024BAG5130.

**Institutional Review Board Statement:** Not applicable.

**Informed Consent Statement:** Not applicable.

**Data Availability Statement:** Data are contained within the article. Further inquiries can be directed to the corresponding author.

**Acknowledgments:** We would like to express our sincere gratitude to Yangtze Normal University and Nankai University for providing the equipment for this research.

**Conflicts of Interest:** The authors declare no conflicts of interest.

## Appendix A. Electronic Structures Analysis

### Appendix A.1. PDOS Analysis

Figure A1 clearly shows hybridization of d orbital of Co, CO, and O<sub>2</sub> during the LH catalytic circle. In the initial state, the O<sub>2</sub> molecule is significantly activated upon adsorption, as evidenced by the elongated O-O bond and the hybridization between Co-d orbitals and O<sub>2</sub> orbitals near the Fermi level. At the transition state, this hybridization intensifies, and a new emerging state indicates electron redistribution towards the formation of the peroxide-



like intermediate, concomitant with O-O bond weakening. Figure A2 displays the active charge redistribution for Co, CO, and O for the Equation (2) mechanism. The Co-adsorbed atomic oxygen site exhibits a highly reactive electronic state. This state readily interacts with the approaching CO molecule, leading to a low-barrier transition state characterized by Co-O-C hybridization. Comparing with Figure 2 and Figure 3 in the main context, the bond cleavage is accompanied by a significant charge redistribution, as revealed by our PDOS analysis above. The electronic structure evolution directly drives the catalytic cycle. Figures A3–A5 present the PDOS analysis for Co-N<sub>3</sub>-gra molecular prototype as SET island, for NO, NO<sub>2</sub>, SO<sub>2</sub>, and CO<sub>2</sub> adsorbed onto the Co-N<sub>3</sub>-gra molecular prototype, and for representative LiPs on Co-N<sub>3</sub> graphene, respectively. It can be found that Co serves as active sites due to clear hybridization between Co-d orbitals and neighboring states of atoms/molecules.

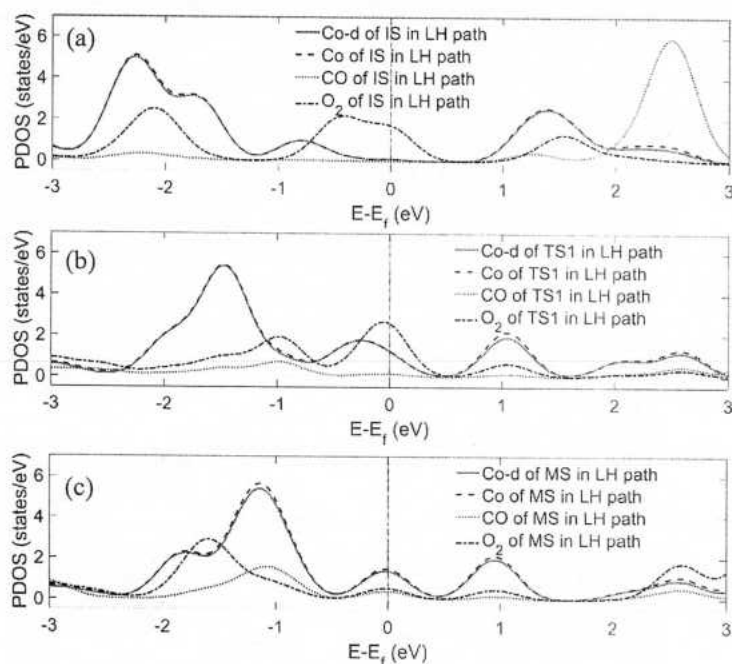


Figure A1. PDOS analysis for (a) IS, (b) TS1, and (c) MS in the LH path.

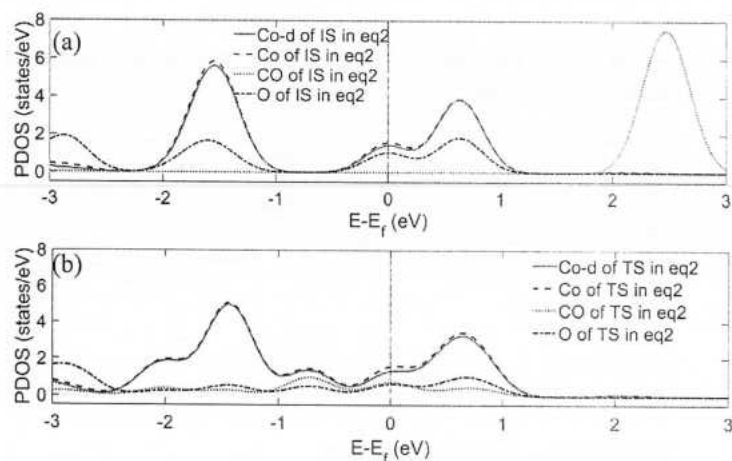


Figure A2. PDOS analysis for (a) IS and (b) TS in the path of Equation (2).



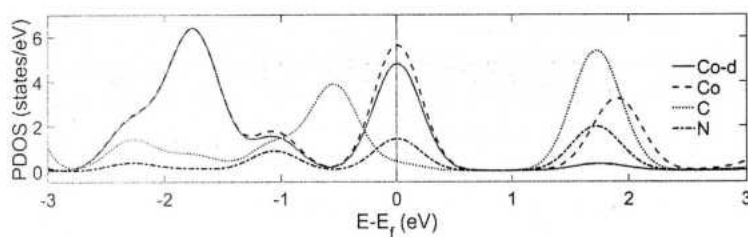


Figure A3. PDOS analysis for the Co-N<sub>3</sub>-gra molecular prototype.

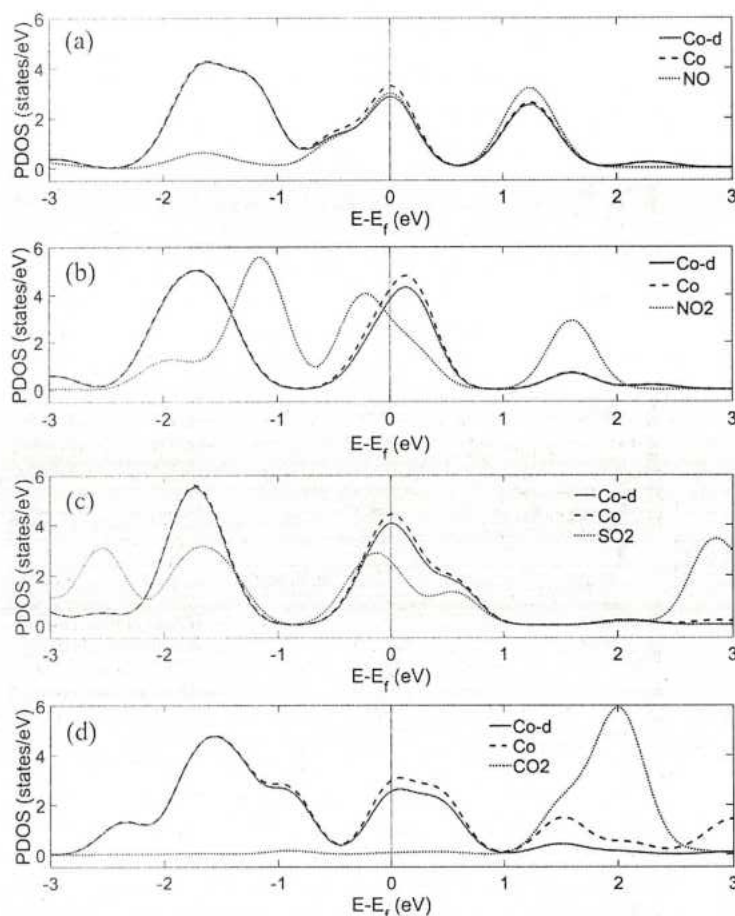


Figure A4. PDOS analysis for (a) NO, (b) NO<sub>2</sub>, (c) SO<sub>2</sub>, and (d) CO<sub>2</sub> adsorbed onto the Co-N<sub>3</sub>-gra molecular prototype.

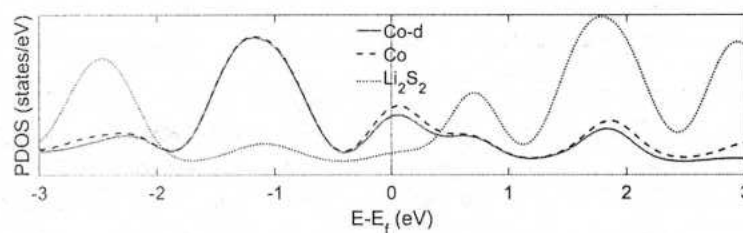
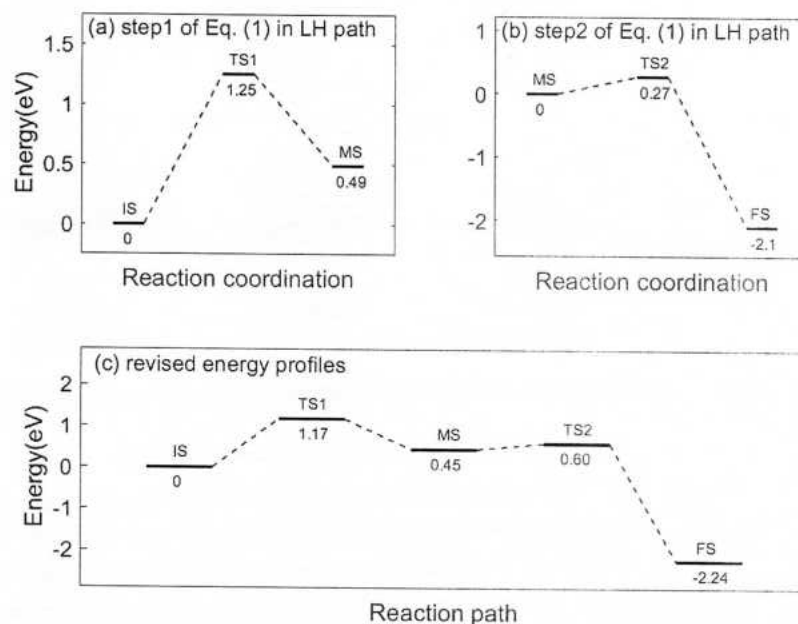


Figure A5. PDOS analysis for LiPs.

#### Appendix A.2. DFT-D Correction

Inclusion of vdW corrections does not alter the overall trends or conclusions of the active reaction pathways (LH and Equation (2)). The relative energy landscape and the identity of the rate-limiting step remain unchanged. The revised energy profiles (with vdW corrections) are now included in the Figures A6 and A7 for transparency.



**Figure A6.** Catalytic reaction's energy profiles for catalytic CO oxidation over Co-3-gra molecular prototype with the LH mechanism. (a) Initial step of Equation (1) transitions from IS to MS via TS1. (b) Second step of Equation (1) moves from MS to FS via TS2. (c) Revised energy profile including temperature corrections. Vdw correction is adopted for related calculations.

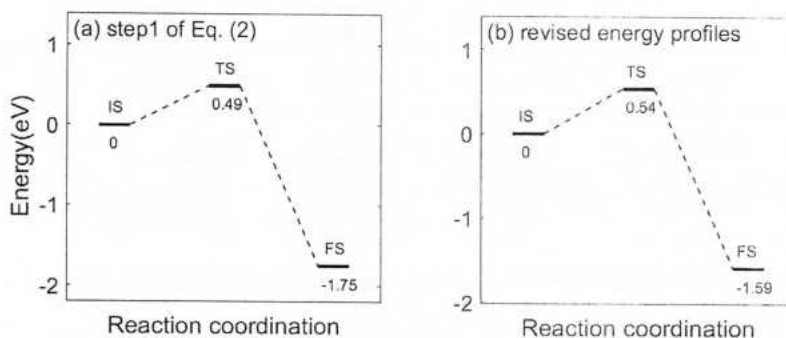


**Figure A7.** (a) Catalytic reaction's energy profiles for Equation (2) advance from IS to FS through TS. (b) Revised energy profile including temperature corrections. Vdw correction is adopted for related calculations.

## Appendix B. Sensing

### Appendix B.1. Charge Transfer Mechanism

The selectivity can be rigorously quantified by the adsorption strength and the amount of charge transfer, as summarized in the above figure. NO<sub>2</sub> exhibits the strongest adsorption (−0.128 eV), confirming it as the most sensitive analyte. This is followed by NO, SO<sub>2</sub>, and CO<sub>2</sub>, which correlates perfectly with the conductance shift trends in Figure 5. This quantitative analysis removes any ambiguity in the selectivity ordering. Furthermore, it directly links the sensing mechanism to the catalytic process: the strong charge transfer to NO<sub>2</sub> mirrors its role as an oxidant in catalytic cycles, unifying the functionality of the Co-N<sub>3</sub> site across different applications.

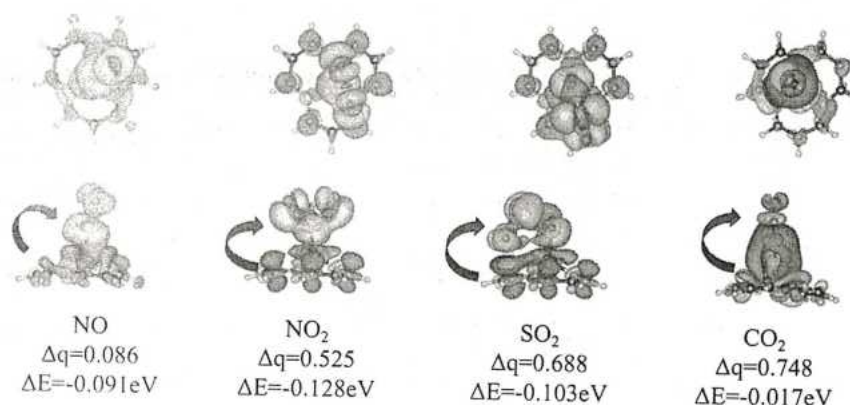


Figure A8. Charge density difference, absorption energy, and Bader charge for air pollutant sensing.

#### Appendix B.2. Detection of Hydrocarbon Radicals

This section illustrates the detection of more complex molecules containing hydrocarbon radicals such as methanol, ethanol, and butanol. Figure A9a illustrates the binding models of butanol, ethanol, and methanol molecules with the Co-N<sub>3</sub>-gra molecular prototype. Figure A9b–d display the effect of gate voltage on charge state at fixed source-drain bias of -15 V, impact of source-drain voltage on charge state at fixed gate bias of 0 V, and influence of source-drain voltage on conductivity at fixed gate bias of 0 V, respectively. Due to the different interactions between the molecules and the SET, it is possible to evaluate their sensitivity to the adsorption of studied molecules.

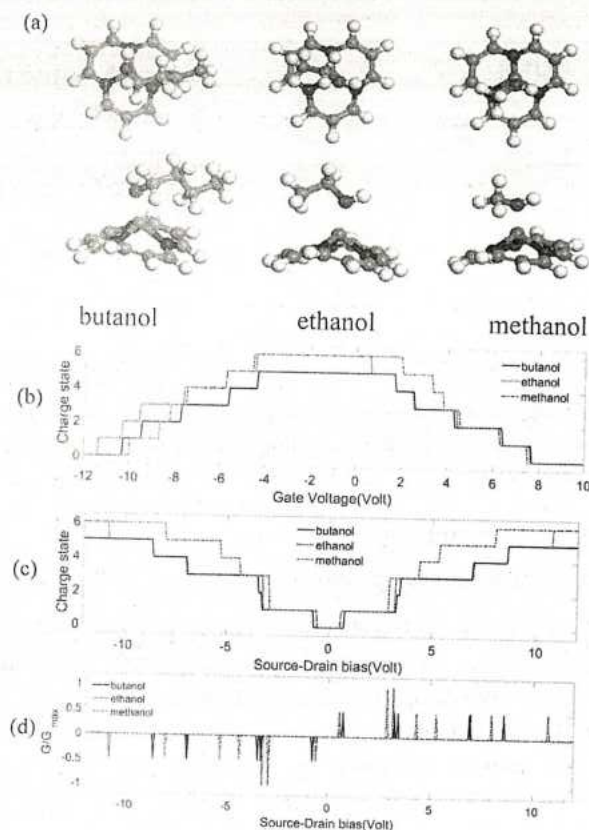


Figure A9. (a) Molecules of methanol, ethanol, and butanol adsorb onto the Co-N<sub>3</sub>-gra molecular prototype. (b) Impact of gate voltage on charge state at fixed source-drain bias of -15 V. (c) Effect of source-drain voltage on charge state at fixed gate bias of 0 V. (d) Influence of source-drain voltage on conductivity at fixed gate bias of 0 V.



## References

- Yang, X.-F.; Wang, A.; Qiao, B.; Li, J.; Liu, J.; Zhang, T. Single-atom catalysts: A new frontier in heterogeneous catalysis. *Accounts Chem. Res.* **2013**, *46*, 1740–1748. [CrossRef] [PubMed]
- Gambardella, P.; Rusponi, S.; Veronese, M.; Dhessi, S.S.; Grazioli, C.; Dallmeyer, A.; Cabria, I.; Zeller, R.; Dederichs, P.H.; Kern, K.; et al. Giant magnetic anisotropy of single cobalt atoms and nanoparticles. *Science* **2003**, *300*, 1130–1133. [CrossRef] [PubMed]
- Ipadeola, A.K.; Chitt, M.; Abdelgawad, A.; Eid, K.; Abdullah, A.M. Graphene-based catalysts for carbon monoxide oxidation: Experimental and theoretical insights. *Int. J. Hydrogen Energy* **2023**, *48*, 17434–17467. [CrossRef]
- Park, J.; Pasupathy, A.N.; Goldsmith, J.I. Coulomb blockade and the Kondo effect in single-atom transistors. *Nature* **2002**, *417*, 722–725. [CrossRef]
- Rani, S.; Ray, S.J. Detection of gas molecule using C<sub>3</sub>N island single electron transistor. *Carbon* **2019**, *144*, 235–240. [CrossRef]
- Shabeeb, M.; Maity, S. Computational investigation on adsorption and activation of atmospheric pollutants co, no and so on small cobalt clusters. *Chem. Phys.* **2024**, *582*, 112291. [CrossRef]
- Wang, F.; Li, J.; Zhao, J.; Yang, Y.; Su, C.; Zhong, Y.L.; Yang, Q.H.; Lu, J. Single-atom electrocatalysts for lithium sulfur batteries: Progress, opportunities, and challenges. *ACS Mater. Lett.* **2020**, *2*, 1450–1463. [CrossRef]
- Ozols, K.; Jang, Y.S.; Cramer, N. Chiral cyclopentadienyl cobalt(iii) complexes enable highly enantioselective 3d-metal-catalyzed c-h functionalizations. *J. Am. Chem. Soc.* **2019**, *141*, 5675–5680. [CrossRef]
- Cao, L.; Luo, Q.; Liu, W.; Lin, Y.; Liu, X.; Cao, Y.; Zhang, W.; Wu, Y.; Yang, J.; Yao, T.; et al. Identification of single-atom active sites in carbon-based cobalt catalysts during electrocatalytic hydrogen evolution. *Nat. Catal.* **2019**, *2*, 134–141. [CrossRef]
- Hood, D.M.; Johnson, R.A.; Carpenter, A.E.; Younker, J.M.; Vinyard, D.J.; Stanley, G.G. Highly active cationic cobalt(ii) hydroformylation catalysts. *Science* **2020**, *367*, 542–548. [CrossRef]
- MacNeil, C.S.; Mendelsohn, L.N.; Pabst, T.P.; Hierlmeier, G.; Chirik, P.J. Alcohol synthesis by cobalt-catalyzed visible-light-driven reductive hydroformylation. *J. Am. Chem. Soc.* **2022**, *144*, 19219–19224. [CrossRef]
- Delolo, F.G.; Yang, J.; Neumann, H.; Dos Santos, E.N.; Gusevskaya, E.V.; Beller, M. Cobalt-catalyzed hydroformylation under mild conditions in the presence of phosphine oxides. *ACS Sustain. Chem. Eng.* **2021**, *9*, 5148–5154. [CrossRef]
- Hebrard, F.; Kalck, P. Cobalt-catalyzed hydroformylation of alkenes: Generation and recycling of the carbonyl species, and catalytic cycle. *Chem. Rev.* **2009**, *109*, 4272–4282. [CrossRef] [PubMed]
- Zhang, B.; Kubis, C.; Franke, R. Hydroformylation catalyzed by unmodified cobalt carbonyl under mild conditions. *Science* **2022**, *377*, 1223–1227. [CrossRef] [PubMed]
- Gao, K.; Yoshikai, N. Low-valent cobalt catalysis: New opportunities for c-h functionalization. *Accounts Chem. Res.* **2014**, *47*, 1208–1219. [CrossRef]
- Nakanowatari, S.; Mei, R.; Feldt, M.; Ackermann, L. Cobalt(iii)-catalyzed hydroarylation of allenes via c-h activation. *ACS Catal.* **2017**, *7*, 2511–2515. [CrossRef]
- Oliveira, J.C.; Dhawa, U.; Ackermann, L. Insights into the mechanism of low-valent cobalt-catalyzed c-h activation. *ACS Catal.* **2021**, *11*, 1505–1515. [CrossRef]
- Li, T.; Shen, C.; Sun, Y.; Zhang, J.; Xiang, P.; Lu, X.; Zhong, G. Cobalt-catalyzed olefinic c-h alkenylation/alkylation switched by carbonyl groups. *Org. Lett.* **2019**, *21*, 7772–7777. [CrossRef]
- Zhang, X.; Lu, Z.; Yang, Z. Single non-noble-metal cobalt atom stabilized by pyridinic vacancy graphene: An efficient catalyst for co oxidation. *J. Mol. Catal. A Chem.* **2016**, *417*, 28–35. [CrossRef]
- Hu, W.; Wang, C.; Tan, H.; Duan, H.; Li, G.; Li, N.; Ji, Q.; Lu, Y.; Wang, Y.; Sun, Z.; et al. Embedding atomic cobalt into graphene lattices to activate room-temperature ferromagnetism. *Nat. Commun.* **2021**, *12*, 1854. [CrossRef]
- Gallagher, C.; Siddiqui, W.; Arnold, T.; Cheng, C.; Su, E.; Zhao, Q. Benchmarking a Molecular Flake Model on the Road to Programmable Graphene-Based Single-Atom Catalysts. *J. Phys. Chem. C* **2024**, *128*, 2876–2883. [CrossRef]
- Graf, H.; Vancea, J.; Hoffmann, H. Single-electron tunneling at room temperature in cobalt nanoparticles. *Appl. Phys. Lett.* **2002**, *80*, 1264–1266. [CrossRef]
- Li, Z.; Wang, Z.; Xi, S.; Zhao, X.; Sun, T.; Li, J.; Yu, W.; Xu, H.; Herng, T.S.; Hai, X.; et al. Tuning the spin density of cobalt single-atom catalysts for efficient oxygen evolution. *ACS Nano* **2021**, *15*, 7105–7113. [CrossRef]
- Wu, D.; Tan, Z.; Feng, X.; Anderson, W.A.; Li, Q. Regeneration of cobalt complexes by thermal decomposition and acid treatment for no absorption. *Chem. Eng. J.* **2017**, *315*, 233–242. [CrossRef]
- Shen, Y.; Deng, J.; Impeng, S.; Li, S.; Yan, T.; Zhang, J.; Shi, L.; Zhang, D. Boosting toluene combustion by engineering co-o strength in cobalt oxide catalysts. *Environ. Sci. Technol.* **2020**, *54*, 10342–10350. [CrossRef] [PubMed]
- Bessell, S. Support effects in cobalt-based fischer-tropsch catalysis. *Appl. Catal. A Gen.* **1993**, *96*, 253–268. [CrossRef]
- Bruce, P.G.; Freunberger, S.A.; Hardwick, L.J.; Tarascon, J.M. Li–O<sub>2</sub> and Li–S batteries with high energy storage. *Nat. Mater.* **2012**, *11*, 19–29. [CrossRef]
- Manthiram, A.; Fu, Y.; Su, Y.S. Challenges and prospects of lithium-sulfur batteries. *Accounts Chem. Res.* **2013**, *46*, 1125–1134. [CrossRef]



29. Yin, H.; He, J.; Xiao, B.; Zhou, M.; Wang, W.; Joao, C.; Chen, Z.; Hou, Z.; Zhang, T.; Yu, Z. Advances and prospects of g-C<sub>3</sub>N<sub>4</sub> in lithium-sulfur batteries. *Nano Res. Energy* **2024**, *3*, e9120138. [CrossRef]
30. Feng, S.; Zhong, H.; Song, J.; Zhu, C.; Dong, P.; Shi, Q.; Liu, D.; Li, J.; Chang, Y.C.; Beckman, S.P.; et al. Catalytic activity of co-x (x = s, p, o) and its dependency on nanostructure/chemical composition in lithium-sulfur batteries. *ACS Appl. Energy Mater.* **2018**, *1*, 7014–7021. [CrossRef]
31. Gu, Z.; Cheng, C.; Yan, T.; Liu, G.; Jiang, J.; Mao, J.; Dai, K.; Li, J.; Wu, J.; Zhang, L. Synergistic effect of Co<sub>3</sub>Fe<sub>7</sub> alloy and n-doped hollow carbon spheres with high activity and stability for high-performance lithium-sulfur batteries. *Nano Energy* **2021**, *86*, 106111. [CrossRef]
32. Huang, T.; Sun, Y.; Wu, J.; Jin, J.; Wei, C.; Shi, Z.; Wang, M.; Cai, J.; An, X.T.; Wang, P.; et al. A dual-functional fibrous skeleton implanted with single-atomic co-nxdispersions for longevous li-s full batteries. *ACS Nano* **2021**, *15*, 14105–14115. [CrossRef]
33. Sun, X.; Qiu, Y.; Jiang, B.; Chen, Z.; Zhao, C.; Zhou, H.; Yang, L.; Fan, L.; Zhang, Y.; Zhang, N. Isolated fe-co heteronuclear diatomic sites as efficient bifunctional catalysts for high-performance lithium-sulfur batteries. *Nat. Commun.* **2023**, *14*, 291. [CrossRef]
34. Yang, C.; Li, Y.; Peng, W.; Zhang, F.; Fan, X. In situ n-doped CoS<sub>2</sub> anchored on mxene toward an efficient bifunctional catalyst for enhanced lithium-sulfur batteries. *Chem. Eng. J.* **2022**, *427*, 131792. [CrossRef]
35. Li, Y.; Wu, J.; Zhang, B.; Wang, W.; Zhang, G.; Seh, Z.W.; Zhang, N.; Sun, J.; Huang, L.; Jiang, J.; et al. Fast conversion and controlled deposition of lithium (poly)sulfides in lithium-sulfur batteries using high-loading cobalt single atoms. *Energy Storage Mater.* **2020**, *30*, 250–259. [CrossRef]
36. Wang, Y.; Chu, F.; Zeng, J.; Wang, Q.; Naren, T.; Li, Y.; Cheng, Y.; Lei, Y.; Wu, F. Single atom catalysts for fuel cells and rechargeable batteries: Principles, advances, and opportunities. *ACS Nano* **2021**, *15*, 210–239. [CrossRef]
37. Liu, X.; Sui, Y.; Duan, T.; Meng, C.; Han, Y. Monodisperse pt atoms anchored on n-doped graphene as efficient catalysts for co oxidation: A first-principles investigation. *Catal. Sci. Technol.* **2015**, *5*, 1658–1667. [CrossRef]
38. Li, Y.; Zhou, Z.; Yu, G.; Chen, W.; Chen, Z. Co catalytic oxidation on iron-embedded graphene: Computational quest for low-cost nanocatalysts. *J. Phys. Chem. C* **2010**, *114*, 6250–6254. [CrossRef]
39. Therrien, A.J.; Hensley, A.J.R.; Marcinkowski, M.D.; Zhang, R.; Lucci, F.R.; Coughlin, B.; Schilling, A.C.; McEwen, J.S.; Sykes, E.C.H. An atomic-scale view of single-site Pt catalysis for low-temperature CO oxidation. *Nat. Catal.* **2018**, *1*, 192–198. [CrossRef]
40. Tang, Y.; Chen, W.; Zhou, J.; Chai, H.; Li, Y.; Cui, Y.; Feng, Z.; Dai, X. Mechanistic insight into the selective catalytic oxidation for no and co on co-doping graphene sheet: A theoretical study. *Fuel* **2019**, *253*, 1531–1544. [CrossRef]
41. Stokbro, K. First-principles modeling of molecular single-electron transistors. *J. Phys. Chem. C* **2010**, *114*, 20461–20465. [CrossRef]
42. Khademhosseini, V.; Dideban, D.; Ahmadi, M.T.; Ismail, R.; Heidari, H. Impact of hydrogen adsorption on the performance of a single electron transistor utilizing fullerene quantum dots. *ECS J. Solid State Sci. Technol.* **2018**, *7*, M191–M194. [CrossRef]
43. Pronin, I.A.; Plugin, I.A.; Kolosov, D.A.; Karmanov, A.A.; Yakushova, N.D.; Varezchnikov, A.S.; Komolov, A.S.; Lazneva, E.F.; Koroleva, A.V.; Moshnikov, V.A.; et al. Sol-gel derived zno film as a gas sensor: Influence of uv processing versus a thermal annealing. *Sens. Actuators A Phys.* **2024**, *377*, 115707. [CrossRef]
44. Zhao, Q.; Liu, Z.; Xu, Z.; Li, B.; Yang, S. rGO/In<sub>2</sub>O<sub>3</sub> heterostructures based gas sensor for efficient ppb-level n-butanol detection. *J. Alloys Compd.* **2024**, *986*, 174154. [CrossRef]
45. Pardeshi, N.M.; Ghuge, R.S.; Birla, P.N.; Chauhan, R.; Bhalekar, S.P.; Shinde, M.D.; Sivalingam, Y.; Kale, R.D.; Rane, S.B. Reduced graphene oxide@bimodal TiO<sub>2</sub> nanocomposites as an efficacious console for room temperature n-butanol gas sensing. *ACS Appl. Electron. Mater.* **2024**, *6*, 4805–4818. [CrossRef]
46. Song, M.K.; Cairns, E.J.; Zhang, Y. Lithium/sulfur batteries with high specific energy: Old challenges and new opportunities. *Nanoscale* **2013**, *5*, 2186–2204. [CrossRef]
47. Nørskov, J.K.; Rossmeisl, J.; Logadottir, A.; Lindqvist, L.; Kitchin, J.R.; Bligaard, T.; Jónsson, H. Origin of the overpotential for oxygen reduction at a fuel-cell cathode. *J. Phys. Chem. B* **2004**, *108*, 17886–17892. [CrossRef] [PubMed]
48. Shen, C.; Xie, J.; Zhang, M.; Andrei, P.; Zheng, J.P.; Hendrickson, M.; Plichta, E.J. A li-li<sub>2</sub>s<sub>4</sub> battery with improved discharge capacity and cycle life at low electrolyte/sulfur ratios. *J. Power Sources* **2019**, *414*, 412–419. [CrossRef]
49. Zhang, H.; Xin, S.; Li, J.; Cui, H.; Liu, Y.; Yang, Y.; Wang, M. Synergistic regulation of polysulfides immobilization and conversion by MOF-derived CoP-HNC nanocages for high-performance lithium-sulfur batteries. *Nano Energy* **2021**, *85*, 106011. [CrossRef]
50. Molavi, R.; Safaiee, R.; Sheikhi, M.H. Oxygen adsorption properties of small cobalt oxide clusters: Application feasibility as oxygen gas sensors. *Phys. Chem. Chem. Phys.* **2020**, *22*, 14889–14899. [CrossRef] [PubMed]
51. Molavi, R.; Safaiee, R.; Sheikhi, M.H.; Hassani, N. Theoretical perspective on co oxidation over small cobalt oxide clusters. *Chem. Phys. Lett.* **2021**, *767*, 138361. [CrossRef]
52. Huang, Z.; Qu, J.; Peng, X.; Liu, W.; Zhang, K.; Wei, X.; Zhong, J. Quantum confinement in graphene quantum dots. *Phys. Status Solidi Rapid Res. Lett.* **2014**, *8*, 436–440. [CrossRef]
53. Zayed, A.O.H.; Daud, M.N.; Zain, S.M. Global structural optimization and growth mechanism of cobalt oxide nanoclusters by genetic algorithm with spin-polarized dft. *J. Alloys Compd.* **2017**, *695*, 2513–2518. [CrossRef]

54. Xie, Y.; Dong, F.; Heinbuch, S.; Rocca, J.J.; Bernstein, E.R. Oxidation reactions on neutral cobalt oxide clusters: Experimental and theoretical studies. *Phys. Chem. Chem. Phys.* **2010**, *12*, 947–959. [CrossRef]
55. Johnson, G.E.; Reveles, J.U.; Reilly, N.M.; Tyo, E.C.; Khanna, S.N.; Castleman, A.W. Influence of stoichiometry and charge state on the structure and reactivity of cobalt oxide clusters with co. *J. Phys. Chem. A* **2008**, *112*, 11330–11340. [CrossRef]
56. Li, M.R.; Chen, J.; Wang, G.C. Reaction mechanism of ethanol on model cobalt catalysts: Dft calculations. *J. Phys. Chem. C* **2016**, *120*, 14198–14208. [CrossRef]

**Disclaimer/Publisher's Note:** The statements, opinions and data contained in all publications are solely those of the individual author(s) and contributor(s) and not of MDPI and/or the editor(s). MDPI and/or the editor(s) disclaim responsibility for any injury to people or property resulting from any ideas, methods, instructions or products referred to in the content.





与原件相符

www.ann-phys.org

JUNE | 2023

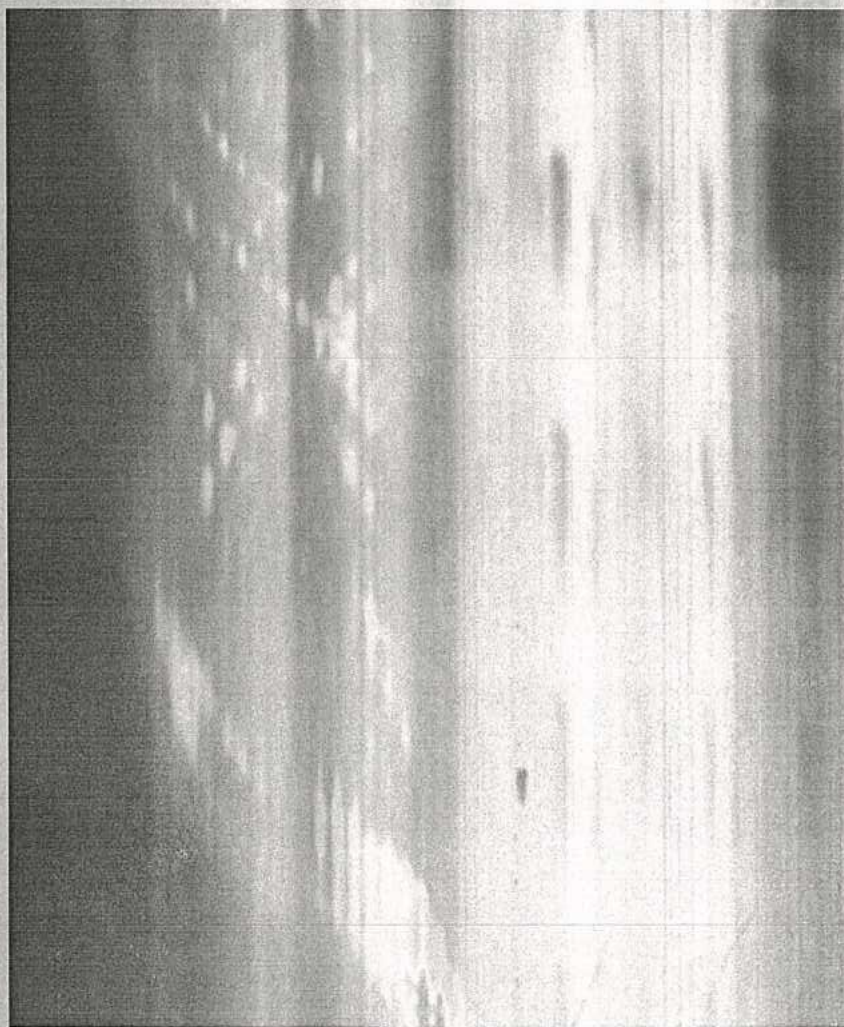
adp

annalen  
der



*Signature*

physik



**Dynamics of Bloch–Zener Oscillations with Tuning Gap**

Zhongkai Huang, Maolin Bo, Chuang Yao

WILEY-VCH

ISSN 0013-3804, Ann. Phys. (Berlin), 535, No 6 (June 2023)







# Dynamics of Bloch–Zener Oscillations with Tuning Gap

Zhongkai Huang,\* Maolin Bo, and Chuang Yao

In this study, the transient dynamics of Bloch–Zener oscillations (BZO) in a 1D qubit chain with a controllable band gap are explored. The chain consists of alternating site energies and is subjected to a constant external field. Several tight-binding models were analyzed, including Bloch and Landau–Zener models, to understand the BZO mechanism. The findings revealed that the band gaps played a crucial role in bridging the intriguing interplay between Bloch oscillations and Landau–Zener transitions. The motion of carriers in real and quasi-momentum spaces is explored and the time evolution of occupancy in mini-bands is calculated. A linearly time-dependent way of tuning the gap is also proposed and non-periodic motion is observed. When the chain is coupled to dispersionless optical phonons, strong coupling leads to large phonon displacements and localizes the carrier wave packets of the qubit states. The findings provide new insights into the behavior of BZO in complex systems and suggest avenues for future studies.

In recent years, tunable platforms have received increasing attention as potential quantum simulators for studying fundamental quantum mechanics phenomena like BZO.<sup>[11–35]</sup> The BZO have been observed directly in various systems, such as light beams in 2D photonic lattices with a refractive index ramp,<sup>[9]</sup> light waves in circularly curved waveguide arrays creating optical binary superlattices,<sup>[12]</sup> atomic rubidium Bose–Einstein condensates in accelerated optical lattice potentials,<sup>[28]</sup> and photonic graphene realized by honeycomb lattices of coupled optical waveguides with an index gradient.<sup>[10]</sup>

Circuit quantum electrodynamics (QED) setups are promising options for quantum simulation and computation due to their ability to provide precise control, scalability, and extended

coherence time.<sup>[16]</sup> These circuits can be arranged in various forms, including single artificial atoms, 1D chains, or 2D lattices.<sup>[37,38]</sup> The versatility of these platforms allows for fulfilling the criteria for universal quantum computation and can be tailored for specific quantum simulation needs.<sup>[39]</sup> Advances in circuit QED technology offer exciting prospects for studying the relationship between BOs and LZ transitions.

Recently, research has been conducted on BOs in various QED systems. In 2017, Ramasesh et al. successfully created BOs in a circuit QED system using a transmon qubit and superconducting cavity.<sup>[40]</sup> Bahmani et al. proposed using a 1D lattice of coupled LC circuits to study BOs and Wannier–Stark ladders.<sup>[41]</sup> Guo et al. showed the existence of BOs in a circuit with 5 superconducting transmon qubits.<sup>[42]</sup> Karamlou et al. showed the existence of BOs in a circuit of 3 × 3 superconducting qubits.<sup>[43]</sup>

Circuit QED devices are also used to examine Landau–Zener (LZ) transitions. In 2004, Izmailkov et al. observed LZ resonances in a circuit with an Al three-junction qubit and a Nb resonant tank.<sup>[44]</sup> Johansson and colleagues studied LZ transitions on a flux qubit in a superconducting chip.<sup>[45]</sup> Hänggi and colleagues investigated the LZ transition probability in circuit QED,<sup>[46]</sup> while Neilinger et al. demonstrated LZ transitions using two types of superconducting qubits: a flux qubit and a phase-slip qubit.<sup>[47]</sup> Circuit QED can be used to study coherent transport in BZO.

Fine-tuning the energy gap of a flux qubit is critical in transforming a one-band crystal model into a two-band one and plays a crucial role in adjusting BZO. Recent progress in the adjustment of the minimum energy splitting or transition energy, also known as the qubit gap of flux qubits, is seen as a positive step toward the realization of BZO. In 2003, Chiorescu et al. were the first to observe the coherent time evolution between two

## 1. Introduction

Bloch oscillations (BOs) and Landau–Zener (LZ) transitions are two essential elements of quantum mechanics that involve the organized movement of quantum particles and waves in repeating media under outside influences.<sup>[1,2]</sup> In repetitive potentials, there are continuous Bloch band structures and Bloch eigenfunctions that spread uniformly throughout the system. The introduction of an external static field results in the formation of discrete Wannier–Stark ladders with localized eigenstates.<sup>[3,4]</sup> When free from scattering and dephasing effects, BOs occur, where carriers experience periodic oscillations in both reciprocal and real space.<sup>[5]</sup> LZ transitions take place when changes to a linear potential from a superimposed field are significant enough to bridge the gap to an adjacent band, allowing for the tunneling of carriers to higher-order bands.<sup>[6,7]</sup> The harmonious combination of BOs and LZ transitions is known as Bloch–Zener oscillations (BZO),<sup>[8–10]</sup> also referred to as Landau–Zener–Bloch oscillations<sup>[11]</sup> or Bloch–Landau–Zener dynamics.<sup>[11]</sup> These concepts have practical applications in fields such as quantum optics,<sup>[12]</sup> solid-state physics,<sup>[13]</sup> and atomic and molecular physics.<sup>[14]</sup>

Z. Huang, M. Bo, C. Yao  
 Key Laboratory of Inorganic Special Functional Materials of Chongqing  
 Yangtze Normal University  
 Chongqing 408100, China  
 E-mail: zhongkaihuang@yznu.edu.cn

The ORCID identification number(s) for the author(s) of this article can be found under <https://doi.org/10.1002/andp.202300101>

DOI: 10.1002/andp.202300101



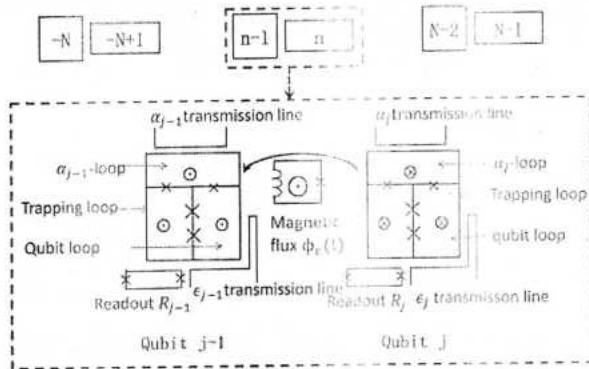


Figure 1. Circuit diagram of the device.

quantum states of a superconducting flux qubit composed of three Josephson junctions in a loop, establishing a strong foundation for solid-state quantum simulation using superconducting flux qubits.<sup>[48]</sup> Paauw et al. experimentally demonstrated the ability to adjust the gap of a superconducting flux qubit in situ using an additional flux loop, allowing the qubit to implement either diagonal or off-diagonal coupling between neighboring qubits.<sup>[49]</sup> The main obstacle in the design of flux qubits is the precise control of the qubit gap while maintaining long and consistent relaxation times. In 2022, Chang et al. produced a large batch of flux qubits and showed excellent reproducibility and control of the qubit gap, relaxation times, and pure echo dephasing times through careful control of e-beam lithography, oxidation parameters of the junctions, and sample surface.<sup>[50]</sup> The continuous progress opens up the possibility of time-dependent manipulation of the band gap in a 1D flux qubit chain.

This study investigates the dynamics of BZOs in a 1D chain of qubits with alternating site energies and under the influence of controllable driving forces. The paper is structured as follows: in Section 2, the model Hamiltonian is presented and the eigenenergies of various subsystems modeled by the proposed qubit scheme are analyzed in detail. In Section 3.1, the fine-tuning of energy structures and BZO dynamics under the commensurate condition is examined, as well as the dynamics of gap tuning that changes linearly with time. The effects of qubit-phonon coupling are explored in Section 3.3 using the multi-D2 ansatz and the Dirac-Frenkel time-dependent variational principle. Finally, conclusions are drawn in section 4.

## 2. Experimental Section

### 2.1. Model

The dynamics of BZOs can be simulated using a tight-binding lattice Hamiltonian. As schematically shown in Figure 1, a 1D chain of gap-tunable qubits is proposed as a quantum circuit to model this. By controlling the site energies of the qubits, this system allowed for the emulation of BZO dynamics.<sup>[50,51]</sup> In the circuit, magnetic fluxes were directed outside in qubit  $n-1$  and inside in qubit  $n$ , resulting in alternating site energies in neighboring qubits. The magnetic flux  $\Phi_e(t)$  represented an external driving force on the qubit array, forming a biperiodic potential system which can be used to study BZO phenomena.

The qubit array consisted of  $2N$  qubits with integer values ranging from  $-N$  to  $N-1$ , which were set up at low temperatures. In a 1D tight-binding model, the total Hamiltonian of the system is made up of three terms: hopping term, on-site energy term, and external field term. These are expressed as

$$\hat{H} = \hat{H}_{\text{hop}} + \hat{H}_{\text{gap}} + \hat{H}_{\text{ext}} \quad (1)$$

$$\hat{H}_{\text{hop}} = -\frac{\Delta}{4} \sum_{n=-N}^{N-1} (\hat{a}_n^\dagger \hat{a}_{n+1} + \text{h.c.}) \quad (2)$$

$$\hat{H}_{\text{gap}} = \frac{\delta(t)}{2} \sum_{n=-N}^{N-1} (-1)^n \hat{a}_n^\dagger \hat{a}_n \quad (3)$$

$$\hat{H}_{\text{ext}} = \sum_{n=-N}^{N-1} F d n \hat{a}_n^\dagger \hat{a}_n \quad (4)$$

The creation and annihilation operators for the excitonic carriers at site  $n$  are represented by  $\hat{a}_n^\dagger$  and  $\hat{a}_n$ , respectively. Each site was limited to two states, the ground and excited state of a qubit, which made the carriers at each site behave like fermions with the relation  $\{\hat{a}_n^\dagger, \hat{a}_m\} = \delta_{n,m}$ . The hopping term in the Hamiltonian only included the coupling between nearest neighbor qubits, with a strength of  $\Delta$ . The on-site energy of each site is  $\frac{\delta(t)}{2}(-1)^n$ , with time  $t$  being a variable. The external influence on each qubit was uniform, with a strength represented by  $F$ , and  $d$  represents the lattice spacing.

The one Bloch band tight-binding subsystem is represented by  $\hat{H}_{\text{hop}}$  (Equation (2)). It contains  $2N$  one-particle states that form the sub Hilbert space  $\mathcal{H}_{\text{hop}}$ . The eigenenergies and eigenstates of this subsystem are well known and have the analytical expressions  $\epsilon_1(k_1) = -\frac{\Delta}{2} \cos(k_1 d)$  and  $|k_1\rangle$ , respectively. These eigenstates are known as Bloch states, which satisfy Bloch's theorem, stating that  $\langle n+1+2N | k_1 \rangle = \langle n+1 | k_1 \rangle = e^{ik_1 d} \langle n | k_1 \rangle$ . The quantum numbers  $k_1$  represent the quasi-momenta.

$$k_1 = \frac{2\pi}{2Nd} s, \quad s \in \mathbb{Z} \quad (5)$$

The  $2N$  Bloch states with the  $k_1$ -quantum numbers ranging from  $-\frac{\pi}{d}$  to  $\frac{\pi}{d}$ , form a complete and orthogonal basis for the sub Hilbert space  $\mathcal{H}_{\text{hop}}$ .

Wannier states,  $|n\rangle = \sum_{|k_1| \in \mathcal{H}_{\text{hop}}} \sqrt{\frac{1}{2N}} e^{-ik_1 n} |k_1\rangle$ , are also a complete and orthonormal set of states in  $\mathcal{H}_{\text{hop}}$ , and are defined for integer values of  $n$  ranging from  $-N$  to  $N-1$ .

Using Fourier transformation, the annihilation (creation) operator  $\hat{a}_n$  ( $\hat{a}_n^\dagger$ ) is

$$\hat{a}_n = \frac{1}{\sqrt{2N}} \sum_{k_1=-\frac{\pi}{d}}^{\frac{\pi}{d}} \hat{a}_{k_1} e^{-ik_1 n} \quad (6)$$

$$\hat{a}_n^\dagger = \frac{1}{\sqrt{2N}} \sum_{k_1=-\frac{\pi}{d}}^{\frac{\pi}{d}} \hat{a}_{k_1}^\dagger e^{ik_1 n}$$

Thus, in momenta space

$$\hat{H}_{\text{hop}}(k_1) = -\frac{\Delta}{2} \cos(k_1 d) \sum_{k_1=-\frac{\pi}{d}}^{\frac{\pi}{d}} \hat{a}_{k_1}^\dagger \hat{a}_{k_1} \quad (7)$$

$\hat{H}_{\text{gap}}$  in Equation (3) represents the difference in energy levels between neighboring sites, which is  $\delta(t)$ . According to our proposed QED scheme,  $\frac{\delta(t)}{2}$  can be adjusted to fine tune the qubit gap. This results in the eigenenergies of  $\hat{H}_{\text{hop}} + \hat{H}_{\text{gap}}$  being split into two minibands,

$$\epsilon_{\pm}^{\pm}(k_z) = \pm \frac{1}{2} \sqrt{[\delta(t)]^2 + [\Delta \cos(k_z d)]^2} \quad (8)$$

with quasi-momenta  $k_z$  ranging in the corresponding first Brillouin zone from  $-\frac{\pi}{2d}$  to  $\frac{\pi}{2d}$ , and a band gap of  $\delta(t)$  when the difference in on-site energy between the two neighboring sites is tuned to  $\delta(t)$ .

When  $N = 1$ , the system became a two-site system that was connected through an off-diagonal coupling. The Hamiltonian of this system is expressed as

$$\hat{H}_{\text{two}} = -\frac{\Delta}{4} \hat{\sigma}_x + \frac{\delta(t)}{2} \hat{\sigma}_z \quad (9)$$

where  $\hat{\sigma}_x$  and  $\hat{\sigma}_z$  are the Pauli matrices. The eigenstates of  $\hat{\sigma}_z$ ,  $|\uparrow\rangle$ , and  $|\downarrow\rangle$ , can also be considered as the excited and ground states of each qubit in the dimer, respectively. This relationship is shown through the equation  $\hat{\sigma}_z = |\uparrow\rangle\langle\uparrow| - |\downarrow\rangle\langle\downarrow| = (-1)^0 \hat{a}_0^\dagger \hat{a}_0 + (-1)^1 \hat{a}_1^\dagger \hat{a}_1$ .

When the gap between the two states changes linearly with time, it creates a Landau-Zener model, described by the Hamiltonian

$$\hat{H}_{\text{LZ}} = -\frac{\Delta}{4} \hat{\sigma}_x + \frac{vt}{2} \hat{\sigma}_z \quad (10)$$

Here, the diabatic states move at a velocity of  $v$ . Transitions between the two diabatic states occurred due to direct coupling between neighboring qubits. The probability of transition from one state to the other at the avoided level-crossing point can be determined using the Landau-Zener formula, which gives  $P_{|\uparrow\rangle \rightarrow |\downarrow\rangle}(\infty) = 1 - \exp(-\frac{\pi \Delta^2}{8\hbar|v|})$ .

The external field along the chain, described by  $\hat{H}_{\text{ext}}$  in Equation (4), leads to a linear shift of the lattice's potential energy. When the  $\delta(t)$  is turned off, Bloch oscillations occur in the one-band system under a constant force  $F$ . In momentum space,  $\hat{H}_{\text{ext}}(k_1)$  is expressed as

$$\hat{H}_{\text{ext}}(k_1) = iF \frac{d}{dk_1} \sum_{k_1=-\frac{\pi}{2d}}^{+\frac{\pi}{2d}} \hat{a}_{k_1}^\dagger \hat{a}_{k_1} \quad (11)$$

By solving the Schrödinger equation for  $\hat{H}_{\text{hop}}(k_1) + \hat{H}_{\text{ext}}(k_1)$ , the eigenenergies are the Wannier-Stark ladders,  $\epsilon_{\text{ws}}(m) = mdF$ , with  $m = 0, \pm 1, \pm 2, \dots$ , and the eigenstates are  $|\text{WS}_m(k_1)\rangle = \sqrt{\frac{d}{2\pi}} e^{-i[mk_1 d + \frac{\Delta}{2dF} \sin(k_1 d)]} |k_1\rangle$ .

In Wannier space, the analytical eigenenergies of  $\hat{H}_{\text{hop}} + \hat{H}_{\text{ext}}$  are given by  $\epsilon_{\text{ws}}(n) = \int_{-\frac{\pi}{2d}}^{+\frac{\pi}{2d}} \epsilon_1(k_1) dk_1 + ndF$ , with  $n = 0, \pm 1, \pm 2, \dots$ , and the eigenstates are the well-known Wannier-Stark states,  $|\text{WS}_m(n)\rangle = \sum_n J_{n-m}(\frac{\Delta}{2dF})$ .

When the qubit system has periodic boundary conditions or when the linear array was shaped into a ring, there can be breaks

in the potential energy at the chain's boundaries.<sup>[52]</sup> However, by utilizing a gauge-transformed vector potential,  $A(t) = -Ft$ , this discontinuity issue can be resolved.<sup>[53]</sup> The expression for  $\hat{H}_{\text{hop}} + \hat{H}_{\text{ext}}$  can then be reformulated as

$$\hat{H}_{\text{gauge}} = -\frac{\Delta}{4} \sum_n \hat{a}_n^\dagger (e^{iA(t)} \hat{a}_{n+1} + e^{-iA(t)} \hat{a}_{n-1}) \quad (12)$$

When the  $\delta(t)$  is turned on, the static external force influenced the two minibands in Equation (8) causing the formation of two miniladders. The energy of these ladders can be expressed as follows:

$$\epsilon_{\text{ws}}^{\text{lad-0}}(n) = E_0 + 2ndF \quad (13)$$

$$\epsilon_{\text{ws}}^{\text{lad-1}}(n) = -E_0 + (2n+1)dFa$$

where the energy offset  $E_0$  depends on system settings of  $\delta$ ,  $\Delta$ ,  $F$ , and  $d$  in Hamiltonian (1).<sup>[54]</sup>

## 2.2. Methods for Dynamics

The single particle wave function's time evolution was described by the Schrödinger equation, which states that

$$i\hbar \frac{d|\Psi(t)\rangle}{dt} = \hat{H}|\Psi(t)\rangle \quad (14)$$

where  $|\Psi(t)\rangle = \sum_{n=-N}^{N-1} \psi_n(t) |n\rangle$ .

There are three different ways to find  $|\Psi(t)\rangle$ . First, the equation can be solved by using the Taylor expansion of  $|\Psi(t)\rangle$

$$|\Psi(t + \Delta t)\rangle = |\Psi(t)\rangle + \sum_{j=1}^{\infty} \frac{1}{j!} \frac{d^j |\Psi(t)\rangle}{dt^j} (\Delta t)^j \quad (15)$$

This method was precise but time-consuming, and required a sixth order expansion with  $\Delta t$  set to  $\approx 10^{-4}$  in the units of  $\hbar/\Delta$ , which resulted in a precision of the order of  $10^{-8}$  in the wave function's norm.

The second method involved using the time evolution operator  $\hat{U} = \exp(-\frac{i}{\hbar} \hat{H} \Delta t)$  to calculate  $|\Psi(t + \Delta t)\rangle = \hat{U}|\Psi(t)\rangle$ . However, this method can become inefficient for very large Hamiltonian matrices.

Finally, the Runge-Kutta method can be used to solve the equations of motion of the coefficients  $\psi_n(t)$ , which are given by

$$i\hbar \dot{\psi}_n(t) = -\frac{\Delta}{4} (e^{-iFt} \psi_{n+1}(t) + e^{iFt} \psi_{n-1}(t)) + \frac{\delta(t)}{2} (-1)^n \psi_n(t) \quad (16)$$

where the reduced plank constant is set to be  $\hbar = 1$  in the rest of paper for convenience. The initial wave packet can be given as

$$|\Psi(t=0)\rangle = \sum_n \psi_n a_n^\dagger |\emptyset\rangle = \sum_n C \exp(-n^2/4\sigma_0^2) a_n^\dagger |\emptyset\rangle \quad (17)$$



### 2.3. Physical Quantity of Interest

The focus is on the time evolution of the carrier probability of the qubit state, which is represented by  $P_n(t, n)$  and  $P_k(t, k)$  in Equation (18).

$$P_n(t, n) = \langle \Psi(t) | \hat{a}_n^\dagger \hat{a}_n | \Psi(t) \rangle \quad (18)$$

$$P_k(t, k_1) = \langle \Psi(t) | \hat{a}_{k_1}^\dagger \hat{a}_{k_1} | \Psi(t) \rangle$$

These equations described the average occupation of the qubit state at time  $t$ , and can be used to determine the occupancy of fermionic carriers on the lower and upper minibands. This information was obtained through the band folding theory, as seen in Equation (19).

$$P_{lw}(t) = \sum_{k_1=-\frac{\pi}{2d}}^{\frac{\pi}{2d}} P_k(t, k_1) \quad (19)$$

$$P_{up}(t) = 1 - P_{lw}(t)$$

The current of the composite system in the presence of an external field can be described by Equation (20).

$$j(t) = \langle \Psi(t) | i \sum_n (e^{iA(t)} \hat{a}_n^\dagger \hat{a}_{n+1} - \text{H.c.}) | \Psi(t) \rangle \quad (20)$$

To understand the movement of the carrier wave packet, the mean value  $c(t)$  and the standard deviation  $\sigma(t)$  are used, as shown in Equation (21).

$$c(t) = \sum_i^n n P_n(t, n)$$

$$\sigma(t)^2 = \sum_i^n (n - c(t))^2 P_n(t, n) \quad (21)$$

It is important to note that the initial standard deviation  $\sigma_0$  has a significant effect on the mean value  $c(t)$  of the carrier wave packet.

## 3. Results and Discussion

### 3.1. BZOs with Fine Tuned Constant Gap

The BOs in a single band case with  $\delta = 0$  have a time period of  $T_B = 2\pi\hbar/F$ .<sup>[54]</sup> However, when  $\delta \neq 0$ , the time periodicity of BZOs satisfying the commensurability condition is usually expressed as  $T_{BZ} = sT_{LZ} = rT_{re}$ , with  $r, s$  being positive integers and  $T_{re}$  being known as the reconstruction period.<sup>[15]</sup> The energy spacing between the Wannier–Stark ladders can be determined by the period of the LZ transition  $T_{LZ} = 2\pi\hbar/(dF - 2E_0(\delta))$ . The reconstruction period is  $T_{re} = \pi\hbar/F = T_B/2$  due to the reduced size of the Brillouin zone for  $\delta \neq 0$ . If  $E_0(\delta) = 0$ , the relationship  $T_{BZ} = 2T_{re} = T_B$  can be obtained. Figure 2a shows a collection of energy offsets of the Wannier–Stark ladders that meet the commensurate condition under the conditions of external field strength of  $F = 1$ , lattice spacing of  $d = 1$ , and hopping strength between neighboring sites of  $\Delta = 24$ . Figure 2b is a slice from

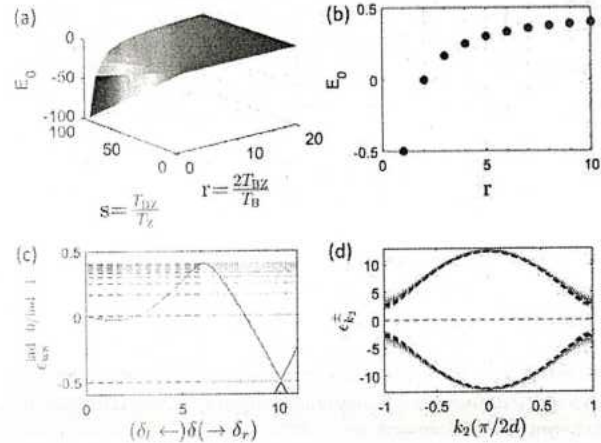
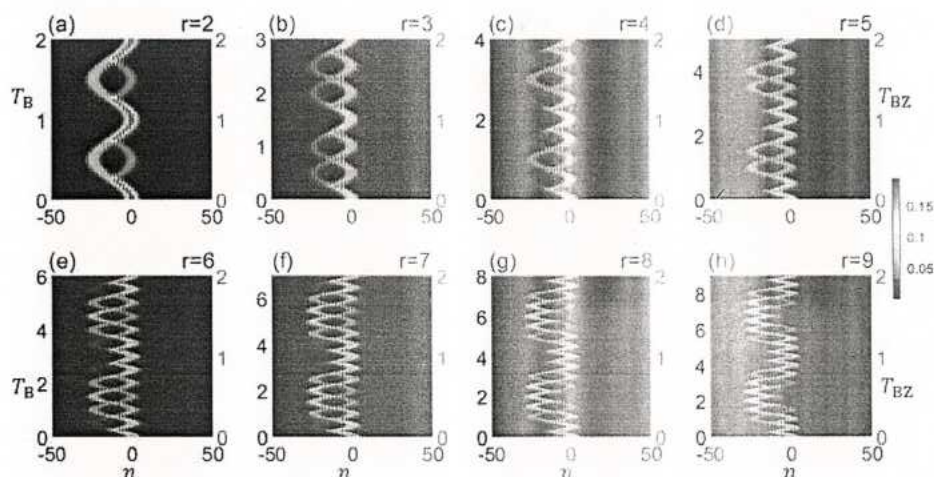


Figure 2. Energy offsets of the Wannier–Stark miniladders for commensurability condition. a) Energy offsets of Wannier–Stark miniladders as a function of  $(r, s)$  denoting commensurability conditions of Bloch–Zener oscillations. b) A slice of (a) for  $s = 1$  and varying  $r$ . c) Energies of the Wannier–Stark miniladders as a function of tuning gaps  $\delta$  are represented by curve lines, and horizontal lines mark calculated energies from (b). d) Band structures of the field free Hamiltonian in the first Brillouin zone with respect to many tuning gaps  $\delta$  of intersection points between the lines in (c). Other parameters include external field strength of  $F = 1$ , lattice spacing of  $d = 1$ , and hopping strength between neighboring sites of  $\Delta = 24$ .

Table 1. Fine tuned gaps for commensurability condition.

$r$	$\frac{T_{BZ}}{T_B}$	$E_0$	$\delta_l$	$\delta_r$
2	1	1/6	2.567495478917847	8.245567380283994
3	1.5	1/4	4.315132382278204	7.557401110701997
4	2	3/10	4.894982447409100	7.184774100703625
5	2.5	1/6	5.221171155059879	6.943559683172581
6	3	1/7	5.440051207299170	6.768519751687520
7	3.5	1/8	5.604562712125939	6.629729206331142
8	4	1/9	5.740726370922797	6.509987772076496
9	4.5	2/5	5.866942796862999	6.394910948173719
10	5	9/22	6.016833838093208	6.016833838093208

Figure 2a and shows how the energy offsets vary with  $r$  for a fixed  $s = 1$ . The energy offset  $E_0$  can be determined by calculating  $\epsilon_{ws}^{lad-0/lad-1}$  in Equation (13) by diagonalizing the Hamiltonian  $\hat{H}$ . A large number of gap values were tested to find the specific gap that produces the required energy offset  $E_0$ . Numerically, the needed gap can be selected with an accuracy of  $10^{-15}$ . There may be several values of  $\delta$  for the same  $E_0$ . In Figure 2c, the green curve denote the energy of  $\epsilon_{ws}^{lad-0}$  ( $n = 0$ ) from Equation (13). The horizontal lines mark the calculated energy values shown in Figure 2b. The dashed line on the left side and the dotted line on the right side cross with curves representing Wannier–Stark miniladder at two sets of gaps, referred to here as  $\delta_l$  and  $\delta_r$ , respectively. With these gap values, the set of minibands is shown in Figure 2d. For clarity, the accurate gap values  $\delta_l$  and  $\delta_r$  are given in Table 1. These carefully selected gaps can produce BZOs with different time periods.



**Figure 3.** Tuning Bloch-Zener oscillation patterns. Time evolution of the carrier probability  $P_n(t, n)$  for tuning gaps  $\delta_i$  from commensurability conditions with  $r$  being a) 2, b) 3, c) 4, d) 5, e) 6, f) 7, g) 8, and h) 9. Other parameters are hopping strength  $\Delta = 24$ ,  $s = 1$ , external field strength  $F = 1$ , and tuning gap  $\delta_i$ . The initial condition is a Gaussian wave packet with  $\sigma_0 = 3$ .

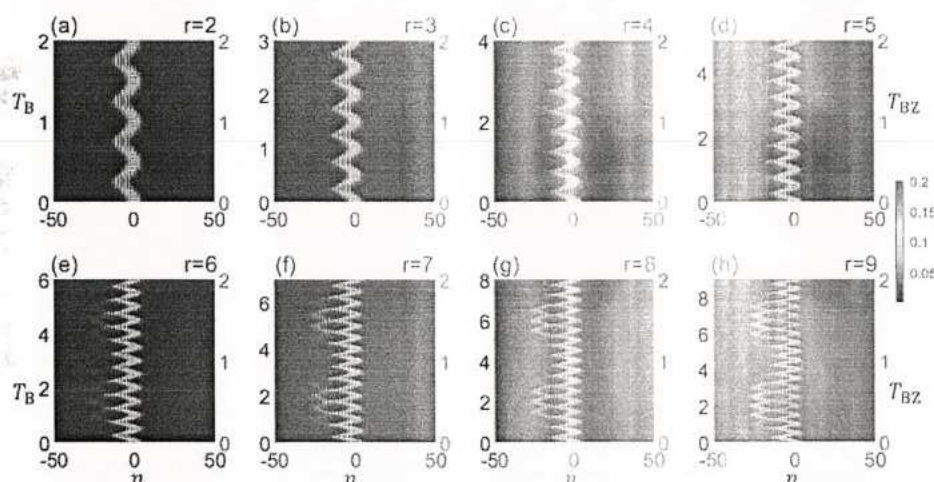


**Figure 4.** Time evolution of the carrier probability  $P_n(t, n)$  for tuning gaps  $\delta_i$  from commensurability conditions with  $r$  being a) 2, b) 3, c) 4, d) 5, e) 6, f) 7, g) 8, and h) 9. Parameters are quite the same with those of Figure 3, except the usage of tuning gap  $\delta_i$ , instead of  $\delta_j$ .

The agreement between the observed dynamic behavior in temporal space in Figures 3 and 4 and the expected time-periods shown in Table 1 further confirms the accuracy of the gap tuning results. Figure 3 shows more apparent BZO patterns due to smaller values of  $\delta$  compared to Figure 4. The tunneling frequency increases as the value of  $r$  grows, leading to longer  $T_{BZ}$  periods, with a fixed field strength and  $T_B = \frac{2\pi\hbar}{dF}$ . Although all evolution in the figures are plotted with  $2T_{BZ}$  for convenience, the wave patterns eventually become similar as  $r$  increases. The largest possible value of  $r$  for a given system can also be inferred from these figures. The evolution starts with a Gaussian wave packet and clearly defined BZO patterns appear, which is in contrast to the behavior of wave packets starting from a single site that display a shrinking breathing mode as shown in the Appendix A.

In Figure 5, we demonstrate the motion in quasi-momentum space, where the tunneling between the upper and lower mini-

bands is made clear. The first column of Figure 5 shows the properties of the motion in Figure 3a, which is the most typical BZO patterns. The second column refers to the motion of same time-periodicity but less transition between two minibands due to the usage of large  $\delta_i$ . The third column shows the  $r = 9$  case as an example of long period evolution with  $T_{BZ} > T_B$ . In Figure 5a-c,  $k_1$ -quantum numbers ranges from  $-\frac{\pi}{d}$  to  $+\frac{\pi}{d}$ , and the Brillouin zone can be reduced to  $[-\frac{\pi}{2d}, +\frac{\pi}{2d}]$  using band-folding theory for the discussed two-band model. That is to say, the lower miniband moves in the range of  $[-\frac{1}{2}, +\frac{1}{2}]/(k_1)$ , while the upper one travels in the range of  $[-1, -\frac{1}{2}]/(k_1)$  and  $[\frac{1}{2}, +1]/(k_1)$ . It can be clearly found that Zener transition between the two bands occur once the wave packets travel to the boundary of the momenta unit region of the Brillouin zone at integer times of  $\frac{1}{4}T_B$ . Before around  $\frac{1}{2}T_{BZ}$ , there is a partial transfer of population from the



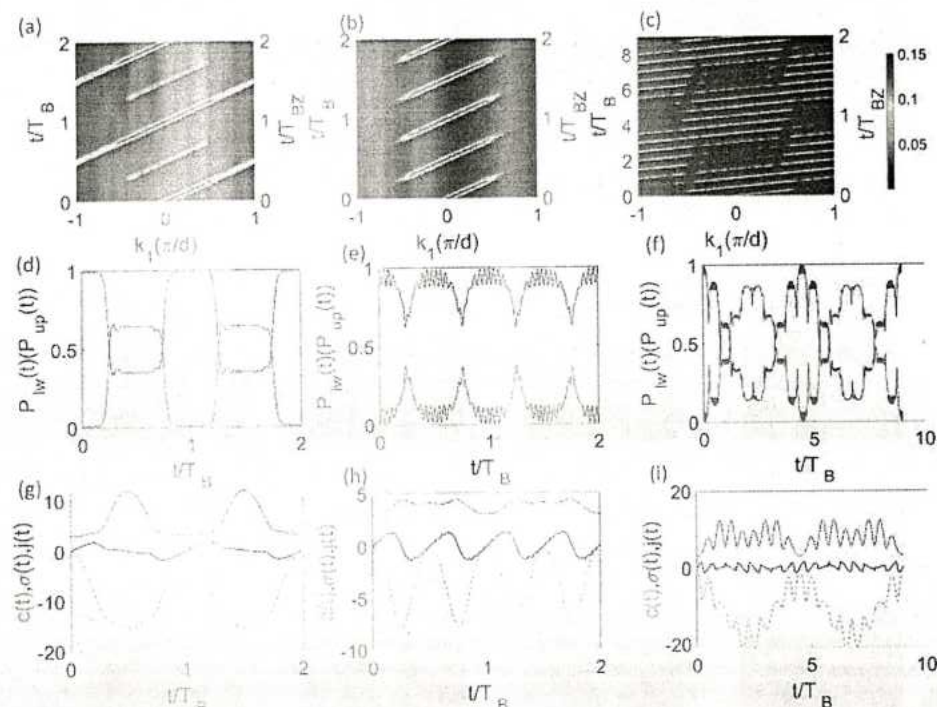


**Figure 5.** Time evolution of carrier probability in quasi-momenta space  $P_k(t, k_1)$  for (a)  $r = 2$  with  $\delta_l$ , b)  $r = 2$  with  $\delta_r$ , and c)  $r = 9$  with  $\delta_l = \delta_r$ . d–f) Time evolution of occupation probability of the lower (upper) band,  $P_{lw}(t)$  ( $P_{up}(t)$ ), denoted by blue (red) line. g–i) Time evolution of standard deviation of carrier probability in real space  $\sigma(t)$  (green color), mean value of carrier probability  $c(t)$  (blue color), and current  $j(t)$  (red color). The three column from left to right corresponds to real space motion in Figures 3a, 4a, and 3h, respectively.

lower miniband to the upper miniband. After  $\frac{1}{2}T_{BZ}$ , the population transfer from the upper band to the lower band until reconstruct the initial condition. Figures 5d–f give the detailed population of each miniband. Figures 5g–i show the wave center, width, and current evolution to quantitatively measure the transferring of the studied BZ.

### 3.2. Linearly Time-Dependent Tuning of Gaps

When the qubit gap is adjusted at a constant rate, the one-site energy term becomes

$$\hat{H}_{gap} = \frac{v_l}{2} \sum_{n=-N}^{N-1} (-1)^n \hat{a}_n^\dagger \hat{a}_n \quad (22)$$

Starting from time  $t = 0$ , the gap increases gradually and the carriers can reach the boundary of the Brillouin zone at a controllable rate. After the first transition, the gap continues to increase and begins to prevent further transitions. This is why the wave center (represented by the green line in Figure 6j–l) oscillates with a small amplitude around a certain value after the first transition. The rate at which the gap is increased significantly affects the center of the wave packet at long times. Since the gap starts from zero, it provides ample opportunities for transitions to occur, which helps to evenly distribute the population between the two minibands. As seen in Figure 6,  $P_{lw}(t)$  and  $P_{up}(t)$  oscillate  $\approx 0.5$  at long times.

### 3.3. Dissipative BZ Dynamics

The operation and performance of a QED device can be affected by its surroundings. In this study, the environmental impact is modeled by coupling the BZO system to a phonon system. The extended Holstein model is constructed through equations of the phonon system with frequency  $\omega_0(\hat{H}_{ph})$  and the carrier–phonon interaction with coupling strength  $g(\hat{H}_{ca-ph})$ .

$$\hat{H}_{ph} = \omega_0 \hat{b}_n^\dagger \hat{b}_n \quad (23)$$

$$\hat{H}_{ca-ph} = -g\omega_0 \sum_n \hat{a}_n^\dagger \hat{a}_n (\hat{b}_n + \hat{b}_n^\dagger)$$

To solve the dynamics of this open quantum system, the Dirac–Frenkel time-dependent variational principle is used in combination with the multi- $D_2$  ansatz,<sup>[55,56]</sup> detailed of the method is in Appendix B.

The time evolution of the carrier probability ( $P_{ca}(t, n)$ ) is calculated through the multi- $D_2$  ansatz,  $|D_2^M\rangle$ , which is shown to be a powerful tool in solving open quantum systems. Additionally, the time evolution of the phonon displacement ( $X_{ph}(t, n)$ ) is also evaluated.

$$P_{ca}(t, n) = \langle D_2^M | \hat{a}_n^\dagger \hat{a}_n | D_2^M \rangle \quad (24)$$

$$X_{ph}(t, n) = \langle D_2^M(t) | \hat{b}_n^\dagger + \hat{b}_n | D_2^M(t) \rangle \quad (25)$$



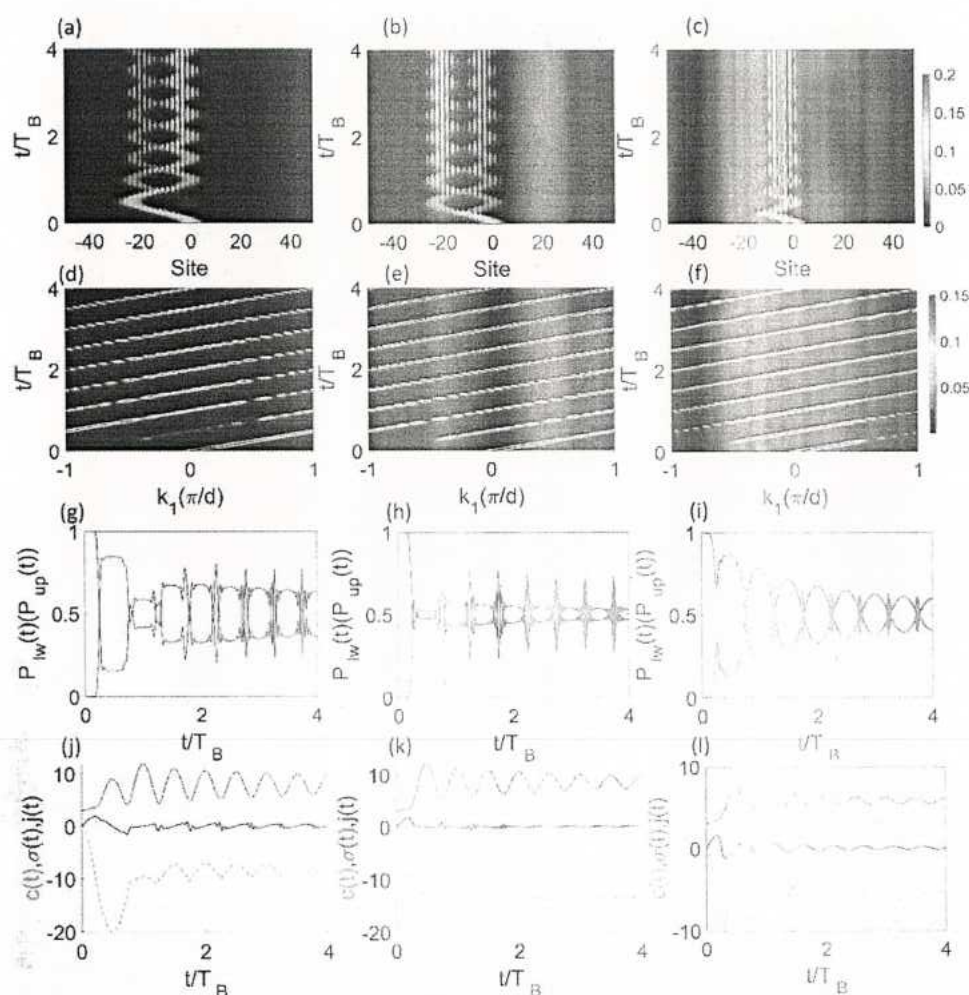


**Figure 6.** Linearly time-dependent gap tuning with  $\delta(t) = \nu t$ . Time evolution of carrier probability in quasi-momentum space  $P_k(t, k_1)$  for linearly tuning rate of a)  $\nu = 1$ , b)  $\nu = 2$ , and c)  $\nu = 4$ . d–f) Time evolution of occupation probability of the lower (upper) band,  $P_w(t)$  ( $P_w(t)$ ), denoted by blue (red) line. g–i) Time evolution of standard deviation of carrier probability in real space  $\sigma(t)$  (green color), mean value of carrier probability  $c(t)$  (blue color), and current  $j(t)$  (red color). Other parameters are hopping strength  $\Delta = 24$ , external field strength  $F = 1$ , and lattice spacing  $d = 1$ .

As seen in Figure 7, the carrier–phonon interaction can lead to the washing out of the periodic behavior of BZOs and the occurrence of dynamic localization when the qubit–phonon coupling is strong. We notice how the range of the colorbars increases with  $g$  in Figure 7c,d, indicating a higher phonon emission rate for an increasing qubit–phonon coupling strength.

#### 4. Conclusion

In conclusion, we have conducted a comprehensive investigation of the transient BZOs dynamics in a 1D qubit chain with a controllable band gap. We considered several tight-binding models, including BOs model and LZs model, and demonstrated the interplay between the BOs and LZ transitions that is bridged by the band gaps. Our findings showed that the energy offset between the Wannier–Stark energy ladders depends on the band gaps, and we explored the impact of fine-tuning the gap values to

meet commensurate conditions. We also analyzed the motion of the carrier in real space and quasi-momentum space, calculated the time evolution of occupancy in the minibands, and captured the behavior of the moving wave packet. Additionally, we proposed a linearly time-dependent way to tune the gap and observed non-periodic motion.

Furthermore, we investigated the impact of the coupling of the qubit chain with dispersionless optical phonons, and found that strong coupling cases resulted in large phonon displacements and localized carrier wave packets. The interplay between BOs and LZ transitions becomes complicated when multiple levels of LZ transitions are superimposed on the BOs in lattice models with multiple bands, and further work is needed in this area. Our study provides valuable insights into the dynamics of the BZOs in complex external fields, and the results have important implications for future work in the field.

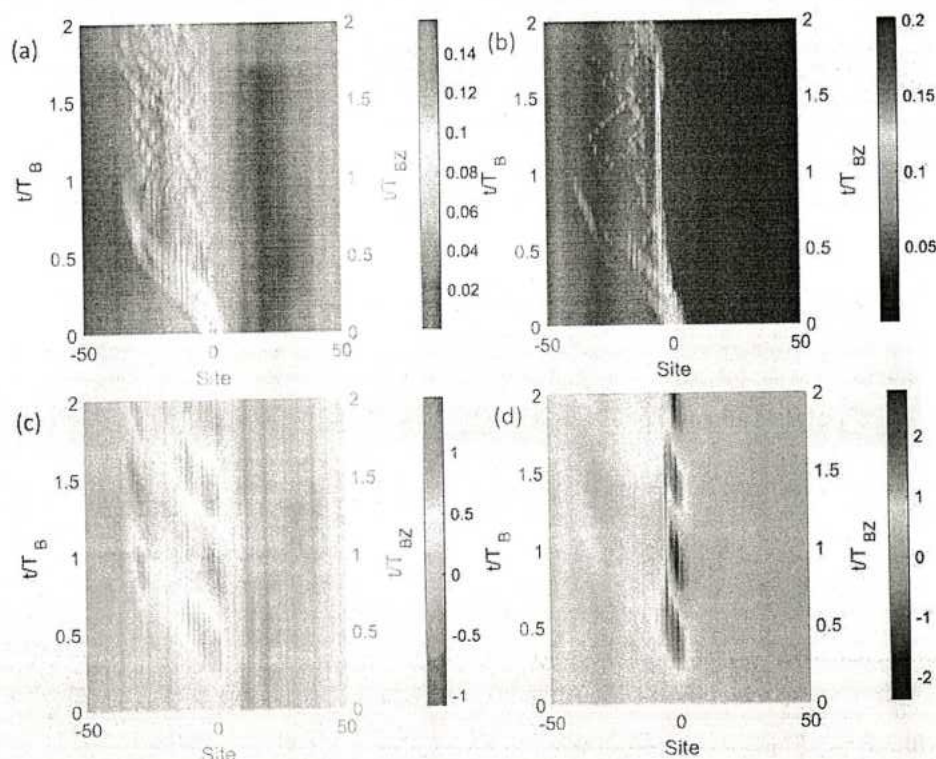


**Figure 7.** a,b) Time evolution of carrier probability  $P_n(t, n)$  for cases with carrier–phonon coupling strength of  $g = 2$  and  $g = 4$ , respectively. c,d) Corresponding time evolution of phonon displacement  $X_{ph}(t)$ . Other parameters are hopping strength  $\Delta = 24$ , external field strength  $F = 1$ , lattice spacing  $d = 1$ , and commensurability condition of  $r = 2$  with  $\delta_l$  and  $s = 1$ .

## Appendix A: BZO Dynamics with Constant Gaps

The wave packets of the qubit states exhibit typical Bloch oscillations in gap-free situations if the wave starts as a broad Gaussian wave packet, whereas standard Bloch–Zener oscillations take place in non-zero gap

cases. Conversely, if the wave packet is initially localized on a single site, it results in a symmetric breathing mode for gap-free conditions and an asymmetric breathing mode for non-zero gap conditions. This can be seen in Figures A1 and A2, which demonstrate the breathing mode for constant gap scenarios.

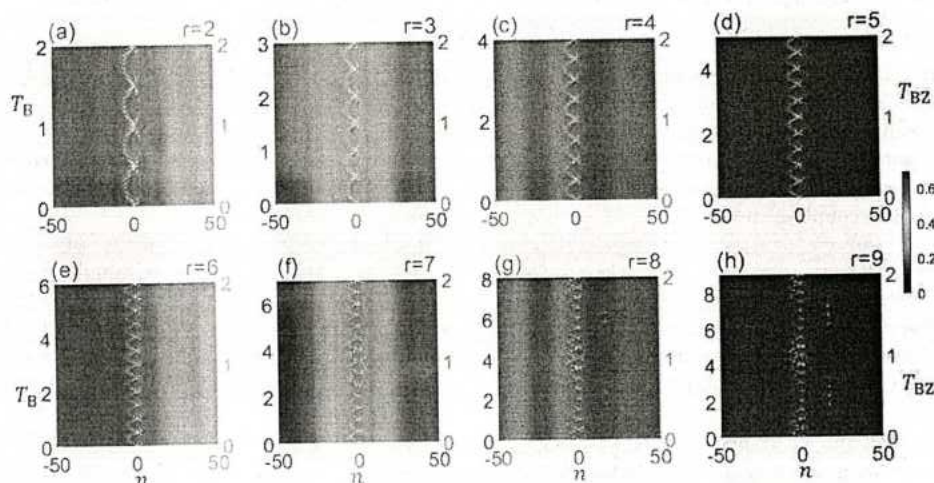


**Figure A1.** Tuning breathing mode Bloch–Zener oscillations with a single site initial condition. Time evolution of carrier probability  $P_n(t, n)$  for tuning gaps  $\delta_l$  from commensurability conditions with  $r$  being a) 2, b) 3, c) 4, d) 5, e) 6, f) 7, g) 8, and h) 9. Other parameters are hopping strength  $\Delta = 24$ , external field strength  $F = 1$ , lattice spacing  $d = 1$ , and  $s = 1$ .



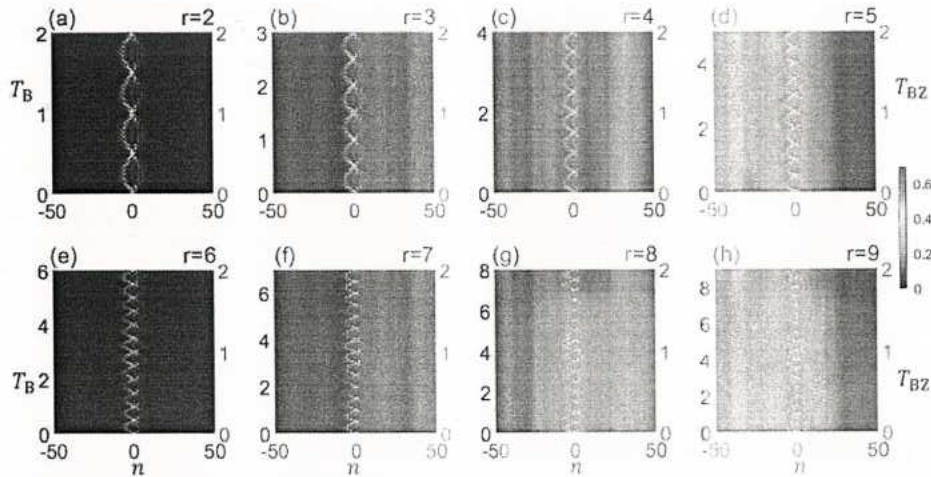


**Figure A2.** Tuning breathing mode Bloch-Zener oscillations with a single site initial condition. Time evolution of carrier probability  $P_n(t, n)$  for commensurability conditions with  $r$  being a) 2, b) 3, c) 4, d) 5, e) 6, f) 7, g) 8, and h) 9. Parameters are quite the same with those of Figure A1, except the usage of  $\delta_j$  instead of  $\delta_l$ .

## Appendix B: The Time Dependent Variational Approach for the Dissipative Bloch-Zener Model

### B.1. Extended Holstein Model

The Hamiltonian terms related to phonons can be expressed in the phonon momentum representation as

$$\hat{H}_{ph} = \sum_q \omega_q \hat{b}_q^\dagger \hat{b}_q \quad (B1)$$

$$\hat{H}_{ca-ph} = -N^{-1/2} g \sum_{n,q} \omega_q \hat{a}_n^\dagger \hat{a}_n (e^{iqn} \hat{b}_q + e^{-iqn} \hat{b}_q^\dagger) \quad (B2)$$

where  $\omega_q$  is the frequency of phonons with momentum  $q$ ,  $\hat{b}_q^\dagger$  and  $\hat{b}_q$  are the creation and annihilation operators of phonons with momentum  $q$ , respectively.  $\hat{b}_q^\dagger$  and  $\hat{b}_q$  can be expressed in terms of  $\hat{b}_n^\dagger$  as follows

$$\hat{b}_q^\dagger = N^{-1/2} \sum_n e^{iqn} \hat{b}_n^\dagger, \quad \hat{b}_n^\dagger = N^{-1/2} \sum_q e^{-iqn} \hat{b}_q^\dagger \quad (B3)$$

The transfer integral and the exciton-phonon coupling strength are represented by  $J$  and  $g$ , respectively. In this study, we are using the Einstein dispersionless model, where all phonons have the same frequency,  $\omega_q = \omega_0$ . For simplicity, the energy unit is set to unity by choosing  $\omega_0 = 1$ .

### B.2. Multiple Davydov Trial States

In this work, we employ the multi- $D_2$  Ansatz. It can be constructed as

$$\begin{aligned} |D_2^M(t)\rangle &= \sum_i^M \sum_n^N \psi_{in}(t) |\lambda_i\rangle \\ &= \sum_i^M \sum_n^N \psi_{in} \hat{a}_n^\dagger |0\rangle_{ex} \exp \left\{ \sum_q \left[ \lambda_{iq} \hat{b}_q^\dagger - \lambda_{iq}^* \hat{b}_q \right] \right\} |0\rangle_{ph} \end{aligned} \quad (B4)$$

The time-dependent variational parameters  $\psi_{in}$  and  $\lambda_{iq}$  for the exciton probability and phonon displacement are defined, with  $n$  representing the site number and  $i$  labeling the coherent superposition state. When  $M = 1$ , the  $|D_2^M(t)\rangle$  Ansatz reduces to the traditional Davydov  $D_2$  trial state. These parameters' equations of motion are obtained by implementing the Dirac-Frenkel variational principle

$$\frac{d}{dt} \left( \frac{\partial L_2}{\partial \dot{\psi}_{in}} \right) - \frac{\partial L_2}{\partial \psi_{in}} = 0$$

$$\frac{d}{dt} \left( \frac{\partial L_2}{\partial \dot{\lambda}_{iq}} \right) - \frac{\partial L_2}{\partial \lambda_{iq}} = 0 \quad (B5)$$

for the multi- $D_2$  Ansatz, and the Lagrangian  $L_2$  is formulated as

$$\begin{aligned} L_2 &= \langle D_2^M(t) | \frac{i}{2} \frac{\partial}{\partial t} - \hat{H} | D_2^M(t) \rangle \\ &= \frac{i}{2} \left[ \langle D_2^M(t) | \frac{\partial}{\partial t} | D_2^M(t) \rangle - \langle D_2^M(t) | \frac{\partial}{\partial t} | D_2^M(t) \rangle \right] \\ &\quad - \langle D_2^M(t) | \hat{H} | D_2^M(t) \rangle \end{aligned} \quad (B6)$$

where the first term yields

$$\begin{aligned} &\frac{i}{2} \left[ \langle D_2^M(t) | \frac{\partial}{\partial t} | D_2^M(t) \rangle - \langle D_2^M(t) | \frac{\partial}{\partial t} | D_2^M(t) \rangle \right] \\ &= \frac{i}{2} \sum_{ij}^M \sum_n^N (\psi_{jn}^* \dot{\psi}_{in} - \dot{\psi}_{jn}^* \psi_{in}) S_{ji} \\ &\quad + \frac{i}{2} \sum_{ij}^M \sum_n^N \psi_{jn}^* \psi_{in} S_{ji} \sum_q \left[ \frac{\lambda_{qn}^* \lambda_{jq} + \lambda_{qn} \lambda_{jq}^*}{2} \right. \\ &\quad \left. - \frac{\lambda_{iq} \lambda_{iq}^* + \lambda_{iq}^* \lambda_{iq}}{2} + \lambda_{jq}^* \lambda_{iq} - \lambda_{iq}^* \lambda_{jq} \right] \end{aligned} \quad (B7)$$



and the second term takes the form

$$\begin{aligned} & \langle D_2^M(t) | \hat{H} | D_2^M(t) \rangle \\ &= \langle D_2^M(t) | \hat{H}_{ex} | D_2^M(t) \rangle + \langle D_2^M(t) | \hat{H}_{ex} | D_2^M(t) \rangle \\ &+ \langle D_2^M(t) | \hat{H}_{ex-ph} | D_2^M(t) \rangle \end{aligned} \quad (B8)$$

where the Debye–Waller factor is formulated as

$$S_{ij} = \exp \left\{ \sum_q \lambda_{iq}^* \lambda_{jq} - \frac{1}{2} \left( |\lambda_{iq}|^2 + |\lambda_{jq}|^2 \right) \right\} \quad (B9)$$

Detailed derivations of the equations of motion for the variational parameters are numerically treated by fourth-order Runge–Kutta method.

## Acknowledgements

This work was supported in part by the Natural Science Foundation of China under Grant No. 11947205, and by the Natural Science Foundation of Chongqing under No. cstc2020jcyj-msxm0003, and the Science and Technology Research project of Chongqing Education Commission under No. KJQN202201421.

## Conflict of Interest

The authors declare no conflict of interest.

## Data Availability Statement

The data that support the findings of this study are available from the corresponding author upon reasonable request.

## Keywords

Bloch–Zener oscillations, carrier–phonon coupling, gap tuning

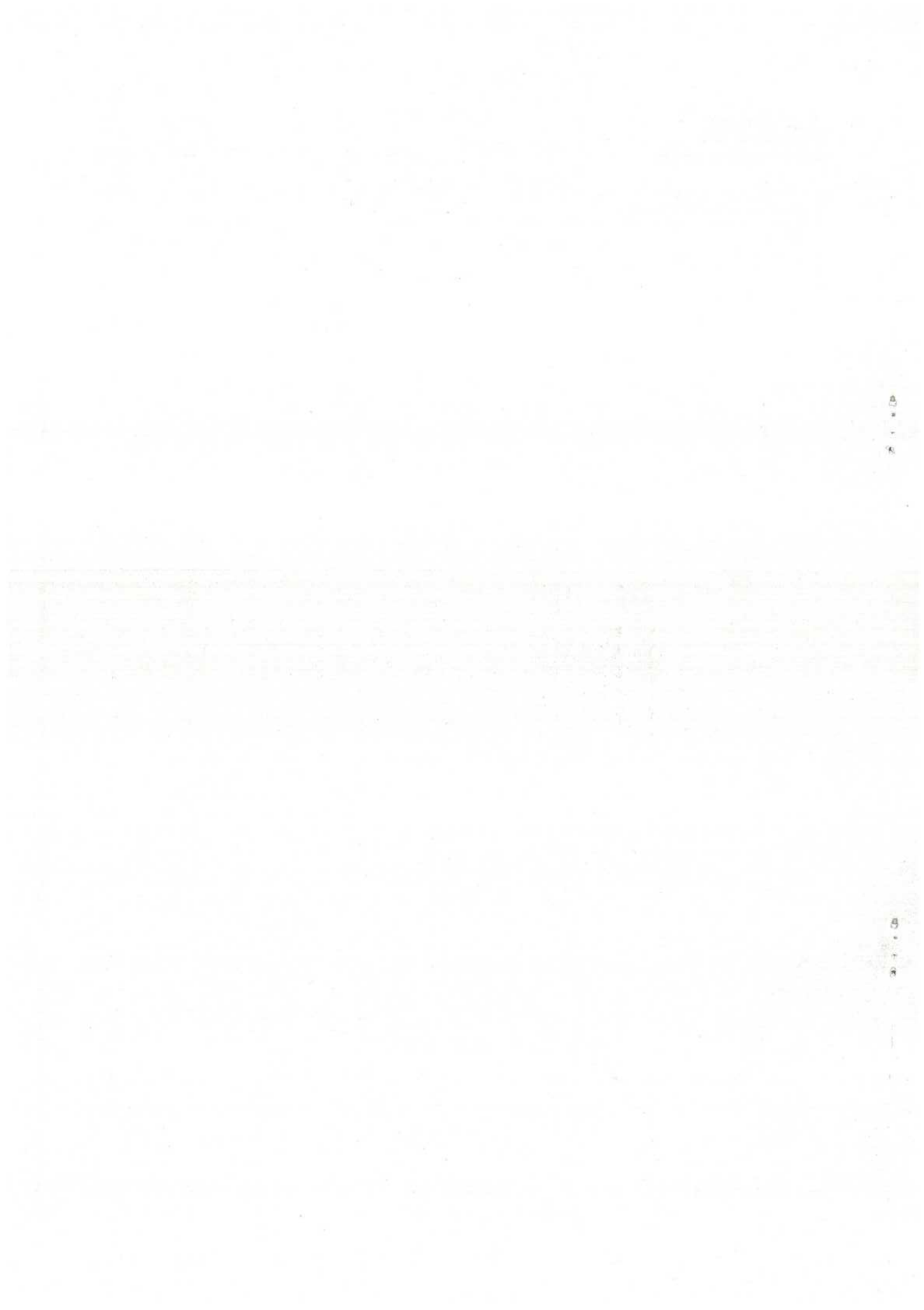
Received: March 10, 2023

Revised: April 8, 2023

Published online:

- [1] F. Bloch, *Z. Phys.* **1929**, 52, 555.
- [2] C. Zener, *Proc. R. Soc. London, Ser. A* **1932**, 137, 696.
- [3] G. H. Wannier, *Phys. Rev.* **1960**, 117, 432.
- [4] J. Zak, *Phys. Rev. Lett.* **1968**, 20, 1477.
- [5] L. Esaki, R. Tsu, *IBM J. Res. Develop.* **1970**, 14, 61.
- [6] M. Holthaus, *J. Opt. B: Quantum Semiclassical Opt.* **2000**, 2, 589.
- [7] A. Watson, M. I. Weinstein, *Commun. Math. Phys.* **2018**, 363, 655.
- [8] B. M. Breid, D. Witthaut, H. J. Korsch, *New J. Phys.* **2006**, 8, 110.
- [9] H. Trompeter, W. Krolkowski, D. N. Neshev, A. S. Desyatnikov, A. A. Sukhorukov, Y. S. Kivshar, T. Pertsch, U. Peschel, F. Lederer, *Phys. Rev. Lett.* **2006**, 96, 53903.
- [10] Y. Sun, D. Leykam, S. Nenni, D. Song, H. Chen, Y. D. Chong, Z. Chen, *Phys. Rev. Lett.* **2018**, 121, 33904.
- [11] A. D’Errico, R. Barboza, R. Tudor, A. Dauphin, P. Massignan, L. Marrucci, F. Cardano, *APL Photonics* **2021**, 6, 20802.
- [12] F. Dreisow, A. Szameit, M. Heinrich, T. Pertsch, S. Nolte, A. Tünnermann, S. Longhi, *Phys. Rev. Lett.* **2009**, 102, 76802.
- [13] J. Y. Romanova, E. V. Demidov, L. G. Mourokh, Y. A. Romanov, *J. Phys.: Condens. Matter* **2011**, 23, 305801.
- [14] Y. Zhang, D. Zhang, Z. Zhang, C. Li, Y. Zhang, F. Li, M. R. Belić, M. Xiao, *Optica* **2017**, 4, 571.
- [15] B. M. Breid, D. Witthaut, H. J. Korsch, *New J. Phys.* **2007**, 9, 62.
- [16] S. Longhi, *Phys. Rev. Lett.* **2020**, 124, 66602.
- [17] X. Qiao, X.-B. Zhang, A.-X. Zhang, Z.-F. Yu, J.-K. Xue, *Phys. Lett. A* **2019**, 383, 3095.
- [18] T.-Y. Du, D. Tang, X.-H. Huang, X.-B. Bian, *Phys. Rev. A* **2018**, 97, 43413.
- [19] R. Takahashi, N. Sugimoto, *Phys. Rev. B* **2017**, 95, 224302.
- [20] N. Bender, H. Li, F. M. Ellis, T. Kottos, *Phys. Rev. A* **2015**, 92, 41803.
- [21] Y. Mizumoto, Y. Kayanuma, *Phys. Rev. A* **2013**, 88, 23611.
- [22] S. Longhi, *J. Phys. B: At., Mol. Opt. Phys.* **2012**, 45, 225504.
- [23] S. Ding, G. Ping Wang, *Appl. Phys. Lett.* **2012**, 100, 151913.
- [24] A. R. Kolovsky, H. J. Korsch, *Phys. Rev. A* **2003**, 67, 63601.
- [25] L.-K. Lim, J.-N. Fuchs, G. Montambaux, *Phys. Rev. Lett.* **2012**, 108, 175303.
- [26] V. Krueckl, K. Richter, *Phys. Rev. B* **2012**, 85, 115433.
- [27] S. Longhi, *Phys. Rev. B* **2012**, 86, 75144.
- [28] S. Kling, T. Salger, C. Grossert, M. Weitz, *Phys. Rev. Lett.* **2010**, 105, 215301.
- [29] M. J. Zheng, C. Wang, K. W. Yu, *Opt. Lett.* **2010**, 35, 3865.
- [30] B. Prasanna Venkatesh, M. Trupke, E. A. Hinds, D. H. J. O’Dell, *Phys. Rev. A* **2009**, 80, 63834.
- [31] S. Longhi, *Phys. Rev. Lett.* **2008**, 101, 193902.
- [32] D. Witthaut, E. M. Graefe, S. Wimberger, H. J. Korsch, *Phys. Rev. A* **2007**, 75, 13617.
- [33] P. He, Z. Li, *New J. Phys.* **2020**, 22, 63031.
- [34] Z.-H. Li, L. Zhou, Y. Li, *J. Phys. B: At., Mol. Opt. Phys.* **2021**, 54, 35004.
- [35] S. Xia, C. Danieli, Y. Zhang, X. Zhao, H. Lu, L. Tang, D. Li, D. Song, Z. Chen, *APL Photonics* **2021**, 6, 126106.
- [36] Y. Makhlin, G. Schön, A. Shnirman, *Rev. Mod. Phys.* **2001**, 73, 357.
- [37] X. Gu, A. F. Kockum, A. Miranowicz, Y.-x. Liu, F. Nori, *Phys. Rep.* **2017**, 718–719, 1.
- [38] A. J. Kollár, M. Fitzpatrick, A. A. Houck, *Nature* **2019**, 571, 45.
- [39] G. Wendin, *Rep. Prog. Phys.* **2017**, 80, 106001.
- [40] V. V. Ramasesh, E. Flurin, M. Rudner, I. Siddiqi, N. Y. Yao, *Phys. Rev. Lett.* **2017**, 118, 130501.
- [41] S. Bahmani, A. N. Askarpour, *Phys. Lett. A* **2020**, 384, 126596.
- [42] X.-Y. Guo, Z.-Y. Ge, H. Li, Z. Wang, Y.-R. Zhang, P. Song, Z. Xiang, X. Song, Y. Jin, K. Xu, D. Zheng, H. Fan, *npj Quantum Inf.* **2020**, 7, 51.
- [43] A. H. Karamlou, J. Braumüller, Y. Yanay, A. Di Paolo, P. M. Harrington, B. Kannan, D. Kim, M. Kjaergaard, A. Melville, S. Muschinske, B. M. Niedzielski, A. Vepsäläinen, R. Winik, J. L. Yoder, M. Schwartz, C. Tahan, T. P. Orlando, S. Gustavsson, W. D. Oliver, *npj Quantum Inf.* **2022**, 8, 35.
- [44] A. Izmalkov, M. Grajcar, E. Il’ichev, N. Oukhanski, T. Wagner, H.-G. Meyer, W. Krech, M. H. S. Amin, A. M. van den Brink, A. M. Zagorskin, *Europhys. Lett.* **2004**, 65, 844.
- [45] Z. Huang, Y. Zhao, *Phys. Rev. A* **2018**, 97, 13803.
- [46] D. Zueco, P. Hänggi, S. Kohler, *New J. Phys.* **2008**, 10, 115012.
- [47] P. Neillinger, S. N. Shevchenko, J. Bogár, M. Rehák, G. Oelsner, D. S. Karpov, U. Hübner, O. Astafiev, M. Grajcar, E. Il’ichev, *Phys. Rev. B* **2016**, 94, 94519.
- [48] I. Chiorescu, Y. Nakamura, C. J. P. M. Harmans, J. E. Mooij, *Science* **2003**, 299, 1869.
- [49] F. G. Paauw, A. Fedorov, C. J. P. M. Harmans, J. E. Mooij, *Phys. Rev. Lett.* **2009**, 102, 90501.

- [50] T. Chang, I. Holzman, T. Cohen, B. C. Johnson, D. N. Jamieson, M. Stern, *Phys. Rev. Appl.* **2022**, *18*, 040602.
- [51] G. Engelhardt, M. Benito, G. Platero, T. Brandes, *Phys. Rev. Lett.* **2017**, *118*, 197702.
- [52] J. Zak, *Phys. Rev. Lett.* **1968**, *20*, 1477.
- [53] J. B. Krieger, G. J. Iafrate, *Phys. Rev. B* **1986**, *33*, 5494.
- [54] T. Hartmann, F. Keck, H. J. Korsch, S. Mossmann, *New J. Phys.* **2004**, *6*, 2.
- [55] N. Zhou, Z. Huang, J. Zhu, V. Chernyak, Y. Zhao, *J. Chem. Phys.* **2015**, *143*, 014113.
- [56] Z. Huang, A. D. Somoza, C. Peng, J. Huang, M. Bo, C. Yao, J. Li, G. Long, *New J. Phys.* **2021**, *23*, 123020.







# Single electron transistor based on twisted bilayer graphene quantum dots

Zhongkai Huang\*, Yuping He, Jing Cao, Qianqian Li, Chen Li, Guichuan Li, Maolin Bo and Chuang Yao

Key Laboratory of Extraordinary Bond Engineering and Advanced Materials Technology of Chongqing, Yangtze Normal University, Chongqing 408100, People's Republic of China

E-mail: zhongkaihuang@yznu.edu.cn

Received 31 August 2023, revised 24 November 2023

Accepted for publication 7 December 2023

Published 15 December 2023



## Abstract

Electrical properties of twisted bilayer graphene exhibit angle-dependent characteristics, sparking a thriving development in the field of twistrionics. However, the application of quantum dots (QDs) made of twisted bilayer graphene in single-electron transistors (SETs) remains largely unexplored so far. We here investigate the electronic properties of twisted bilayer graphene QDs (TBG QDs) within a SET configuration. We compare the performance of conventional and double-gated SET structures and find that the double-gated configuration provides enhanced control over the electronic properties of TBG QDs. We analyze the influence of rotation angles on the charge stability diagrams and observe that the linear and quadratic gate-island coupling strengths generally decrease as the rotation angle decreases. Furthermore, we quantify the effect of QD size on the charge stability diagrams and find that the size of the diamond-shaped regions decreases as the TBG QD size increases. Results presented herein may help pave the way for realization and application of TBG QDs based SET.

Supplementary material for this article is available online

Keywords: single electron transistor, twisted bilayer graphene, quantum dots

## 1. Introduction

Twisted bilayer graphene (TBG), a van der Waals heterostructure, has attracted widespread interest due to its tunable electronic properties, notably the emergence of flat bands and correlated insulator states at the 'magic angle' [1]. In the past three years, there has been a significant increase in research on quantum dots (QDs) made of TBG. In recent studies, Wang and Yang have explored the interlayer interaction in TBG and its QDs, uncovering angle-dependent variations and contributions from different interactions, providing insights into interlayer coupling and decoupling mechanisms [2]. Moreover, they proposed a method to determine interlayer coupling strength in TBG QDs by analyzing electric dipole polarizability, revealing the dominant role of interlayer

coupling in polarizability variation and highlighting its significance even at small twist angles [3].

The investigation of TBG QDs with varying twist angles and external electric fields has revealed the widening of size-dependent band gaps through interlayer twist and the narrowing of gaps through applied fields. Notably, the coupling between twist and field induces an enhanced Stark response, allowing for tunable band engineering of TBG QDs [4]. Additionally, TBG QDs exhibit remarkably strong chiral optical activity, surpassing that of semiconductor QDs and small chiral molecules, offering potential applications in chiral nanophotonics [5]. Furthermore, the fabrication of graphene QDs in TBG using nanoscale p-n junctions enables the confinement of low-energy massless Dirac fermions and showcases the modification of electronic states, highlighting the unique interlayer coupling variations induced by graphene QDs in TBG [6].

Investigations on circular bilayer graphene QDs reveal the localization of low-energy states at AA-stacked regions

\* Author to whom any correspondence should be addressed.



and the closing of the energy gap with edge states under a perpendicular magnetic field, suggesting potential experimental probing using scanning tunneling microscopy [7]. Polarization-dependent selection rules have been extended to TBG QDs, offering a comprehensive atlas of optical conductivity spectra and providing insights into size-scaling behavior dominated by the twist angle, enabling the manipulation of optical properties for integrated carbon optoelectronics [8]. Additionally, large-angle twisting in single-layer graphene has been investigated, emphasizing the potential of adjusting position symmetry in graphene systems [9]. Finally, the dominance of interlayer polarizability and charge transfer at small twist angles in TBG sheds light on interlayer coupling and charge transfer potential in graphene-based nanomaterials [10].

In summary, these studies contribute to our understanding of TBG QDs, providing insights into interlayer coupling, optical properties, band engineering, and charge transfer mechanisms. These findings pave the way for the development of novel applications and devices based on TBG QDs.

The single-electron transistor (SET) is a nanoscale device that exhibits remarkable control over individual electron transport and charge states [11]. At the heart of an SET lies an isolated conducting island, which plays a crucial role in confining and manipulating individual electrons. The island must possess a low capacitance and exhibit a discrete energy spectrum to enable the well-defined charging and discharging of electrons [12].

The atomically thin nature of TBG QDs and their tunable electronic structure provide a versatile platform for tailoring the energy spectrum and manipulating electron-electron interactions [13]. Treating TBG QDs as the island of SET offers several advantages. Firstly, SETs enable the precise manipulation and detection of single electrons, facilitating the exploration of fundamental charge transport properties in TBG QDs. Secondly, the strong electrostatic coupling between the SET and TBG QD allows for the realization of robust functionalities such as gate-tunable spin qubits and QDs. Lastly, the integration of SETs with TBG QDs holds immense potential for applications in quantum computing [14], quantum information processing [15], and ultra-sensitive sensing [16]. However, SET configurations discussed before have not been specifically designed for TBG QDs and cannot adequately explore the electronic properties of TBG QDs.

In this study, we present and investigate a double-gated SET configuration utilizing TBG QDs as the conducting island. Our investigation into the electronic features of TBG QDs within SET is conducted using density functional theory (DFT) and the density functional tight binding framework (DFTB) [17–19]. The work is formulated as follows: In section 2, we provide details on the construction of TBG QDs from commensurate TBG, the proposed double-gated SET configuration, and the calculation methodology employed. Section 3.1 focuses on the study of the influence of conventional and double-gated SET environments on the electronic properties of TBG QDs. In section 3.2, we characterize the electronic features, including the charge stability diagrams, for varying rotation angles. Additionally, in section 3.3, we

examine the size effect using the proposed device. Finally, we draw conclusions in section 4.

## 2. Methodology

### 2.1. System description

Utilizing the inherent versatility of TBG thin films with a Moiré pattern, we propose a path to study QDs with tailored electronic characteristics. A TBG model is first constructed, and then the desired QDs structure is extracted from it for analysis.

Graphene, a 2D material with a hexagonal honeycomb lattice, serves as the foundation for our study. To construct a TBG model, we begin by depicting its lattice structure in figure 1. Assuming the lattice constant  $a_0$ , we define the primitive cell basis vectors as  $\mathbf{a}_1 = (\frac{\sqrt{3}}{2}, -\frac{1}{2})a_0$  and  $\mathbf{a}_2 = (\frac{\sqrt{3}}{2}, \frac{1}{2})a_0$ . To elucidate the TBG structure, we introduce super cell basis vectors:  $\mathbf{t}_1 = n\mathbf{a}_1 + (n+1)\mathbf{a}_2$  and  $\mathbf{t}_2 = -(n+1)\mathbf{a}_1 + (2n+1)\mathbf{a}_2$ , where  $n$  is a non-negative integer. Upon a clockwise super lattice rotation by a twisting angle  $\theta$ , the rotated super cell assumes the basis vectors  $\mathbf{t}'_1 = (n+1)\mathbf{a}_1 + n\mathbf{a}_2$  and  $\mathbf{t}'_2 = -n\mathbf{a}_1 + (2n+1)\mathbf{a}_2$ . The rotation angle can be determined by calculating the dot product of the super cell basis vectors:

$$\cos(\theta_n) = \frac{\mathbf{t}_1 \cdot \mathbf{t}'_1}{|\mathbf{t}_1| |\mathbf{t}'_1|} = \frac{6n^2 + 6n + 1}{6n^2 + 6n + 2}.$$

Utilizing the aforementioned twist angle formula, we have fabricated a TBG structure with the minimal surface area of super cells, as depicted in figure 1(b). The twist angle of TBG in the figure is  $21.78^\circ$ , which corresponds to the smallest super cell area among various commensurate twist angles. Details of TBG super cell are listed, as shown in table 1,  $n$  is the index of the supercell,  $\theta$  is the rotation angle, and the number of carbon atoms in the supercell ( $N$ ) is given in the third row. After constructing the TBG structure, we employed black circles to trim the graphene QDs along the edges, thereby defining the boundary of the TBG flake to be studied.

Circular QDs of varying radii were carved from the obtained supercells, followed by hydrogenation at their boundaries to achieve sp<sup>2</sup> hybridization and resolve the issue of broken bonds. As shown in figure 2, a detailed analysis was primarily conducted on four distinct sizes of QDs, consisting of 26, 74, 122, and 146 carbon atoms. In order to investigate the influence of twist angles, multiple QDs at different rotation angles were analyzed for each size, with figure 2 illustrating the case of  $21.78^\circ$ .

As depicted in figure 3, the setup of the SET comprises gate electrodes, metallic source, drain, as well as a TBG QD functioning as an isolated island. The transport process in the SET is characterized by sequential tunneling rather than coherent tunneling. Owing to the feeble interaction between the TBG QDs and the source/drain electrodes, the charge carrier traverses the configuration while preserving minimal information. During this electron motion stage, the charge carrier migrates individually from the drain electrode to the source electrode through TBG QDs. Gate-t and Gate-b



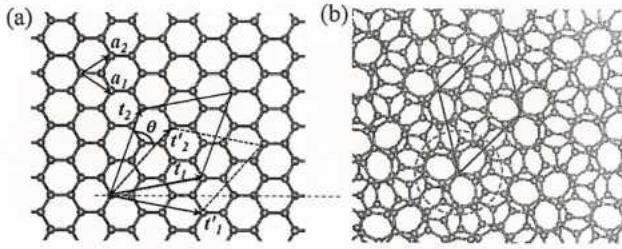


**Figure 1.** (a) Construction of a commensurate twisted bilayer graphene.  $a_1$  and  $a_2$  denote lattice vectors characterizing the primitive cell of graphene.  $t_1$  ( $t'_1$ ) and  $t_2$  ( $t'_2$ ) represent the corresponding lattice vectors for the original (rotated) supercell in the process of constructing the twisted structure. A rotation angle of  $\theta$  is employed to achieve the formation of commensurate Moiré patterns. (b) Top view of twisted bilayer graphene with twisting angle of  $21.78^\circ$ . The blue diamond with solid line refers to the supercell, and red circle with dotted line indicates the cutting edge of quantum dots.

**Table 1.** A series of selected twisted bilayer graphene structures is examined for quantum dots formation. The rotation angle,  $\theta_n$ , is determined by the relation  $\theta_n = \arccos(\frac{6n^2+6n+1}{6n^2+6n+2})$ , where  $n$  represents a non-negative integer. The resulting number of atoms, denoted as  $N$ , is given by  $N = 4 * (3n^2 + 3n + 1)$  in the unit cell of corresponding Moiré structure.

$n$	0	1	2	3	4	5	6	7	8	9
$\theta_n$	$60^\circ$	$21.78^\circ$	$13.17^\circ$	$9.43^\circ$	$7.23^\circ$	$6.01^\circ$	$5.09^\circ$	$4.41^\circ$	$3.89^\circ$	$3.48^\circ$
$N$	4	28	76	148	244	364	508	676	868	1084

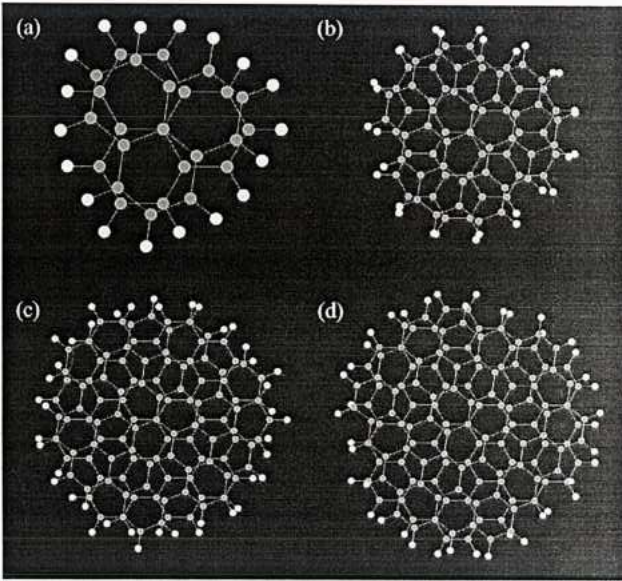


**Figure 2.** Quantum dots made of commensurate twisted bilayer graphene. The dots consist of (a) 26, (b) 74, (c) 122, and (d) 146 carbon atoms. The white dots refer to hydrogen atoms.

are used to modulate the electron affinity energies, thereby enabling the regulation of electron transport and the opening and closure of the conductive pathway.

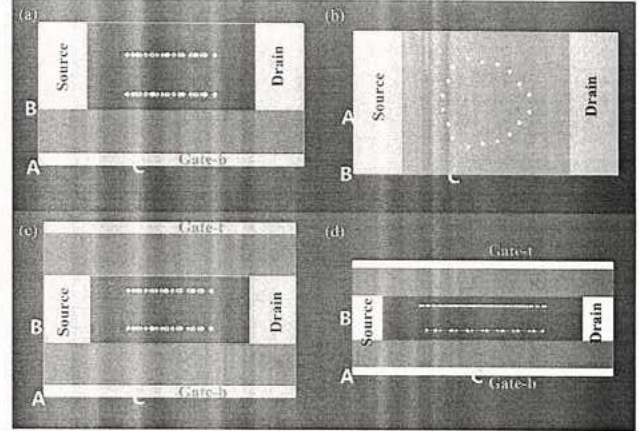


**Figure 3.** Two types of single electron transistors structures. (a) Side and (b) top view of conventional structure with a dielectric layer and bottom gate electrode (Gate-b). Side view of double-gated structure with additional top gate (Gate-t) and sandwiched TBG QD island of (c) 26 and (d) 146 carbon atoms.

## 2.2. Computational procedure

In the investigation of SETs using TBG QDs, electronic properties have been extensively explored through DFT and DFTB calculations. To account for electrostatic interactions, SET simulations employed pseudo-potentials and additional charges, effectively screening these interactions. The calculations were carried out using the QuantumATK package [18], which facilitated simulations employing methods of DFT, DFTB, and the nonequilibrium Green's function (NEGF) formalism.

The DFT-NEGF approach, initially applied to non-equilibrium systems [20, 21], was employed and subsequently further developed to consider cases under the standard equilibrium condition [22, 23]. Within the NEGF-DFT framework of Quantum Wise [17], charging energies of molecules within SETs were investigated. This approach has been successfully applied to explore a variety of single molecule transistors [24–31]. Furthermore, the self-consistent-charge DFTB method [19] was utilized to examine the electronic properties of TBG QDs within SETs.

These comprehensive calculations have yielded valuable insights into the electronic properties of TBG QDs within SETs, shedding light on their potential applications in electronic devices.

## 3. Results and discussion

### 3.1. Effects of SET structure

The SET structures, as depicted in figure 3 illustrate two distinct configurations. The conventional SET structure, depicted in figure 3(a) consists of source/drain electrodes positioned at the left and right side of the device. A dielectric layer located beneath the electrodes has a dielectric constant of  $10\epsilon_0$  and a thickness of  $3.7 \text{ \AA}$ . A gate electrode, denoted as Gate-b, with



a thickness of 1 Å covers the entire area beneath the dielectric layer. The electrodes are composed of metallic materials with a work function of 5.28 eV, specifically Au. Thicknesses of both the source and drain electrodes are 12 Å along the *A*-axis and the two electrodes are horizontally separated by 14 Å along the *C*-axis. Along the *B*-axis, the height of both electrodes is 7.3 Å. The size of the conventional SET structure is comparable to previously reported graphene-based [32] and silicon-based [33] nanopores.

In the current work, a novel double-gated SET structure is proposed, as illustrated in figure 3(b). This structure incorporates another gate on top, i.e. Gate-t. Identical configuration is used for both Gate-t and Gate-b. This setup couples the top (bottom) gate to the up (down) layer of TBG QDs, thereby amplifying the influence of twisting angles on the two-layer dots and device performance.

As depicted in figure 4 the charge stability diagram offers a comprehensive portrayal of the electrostatic dynamics and the conduction characteristics within a SET. In the event of weak coupling between the TBG QDs and the source/drain electrodes, sequential tunneling serves as the conduit for conduction, a process wherein an electron traverses from the source to the island before finally transitioning to the drain to fulfill the conduction cycle. The coupling strengths of the QD-source and the QD-drain primarily dictate the tunneling rate. In the SET scenario where a substantial separation exists between the source and drain, the incoming charge carrier state is approximately independent of the outgoing state. By measuring a large amount of gate voltage  $V_g$  along a fixed direction while sustaining a constant source-drain bias  $V_d$ , a pattern of periodic peaks emerges, signifying the addition or subtraction of a charge carrier from TBG QDs. Executing this continuous measuring procedure within a balanced range of  $V_d$  would reveal diamond-shaped zones within the  $V_g - V_d$  plane, a representation commonly referred to as the charge stability diagram. Mathematical details on obtaining charge stability diagram is outlined in the Supporting Information. Within these diamond regions, no conduction is observed, and a unit change in charge population is noted between adjacent diamonds. Consequently, SET configurations employing a range of TBG QDs can yield charge stability diagrams with distinct attributes.

Figures 4(a) and (c) exhibit the charge stability diagrams corresponding to the single-gated configuration of the SET illustrated in figures 3(a) and (b). Meanwhile, figures 4(c)–(h) pertain to the double-gated SET configuration. In the left column of figure 4, the QD utilized as the island consists of 26 carbon atoms and possesses a rotation angle of  $21.78^\circ$ , whereas the right column subfigures employ a QD with a rotation angle of  $9.43^\circ$ . These two distinct angles are employed to exemplify the influence of the rotation angle.

Figures 4(a) and (b) exhibit strikingly similar characteristics, implying that the rotation angle in a single-gated SET predominantly affects its performance. Regarding the impact of rotation angle on the charge stability diagram, a comprehensive investigation of this phenomenon is elucidated in the supplementary information, providing detailed insights into its

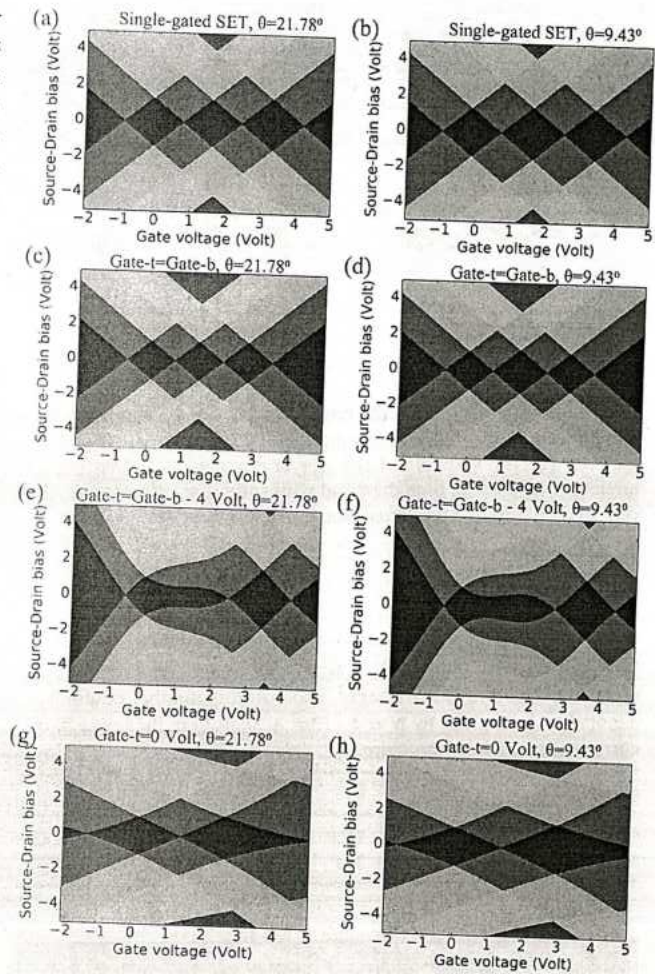


**Figure 4.** Charge stability diagrams of different configurations of single electron transistors for quantum dots composed of 26 carbon atoms are presented. The twisting angle for the first (second) column is  $21.78^\circ$  ( $9.43^\circ$ ). Single-gated structures are employed for (a) and (b), while double-gated structures are utilized for (c)–(h). In the second row, the gate voltage of Gate-t and Gate-b are set to be equal. In the third row, the voltage of Gate-t is consistently 4 V lower than that of Gate-b. In the fourth row, the voltage of Gate-t is held at zero. The horizontal gate voltage in the figures corresponds to that of Gate-b. The color scheme of dark blue, blue, green, yellow, red indicates the number of charge states of 0, 1, 2, 3, 4, respectively.

effects. In contrast, when the gate voltage of Gate-t and Gate-b are set to be equal in the double-gated SET, figures 4(c) and (d) display visually distinct diamond sizes in the central region of each pattern. Furthermore, if the voltage of Gate-t consistently remains 4 V lower than that of Gate-b, figures 4(e) and (f) illustrate the variation in size between gate voltages of 0 and 2.5 V in the middle region. Conversely, when the top gate is grounded (i.e. Gate-t = 0), figures 4(g) and (h) exhibit noticeable differences at the left and right boundaries around a source-drain bias of 0 V. This observation implies that the rotation angle of TBG QDs exerts a discernible impact on the charge stability diagram within the double-gated SET environment. Consequently, the double-gated SET configuration is preferred for subsequent discussions.



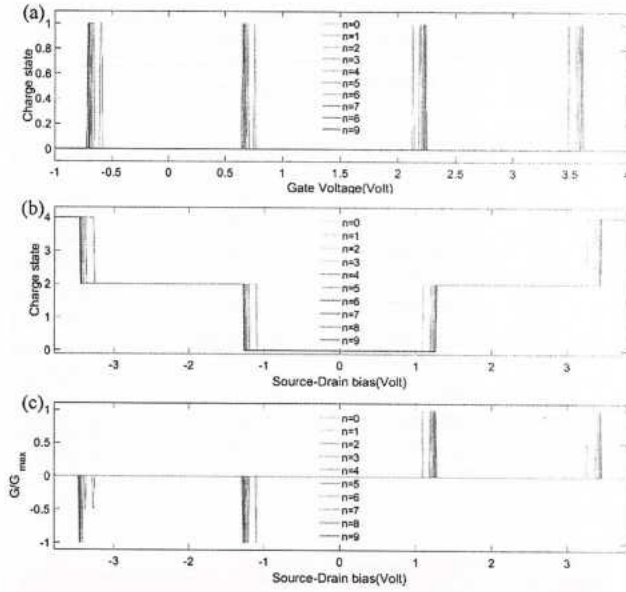


**Figure 5.** Detailed study of charge stability diagram for configurations with Gate-t = Gate-b and 26 carbon atoms. Line scans taken along (a) gate voltage with source-drain bias equal to zero and (b) along source-drain bias with max central diamond (gate voltage = 1.45 V) for various twisted bilayer quantum dots. (c) Normalized differential conductance with respect to source-drain bias referring to (b).

Line scans at varying source-drain bias and gate voltage values were conducted for the charge stability diagram to analyze the diagram's characteristics. Behavior of double-gated structure with Gate-t = Gate-b is shown here in figure 5, corresponding to diagram in figures 4(b) and (c). Analysis for diagram of double-gated structure with Gate-t = Gate-b - 4 V and Gate-t = 0 V can be found in the Supporting Information. Figure 5(a) exhibits periodic charge peaks in gate voltage line scans, signifying charge additions or removals at a fixed zero bias. Increasing the twisting angle results in a narrowing of the gate voltage window, facilitating enhanced observation of charge states. In figure 5(b), line scans along the source-drain bias reveal symmetric step-like features, indicating distinct island configurations and balanced tunnel barriers. As the voltage increases from zero bias, transitions between charge states occur, leading to Coulomb blockade and conduction blockages. The width of these plateaus provides valuable insights into the charging energy of excited states. Notably, a decrease in the twisting angle enlarges the blockade region, indicating a higher charging energy required to excite the TBG QDs. In experimental settings, the charge stability diagram is obtained through current/conductance measurements on a voltage plane. Figure 5(c) displays the normalized differential conductance behavior derived from line scans, featuring distinct conductance peaks corresponding to specific QD configurations. The separation between adjacent peaks represents the non-uniform charging energy between consecutive excited states for a given gate voltage. Negative conductance peaks are observed in the negative bias region. Increasing the

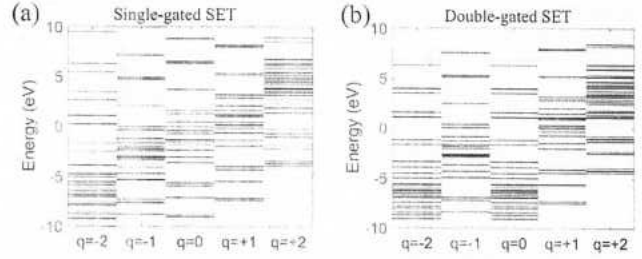


**Figure 6.** Molecular energy spectra of quantum dots composed of 26 carbon atoms and twisted at  $\theta = 21.78^\circ$  are investigated for five charge states under two distinct single electron transistor configurations: (a) single-gated and (b) double-gated. These investigations are conducted under the condition where the gate voltage is set to zero.

rotation angle narrows the source-drain bias window for conductance observation, suggesting a reduced charging energy required to excite the QDs. By comparing line scans along different bias/voltage axes, the effects of the rotation angle can be discerned.

In the realm of energy space, we have chosen the TBG QD with a rotation angle of  $21.78^\circ$  and composed of 26 carbon atoms within the SET as a representative example for investigating the electronic energy levels in various charging states, as depicted in figure 6. Throughout the operation of the SET device, the molecular energy spectrum of TBG QDs maintains its inherent electronic structure. However, the energy levels undergo distinct shifts to accommodate the net charges entering or leaving the TBG QD. Specifically, when the TBG QD bears a negative charge, the electronic energy levels shift entirely downwards, whereas they shift upwards as the charge carrier moves away from the TBG QD. Figure 6(a) illustrates a nearly linear shift of energy levels in the conventional SET configuration. In contrast, due to the combined electrostatic effects from the double-gated SET environment, the energy shift deviates from a linear trend as the charge state varies. This behavior indicates the nonlinear boundaries observed in the diamond-shaped charge stability diagrams of figures 4(e)–(h).

Furthermore, it is worth noting that the device is capable of operating at room temperature. Typically, the featured charging energy must exceed the thermal energy of the charge carriers for Coulomb blockade to be observable. The charging energy represents the energy needed to charge the TBG QD with a single unitary charge. The energies employed for charging the studied TBG QDs are sufficiently high to prevent electron transport induced by thermal fluctuations. As a result, the SET device can function effectively across a wide temperature range, including room temperature.

### 3.2. Impact of rotation angles

The rotation angles of each TBG QD employed as the SET island have an important effect on the performance of the SET. In this section, we further investigate the effect of rotation angles on the system.



**Table 2.** Linear gate coupling strengths between gates and island quantum dots (26 carbon atoms) of double-gated SET configurations.

Rotation index $n$	Linear gate-island coupling strength( $\alpha$ )		
	Gate-t = Gate-b	Gate-t = Gate-b - 4	Gate-t = 0
0	0.801 097	0.801 109	0.400 671
1	0.800 487	0.800 529	0.400 419
2	0.800 426	0.800 454	0.400 377
3	0.800 329	0.800 349	0.400 314
4	0.800 238	0.800 255	0.400 261
5	0.800 171	0.800 185	0.400 224
6	0.800 120	0.800 133	0.400 174
7	0.800 083	0.800 095	0.400 194
8	0.800 052	0.800 064	0.400 156
9	0.800 027	0.800 038	0.400 144

**Table 3.** Quadratic gate coupling strengths between quantum dots (26 carbon atoms) and gates of double-gated SET configurations.

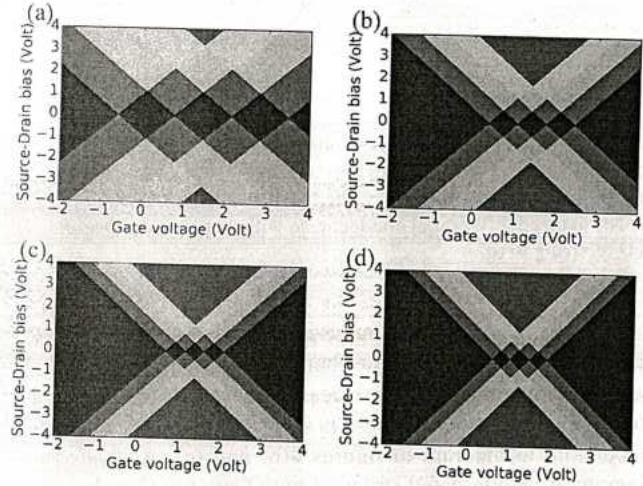
Rotation index $n$	Quadratic coupling strength( $\beta$ (eV <sup>-1</sup> ))		
	Gate-t = Gate-b	Gate-t = Gate-b - 4	Gate-t = 0
0	-0.001 757	-0.003 188	-0.019 021
1	-0.001 765	-0.003 457	-0.020 454
2	-0.001 765	-0.003 292	-0.019 669
3	-0.001 772	-0.003 247	-0.019 370
4	-0.001 777	-0.003 231	-0.019 231
5	-0.001 782	-0.003 224	-0.019 158
6	-0.001 786	-0.003 222	-0.019 086
7	-0.001 789	-0.003 219	-0.019 114
8	-0.001 792	-0.003 218	-0.019 066
9	-0.001 794	-0.003 218	-0.019 053

To comprehend the underlying electronic properties of TBG QD-based SET, we examine how the total energy depends on the gate electrode. Through DFT and DFTB calculations, we obtain the total energies of the TBG QD in the SET scenario for many charge states. Based on these obtained energies, a quadratic function can be fit appropriately using following expression:

$$E(q, V_g) = E_0 + qW + \alpha qV_g + \beta (eV_g)^2. \quad (1)$$

The above energy expression consists of several terms. The first term,  $E_0$ , corresponds to the zeroth-order term and represents a constant energy component. The second term, denoted as  $qW$ , represents the reservoir energy, where  $q$  denotes the charge of the TBG QDs, and  $W$  represents the work function of the electrode. In our simulations, a value of  $W = 5.28$  eV is adopted, being a characteristic value for a gold electrode. To account for the direct coupling between the TBG QD and the gate electrode, the third term in equation (1) is included. This term is proportional to the charge  $q$  on the QD and exhibits a linear relationship with respect to the gate voltage  $V_g$ . The strength of this linear coupling is denoted as  $\alpha$ , which depends on the spacial relation between the TBG QD and the gate, specific to the molecule under investigation. The fourth term in the energy expression has nothing to do with the charge state and exhibits a quadratic dependence on the gate voltage  $V_g$ . This term captures the contribution of electrical polarization influenced by an electric field. The quadratic coupling strength is represented by  $\beta$ . To determine the values of the coupling strengths, namely  $\alpha$  and  $\beta$ , we perform a least squares fit to the total energies obtained from the DFT/DFTB calculations. This fitting procedure allows us to estimate the optimal values of the coupling strengths that best describe the system's behavior in our model. The coupling strengths corresponding to various rotation angles are listed in tables 2 and 3.

Observations reveal that both the linear and quadratic gate-island coupling strengths generally decrease as the rotation angle decreases. This finding suggests that the influence of electrical polarization in the charge stability diagrams of double-gated SET devices depends on the specific rotation

**Figure 7.** Charge stability diagrams of twisted bilayer graphene quantum dots of various sizes with (a) 26, (b) 74, (c) 122, and (d) 146 carbon atoms under double-gated single electron transistor. Gate voltage condition of Gate-t = Gate-b is used. The rotation angle for all cases is fixed at 21.78°. The number of charge states of 4, 3, 2, 1, 0, are represented by the color of red, yellow, green, blue, and dark blue, respectively.

angles of the studied TBG QDs. Consequently, this further corroborates the suitability of double-gated SET configurations for the identification and characterization of TBG QDs.

### 3.3. Effect of QD sizes

In this section, we thoroughly investigate the charge stability diagrams of TBG QDs with varying sizes within a double-gated SET configuration. Specifically, we examine TBG QDs comprised of 26, 74, 122, and 146 carbon atoms, as illustrated in figure 7. The gate voltage condition employed is Gate-t = Gate-b, indicating that the potentials of the top and bottom gates are set to be equal.

By carefully analyzing these charge stability diagrams, we observe a clear reduction in the size of the diamond-shaped



**Table 4.** Linear gate coupling strengths between gates and various island quantum dots of double-gated SET configurations with Gate-t = Gate-b.

Rotation index $n$	Linear gate-island coupling strength( $\alpha$ )		
	74 C atoms	122 C atoms	146 C atoms
0	0.853 411	0.882 212	0.951 942
1	0.853 446	0.881 428	0.951 879
2	0.853 218	0.881 672	0.951 870
3	0.853 049	0.881 709	0.951 818
4	0.852 925	0.881 683	0.951 770
5	0.852 842	0.881 654	0.951 734
6	0.852 783	0.881 631	0.951 707
7	0.852 741	0.881 613	0.951 688
8	0.852 708	0.881 596	0.951 674
9	0.852 682	0.881 582	0.951 662

regions as the TBG QD island increases in size. This reduction can be attributed to the suppression of energy levels as the number of atoms within the nano clusters grows.

Additionally, we investigate the linear and quadratic gate coupling strengths between the gates and the TBG QD islands composed of 74, 122, and 146 carbon atoms. As presented in tables 4 and 5, we find that these coupling strengths decrease as the twisting angles become smaller. Remarkably, for each twisting angle investigated, the linear gate-island coupling becomes stronger as the size of the TBG QD increases.

In addition, graphene QD-based single-electron transistors in van der Waals hybrids have attracted considerable attention in recent studies. Noteworthy achievements include the fabrication of graphene QDs with varying diameters, ranging from 60 to 350 nm [34], exhibiting charging energies of approximately 3 meV [35]. Additionally, an Al nanocluster/MoS<sub>2</sub> device with a 250 nm channel length demonstrated a charging energy of 4 meV [36]. Investigations have also explored the size distribution of Ni grains and graphene domains on substrates, ranging from a few micrometers to nearly 100  $\mu$ m [37]. Hybrid structures comprising graphene QDs on hexagonal boron nitride layers, with dot sizes of 13 nm, exhibited intriguing single-electron charging effects [38]. Present research focuses on simulating QDs with diameters and channels smaller than 4 nm, resulting in charging energies spanning 0.5 to 3.5 eV. These energy ranges stem from the significant energy gap between the highest occupied molecular orbital (HOMO) and the lowest unoccupied molecular orbital (LUMO) of the QDs. Simulations aim to meet the demands of ongoing experiments by considering large-scale QD systems.

The charge stability diagram plays a crucial role in investigating single-electron charging phenomena. Prior studies utilized the orthodox method to simulate the charge stability diagram of an Al nanocluster/MoS<sub>2</sub> device [36], suited for metallic nanoclusters of around 10 nm. However, the discrete energy spectrum exhibited by the islands in our cases precludes the orthodox method, as these islands lack metallic behavior. Thus, an alternative simulation approach based on first-principles calculations of the molecule's total

**Table 5.** Quadratic gate coupling between various quantum dots and gates of double-gated SET configurations with Gate-t = Gate-b.

Rotation index $n$	Quadratic coupling strength( $\beta$ (eV <sup>-1</sup> ))		
	74 C atoms	122 C atoms	146 C atoms
0	-0.006 352	-0.010 347	-0.002 266
1	-0.006 280	-0.010 316	-0.002 264
2	-0.006 281	-0.010 340	-0.002 253
3	-0.006 295	-0.010 374	-0.002 249
4	-0.006 309	-0.010 401	-0.002 225
5	-0.006 320	-0.010 42	-0.002 251
6	-0.006 329	-0.010 434	-0.002 253
7	-0.006 335	-0.010 444	-0.002 254
8	-0.006 340	-0.010 452	-0.002 255
9	-0.006 344	-0.010 459	-0.002 255

energy within an electrostatic environment was employed [17]. Although the current method has limitations in accurately capturing quantum capacitance and transmission processes between the source/drain and islands, future endeavors aim to integrate orthodox theory with quantum chemistry calculations for precise simulations of molecular-level single-electron transistors.

Moreover, the observation in graphene that quantum capacitance is directly proportional to its density of states highlights the relationship between these two quantities [39]. However, when it comes to precise measurement and simulation of capacitance in TBG QD based SETs, the presence of non-uniformly spaced energy levels in TBG QDs necessitates the development of novel approaches [40]. These approaches are essential to accurately capture the capacitance behavior in TBG QDs and facilitate comprehensive understanding and analysis of their electronic properties.

#### 4. conclusion

In conclusion, we have investigated the electronic properties of TBG QDs within a SET configuration. We compared the performance of conventional and double-gated SET structures and found that the double-gated configuration provides enhanced control over the electronic properties of TBG QDs. We identified the influence of rotation angles on the charge stability diagrams and observed that the linear and quadratic gate-island coupling strengths decrease as the rotation angle decreases. Moreover, we quantified the effect of QD size on the charge stability diagrams and found that the size of the diamond-shaped regions decreases as the TBG QD size increases. Our findings provide valuable insights into the electronic properties of TBG QDs based SET and demonstrate the potential of realization of the configuration. Further studies are warranted to explore the unique interlayer coupling variations induced by TBG QDs under SET environment and the crossover from sequential transport to coherent transport.



## Data availability statement

All data that support the findings of this study are included within the article (and any supplementary files).

## Acknowledgments

Supported by the Natural Science Foundation of China under Grant No. 11947205, by the Natural Science Foundation of Chongqing Under No. cstc2020jcyj-msxmX0003, Science and Technology Research project of Chongqing Education Commission Under No. KJQN202201421, and Educational Reform Project Fund of Yangtze Normal University (No. JG2019234).

## ORCID iD

Zhongkai Huang  <https://orcid.org/0000-0002-4062-0402>

## References

- [1] Cao Y, Fatemi V, Fang S, Watanabe K, Taniguchi T, Kaxiras E and Jarillo-Herrero P 2018 Unconventional superconductivity in magic-angle graphene superlattices *Nature* **556** 43–50
- [2] Wang X and Yang M 2022 Enhanced interlayer coupling in twisted bilayer graphene quantum dots *Appl. Surf. Sci.* **600** 154148
- [3] Wang X, Shengping Yu L, Yang M and Jackson K 2021 Interlayer polarizability in twisted bilayer graphene quantum dots *Phys. Rev. B* **104** 155411
- [4] Wang X, Cui Y, Zhang Li and Yang M 2021 Enhanced second-order Stark effect in twisted bilayer graphene quantum dots *Nano Res.* **14** 3935–41
- [5] Tepliakov N, Orlov A, Kundelev E and Rukhlenko I 2020 Twisted bilayer graphene quantum dots for chiral nanophotonics *J. Phys. Chem. C* **124** 22704–10
- [6] Zhou X-F, Liu Y-W, Yan H-Y, Fu Z-Q, Liu H and He L 2021 Electronic confinement in quantum dots of twisted bilayer graphene *Phys. Rev. B* **104** 235417
- [7] Mirzakhani M, Peeters F M and Zarenia M 2020 Circular quantum dots in twisted bilayer graphene *Phys. Rev. B* **101** 075413
- [8] Wang Y, Yu G, Rösner M, Katsnelson M, Lin H-Q and Yuan S 2022 Polarization-dependent selection rules and optical spectrum atlas of twisted bilayer graphene quantum dots *Phys. Rev. X* **12** 021055
- [9] Bucko J and sek Herman F 2021 Large twisting angles in bilayer graphene Moiré quantum dot structures *Phys. Rev. B* **103** 075116
- [10] Liu X, Wang X, Yu S, Wang G, Li B, Cui T, Lou Z and Ge H 2023 Polarizability characteristics of twisted bilayer graphene quantum dots in the absence of periodic Moiré potential *RSC Adv.* **13** 23590–600
- [11] Kastner M A 1992 The single-electron transistor *Rev. Mod. Phys.* **64** 849–58
- [12] Grabert H and Devoret M H 2013 *Single Charge Tunneling: Coulomb Blockade Phenomena In Nanostructures (NATO Science Series B)* (Springer)
- [13] Rozhkov A V, Sboychakov A O, Rakhmanov A L and Nori F 2017 Single-electron gap in the spectrum of twisted bilayer graphene *Phys. Rev. B* **95** 045119
- [14] Maeda K, Okabayashi N, Kano S, Takeshita S, Tanaka D, Sakamoto M, Teranishi T and Majima Y 2012 Logic operations of chemically assembled single-electron transistor *ACS Nano* **6** 2798–803
- [15] Keith D, House M G, Donnelly M B, Watson T F, Weber B and Simmons M Y 2019 Single-shot spin readout in semiconductors near the shot-noise sensitivity limit *Phys. Rev. X* **9** 041003
- [16] Rani S and Ray S J 2019 Detection of gas molecule using C<sub>3</sub>N island single electron transistor *Carbon* **144** 235–40
- [17] Stokbro K 2010 First-principles modeling of molecular single-electron transistors *J. Phys. Chem. C* **114** 20461–5
- [18] S Smidstrup et al 2019 Quantumatk: an integrated platform of electronic and atomic-scale modelling tools *J. Phys.: Condens. Matter* **32** 015901
- [19] Elstner M, Porezag D, Jungnickel G, Elsner J, Haugk M, Frauenheim T, Suhai S and Seifert G 1998 Self-consistent-charge density-functional tight-binding method for simulations of complex materials properties *Phys. Rev. B* **58** 7260–8
- [20] Brandbyge M, Mozos J-L, Ordejón P, Taylor J and Stokbro K 2002 Density-functional method for nonequilibrium electron transport *Phys. Rev. B* **65** 165401
- [21] Kaasbjerg K and Flensberg K 2008 Strong polarization-induced reduction of addition energies in single-molecule nanojunctions *Nano Lett.* **8** 3809–14
- [22] Brandbyge M, Kobayashi N and Tsukada M 1999 Conduction channels at finite bias in single-atom gold contacts *Phys. Rev. B* **60** 17064–70
- [23] Taylor J, Guo H and Wang J 2001 *Ab initio* modeling of open systems: Charge transfer, electron conduction and molecular switching of a C<sub>60</sub> device *Phys. Rev. B* **63** 121104
- [24] Ray S J 2014 Single atom impurity in a single molecular transistor *J. Appl. Phys.* **116** 154302
- [25] Ray S J 2014 Single molecule transistor based nanopore for the detection of nicotine *J. Appl. Phys.* **116** 244307
- [26] Ray S J 2015 Humidity sensor using a single molecular transistor *J. Appl. Phys.* **118** 044307
- [27] Ray S J 2015 Single molecular transistor as a superior gas sensor *J. Appl. Phys.* **118** 034303
- [28] Ray S J 2016 Gate engineered performance of single molecular transistor *J. Appl. Phys.* **119** 204302
- [29] Ray S J and Chowdhury R 2014 Double gated single molecular transistor for charge detection *J. Appl. Phys.* **116** 034307
- [30] Anu, Srivastava A and Khan M 2018 Charge stability diagram and addition energy spectrum for single-electron transistor based on Ni-dithiolene derivatives *Org. Electron.* **59** 125–30
- [31] Guo Y-D, Yan X-H and Xiao Y 2012 Computational investigation of dna detection using single-electron transistor-based nanopore *J. Phys. Chem. C* **116** 21609–14
- [32] Garaj S, Hubbard W, Reina A, Kong J, Branton D and Golovchenko J A 2010 Graphene as a subnanometre trans-electrode membrane *Nature* **467** 190–3
- [33] Li J, Stein D, McMullan C, Branton D, Aziz M and Golovchenko J 2001 Ion-beam sculpting at nanometre length scales *Nature* **412** 166–9
- [34] Güttinger J, Molitor F, Stampfer C, Schnez S, Jacobsen A, Dröscher S, Ihn T and Ensslin K 2012 Transport through graphene quantum dots *Rep. Prog. Phys.* **75** 126502
- [35] Stampfer C, Schurtenberger E, Molitor F, Güttinger J, Ihn T and Ensslin K 2008 Tunable graphene single electron transistor *Nano Lett.* **8** 2378–83
- [36] DonaldNotemngnou Mouafo L et al 2021 0D/2D heterostructures vertical single electron transistor *Adv. Funct. Mater.* **31** 2008255
- [37] Godel F, DonaldNotemngnou Mouafo L, Froehlicher G, Doudin B, Berciaud S, Henry Y, Dayen J-F and Halley D

- 2017 Conductance oscillations in a graphene/nanocluster hybrid material: toward large-area single-electron devices *Adv. Mater.* **29** 1604837
- [38] Kim G *et al* 2019 Planar and van der Waals heterostructures for vertical tunnelling single electron transistors *Nat. Commun.* **10** 230
- [39] Dröschner S, Roulleau P, Molitor F, Studerus P, Stampfer C, Ensslin K and Ihn T 2010 Quantum capacitance and density of states of graphene *Appl. Phys. Lett.* **96** 152104
- [40] Weis J 2005 *Single-Electron Devices BT - CFN Lectures on Functional Nanostructures* vol 1 (Springer) pp 87–121





PAPER • OPEN ACCESS

# Polaron dynamics of Bloch–Zener oscillations in an extended Holstein model

To cite this article: Zhongkai Huang *et al* 2021 *New J. Phys.* 23 123020

View the [article online](#) for updates and enhancements.

与原件相符



A handwritten signature in black ink, appearing to be 'Zhongkai Huang'.



## PAPER

## OPEN ACCESS

RECEIVED  
11 July 2021REVISED  
24 October 2021ACCEPTED FOR PUBLICATION  
17 November 2021PUBLISHED  
10 December 2021Original content from  
this work may be used  
under the terms of the  
Creative Commons  
Attribution 4.0 licence.Any further distribution  
of this work must  
maintain attribution to  
the author(s) and the  
title of the work, journal  
citation and DOI.

## Polaron dynamics of Bloch–Zener oscillations in an extended Holstein model

Zhongkai Huang<sup>1,2,3,\*</sup>, Alejandro D Somoza<sup>1,4</sup>, Cheng Peng<sup>1,\*</sup>, Jin Huang<sup>2,\*</sup>,  
Maolin Bo<sup>5</sup>, Chuang Yao<sup>5</sup>, JiBiao Li<sup>5</sup> and Guankui Long<sup>6</sup><sup>1</sup> Key Laboratory of Inorganic Special Functional Materials of Chongqing, Yangtze Normal University, Chongqing 408100, People's Republic of China<sup>2</sup> School of Chemistry and Chemical Engineering, Chongqing Key Laboratory of Soft-Matter Material Chemistry and Function Manufacturing, Southwest University, Chongqing 400715, People's Republic of China<sup>3</sup> Department of Physics, Chongqing University, Chongqing 401330, People's Republic of China<sup>4</sup> German Aerospace Center (DLR), Stuttgart 70569, Germany<sup>5</sup> Key Laboratory of Extraordinary Bond Engineering and Advanced Materials Technology of Chongqing, Yangtze Normal University, Chongqing 408100, People's Republic of China<sup>6</sup> School of Materials Science and Engineering, Nankai University, Tianjin 300071, People's Republic of China

\* Authors to whom any correspondence should be addressed.

E-mail: zhongkaihuang@yznu.edu.cn, 20090008@yznu.edu.cn and huangjin2015@swu.edu.cn

Keywords: Bloch–Zener oscillations, phonons effect, open quantum system

## Abstract

Recent developments in qubit engineering make circuit quantum electrodynamics devices promising candidates for the study of Bloch oscillations (BOs) and Landau–Zener (LZ) transitions. In this work, a hybrid circuit chain with alternating site energies under external electric fields is employed to study Bloch–Zener oscillations (BZO), i.e. coherent superpositions of BOs and LZ transitions. We couple each of the tunable qubits in the chain to dispersionless optical phonons and build an extended Holstein polaron model with the purpose of investigating vibronic effects in the BZO. We employ an extension of the Davydov ansatz in combination with the Dirac–Frenkel time-dependent variational principle to simulate the dynamics of the qubit chain under the influence of high-frequency quantum harmonic oscillators. Band gaps emerge due to energy differences in site energies at alternating qubit sites, and are shown to play key roles in tuning band structures and time periodic reconstructions of the wave patterns. In the absence of qubit–phonon interactions, the qubits undergo either standard BZO or breathing modes, depending on whether the initial wave packet is formed by a broad or narrow Gaussian wave packet, respectively. The BZO can get localized in space if the band gaps are sufficiently large. In the presence of qubit–phonon coupling, the periodic behavior of BZO can be washed out and undergo dynamic localization. The influence of an ohmic bath on the dynamics of BZO is investigated by means of a Markovian master equation approach. Finally, we calculate the von Neumann entropy as a measure of the entanglement between qubits and phonons.

## 1. Introduction

Bloch oscillations (BOs) and Landau–Zener (LZ) transitions are two fundamental phenomena in quantum mechanics associated with coherent transport of quantum particles and waves in periodic media under external driving forces [1, 2]. In periodic potentials, there are continuous Bloch band structures and delocalized Bloch eigenfunctions that are uniformly distributed over the whole system. When an electric field is introduced in the form of a direct current (DC), the qubit chain exhibits discrete localized eigenstates that receive the name of Wannier–Stark ladders [3, 4]. In the absence of scattering and dephasing effects, BOs refer to the periodic motion of charged carriers in reciprocal and real space [5]. When the variation of a linear potential due to a superimposed field is comparable with the smallest gaps to an adjacent band, the LZ transitions emerge and carriers may successively tunnel to higher-order



bands [6, 7]. Coherent superpositions of BOs and LZ transitions receive the name of Bloch-Zener oscillations (BZO) [8–10] or Landau-Zener-Bloch oscillations [10], and have found applications in various fields, including quantum optics [11], solid-state physics [12], or atomic and molecular physics [13]. In fact, BZOs have already been directly observed in a variety of systems, such as light beams in two-dimensional, square photonic lattices [9], light waves in optical, binary superlattices [11], or rubidium Bose-Einstein condensates [14], to name a few.

In recent decades, a growing interest has been paid to tunable platforms that are based on circuit quantum electrodynamics (QED) because of their high-precision control, scalability, and long decoherence time [15]. For these reasons, the application of circuit QED setups as quantum simulators may provide relevant insights into the fundamental problems of quantum mechanics [11–33]. These circuits can be implemented on various physical platforms, ranging from an individual artificial atom, to one- and two-dimensional lattices [34, 35]. Versatile platforms can meet requirements of universal quantum computations and can be designed for specific quantum simulation tasks [36]. More importantly, rapid progresses in circuit QED devices have opened the door to the investigation of the interplay between BOs and LZ transitions, which is the focus of this work. Recently, several QED experiments have been dedicated to the analysis of BOs. In 2017, Ramasesh *et al* realized Bloch-oscillating quantum walks in a circuit QED protocol which is formed by a transmon qubit and a superconducting cavity mode [37]. Bahmani *et al* theoretically proposed a one-dimensional chain of coupled resonant circuits to probe the BOs and Wannier-Stark ladders [38]. Guo *et al* demonstrated the presence of BOs on a circuit processor of 5 superconducting transmon qubits [39].

Circuit QED experiments have also been performed to investigate LZ transitions. Izmailkov *et al* observed in 2004 the LZ transitions in a macroscopic circuit composed by an Al three-junction qubit and a Nb resonant tank [40]. Johansson *et al* measured the LZ transitions on an individual flux qubit within a superconducting chip of device qubits [41]. Hänggi and co-workers studied the LZ transition probability at long times in circuit QED [42]. Neillinger *et al* demonstrated the LZ transitions in two experiments utilizing circuit QED arrangements with two types of superconducting qubits: the flux qubit on the basis of conventional Josephson junctions, and the phase-slip qubit based on niobium nitride nanowires [43]. Coherent transport in the BZOs can therefore be investigated by employing a circuit QED configuration.

Nevertheless, the quantum states of the qubits in the circuit QED platform will inevitably be affected by surrounding environments. The interaction between qubits and their environments has been probed in a variety of circuit QED setups [44–46]. Dissipative effects and the interaction between BOs, LZ transitions and phonons can be studied in hybrid circuit QED setups that incorporate for example mechanical resonators or microwave cavities [47, 48]. O'Connell *et al* realized single-phonon control in a microwave-frequency mechanical resonator coupled to a flux qubit [49]. Riedinger *et al* demonstrated the correlated photon-phonon pairs based on a Duan-Lukin-Cirac-Zoller protocol [50]. Manenti *et al* measured average coherent phonon populations in a circuit QED architecture containing a superconducting qubit coupled to a surface acoustic wave cavity via piezoelectric effects [51]. In spite of these experimental efforts, the influence of quantized oscillators in the dynamics of BOs and LZ transitions is yet not fully understood.

A variational method that employs a multi-mode representation of a Davydov ansatz called multi-D2 has been developed for the simulation of open quantum systems with applications to fermions and bosons [52, 53]. Here, the accuracy of the variational ansatz is increased by adding more modes until the value of the error, a measure based on a geometrical interpretation of the variational manifold, is maintained below a desired accuracy. In that respect we say that the method is numerically accurate within the theoretical model of the system. The method has been applied to a multitude of systems, including a Holstein model of polaron dynamics in the presence of external fields [54–56], phase transitions in the spin-boson model [57] or singlet fission model [58], a dissipative LZ model that is based on QED protocols [41, 59] and other investigations in quantum optics [60, 61].

In the present work, we employ the aforementioned multi-D2 ansatz to perform numerically accurate simulations of BZOs in a one-dimensional model of a qubit chain with alternating site energies under the influence of a constant electric field and phonon. Our focus here will be the interaction between the qubits and the high frequency, optical phonons that have an intramolecular origin. The remainder of the paper is organized as follows. In section 2, we show the model Hamiltonian and explain the properties of the multi-D2 ansatz as the trial wave function. In section 3.1, the energy structures and transitions of a purely electronic qubit chain is studied. In section 3.2, the effects of different initial conditions and band gaps on the BZO dynamics of a free excitation are investigated. In section 3.3, the effects of undamped, high-frequency phonon modes on the BZO dynamics are studied. Finally, the influence of dephasing Ohmic bath on the dynamics of BZOs is examined in section 3.4. Conclusions are drawn in section 4.



## 2. Methodology

### 2.1. Model

An schematic of the one-dimensional quantum circuit used in this work is shown in figure 1. The qubits are gap-tunable and the site energies of the model can thus be controlled [62]. The signs  $\odot$  in qubit  $j-1$  and  $\otimes$  in qubit  $j$  illustrate that the magnetic fluxes at consecutive sites point at opposite directions, which also affects the sign of their site energies. The magnetic flux  $\Phi_e(t)$  represents an external driving force acting on the qubit array. The resultant biperiodic potential serves as an ideal platform for the investigation of BZOs [8]. The Hamiltonian of the one-dimensional qubit chain schematically shown in figure 1 is given by

$$\hat{H}_{\text{qu}} = -J \sum_n \hat{a}_n^\dagger (\hat{a}_{n+1} + \hat{a}_{n-1}) + \frac{\delta}{2} \sum_n (-1)^n \hat{a}_n^\dagger \hat{a}_n + F \sum_n n \hat{a}_n^\dagger \hat{a}_n, \quad (1)$$

where  $J$  is the nearest-neighbours hopping integral,  $\delta$  is the difference in the site energies at alternating sites,  $F$  denotes an external electric field,  $\hat{a}_n$  ( $\hat{a}_n^\dagger$ ) is the annihilation (creation) operator of the electronic excitation at site  $n$ , and the distance between neighbouring sites is set to unity for simplicity. Periodic boundary conditions can be introduced by bending the linear array into a ring structure, leading to discontinuities in the applied electric potential at the boundaries due to the constant nature of the external field (DC-current) [4]. Thanks to the usage of a gauge transformed vector potential,  $A(t) = -Ft$ , this discontinuity problem can be avoided [63], and equation (1) can be recast as follows

$$\hat{H}_{\text{qu}} = -J \sum_n \hat{a}_n^\dagger (e^{iA(t)} \hat{a}_{n+1} + e^{-iA(t)} \hat{a}_{n-1}) + \frac{\delta}{2} \sum_n (-1)^n \hat{a}_n^\dagger \hat{a}_n. \quad (2)$$

Taking into consideration the high-frequency optical phonons at each site, the Hamiltonian of the complete electronic-vibrational (vibronic) system can be written as

$$\hat{H} = \hat{H}_{\text{qu}} + \hat{H}_{\text{ph}} + \hat{H}_{\text{qu-ph}}. \quad (3)$$

These undamped high-frequency phonon modes have been shown to strongly influence the excitation transfer and optical properties of organic semiconductors, photosynthetic molecular complexes [64], and qubit-resonator systems [65]. The phonon Hamiltonian  $\hat{H}_{\text{ph}}$  and qubit-phonon coupling Hamiltonian  $\hat{H}_{\text{qu-ph}}$  terms take the following form

$$\hat{H}_{\text{ph}} = \omega_0 \sum_n \hat{b}_n^\dagger \hat{b}_n, \quad (4)$$

$$\hat{H}_{\text{qu-ph}} = -g\omega_0 \sum_n \hat{a}_n^\dagger \hat{a}_n (\hat{b}_n + \hat{b}_n^\dagger), \quad (5)$$

where  $g$  is the diagonal qubit-phonon coupling strength and  $\hat{b}_n$  ( $\hat{b}_n^\dagger$ ) denotes the annihilation (creation) operator of the phonons with site  $n$ . Next we transform the bosonic operators from real space to momentum space by expanding them in a Fourier series

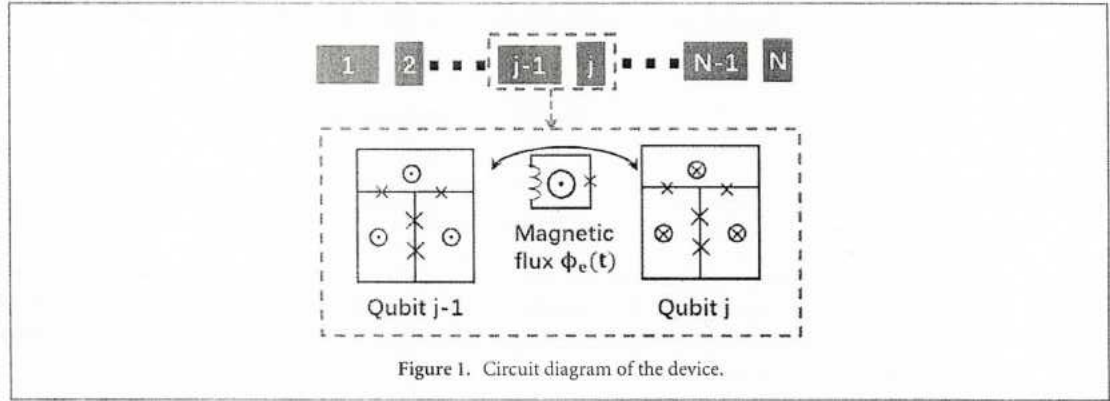
$$\hat{b}_q^\dagger = N^{-1/2} \sum_n e^{iqn} \hat{b}_n^\dagger, \quad \hat{b}_n^\dagger = N^{-1/2} \sum_q e^{-iqn} \hat{b}_q^\dagger, \quad (6)$$

and rewrite the terms  $\hat{H}_{\text{qu}}$ ,  $\hat{H}_{\text{qu-ph}}$  of the Hamiltonian as follows,

$$\hat{H}_{\text{ph}} = \sum_q \omega_q \hat{b}_q^\dagger \hat{b}_q, \quad (7)$$

$$\hat{H}_{\text{qu-ph}} = -N^{-1/2} g \sum_{n,q} \omega_q \hat{a}_n^\dagger \hat{a}_n (e^{iqn} \hat{b}_q + e^{-iqn} \hat{b}_q^\dagger), \quad (8)$$

in which  $\omega_q$  is the phonon frequency of the mode with momentum  $q$ . Here we use dispersionless, Einstein phonons with  $\omega_q = \omega_0$ , and set the value of  $\omega_0$  to unity as the reference energy scale of this work. It is noted that the phonon related terms (equations (4) and (5)) in this work are the same with those in the standard Holstein model, which can be written as  $\hat{H}_{\text{Holstein}} = -J \sum_n \hat{a}_n^\dagger (\hat{a}_{n+1} + \hat{a}_{n-1}) + \omega_0 \sum_n \hat{b}_n^\dagger \hat{b}_n - g\omega_0 \sum_n \hat{a}_n^\dagger \hat{a}_n (\hat{b}_n + \hat{b}_n^\dagger)$  and describes non-interacting electrons in a one-dimensional lattice coupled to dispersionless phonons [66, 67]. The electronic terms in our work describe one electronic excitation in a double-band lattice under the external constant field, and is an extension of the electronic parts of the standard Holstein model. Therefore, our model can be treated as a type of extended Holstein model in terms of the Holstein language. In the Holstein system, a bare electron is dressed by a cloud of bosonic excitations, and form a quasiparticle called polaron. Polaron dynamics in the Holstein model have been continuingly studied using the following variational method [52–56].



## 2.2. Multi-D2 ansatz

The variational ansatz that we employ in this work is the multi-D2 Davydov ansatz [52, 55, 56], a superposition of electronic excitations and coherent states that takes the following form

$$|D_2^M(t)\rangle = \sum_i^M \sum_n^N \psi_{in} |n\rangle |\lambda_i\rangle = \sum_i^M \sum_n^N \psi_{in} \hat{a}_n^\dagger |0\rangle_{\text{ex}} \exp \left\{ \sum_q [\lambda_{iq} \hat{b}_q^\dagger - \lambda_{iq}^* \hat{b}_q] \right\} |0\rangle_{\text{ph}} \quad (9)$$

where  $M$  is the multiplicity of the ansatz and measures the number of different coherent states per site and  $i$  labels the  $i$ th coherent state.  $\psi_{in} \in \mathbb{C}$  denotes the time-dependent excitation amplitude of the  $n$ th qubit and  $\lambda_{iq} \in \mathbb{C}$  is the phonon displacement of the  $q$ th mode. The time evolution of the time-dependent variational parameters ( $u_i = \psi_{in}, \lambda_{iq}$ ) are determined by the Dirac–Frenkel time-dependent variational principle

$$\frac{d}{dt} \left( \frac{\partial \mathcal{L}}{\partial u_i^*} \right) - \frac{\partial \mathcal{L}}{\partial u_i} = 0, \quad (10)$$

where the Lagrangian  $\mathcal{L}$  is to be found in appendix A. The integration of equations of motion for the variational variables  $u_i$  can result in numerical instabilities [57]. An *apoptosis* procedure has been implemented to circumvent the singularity problem of the numerical solver that makes the multi-D2 ansatz a rather stable tool in the study of polaron dynamics [68]. Using this ansatz, we can provide numerically stable and accurate dynamics for both electronic and bosonic degrees of freedom. The validity of the variational approach has been extensively investigated and confirmed in previous works [41, 52, 55]. The accuracy of the multi-D2 ansatz is again certified in this work for sufficiently high multiplicity  $M$ . More details on the accuracy test can be found in appendix B.

Observables of interest include the time evolution of the excitation probability of the qubit state,  $P_{\text{qu}}(t, n)$ , and the time evolution of phonon displacement,  $X_{\text{ph}}(t, n)$ , as follows

$$\begin{aligned} P_{\text{qu}}(t, n) &= \langle D_2^M(t) | \hat{a}_n^\dagger \hat{a}_n | D_2^M(t) \rangle, \\ X_{\text{ph}}(t, n) &= \langle D_2^M(t) | \hat{b}_n^\dagger + \hat{b}_n | D_2^M(t) \rangle. \end{aligned} \quad (11)$$

In the presence of the external electric field, the current of the composite system can be described as

$$j(t) = \langle D_2^M(t) | i \sum_n (e^{iA(t)} \hat{a}_n^\dagger \hat{a}_{n+1} - \text{h.c.}) | D_2^M(t) \rangle.$$

Furthermore, the expected value  $c(t)$  of the excitation's position is utilized to characterize the centroid of the wave packet, and the standard deviation of the excitation wave packet  $\sigma(t)$  is used to describe how far it moves away from the origin,

$$\begin{aligned} c(t) &= \sum_i^N i P_{\text{qu}}(t, i), \\ \sigma(t)^2 &= \sum_i^N (i - c(t))^2 P_{\text{qu}}(t, i). \end{aligned} \quad (12)$$

The shape of the initial standard deviation  $\sigma_0$  has a significant impact on the mean value  $c(t)$  of the excitations' position [55]. Based on the multi-D2 trial state, the qubit energy, phonon energy,



qubit–phonon coupling energy, and total energy of the system can be respectively written by

$$E_{\text{qu}}(t) = \langle D_2^M(t) | \hat{H}_{\text{qu}} | D_2^M(t) \rangle, \quad (13)$$

$$E_{\text{ph}}(t) = \langle D_2^M(t) | \hat{H}_{\text{ph}} | D_2^M(t) \rangle, \quad (14)$$

$$E_{\text{qu-ph}}(t) = \langle D_2^M(t) | \hat{H}_{\text{qu-ph}} | D_2^M(t) \rangle, \quad (15)$$

$$E_{\text{tot}}(t) = E_{\text{qu}}(t) + E_{\text{ph}}(t) + E_{\text{qu-ph}}(t). \quad (16)$$

In order to better characterize the effects of phonons on the qubit system, the bipartite quantum entanglement is investigated. In particular, we calculate the von Neumann entropy as a measure of the amount of entanglement between the qubit system and the optical phonons [69]. The time evolution of the von Neumann entropy can be written as

$$S_{\text{vN}}(t) = -\text{Tr}(\hat{\rho}_{\text{qu}}(t) \ln \hat{\rho}_{\text{qu}}(t)), \quad (17)$$

where the reduced single-excitation density matrix,  $\hat{\rho}_{\text{qu}}(t) = \text{Tr}_{\text{ph}} \hat{\rho}(t)$ , is the partial trace of the full density matrix,  $\hat{\rho}(t) = |D_2^M(t)\rangle \langle D_2^M(t)|$ , by tracing over the environmental phonon degrees of freedom at time  $t$ .

### 3. Results and discussion

#### 3.1. Spectral properties of BZO phenomenon

We start by discussing the spectral properties, band structure and miniband transitions of the Hamiltonian of equation (1). We consider the Hamiltonian (1) in the Bloch representation to study energy properties in the reciprocal space. In this representation, the electronic ground state of the periodic system is usually described in terms of extended Bloch orbitals, simultaneous eigenstates of the periodic Hamiltonian and of the direct lattice translations. In the absence of an external electric field ( $F = 0$ ), the eigenenergies are given by

$$E_{\mu,k} = \frac{\eta}{2}(-1)^{\mu+1} \sqrt{\delta^2 + 16J^2 \cos^2(k)}, \quad (18)$$

where  $\mu = 0, 1$  is the miniband index,  $k$  is the wave vector index, and  $\eta = \text{sgn}(\delta)$ . The electronic band structure in a reduced Brillouin zone of the qubit Hamiltonian of equation (1) in the absence of an external field or coupling to vibrations is shown in figure 2(a) for  $J = 0.2$ ,  $F = 0$  and  $g = 0$ . The energy difference between alternating sites  $\delta$  is equal to the energy difference between two minibands at the edge of the Brillouin zone. The case when the chain is energetically homogeneous ( $\delta = 0$ ), a Bloch band of width  $4J$  is formed, as shown in the black curve of figure 2(a) (plus sign markers). When an energetic bias is introduced  $\delta \neq 0$ , a pair of minibands separated by  $\delta$  emerge at the edge of the Brillouin zone, as shown in figure 2(a) for various values of  $\delta$ .

In the presence of an external field ( $F \neq 0$ ), the transition matrix elements of  $\hat{H}_{\text{qu}}$  between minibands  $\mu = 0, 1$  with momentum  $k, k'$  can be expressed as  $\langle \phi_{1,k'} | \hat{H}_{\text{qu}} | \phi_{0,k} \rangle = T_k \delta_{\pi}(k - k')$ , where  $|\phi_{\mu,k}\rangle$  represents a Bloch miniband  $\mu$  of momentum  $k$  and the delta function  $\delta_{\pi}(k - k')$  ensures that only direct interband transitions take place. The integrated transition matrix element  $T_k$  is

$$T_k = -\frac{i4FJ\delta \sin(k)e^{ik}}{2\delta^2 + 32J^2 \cos^2(k)}. \quad (19)$$

Transitions occur mainly around the edge of the reduced Brillouin zone and, due to the large energy difference between minibands, almost no transitions take place at the center of the zone. This effect has been verified in experiments [9].

As an example, we take the value  $J = 0.2$  for the electronic coupling strength between qubits in an external electric field  $F = 0.1$  to study the transition amplitudes  $T_k$ , whose absolute value is shown in figure 2(b). The case with the smallest energy difference between consecutive sites ( $\delta = 0.2287$ ) exhibits the largest values, while the transition amplitudes vanish for a gap-free case. In the Wannier representation, the solution to the eigenvalue problem  $\hat{H}_{\text{qu}} |\psi_{\nu,n}\rangle = E_{\nu,n} |\psi_{\nu,n}\rangle$  in a two-band model of the qubit chain gives rise to Wannier–Stark states  $|\psi_{\nu,n}\rangle$  that are indexed by what is known as the mini-ladder index  $\nu = 0, 1$  and are  $2n$  periodic in the lattice. The two energy ladders are equally spaced and have an energy offset of  $2E_0(\delta)$ ,

$$\begin{aligned} E_{0,n} &= E_0(\delta) + 2nF, \\ E_{1,n} &= -E_0(\delta) + (2n + 1)F. \end{aligned} \quad (20)$$

The spectrum of  $E_{\nu,n}(\delta)$  is shown in figure 2(c) and an enlarged plot at zero energy is also shown in figure 2(d). The orange curve in figure 2(d) corresponds to the results of a numerical simulation with

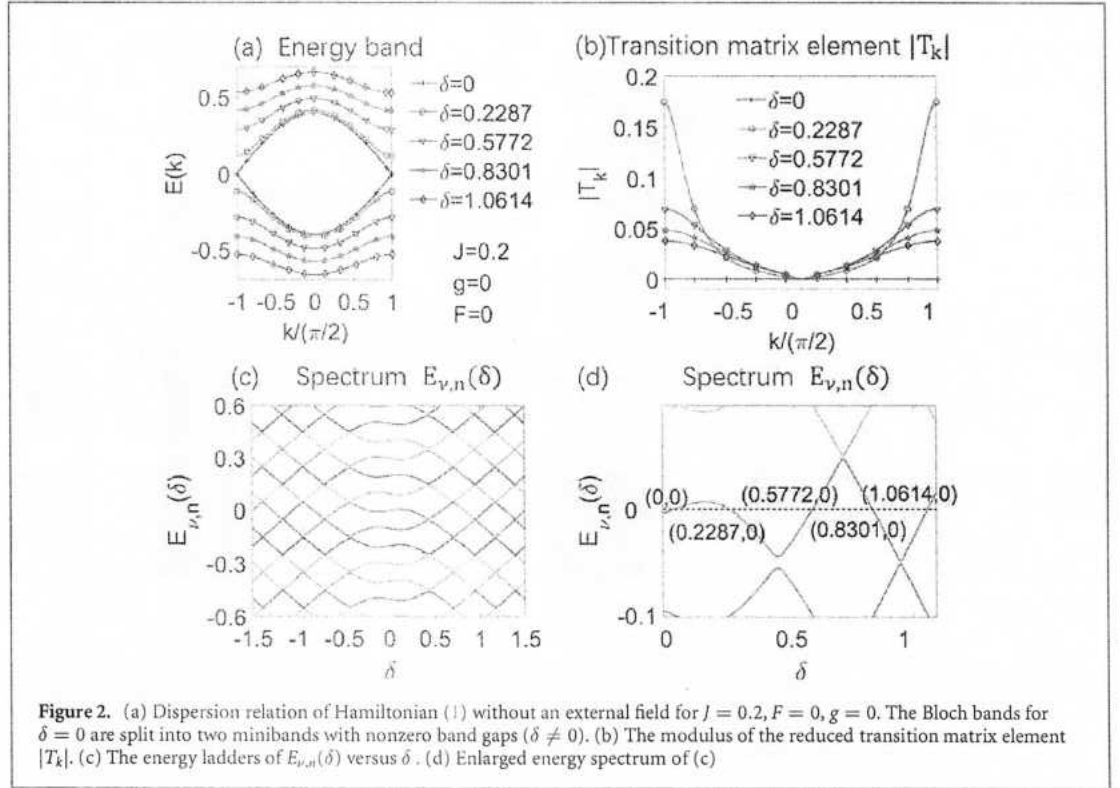


**Figure 2.** (a) Dispersion relation of Hamiltonian (1) without an external field for  $J = 0.2, F = 0, g = 0$ . The Bloch bands for  $\delta = 0$  are split into two minibands with nonzero band gaps ( $\delta \neq 0$ ). (b) The modulus of the reduced transition matrix element  $|T_k|$ . (c) The energy ladders of  $E_{\nu,n}(\delta)$  versus  $\delta$ . (d) Enlarged energy spectrum of (c)

ladder index  $\nu = 0$  at the 0th site ( $n = 0$ ). For the single band case of  $\delta = 0$ , the BOs have a time period of  $T_B = 2\pi\hbar/F$  [70]. When  $\delta \neq 0$ , the excitation undergoes BZO as a combined phenomenon involving both BOs and LZ transitions [16]. The time periodicity of BZO is dominated by the LZ transition, and the time period is usually expressed as  $T_{BZ} = sT_{LZ} = rT_{re}$ , with  $r, s \in \mathbb{N}$  and  $T_{re}$  is known as the reconstruction period, and reference [16] describes these time periodicities in great detail. The energy spacing between the Wannier–Stark ladders is reflected in the period of the LZ transition  $T_{LZ} = 2\pi\hbar/(F - 2E_0(\delta))$ . The reconstruction period is  $T_{re} = \pi\hbar/F = T_B/2$  because the size of the reduced Brillouin zone for  $\delta \neq 0$  is half of that for  $\delta = 0$ . When  $E_0(\delta) = 0$ , we can obtain a relation of  $T_{BZ} = 2T_{re} = T_B$ .

### 3.2. BZO dynamics of a free excitation

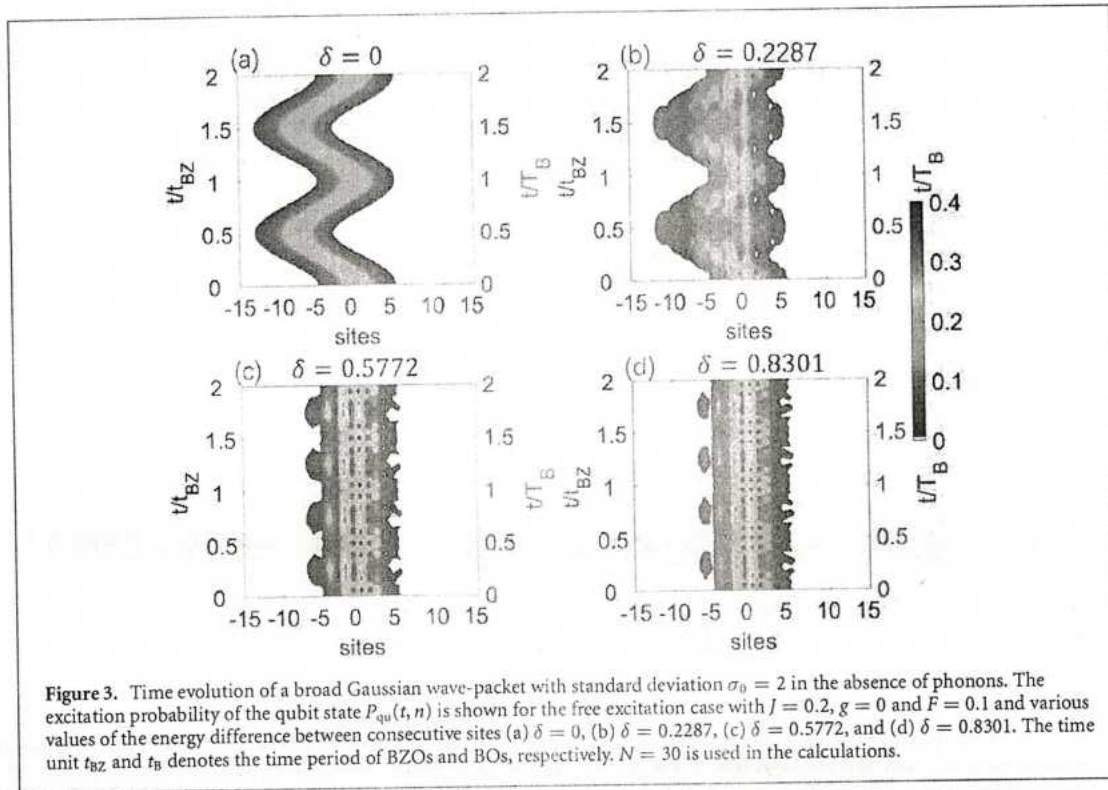
Next we investigate the dynamics of BZO under a wide range of parameters. We remark how the sensitive dependence of electronic dynamics on the energy difference between consecutive sites  $\delta$  can be exploited to manipulate the evolution of the wave packet. For simplicity, we assume that the initial wave packet in the qubit chain is shaped as a Gaussian function of the form

$$|\Psi(t=0)\rangle = \sum_n \psi_n a_n^\dagger |0\rangle_{qu} |0\rangle_{ph} = \sum_n C \exp(-n^2/4\sigma_0^2) a_n^\dagger |0\rangle_{qu} |0\rangle_{ph} \quad (21)$$

in which  $C$  represents a normalization coefficient and  $\sigma_0$  is the initial standard deviation of the Gaussian wave function [55]. We shall assume thereon that the initial state is centered at the site  $n = 0$ , with zero momentum.

We start by studying the purely electronic case in the absence of phonons. Figure 3 shows the excitation dynamics for various values of  $\delta$  and a broad initial state of spatial width  $\sigma_0 = 2$ . When the qubit chain is energetically homogeneous ( $\delta = 0$ ) we obtain the distinctive pattern of BOs with oscillation of the center-of-mass and essentially constant wave shape, as shown in figure 3(a). When an energetic bias is introduced  $\delta \neq 0$ , interband tunneling induces coherent superpositions of BOs and LZ transitions. As the LZ transitions take place mainly when the wave packet is close to the boundary of the energy band, transitions zones can be characterized at times  $t = T_{BZ}/4$  and  $3T_{BZ}/4$  in one  $T_{BZ}$  period. Before  $t = T_{BZ}/4$ , the wave packet mainly propagates in a lower miniband and the travelling direction is orthogonal to the band curve. At  $T_{BZ}/4$ , part of the wave tunnels to a higher miniband and travels along different spatial paths. Around  $3T_{BZ}/4$ , the LZ transitions occur again and the two branches are combined to reconstruct the original wave shape. The BZO pattern is most obvious in the case of  $\delta = 0.2287$  where the interband transitions dominate, as shown in figures 2(b) and 3(b). As depicted in figures 3(c) and (d) for  $\delta = 0.5772$





and 0.8301, the wave packet starts to get localized for higher values of  $\delta$ , although the characteristic structure of BZO can still be inferred. Further localization of the wave packet ensues as  $\delta/J \sim 1$ , as shown in more detail in appendix C

In addition to the initially broad Gaussian wave packet, we also consider a narrow initial state in figure 4 with standard deviation  $\sigma_0 = 0.1$ . Here, the wave packet is initially localized at site  $n = 0$ . When the chain is energetically homogeneous ( $\delta = 0$ ), the characteristic motion of a breathing mode is shown in figure 4(a). The wave packets widen and shrink in space around the origin in a symmetric manner with precise time periodicity. The dynamics of the qubit chain in the presence of an energetic bias  $\delta \neq 0$  is shown in figures 4(b)–(d). Interestingly, the spatial symmetry is destroyed, while the temporal periodicity is preserved. The localization effects are also clearly shown in the plots with large values of  $\delta$ . In addition, we show in figure 5 the time evolution of various observables of interest, such as the mean value of the position of the excitation  $\langle c(t) \rangle$ , the standard deviation of the initial state  $\sigma(t)$ , and the currents  $j(t)$ . For the broad, Gaussian initial condition, the values of  $\langle c(t) \rangle$  in the case of BOs is larger than those of BZO as shown in figure 5(a). The case of  $\delta = 0.2287$  has the largest displacement  $\sigma(t)$  due to its stronger tunneling, as shown in figure 5(c). We show in figure 5(e) that the amplitude of the current  $j(t)$  gets reduced and oscillations become more prominent as the energetic bias  $\delta$  is increased. When the particle is initially localized at the origin as in the case of a narrow Gaussian wave packet, the center of the wave packet oscillates for cases with nonzero  $\delta$ , as shown in figure 5(b), the amplitude of  $\sigma(t)$  decreases as  $\delta$  increases, and the current  $j(t)$  is no longer equal to zero for cases with  $\delta \neq 0$ , as shown in figure 5(e).

### 3.3. Effects of the optical phonon

In this subsection, we proceed to investigate the BZO dynamics of the qubit chain in the presence of dispersionless optical phonons, using the linear, vibronic coupling model described by the extended Holstein Hamiltonian of equation (3). In all following simulations, we take  $\delta = 0.2287$  as the energy difference between consecutive sites as we did in the purely electronic case for an initially broad or narrow wave packet in figures 3(b) and 4(b), respectively. This value of  $\delta$  is chosen so that  $T_{BZ} = T_B$ . In addition we fix the number of sites to  $N = 30$ , with electronic coupling ( $J = 0.2$ ) and the strength of the external field ( $F = 0.1$ ).

In analogy with the previous section, we first study the time evolution in figure 6 of a broad Gaussian packet with standard deviation  $\sigma_0 = 2$ . The characteristic patterns of BZO are washed out as the qubit-phonon coupling is increased from  $g = 0.1$  (figure 6(a)) to  $g = 1.4$  (figure 6(d)). When the qubit-phonon coupling is sufficiently weak, the contour profile of the BZO can still be recognized, as shown in figure 6(a). For intermediate coupling, the structure of BZO start to smear out after time  $3t_{BZ}/4$ ,



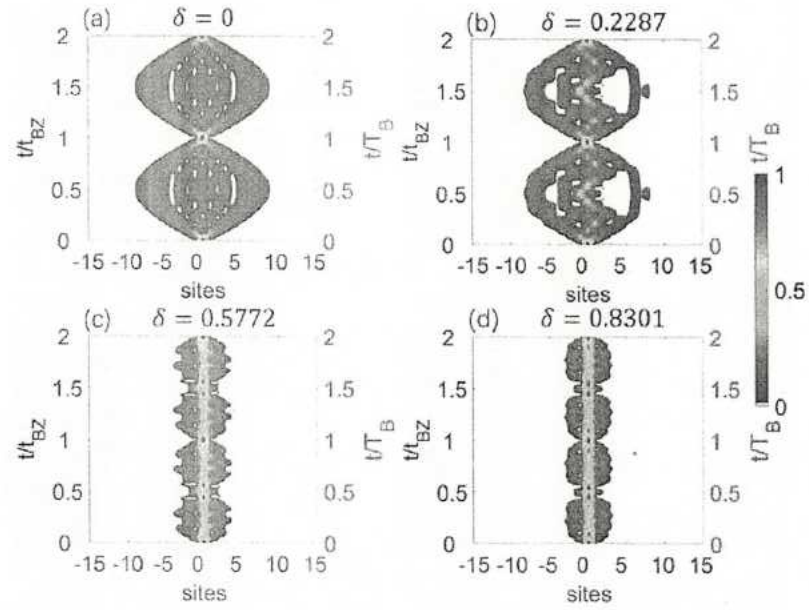


**Figure 4.** Time evolution of a narrow Gaussian wave-packet with standard deviation  $\sigma_0 = 0.1$  in the absence of phonons. The excitation probability of the qubit state  $P_{qu}(t, n)$  is shown for the free excitation case. The same parameters used in figure 3 are employed,  $J = 0.2$ ,  $g = 0$  and  $F = 0.1$ .

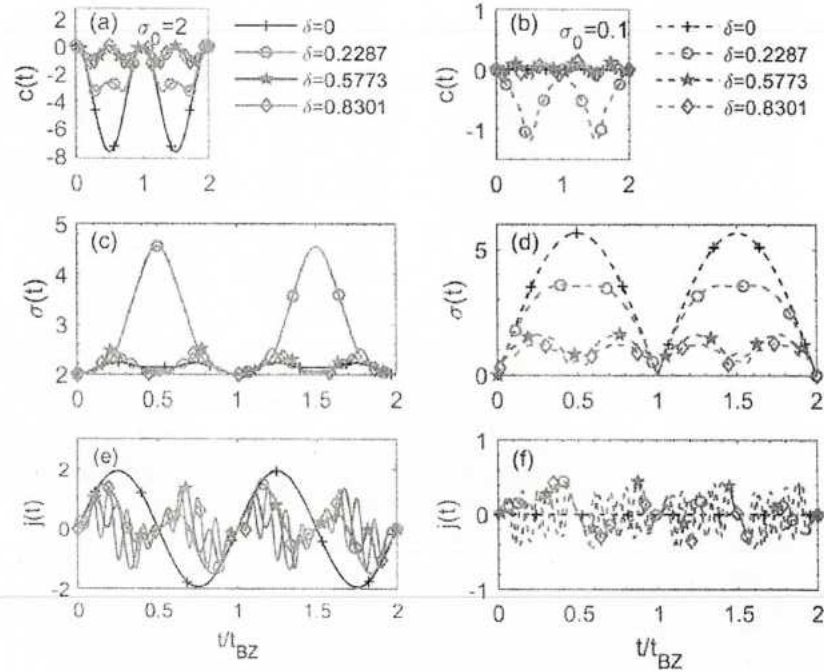
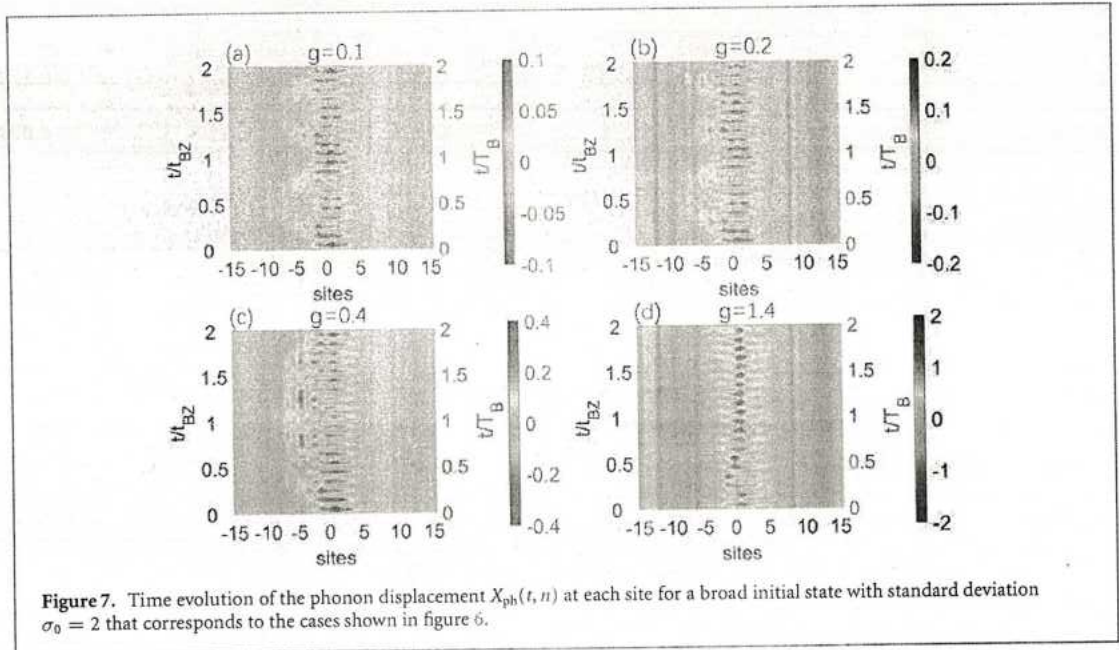
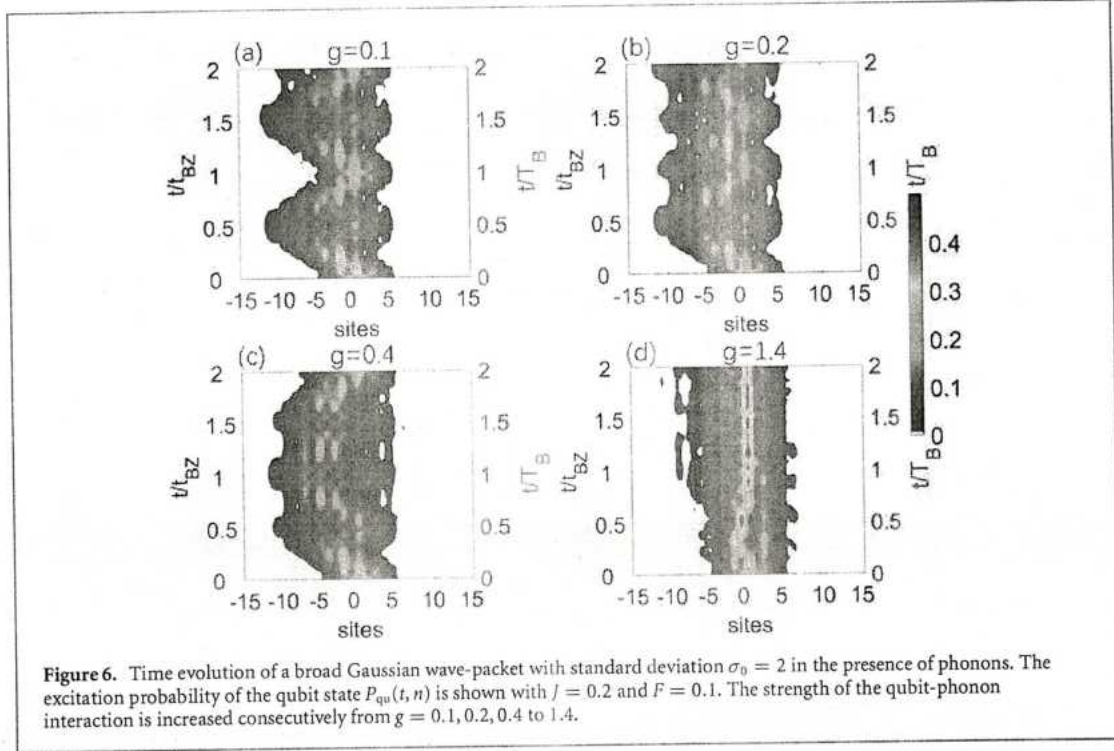


**Figure 5.** Time evolution of the mean values  $c(t)$ , the standard deviations of the wavepackets  $\sigma(t)$ , and the currents  $j(t)$  for the cases of  $J = 0.2$ ,  $F = 0.1$ ,  $g = 0$  with various  $\delta$  of 0, 0.2287, 0.5773 and 0.8301. The left panels ((a), (c) and (e)) and right panels ((b), (d) and (f)) use initial conditions of Gaussian wave packets with the initial widths of  $\sigma_0 = 2$  and  $\sigma_0 = 0.1$ , respectively.

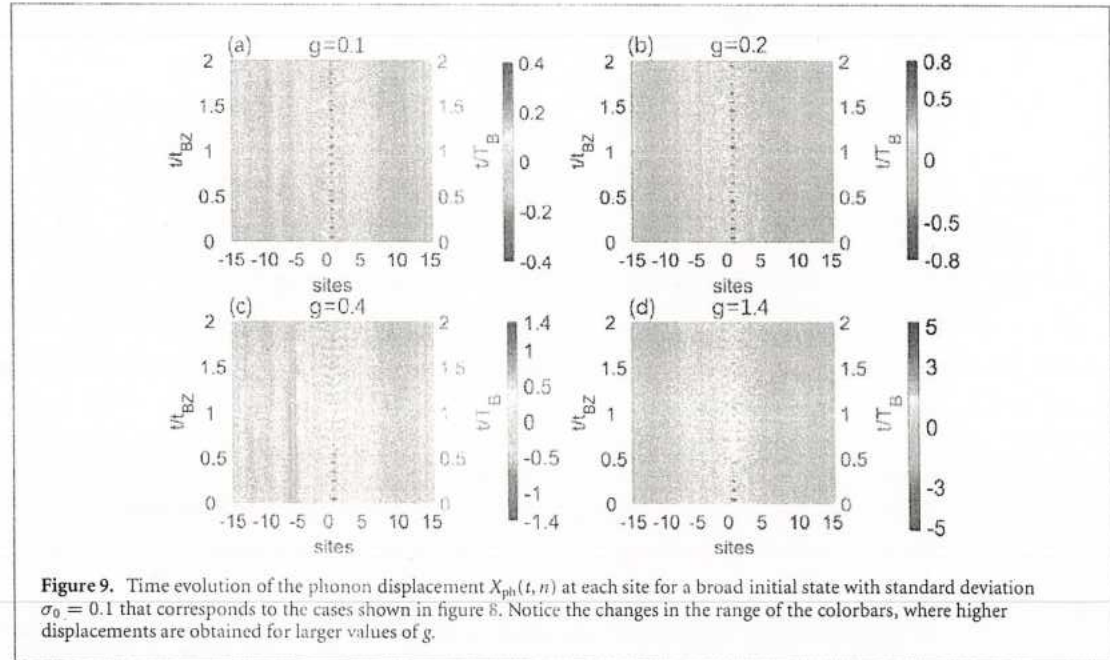
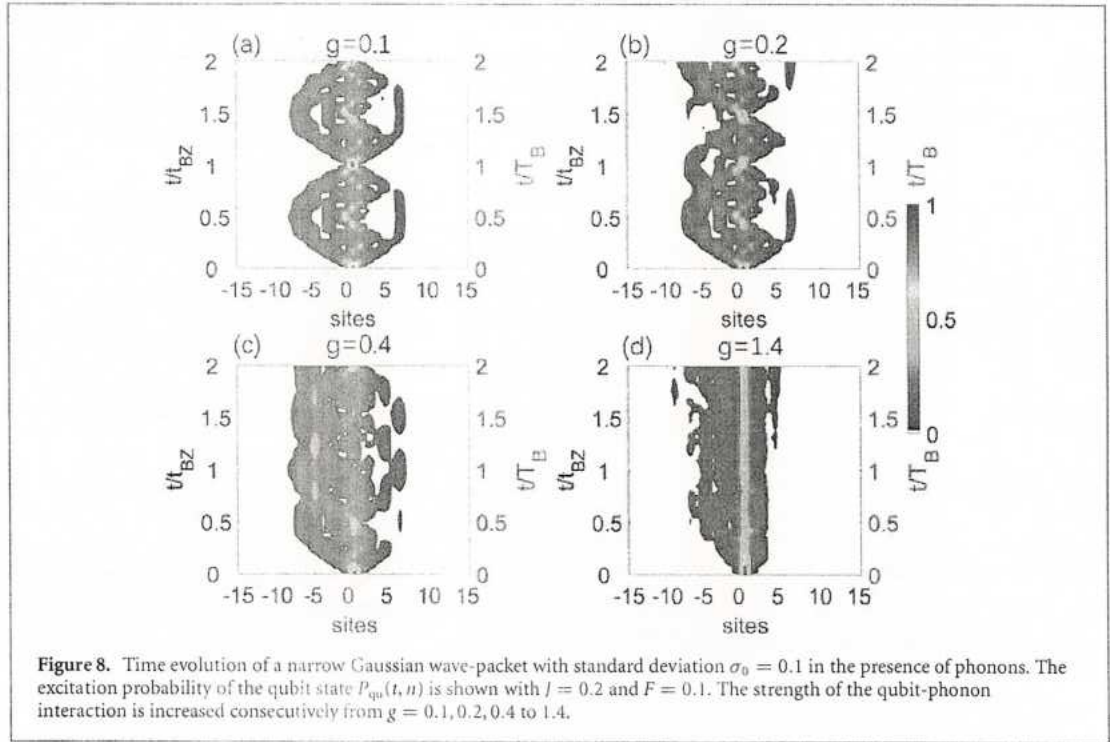
as displayed in figures 6(b) and (c). In the strong coupling regime, the center of the wave packet becomes localized, as visualized in figure 6(d). The time evolution of the phonon displacement  $X_{ph}(t, n)$  at each site is shown in figure 7 for the initially broad Gaussian state. Initially the phonons are in the vacuum state. As the electronic excitation travels along the chain, phonons are emitted across the chain following the dynamics of the electronic wave packet. Subsequently, the emitted phonons are scattered by the electronic excitation, leading to the aforementioned vague patterns of BZOs. The BZOs frequency  $\omega_{BZ}$  is equal to the BOs frequency  $\omega_B$  since the value  $\delta = 0.2287$  was chosen to satisfy  $T_{BZ} = T_B$ . Since the external field



$F = 0.1$ ,  $\omega_{BZ}(\omega_{BZ} = F)$  is ten times smaller than the phonon's frequency  $\omega_0 = 1$ , ten peaks can be found in one period of the BZOs.

Complementary to the evolution of an initially broad wave packet, we show in figure 8 the time evolution of an initially narrow wave packet in the presence of phonons for various values of the qubit-phonon coupling strength. As the qubit-phonon coupling strength is increased in figures 8(a)–(c), the spatial symmetry of the left and right branches around the origin is broken, and irregular excitation motion ensues. The localization effect by the strong coupling on the evolution of the excitation populations can be clearly seen in figure 8(d). We notice how the range of the colorbars increases with  $g$  in figure 9, indicating a higher phonon emission rate for an increasing qubit-phonon coupling strength. Additionally, figure 10 illustrates the effects of phonons on the expected value of the particle's position  $c(t)$ , the standard deviation  $\sigma(t)$  of the wave packet and the currents  $j(t)$ . Our results show that the excitation of the qubit states can be manipulated by the external field and qubit-phonon coupling.





In order to better understand the interaction between the qubit chain and the surrounding phonons, we have analyzed the time evolution of various energy variables, such as the kinetic energy of the excitation  $E_{\text{qu}}(t)$ , the total energy of the high-frequency phonons  $E_{\text{ph}}(t)$  and the interaction energy between the qubits and the phonons  $E_{\text{qu-ph}}(t)$ . The total energy  $E_{\text{tot}}(t)$  of the whole system is conserved if no external field is added ( $F = 0$ ). As shown in figure 11, the total energy varies with time when an external field is applied to the qubit chain. In the presence of an external field  $F = 0.1$ , the qubit chain undergoes either BZOs or a breathing mode when the qubit-phonon interaction is turned off ( $g = 0$ ), as shown in figures 11(a) and (b) for the initially broad and narrow cases, respectively. When  $g > 0$  the energy of the high-frequency phonons quickly grows from zero and starts to oscillate with high-frequency, as evidenced by the high value of the ratio  $\omega_0/J = 5$ , as shown in figures 11(c) and (d) for the broad and narrow case, respectively.

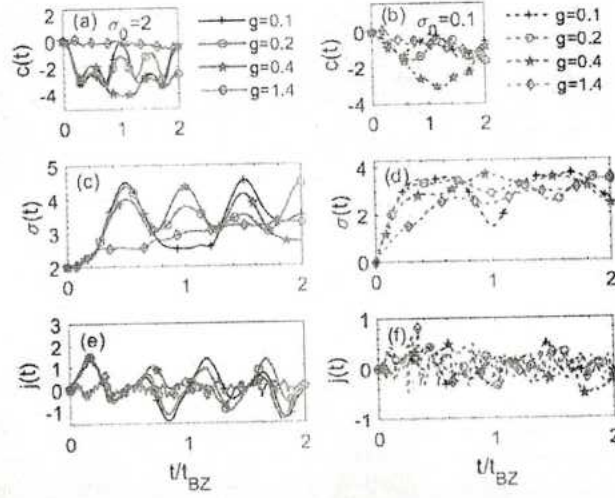


**Figure 10.** Time evolution of the mean values  $c(t)$ , the standard deviations of the wavepackets  $\sigma(t)$ , and the currents  $j(t)$  for the cases of  $J = 0.2$ ,  $F = 0.1$ ,  $\delta = 0.2287$  with various qubit-phonon coupling strengths of  $g = 0.1, 0.2, 0.4$  and  $1.4$ . The left panels ((a), (c) and (e)) and right panels ((b), (d) and (f)) use initial conditions of Gaussian wave packets with the initial widths of  $\sigma_0 = 2$  and  $\sigma_0 = 0.1$ , respectively.

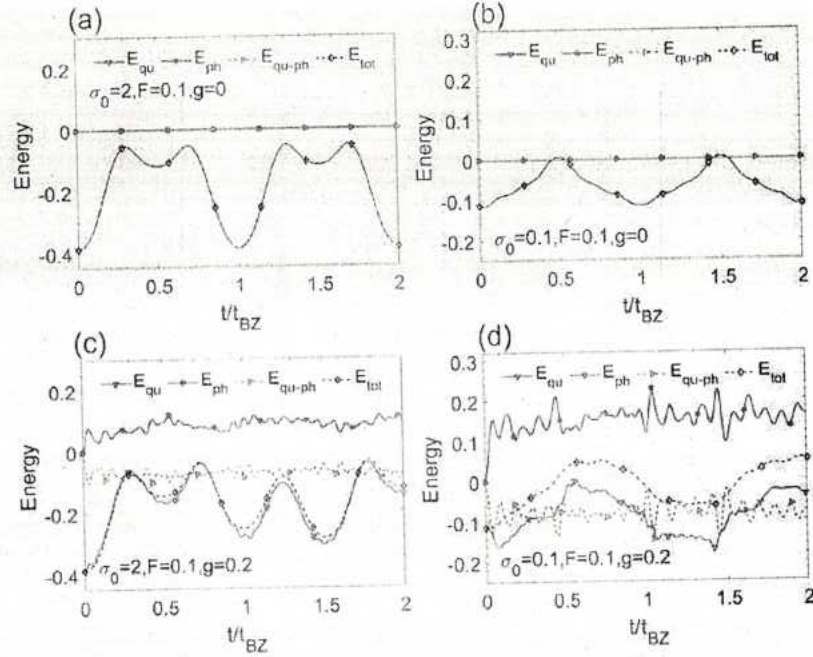


**Figure 11.**  $E_{qu}$ ,  $E_{ph}$ ,  $E_{qu-ph}$ , and  $E_{tot}$  calculated by the multi-D2 ansatz for the cases of (a)  $\sigma_0 = 2$ ,  $F = 0.1$ ,  $g = 0$ , (b)  $\sigma_0 = 0.1$ ,  $F = 0.1$ ,  $g = 0$ , (c)  $\sigma_0 = 2$ ,  $F = 0.1$ ,  $g = 0.2$ , and (d)  $\sigma_0 = 0.1$ ,  $F = 0.1$ ,  $g = 0.2$ . The nearest neighbor hopping integral is  $J = 0.2$  and difference in the site energies of alternating sites is  $\delta = 0.2287$ .

Next we proceed to evaluate the quantum correlations between qubits and phonons by analyzing the time evolution of the von Neumann entropy, given by equation (17). First, we vary the qubit-phonon coupling strength and calculate the von Neumann entropy  $S_{vN}$  in figure 12 for different values of the qubit-phonon coupling and band gaps. It can be found that large band gaps  $\delta$  restrict the entanglement between the qubit and phonons. For an initially broad Gaussian wave packet and fixed  $\delta$ , increasing the qubit-phonon coupling strength  $g$  the large amplitude of the oscillatory dynamics of the von Neumann entanglement entropy are dramatically reduced as  $g \sim 1$ . This can be interpreted as a signature of the dynamic localization of the particle. In contrast, when the excitation starts from a narrow Gaussian wave packet and  $g \geq J$ , the entanglement entropy increase steadily  $S_{vN}(t) \propto t^\kappa$  for some  $\kappa < 1$ .



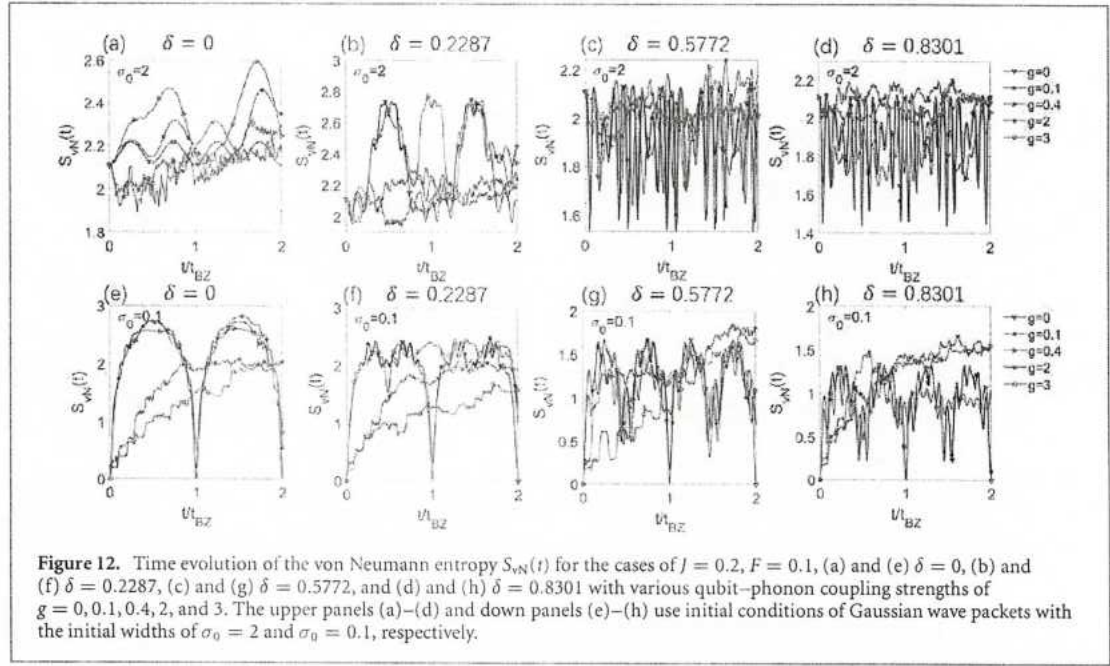


**Figure 12.** Time evolution of the von Neumann entropy  $S_{vN}(t)$  for the cases of  $J = 0.2$ ,  $F = 0.1$ , (a) and (e)  $\delta = 0$ , (b) and (f)  $\delta = 0.2287$ , (c) and (g)  $\delta = 0.5772$ , and (d) and (h)  $\delta = 0.8301$  with various qubit–phonon coupling strengths of  $g = 0, 0.1, 0.4, 2$ , and  $3$ . The upper panels (a)–(d) and down panels (e)–(h) use initial conditions of Gaussian wave packets with the initial widths of  $\sigma_0 = 2$  and  $\sigma_0 = 0.1$ , respectively.

In all the simulations so far we have taken  $J = 0.2\omega_0$  as the electronic coupling strength between neighbouring qubits (we remind the reader that  $\omega_0 = 1$  is taken as energy unit throughout this work). That is to say, the studied cases above focus on the anti-adiabatic regime ( $\omega_0 \gg J$ ). We now vary the adiabaticity ratio  $\omega_0/J$  for fixed qubit–phonon coupling strength  $g = 0.2$  to clarify the different energy scales involved in the dynamics. As shown in figures 13(a) and (d), the effects of phonons on the qubits are accentuated in the anti-adiabatic limit when compared with the adiabatic case. In the adiabatic regime  $\omega_0/J = 1$ , energy resonance between the electronic and vibrational subsystems are established. In the adiabatic regime ( $\omega_0/J = 1$ ), we show the dynamics of  $S_{vN}(t)$  for weak (figures 12(b) and (e)) and strong (figures 12(c) and (f)) qubit–phonon coupling strength  $g$ . The effect of qubit–phonon interactions in the entanglement entropy is overall less pronounced as in the anti-adiabatic case as a result of the higher electronic coupling strength. In comparison with the anti-adiabatic case of figure 12, the entanglement entropy reaches higher values in the adiabatic case for strong values of the qubit–phonon coupling strength, as shown in figures 13(c) and (f).

### 3.4. Dissipative dynamics of BZO in an ohmic environment

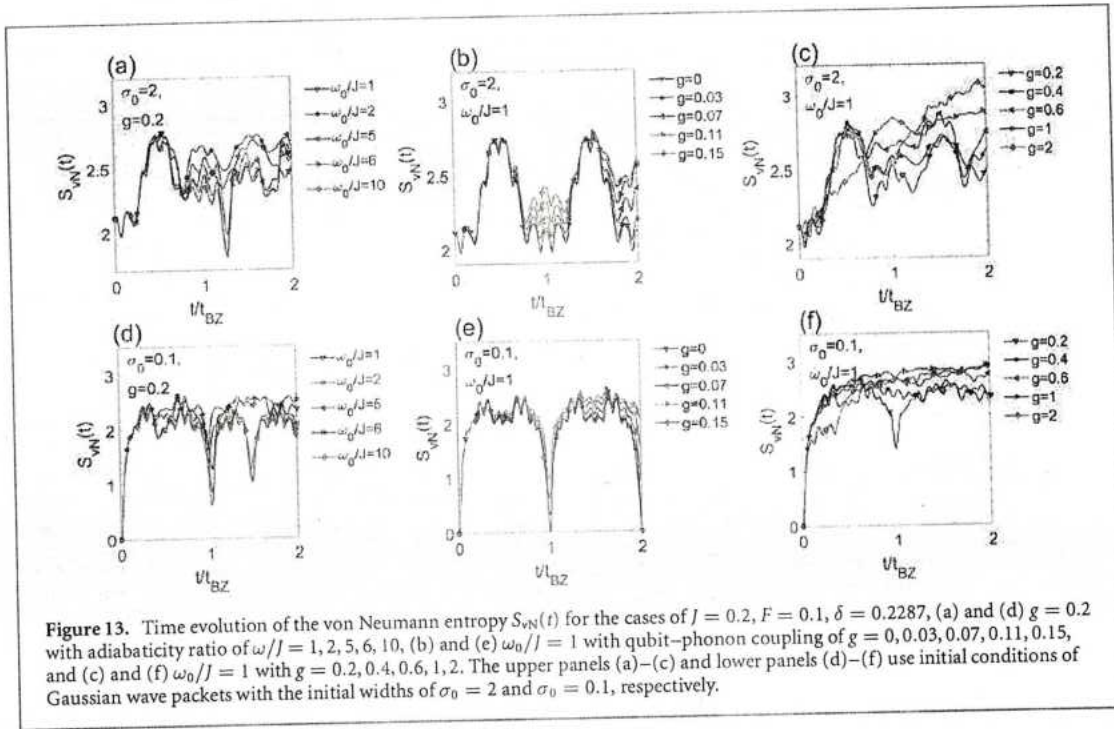
Recent developments in circuit QED have shown that qubits can be experimentally coupled to an ohmic phonon bath [41]. We proceed to study the effects of an Ohmic vibrational environment on the dynamics of BZO. We introduce the Hamiltonian of the phonon reservoir  $\hat{H}_R$  (equation (4)) with a linear vibronic interaction term  $\hat{H}_{qu-R}$  (equation (5)),

$$\hat{H}_R = \sum_{n,\xi} \hbar \omega_{n\xi} \hat{b}_{n\xi}^\dagger \hat{b}_{n\xi}, \quad (22)$$

and

$$\hat{H}_{qu-R} = \sum_n \hat{a}_n^\dagger \hat{a}_n \sum_\xi g_{n\xi} (\hat{b}_{n\xi}^\dagger + \hat{b}_{n\xi}), \quad (23)$$

in which  $\hat{a}_n$  ( $\hat{a}_n^\dagger$ ) is the annihilation (creation) operator of the excitation at site  $n$ ,  $\hat{b}_{n\xi}$  ( $\hat{b}_{n\xi}^\dagger$ ) is the annihilation (creation) operator of the  $\xi$ th phonon mode with frequency  $\omega_{n\xi}$ , and  $g_{n\xi}$  denotes the coupling strength of the  $\xi$ th phonon mode at site  $n$ . We notice that the interaction term of equation (23) has the structure  $\hat{H}_{qu-R} = \sum_n \hat{A}_n \otimes \hat{B}_n$  with  $\hat{A}_n = \hat{a}_n^\dagger \hat{a}_n$  and  $\hat{B}_n = \sum_\xi g_{n\xi} (\hat{b}_{n\xi}^\dagger + \hat{b}_{n\xi})$  operating on the electronic and vibrational subsystems, respectively. After bringing the number of oscillators in the environment to infinity, the coupling between the qubits and the bosonic reservoir can be characterized by the corresponding spectral density function,  $J_R(\omega) = \pi \sum_\xi g_{n\xi}^2 \delta(\omega - \omega_{n\xi}) = 2\alpha\omega e^{-\omega/\omega_c}$ , where  $\alpha$  is the dimensionless coupling strength and  $\omega_c$  is the cut-off frequency of the ohmic environment. In order to simulate the dissipative



dynamics of BZOs, we employ the following Markovian master equation [71],

$$\frac{d}{dt} \hat{\rho}_{\text{qu}}(t) = -i [\hat{H}_{\text{qu}}, \hat{\rho}_{\text{qu}}(t)] + \mathcal{D}(\hat{\rho}_{\text{qu}}(t)) \quad (24)$$

where the reduced density matrix,  $\hat{\rho}_{\text{qu}}(t) = \text{Tr}_{\text{R}} \hat{\rho}(t)$ , is the partial trace of the density matrix of the total system over the reservoir's degrees of freedom, and the dissipator  $\mathcal{D}$  takes the form

$$\mathcal{D} \hat{\rho}_{\text{qu}} = \sum_{\omega} \sum_{n,m} \gamma_{nm}(\omega) \left( \hat{A}_m(\omega)^\dagger \hat{\rho}_{\text{qu}} \hat{A}_n(\omega) - \frac{1}{2} \left\{ \hat{A}_n(\omega)^\dagger \hat{A}_m(\omega), \hat{\rho}_{\text{qu}} \right\} \right) \quad (25)$$

with

$$\hat{A}_n(\omega) = \sum_{\epsilon' = \epsilon - \omega} \hat{\Pi}(\epsilon) \hat{A}_n \hat{\Pi}(\epsilon') \quad (26)$$

and  $\hat{\Pi}(\epsilon) = \sum_{\epsilon_k} |\epsilon_k\rangle \langle \epsilon_k|$  is a projector onto the subspace of qubit eigenstates with energy  $\epsilon_k$ . The parameter  $\gamma_{nm}(\omega)$  sets the dissipation rate at each frequency and is given by

$$\gamma_{nm}(\omega) = \int_0^\infty dt e^{i\omega s} \langle \hat{B}_n^\dagger(s) \hat{B}_m(0) \rangle \quad (27)$$

in which the reservoir correlation functions  $\langle \hat{B}_n^\dagger(s) \hat{B}_m(0) \rangle = \text{Tr}_{\text{ph}} [\hat{\rho}_{\text{ph}} e^{iH_{\text{ph}} s} \hat{B}_n e^{-iH_{\text{ph}} s} \hat{B}_m]$  in the interaction picture. We assume that each qubit is subject to independent (uncorrelated) environments, i.e.

$\gamma_{nm}(\omega) = \gamma_{mn}(\omega) = \delta_{n,m} C(\omega)$ , equation (25) simplifies significantly and

$$C(\omega) = \begin{cases} 2\pi J(\omega)(n(\omega) + 1) & \text{if } \omega > 0 \\ 2\pi J(|\omega|)(n(|\omega|)) & \text{if } \omega < 0 \\ \lim_{\omega \rightarrow 0} 2\pi J(\omega)(n(\omega) + 1) & \text{if } \omega = 0 \\ = 4\pi \alpha k_B T & \end{cases} \quad (28)$$

where  $n(\omega) = (\exp(\omega/k_B T) - 1)^{-1}$  represents the mean phonon number of a phonon mode with a frequency  $\omega$  at temperature  $T$ , and  $J(\omega)$  is given by the Ohmic spectral density.

The polaron dynamics of BZOs in the presence of an Ohmic environment are shown in figure 14, where the excitation probabilities  $P_{\text{qu}}(t, n) = \hat{\rho}_{nn}(t)$  ( $n = 1, 2, \dots, N$ ) are calculated. In the current paper,  $T = 0$  is adopted as QED devices work at extremely low temperatures and energies of electronic excitation and phonons are high in comparison with the thermal energy  $k_B T$  in a wide range [44]. When the initial state is



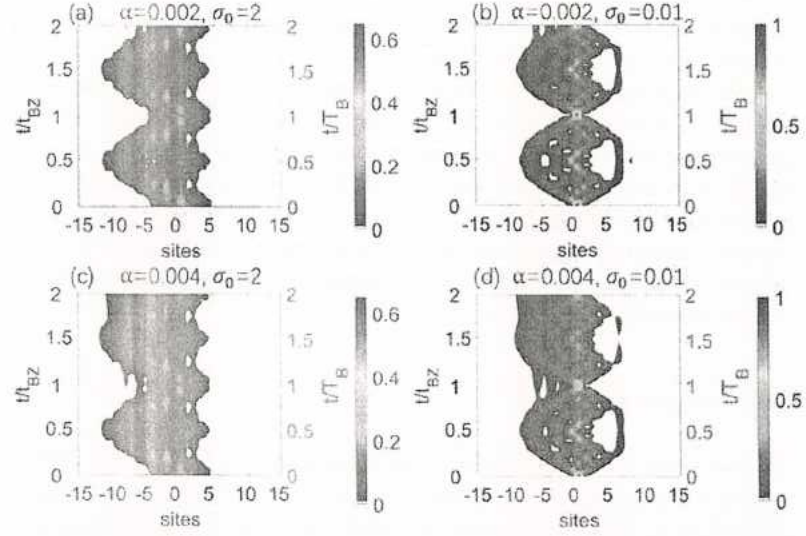


**Figure 14.** Time evolution of the excitation probability of the qubit state  $P_{qu}(t, n)$  for the coupling case of  $J = 0.2$ ,  $\delta = 0.2287$  and  $F = 0.1$  is obtained with qubit–phonon coupling strengths of ((a) and (b))  $\alpha = 0.002$ , and ((c) and (d))  $\alpha = 0.004$ . The initial Gaussian wave packets have an initial standard deviation of  $\sigma_0 = 2$  and  $0.1$ , in the left and right panels, respectively.

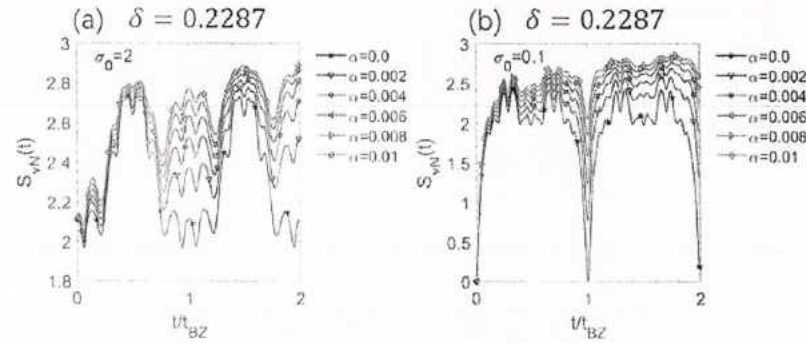


**Figure 15.** Time evolution of the von Neumann entropy  $S_{vN}(t)$  for the cases of  $J = 0.2$ ,  $F = 0.1$ ,  $\delta = 0.2287$  with various qubit–phonon coupling strengths of  $\alpha = 0, 0.002, 0.004, 0.006, 0.008$ , and  $0.01$ . The left panel (right) panel use initial conditions of Gaussian wave packets with the initial widths of  $\sigma_0 = 2$  ( $\sigma_0 = 0.1$ ).

a wide Gaussian wave packet (figures 14(a) and (c)), the BZO's are less pronounced as a consequence of the dephasing environment. If the initial state is narrow, strong differences between the left and right branches of the wave function start to appear, as shown in figures 14(b) and (d). Finally, we have calculated in figure 15 the von Neumann entropy for various values  $\alpha$  of the overall coupling of the qubits to their respective environments.

#### 4. Conclusion

In this work, we have built an extended Holstein model to describe a one-dimensional qubit chain with alternating site energies under the influence of a constant, electric field and high-frequency, dispersionless phonons. To investigate the transient polaron dynamics in the extended Holstein model, we have employed a time-dependent variational method based on an extension of the Davydov ansatz that becomes numerically accurate for sufficiently high values of the multiplicity parameter. This quantity is a measure of the complexity of the trial wave function and is related to the number of variational degrees of freedom in the ansatz. We have first studied the spectral properties and the band structure of the electronic Hamiltonian under various conditions. A tight-binding model (equation (1)) with near-neighbours interactions in the reciprocal and Wannier–Stark representations has been employed. The energy difference between consecutive site energies equals to the gap between the two minibands at the edges of the Brillouin zone. We have discussed the dependence of the energy offset between the Wannier–Stark energy ladders on

the band gaps, and calculated the values for which the commensurate condition is satisfied, so that the time period of BZO is equal to the period of BOs. We observe in our simulations that the band gap has a strong influence on the dynamics of BZO.

After considering the coupling to the dispersionless optical phonon, we have carefully checked the validity of the multi-D2 ansatz by performing convergence tests and relative error calculations in order to demonstrate the accuracy of the method employed. Overall, the BZO patterns and the corresponding breathing modes are smeared out by phonons. For weak qubit–phonon coupling strengths, the time periodicity of electronic motion is maintained and the spatial periodicity starts to break down when the coupling strength becomes comparable to the electronic interaction between qubits. Finally, we have numerically simulated the dissipative dynamics of BZO employing a Markovian master equation and a vibrational ohmic environment.

## Acknowledgments

This work was supported in part by the Natural Science Foundation of China under Grant Nos. 11947205 and 12047564, by the Fundamental Research Funds for the Central Universities under Grant No. 2020CDJQY-Z003, by the Natural Science Foundation of Chongqing under No.cstc2020jcyj-msxmX0003, Yu Ren She [2019] No. 298, and by China Postdoctoral Science Foundation under Grant No. 2019M663877XB.

## Appendix A. The Lagrangian for Bloch–Zener model coupled to phonons

The Lagrangian is formulated as

$$\begin{aligned} \mathcal{L} &= \langle D_2^M(t) | \frac{i\hbar}{2} \frac{\overleftrightarrow{\partial}}{\partial t} - \hat{H} | D_2^M(t) \rangle \\ &= \frac{i\hbar}{2} \left[ \langle D_2^M(t) | \frac{\overrightarrow{\partial}}{\partial t} | D_2^M(t) \rangle - \langle D_2^M(t) | \frac{\overleftarrow{\partial}}{\partial t} | D_2^M(t) \rangle \right] - \langle D_2^M(t) | \hat{H} | D_2^M(t) \rangle. \end{aligned} \quad (\text{A1})$$

where  $f \overleftrightarrow{\partial}_t g \equiv f (\partial_t g) - (\partial_t f) g$  and  $\partial_t \varphi = \partial \varphi / \partial t$  [72]. The first term yields

$$\begin{aligned} &\frac{i\hbar}{2} \left[ \langle D_2^M(t) | \frac{\overrightarrow{\partial}}{\partial t} | D_2^M(t) \rangle - \langle D_2^M(t) | \frac{\overleftarrow{\partial}}{\partial t} | D_2^M(t) \rangle \right] \\ &= \frac{i\hbar}{2} \sum_{ij} \sum_n \left( \psi_{jn}^* \dot{\psi}_{in} - \dot{\psi}_{jn}^* \psi_{in} \right) S_{ji} + \frac{i\hbar}{2} \sum_{ij} \sum_n \psi_{jn}^* \psi_{in} S_{ji} \sum_q \left[ \frac{\dot{\lambda}_{iq}^* \lambda_{jq} + \lambda_{jq}^* \dot{\lambda}_{inq}}{2} \right. \\ &\quad \left. - \frac{\dot{\lambda}_{iq} \lambda_{iq}^* + \lambda_{iq} \dot{\lambda}_{iq}^*}{2} + \lambda_{jq}^* \dot{\lambda}_{iq} - \dot{\lambda}_{jq}^* \lambda_{iq} \right], \end{aligned} \quad (\text{A2})$$

and the second term takes the form

$$\langle D_2^M(t) | \hat{H} | D_2^M(t) \rangle = \langle D_2^M(t) | \hat{H}_{\text{qu}} | D_2^M(t) \rangle + \langle D_2^M(t) | \hat{H}_{\text{ph}} | D_2^M(t) \rangle + \langle D_2^M(t) | \hat{H}_{\text{qu-ph}} | D_2^M(t) \rangle \quad (\text{A3})$$

where the Debye–Waller factor is formulated as

$$S_{ij} = \exp \left\{ \sum_q \lambda_{iq}^* \lambda_{jq} - \frac{1}{2} (|\lambda_{iq}|^2 + |\lambda_{jq}|^2) \right\}. \quad (\text{A4})$$

## Appendix B. Validity of variation for BZO dynamics affected by phonons

In this section, we demonstrate that the multi-D2 ansatz with sufficiently large multiplicity  $M$  can provide quantitatively accurate calculations to the BZO dynamics affected by phonons. As a proof of principle, we here only show the case with system parameters of  $J = 0.2$ ,  $\delta = 0.2287$ ,  $g = 0.2$  and  $F = 0.1$ , and a two-site-centered initial condition of  $\psi_n(t=0) = (\delta_{n,N/2} + \delta_{n,N/2+1})/\sqrt{2}$ .

First, in the presence of the external field, a convergence test is performed using the multi-D2 ansatz with various multiplicity  $M$  for the qubit states in the qubit chain with alternating site energies and diagonal



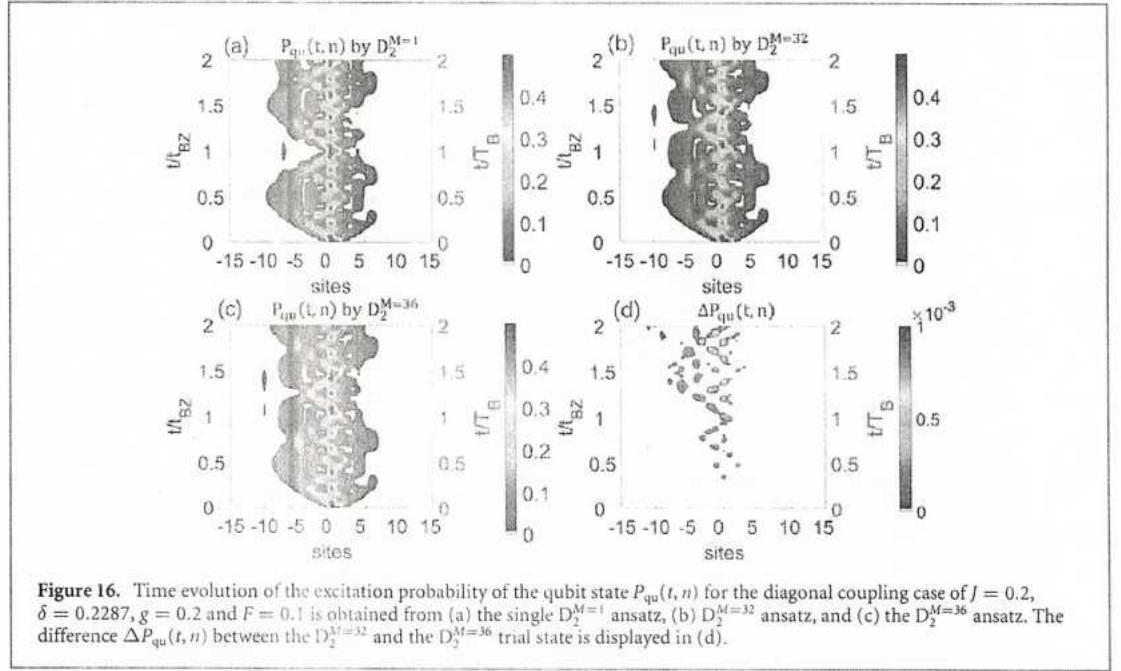


**Figure 16.** Time evolution of the excitation probability of the qubit state  $P_{qu}(t, n)$  for the diagonal coupling case of  $J = 0.2$ ,  $\delta = 0.2287$ ,  $g = 0.2$  and  $F = 0.1$  is obtained from (a) the single  $D_2^{M=1}$  ansatz, (b)  $D_2^{M=32}$  ansatz, and (c) the  $D_2^{M=36}$  ansatz. The difference  $\Delta P_{qu}(t, n)$  between the  $D_2^{M=32}$  and the  $D_2^{M=36}$  trial state is displayed in (d).

qubit-phonon coupling. As shown in figure 16, the time evolution of the excitation probability of the qubit state  $P_{qu}(t, n)$  is calculated by the  $D_2^{M=1}$ ,  $D_2^{M=32}$ , and  $D_2^{M=36}$  ansatz, respectively. Figures 16(b) and (c) exhibit quite identical plots and both show large difference from figure 16(a). As given in figure 16(d),  $\Delta P_{qu}(t, n)$  is the difference between  $P_{qu}(t, n)$  calculated by the  $D_2^{M=32}$  and  $D_2^{M=36}$ , and its value is smaller than that of  $P_{qu}(t, n)$  by two orders of magnitude. The comparison here presents the nearly converged results calculated from  $D_2^{M=32}$  ansatz, showing the superior accuracy of our variational approach.

Second, validity of the variational approach is carefully checked by testing how faithfully the calculations obey the Schrödinger equation. At the moment  $t$ ,  $|\Psi(t)\rangle$  serves as the real wave function, and we assume the trial state  $|\tilde{D}_2^M(t)\rangle = |\Psi(t)\rangle$ . Then a deviation vector  $\vec{\delta}(t)$  is introduced to measure the accuracy of dynamics obtained by the multi-D2 trial state,

$$\begin{aligned}\vec{\delta}(t) &= \vec{\chi}(t) - \vec{\gamma}(t) \\ &= \frac{\partial}{\partial t} |\Psi(t)\rangle - \frac{\partial}{\partial t} |\tilde{D}_2^M(t)\rangle.\end{aligned}\quad (\text{B1})$$

in which the vectors  $\vec{\gamma}(t)$  and  $\vec{\chi}(t)$  follow the Dirac–Frenkel time-dependent variational dynamics  $\vec{\gamma}(t) = \partial |\tilde{D}_2^M\rangle / \partial t$  in equation (10) and the Schrödinger equation  $\vec{\chi}(t) = \partial |\Psi(t)\rangle / \partial t = \frac{1}{i\hbar} \hat{H} |\Psi(t)\rangle$ , respectively. Based on the Schrödinger equation as well as the relationship  $|\Psi(t)\rangle = |\tilde{D}_{1,2}^M(t)\rangle$  at the time  $t$ , the deviation vector  $\vec{\delta}(t)$  can be written as

$$\vec{\delta}(t) = \frac{1}{i\hbar} \hat{H} |\tilde{D}_2^M(t)\rangle - \frac{\partial}{\partial t} |\tilde{D}_2^M(t)\rangle. \quad (\text{B2})$$

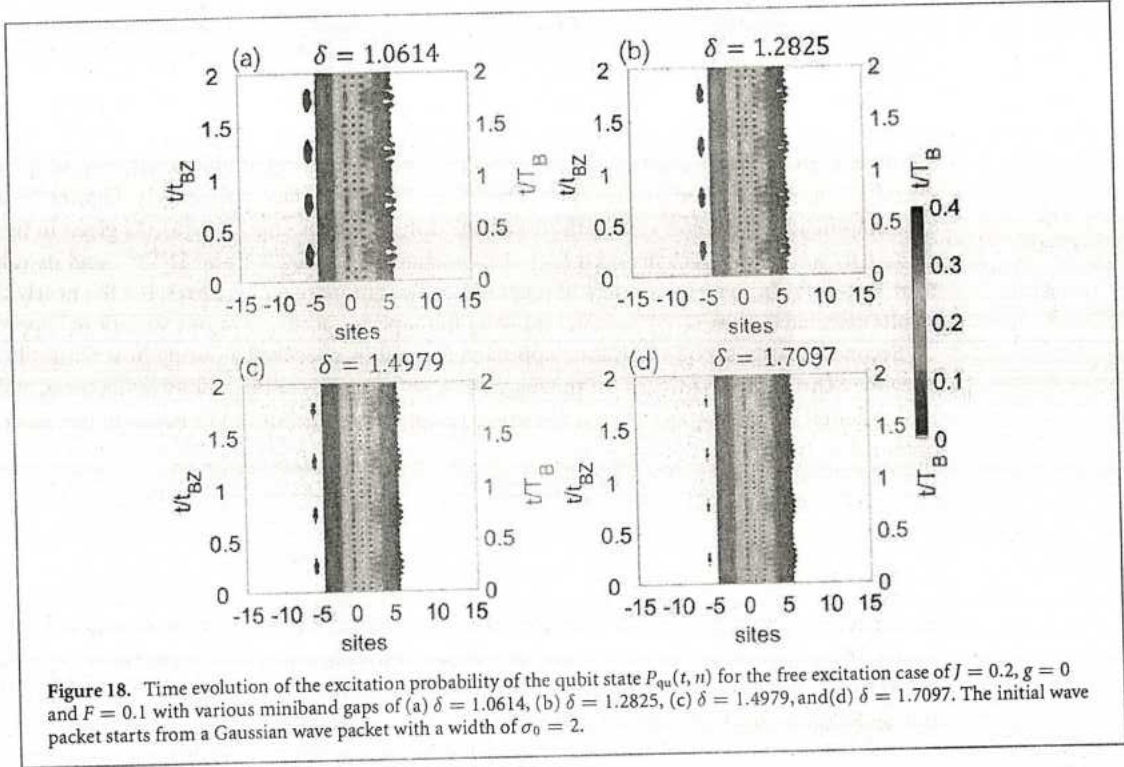
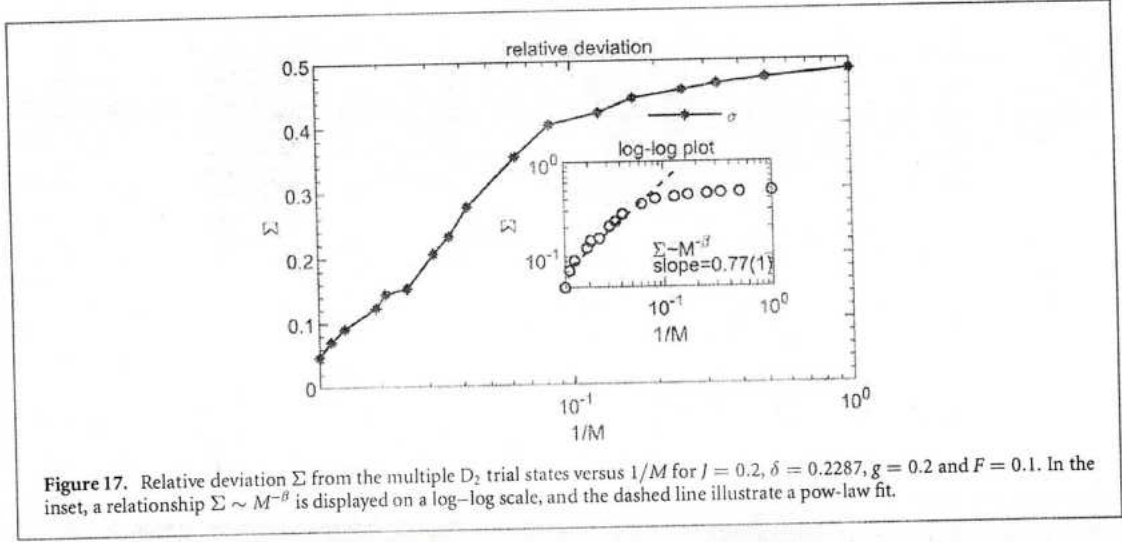
Thus, we can use the amplitude of the deviation vector  $\Delta(t) = \|\vec{\delta}(t)\|$  to estimate the accuracy of the results calculated by the multi-D2 ansatz. To better verify the deviation in the parameter space  $(\delta, J, g)$ , we define a dimensionless relative deviation  $\Sigma$  as follows

$$\Sigma = \frac{\max\{\Delta(t)\}}{\text{mean}\{N_{\text{err}}(t)\}}, \quad t \in [0, t_{\text{max}}]. \quad (\text{B3})$$

in which  $N_{\text{err}}(t) = \|\vec{\chi}(t)\|$  denotes the amplitude of the time derivative of the wave function,

$$\begin{aligned}N_{\text{err}}(t) &= \sqrt{-\left\langle \frac{\partial}{\partial t} \Psi(t) \left| \frac{\partial}{\partial t} \Psi(t) \right\rangle} \\ &= \sqrt{\langle \tilde{D}_2^M(t) | \hat{H}^2 | \tilde{D}_2^M(t) \rangle}.\end{aligned}\quad (\text{B4})$$

As illustrated in figure 17, the relative deviation  $\Sigma$  drops when the multiplicity  $M$  of the multi-D2 ansatz grows. As supported by the relationship of  $\Sigma \sim M^{-\beta}$  with an exponent of  $\beta = 0.77$  in the inset of figure 17,



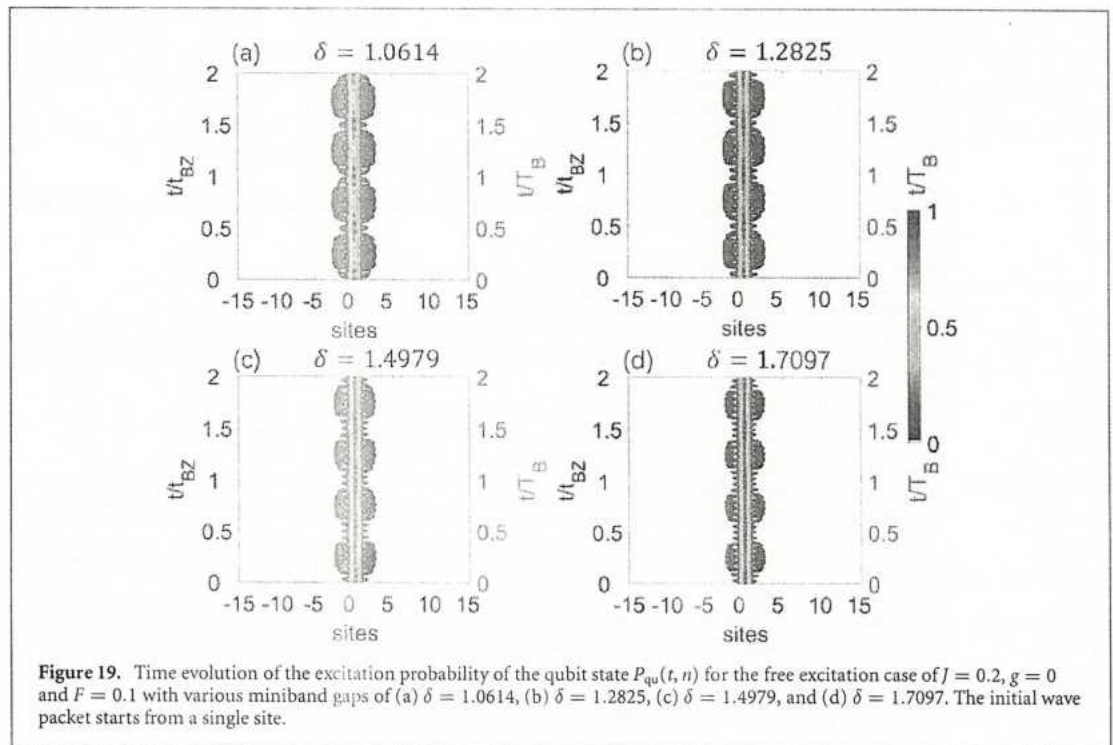
the value of  $\Sigma$  gets close to zero as  $M$  increases to infinity. In the limit of large  $M$ , the variational approach with the multi- $D_2$  ansatz yields numerically exact BZO dynamics affected by phonons according to the time-dependent Schrödinger equation.

In this work, a multiplicity of  $M = 32$  is used in balance with the computational efficiency to obtain sufficiently accurate results for the investigation of the BZO dynamics affected by phonons.

### Appendix C. Pure BZOs for various gaps

In this section, we further illustrate the effects of the band gap  $\delta$  on the evolution of the excitation wave patterns if we initially use a broad (narrow) Gaussian wave packet with an initial spatial width of  $\sigma_0 = 2$  ( $\sigma_0 = 0.1$ ), as shown in figure 18 (figure 19). The temporal periodicities are well reserved in studied cases displayed here while the BZO patterns become hardly identifiable. As the gap  $\delta$  grows larger, the wave packets turn out to be slightly more localized, demonstrating the localization effect of large gaps  $\delta$  on the excitation wave packets.





## ORCID iDs

Zhongkai Huang <https://orcid.org/0000-0002-4062-0402>

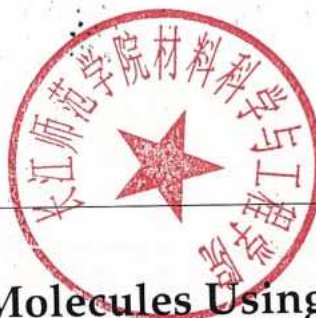
Alejandro D Somoza <https://orcid.org/0000-0002-4973-8052>

## References

- [1] Bloch F 1929 *Z. Phys.* 52 555–600
- [2] Zener C 1932 *Proc. R. Soc. A* 137 696–702
- [3] Wannier G H 1960 *Phys. Rev.* 117 432–9
- [4] Zak J 1968 *Phys. Rev. Lett.* 20 1477–81
- [5] Esaki L and Tsu R 1970 *IBM J. Res. Dev.* 14 61–5
- [6] Holthaus M 2000 *J. Opt. B: Quantum Semiclassical Opt.* 2 589
- [7] Watson A and Weinstein M I 2018 *Commun. Math. Phys.* 363 655–98
- [8] Breid B M, Witthaut D and Korsch H J 2006 *New J. Phys.* 8 110
- [9] Trompeter H, Krolkowski W, Neshev D N, Desyatnikov A S, Sukhorukov A A, Kivshar Y S, Pertsch T, Peschel U and Lederer F 2006 *Phys. Rev. Lett.* 96 53903
- [10] Sun Y, Leykam D, Nenni S, Song D, Chen H, Chong Y D and Chen Z 2018 *Phys. Rev. Lett.* 121 33904
- [11] Dreisow F, Szameit A, Heinrich M, Pertsch T, Nolte S, Tünnermann A and Longhi S 2009 *Phys. Rev. Lett.* 102 76802
- [12] Romanova J Y, Demidov E V, Mouroukh L G and Romanov Y A 2011 *J. Phys.: Condens. Matter* 23 305801
- [13] Zhang Y, Zhang D, Zhang Z, Li C, Zhang Y, Li F, Belić M R and Xiao M 2017 *Optica* 4 571–5
- [14] Kling S, Salger T, Grossert C and Weitz M 2010 *Phys. Rev. Lett.* 105 215301
- [15] Makhlin Y, Schön G and Shnirman A 2001 *Rev. Mod. Phys.* 73 357–400
- [16] Breid B M, Witthaut D and Korsch H J 2007 *New J. Phys.* 9 62
- [17] D'Errico A, Barboza R, Tudor R, Dauphin A, Massignan P, Marrucci L and Cardano F 2021 *APL Photon.* 6 20802
- [18] Longhi S 2020 *Phys. Rev. Lett.* 124 06602
- [19] Qiao X, Zhang X-B, Zhang A-X, Yu Z-F and Xue J-K 2019 *Phys. Lett. A* 383 3095–100
- [20] Du T-Y, Tang D, Huang X-H and Bian X-B 2018 *Phys. Rev. A* 97 43413
- [21] Takahashi R and Sugimoto N 2017 *Phys. Rev. B* 95 224302
- [22] Bender N, Li H, Ellis F M and Kottos T 2015 *Phys. Rev. A* 92 41803
- [23] Mizumoto Y and Kayanuma Y 2013 *Phys. Rev. A* 88 23611
- [24] Longhi S 2012 *J. Phys. B: At. Mol. Opt. Phys.* 45 225504
- [25] Ding S and Ping Wang G 2012 *Appl. Phys. Lett.* 100 151913
- [26] Kolovsky A R and Korsch H J 2003 *Phys. Rev. A* 67 63601
- [27] Lim L-K, Fuchs J-N and Montambaux G 2012 *Phys. Rev. Lett.* 108 175303
- [28] Krueckl V and Richter K 2012 *Phys. Rev. B* 85 115433
- [29] Longhi S 2012 *Phys. Rev. B* 86 75144
- [30] Zheng M J, Wang G and Yu K W 2010 *Opt. Lett.* 35 3865–7
- [31] Prasanna Venkatesh B, Trupke M, Hinds E A and O'Dell D H J 2009 *Phys. Rev. A* 80 63834

- [32] Longhi S 2008 *Phys. Rev. Lett.* 101 193902
- [33] Witthaut D, Graefe E M, Wimberger S and Korsch H J 2007 *Phys. Rev. A* 75 13617
- [34] Gu X, Kockum A F, Miranowicz A, Liu Y-x. and Nori F 2017 *Phys. Rep.* 718–719 1–102
- [35] Kollár A J, Fitzpatrick M and Houck A A 2019 *Nature* 571 45–50
- [36] Wendin G 2017 *Rep. Prog. Phys.* 80 106001
- [37] Ramasesh V V, Flurin E, Rudner M, Siddiqi I and Yao N Y 2017 *Phys. Rev. Lett.* 118 130501
- [38] Bahmani S and Askarpour A N 2020 *Phys. Lett. A* 384 126596
- [39] Guo X Y et al 2020 Observation of Bloch oscillations and Wannier–Stark localization on a superconducting processor (arXiv:2007.08853)
- [40] Izmailkov A et al 2004 *Europhys. Lett.* 65 844–9
- [41] Huang Z and Zhao Y 2018 *Phys. Rev. A* 97 13803
- [42] Zueco D, Hänggi P and Kohler S 2008 *New J. Phys.* 10 115012
- [43] Neillinger P et al 2016 *Phys. Rev. B* 94 94519
- [44] Wallraff A, Schuster D I, Blais A, Frunzio L, Huang R S, Majer J, Kumar S, Girvin S M and Schoelkopf R J 2004 *Nature* 431 162–7
- [45] Ye Y et al 2019 *Phys. Rev. Lett.* 123 50502
- [46] Stojanović V M and Salom I 2019 *Phys. Rev. B* 99 134308
- [47] Clerk A A, Lehnert K W, Bertet P, Petta J R and Nakamura Y 2020 *Nat. Phys.* 16 257–67
- [48] Delsing P et al 2019 *J. Phys. D: Appl. Phys.* 52 353001
- [49] O’Connell A D et al 2010 *Nature* 464 697–703
- [50] Riedinger R, Hong S, Norte R A, Slater J A, Shang J, Krause A G, Anant V, Aspelmeyer M and Gröblacher S 2016 *Nature* 530 313–6
- [51] Manenti R, Kockum A F, Patterson A, Behrle T, Rahamim J, Tancredi G, Nori F and Leek P J 2017 *Nat. Commun.* 8 975
- [52] Zhou N, Huang Z, Zhu J, Chernyak V and Zhao Y 2015 *J. Chem. Phys.* 143 014113
- [53] Huang Z 2018 The multiple Davydov D2 ansatz and its applications *Doctoral Thesis* Nanyang Technological University, Singapore
- [54] Huang Z, Wang L, Wu C, Chen L, Grossmann F and Zhao Y 2017 *Phys. Chem. Chem. Phys.* 19 1655–68
- [55] Huang Z, Chen L, Zhou N and Zhao Y 2017 *Ann. Phys., Lpz.* 529 1600367
- [56] Huang Z, Hoshina M, Ishihara H and Zhao Y 2019 *Ann. Phys., Lpz.* 531 1800303
- [57] Werther M and Grossmann F 2020 *Phys. Rev. B* 101 174315
- [58] Huang Z, Fujihashi Y and Zhao Y 2017 *J. Phys. Chem. Lett.* 8 3306–12
- [59] Werther M, Grossmann F, Huang Z and Zhao Y 2019 *J. Chem. Phys.* 150 234109
- [60] Huang Z, Zheng F, Zhang Y, Wei Y and Zhao Y 2019 *J. Chem. Phys.* 150 184116
- [61] Werther M and Grossmann F 2020 *Phys. Rev. A* 102 63710
- [62] Engelhardt G, Benito M, Platero G and Brandes T 2017 *Phys. Rev. Lett.* 118 197702
- [63] Krieger J B and lafrate G J 1986 *Phys. Rev. B* 33 5494–500
- [64] Yeh S-H, Hoehn R D, Allodi M A, Engel G S and Kais S 2019 *Proc. Natl Acad. Sci.* 116 18263–8
- [65] Mei F, Stojanović V M, Siddiqi I and Tian L 2013 *Phys. Rev. B* 88 224502
- [66] Holstein T 1959 *Ann. Phys., NY* 8 325–42
- [67] Holstein T 1959 *Ann. Phys., NY* 8 343–89
- [68] Werther M, Choudhury S L and Grossmann F 2021 *Int. Rev. Phys. Chem.* 40 81–125
- [69] Dorfner F, Vidmar L, Brockt C, Jeckelmann E and Heidrich-Meisner F 2015 *Phys. Rev. B* 91 104302
- [70] Hartmann T, Keck F, Korsch H J and Mossmann S 2004 *New J. Phys.* 6 2
- [71] Breuer H P and Petruccione F 2002 *The Theory of Open Quantum Systems* (Oxford: Oxford University Press)
- [72] Srednicki M 2007 *Quantum Field Theory* (Cambridge: Cambridge University Press)





Article

# Detecting Air Pollutant Molecules Using Tube-Shaped Single Electron Transistor

Zhongkai Huang <sup>1,2</sup>, Xiangyang Peng <sup>3,\*</sup>, Cheng Peng <sup>2,\*</sup>, Jin Huang <sup>1,\*</sup>, Maolin Bo <sup>4</sup>, Chuang Yao <sup>4</sup> and Jibiao Li <sup>4</sup>

- <sup>1</sup> School of Chemistry and Chemical Engineering, Chongqing Key Laboratory of Soft-Matter Material Chemistry and Function Manufacturing, Southwest University, Chongqing 400715, China; zhongkaihuang@yznu.edu.cn
  - <sup>2</sup> Key Laboratory of Inorganic Special Functional Materials of Chongqing, Yangtze Normal University, Chongqing 408100, China
  - <sup>3</sup> Hunan Key Laboratory of Micro-Nano Energy Materials and Devices, Xiangtan University, Xiangtan 411105, China
  - <sup>4</sup> Key Laboratory of Extraordinary Bond Engineering and Advanced Materials Technology of Chongqing, Yangtze Normal University, Chongqing 408100, China; bmlwd@yznu.edu.cn (M.B.); yaochuang@yznu.cn (C.Y.); jibiaoli@yznu.edu.cn (J.L.)
- \* Correspondence: xiangyang\_peng@xtu.edu.cn (X.P.); 20090008@yznu.edu.cn (C.P.); huangjin2015@swu.edu.cn (J.H.)



**Citation:** Huang, Z.; Peng, X.; Peng, C.; Huang, J.; Bo, M.; Yao, C.; Li, J. Detecting Air Pollutant Molecules Using Tube-Shaped Single Electron Transistor. *Molecules* **2021**, *26*, 7098. <https://doi.org/10.3390/molecules26237098>

Academic Editors: Yuanfu Chen, Qian Chen, Guankui Long, Yiming Wang and Afang Zhang

Received: 29 October 2021

Accepted: 20 November 2021

Published: 24 November 2021

**Publisher's Note:** MDPI stays neutral with regard to jurisdictional claims in published maps and institutional affiliations.



Copyright: © 2021 by the authors. Licensee MDPI, Basel, Switzerland. This article is an open access article distributed under the terms and conditions of the Creative Commons Attribution (CC BY) license (<https://creativecommons.org/licenses/by/4.0/>).

**Abstract:** An air pollution detector is proposed based on a tube-shaped single-electron transistor (SET) sensor. By monitoring the flow control component of the detector, each air pollutant molecule can be placed at the center of a SET nanopore and is treated as an island of the SET device in the same framework. Electron transport in the SET was incoherent, and the performances of the SET were sensitive at the single molecule level. Employing first-principles calculations, electronic features of an air pollutant molecule within a tube-shaped SET environment were found to be independent of the molecule rotational orientations with respect to axis of symmetry, unlike the electronic features in a conventional SET environment. Charge stability diagrams of the island molecules were demonstrated to be distinct for each molecule, and thus they can serve as electronic fingerprints for detection. Using the same setup, quantification of the air pollutant can be realized at room temperature as well. The results presented herein may help provide guidance for the identification and quantification of various types of air pollutants at the molecular level by treating the molecule as the island of the SET component in the proposed detector.

**Keywords:** tube-shaped single electron transistors; incoherent transport; air pollutant molecule; first-principle calculations; identification and quantification

## 1. Introduction

Air pollution occurs when harmful or excessive quantities of substances are introduced into Earth's atmosphere, leading to public health and environmental problems [1]. On the public health side, the toxic effects of air pollution have been individually identified in various organs of the body, leading to eighteen outpatient diseases, including cancer [2]. In addition to the documented physical effects of air pollution on humans, there are negative effects of air pollution on subjective well-being [3]. On the environmental side, air pollution can damage ecosystem functions and structures and result in global warming, acid rain, and deterioration of the ozone (O<sub>3</sub>) layer [4]. The impact of air pollution on materials is also notorious, as chemical reactions between the polluted air and material matrices coating buildings or within structures may result in large maintenance costs [5].

Air pollutants are the source of air pollution, and they can be classified as "criteria pollutants" and "hazardous air pollutants" [6]. Criteria pollutants are used to determine if one region meets air quality standards. The most common criteria pollutants include



particulate matter (PM), carbon monoxide (CO), nitrogen dioxide (NO<sub>2</sub>), tropospheric ozone (O<sub>3</sub>), and sulfur dioxide (SO<sub>2</sub>) [7]. Hazardous air pollutants, known as “air toxics”, are chemical species that may cause cancer and other chronic human health risks. Frequently encountered hazardous air pollutants include benzene (C<sub>6</sub>H<sub>6</sub>), formaldehyde (CH<sub>2</sub>O), toluene (C<sub>7</sub>H<sub>8</sub>), xylene (C<sub>8</sub>H<sub>10</sub>), and benzo (a) pyrene (as a marker for polycyclic aromatic hydrocarbons) [8].

Various approaches have been developed to identify and quantify air pollutants in the atmosphere and determine the air quality. Direct and indirect measurements are used. Direct measurements include the sizes and concentrations of particles caught on filters, the concentrations of gases collected in traps, the pH values of liquid droplets, the temperature, and the humidity. Other measurements are indirect. For example, light scattering methods are used to determine the number of aerosol particles in the air [9].

However, as air pollutants have various types, individual detection methods must be tailored to specific features of the measured species. For instance, a primary method to detect carbon monoxide is based on nondispersive infrared photometry. The current method to identify sulfur dioxide employs ultraviolet fluorescence. Methane and other non-methane volatile organic compounds are measured using gas chromatography with a calibrated flame ionization detector [9]. Therefore, more technologically advanced methods are necessary to unify the measurements of various air pollutant species.

Given the wide application of semiconductors in gas sensing, the use of semiconductor devices to measure air pollution is promising. In recent decades, low-dimensional nanostructures have received considerable attention for gas sensing, as the resistance changes drastically due to the absorption of foreign molecules on materials with high surface-to-volume ratios [10]. High gas-sensing abilities have been found in low-dimensional nanostructures, such as carbon nanotubes [11], ZnO nanobelts [12], silicon [13], In<sub>2</sub>O<sub>3</sub> [14], and SnO<sub>2</sub> [15] nanowire-based sensors, and two-dimensional materials, such as graphene [16] and MoS<sub>2</sub> [17]. However, those sensors are mostly based on coherent electronic transport [18]. Inevitably, electric heat will be produced during the operation of these sensors, and their large power costs will affect the high sensitivities of the sensors.

Based on sequential transport, single-electron transistors (SETs) can avoid the aforementioned problems induced by the coherent transport [19]. A SET consists of source, drain, and gate electrodes and an island [20]. There are tunnel barriers between the source/drain electrode and the island, and electronic conduction takes place via sequential quantum tunneling through the barriers. The gate electrode is designed such that the electrostatic potential of the island is in a Coulomb blockade state. Based on the scanning values of the gate voltage ( $V_g$ ) and source-drain bias ( $V_b$ ), a phase diagram called the charge stability diagram can be obtained to unveil the conduction behaviors of the electrons in an SET [21,22]. According to the underlying physics of the physical quantities observed, potential applications of SETs have been found in logic operations [23,24], quantum computation [25], and sensing [26–28]. Gas molecules have been proposed to be the island of the SET for sensing. Ray et al. studied a series of molecules using SET with conventional structures and investigated the effects of gates tuning on the performance of SET [29–34]. Recent studies have shown that the types of island molecules can be identified by unique electronic signals from corresponding SET devices [34]. However, previous SET schemes were not designed for the purpose of air pollutant detection and cannot adequately meet the requirements for the identification and quantification of air pollutants at a molecular level.

In the present work, an air pollutant measurement system was designed based on a tube-shaped SET sensor, which was the key component of the detector. Monitored by the flow control component, an air pollutant molecule could flow to the center of the SET nanopore and act as an SET island. The electronic properties of island molecules under the SET environment were investigated using first-principles-based density functional theory (DFT) [35]. In detail, we examined the performances of SET configurations by calculating the physical quantities of interest, including the total energies as functions of the gate voltage, energy density, molecular energy spectra, and the charge stability diagrams.



The remainder of the paper is structured as follows. In Section 2, we present the proposed measurement system and the calculation method. In Section 3.1, the influence of conventional and tube-shaped SET environments is studied for a certain molecule with various orientations. In Section 3.2, the electronic features, such as the charge stability diagrams, are characterized for the identification of individual air pollutant molecules. In Section 3.3, the quantification of the air pollutants is examined using the proposed device. Conclusions are drawn in Section 4.

## 2. Materials and Methods

### 2.1. System Description

The proposed air pollution detector is depicted in Figure 1a. The setup consists of a particulate filter to clean particulate matter from the measured air, an air sample chamber to sample the ambient air, a flow control subsystem to move the sampled air into an SET sensor, an SET sensor with a suitable configuration, and a data acquisition subsystem for analyzing signals obtained from the SET sensor. In real application, the flow control subsystem would drive the molecules to small tubes whose sizes allow only single molecules to enter, and the molecule would then be precisely pulled through the pore in the SET sensor by a vertical electric field. The time for identifying a molecule included the time for pulling of the molecule into required positions in the sensor, time for completing an individual measurement, and the time for analyzing the measured data. During the measurement process, the molecule is treated as a static island of the SET device. Using the proposed setup, our objective is to guide the experimental development of the air pollutant detection using theory. Though it is not explicitly described here, it should be pointed out that other conditioning components are needed in experiments to minimize the measurement interference induced by the unsuitable flow control operations and to maximize the measurement processing ability.

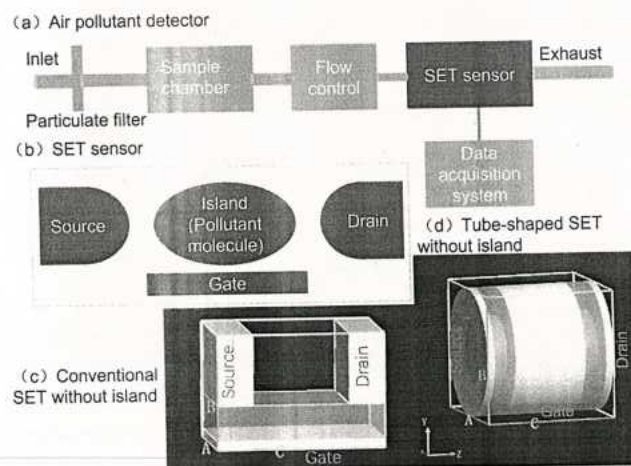


**Figure 1.** Schematic of an air pollutant detector based on a single-electron transistor (SET) sensor.

As shown in Figure 1b, the geometry of the SET sensor included metallic source, drain, and gate electrodes and an island. If the coupling between the island and source/drain gates is strong, the coherent lifetime of the charge carrier is much longer than the propagating time on the island, and coherent transport thus dominates. If the island is weakly coupled to the source/drain gates, the charge carrier transfers from the source to the island and loses all information about its original quantum state due to sufficiently long staying time on the island. Together with a subsequent tunneling process into the drain electrode, the whole process is referred to as the sequential transport. As an example, Figure 1c,d plots conventional and tube-shaped SET structures without islands, respectively. The transport mechanism in the SET was sequential tunneling instead of coherent tunneling.

Because of the weak coupling between the island and the source and drain electrodes, the electron moves through the SET and loses the information about its initial quantum state. In this transport step, the electron propagates independently from the drain electrode to the island and from the island to the source electrode. The gate potential of the gate electrode can tune the electron affinity levels and allows for opening and closing of the electron transport. Explicit principles for the SET operations are described in Appendix A.

Two types of SET structures are illustrated in Figure 2. A conventional structure is represented in the upper panels of Figure 2. The source and drain electrodes were at the two ends of the SET. Below these two electrodes was a dielectric layer with a dielectric constant of  $10\epsilon_0$  and a thickness of 4 Å. Beneath this layer, a gate electrode covered the entire area with a thickness of 1 Å. The three electrodes were metallic and used the work function of gold with a value of  $W = 5.28$  eV. To guide the experimental fabrication, these electrodes were considered to be made of other metals. The thickness along the x-axis was 12 Å for both the source and drain electrodes. The two electrodes had a horizontal separation of 11 Å along the z-axis. Along the y-axis, the two electrodes had the same height of 8 Å. The nanopore can be seen as a pore cross section with an area of  $8 \text{ Å} \times 11 \text{ Å}$ . The thickness of the whole SET structure was 12 Å along the x-axis. The size was comparable to those of earlier reported graphene- [36] and silicon-based [37] nanopores.

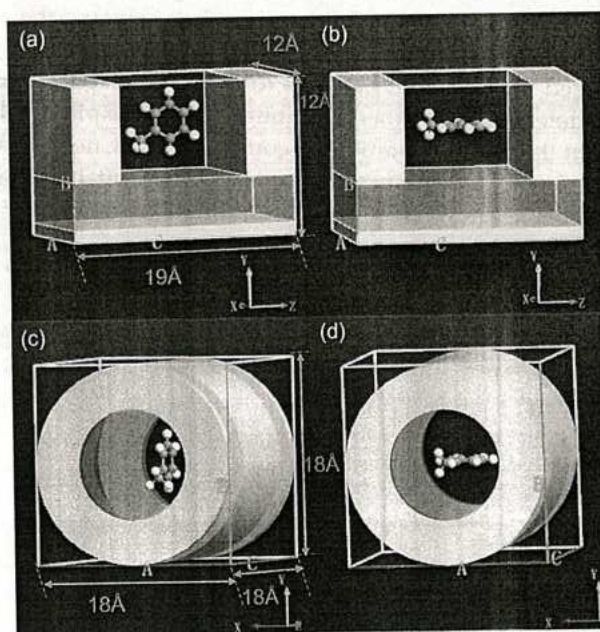


**Figure 2.** SET configurations with  $C_7H_8$  as the SET island. The molecule was perpendicular to the in the left column (a,c) and parallel to xz-plane in the right column (b,d). The molecular center was aligned with the nanopore center.

A tube-shaped SET structure is proposed in the current work, as shown in lower panels of Figure 2. This device was significantly different from the conventional one. The source and drain electrodes had the same metallic tube sections with inner radii of 5 Å, thicknesses of 4 Å, and lengths of 1 Å along the z-axis. The central part of the SET is the gate electrode with a length of 10 Å along the z-axis. The gate and source/drain electrodes were separated by a dielectric tube with a length of 3 Å at each end. The two dielectric tubes had the same inner radius and thickness as those of the source/drain electrodes. The tubular gate electrode had a thickness of 1 Å. The usage of 1 Å has been widely used, though it is even less than the radius of an atomic radius because it is sufficient to model the metal gate effect [33,34]. A dielectric layer with a thickness of 3 Å was placed underneath the gate and surrounded the nanopore of this SET structure. Compared to conventional SET devices, the newly proposed tube-shaped setup possessed several peculiar characteristics: (a) the



source, drain, and gate electrodes were all tube-shaped, allowing a molecule to tunnel through the device before and after the measurements; (b) the gate electrode surrounded the entire channel and could provide stronger control over the electrostatics of the island compared to the conventional SET; and (c) the rotational angle along the  $z$ -axis was flexible due to rotational symmetry.

A pollutant molecule was placed at the center of the nanopore as the SET island with various orientations to examine the capabilities of each SET structure. As a proof of principle, the  $C_7H_8$  molecule was adopted in this section. The molecules in Figure 2a,c as well as Figure 2b,d were perpendicular to and parallel to the  $xz$ -plane, respectively. In all cases, the center of the molecule was placed at the center of the nanopore. In the experiments, the molecule entered the nanopore with various orientations relative to the gate. The SET responded correspondingly to the orientations, and the responses were examined. Influences of the orientation on the performance of the SET were revealed by investigating various physical properties of interest, such as the charge stability diagram.

## 2.2. Computational Procedure

Within the SET environment, the electronic properties of the air pollutant molecule were estimated using DFT calculations. The SET simulations not only used the pseudo-potential, but also introduced compensation charges at each atomic site to screen the electrostatic interactions. The method was implemented within the QuantumATK package [38], which performs calculations based on DFT and nonequilibrium Green's function (NEGF) formalism. The DFT-NEGF-based methodology was developed [39,40] and introduced for non-equilibrium systems initially [41], and it was later expanded to the standard equilibrium case [42]. Stokbro completed this approach in the NEGF-DFT framework of Quantum Wise [35]. The self-consistent calculations employ the generalized gradient approximation of the Perdew–Burke–Ernzerhof exchange–correlation functional [43]. Metallic electrodes were used to fix the potential at a specified voltage on each electrode. To elucidate the absence of the perpendicular components of the electric fields from the metallic surfaces, Neumann boundary conditions were applied when solving the Poisson equation. This method has been successfully applied to estimate the charging energies of a variety of molecules within SETs [29–34,44,45].

## 3. Results and Discussion

### 3.1. Effects of SET Structure

As presented in Figure 3, the charge stability diagram illustrates the electrostatics and the nature of conduction within a SET in detail. If the island and source/drain electrodes are weakly coupled, conduction takes place via the way of sequential tunneling, where an electron goes from the source to the island and finally transfers to the drain so as to complete the conduction path. The island–source coupling and the island–drain coupling strengths determine the tunneling rate. In the case of an SET with a large source–drain separation, the incoming state of the electron is roughly uncorrelated with the outgoing state. Scanning a line along the gate voltage  $V_g$  at a fixed source–drain bias  $V_d$  would lead to a series of periodic peaks, which would indicate the addition of an electron to or removal of an electron from the island. If the scanning process in a symmetric range of  $V_d$  was repeated, diamond-shaped regions would be found on the  $V_g - V_d$  plane, which is known as the charge stability diagram. No conduction occurred within each of the diamond regions, and the charge population change by 1 between neighboring diamonds. Details of the mathematical descriptions of the charge stability diagram are interpreted in Appendix A. Therefore, the SET configurations with molecules of various orientations can provide charge stability diagrams with certain features. Figure 3a–d shows the charge stability diagrams of the configurations shown in Figure 2a–d, respectively. Figure 3a,b shows quite different features, indicating that the molecule orientation in a conventional SET can strongly affect the SET performance. In contrast, Figure 3c,d presents the same



figure patterns, implying that the molecule orientation in the tube-shaped SET had a negligible influence on its charge stability diagram.

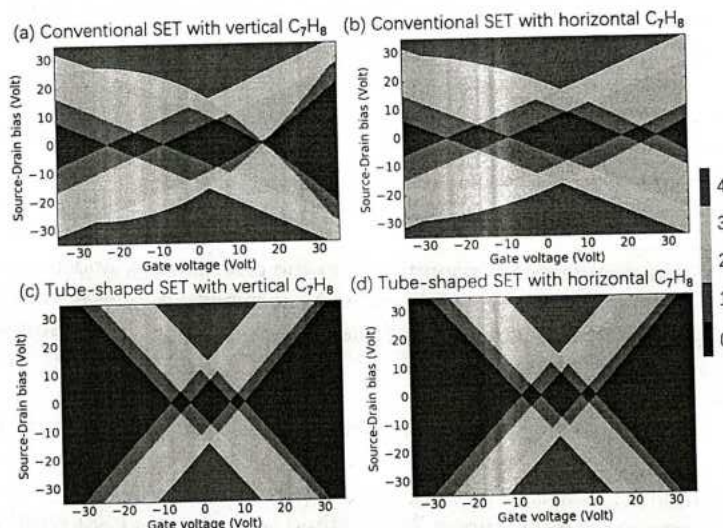


**Figure 3.** (a–d) Charge stability diagrams of various SET configurations for  $C_7H_8$ . For certain gate voltage and source–drain biases, the number of charge states within the bias window is indicated by color: red (4), yellow (3), green (2), blue (1), and dark blue (0).

Next, the electronic structures of the molecule were calculated to clarify the SET environmental effect on and the charging process of the island molecule. In the real space, the electron density of an isolated molecule can be altered by the SET electrostatic potential and the additional charge. Under the conventional SET environment, Figure 4 shows the distribution of electron density of an additional net charge of +1 on  $C_7H_8$ , i.e., the differences between electron densities of  $C_7H_8$  with charge states of  $q = +1$  and  $q = 0$ . The major differences between the electron densities of molecules oriented vertically and horizontally are evident in the figure. For example, the electron density on atom H1 in the vertically positioned  $C_7H_8$  was lower than that in the horizontal  $C_7H_8$ , as shown by the red regions inside the white circles in the upper and lower panels. In contrast, a greater electron density was found on atom H2 (inside the green circles) in the vertical  $C_7H_8$  than in the horizontal  $C_7H_8$ . Under tube-shaped SET environment, the distributions of the additional net charge were the same for the vertical and horizontal  $C_7H_8$ , as shown in Figure A6 of Appendix D. This agrees with that fact that the charge stability diagram in the conventional SET relies on the orientation of the island molecule, while that in the tube-shaped SET was independent of the molecule orientation along the z-axis.

In the energy space, we considered the vertically positioned  $C_7H_8$  in the tube-shaped SET as an example to study the energy levels in various charging states, as illustrated in Figure 5. The molecular energy spectrum for the island molecule retained its structure during the operation of the SET device. However, the energy levels shifted by certain amounts to let the net charges enter or leave the island molecule. The energy levels entirely shifted upward when the island molecule was negatively charged, while they shifted downward as the electron moved away from the molecule. For example, if one electron was added to the island molecule, the originally lowest unoccupied molecular orbital (LUMO) in the neutral state shown in Figure 5c will become occupied by one electron, becoming the highest occupied molecular orbital (HOMO) in the charge state of  $q = -1$ , as presented in Figure 5d. Figure A7 in Appendix D presents the energy levels of the horizontally placed  $C_7H_8$  in the tube-shaped SET, and the spectra were the same as those of the case discussed here. In addition, Figures A8 and A9 in Appendix D show the energy levels of the vertical and horizontal  $C_7H_8$  in a conventional SET, and they have same



spectral structure as those of the cases in the tube-shaped SET. However, slight energy shifting occurred due to the electrostatic effect from the SET environment.

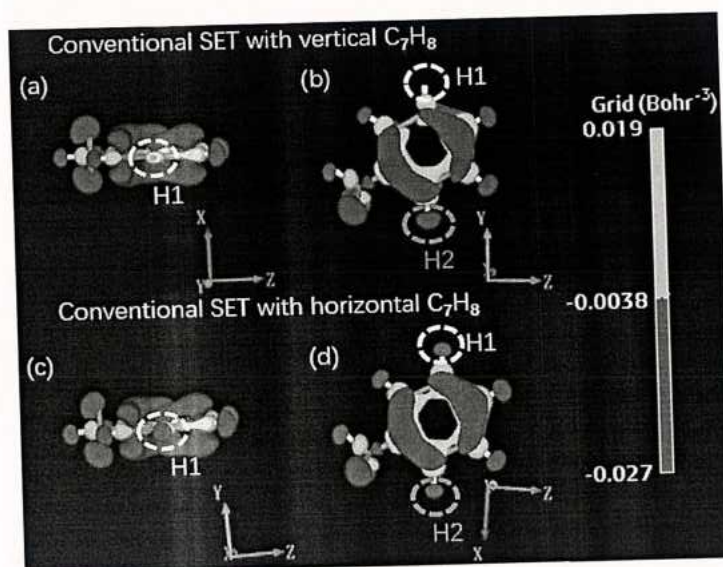


**Figure 4.** (a–d) Electron density of an additional net charge of +1 distributed on  $C_7H_8$  under a conventional SET environment. The upper and lower panels represent the cases with vertical and horizontal  $C_7H_8$  molecules, respectively. The charge clouds are illustrated from different viewpoints in the left and right columns.

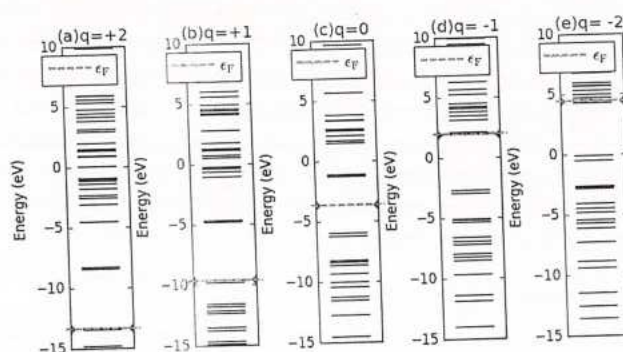


**Figure 5.** (a–e) Molecular energy spectra of vertically positioned  $C_7H_8$  with various charge states under the tube-shaped SET environment. The fermion energy level is marked in each subplot with green dots.

The dependence of the total energy on the gate potential was then studied to further understand the underlying electronic properties of the two types of SET structures. Based on the DFT calculations, the total energies of the island molecule within the SET environment were obtained for various charge states, as shown in Figure A3 in Appendix C. Using the calculated total energy, we fit a quadratic function as follows [32,35]:

$$E(q, V_g) = E_0 + qW + \alpha qV_g + \beta(eV_g)^2, \quad (1)$$

in which  $E_0$  denotes the zeroth-order term, which corresponds to a constant energy. The second term  $qW$  is the reservoir energy, where  $q$  represents the charge of the island molecule,  $W$  denotes the work function of the electrode, and a value of  $W = 5.28$  eV was used to model a gold electrode. The third term in Equation (1), which represents the direct coupling between the island molecule and the gate electrode, is proportional to the charge  $q$  on the molecule and is linear with respect to the gate voltage  $V_g$ . The linear coupling strength,  $\alpha$ ,

depends on the relative position/orientation between the island and the gate for a certain type of molecule. The fourth term is independent of the charge state and has a quadratic dependence on the gate voltage  $V_g$ . The quadratic coupling strength,  $\beta$ , estimates the contribution of electrical polarization under the influence of an electric field. The values of the coupling strengths were estimated by making a least squares fit to the total energies from the DFT calculations, and those of the configurations in Figure 2 are listed in Table 1.

**Table 1.** Gate coupling strengths between gates and island molecules.

SET Configuration			Gate-Island Coupling Strength	
SET Structure	ISLAND Molecule	Molecule Posture	Linear $\alpha$	Quadratic $\beta$ (eV <sup>-1</sup> )
Conventional	C <sub>7</sub> H <sub>8</sub>	Vertical	0.3417	−0.0056
Conventional	C <sub>7</sub> H <sub>8</sub>	Horizontal	0.3004	−0.0023
Tube-shaped	C <sub>7</sub> H <sub>8</sub>	Vertical	0.7962	−0.0006
Tube-shaped	C <sub>7</sub> H <sub>8</sub>	Horizontal	0.7962	−0.0006

For conventional SET configurations shown in Figure 2a,b, the coupling strengths strongly depended on the orientation of the island molecule. As shown in Table 1, the vertically placed molecule caused stronger quadratic gate–island coupling than the horizontally oriented molecule. The strong dependence of the gate–island coupling on the orientation of the molecule in the SET suggested that the conventional SET is not suitable for the detection of pollutant molecules, as the molecules would arrive the nanopore with various orientations. As shown in the last two lines of Table 1, for the configurations shown in Figure 2c,d, the total energy was almost linearly dependent on  $V_g$ , indicating the minimal polarization contribution in the tube-shaped geometry. This minimum is possible because of the large coverage of the gate electrode on the island area from all different sides. The gate–island coupling strengths are identical for the configurations shown in Figure 2c,d. Thus, we concluded that the rotational symmetry of the tube-shaped device provided greater convenience for identifying the types of various molecules than the conventional SET. In the remainder of the manuscript, the tube-shaped SET will be employed to detect the pollutant molecules.

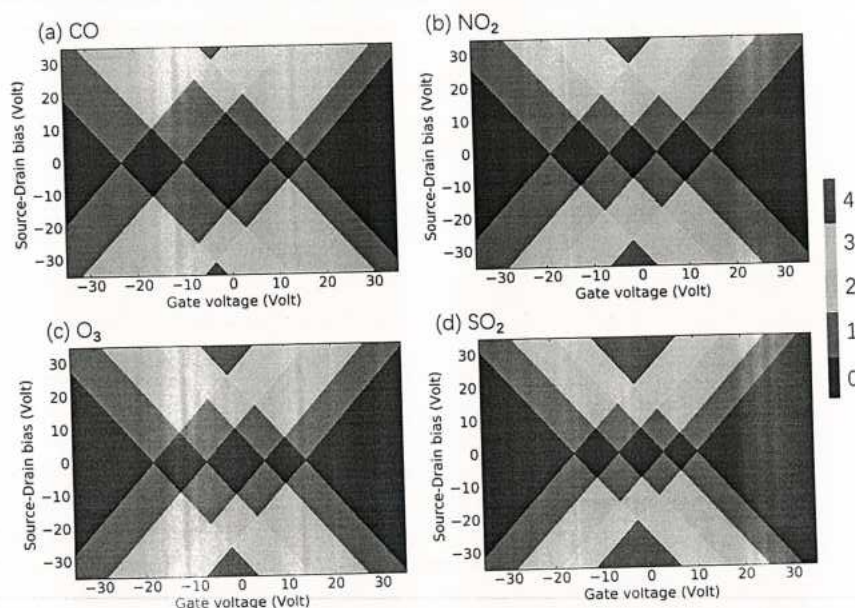
### 3.2. Identification of Air Pollutants

In this work, each air pollutant molecule served as the SET island and determined the performance of the SET. A slew of gas-phase air pollution molecules, including criteria pollutants and hazardous air pollutant molecules, were studied for the purpose of detection.

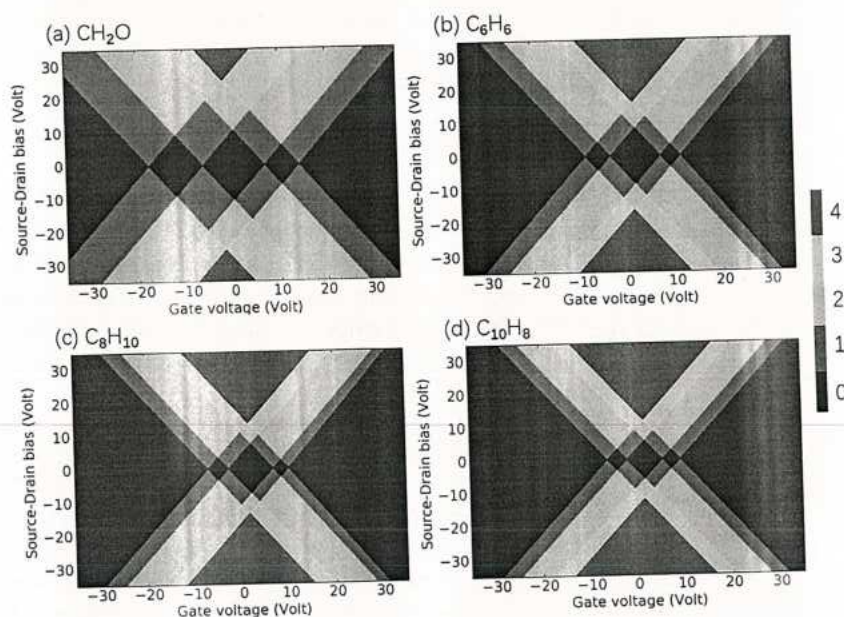
In this section, we investigate the commonly met criteria pollutants molecules CO, NO<sub>2</sub>, O<sub>3</sub>, and SO<sub>2</sub> [46], as well as several typical hazardous pollutants molecules CH<sub>2</sub>O, C<sub>6</sub>H<sub>6</sub>, C<sub>7</sub>H<sub>8</sub>, C<sub>8</sub>H<sub>10</sub>, and C<sub>10</sub>H<sub>8</sub>, as examples of polycyclic aromatic hydrocarbons [47]. The molecules and the SET configurations are shown in Appendix B. The total energy of the investigated criteria pollutant and hazardous air pollutant molecules in the electrostatic environment is shown in Figures A4 and A5 of Appendix C, respectively. Based on these total energies, the charge stability diagrams for the SET configurations with the criteria and hazardous air pollutant molecules were obtained and are illustrated in Figures 6 and 7, respectively. The individual diagrams of the studied molecules had specific patterns, and the corresponding criteria pollutant and hazardous air pollutant molecules could be identified easily after the measured signals were analyzed by the data acquisition subsystem in Figure 1. The transport performance in the SET device was primarily decided by the electronic structure of the island molecule. The electronic structures of each criteria pollutant or hazardous air pollutant molecule differed, as shown in Appendix D. The electronic levels of the island molecule were well maintained during the operation of the SET due to the weak coupling between the electrodes and the molecule, and the pattern of the charge stability diagram was determined by the molecular electronics. Thus, the



diagram can represent the intrinsic and unique features for each criteria pollutant and hazardous air pollutant molecule and can be treated as fingerprints of the molecules. For example, the size of the central Coulomb diamond in the charge stability diagram varied for all the studied molecules, as shown in Table A1 in Appendix B.



**Figure 6.** Charge stability diagrams of criteria pollutant molecules of (a) CO, (b) NO<sub>2</sub>, (c) O<sub>3</sub>, and (d) SO<sub>2</sub>. For certain gate voltage and source–drain bias, the number of charge states within the bias window is indicated by the color: red (4), yellow (3), green (2), blue (1), and dark blue (0).



**Figure 7.** Charge stability diagrams of hazardous pollutant molecules of (a) CH<sub>2</sub>O, (b) C<sub>6</sub>H<sub>6</sub>, (c) C<sub>8</sub>H<sub>10</sub>, and (d) C<sub>10</sub>H<sub>8</sub>. For certain gate voltage and source–drain bias, the number of charge states within the bias window is indicated by the color: red (4), yellow (3), green (2), blue (1), and dark blue (0).

In addition, we investigated the coupling between the aforementioned molecules and the gate in the proposed device, and the results are shown in Table 2. The linear gate–island coupling dominated the interaction between the gate and air pollutant molecules,

indicating that contribution of electrical polarization in the tube-shaped SET was negligible. The coupling strengths for each investigated molecule differed, further confirming the validity of the tube-shaped SET for identification of air pollutant molecules.

**Table 2.** Gate coupling strengths between gates and island molecules of tube-shaped SET configurations.

Island Molecule	Gate–Island Coupling Strength	
	Linear $\alpha$	Quadratic $\beta$ (eV <sup>−1</sup> )
CO	0.8020	0.0000
NO <sub>2</sub>	0.8029	0.0000
O <sub>3</sub>	0.8138	0.0000
SO <sub>2</sub>	0.8005	−0.0001
CH <sub>2</sub> O	0.8035	0.0000
C <sub>6</sub> H <sub>6</sub>	0.8031	−0.0004
C <sub>8</sub> H <sub>10</sub>	0.7954	−0.0009
C <sub>10</sub> H <sub>8</sub>	0.7768	−0.0009

### 3.3. Quantification of Air Pollutants

Identification and quantification of air pollutants are the two major goals of testing a sample of ambient air. Traditionally, the entire process includes multiple stages, and different pieces of equipment are used in identification and quantification stages. For instance, the early procedures for the detection and quantitative measurements of the amount of SO<sub>2</sub> varied, and different measurement devices were used in each process [9].

In our case, the proposed setup for the identification can be utilized for quantification as well. As shown in Figure 1, the quantification can be realized after the pollutant molecules go through the flow control component and flow to the center of the nanopore of the SET sensor. Using the air pollutant molecule as the island, the charge stability diagram can be produced after the operation of the SET device [21,22]. In the data acquisition subsystem, we can analyze the information gathered and obtain the concentration  $c_X$  of each type of air pollutant X, as follows:

$$c_X = N_X m_X / V \quad (2)$$

where  $N_X$  denotes the number of molecules X identified during the measurement process,  $m_X$  is the molecular weight of the molecule X, and  $V$  is the volume of air that went through the SET sensor for quantification. Each type of molecule must be well mixed in the tested sample air, and the testing time must be sufficiently long to obtain convergent results. To speed up the measurement process  $M$  times, the SET sensor can be replaced by an integrated sensor with  $M$  parallel SET devices. More details of the parallelization of SET can be found in [31].

Finally, the device can operate at room temperature. Normally, the characteristic charging energy will be larger than the thermal energy of the charge carriers only if the temperature is low enough, making the Coulomb blockade observable [48]. The charging energy  $\Delta E^i(I)$  is needed to charge the island with one elementary charge. As listed in Table A2 of Appendix C, the energies used to charge different air pollutant molecules are sufficiently high ( $k_B T_{300K} \ll |\Delta E^i(I)|$ ) to avoid the electron transport induced by the thermal fluctuations, in agreement with other molecule SET papers [30,31]. The SET device can thus operate over a large temperature range, including room temperature.

## 4. Conclusions

In the present work, based on the newly designed tube-shaped SET, an air pollutant measurement system was proposed to examine the air pollutants at the molecular level. First, we compared our new SET sensor with the conventional one. In each SET, the molecule was treated as the island after flowing to the center of the SET nanopore.



The island molecule was placed along the *z*-axis with different orientations, i.e., either vertically or horizontally to the *xy*-plane in the studied cases. Operation and performance analysis of the SET sensor was performed using DFT-based *ab initio* calculations. We then studied the electronic properties of the island molecule under each SET environment, including the charge stability diagrams, electron densities, molecular energy spectra, total energies as functions of the gate voltages, and gate–island coupling. The effect of molecular orientation on the performance of the tube-shaped SET was found to be negligible, while it was not negligible for the conventional SET, demonstrating the advantage of our new sensor. Second, the new device was used to identify commonly encountered air pollutant molecules. The calculated charge stability diagrams were unique for each molecule, and thus they can be used as a fingerprint for detection. Third, we showed that the device prototype could identify and quantify the criteria pollutants and hazardous air pollutants in a unified framework. Our device was illustrated to operate over a broad range around room temperature, owing to the high charging energy of the molecules within it. In conclusion, this tube-shaped SET sensor has many potential applications. Its great versatility, high sensitivity, and elevated temperature of operation are significant advantages, making this SET-based detector a promising candidate for testing air quality at the molecular level. Research on the applications of the proposed device for testing other toxic molecules and designing more flexible detection setups for the dynamic sensing of air pollutant molecules is ongoing.

**Author Contributions:** Conceptualization, Z.H. and X.P.; methodology, Z.H. and X.P.; software, Z.H. and M.B.; validation, J.L. and C.Y.; formal analysis, Z.H. and X.P.; investigation, Z.H.; resources, C.P. and J.H.; writing—original draft preparation, Z.H.; writing—review and editing, X.P.; visualization, Z.H.; supervision, X.P., C.P., and J.H.; project administration, Z.H.; funding acquisition, Z.H. All authors have read and agreed to the published version of the manuscript.

**Funding:** This research was funded by China Postdoctoral Science Foundation (No. 2019M663877XB), Natural Science Foundation of Chongqing (No. cstc2020jcyj-msxmX0003), Yu Ren She [2019] No. 298, and Educational Reform Project Fund of Yangtze Normal University (No. JG2019234).

**Institutional Review Board Statement:** Not applicable.

**Informed Consent Statement:** Not applicable.

**Data Availability Statement:** The datasets used and/or analyzed during the current study are available from the corresponding author on reasonable request.

**Acknowledgments:** Zhongkai Huang would like to thank Ziyi Yang for fruitful discussion.

**Conflicts of Interest:** The authors declare no conflicts of interest.

## Appendix A. Working Principle of SET for Detection of Air Pollutant Molecules

Coupling between the source/drain electrodes and the island was weak within the SET device. An electron would tunnel from the source to the drain electrode via the island. During the transport, because of the localization and long stay of an electron in the island, the original and final quantum states of the electron would become uncorrelated, and the electron would undergo subsequent tunneling instead of coherent tunneling. This process is known as the Coulomb blockade.

In detail, when the electron tunnels through the barrier between the source electrode and the island, the energy of the electron on the island must be lower than that of the electron in the source electrode,

$$E^s(S) + E^i(I) \geq E^s(S-1) + E^i(I+1), \quad (\text{A1})$$

where *S* and *I* are the initial numbers of electrons on the island and in the source electrode, respectively.  $E^s(q)$ ,  $E^i(q)$ , and  $E^d(q)$  give the total energy of the source electrode, island, and drain electrode as functions of the number of electrons *q*, respectively.

Similarly, if the electron transfers from the island to the drain electrode, the energy of the electron on the island must be higher than that in the drain electrode. Moreover, to move the electron from the island to the drain electrode, it must have a lower energy in the drain electrode,

$$E^d(D) + E^i(I + 1) \geq E^d(D + 1) + E^i(I), \quad (\text{A2})$$

where  $D$  is the initial number of electrons in the drain electrode.

The maximum energy of the electron in the source electrode is  $-W + eV_b/2$ , where  $W$  is the work function of the electrode and  $V_b$  is the applied bias. Assuming that the electron with maximum energy tunnels onto the island, then the energy is

$$E^s(S) - E^s(S - 1) = -W + eV_b/2. \quad (\text{A3})$$

Using the above tunneling criterion, we obtain the condition

$$-W + eV_b/2 + E^i(I) \geq E^i(I + 1). \quad (\text{A4})$$

Similarly,  $-W - eV_b/2$  is the minimum energy of an electron in the drain electrode, and thus

$$E^i(I + 1) \geq -W - eV_b/2 + E^i(I). \quad (\text{A5})$$

The requirement for a current to flow in the device is therefore

$$e|V_b|/2 \geq \Delta E^i(I) + W \geq -e|V_b|/2, \quad (\text{A6})$$

where  $\Delta E^i(I) = E^i(I + 1) - E^i(I)$  is the charging energy of the island.

In this work, the charging energies of different molecular SETs were calculated, and Equation (A6) was used to obtain the so-called charge stability diagram, which shows the number of charge states inside the bias window as a function of the gate and source-drain voltages. In detail, the sizes of the central diamonds in the charge stability diagrams for the investigated air pollutant molecules are shown in Table A1.

**Table A1.** Size of the central diamond in the charge stability diagram of tube-shaped SET configurations with an individual island molecule.

Island Molecule	CO	NO <sub>2</sub>	O <sub>3</sub>	SO <sub>2</sub>	CH <sub>2</sub> O	C <sub>6</sub> H <sub>6</sub>	C <sub>7</sub> H <sub>8</sub>	C <sub>8</sub> H <sub>10</sub>	C <sub>10</sub> H <sub>8</sub>
Length of a diagonal line in the central diamond along the gate voltage axis (V)	18.5	9.9	12.3	9.3	13.1	10.4	9.9	9.4	7.4
Length of a diagonal line in the central diamond along the source-drain bias (V)	29.6	16.0	20.0	14.8	21	16.8	15.6	14.9	11.2

## Appendix B. SET Configurations with Various Air Pollutant Molecules

The SET configurations for investigating criteria pollutant molecules and hazardous air pollutant molecules are illustrated in Figures A1 and A2, respectively.



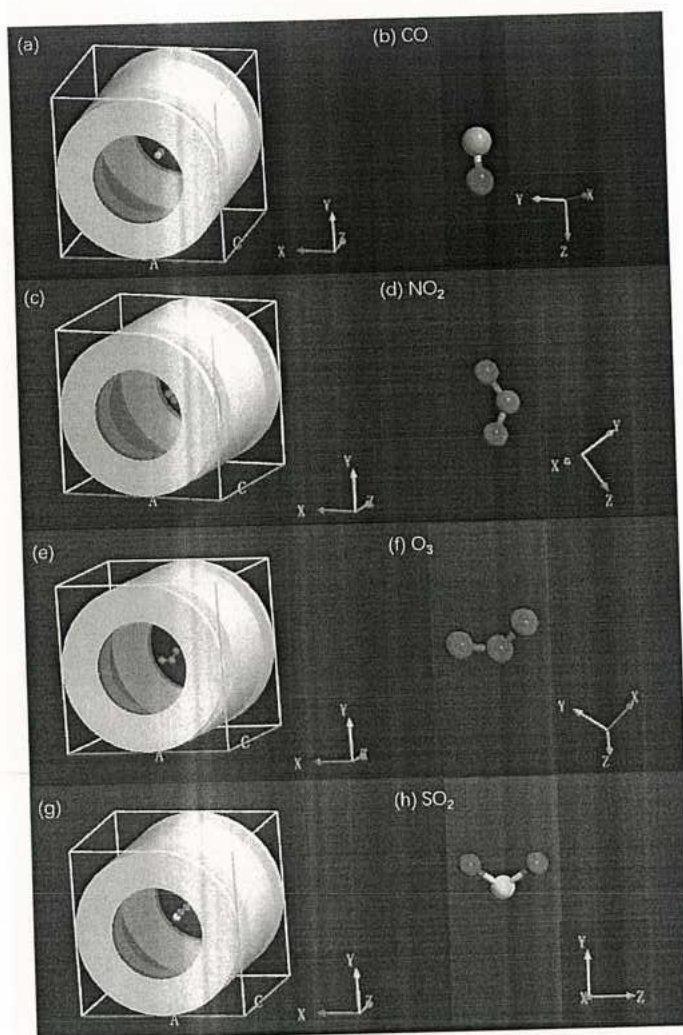


**Figure A1.** (a) Tube-shaped SET with a CO molecule as the island, (b) CO molecule, (c) tube-shaped SET with an NO<sub>2</sub> molecule as the island, (d) NO<sub>2</sub> molecule, (e) tube-shaped SET with an O<sub>3</sub> molecule as the island, (f) O<sub>3</sub> molecule, (g) tube-shaped SET with an SO<sub>2</sub> molecule as the island, and (h) SO<sub>2</sub> molecule.

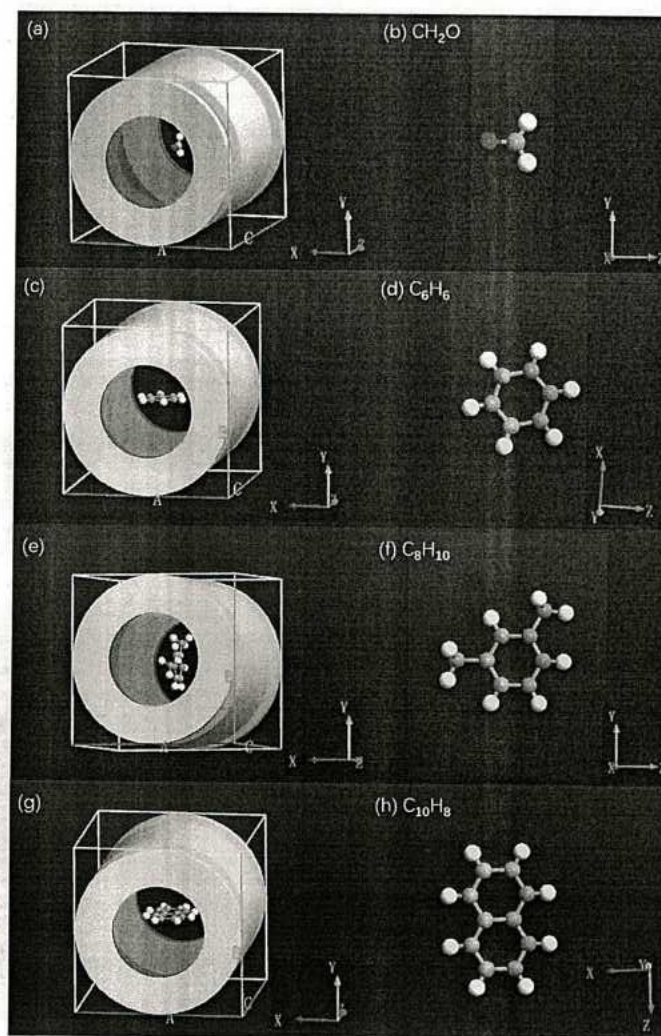


**Figure A2.** (a) Tube-shaped SET with a  $\text{CH}_2\text{O}$  molecule as the island, (b)  $\text{CH}_2\text{O}$  molecule, (c) tube-shaped SET with a  $\text{C}_6\text{H}_6$  molecule as the island, (d)  $\text{C}_6\text{H}_6$  molecule, (e) tube-shaped SET with a  $\text{C}_8\text{H}_{10}$  molecule as the island, (f)  $\text{C}_8\text{H}_{10}$  molecule, (g) tube-shaped SET with a  $\text{C}_{10}\text{H}_8$  molecule as the island, and (h)  $\text{C}_{10}\text{H}_8$  molecule.

### Appendix C. Total Energy as Function of Gate Voltage

The total energy of  $\text{C}_7\text{H}_8$  in each SET environment as a function of the gate voltage is shown in Figure A3. The total energies of the criteria pollutant molecules and hazardous air pollutant molecules in the tube-shaped SET environment as functions of the gate voltage are displayed in Figures A4 and A5, respectively.



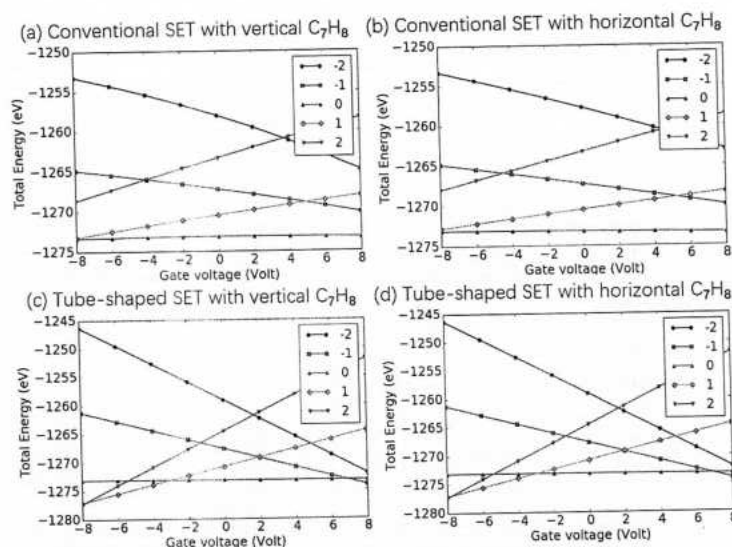


**Figure A3.** Total energy as a function of the gate voltage for  $C_7H_8$  in the (a) conventional SET with the island molecule vertically oriented, (b) conventional SET with the island molecule horizontally oriented, (c) tube-shaped SET with the island molecule vertically oriented, and (d) tube-shaped SET with the island molecule horizontally oriented. Different curves correspond to charge states  $-2$ ,  $-1$ ,  $0$ ,  $+1$ ,  $+2$ .

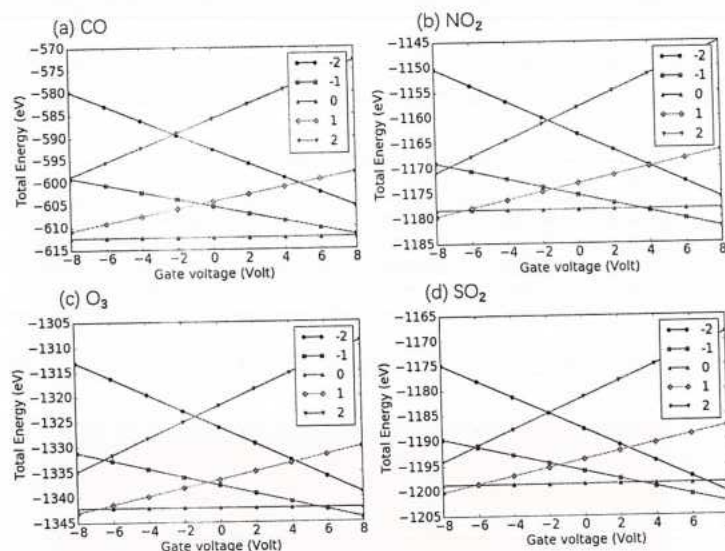


**Figure A4.** Total energy as a function of the gate voltage for criteria pollutant molecules (a) CO, (b)  $NO_2$ , (c)  $O_3$ , and (d)  $SO_2$  in the tube-shaped SET environment. Different curves correspond to charge states  $-2$ ,  $-1$ ,  $0$ ,  $+1$ ,  $+2$ .

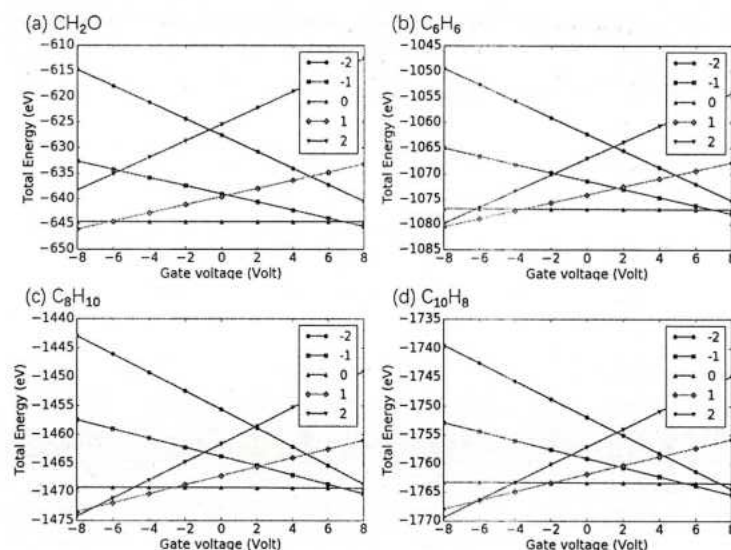


**Figure A5.** Total energy as a function of the gate voltage for criteria pollutant molecules (a)  $\text{CH}_2\text{O}$ , (b)  $\text{C}_6\text{H}_6$ , (c)  $\text{C}_8\text{H}_{10}$ , and (d)  $\text{C}_{10}\text{H}_8$  in the tube-shaped SET environment. Different curves correspond to charge states  $-2$ ,  $-1$ ,  $0$ ,  $+1$ ,  $+2$ .

The charging energies of the island molecules were deduced from the total energies obtained from the first-principle calculations, as illustrated in Table A2.

**Table A2.** Charging energy for state  $I$  is  $\Delta E^I(I) = E^I(I+1) - E^I(I)$  at zero gate voltage, where  $E^I(I)$  is the total energy of the island molecule with a net charge  $I$ . The charging energy of the investigated air pollutant molecule for various states are shown.

Island Molecule	CO	$\text{NO}_2$	$\text{O}_3$	$\text{SO}_2$	$\text{CH}_2\text{O}$	$\text{C}_6\text{H}_6$	$\text{C}_7\text{H}_8$	$\text{C}_8\text{H}_{10}$	$\text{C}_{10}\text{H}_8$
$\Delta E^I(+1)$ (eV)	23.7019	20.3182	19.9398	17.6599	19.4065	12.3559	11.4820	10.8229	10.0120
$\Delta E^I(0)$ (eV)	13.2354	10.4107	10.8392	10.1616	10.2545	8.1345	7.6662	7.3421	6.7887
$\Delta E^I(-1)$ (eV)	-1.5923	2.4329	0.8093	2.6771	-0.2429	-0.2895	-0.2405	-0.1665	1.0380
$\Delta E^I(-2)$ (eV)	-7.4722	-6.8920	-6.2228	-3.0606	-6.1735	-3.8604	-3.2489	-2.8812	-1.9152

#### Appendix D. Electronic Structures of the Investigated Molecules

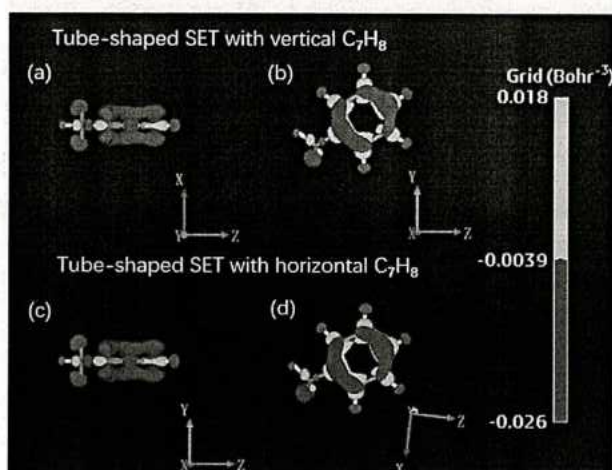


**Figure A6.** (a–d) Electron density of an additional net charge of  $+1$  distributed on  $\text{C}_7\text{H}_8$  under the tube-shaped SET environment. The upper and lower panels represent those with vertical and horizontal  $\text{C}_7\text{H}_8$ , respectively. The charge clouds are illustrated from different viewpoints in the left and right columns.



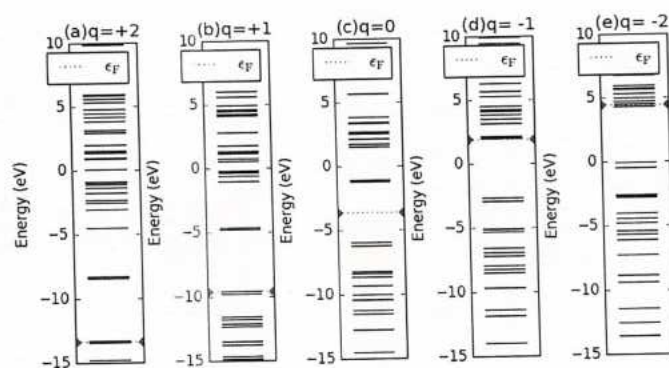


**Figure A7.** (a–e) Molecular energy spectra of horizontally oriented  $C_7H_8$  with various charge states under the tube-shaped SET environment. The fermion energy level is marked in each subplot with green dots.

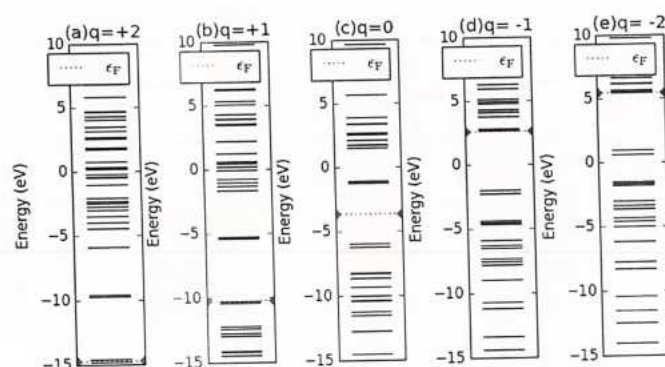


**Figure A8.** (a–e) Molecular energy spectra of vertically oriented  $C_7H_8$  with various charge states under the conventional SET environment. The fermion energy level is marked in each subplot with green dots.

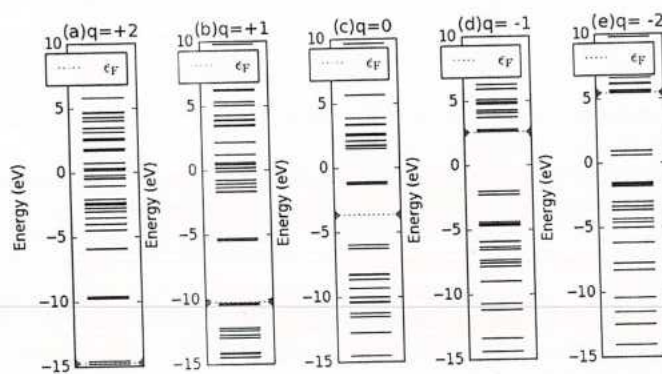


**Figure A9.** (a–e) Molecular energy spectra of horizontally oriented  $C_7H_8$  with various charge states under the conventional SET environment. The fermion energy level is marked in each subplot with green dots.

The molecular energy spectra of the investigated criteria pollutant and hazardous pollutant molecules are illustrated in Figures A10 and A11, respectively. It is evident that these spectra differed, indicating the validity of the tube-shaped SET for identifying corresponding molecules.

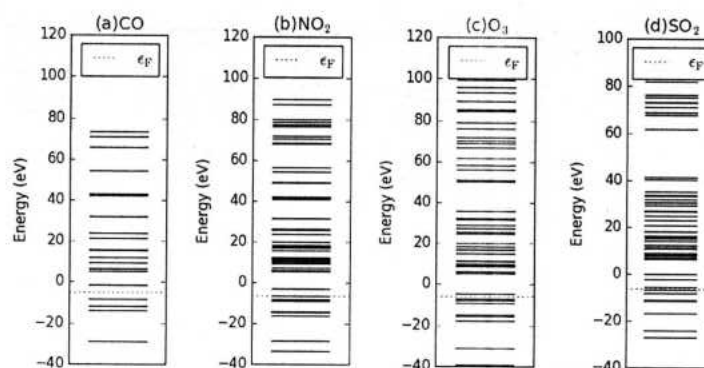


**Figure A10.** Molecular energy spectra of neutralized criteria pollutant molecules of (a) CO, (b) NO<sub>2</sub>, (c) O<sub>3</sub>, and (d) SO<sub>2</sub> in tube-shaped SET environment. The fermion energy level is marked in each subplot with green dots.

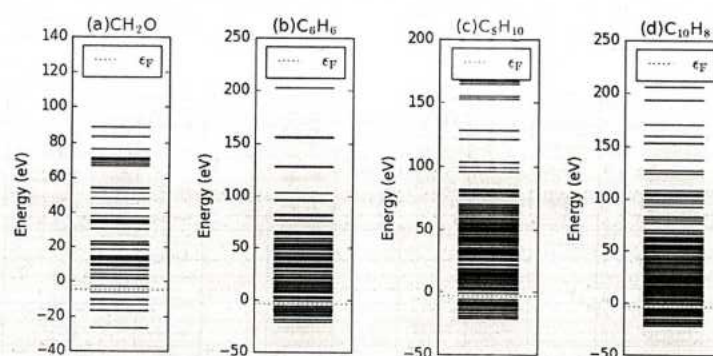


**Figure A11.** Molecular energy spectra of neutralized hazardous air pollutant molecules of (a) CH<sub>2</sub>O, (b) C<sub>6</sub>H<sub>6</sub>, (c) C<sub>8</sub>H<sub>10</sub>, and (d) C<sub>10</sub>H<sub>8</sub> in tube-shaped SET environment. The fermion energy level is marked in each subplot with green dots.

## References

- Vallero, D.A. Air Pollution. In *Kirkthmer Encyclopedia of Chemical Technology*; John Wiley Sons, Inc.: Hoboken, NJ, USA, 2015; pp. 1–48. [CrossRef]
- Chau, T.T.; Wang, K.Y. An association between air pollution and daily most frequently visits of eighteen outpatient diseases in an industrial city. *Sci. Rep.* **2020**, *10*, 2321. [CrossRef] [PubMed]
- Li, Y.; Guan, D.; Yu, Y.; Westland, S.; Wang, D.; Meng, J.; Wang, X.; He, K.; Tao, S. A psychophysical measurement on subjective well-being and air pollution. *Nat. Commun.* **2019**, *10*, 5473. [CrossRef] [PubMed]
- Vallero, D., Chapter 14—Air Pollution's Impact on Ecosystems. In *Fundamentals of Air Pollution*, 5th ed.; Vallero, D., Ed.; Academic Press: Boston, MA, USA, 2014; pp. 341–368. [CrossRef]
- Vallero, D., Chapter 15—Air Pollution's Impact on Materials and Structures. In *Fundamentals of Air Pollution*, 5th ed.; Vallero, D., Ed.; Academic Press: Boston, MA, USA, 2014; pp. 369–378. [CrossRef]
- Vallero, D., Chapter 7—Air Pollutant Hazards. In *Fundamentals of Air Pollution*, 5th ed.; Vallero, D., Ed.; Academic Press: Boston, MA, USA, 2014; pp. 197–214. [CrossRef]
- Johannson, K.A.; Balmes, J.R.; Collard, H.R. Air Pollution Exposure: A Novel Environmental Risk Factor for Interstitial Lung Disease? *CHEST* **2015**, *147*, 1161–1167. [CrossRef]
- Ham, B. Indoor chemical pollution impacts often remain invisible. *Science* **2019**, *366*, 1084. [CrossRef]
- Vallero, D., Chapter 25—Methods for Measuring Air Pollutants. In *Fundamentals of Air Pollution*, 5th ed.; Vallero, D., Ed.; Academic Press: Boston, MA, USA, 2014; pp. 579–626.
- Kong, J.; Franklin, N.R.; Zhou, C.; Chapline, M.G.; Peng, S.; Cho, K.; Dai, H. Nanotube Molecular Wires as Chemical Sensors. *Science* **2000**, *287*, 622–625. [CrossRef]
- Iijima, S. Helical microtubules of graphitic carbon. *Nature* **1991**, *354*, 56–58. [CrossRef]
- Li, Y.B.; Bando, Y.; Sato, T.; Kurashima, K. ZnO nanobelts grown on Si substrate. *Appl. Phys. Lett.* **2002**, *81*, 144–146. [CrossRef]
- Morales, A.M.; Lieber, C.M. A Laser Ablation Method for the Synthesis of Crystalline Semiconductor Nanowires. *Science* **1998**, *279*, 208–211. [CrossRef]



14. Li, C.; Zhang, D.; Liu, X.; Han, S.; Tang, T.; Han, J.; Zhou, C. In<sub>2</sub>O<sub>3</sub> nanowires as chemical sensors. *Appl. Phys. Lett.* **2003**, *82*, 1613–1615. [CrossRef]
15. Kolmakov, A.; Zhang, Y.; Cheng, G.; Moskovits, M. Detection of CO and O<sub>2</sub> Using Tin Oxide Nanowire Sensors. *Adv. Mater.* **2003**, *15*, 997–1000. [CrossRef]
16. Schedin, F.; Geim, A.K.; Morozov, S.V.; Hill, E.W.; Blake, P.; Katsnelson, M.I.; Novoselov, K.S. Detection of individual gas molecules adsorbed on graphene. *Nat. Mater.* **2007**, *6*, 652–655. [CrossRef]
17. Li, H.; Yin, Z.; He, Q.; Li, H.; Huang, X.; Lu, G.; Fam, D.W.H.; Tok, A.I.Y.; Zhang, Q.; Zhang, H. Fabrication of Single- and Multilayer MoS<sub>2</sub> Film-Based Field-Effect Transistors for Sensing NO at Room Temperature. *Small* **2012**, *8*, 63–67. [CrossRef] [PubMed]
18. Chen, L.C.; Zheng, J.; Liu, J.; Gong, X.T.; Chen, Z.Z.; Guo, R.X.; Huang, X.; Zhang, Y.P.; Zhang, L.; Li, R.; et al. Nonadditive Transport in Multi-Channel Single-Molecule Circuits. *Small* **2020**, *16*, 2002808. [CrossRef] [PubMed]
19. Kastner, M.A. The single-electron transistor. *Rev. Mod. Phys.* **1992**, *64*, 849–858. [CrossRef]
20. Bitton, O.; Gutman, D.B.; Berkovits, R.; Frydman, A. Multiple periodicity in a nanoparticle-based single-electron transistor. *Nat. Commun.* **2017**, *8*, 402. [CrossRef] [PubMed]
21. Matsumoto, K.; Ishii, M.; Segawa, K.; Oka, Y.; Vartanian, B.J.; Harris, J.S. Room temperature operation of a single electron transistor made by the scanning tunneling microscope nanooxidation process for the TiO<sub>x</sub>/Ti system. *Appl. Phys. Lett.* **1996**, *68*, 34–36. [CrossRef]
22. Shin, S.J.; Lee, J.J.; Kang, H.J.; Choi, J.B.; Yang, S.R.E.; Takahashi, Y.; Hasko, D.G. Room-Temperature Charge Stability Modulated by Quantum Effects in a Nanoscale Silicon Island. *Nano Lett.* **2011**, *11*, 1591–1597. [CrossRef] [PubMed]
23. Maeda, K.; Okabayashi, N.; Kano, S.; Takeshita, S.; Tanaka, D.; Sakamoto, M.; Teranishi, T.; Majima, Y. Logic Operations of Chemically Assembled Single-Electron Transistor. *ACS Nano* **2012**, *6*, 2798–2803. [CrossRef]
24. Tsukanov, A.V. Measurement of a charge qubit using a single-electron transistor based on a triple quantum dot. *Phys. Rev. A* **2019**, *100*, 062305. [CrossRef]
25. Keith, D.; House, M.; Donnelly, M.; Watson, T.; Weber, B.; Simmons, M. Single-Shot Spin Readout in Semiconductors Near the Shot-Noise Sensitivity Limit. *Phys. Rev. X* **2019**, *9*, 041003. [CrossRef]
26. Rani, S.; Ray, S.J. Detection of gas molecule using C<sub>3</sub>N island single electron transistor. *Carbon* **2019**, *144*, 235–240. [CrossRef]
27. Sharma, A.; Husain, M.; Srivastava, A.; Khan, M.S. Anti-site defected MoS<sub>2</sub> sheet-based single electron transistor as a gas sensor. *AIP Conf. Proc.* **2018**, *1953*, 140075. [CrossRef]
28. Sharma, A.; Anu, A.; Khan, M.S.; Husain, M.; Khan, M.S.; Srivastava, A. Sensing of CO and NO on Cu-Doped MoS<sub>2</sub> Monolayer-Based Single Electron Transistor: A First Principles Study. *IEEE Sens. J.* **2018**, *18*, 2853–2860. [CrossRef]
29. Ray, S.J. Single molecule transistor based nanopore for the detection of nicotine. *J. Appl. Phys.* **2014**, *116*, 244307. [CrossRef]
30. Ray, S.J. Humidity sensor using a single molecular transistor. *J. Appl. Phys.* **2015**, *118*, 044307. [CrossRef]
31. Ray, S.J. Single molecular transistor as a superior gas sensor. *J. Appl. Phys.* **2015**, *118*, 034303. [CrossRef]
32. Ray, S.J. Gate engineered performance of single molecular transistor. *J. Appl. Phys.* **2016**, *119*, 204302. [CrossRef]
33. Ray, S.J.; Chowdhury, R. Double gated single molecular transistor for charge detection. *J. Appl. Phys.* **2014**, *116*, 034307. [CrossRef]
34. Anu, A.; Srivastava, A.; Khan, M.S. Charge stability diagram and addition energy spectrum for single-electron transistor based on Ni-dithiolene derivatives. *Org. Electron.* **2018**, *59*, 125–130. [CrossRef]
35. Stokbro, K. First-Principles Modeling of Molecular Single-Electron Transistors. *J. Phys. Chem. C* **2010**, *114*, 20461–20465. [CrossRef]
36. Garaj, S.; Hubbard, W.; Reina, A.; Kong, J.; Branton, D.; Golovchenko, J.A. Graphene as a subnanometre trans-electrode membrane. *Nature* **2010**, *467*, 190–193. [CrossRef] [PubMed]
37. Li, J.; Stein, D.; McMullan, C.; Branton, D.; Aziz, M.J.; Golovchenko, J.A. Ion-beam sculpting at nanometre length scales. *Nature* **2001**, *412*, 166–169. [CrossRef]
38. Smidstrup, S.; Markussen, T.; Vancraeyveld, P.; Wellendorff, J.; Schneider, J.; Gunst, T.; Verstichel, B.; Stradi, D.; Khomyakov, P.A.; Vej-Hansen, U.G.; et al. QuantumATK: an integrated platform of electronic and atomic-scale modelling tools. *J. Phys. Condens. Matter* **2019**, *32*, 015901. [CrossRef] [PubMed]
39. Brandbyge, M.; Kobayashi, N.; Tsukada, M. Conduction channels at finite bias in single-atom gold contacts. *Phys. Rev. B* **1999**, *60*, 17064–17070. [CrossRef]
40. Taylor, J.; Guo, H.; Wang, J. Ab initio modeling of open systems: Charge transfer, electron conduction, and molecular switching of a C<sub>60</sub> device. *Phys. Rev. B* **2001**, *63*, 121104. [CrossRef]
41. Brandbyge, M.; Mozos, J.L.; Ordejón, P.; Taylor, J.; Stokbro, K. Density-functional method for nonequilibrium electron transport. *Phys. Rev. B* **2002**, *65*, 165401. [CrossRef]
42. Kaasbjerg, K.; Flensberg, K. Strong Polarization-Induced Reduction of Addition Energies in Single-Molecule Nanojunctions. *Nano Lett.* **2008**, *8*, 3809–3814. [CrossRef]
43. Perdew, J.P.; Burke, K.; Ernzerhof, M. Generalized Gradient Approximation Made Simple. *Phys. Rev. Lett.* **1996**, *77*, 3865–3868. [CrossRef]
44. Ray, S.J. Single atom impurity in a single molecular transistor. *J. Appl. Phys.* **2014**, *116*, 154302. [CrossRef]
45. Guo, Y.D.; Yan, X.H.; Xiao, Y. Computational Investigation of DNA Detection Using Single-Electron Transistor-Based Nanopore. *J. Phys. Chem. C* **2012**, *116*, 21609–21614. [CrossRef]

46. Zhang, Y.; Heath, G.; Carpenter, A.; Fisher, N. Air pollutant emissions inventory of large-scale production of selected biofuels feedstocks in 2022. *Biofuels Bioprod. Biorefining* **2016**, *10*, 56–69. [CrossRef]
47. Aaroe, W.H.; Light, E. Indoor air pollution. *Science* **1984**, *223*, 6. [CrossRef]
48. Zharinov, V.S.; Picot, T.; Scheerder, J.E.; Janssens, E.; Van de Vondel, J. Room temperature single electron transistor based on a size-selected aluminium cluster. *Nanoscale* **2020**, *12*, 1164–1170. [CrossRef] [PubMed]





*[Handwritten signature]*

与原件相符

# Dissipative dynamics in a tunable Rabi dimer with periodic harmonic driving

Cite as: J. Chem. Phys. **150**, 184116 (2019); <https://doi.org/10.1063/1.5096071>

Submitted: 14 March 2019 . Accepted: 24 April 2019 . Published Online: 14 May 2019

Zhongkai Huang, Fulu Zheng, Yuyu Zhang, Yadong Wei , and Yang Zhao



View Online



Export Citation



CrossMark

## ARTICLES YOU MAY BE INTERESTED IN

Dynamics in reactions on metal surfaces: A theoretical perspective

The Journal of Chemical Physics **150**, 180901 (2019); <https://doi.org/10.1063/1.5096869>

Quantum-classical path integral with a harmonic treatment of the back-reaction

The Journal of Chemical Physics **150**, 184102 (2019); <https://doi.org/10.1063/1.5091725>

Removing instabilities in the hierarchical equations of motion: Exact and approximate projection approaches

The Journal of Chemical Physics **150**, 184109 (2019); <https://doi.org/10.1063/1.5092616>

The Journal  
of Chemical Physics

Submit Today

The Emerging Investigators Special Collection and Awards  
Recognizing the excellent work of early career researchers!



# Dissipative dynamics in a tunable Rabi dimer with periodic harmonic driving

Cite as: J. Chem. Phys. 150, 184116 (2019); doi: 10.1063/1.5096071

Submitted: 14 March 2019 • Accepted: 24 April 2019 •

Published Online: 14 May 2019



View Online



Export Citation



CrossMark

Zhongkai Huang,<sup>1,2,a)</sup> Fulu Zheng,<sup>1,3,a)</sup> Yuyu Zhang,<sup>4</sup> Yadong Wei,<sup>3</sup> and Yang Zhao<sup>1,b)</sup>

## AFFILIATIONS

<sup>1</sup>Division of Materials Science, Nanyang Technological University, Singapore 639798, Singapore

<sup>2</sup>College of Materials Science and Engineering, Yangtze Normal University, Chongqing 408100, China

<sup>3</sup>School of Physics and Energy, Shenzhen University, Shenzhen 518060, China

<sup>4</sup>Department of Physics, Chongqing University, Chongqing 404100, China

**Note:** This paper is part of a JCP Special Topic on Dynamics of Open Quantum Systems.

<sup>a)</sup>Z. Huang and F. Zheng contributed equally to this work.

<sup>b)</sup>Electronic mail: YZhao@ntu.edu.sg

## ABSTRACT

Recent progress on qubit manipulation allows application of periodic driving signals on qubits. In this study, a harmonic driving field is added to a Rabi dimer to engineer photon and qubit dynamics in a circuit quantum electrodynamics device. To model environmental effects, qubits in the Rabi dimer are coupled to a phonon bath with a sub-Ohmic spectral density. A nonperturbative treatment, the Dirac-Frenkel time-dependent variational principle together with the multiple Davydov  $D_2$  ansatz, is employed to explore the dynamical behavior of the tunable Rabi dimer. In the absence of the phonon bath, the amplitude damping of the photon number oscillation is greatly suppressed by the driving field, and photons can be created, thanks to the resonance between the periodic driving field and the photon frequency. In the presence of the phonon bath, one can still change the photon numbers in two resonators and indirectly alter the photon imbalance in the Rabi dimer by directly varying the driving signal in one qubit. It is shown that qubit states can be manipulated directly by the harmonic driving. The environment is found to strengthen the interqubit asymmetry induced by the external driving, opening up a new venue to engineer the qubit states.

Published under license by AIP Publishing. <https://doi.org/10.1063/1.5096071>

## I. INTRODUCTION

Originally proposed to study the effect of a weak, rapidly rotating magnetic field on an atom possessing a nuclear spin,<sup>1,2</sup> the Rabi model represents the simplest interaction between a two-level atom and a light field and continues to inspire exciting developments in both mathematics and physics.<sup>3</sup> Since the two-level system in the Rabi model and its variants can describe qubits, the Rabi model has a considerable impact on practical applications in quantum computation and information science.<sup>4</sup> Recently, the Rabi model has been used to describe various quantum systems, such as microwave and optical-cavity quantum electrodynamics (QED),<sup>5</sup> ion traps,<sup>6</sup> quantum dots,<sup>7</sup> and superconducting qubits in circuit QED.<sup>8</sup>

Such systems are interesting both for fundamental study of quantum phenomena, such as Landau-Zener transitions,<sup>9,10</sup> on the mesoscopic scale, as well as for promising design of future electronic

devices. Multiphoton transitions have been proposed and realized in Josephson-junction qubits.<sup>11</sup> For example, Temchenko *et al.* studied the transition between two flux qubits that are biased by independent constant magnetic fluxes and coupled to each other as well as to an unavoidable dissipative environment.<sup>12</sup> Zheng *et al.* reported new results on dynamical photon localization and delocalization in a Rabi dimer model with a dissipative bath.<sup>13</sup>

In particular, advances in QED devices and quantum dots make them promising candidates for the exploration of a tunable Rabi model due to their potential scalability and tunable parameters over a broad range.<sup>7,14–17</sup> One way is to apply an external driving field to the cavity,<sup>18,19</sup> and the other is to impose the driving force on the qubit.<sup>11,15,20</sup> It is more common to tune the energy spacing of the qubit by changing the magnetic flux in the superconducting quantum interference device qubits,<sup>21</sup> or by applying an external magnetic field on a spin qubit in a Si/SiGe quantum dot.<sup>7</sup>



Dynamics of the tunable qubits is inevitably influenced by their environments. Environmentally induced fluctuations in the qubit energies are such an example. The qubit-environment coupling has been demonstrated to exist in various experiments, such as in a superconducting charge qubit coupled to an on-chip microwave resonator in the strong coupling regime,<sup>20</sup> in a circuit QED device with seven qubits,<sup>22</sup> and in a circuit QED implementation with a time-dependent transverse magnetic field.<sup>23</sup> QED devices typically work at extremely low temperatures. Dominant noise sources could be modeled by sub-Ohmic spectral densities or  $1/f$  low-frequency noises.<sup>24</sup> For example, Egger and Wilhelm have shown that a sub-Ohmic type spectral density can characterize the qubit-bath coupling in a multimode circuit QED setup with hybrid metamaterial transmission lines.<sup>25</sup> However, the effects of qubit-phonon coupling on qubit dynamics have not been sufficiently investigated. Recently, the multiple Davydov  $D_2$  ansatz has been developed to accurately treat dynamics of the generalized Holstein model with simultaneous diagonal and off-diagonal system-bath coupling.<sup>26,27</sup> Influences of qubit-phonon coupling have also been probed in the dissipative Landau-Zener model using our variational approach.<sup>28</sup>

In a previous study,<sup>13</sup> photon delocalization in a Rabi dimer has been studied by employing the multiple Davydov trial states. The external control of the qubit population can be realized in the same experimental setup to engineer photon delocalization in the Rabi dimer by applying two independent magnetic fields on the two qubits. It is, thus, necessary to extend the successful method to study the dynamics of the tunable Rabi dimer in a dissipative bath.<sup>20,29–31</sup> With respect to the dynamics of the tunable Rabi dimer, qubit polarization and photon dynamics affected by qubit-photon and qubit-phonon interactions have not received adequate attention. Here, we continue our endeavor with an accurate treatment of the many-body quantum dynamics in a tunable Rabi dimer.

In this work, we apply periodic harmonic driving to a qubit of the Rabi dimer and explore its effects on the qubit polarizations. We investigate the impacts of qubit-photon coupling and qubit-phonon coupling on the photon dynamics in the tunable Rabi dimer using the multi- $D_2$  ansatz with the Dirac-Frenkel variational principle. Good convergence has been obtained using the employed method, justifying the validity of our method.

The remainder of this paper is structured as follows: In Sec. II, we present the Hamiltonian and our trial wave function, the multi- $D_2$  ansatz. In Sec. III, using the Dirac-Frenkel time-dependent variational principle, we proceed to study quantum dynamics of the composite system when one qubit of the Rabi dimer is under harmonic driving and the energy splitting of the other qubit is kept constant. Environmental effects are examined by coupling the qubits to a sub-Ohmic phonon bath. Photon dynamics in the left and right resonators is discussed in Sec. III A, and qubit dynamics is investigated in Sec. III B. Conclusions are drawn in Sec. IV.

## II. METHODOLOGY

### A. Hamiltonian of the hybrid system

As illustrated in Ref. 13, we model a Rabi dimer composed of two coupled transmission line resonators with each interacting with a qubit. The environmental effects on the device result from the

coupling of the qubits to multimode micromechanical resonators, which are described by a collection of harmonic oscillators. By controlling the magnetic flux through the qubits in the dimer, harmonic driving can be applied onto the qubits, as shown in Fig. 1. The Hamiltonian for the hybrid system can be written as follows:

$$H = H_{RD} + H_B + H_{BQ}. \quad (1)$$

The Rabi dimer can be described by the following Hamiltonian ( $\hbar = 1$ ):

$$H_{RD} = H_L^{\text{Rabi}} + H_R^{\text{Rabi}} - J(a_L^\dagger a_R + a_R^\dagger a_L), \quad (2)$$

where  $J$  is the photon tunneling amplitude. The energy spacings of left and right qubits are constants in Ref. 13, and here, we make them tunable. To be specific, an external driving field can be independently imposed on each of the two qubits. The left (L) and right (R) Rabi Hamiltonians  $H_{i=L/R}^{\text{Rabi}}$  are given by<sup>1,2,30,31</sup>

$$H_{i=L/R}^{\text{Rabi}} = \frac{A_i}{2} \cos(\Omega_i t + \Phi_i) \sigma_z^i + \omega_i a_i^\dagger a_i - g_i (a_i^\dagger + a_i) \sigma_x^i,$$

where  $\frac{A_i}{2} \cos(\Omega_i t + \Phi_i)$  serves as the periodic harmonic driving field on the  $i$ th qubit and imply tunable energy spacing of the qubit.  $\Phi_L = \Phi_R = 0$  is set to simplify the simulations.  $\omega_i$  is the frequency of the photon mode in the  $i$ th Rabi system.  $\sigma_x^i$  and  $\sigma_z^i$  are the usual Pauli matrices, and  $a_i$  ( $a_i^\dagger$ ) is the annihilation (creation) operator of the  $i$ th photon mode.  $g_i$  characterizes the coupling strength between the qubits and the photons. We assume that the frequencies of the photon modes and the qubit-photon coupling strengths are identical in the tunable dimer, i.e.,  $\omega_L = \omega_R = \omega_0$ , and  $g_L = g_R = g$ .

To study the dynamics of the tunable Rabi dimer in the presence of an environment, we model a phonon bath of  $N$  quantum harmonic oscillators by the Hamiltonian  $H_B$  and the qubit-phonon coupling by the Hamiltonian  $H_{BQ}$ ,

$$H_B = \sum_{k=1}^N \omega_k b_k^\dagger b_k \quad (3)$$

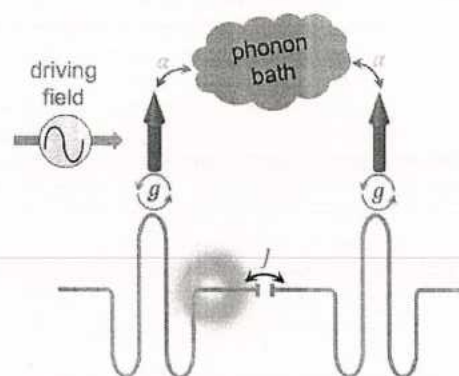


FIG. 1. Sketch of a tunable circuit QED system studied in this work. Photons hop between two transmission line resonators with a tunneling rate of  $J$ . An external periodic driving field is applied to the left qubit. Left (right) qubit is coupled to the photon mode in the left (right) resonator with a coupling strength of  $g$ . Two qubits interact with a sub-Ohmic phonon bath with a strength of  $\alpha$ .



and

$$H_{\text{BQ}} = \sum_{k=1}^N \phi_k (b_k^\dagger + b_k) (\sigma_z^L + \sigma_z^R), \quad (4)$$

where  $b_k$  ( $b_k^\dagger$ ) is the annihilation (creation) operator of the  $k$ th bath mode with frequency  $\omega_k$ , and  $\phi_k$  is the coupling strength between the  $k$ th mode and the qubits. The qubit-bath coupling is characterized by a spectral density function,

$$J(\omega) = \sum_k \phi_k^2 \delta(\omega - \omega_k) = 2\alpha\omega_c^{1-s} \omega^s e^{-\omega/\omega_c}, \quad (5)$$

with  $\omega_c$  being the cut-off frequency and the dimensionless parameter  $\alpha$  quantifying the qubit-bath coupling strength.<sup>32</sup> Since the focus of this work is the application of an external field on the Rabi dimer, we use a weak photon tunneling strength  $J$ , producing energy levels with small gaps in the spectrum of the Rabi dimer. Low frequency bath modes are crucially important to the dynamics, as these modes may be at resonance with some transitions in the Rabi dimer. Therefore, a sub-Ohmic bath spectral density with  $s = 0.5$  is chosen in this work. The logarithmic discretization procedure is adopted to parameterize the low frequency bath modes with balanced numerical accuracy and efficiency.<sup>32</sup> The cut-off frequency for the bath modes is set to  $\omega_c = \omega_0$ , and the maximum frequency used in the discretization is  $\omega_{\text{max}} = 20 \omega_c$ .

If the energies corresponding to frequencies of the photon and phonon modes are high in comparison with the thermal energy  $k_B T$ , the oscillators are thermally inactive, and thus, the dynamics influenced by the bath modes is temperature independent in a wide temperature range.<sup>8,20</sup> QED devices typically work at extremely low temperatures. Therefore,  $T = 0$  is adopted in the current study. It is straightforward to include the temperature effects in this methodology by applying Monte Carlo importance sampling.<sup>37</sup> Simulations at finite temperatures require relatively more computational resources and will be performed in future studies.

## B. The multi- $D_2$ ansatz

The multiple Davydov  $D_2$  ansatz with multiplicity  $M$  are essentially  $M$  copies of the single Davydov  $D_2$  ansatz.<sup>33,34</sup> It is also known as the multi- $D_2$  ansatz and has been employed to study the static and dynamic properties of various systems, producing excellent numerical efficiency and accuracy in a broad parameter regime in the presence of both the diagonal and off-diagonal system-bath coupling.<sup>13,26–28,35–40</sup> In this work, the multi- $D_2$  ansatz is employed to treat accurately both the off-diagonal qubit-photon coupling and the diagonal qubit-phonon coupling in Eq. (1) and can be constructed as

$$|D_2^M(t)\rangle = \sum_{n=1}^M [A_n(t)|\uparrow\uparrow\rangle + B_n(t)|\uparrow\downarrow\rangle + C_n(t)|\downarrow\downarrow\rangle + D_n(t)|\downarrow\uparrow\rangle] \otimes |\mu_n\rangle_L |\nu_n\rangle_R |\eta_n\rangle_B, \quad (6)$$

where  $|\uparrow\downarrow\rangle = |\uparrow\rangle_L \otimes |\downarrow\rangle_R$  with  $\uparrow$  ( $\downarrow$ ) indicating the up (down) state of the qubits.  $|\mu_n\rangle_L$  and  $|\nu_n\rangle_R$  are coherent states of the photon modes

$$|\mu_n\rangle_L = \exp[\mu_n(t)a_L^\dagger - \mu_n^*(t)a_L]|0\rangle_L, \quad (7)$$

$$|\nu_n\rangle_R = \exp[\nu_n(t)a_R^\dagger - \nu_n^*(t)a_R]|0\rangle_R, \quad (8)$$

where  $|0\rangle_{L(R)}$  is the photon vacuum state of the left (right) resonator.  $|\eta_n\rangle_B$  is the coherent state of the phonon bath

$$|\eta_n\rangle_B = \exp\left[\sum_k \eta_{nk}(t)b_k^\dagger - \eta_{nk}^*(t)b_k\right]|0\rangle_B, \quad (9)$$

with  $|0\rangle_B$  being the vacuum state of the phonon bath. In Eq. (6),  $A_n(t)$ ,  $B_n(t)$ ,  $C_n(t)$ ,  $D_n(t)$ ,  $\mu_n(t)$ ,  $\nu_n(t)$ , and  $\eta_{nk}(t)$  are time-dependent variational parameters to be determined via the time-dependent variational principle.  $A_n$  is the probability amplitude in the state  $|\uparrow\uparrow\rangle |\mu_n\rangle_L |\nu_n\rangle_R |\eta_n\rangle_B$ ,  $\mu_n$  ( $\nu_n$ ) is the displacement of the left (right) photon mode, and  $\eta_{nk}$  is the displacement of the  $k$ th bath mode.

## C. The time-dependent variational principle

Equations of motion for the variational parameters are derived by adopting the Dirac-Frenkel time-dependent variational principle,

$$\frac{d}{dt} \left( \frac{\partial L}{\partial \dot{\alpha}_n} \right) - \frac{\partial L}{\partial \alpha_n} = 0, \quad (10)$$

where  $\alpha_n$  are the variational parameters, i.e.,  $A_n(t)$ ,  $B_n(t)$ ,  $C_n(t)$ ,  $D_n(t)$ ,  $\mu_n(t)$ ,  $\nu_n(t)$ , and  $\eta_{nk}(t)$ . The Lagrangian  $L$  is given by

$$L = \frac{i}{2} \langle D_2^M(t) | \frac{\partial}{\partial t} - \frac{\partial}{\partial t} | D_2^M(t) \rangle - \langle D_2^M(t) | H | D_2^M(t) \rangle. \quad (11)$$

Details of the derivations can be found in the Appendix.

## D. Observables

Employing the Dirac-Frenkel time-dependent variational principle with the multi- $D_2$  ansatz, we investigate the bath induced dynamics of a Rabi dimer with specific contributions from individual bath modes presented explicitly. The time evolution of photon numbers in two resonators is given by

$$\begin{aligned} N_L(t) &= \langle D_2^M(t) | a_L^\dagger a_L | D_2^M(t) \rangle \\ &= \sum_{l,n}^M [A_l^*(t)A_n(t) + B_l^*(t)B_n(t) + C_l^*(t)C_n(t) \\ &\quad + D_l^*(t)D_n(t)] \mu_l^*(t)\mu_n(t) S_{ln}(t), \end{aligned} \quad (12)$$

$$\begin{aligned} N_R(t) &= \langle D_2^M(t) | a_R^\dagger a_R | D_2^M(t) \rangle \\ &= \sum_{l,n}^M [A_l^*(t)A_n(t) + B_l^*(t)B_n(t) + C_l^*(t)C_n(t) \\ &\quad + D_l^*(t)D_n(t)] \nu_l^*(t)\nu_n(t) S_{ln}(t), \end{aligned} \quad (13)$$

where  $S_{ln}(t)$  is the Debye-Waller factor,

$$\begin{aligned} S_{ln} &= \exp\left[\mu_l^*(t)\mu_n(t) - \frac{1}{2}|\mu_l(t)|^2 - \frac{1}{2}|\mu_n(t)|^2\right] \\ &\quad \cdot \exp\left[\nu_l^*(t)\nu_n(t) - \frac{1}{2}|\nu_l(t)|^2 - \frac{1}{2}|\nu_n(t)|^2\right] \\ &\quad \cdot \exp\left[\sum_k \left(\eta_{lk}^*(t)\eta_{nk}(t) - \frac{1}{2}|\eta_{lk}(t)|^2 - \frac{1}{2}|\eta_{nk}(t)|^2\right)\right]. \end{aligned} \quad (14)$$



The time evolution of the photon imbalance is  $Z(t) = N_L(t) - N_R(t)$  and that of the total photon number is  $N(t) = N_L(t) + N_R(t)$ . These quantities are used to characterize photon localization and delocalization.

In addition to photon dynamics, the time evolution of the qubit states is recorded during the simulations by measuring the time evolution of the qubit polarization via

$$\begin{aligned} \langle \sigma_z^L(t) \rangle &= \langle D_2^M(t) | \sigma_z^L | D_2^M(t) \rangle \\ &= \sum_{l,n}^M \left[ A_l^*(t) A_n(t) + B_l^*(t) B_n(t) \right. \\ &\quad \left. - C_l^*(t) C_n(t) - D_l^*(t) D_n(t) \right] S_{ln}(t), \end{aligned} \quad (15)$$

$$\begin{aligned} \langle \sigma_z^R(t) \rangle &= \langle D_2^M(t) | \sigma_z^R | D_2^M(t) \rangle \\ &= \sum_{l,n}^M \left[ A_l^*(t) A_n(t) - B_l^*(t) B_n(t) \right. \\ &\quad \left. + C_l^*(t) C_n(t) - D_l^*(t) D_n(t) \right] S_{ln}(t). \end{aligned} \quad (16)$$

As given in Hamiltonian (1), the qubits serve as a bridge to connect the photon and the phonon modes, transferring bath-induced impacts to the photons. Combining influences from the photons and the bath, our calculated qubit dynamics reflects the complex interactions between the photon modes and the phonon bath.

Thanks to the methodology adopted here, the temporal evolution of the phonon bath can also be obtained explicitly. To reveal the participation of individual phonon modes in the Rabi dimer dynamics, we calculate the population on the  $k$ th mode as follows:

$$\begin{aligned} N_k^B(t) &= \langle D_2^M(t) | b_k^\dagger b_k | D_2^M(t) \rangle \\ &= \sum_{l,n}^M \left[ A_l^*(t) A_n(t) + B_l^*(t) B_n(t) + C_l^*(t) C_n(t) \right. \\ &\quad \left. + D_l^*(t) D_n(t) \right] \eta_{lk}^*(t) \eta_{nk}(t) S_{ln}(t). \end{aligned} \quad (17)$$

Through interacting with the qubits, the phonon bath gradually gains sufficient energy from the Rabi dimer to affect the dynamics of the photons and the qubits. In return, the influences of the QED system on the bath modes can be investigated by calculating the populations dynamics  $N_k^B(t)$ .

### III. RESULTS AND DISCUSSION

Used as comparison is a case where the qubits and the photons are at resonance in the absence of a driving field. The parameter set chosen is  $A_L/\omega_0 = A_R/\omega_0 = 1$ ,  $\Omega_L = \Omega_R = 0$ , and  $\Phi_L = \Phi_R = 0$ . In the absence of a phonon bath and a driving field, the photon dynamics is determined by the cooperation between  $J$  and  $g$ . A relatively weak photon tunneling rate  $J = 0.05\omega_0$  is adopted here, and the quadrature-quadrature coupling between the two photon modes is neglected.<sup>41,42</sup> According to recent experiment,<sup>43</sup> ultrastrong qubit-photon coupling (USC) is preferred; thus, the qubit-photon coupling strength is set to  $g = 0.3\omega_0$ . The combined effects of  $J$  and  $g$  used here lead to photon delocalization over two resonators in a bare Rabi dimer.<sup>44</sup> We choose a qubit-bath coupling strength of  $\alpha = 0.1$  to model the phonon effect. A two-qubit gate has been studied by

Hänggi *et al.*, and an ac field was acted upon one of the qubits to induce a time-dependent level splitting.<sup>45</sup> Here, a harmonic driving field is applied to the left qubit without loss of generality. Similar to previous experimental and theoretical work,<sup>13,43</sup> a fully localized photon state is prepared by pumping  $N(0) = 20$  photons into the left resonator while keeping the right one in a photon vacuum with  $\mu_1(t=0) = \sqrt{20}$  and  $\mu_{n \neq 1}(t=0) = \nu_n(t=0) = 0$ . The qubits in the two resonators start to evolve from their down states with  $A_n(t=0) = B_n(t=0) = C_n(t=0) = D_n(t=0) = 0$  and  $D_1(t=0) = 1$ . The phonon bath is initially in a vacuum state with  $\eta_{nk}(t=0) = 0$ . The validity of our approach has been extensively tested in the previous work, and calculations are performed with a sufficiently large multiplicity  $M$  in this work. The multiplicity  $M = 8$  and number of phonon modes  $N_{\text{bath}} = 0$  are set for cases of  $\alpha = 0$ , while  $M = 6$  and  $N_{\text{bath}} = 60$  is used for cases of  $\alpha = 0.1$ . The reader is referred to Ref. 13 for details of the validity study.

As the driving force is exerted on the left qubit, the site energy on the qubit can be directly controlled by following parameters: the driving field strength  $A_L$ , the harmonic driving frequency  $\Omega_L$ , and the ratio between them  $R = A_L/\Omega_L$ . The effect of the driving field will be transferred to the left photon mode via the qubit-photon coupling  $g$ . In the proposed QED device shown in Fig. 1, the photons initially created will hop between two resonators with a tunneling rate of  $J$ .

#### A. Photon dynamics

We first study the photon dynamics in the composite system. Shown in Fig. 2 are the time-dependent photon numbers in two resonators in the absence of the phonon bath. The photons hop between the resonators due to the interresonator tunneling rate  $J$ . For the case without a driving field and a phonon bath, as shown in Fig. 2(a), the photon number in an individual resonator approaches half of the initial total photon number, indicating photon delocalization with quasiequilibration in two resonators at long times.<sup>13</sup> Due to the qubit-photon coupling, the oscillation amplitude decays as time evolves. The decrease in the oscillation amplitude can be seen as a purity loss in one Rabi model or the decoherence in the Rabi dimer.<sup>45</sup> Upon applying a harmonic driving field to the left qubit, the external field provides energy to the Rabi dimer and the oscillation amplitude damping of the photon numbers is suppressed, as displayed in Figs. 2(b)–2(d). Hänggi *et al.* discovered that the decoherence in the two-qubit system at low temperatures can be significantly slowed due to the application of the harmonic driving, and the purity loss depends on the ratio  $R$  between the driving field strength  $A_L$  and the driving frequency  $\Omega_L$ .<sup>45</sup> As expected, Figs. 2(b)–2(d) show that the decay of the oscillation amplitude of the photon number is decelerated by an increasing ratio  $R$  with the fixed driving field strength  $A_L = \omega_0$ .

Upon turning on the qubit-bath coupling, the photon numbers in two resonators deviate dramatically from those without a phonon bath, as shown in Figs. 2 and 3. In the absence of the driving field, the oscillation amplitude of the photon numbers in Fig. 3(a) drops faster than those in Fig. 2(a), since the phonon bath absorbs the energy from the qubit via the qubit-bath coupling, leaving few photons active in the resonators at long times. Our results are in agreement with the conclusion that the environmental noise may lead to strong purity loss in a Rabi model.<sup>45</sup> The field applied in



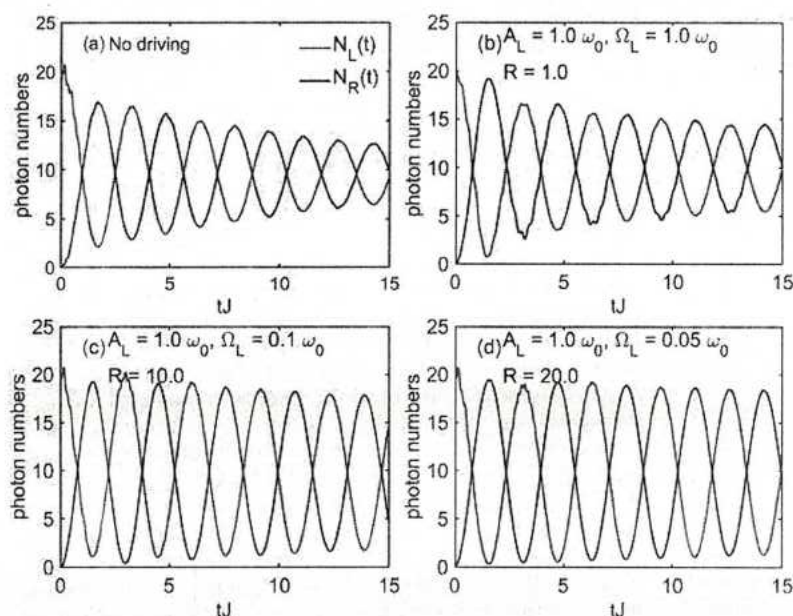


FIG. 2. Time evolution of the photon numbers in the left  $[N_L(t)]$  and right  $[N_R(t)]$  resonators without phonon bath ( $\alpha = 0$ ). Various fields are applied to the left qubit: (a)  $A_L = A_R = \omega_0$ ,  $\Omega_L = \Omega_R = 0$ , (b)  $A_L = \omega_0$  and  $\Omega_L = \omega_0$ , (c)  $A_L = \omega_0$  and  $\Omega_L = 0.1 \omega_0$ , and (d)  $A_L = \omega_0$  and  $\Omega_L = 0.05 \omega_0$ . There is no field on the right qubit ( $A_R = 0$ ) in (b)–(d).

Fig. 3(b) is the same as that for Fig. 2(b). It is found that a driving field with strength  $A_L = \omega_0$  is incapable of keeping the photons active and cannot significantly offset the photon dynamics.

In order to offset the dissipative effects from the phonon bath, the driving field strength is increased to a larger value of  $A_L = 10 \omega_0$ , and the ratio  $R = A_L/\Omega_L$  varies from 10 to 200, as shown in Fig. 4. The phononic effects on the photon dynamics under a strong field are much weaker than those under a weak field. As shown in Fig. 4, a larger ratio  $R$  implies a lower harmonic driving frequency, and the oscillation amplitude of the photon numbers generally decay faster as  $R$  increases in the presence of the phonon bath. In contrast, the decay of the oscillation amplitude becomes slower as  $R$  grows larger when the phonon bath is absent, as shown in Fig. 2. This is because the photon bath has only one mode with the frequency of  $\omega_0$ , while the phonon bath includes more low-frequency modes. The sub-Ohmic phonon bath has strong dissipative effects on the photon dynamics for low-frequency driving. Detailed phononic effects on the photon numbers can be better understood by the corresponding population dynamics of the

bath modes, as shown in Fig. 9. It is found that a strong driving field can significantly suppress the decay of the oscillation amplitude of the photon numbers even in the presence of the phonon bath.

Next, we study the time evolution of the photon imbalance in the presence of the qubit-bath coupling of  $\alpha = 0.1$ . As shown in Fig. 5, the oscillation amplitude for the no driving case decreases to 2 around  $t/J = 14$ . In comparison, slower decay is presented as the driving field strength increases with a harmonic driving frequency of  $\Omega_L = 0.5 \omega_0$ . This is because the oscillation amplitude of the photon number evolution decreases more gradually when the ratio of the field-strength and frequency is raised. Varying the driving field strength is similar to tuning the qubit-photon coupling strength and the tunneling rate, leading to a more delocalized photon state.<sup>47</sup> As extensively studied by Savel'ev *et al.*, manipulation of one qubit can be realized by applying an ac signal to an adjacent qubit coupled with it via interqubit interaction.<sup>46,48–50</sup> We have a more sophisticated system with two photon modes and one phonon bath, but we still can indirectly alter the photon imbalance between the two

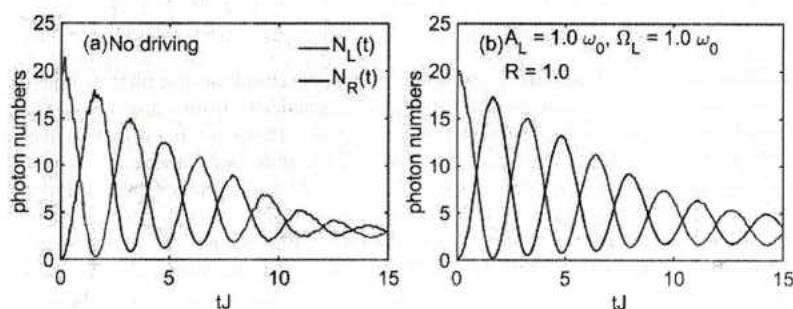


FIG. 3. Time evolution of the photon numbers in the left  $[N_L(t)]$  and right  $[N_R(t)]$  resonators with phonon bath ( $\alpha = 0.1$ ). Following fields are added to the left qubit: (a)  $A_L = A_R = \omega_0$ ,  $\Omega_L = \Omega_R = 0$ ; (b)  $A_L = \omega_0$ ,  $A_R = 0$ , and  $\Omega_L = \omega_0$ . The multiplicity  $M$  and the number of phonon modes  $N_{\text{bath}}$  used in the related calculations are  $M = 6$  and  $N_{\text{bath}} = 60$ .



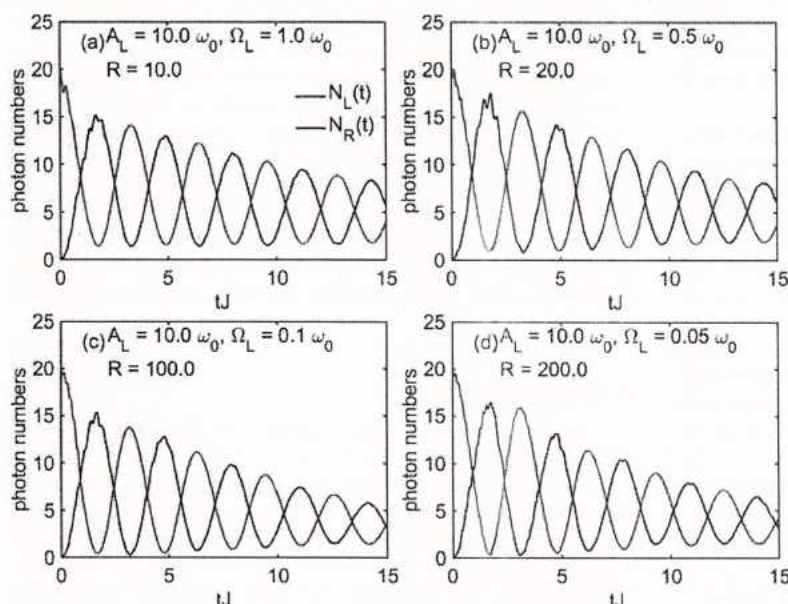


FIG. 4. Time evolution of the photon numbers in the left  $[N_L(t)]$  and right  $[N_R(t)]$  resonators with phonon bath ( $\alpha = 0.1$ ). Following fields are added to the left qubit: (a)  $A_L = 10.0 \omega_0$  and  $\Omega_L = \omega_0$ ; (b)  $A_L = 10.0 \omega_0$  and  $\Omega_L = 0.5 \omega_0$ ; (c)  $A_L = 10.0 \omega_0$  and  $\Omega_L = 0.1 \omega_0$ ; and (d)  $A_L = 10.0 \omega_0$  and  $\Omega_L = 0.05 \omega_0$ . There is no field on the right qubit ( $A_R = 0$ ). The multiplicity  $M$  and the number of phonon modes  $N_{\text{bath}}$  used for the figure are  $M = 6$  and  $N_{\text{bath}} = 60$ .

resonators by changing the driving signal in one qubit coupled to its related resonator. The photon dynamics in one resonator can be further controlled by manipulation of the driving field on the qubit coupled to the neighboring resonator. With a fixed qubit-phonon coupling strength, it is the competitive qubit-photon interaction

$g$  and interresonator photon tunneling  $J$  that determine the photon dynamics in a Rabi dimer. Hausinger and Grifoni have shown that the external driving field on the qubit can amplify the effects of qubit-photon coupling.<sup>47</sup> Therefore,  $J$  appears relatively weaker compared to the effective  $g$  as the driving field strength

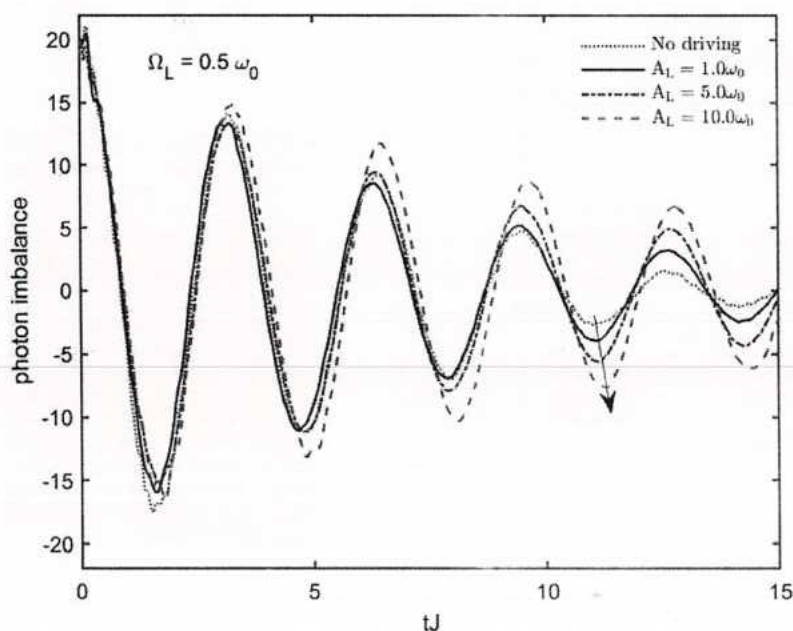


FIG. 5. Time evolution of the photon imbalance  $Z(t)$  with phonon bath ( $\alpha = 0.1$ ). Following fields are added to the left qubit:  $A_L = A_R = \omega_0$  and  $\Omega_L = \Omega_R = 0$  for the red dotted line,  $A_L = \omega_0$  for the black solid line,  $A_L = 5.0 \omega_0$  for the blue dashed-dotted line, and  $A_L = 10.0 \omega_0$  for the green dashed line. The driving field frequency is  $\Omega_L = 0.5 \omega_0$ . There is no field on the right qubit ( $A_R = 0$ ) for nonzero  $A_L$ . The arrow indicates changes in oscillation periods due to increasing driving field amplitudes. The multiplicity  $M$  and the number of phonon modes  $N_{\text{bath}}$  used in the corresponding simulations are  $M = 6$  and  $N_{\text{bath}} = 60$ .



is increased,<sup>44</sup> leading to longer period oscillations of the photon imbalance as shown in Fig. 5. This longer period for stronger  $A_L$  is detectable at long times as illustrated by the arrow at around  $tJ = 11.3$ .

We then explore the time evolution of the total photon number to study photon creation in the absence of the phonon bath, as shown in Figs. 6(a) and 6(b). Initially, the total photon number is 20, and all the photons are found in the left resonator. Without the external field, the photon number decreases at short times because the right photon mode is in its initial vacuum state. The high-frequency oscillations in the time evolution of the total photon number have the same frequency as the photons, which is much larger than the photon tunneling amplitude  $J = 0.05 \omega_0$ . At long times, though the qubit-photon coupling  $g = 0.3 \omega_0$  is strong enough to ensure photon delocalization over two resonators in a bare Rabi dimer, the photon numbers stay almost constant during interresonator tunneling, as presented by the red dotted line in Fig. 6(a). The application of various harmonic driving fields scarcely affects the total photon number if the driving field frequency  $\Omega_L$  is off-resonant with the photon frequency  $\omega_0$ . With a fixed photon frequency  $\omega_0$ , we can vary the frequency of the harmonic driving  $\Omega_L$ . If  $\Omega_L$  is in resonance or near resonance with  $\omega_0$ , the total photon number is found to increase with time, as shown in Fig. 6(b). Even in simple driving models with a single qubit, rich physics has sometimes been uncovered, thanks to the resonance between the periodic driving field and the energy splitting in the qubit systems.<sup>15,47,51,52</sup> In a strongly driven superconducting qubit, a fringe pattern can be found in the peaks of interqubit transition probability around multiphoton resonance positions.<sup>15,51</sup> Cao and Zheng studied a driven spin-boson model with the driving field frequency in resonance with the tunneling in the two level system and found a damped oscillation for weak driving and an undamped, large-amplitude coherent oscillation for

strong driving.<sup>52</sup> In our model, after the application of the harmonic driving of  $\Omega_L = \omega_0$  to the left qubit, the total photon number is kept larger than the initial total photon number due to the resonance between the periodic driving field and the photon frequency, as displayed in Fig. 6(b). In contrast, the addition of a phonon bath leads to the decrease in the total photon number, as shown in Figs. 6(c) and 6(d). Even in the presence of the phonon bath, the total photon number can be compensated by applying a driving field of a sufficiently large amplitude, comparing to that without the field. As indicated in Figs. 6(c) and 6(d), the total photon numbers can be more easily controlled using a resonant driving field than using an off-resonant one.

## B. Qubit dynamics

In addition to the photon dynamics, the time evolution of the qubit polarization can be monitored. As shown in Fig. 7, the qubit dynamics can be directly tuned by the external driving field. When the phonon bath is absent, the left qubit is controlled by the driving field, the photon mode, and the photon tunneling. Here, we choose a driving field with  $A_L = 10 \omega_0$  and  $\Omega_L = 0.1 \omega_0$ , and examine the influence of the field and the photon mode on the polarization of the left qubit. The qubit is initially in its down state. As time evolves, the mixing effects lead to segmented oscillations in the left qubit polarization, as displayed in Fig. 7(b). There are at least four types of energy contributions to the oscillation of the left qubit polarization: the energy of driving field with frequency  $\Omega_L$ , the photon energy with frequency  $\omega_0$ , the photon tunneling energy  $2J$ , and the splitting energy  $F(t) = A_L \cos(\Omega_L t)$  in the left qubit. It can be found that the driving field determines the pattern with the frequency of  $\Omega_L$ , by comparing Figs. 7(a) and 7(b). In the first plateau of Fig. 7(b), the left qubit polarization oscillates with small amplitudes and the

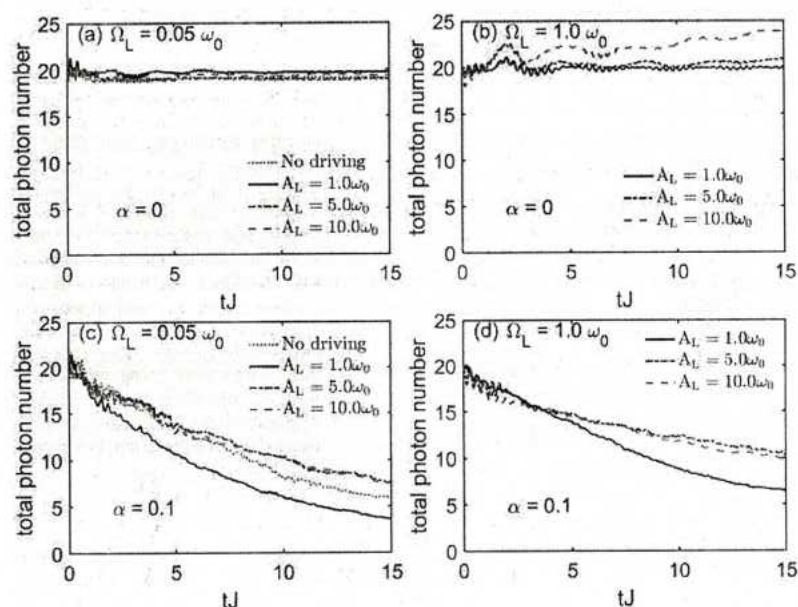


**FIG. 6.** Time evolution of total photon number. The qubit-bath coupling  $\alpha$  and the driving field frequency  $\Omega_L$  are (a)  $\alpha = 0$  and  $\Omega_L = 0.05 \omega_0$ ; (b)  $\alpha = 0$  and  $\Omega_L = 1.0 \omega_0$ ; (c)  $\alpha = 0.1$  and  $\Omega_L = 0.05 \omega_0$ ; and (d)  $\alpha = 0.1$  and  $\Omega_L = 1.0 \omega_0$ . In each subplot, the following fields are added to the left qubit:  $A_L = A_R = \omega_0$  and  $\Omega_L = \Omega_R = 0$  for the red dotted line,  $A_L = 1.0 \omega_0$  for the black solid line,  $A_L = 5.0 \omega_0$  for the blue dashed-dotted line, and  $A_L = 10.0 \omega_0$  for the green dashed line. There is no field on the right qubit ( $A_R = 0$ ) for nonzero  $A_L$ . The multiplicity  $M$  and the number of phonon modes  $N_{\text{bath}}$  used in the calculations are  $M = 8$  and  $N_{\text{bath}} = 0$  for (a) and (b) and  $M = 6$  and  $N_{\text{bath}} = 60$  for (c) and (d).



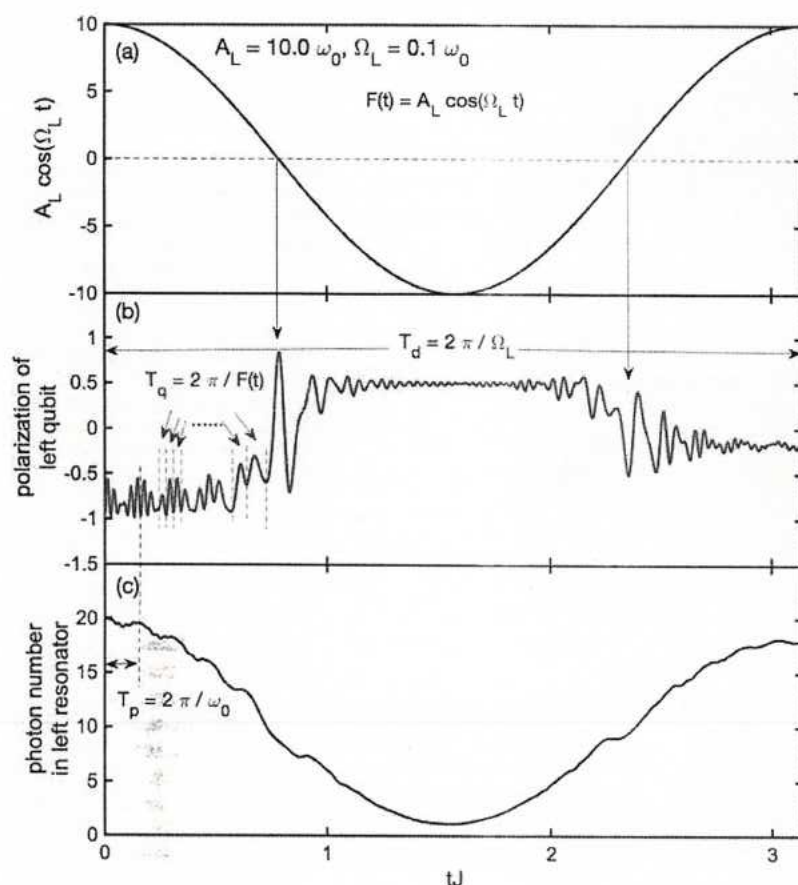


**FIG. 7.** (a) Harmonic driving field, (b) time evolution of the left qubit polarization  $\langle \sigma_z^L(t) \rangle$ , and (c) time evolution of the photon numbers in the left  $[N_L(t)]$  resonator.  $A_L = 10.0 \omega_0$  and  $\Omega_L = 0.1 \omega_0$ . There is no field on the right qubit ( $A_R = 0$ ). There is no phonon bath. The multiplicity used in the related calculations is  $M = 8$ .

time-dependent frequency of  $F(t)$ , as indicated by the red arrows. Once the energy difference between the up and down states of the left qubit approaches zero, the left qubit flips from the down (up) state to the up (down) state as denoted by the black down arrows, leading to the second (third) plateau in the overall trend. After flipping at  $tJ = \pi/4$ , the splitting  $F(t)$  becomes larger and prevents further flipping until  $F(t)$  is close to zero again at  $tJ = 3\pi/4$ . In each plateau, the qubit polarization oscillates with a small amplitude and a high frequency due to the combined effects of photon oscillations and the changing qubit splitting energy. This small amplitude can be understood as follows: The photons flow from the left (right) to the right (left) resonator, as shown in Fig. 7(c). Too few photons in the left resonator are available to affect the qubit polarization at around  $tJ = \pi/2$ , leading to small amplitude oscillations in the second plateau of the qubit polarization.

As shown Fig. 8, the external driving creates asymmetry between the left and right qubit polarization. In Figs. 8(a) and 8(b), there is no phonon bath, and the oscillation amplitude decrease in the absence of a phonon bath, the interqubit asymmetry (i.e., the difference between the blue and red curves) grows as the field strength is increased. The oscillation amplitude of the right qubit polarization (blue) vanishes at shorter times in Fig. 8(a) than that in

Fig. 8(b). Segmented oscillations (square-wave like patterns) appear in the left qubit polarization (red) and are strengthened as the field strength is increased. In Figs. 8(c) and 8(d), when the bath is present, the segmented oscillation shows a higher oscillation amplitude compared to its counterpart without a phonon bath. In particular, the qubit polarization shows a time periodicity of  $2\pi/\Omega_L$  under a strong driving field. In Figs. 8(c) and 8(d), the asymmetry between the left and right qubit polarization becomes more obvious, when the phonon bath is present. The phonon bath is diagonally coupled to the qubits and can be treated as a bias on the qubits. The bath can then trap the qubit in its up or down state, resulting in more pronounced asymmetry between the left and right qubits. It can also be understood as follows: Due to the driving field, it is more difficult for the left qubit to flip than the right qubit, as the left qubit flips only when  $F(t) = 0$ . The results of qubit polarization indicate that we can manipulate the qubit state directly by harmonic driving. Moreover, the asymmetry between the two qubits can be strengthened by the environmental phonons, leading to a new venue to engineer the qubit states.

In order to gauge the participation of individual phonon bath modes in the tunable Rabi dimer dynamics, we study population evolution of the bath modes. Thanks to our wave function based

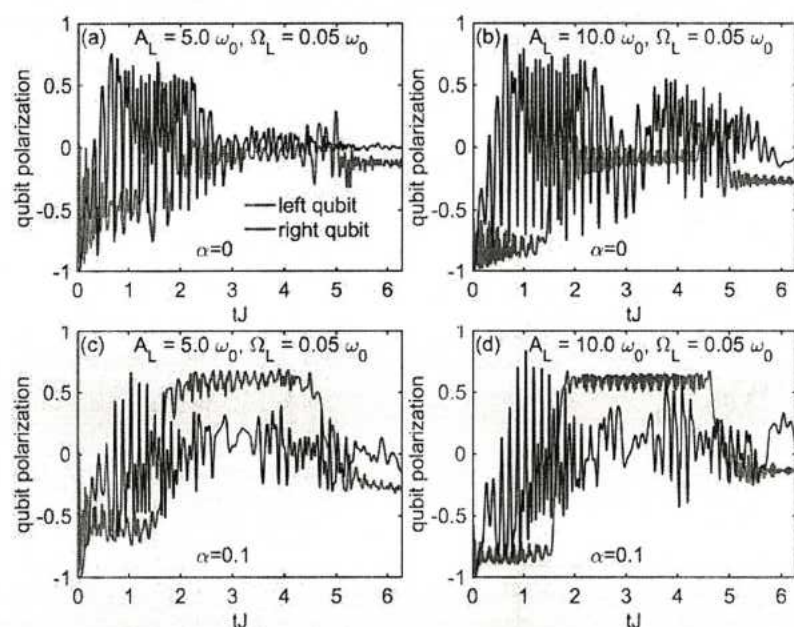


FIG. 8. Time evolution of the qubit polarization  $\langle \sigma_z^L(t) \rangle$  and  $\langle \sigma_z^R(t) \rangle$ . The qubit-bath coupling  $\alpha$  and the driving field parameters are (a)  $\alpha = 0$ ,  $A_L = 5.0 \omega_0$ , and  $\Omega_L = 0.05 \omega_0$ ; (b)  $\alpha = 0$ ,  $A_L = 10.0 \omega_0$ , and  $\Omega_L = 0.05 \omega_0$ ; (c)  $\alpha = 0.1$ ,  $A_L = 5.0 \omega_0$ , and  $\Omega_L = 0.05 \omega_0$ ; and (d)  $\alpha = 0.1$ ,  $A_L = 10.0 \omega_0$ , and  $\Omega_L = 0.05 \omega_0$ . There is no field on the right qubit ( $A_R = 0$ ). The multiplicity  $M$  and the number of phonon modes  $N_{\text{bath}}$  used in the calculations are  $M = 8$  and  $N_{\text{bath}} = 0$  for (a) and (b) and  $M = 6$  and  $N_{\text{bath}} = 60$  for (c) and (d).

method, detailed phonon dynamics is available to shed light on the interplay between the electronic and phononic degrees of freedom (DOFs). In contrast, the phononic DOFs are traced out when constructing the reduced density matrix in the density matrix based methods, and explicit information of the bath dynamics is lost.<sup>45,52</sup> Without the driving field, two qubits can freely flip and the total

photon number decreases continuously, exciting a large number of phonon modes via the qubit-phonon coupling.<sup>13</sup> After application of the harmonic driving, interesting physics can be obtained from detailed phonon dynamics. As shown in Fig. 9(a), the phonon bath is at its vacuum state at  $t = 0$ . At short times, there is an energy influx into the bath modes with frequencies near  $1.5 \omega_0$ .<sup>13</sup> After  $tJ = 2$ , there

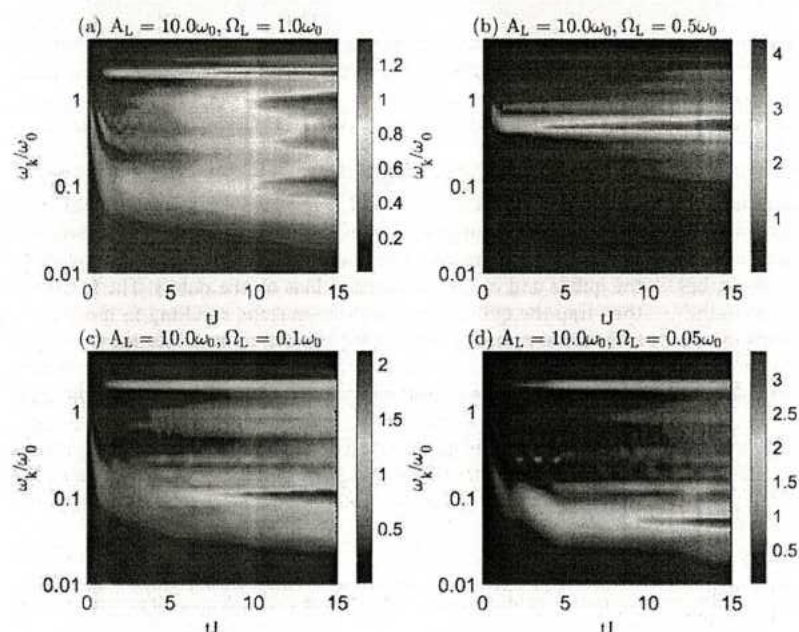


FIG. 9. Population dynamics of the bath modes. The following fields are added to the left qubit: (a)  $A_L = 10.0 \omega_0$  and  $\Omega_L = \omega_0$ ; (b)  $A_L = 10.0 \omega_0$  and  $\Omega_L = 0.5 \omega_0$ ; (c)  $A_L = 10.0 \omega_0$  and  $\Omega_L = 0.1 \omega_0$ ; and (d)  $A_L = 10.0 \omega_0$  and  $\Omega_L = 0.05 \omega_0$ . There is no field on the right qubit ( $A_R = 0$ ). The multiplicity  $M$  and the number of phonon modes  $N_{\text{bath}}$  used in the calculations are  $M = 6$  and  $N_{\text{bath}} = 60$ .



is an increase in the population of  $\omega_k = 2.0 \omega_0$ , which is attributed to the energy passed by the two qubits from their coupled photon modes with the frequency of  $\omega_0$  to the phonon modes. Since the left qubit flipping is determined by the driving field, the population of phonons that are in resonance with the driving field frequency  $\Omega_L = 1.0 \omega_0$  grows larger. Low-frequency phonons are gradually excited at long times because the sub-Ohmic phonon bath is featured at low-frequency regimes. As presented in Figs. 9(b)–9(d), the phonon modes in resonance with the periodic driving field frequency  $\Omega_L$  dominate the phonon dynamics, if  $\Omega_L$  is smaller than  $\omega_0$ . This is because the qubits are directly coupled to the phonon bath, and the left qubit continuously receives external energy from the strong field  $A_L = 10\omega_0$  and switches its orientation at a low frequency  $\Omega_L < \omega_0$ . In Fig. 9(b), phonon dynamics is dominated by active phonons with frequencies around  $0.5 \omega$ . Among the four cases shown in Fig. 9, more low-frequency phonon modes are found in Figs. 9(c) and 9(d) to contribute to the dissipative effect. Therefore, a smaller oscillation amplitude of the photon numbers in the left and the right resonator is observed at  $tJ = 15$  in Figs. 4(c) and 4(d), compared to those in Figs. 4(a) and 4(b).

#### IV. CONCLUSION

In our previous work,<sup>13</sup> we studied the intriguing role played by the qubit-phonon coupling in engineering photon delocalization in a dissipative Rabi dimer in the absence of external fields. In this work, we extend our formalism to investigate the influence of a harmonic driving field in the vicinity of one of the qubits on the dynamics of the composite system. Following the Dirac-Frenkel time-dependent variation principle, the photon and the qubit dynamics are probed by employing the multi-D<sub>2</sub> ansatz. The external harmonic driving field can provide energy to the Rabi dimer and slow the amplitude damping of photon number oscillations induced by qubit-photon coupling in the absence of a phonon bath. Especially, the total photon number is found to be larger than, or equal to, its initial value due to the resonance between the periodic driving field and the photon frequency. In the presence of the phonon bath, the photon numbers are dramatically reduced and the reduction can be partially compensated by strong driving fields. It is revealed that the qubit polarization can be tuned by the harmonic driving. Low-frequency segmented oscillations can be found in the time evolution of the left qubit polarization if the driving field frequency is not high. Environmental effects can strengthen the qubit state asymmetry induced by the driving field. Finally, our phonon dynamics analyses based on the multi-D<sub>2</sub> ansatz can successfully identify the contribution of specific phonon modes to the time evolution of the photon numbers and the qubit polarization. Recently, simultaneous manipulation of the two qubits has been proposed in a system of two superconducting flux qubits interacting with each other through their mutual inductance.<sup>5,7</sup> Work on simulating photon and qubit dynamics is in progress by applying separate external fields on the two qubits.

#### ACKNOWLEDGMENTS

The authors thank Cao Xiufeng for useful discussion. Support from the Singapore National Research Foundation through the

Competitive Research Programme (CRP) under Project No. NRF-CRP5-2009-04 and from the Singapore Ministry of Education Academic Research Fund Tier 1 (Grant Nos. RG106/15, RG102/17, and RG190/18) is gratefully acknowledged.

#### APPENDIX: THE TIME DEPENDENT VARIATIONAL APPROACH

The Dirac-Frenkel variational principle results in equations of motion of the variational parameters as follows:

$$i \sum_{n=1}^M (\dot{A}_n + A_n \Xi_{nl}) S_{ln} = \sum_{n=1}^M \left\{ A_n \cdot \left[ \frac{\Delta_L(t) + \Delta_R(t)}{2} + \Pi_{nl} + 2 \sum_k \phi_k (\eta_{lk}^* + \eta_{nk}) \right] - g[(\mu_l^* + \mu_n)C_n + (\nu_l^* + \nu_n)B_n] \right\} S_{ln}, \quad (A1)$$

$$i \sum_{n=1}^M (\dot{B}_n + B_n \Xi_{nl}) S_{ln} = \sum_{n=1}^M \left\{ B_n \cdot \left[ \frac{\Delta_L(t) - \Delta_R(t)}{2} + \Pi_{nl} \right] - g[(\mu_l^* + \mu_n)D_n + (\nu_l^* + \nu_n)A_n] \right\} S_{ln}, \quad (A2)$$

$$i \sum_{n=1}^M (\dot{C}_n + C_n \Xi_{nl}) S_{ln} = \sum_{n=1}^M \left\{ C_n \cdot \left[ \frac{-\Delta_L(t) + \Delta_R(t)}{2} + \Pi_{nl} \right] - g[(\mu_l^* + \mu_n)A_n + (\nu_l^* + \nu_n)D_n] \right\} S_{ln}, \quad (A3)$$

$$i \sum_{n=1}^M (\dot{D}_n + D_n \Xi_{nl}) S_{ln} = \sum_{n=1}^M \left\{ D_n \cdot \left[ \frac{-\Delta_L(t) - \Delta_R(t)}{2} + \Pi_{nl} - 2 \sum_k \phi_k (\eta_{lk}^* + \eta_{nk}) \right] - g[(\mu_l^* + \mu_n)B_n + (\nu_l^* + \nu_n)C_n] \right\} S_{ln}, \quad (A4)$$

$$i \sum_{n=1}^M \left[ (A_l^* \dot{A}_n + B_l^* \dot{B}_n + C_l^* \dot{C}_n + D_l^* \dot{D}_n) \mu_n + \Theta_{nl}^a (\mu_n + \mu_n \Xi_{nl}) \right] S_{ln} = \sum_{n=1}^M \left\{ \left[ \frac{\Delta_L(t)}{2} \Theta_{nl}^b + \frac{\Delta_R(t)}{2} \Theta_{nl}^c \right] \mu_n + \Theta_{nl}^a (\omega_L \mu_n - J \nu_n + \mu_n \Pi_{nl}) - g \Theta_{nl}^d [1 + \mu_n (\mu_l^* + \mu_n)] - g \Theta_{nl}^e \mu_n (\nu_l^* + \nu_n) + 2(A_l^* A_n - D_l^* D_n) \mu_n \sum_k \phi_k (\eta_{lk}^* + \eta_{nk}) \right\} S_{ln}, \quad (A5)$$

$$\begin{aligned}
 & i \sum_{n=1}^M \left[ (A_i^* \dot{A}_n + B_i^* \dot{B}_n + C_i^* \dot{C}_n + D_i^* \dot{D}_n) v_n + \Theta_{nl}^a (\dot{v}_n + v_n \Xi_{nl}) \right] S_{ln} \\
 &= \sum_{n=1}^M \left\{ \left[ \frac{\Delta_L(t)}{2} \Theta_{nl}^b + \frac{\Delta_R(t)}{2} \Theta_{nl}^c \right] v_n + \Theta_{nl}^a (\omega_R v_n - J \mu_n + v_n \Pi_{nl}) \right. \\
 &\quad \left. - g \Theta_{nl}^d v_n (\mu_l^* + \mu_n) - g \Theta_{nl}^e [1 + v_n (v_l^* + v_n)] \right. \\
 &\quad \left. + 2(A_i^* A_n - D_i^* D_n) v_n \sum_k \phi_k (\eta_{lk}^* + \eta_{nk}) \right\} S_{ln}, \quad (A6)
 \end{aligned}$$

$$\begin{aligned}
 & i \sum_{n=1}^M \left[ (A_i^* \dot{A}_n + B_i^* \dot{B}_n + C_i^* \dot{C}_n + D_i^* \dot{D}_n) \eta_{nk'} + \Theta_{nl}^a (\dot{\eta}_{nk'} + \eta_{nk'} \Xi_{nl}) \right] S_{ln} \\
 &= \sum_{n=1}^M \left\{ \left[ \frac{\Delta_L(t)}{2} \Theta_{nl}^b + \frac{\Delta_R(t)}{2} \Theta_{nl}^c \right] \eta_{nk'} + \Theta_{nl}^a (\omega_k \eta_{nk'} + \eta_{nk'} \Pi_{nl}) \right. \\
 &\quad \left. - g \Theta_{nl}^d \eta_{nk'} (\mu_l^* + \mu_n) - g \Theta_{nl}^e \eta_{nk'} (v_l^* + v_n) \right. \\
 &\quad \left. + 2(A_i^* A_n - D_i^* D_n) [\phi_{k'} + \eta_{nk'} \sum_k \phi_k (\eta_{lk}^* + \eta_{nk})] \right\} S_{ln}, \quad (A7)
 \end{aligned}$$

where the auxiliary terms are

$$\begin{aligned}
 \Xi_{nl} &= \dot{\mu}_n \mu_l^* - \frac{1}{2} \dot{\mu}_n \mu_n^* - \frac{1}{2} \mu_n \dot{\mu}_n^* + \dot{v}_n v_l^* - \frac{1}{2} \dot{v}_n v_n^* - \frac{1}{2} v_n \dot{v}_n^* \\
 &\quad + \sum_k (\dot{\eta}_{nk} \eta_{lk}^* - \frac{1}{2} \dot{\eta}_{nk} \eta_{nk}^* - \frac{1}{2} \eta_{nk} \dot{\eta}_{nk}^*), \quad (A8)
 \end{aligned}$$

$$\Pi_{nl} = (\omega_L \mu_l^* \mu_n + \omega_R v_l^* v_n) - J(\mu_l^* v_n + v_l^* \mu_n) + \sum_k (\omega_k \eta_{lk}^* \eta_{nk}), \quad (A9)$$

$$\Delta_L(t) = A_L \cos(\Omega_L t + \Phi_L), \quad (A10)$$

$$\Delta_R(t) = A_R \cos(\Omega_R t + \Phi_R), \quad (A11)$$

$$\Theta_{nl}^a = A_i^* A_n + B_i^* B_n + C_i^* C_n + D_i^* D_n, \quad (A12)$$

$$\Theta_{nl}^b = A_i^* A_n + B_i^* B_n - C_i^* C_n - D_i^* D_n, \quad (A13)$$

$$\Theta_{nl}^c = A_i^* A_n - B_i^* B_n + C_i^* C_n - D_i^* D_n, \quad (A14)$$

$$\Theta_{nl}^d = A_i^* C_n + B_i^* D_n + C_i^* A_n + D_i^* B_n, \quad (A15)$$

$$\Theta_{nl}^e = A_i^* B_n + B_i^* A_n + C_i^* D_n + D_i^* C_n. \quad (A16)$$

By numerically solving these equations at each time  $t$ , one can calculate the values of  $\dot{A}_n$ ,  $\dot{B}_n$ ,  $\dot{C}_n$ ,  $\dot{D}_n$ ,  $\dot{\mu}_n$ ,  $\dot{v}_n$ , and  $\dot{\eta}_{nk}$  accurately. The fourth-order Runge-Kutta method is then adopted for the time evolution of the tunable Rabi dimer, including the time-dependent photon numbers, qubit polarization, and population of the bath modes.

## REFERENCES

- I. I. Rabi, *Phys. Rev.* **49**, 324–328 (1936).
- I. I. Rabi, *Phys. Rev.* **51**, 652–654 (1937).
- D. Braak, Q.-H. Chen, M. T. Batchelor, and E. Solano, *J. Phys. A: Math. Theor.* **49**, 300301 (2016).
- C. H. Alderete and B. M. Rodríguez-Lara, *J. Phys. A: Math. Theor.* **49**, 414001 (2016).
- J. M. Raimond, M. Brune, and S. Haroche, *Rev. Mod. Phys.* **73**, 565 (2001).
- D. Leibfried, R. Blatt, C. Monroe, and D. Wineland, *Rev. Mod. Phys.* **75**, 281 (2003).
- P. Scarlino, E. Kawakami, D. R. Ward, D. E. Savage, M. G. Lagally, M. Friesen, S. N. Coppersmith, M. A. Eriksson, and L. M. K. Vandersypen, *Phys. Rev. Lett.* **115**, 106802 (2015).
- I. Chiorescu, P. Bertet, K. Semba, Y. Nakamura, C. J. P. M. Harmans, and J. E. Mooij, *Nature* **431**, 159 (2004).
- C. Zener, *Proc. R. Soc. A* **137**, 696 (1932).
- L. D. Landau, *Phys. Z. S.* **2**, 46 (1932).
- S. N. Shevchenko, A. N. Omelyanchouk, and E. Il'ichev, *Low Temp. Phys.* **38**, 283 (2012).
- E. A. Temchenko, S. N. Shevchenko, and A. N. Omelyanchouk, *Phys. Rev. B* **83**, 144507 (2011).
- F. Zheng, Y. Zhang, L. Wang, Y. Wei, and Y. Zhao, *Ann. Phys.* **530**, 1800351 (2018).
- K. Saito, M. Wubs, S. Kohler, P. Hänggi, and Y. Kayanuma, *Europhys. Lett.* **76**, 22 (2006).
- W. D. Oliver, Y. Yu, J. C. Lee, K. K. Berggren, L. S. Levitov, and T. P. Orlando, *Science* **310**, 1653 (2005).
- T. Niemczyk, F. Deppe, H. Huebl, E. P. Menzel, F. Hocke, M. J. Schwarz, J. J. García-Ripoll, D. Zueco, T. Hummer, E. Solano, A. Marx, and R. Gross, *Nat. Phys.* **6**, 772 (2010).
- S. Javanbakht, P. Nalbach, and M. Thorwart, *Phys. Rev. A* **91**, 052103 (2015).
- L. S. Bishop, E. Ginossar, and S. M. Girvin, *Phys. Rev. Lett.* **105**, 100505 (2010).
- L. Henriot, Z. Ristivojevic, P. P. Orth, and K. Le Hur, *Phys. Rev. A* **90**, 023820 (2014).
- A. Wallraff, D. I. Schuster, A. Blais, L. Frunzio, R.-S. Huang, J. Majer, S. Kumar, S. M. Girvin, and R. J. Schoelkopf, *Nature* **431**, 162 (2004).
- J. Johansson, M. H. S. Amin, A. J. Berkley, P. Bunyk, V. Choi, R. Harris, M. W. Johnson, T. M. Lanting, S. Lloyd, and G. Rose, *Phys. Rev. B* **80**, 012507 (2009).
- A. A. Houck, J. A. Schreier, B. R. Johnson, J. M. Chow, J. Koch, J. M. Gambetta, D. I. Schuster, L. Frunzio, M. H. Devoret, S. M. Girvin, and R. J. Schoelkopf, *Phys. Rev. Lett.* **101**, 080502 (2008).
- O. Viehmann, J. von Delft, and F. Marquardt, *Phys. Rev. Lett.* **110**, 030601 (2013).
- H.-N. Xiong, P.-Y. Lo, W.-M. Zhang, D. H. Feng, and F. Nori, *Sci. Rep.* **5**, 13353 (2015).
- D. J. Egger and F. K. Wilhelm, *Phys. Rev. Lett.* **111**, 163601 (2013).
- N. Zhou, Z. Huang, J. Zhu, V. Chernyak, and Y. Zhao, *J. Chem. Phys.* **143**, 014113 (2015).
- Z. Huang, L. Chen, N. Zhou, and Y. Zhao, *Ann. Phys.* **529**, 1600367 (2017).
- Z. Huang and Y. Zhao, *Phys. Rev. A* **97**, 013803 (2018).
- P. Nalbach, N. Klinkenberg, T. Palm, and N. Müller, *Phys. Rev. E* **96**, 042134 (2017).
- D. Braak, *Phys. Rev. Lett.* **107**, 100401 (2011).
- H. Zhong, Q. Xie, X. Guan, M. T. Batchelor, and C. Lee, *J. Phys. A: Math. Theor.* **50**, 113001 (2017).
- L. Wang, L. Chen, N. Zhou, and Y. Zhao, *J. Chem. Phys.* **144**, 024101 (2016).
- Y. Zhao, B. Luo, Y. Zhang, and J. Ye, *J. Chem. Phys.* **137**, 084113 (2012).
- Y. Zhao, D. W. Brown, and K. Lindenberg, *J. Chem. Phys.* **107**, 3159 (1997); **107**, 3179 (1997).
- N. Zhou, L. Chen, Z. Huang, K. Sun, Y. Tanimura, and Y. Zhao, *J. Phys. Chem. A* **120**, 1562 (2016).
- L. Chen, R. Borrelli, and Y. Zhao, *J. Phys. Chem. A* **121**, 8757–8770 (2017).



- <sup>37</sup> L. Wang, Y. Fujihashi, L. Chen, and Y. Zhao, *J. Chem. Phys.* **146**, 124127 (2017).
- <sup>38</sup> Z. Huang, L. Wang, C. Wu, L. Chen, F. Grossmann, and Y. Zhao, *Phys. Chem. Chem. Phys.* **19**, 1655 (2017).
- <sup>39</sup> Z. Huang, Y. Fujihashi, and Y. Zhao, *J. Phys. Chem. Lett.* **8**, 3306 (2017).
- <sup>40</sup> Z. Huang, M. Hoshina, H. Ishihara, and Y. Zhao, *Ann. Phys.* **531**, 1800303 (2019).
- <sup>41</sup> D. Z. Rossatto, S. Felicetti, H. Eneriz, E. Rico, M. Sanz, and E. Solano, *Phys. Rev. B* **93**(9), 094514 (2016).
- <sup>42</sup> Y. Wang, J. Zhang, C. Wu, J. Q. You, and G. Romero, *Phys. Rev. A* **94**(1), 012328 (2016).
- <sup>43</sup> J. Raftery, D. Sadri, S. Schmidt, E. Türeci, and A. A. Houck, *Phys. Rev. X* **4**, 031043 (2014).
- <sup>44</sup> M. J. Hwang, M. S. Kim, and M. S. Choi, *Phys. Rev. Lett.* **116**, 153601 (2016).
- <sup>45</sup> K. M. Fonseca-Romero, S. Kohler, and P. Hänggi, *Phys. Rev. Lett.* **95**, 140502 (2005).
- <sup>46</sup> S. E. Savel'ev, Z. Washington, A. M. Zagoskin, and M. J. Everitt, *Phys. Rev. A* **86**, 065803 (2012).
- <sup>47</sup> J. Hausinger and M. Grifoni, *Phys. Rev. A* **83**, 030301 (2011).
- <sup>48</sup> S. Savel'ev, A. L. Rakhmanov, and F. Nori, *Phys. Rev. E* **72**, 056136 (2005).
- <sup>49</sup> S. Savel'ev, A. M. Zagoskin, A. N. Omelyanchouk, and F. Nori, *Chem. Phys.* **375**, 180 (2010).
- <sup>50</sup> S. Savel'ev, A. M. Zagoskin, A. L. Rakhmanov, A. N. Omelyanchouk, Z. Washington, and F. Nori, *Phys. Rev. A* **85**, 013811 (2012).
- <sup>51</sup> S.-K. Son, S. Han, and S.-I. Chu, *Phys. Rev. A* **79**, 032301 (2009).
- <sup>52</sup> X. Cao and H. Zheng, *Phys. Rev. A* **75**, 062121 (2007).
- <sup>53</sup> K. Xia, M. Macovei, J. Evers, and C. H. Keitel, *Phys. Rev. B* **79**, 024519 (2009).







# Transient Dynamics of Super Bloch Oscillations of a 1D Holstein Polaron under the Influence of an External AC Electric Field

Zhongkai Huang, Masayuki Hoshina, Hajime Ishihara, and Yang Zhao\*

Theoretical formalism for DC-field polaron dynamics is extended to the dynamics of a 1D Holstein polaron in an external AC electric field using multiple Davydov trial states. Effects of carrier–phonon coupling on detuned and resonant scenarios are investigated for both phase and nonzero phase. For slightly off-resonant or detuned cases, a beat between the usual Bloch oscillations and an AC driving force results in super Bloch oscillations, that is, rescaled Bloch oscillations in both the spatial and the temporal dimension. Super Bloch oscillations are damped by carrier–phonon coupling. For resonant cases, if the carrier is created on two nearest-neighboring sites, the carrier wave packet spreads with small-amplitude oscillations. Adding carrier–phonon coupling localizes the carrier wave packet. If an initial broad Gaussian wave packet is adopted, the centroid of the carrier wave packet moves with a certain velocity and with its shape unchanged. Adding carrier–phonon coupling broadens the carrier wave packet and slows down the carrier movement. Our findings may help provide guiding principles on how to manipulate the dynamics of the super Bloch oscillations of carriers in semiconductor superlattice and optical lattices by modifying DC and AC field strengths, AC phases, and detuning parameters.

the oscillation and dynamical localization of electrons in spatial and temporal domains have attracted great attention.<sup>[1]</sup> In perfect crystals, lattices generate a periodic potential and the Bloch theorem predicts that electronic states can extend uniformly over the whole system. However, when a uniform electrical field  $F$  is applied, all eigenstates of the single-electron tight-binding Hamiltonian become spatially localized Wannier–Stark states due to Bragg reflections, while electrons keep oscillating within a finite volume if scattering effects are neglectable. The periodic motion occurs in real and reciprocal space, and is known as the BOs.<sup>[2]</sup> The center-of-mass of an electronic wave packet performs a periodic oscillation with an amplitude given by the Stark localization length  $L = J/aF$ , where  $J$  is a tunneling coefficient and  $a$  refers to the lattice constant along the field direction.<sup>[3–6]</sup>

Since scattering processes are induced by defects and environment effects, an experimental detection of the BOs is highly nontrivial. In the 1970s, Esaki et al. firstly proposed that the BOs are achievable in semiconductor superlattices.<sup>[7]</sup> By 1992, the first observation of the BOs was reported by Feldmann et al. in superlattices under an external electric field.<sup>[1]</sup> More recently, cold atoms and Bose–Einstein condensates (BECs) in optical lattices have been revealed as a very convenient quasiparticles to undergo the BOs since the scattering processes can be significantly reduced.<sup>[8–10]</sup> To probe the mechanism by which the BOs take place, the dynamics of the carrier wave packet has been extensively studied in various physical systems,<sup>[11–21]</sup> including a semiconductor waveguide<sup>[22]</sup> and a thermo-optic polymer array subjected to a temperature gradient.<sup>[23]</sup>

In the last decade, there has emerged much interest in dynamics of a quasiparticle affected not only by a direct current (DC) field but also by a superimposed alternating current (AC) field.<sup>[24–29]</sup> Influences of the DC and AC field have been theoretically and experimentally reported for the BECs in optical lattices,<sup>[30,31]</sup> for charge carriers in organic materials,<sup>[25]</sup> for light in periodic optical waveguide arrays,<sup>[24,32]</sup> for carriers in a 1D quantum-dot superlattice,<sup>[33]</sup> and in a semiconductor superlattice.<sup>[34]</sup> It has been shown that particular AC fields result in localized wave packet for certain AC frequencies.<sup>[33,35,36]</sup>

## 1. Introduction

Since the first experimental report of time-domain Bloch oscillations (BOs) in superlattices under an external electric field,

Z. Huang  
College of Mechanical and Electrical Engineering  
Yangtze Normal University  
Chongqing 408100, China

Z. Huang, M. Hoshina, Prof. Y. Zhao  
Division of Materials Science  
Nanyang Technological University  
Singapore 639798, Singapore  
E-mail: YZhao@ntu.edu.sg

M. Hoshina, Prof. H. Ishihara  
Department of Physics and Electronics  
Osaka Prefecture University  
1-1 Gakuen-cho, Naka-ku, Sakai, Osaka 599-8531, Japan  
Prof. H. Ishihara  
Division of Frontier Materials Science  
Osaka University  
1-3 Machikaneyama-cho, Toyonaka, Osaka 560-8531, Japan



The ORCID identification number(s) for the author(s) of this article can be found under <https://doi.org/10.1002/andp.201800303>

DOI: 10.1002/andp.201800303



This kind of localization is known as dynamical localization and it is conceptually different from Anderson localization.<sup>[37,38]</sup> Dynamical localization has been experimentally reported in cold atoms and the BECs in 1D optical lattices.<sup>[39,40]</sup> Remarkably, it was demonstrated that a weakly interacting BEC in a harmonically driven tilted potential can support directed transport or large amplitude oscillations of the wave function, depending on the driven frequency.<sup>[31,41,42]</sup> In 2010, Haller et al. observed giant center-of-mass oscillations of a weakly interacting atomic BEC in real space with a displacement across hundreds of lattice sites when they added a periodic modulation to the force near the Bloch frequency, and firstly named the oscillations as super Bloch oscillations (SBOs).<sup>[43]</sup> Kolovsky et al. soon followed up with a theoretical explanation: when the AC frequency is close to the Bloch frequency, the difference between the two frequencies leads to the SBOs, and a near resonant driving transforms Wannier–Stark states into new “super” Wannier–Stark states with a localization length  $\tilde{L} \approx \tilde{J}/a\tilde{F}$ , where  $\tilde{J}$  is an effective tunneling coefficient, and  $\tilde{F}$  corresponds to an effective field.<sup>[44–46]</sup> The term “super” refers to the fact that the amplitude in position space of such an oscillation is several orders of magnitude larger than that for usual BOs.<sup>[24,47]</sup>

Environmental effects are of essential importance to dynamics of the BOs and SBOs in target systems such as semiconductor superlattices, organic materials, and quantum dots. Due to the complexity of system–bath interactions, it is difficult to devise exact analytical solutions to the dynamics of these systems under the influence of external electric fields. Fröhlich’s model of polaron was employed in 1970 by Feynman et al. to study the motion of an electron in a polar crystal in a strong electric field.<sup>[48]</sup> Later, much theoretical work focused on transition rate probabilities, which can be derived from the rate equations or the Boltzmann equation.<sup>[49,50]</sup> In the 1990s, Holthaus et al. proposed to use AC fields to localize the carrier in disordered semiconductor superlattices,<sup>[51]</sup> and carried out a systematic study on carrier localization in AC-field-driven tight-binding lattices.<sup>[37]</sup> However, a fully quantum mechanical modeling of polaron dynamics under the simultaneous presence of the DC and AC fields has not received much-deserved attention over the last decades. Moreover, regardless of the rapid experimental progress on the SBOs,<sup>[31,43]</sup> little theoretical work has been devoted to study the dynamics of the SBOs.<sup>[27,52]</sup>

Despite extensive studies on the BOs, roles of the complex interplay between the carrier and its accompanying phonon cloud still remain an open question.<sup>[53]</sup> With respect to dynamics of the BOs in the Su–Schrieffer–Heeger model for polymers<sup>[15,16,54,55]</sup> and the Peyrard–Bishop–Holstein model for DNA,<sup>[56]</sup> the phonon bath is treated classically and the associated carrier–phonon coupling is treated semiclassically. In 1997, Bonča and Trugman used the 1D Holstein molecular crystal model to study dynamics of an electron coupled to optical phonons under a strong electric field. Their work retained full quantum coherence in the description of nonequilibrium dynamics of a polaron.<sup>[53,57–59]</sup> Recently, the crux of transient dynamics of the BOs was laid out in our previous study by employing the multiple Davydov trial states.<sup>[13]</sup> Since the dynamical control of the SBOs can be realized in the same experimental setup for the engineering of the BOs, it is necessary to extend the successful method for the dynamics of the BOs to study the influence of carrier–phonon coupling on the SBOs.<sup>[37]</sup> With

respect to the SBOs, spatial and temporal dynamics affected by carrier–phonon interactions has not received adequate attention. In fact, little can be found in the literature on how system–bath interactions affect the dynamics of the SBOs. Here, we continue our endeavor with an accurate theoretical treatment of dynamics of the SBOs of a carrier coupled to phonons.

In this work, we investigate the impact of diagonal carrier–phonon coupling on polaron dynamics in a ring system in the presence of the DC and AC electric fields using the multiple Davydov  $D_2$  trial state with the Dirac–Frenkel variational principle. The rest of the paper is structured as follows. In Section 2, we present the Hamiltonian in the gauge transformed form and our trial wave function, the multi- $D_2$  Ansatz. Dynamics of the SBOs is examined in Section 3. Polaron dynamics for the detuned and resonant cases is discussed in Section 3.1. Finally, polaron dynamics for nonzero AC phase is described in Section 3.2. Conclusions are drawn in Section 4.

## 2. Methodology

### 2.1. Model

The Hamiltonian of the 1D Holstein polaron reads

$$\hat{H} = \hat{H}_{\text{ca}} + \hat{H}_{\text{ph}} + \hat{H}_{\text{ca-ph}} \quad (1)$$

where  $\hat{H}_{\text{ca}}$ ,  $\hat{H}_{\text{ph}}$ , and  $\hat{H}_{\text{ca-ph}}$  are the charge carrier Hamiltonian, the bath (phonon) Hamiltonian, and the carrier–phonon coupling Hamiltonian, respectively. An extra term

$$[F_{\text{dc}} + F_{\text{ac}} \cos(\omega_{\text{ac}}t + \phi_{\text{ac}})] \sum_n n a_n^\dagger a_n \quad (2)$$

is added to represent the scalar potential interactions induced by the external electric field.  $F_{\text{dc}}$  denotes a DC field and  $F_{\text{ac}} \cos(\omega_{\text{ac}}t + \phi_{\text{ac}})$  serves as an AC field. In the presence of the external field, the potential of the field at the boundary of the system was found to become discontinuous if the periodic boundary conditions were taken into consideration via bending a linear chain into a ring.<sup>[60]</sup> This problem can be circumvented by adopting a gauge transformed vector potential, that is,  $A(t) = -F_{\text{dc}}t - \frac{F_{\text{ac}}}{\omega_{\text{ac}}} \sin(\omega_{\text{ac}}t + \phi_{\text{ac}})$ .<sup>[61,62]</sup> Then, we can recast Equations (1) and (2) as a gauge transformed Hamiltonian for the ring system under the external electric field

$$\begin{aligned} \hat{H}_{\text{ca}} &= -J \sum_n a_n^\dagger (e^{iA(t)} a_{n+1} + e^{-iA(t)} a_{n-1}) \\ \hat{H}_{\text{ph}} &= \omega_0 \sum_n b_n^\dagger b_n \\ \hat{H}_{\text{ca-ph}} &= -g \omega_0 \sum_n a_n^\dagger a_n (b_n + b_n^\dagger) \end{aligned} \quad (3)$$

where  $\hat{a}_n^\dagger$  ( $\hat{a}_n$ ) and  $\hat{b}_n^\dagger$  ( $\hat{b}_n$ ) are the carrier and phonon creation (annihilation) operators for the  $n$ -th site, respectively. Written in the phonon momentum space, one has

$$\hat{H}_{\text{ph}} = \sum_q \omega_q \hat{b}_q^\dagger \hat{b}_q \quad (4)$$

$$\hat{H}_{\text{ca-ph}} = -N^{-1/2} g \sum_{n,q} \omega_q \hat{a}_n^\dagger \hat{a}_n (e^{iqn} \hat{b}_q + e^{-iqn} \hat{b}_q^\dagger) \quad (5)$$



where  $\omega_q$  is the phonon frequency with momentum  $q$ , and  $\hat{b}_q^\dagger$  ( $\hat{b}_q$ ) is the creation (annihilation) operator of a phonon with the momentum  $q$

$$\hat{b}_q^\dagger = N^{-1/2} \sum_n e^{iqn} \hat{b}_n^\dagger, \quad \hat{b}_n^\dagger = N^{-1/2} \sum_q e^{-iqn} \hat{b}_q^\dagger \quad (6)$$

$J$  and  $g$  are the transfer integral and the diagonal carrier–phonon coupling strength, respectively. There has been related theoretical work that using the Holstein model to describe an electron interacting locally with dispersionless phonons under a strong electric field in an inelastic quantum transport process.<sup>[50]</sup> The full quantum coherence was revealed to be retained in the model and dispersionless phonons were found to absorb the excess energy from the external field to avoid infinite drift velocity of the electron.<sup>[53,63]</sup> In this work, we consider dispersionless phonons, that is,  $\omega_q = \omega_0$ . In the remainder of the paper,  $\omega_0$  is set to unity as the energy unit.

## 2.2. Multiple Davydov Trial States

The multiple Davydov trial states with a multiplicity  $M$ , which are essentially  $M$  copies of the corresponding single Davydov Ansatz, have been developed to investigate the time evolution of the Holstein polaron following the Dirac–Frenkel variational principle.<sup>[64]</sup> A series of multiple Davydov trial states, that is, the multiple Davydov  $D_1$ ,  $D_{1.5}$ , and  $D_2$  Ansätze, have been proposed, demonstrating significant improvements over single Davydov states in the flexibility and the accuracy of the trial states.<sup>[65–67]</sup> Recently, the multiple Davydov  $D_2$  trial state, also known as the multi- $D_2$  Ansatz, has been successfully applied to obtain accurate dynamics of a variety of open quantum systems,<sup>[68–70]</sup> including the singlet fission model<sup>[71]</sup> and the dissipative Landau–Zener model.<sup>[72,73]</sup>

The multi- $D_2$  Ansatz employed in this work can be constructed as

$$\begin{aligned} |D_2^M(t)\rangle &= \sum_i^M \sum_n^N \psi_{in} |n\rangle |\lambda_i\rangle \\ &= \sum_i^M \sum_n^N \psi_{in} \hat{a}_n^\dagger |0\rangle_{ca} \exp \left\{ \sum_q [\lambda_{iq} \hat{b}_q^\dagger - \lambda_{iq}^* \hat{b}_q] \right\} |0\rangle_{ph} \end{aligned} \quad (7)$$

where  $\psi_{in}$  and  $\lambda_{iq}$  are time-dependent variational parameters for the carrier probability and the phonon displacement, respectively,  $n$  represents the site number, and  $i$  is the coherent superposition index. If  $M = 1$ , the  $|D_2^M(t)\rangle$  Ansatz is restored to the usual Davydov  $D_2$  trial state. The equations of motion of the variational parameters  $\psi_{in}$  and  $\lambda_{iq}$  are then derived by adopting the Dirac–Frenkel variational principle

$$\begin{aligned} \frac{d}{dt} \left( \frac{\partial L_2}{\partial \psi_{in}^*} \right) - \frac{\partial L_2}{\partial \psi_{in}} &= 0 \\ \frac{d}{dt} \left( \frac{\partial L_2}{\partial \lambda_{iq}^*} \right) - \frac{\partial L_2}{\partial \lambda_{iq}} &= 0 \end{aligned} \quad (8)$$

For the multi- $D_2$  Ansatz, and the Lagrangian  $L_2$  is formulated as

$$\begin{aligned} L_2 &= \langle D_2^M(t) | \frac{i}{2} \frac{\overleftrightarrow{\partial}}{\partial t} - \hat{H} | D_2^M(t) \rangle \\ &= \frac{i}{2} \left[ \langle D_2^M(t) | \frac{\overrightarrow{\partial}}{\partial t} | D_2^M(t) \rangle - \langle D_2^M(t) | \frac{\overleftarrow{\partial}}{\partial t} | D_2^M(t) \rangle \right] \\ &\quad - \langle D_2^M(t) | \hat{H} | D_2^M(t) \rangle \end{aligned} \quad (9)$$

where the first term yields

$$\begin{aligned} &\frac{i}{2} \left[ \langle D_2^M(t) | \frac{\overrightarrow{\partial}}{\partial t} | D_2^M(t) \rangle - \langle D_2^M(t) | \frac{\overleftarrow{\partial}}{\partial t} | D_2^M(t) \rangle \right] \\ &= \frac{i}{2} \sum_{i,j}^M \sum_n^N (\psi_{jn}^* \dot{\psi}_{in} - \dot{\psi}_{jn}^* \psi_{in}) S_{ji} \\ &\quad + \frac{i}{2} \sum_{i,j}^M \sum_n^N \psi_{jn}^* \dot{\psi}_{in} S_{ji} \sum_q \left[ \frac{\dot{\lambda}_{jq}^* \lambda_{jq} + \lambda_{jq}^* \dot{\lambda}_{jq}}{2} \right. \\ &\quad \left. - \frac{\dot{\lambda}_{iq} \lambda_{iq}^* + \lambda_{iq} \dot{\lambda}_{iq}^*}{2} + \lambda_{jq}^* \dot{\lambda}_{iq} - \lambda_{iq} \dot{\lambda}_{jq}^* \right] \end{aligned} \quad (10)$$

and the second term takes the form

$$\begin{aligned} &\langle D_2^M(t) | \hat{H} | D_2^M(t) \rangle \\ &= \langle D_2^M(t) | \hat{H}_{ca} | D_2^M(t) \rangle + \langle D_2^M(t) | \hat{H}_{ph} | D_2^M(t) \rangle \\ &\quad + \langle D_2^M(t) | \hat{H}_{ca-ph} | D_2^M(t) \rangle \end{aligned} \quad (11)$$

with  $S_{ij}$  being the Debye–Waller factor

$$S_{ij} = \exp \left\{ \sum_q \lambda_{iq}^* \lambda_{jq} - \frac{1}{2} (|\lambda_{iq}|^2 + |\lambda_{jq}|^2) \right\} \quad (12)$$

Detailed derivations of the equations of motion for the variational parameters are given in the Supporting Information. In the numerical calculations, the fourth-order Runge–Kutta method is used to integrate the equations of motion.

It is noted that our multi- $D_2$  Ansatz is essentially improved on the Ansatz in the multi-configurational Ehrenfest (MCE) method independently proposed by Shalashilin et al.<sup>[74–76]</sup> The formulation notations may be different. In the language of the MCE approach,  $\lambda_{iq}$  is called coherent state  $Z_{iq}$ , and the multiplicity  $M$  refers to the number of Ehrenfest configurations or simply the Ehrenfest basis set size. The two methods differ in equations of motion. The MCE approach relies on the predetermined equations of motion of the coherent state, which are chosen to be the Ehrenfest equations. In contrast, our variational method with the multi- $D_2$  Ansatz uses fully the Dirac–Frenkel variational principle and its equations of motion are more computationally expensive and accurate. Validity of our approach has been extensively tested in the previous work, and calculations are performed with



a sufficiently large multiplicity  $M$  in this work. For details of the accuracy test, please refer to ref. [13].

Time evolution of the carrier probability  $P_{ca}(t, n)$  is calculated as

$$P_{ca}(t, n) = \langle D_2^M(t) | \hat{a}_n^\dagger \hat{a}_n | D_2^M(t) \rangle \quad (13)$$

We further study the current of the system under an external field

$$\begin{aligned} j(t) &= \langle D_2^M(t) | i \left( \sum_n e^{iA(t)} \hat{a}_n^\dagger \hat{a}_{n+1} - H.c. \right) | D_2^M(t) \rangle \\ &= i \sum_{i,j} \sum_n \psi_{j,n}^*(t) [e^{iA(t)} \psi_{i,n+1}(t) - e^{-iA(t)} \psi_{i,n-1}(t)] S_{ji} \end{aligned} \quad (14)$$

We also define a mean value  $c(t)$  and a standard deviation  $\sigma(t)$  of the centroid position of the carrier wave packet as follows

$$\begin{aligned} c(t) &= \sum_i n P_{ca}(t, n) \\ \sigma(t)^2 &= \sum_i (n - c(t))^2 P_{ca}(t, n) \end{aligned} \quad (15)$$

It is noted that the mean value  $c(t)$  is sensitive to the initial standard deviation  $\sigma_0$  of the carrier wave packet.

### 3. Numerical Results and Discussions

In the absence of the carrier-phonon coupling, if the field  $F_{dc} + F_{ac} \cos(\omega_{ac}t + \phi_{ac})$  is applied to the carrier, the inherent localization of the BOs and SBOs is circumvented under some suitable conditions of AC frequency  $\omega_{ac}$  and phase  $\phi_{ac}$ . Dignam et al. examined the conditions for dynamic localization of electrons in a periodic potential due to an applied AC electric field. Haller et al. investigated particle transport in a lattice potential subjected to harmonic driving and reported that details of the motion depend on the ratio between the AC frequency  $\omega_{ac}$  and the Bloch frequency  $\omega_B$ .<sup>[43]</sup> If the AC field is absent ( $F_{ac} = 0$ ), the BOs occur at the Bloch frequency  $\omega_B = F_{dc}$ , where  $\omega_B = 2\pi/T_B$  with  $T_B$  denoting the time period of the BOs. When the AC frequency is detuned from the Bloch frequency, the SBOs arise. A small detuning  $\omega_{ac} - \omega_B$  results in a beat between the Bloch cycle and the harmonic driving, with a drastic change of the particle motion. On top of the BOs, the SBOs motion has a much larger amplitude of oscillation in position space that extends over hundreds of lattice sites. Those SBOs directly correspond to the motion of normal BOs, just rescaled in the spatial and temporal dimension. In other words, the SBOs are observed when  $\omega_{ac}$  satisfies the condition

$$N_{int}\omega_{ac} = \omega_B(1 + \delta) = F_{dc}(1 + \delta) \quad (16)$$

for some nonvanishing integer  $N_{int}$ , where  $|\delta| \ll 1$  is a small dimensionless detuning parameter controlling the period of the SBOs.  $N_{int} = 1$  was most commonly used in theoretical and experimental studies,<sup>[27,43,45]</sup> and is thus adopted in this work as well. The time period of the SBOs is given by  $T_{SB} = 2\pi/(\delta\omega_B) = 2\pi/(\delta F_{dc})$ . When the detuning parameter  $\delta$  vanishes,  $T_{SB}$  diverges.<sup>[52]</sup>

#### 3.1. Detuned and Resonant Cases

Experimental realizations of SBOs are recently given by a tunable BEC in modulated standing light waves or semiconductor superlattices in far-infrared laser fields.<sup>[37]</sup> Using BECs in optical lattice potentials generated by interfering laser waves, the BOs and SBOs can be engineered by a force that is provided by gravity or by acceleration of the lattice potential. Haller et al. observed the SBOs for a BEC subjected to harmonic driving, by changing the lattice tilt as an external force as well as lattice depth and spacing.<sup>[43]</sup> Alberti et al. managed to control the quantum transport of cold Sr atoms that are trapped in an optical lattice aligned along the Earth's gravity field.<sup>[31]</sup> The carrier motion will inevitably be influenced by the environmental fluctuation on the optical lattice potential or the lattice vibration in the semiconductor superlattice.<sup>[8–10,77]</sup> The influence of surroundings on the carrier can be modeled as phonons,<sup>[1]</sup> and thus the key issue of this work is the effects of carrier-phonon coupling. As shown in Hamiltonian (1), carrier-phonon interactions included in the Holstein model are in the form of the diagonal coupling as a nontrivial dependence of the carrier site energies on the lattice coordinates.<sup>[78]</sup>

We will study the influence of carrier-phonon coupling in two typical categories: resonant ( $\delta = 0$ ) type and detuned ( $\delta \neq 0$ ) type of carrier motion. These two types have been reported previously in the observation of the SBOs of a BEC under superposed DC and AC forces.<sup>[43]</sup> After experimental investigation in 1D optical lattice, the two types of movement have also been analyzed numerically using a semiclassical approach.<sup>[47]</sup> Generally, for a simple resonant AC field with frequency  $\omega_{ac} = \omega_B$ , the wave function of the carrier performs a directed motion with oscillatory features and drift velocity depending on the phase  $\phi_{ac}$ . On the contrary, if the frequency of the AC field  $\omega_{ac}$  is detuned with respect to  $\omega_B$ , the wave packet exhibits a beating effect of the SBOs. These two scenarios were referred to as resonant and detuned types. In this work, we will focus on certain sets of parameters as representative values of these two situations under the influence of carrier-phonon coupling.

Being strongly dependent on the initial conditions, the motion of the carrier wave packet subject to the DC and AC electric field has been found to exhibit a breathing mode or the typical BOs/SBOs,<sup>[13,43,79]</sup> thus here we discuss the initial conditions before moving on to specific calculations. Effects of initial Gaussian wave packets have been investigated by Caetano et al. under the superposed DC and AC field.<sup>[24,47]</sup> The outcomes of initial Gaussian wave packets of different widths  $\sigma_0$  are speculated first.<sup>[44]</sup> For a very narrow initial Gaussian wave packet, the carrier is almost created on only one site and there are no typical oscillations for the centroid of the carrier wave packet, which is denoted by



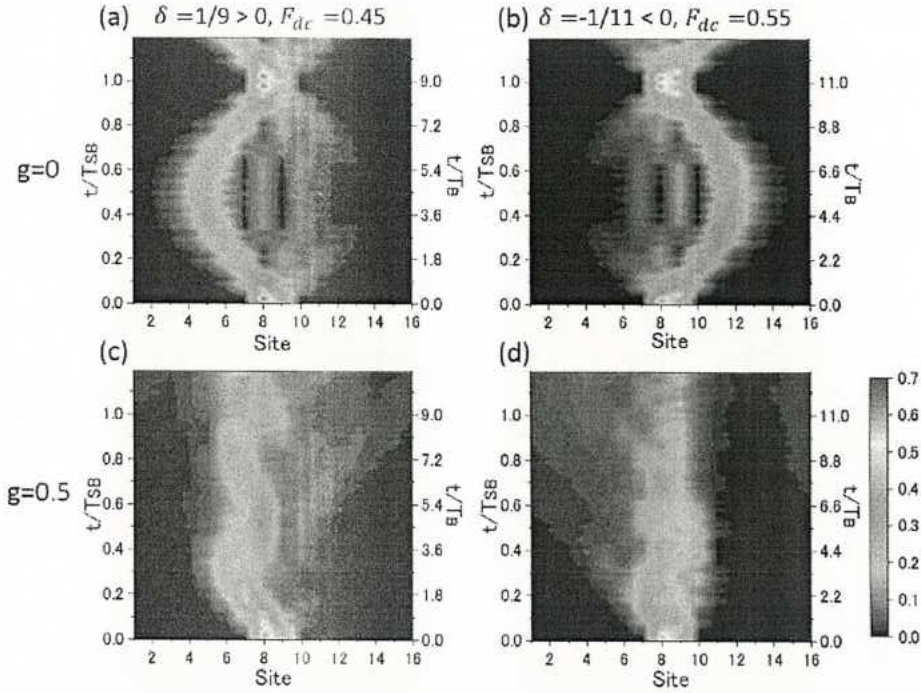


**Figure 1.** Time evolution of the carrier probability  $P_{ca}(t, n)$  for detuned cases ( $\delta \neq 0$ ) with the two-site-centered initial condition. In the left panels,  $\delta = 1/9$  and  $F_{dc} = 0.45$ . In the right panels,  $\delta = -1/11$  and  $F_{dc} = 0.55$ . The carrier–phonon coupling strength is  $g = 0$  in the upper panels, and  $g = 0.5$  in the lower panels. Other parameters are  $M = 16$ ,  $N = 16$ ,  $J = 0.1$ ,  $F_{ac} = 1.0$ ,  $\omega_{ac} = 0.5$ , and  $\phi_{ac} = 0$ .

$c(t)$ . The application of a DC field leads to a symmetric breathing mode with unchanged  $c(t)$  and an oscillatory wave-packet width

$$\sigma(t) = \sqrt{\sigma_0^2 + 2 \left[ 2 \frac{J}{F_{dc}} \sin\left(\frac{\omega_B t}{2}\right) \right]^2} \quad (17)$$

While the introduction of an AC field in the detuned cases leads to a symmetric motion of fixed  $c(t)$  and a varying width

$$\sigma(t) = \sqrt{\sigma_0^2 + 2 |\chi(t)|^2} \quad (18)$$

with

$$\chi(t) = 2J \sum_{n=-\infty}^{\infty} \mathcal{J}_n\left(\frac{F_{ac}}{\omega_{ac}}\right) \frac{1}{\delta\omega_B} \exp\left(-i\frac{\delta\omega_B}{2}t\right) \sin\left(\frac{\delta\omega_B}{2}t\right) \quad (19)$$

where  $\mathcal{J}_n$  is the ordinary Bessel function of order  $n$ . For the resonant case, the AC field results in a symmetrically spreading wave packet with width

$$\sigma(t) = \sum_{n=-\infty}^{\infty} \mathcal{J}_n\left(\frac{F_{ac}}{\omega_{ac}}\right) \sqrt{2} J t \quad (20)$$

As the initial width of the Gaussian wave packet increases, the oscillation amplitude of  $c(t)$  converges to those of the semiclassical

cases, in which the motion of wave packet centroid agrees with the movement of particles.<sup>[24,47]</sup> Using a broad initial Gaussian wave packet, the carrier movement exhibits the typical SBOs in the detuned scenario and a linear movement with superimposed small-amplitude oscillation in the resonant case, also defined as the directed motion of the carrier.<sup>[43,52]</sup>

When a two-site-centered initial state is adopted, the carrier is created on two nearest neighboring sites,  $\psi_n(t=0) = (\delta_{n,N/2} + \delta_{n,N/2+1})/\sqrt{2}$ .<sup>[64]</sup> Using this initial condition, the carrier exhibits partial BOs in the presence of only the DC field, conveying the quantum feature of the carrier wave packet explicitly.<sup>[13]</sup> However, the influence of the AC field on the movement of the carrier wave packet using this initial condition has not been investigated. In this study, the two-site-centered state is used as the initial condition, and the phonon displacement  $\lambda_{i,q}(t=0) = 0$  is set.

First, let us analyze how the polaron wave function evolves as the field is applied. The time-domain evolution of the carrier wave packet is shown in Figure 1 for the detuned cases. We fix  $J = 0.1$ ,  $F_{ac} = 1.0$ ,  $\omega_{ac} = 0.5$ , and  $\phi_{ac} = 0$ , and vary the set of  $\delta$  and  $F_{dc}$ . Figure 1a is for  $\delta = 1/9$  and  $F_{dc} = 0.45$ , and the corresponding wave packet moves to the left-hand side. In comparison, the carrier wave packet shifts to the right-hand side with  $\delta = -1/11$  and  $F_{dc} = 0.55$ , as shown in Figure 1b. Both detuned cases show that the carrier performs the SBOs. The oscillation amplitudes for the two-site-centered condition are smaller than those for the broad initial Gaussian wave packet, since the latter yields the largest oscillation amplitudes among all types of initial conditions.<sup>[44]</sup> It can be also revealed that the direction of the carrier wave



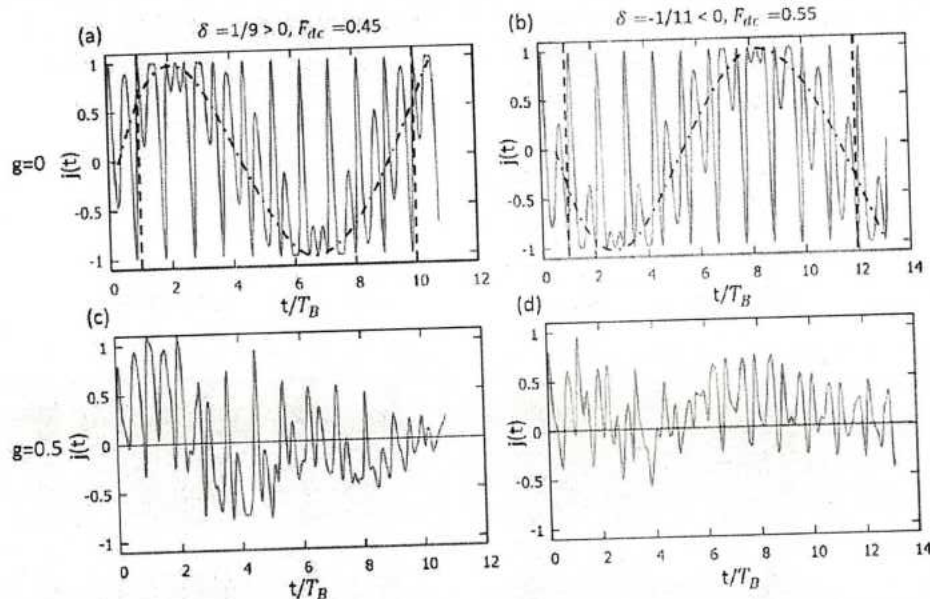


**Figure 2.** Currents for detuned cases of Figure 1.

package centroid movement can be engineered by tuning  $\delta$  and  $F_{dc}$ .

As presented in Figure 1c,d, a coupling strength of  $g = 0.5$  is used. It is shown that by increasing the strength of the carrier–phonon coupling, the carrier states become more localized. Holthaus et al. has reported that the dynamical localization of the wave packet can be manipulated by varying the strength of the electric field in disordered semiconductor superlattices.<sup>[51]</sup> This conclusion has been well supported by several studies,<sup>[39,44]</sup> and is also in agreement with our simulation. Our findings imply that changing the carrier–phonon coupling strength is another promising way to engineer the dynamical localization of the SBOs.

In view of the oscillatory behavior of the carrier wave packet described in Figure 1 for the detuned cases, it is reasonable to expect that the electric current behaves in a similar manner. An observable of interest, the current is numerically calculated according to Equation (14). As shown in Figure 2a,b, currents  $j(t)$  display well-defined oscillatory behavior in the detuned cases. Relevant movement directions and temporal periods of the currents match perfectly those obtained from the carrier wave packet. As presented in Figures 1a and 2a,  $\delta = 1/9$  leads to  $T_{SB} = 9T_B$ .  $T_{SB} = 11T_B$  in Figures 1b and 2b results from  $\delta = -1/11$ . The current of DC cases in the previous study shows oscillations in a purely sine function form.<sup>[13]</sup> In comparison, the currents in the simultaneous presence of AC and DC fields have two features: low-frequency oscillations marked by dash-dotted line due to the AC field, and high-frequency oscillations induced by the DC field. Figure 2c,d shows the decay of amplitudes of current oscillations due to dissipation effects of the carrier–phonon coupling, in agreement with quenching of the BOs due to strong carrier–phonon coupling.<sup>[17–20]</sup> It can be found that both the high-frequency and low-frequency oscillations of the

current are damped, in accord with the breakdown of the SBOs patterns of the carrier wave packet.

We proceed to the resonant case of  $\delta = 0$  in this subsection. If the broad initial Gaussian wave packet is applied, the center-of-mass of the wave packet moves almost linearly with superimposed high-frequency and small-amplitude oscillations while its shape is essentially unchanged, that is to say, resonant modulation of the detuning parameter causes directed motion of the wave packet's center-of-mass.<sup>[47]</sup> When the carrier is created at two nearest neighboring sites, there is no directed motion observed. Instead, the carrier wave packet spreads over the ring at a certain velocity with small-amplitude and high-frequency oscillations, as presented in Figure 3a,b, leading to negligible wave packet centroid movement from the initial positions. This movement can be denoted as bifurcated motion. After the carrier–phonon coupling of  $g = 0.5$  is added, the wave packets become localized and their averaged center substantially shifts away from the original position during the evolution, as shown in Figure 3c,d. Because the external DC fields have opposite directions in the left ( $F_{dc} = 0.5$ ) and right ( $F_{dc} = -0.5$ ) panels, the wave packet in Figure 3c is found to shift to the left-hand side while that in Figure 3d moves to the right-hand side. As shown in Figure 4, the currents exhibit corresponding oscillation features. In upper panels of Figures 3 and 4, only values of  $T_B$  are listed because the  $T_{SB}$  approaches infinity. In the lower panels, dissipation features are again observed after the addition of carrier–phonon interactions. Domínguez et al. have considered the Peyrard–Bishop–Holstein model of charge transport in DNA to study the SBOs of the charge carrier semiclassically, and the current oscillation in resonant cases was found to be modulated without decay in time.<sup>[25]</sup> In contrast, the periodicity is broken and the amplitude of the oscillatory current is smaller in our fully quantum mechanical results.



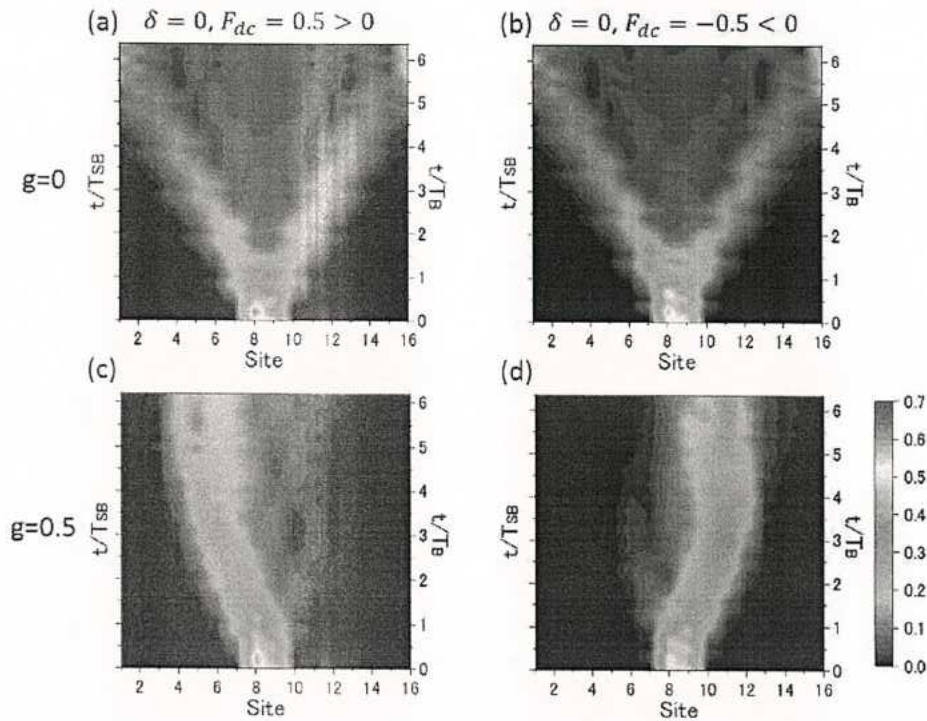


**Figure 3.** Time evolution of the carrier probability  $P_{ca}(t, n)$  for resonant cases ( $\delta = 0$ ) with the two-site-centered initial condition. In the left panels,  $F_{dc} = 0.5$ . In the right panels,  $F_{dc} = -0.5$ , denoting that electric field is in an opposite direction of that in the left panels. The carrier-phonon coupling strength is  $g = 0$  in the upper panels, and  $g = 0.5$  in the lower panels. Other parameters are  $M = 16$ ,  $N = 16$ ,  $J = 0.1$ ,  $F_{ac} = 1.0$ ,  $\omega_{ac} = 0.5$ , and  $\phi_{ac} = 0$ .

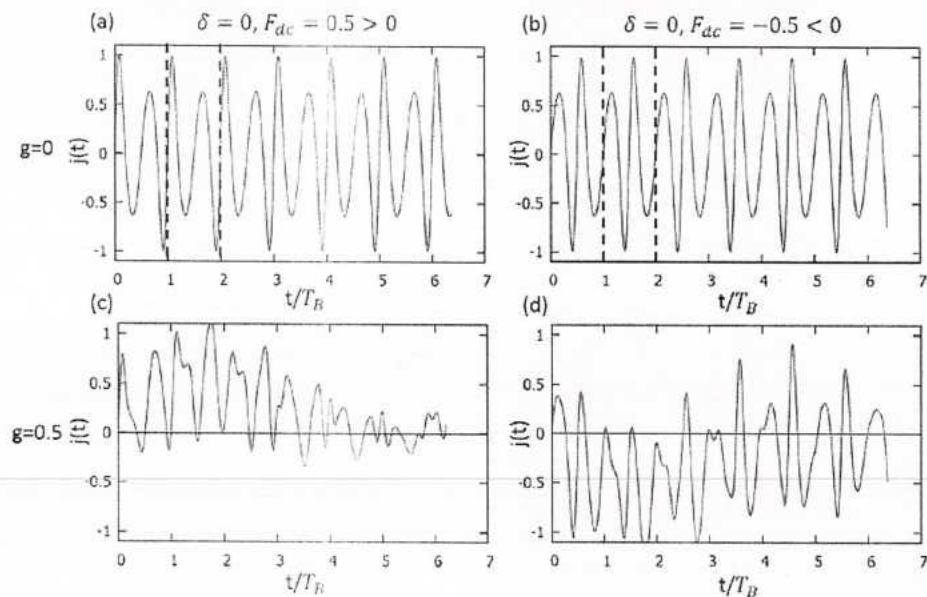


**Figure 4.** Currents for detuned cases of Figure 3.

### 3.2. AC Phase Modulation

Recent observations of cold atoms in optical lattices include global motion of the atom cloud, pointing to the importance of AC phase correction.<sup>[27]</sup> By appropriate modulation of the

phase, the carrier transport can be precisely engineered. Figure 5 presents a quantitative study of the AC phase and time-dependent amplitudes of such SBOs. Figure 5a,b show the time evolution of the carrier wave packet for  $\phi_{ac}$  of 0,  $\pi/4$ ,  $3\pi/8$ , and  $\pi/2$ . In Figure 5e, we plot the time evolution of the wave packet

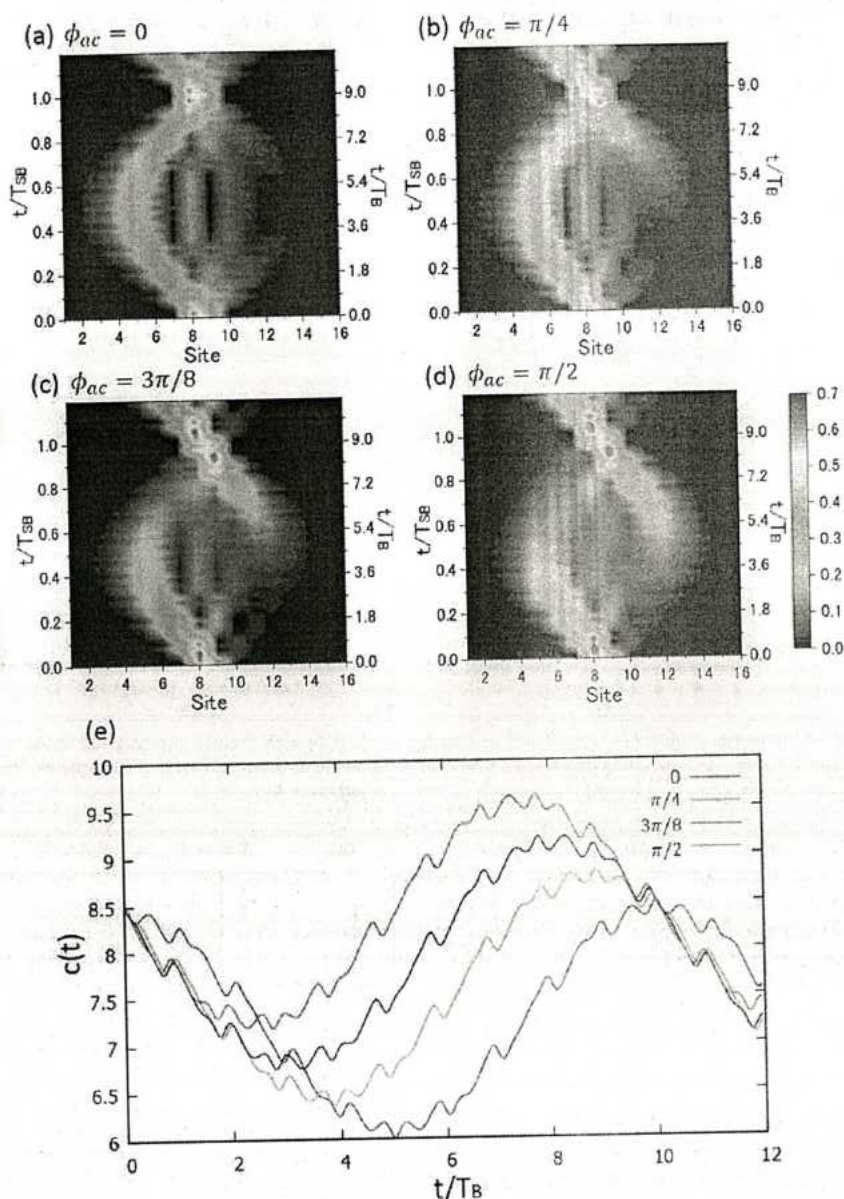


**Figure 5.** Time evolution of the carrier probability  $P_{ca}(t, n)$  for various phases a)  $\phi_{ac} = 0$ , b)  $\phi_{ac} = \pi/4$ , c)  $\phi_{ac} = 3\pi/8$ , and d)  $\phi_{ac} = \pi/2$ , in the absence of carrier–phonon coupling ( $g = 0$ ). e) Mean values  $c(t)$  of the carrier wave packets. The two-site-centered initial condition is used. Other parameters are  $M = 1$ ,  $N = 16$ ,  $J = 0.1$ ,  $F_{dc} = 0.45$ ,  $F_{ac} = 1.0$ ,  $\omega_{ac} = 0.5$ , and  $\delta = 1/9$ .

centroid for these AC phases. It can be found that the motion corresponding to each phase is shifted with an unchanged temporal period.

Effects of the carrier–phonon coupling for  $\phi_{ac} = \pi/2$  are presented in Figures 6 and 7. Figure 6 shows the SBO features in two detuned cases of  $\delta = 1/9$  and  $-1/11$ . It is worth noting that phase manipulations can lead to similar carrier motion patterns for different parameter sets, as shown in Figure 6a,b. This similarity is destroyed after adding the carrier–phonon coupling, as shown in Figure 6c,d. Since the DC field strength in Figure 6d is larger than that in Figure 6c, the carrier wave packet

in Figure 6c becomes more localized than its counterpart in Figure 6d.

Figure 7 is for the resonant cases of  $\delta = 0$ . Figure 7a characterizes the time evolution of the carrier wave packet between the bifurcated motion and the directed motion. As the phase  $\phi_{ac}$  increases from 0 to  $\pi/2$ , the bifurcated motion of the carrier wave packet morphs toward the directed motion, but cannot turn into complete directed motion due to the two-site-centered initial condition. Figure 7b shows the directed motion of the polaron as well as superimposed BOs, if a Gaussian wave packet of  $\sigma_0 = 2.0$  is used initially. The center-of-mass of the carrier wave packet



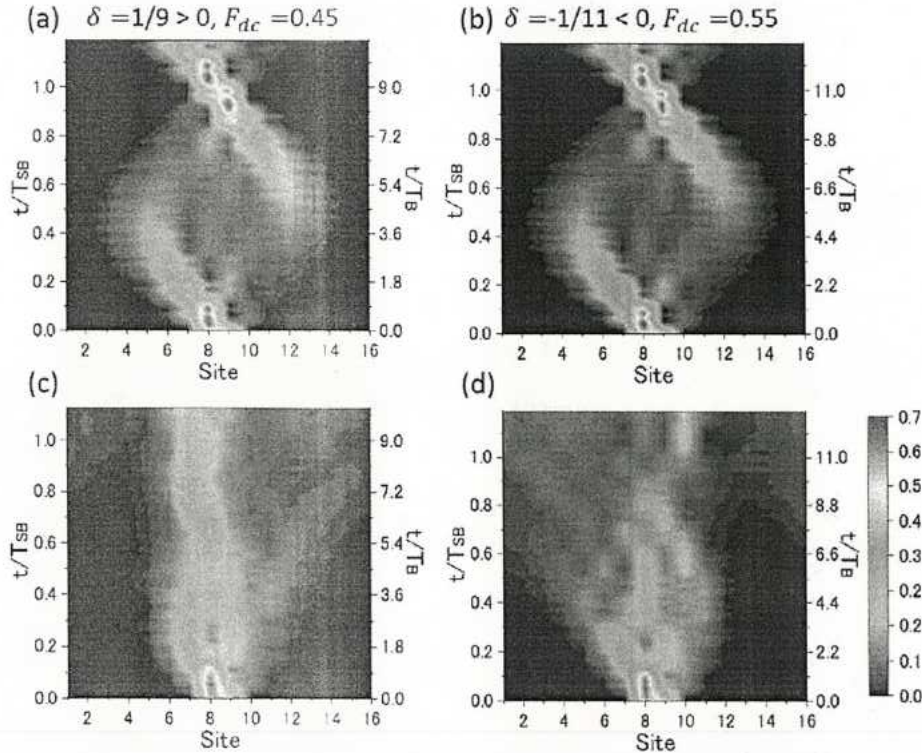


**Figure 6.** Time evolution of the carrier probability  $P_{ca}(t, n)$  for detuned cases with the nonzero phase  $\phi_{ac} = \pi/2$ . In the left panels,  $\delta = 1/9$  and  $F_{dc} = 0.45$ . In the right panels,  $\delta = -1/11$  and  $F_{dc} = 0.55$ . The carrier–phonon coupling strength is  $g = 0$  in the upper panels, and  $g = 0.5$  in the lower panels. The two-site-centered initial condition is used. Other parameters are  $M = 16$ ,  $N = 16$ ,  $J = 0.1$ ,  $F_{ac} = 1.0$ , and  $\omega_{ac} = 0.5$ .

moves with a certain speed to the left-hand side and with its wave packet shape kept. It can be found that the velocity of the carrier in Figure 7b agrees with that of the main branch in Figure 7a. The group velocity of the carrier is

$$v_g = -J \cos \left( k + \frac{F_{ac}}{\omega_{ac}} \cos \phi_{ac} - \phi_{ac} + \delta \omega t \right) \mathcal{J}_1 \left( \frac{F_{ac}}{\omega_{ac}} \right) \quad (21)$$

where  $k$  is the carrier momentum and  $\mathcal{J}_1$  is the Bessel function of order  $n = 1$ .<sup>[27]</sup> Due to  $\delta = 0$  in the resonant cases, the group velocity becomes a time-independent constant value of  $J \cos(k + \frac{F_{ac}}{\omega_{ac}} \cos \phi_{ac} - \phi_{ac}) \mathcal{J}_1(\frac{F_{ac}}{\omega_{ac}})$ , leading to the directed motion of the carrier. By the addition of the carrier–phonon coupling in the resonant cases with a nonzero AC phase, the wave packet is broadened during the evolution and the carrier motion becomes slower than the movement of the bare carrier. Haller et al. has reported that by varying the AC phases and detuning parameters, the shape of the wave packet can be greatly changed.<sup>[43]</sup> Their conclusion agrees with our findings in the absence of the carrier–phonon coupling in this section. In addition, our study shows that the application of carrier–phonon coupling allows for adjustment of the shape of the wave packet and the oscillation amplitude.

#### 4. Conclusion

In our previous work,<sup>[13]</sup> we studied the intriguing role played by the carrier–phonon coupling in the dynamics of a Holstein po-

laron under the influence of a DC external field. In this work, we extend our formulism to investigate the influence of an AC external field. Following the Dirac–Frenkel time-dependent variational principle, the polaron dynamics under the AC field is probed by employing the multi- $D_2$  Ansatz. It is revealed that the direction of carrier wave package centroid movement can be engineered by tuning  $\delta$  and  $F_{dc}$  under the two-site-centered initial condition. The carrier transport can also be modulated by varying the AC phase  $\phi_{ac}$ . If  $\phi_{ac} = 0$ , SBOs appear in the detuned case of  $\delta \neq 0$ , while bifurcated motion of the wave packet is found in the resonant case of  $\delta = 0$ . After adding the carrier–phonon coupling, the carrier states become localized in the detuned scenarios, leading to clear suppression of the carrier wave packet motion. For the resonant cases, the carrier–phonon coupling breaks the bifurcated motion of the carrier wave packet, and shifts the carrier away from the original positions. If  $\phi_{ac} = \pi/2$ , the carrier–phonon coupling destroys the modulated patterns of the SBOs in the detuned case. Using a broad Gaussian wave packet as the initial state, the centroid of carrier wave packet moves with a certain velocity and with its shape unchanged in the resonant cases. Adding the carrier–phonon coupling broadens the carrier wave packet and slows down the carrier movement. A detailed understanding of the transport mechanism of multiple carriers under an external field is of great interest and awaits future investigations. In addition, the coherent superpositions of BOs and Zener tunneling between minibands of a binary lattice, also known as Bloch–Zener oscillations,<sup>[80,81]</sup> have been experimentally demonstrated for light waves in curved femtosecond

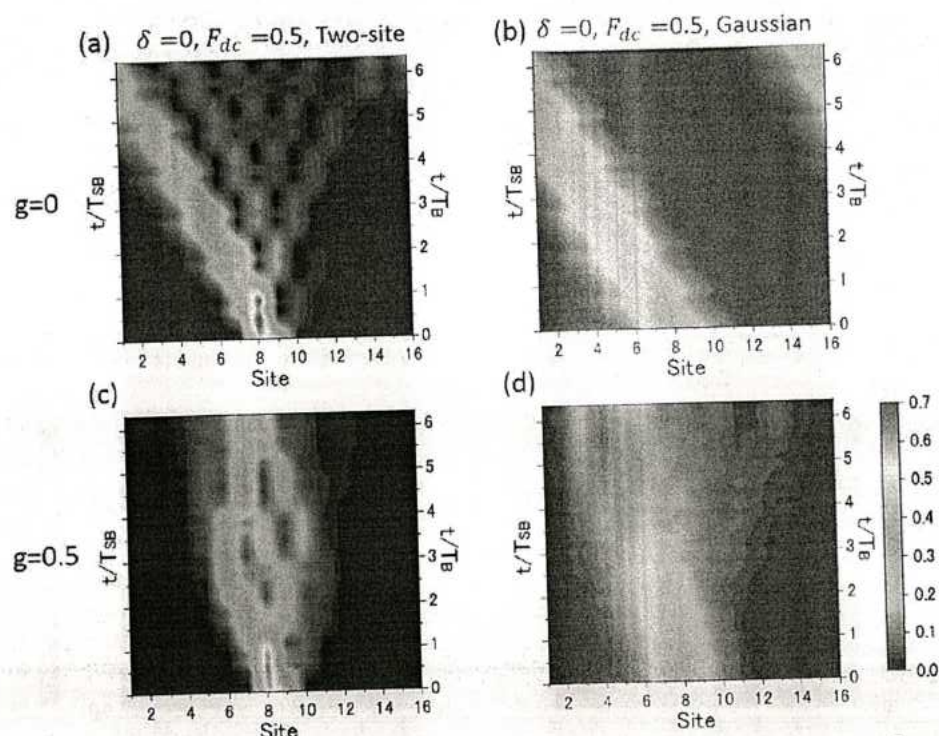


**Figure 7.** Time evolution of the carrier probability  $P_{\text{ex}}(t, n)$  for resonant cases ( $\delta = 0$ ) with the nonzero phase  $\phi_{\text{ac}} = \pi/2$ . Left panels with the two-site-centered initial condition, and right panels with the Gaussian initial condition of  $\sigma_0 = 2$ . The carrier-phonon coupling strength is  $g = 0$  in the upper panels, and  $g = 0.5$  in the lower panels. Other parameters are  $M = 16$ ,  $N = 16$ ,  $J = 0.1$ ,  $F_{\text{ac}} = 1.0$ , and  $\omega_{\text{ac}} = 0.5$ .

laser-written waveguide arrays.<sup>[82]</sup> Work on simulating Bloch-Zener dynamics is in progress.

Received: August 13, 2018  
Revised: November 1, 2018  
Published online: December 10, 2018

## Supporting Information

Supporting Information is available from the Wiley Online Library or from the author.

## Acknowledgements

Support from the Singapore National Research Foundation through the Competitive Research Programme (Project No. NRF-CRP5-2009-04) and the Singapore Ministry of Education Academic Research Funds (Grant Nos. RG106/15 and RG102/17) is gratefully acknowledged.

## Conflict of Interest

The authors declare no conflict of interest.

## Keywords

carrier-phonon coupling, Davydov Ansatz, polaron dynamics, super Bloch oscillations

- [1] J. Feldmann, K. Leo, J. Shah, D. A. B. Miller, J. E. Cunningham, T. Meier, G. von Plessen, A. Schulze, P. Thomas, S. Schmitt Rink, *Phys. Rev. B* **1992**, 46, 7252.
- [2] F. Bloch, *Zeitschrift Für Phys.* **1928**, 52, 555.
- [3] C. Zener, *Proc. R. Soc. A* **1934**, 145, 523.
- [4] J. N. Churchill, F. E. Holmstrom, *Phys. Scr.* **1983**, 27, 91.
- [5] G. H. Wannier, *Phys. Rev.* **1960**, 117, 432.
- [6] W. V. Houston, *Phys. Rev.* **1940**, 57, 184.
- [7] L. Esaki, R. Tsu, *IBM J. Res. Dev.* **1970**, 14, 61.
- [8] B. P. Anderson, M. A. Kasevich, *Science* **1998**, 282, 1686.
- [9] A. R. Kolovsky, E. A. Gomez, H. J. Korsch, *Phys. Rev. A* **2010**, 81, 025603.
- [10] M. Cristiani, O. Morsch, J. H. Müller, D. Ciampini, E. Arimondo, *Phys. Rev. A* **2002**, 65, 063612.
- [11] M. Holthaus, D. W. Hone, *Phil. Mag. B* **1996**, 74, 105.
- [12] H. Fukuyama, R. A. Bari, H. C. Fogedby, *Phys. Rev. B* **1973**, 8, 5579.
- [13] Z. Huang, L. Chen, N. Zhou, Y. Zhao, *Ann. Phys. (Berlin)* **2017**, 529, 1600367.
- [14] L. A. Ribeiro, W. F. da Cunha, P. H. de Oliveria Neto, R. Gargano, G. M. e Silva, *New J. Chem.* **2013**, 37, 2829.
- [15] L. A. Ribeiro Junior, S. Stafström, *Phys. Chem. Chem. Phys.* **2015**, 17, 8973.
- [16] M. L. Pereira Junior, L. A. Ribeiro Junior, *J. Mol. Model.* **2017**, 23, 257.



- [17] a) V. D. Lakhno, N. S. Fialko, *Pis'ma v Zh. Èksper. Teoret. Fiz.* **2004**, 79, 575; b) *J. Exp. Theor. Phys. Lett.* **2004**, 79, 464.
- [18] V. D. Lakhno, A. N. Korshunova, *Eur. Phys. J. B* **2007**, 55, 85.
- [19] V. D. Lakhno, *Int. J. Quantum Chem.* **2010**, 110, 127.
- [20] V. D. Lakhno, A. N. Korshunova, *Eur. Phys. J. B* **2011**, 79, 147.
- [21] B. Friedrich, D. R. Herschbach, J.-M. Rost, H.-G. Rubahn, M. Renger, M. Verbeek, *J. Chem. Soc. Faraday Trans.* **1993**, 89, 1539.
- [22] R. Morandotti, U. Peschel, J. S. Aitchinson, H. S. Eisenberg, Y. Silberberg, *Phys. Rev. Lett.* **1999**, 83, 4756.
- [23] T. Pertsch, P. Dannberg, W. Elfein, A. Bräuer, *Phys. Rev. Lett.* **1999**, 83, 4752.
- [24] Z. Turker, C. Yuce, *Phys. Lett. A* **2016**, 380, 2260.
- [25] C. Herrero-Gómez, E. Díaz, F. Domínguez-Adame, *Phys. Lett. A* **2012**, 376, 555.
- [26] K. Kudo, T. Boness, T. S. Monteiro, *Phys. Rev. A* **2009**, 80, 63409.
- [27] K. Kudo, T. S. Monteiro, *Phys. Rev. A* **2011**, 83, 53627.
- [28] P. Rivière, O. Uhden, U. Saalmann, J. M. Rost, *New J. Phys.* **2009**, 11, 53011.
- [29] C. Gnodtke, U. Saalmann, J. M. Rost, *Phys. Rev. A* **2009**, 79, 41201.
- [30] A. Alberti, V. V. Ivanov, G. M. Tino, G. Ferrari, *Nat. Phys.* **2009**, 5, 547.
- [31] A. Alberti, G. Ferrari, V. V. Ivanov, M. L. Chiofalo, G. M. Tino, *New J. Phys.* **2010**, 12, 65037.
- [32] G. Lenz, R. Parker, M. C. Wanke, C. M. de Sterke, *Opt. Commun.* **2003**, 218, 87.
- [33] D. Huang, S. K. Lyo, G. Gumbs, *Phys. Rev. B* **2009**, 79, 155308.
- [34] R.-B. Liu, B.-F. Zhu, *Phys. Rev. B* **1999**, 59, 5759.
- [35] D. H. Dunlap, V. M. Kenkre, *Phys. Rev. B* **1986**, 34, 3625.
- [36] D. Cai, A. R. Bishop, N. Gronbech-Jensen, M. Salerno, *Phys. Rev. Lett.* **1995**, 74, 1186.
- [37] M. Holthaus, D. W. Hone, *Philos. Mag. Part B* **1996**, 74, 41.
- [38] M. M. Dignam, C. M. de Sterke, *Phys. Rev. Lett.* **2002**, 88, 46806.
- [39] B. J. Keay, S. Zeuner, S. J. Allen, K. D. Maranowski, A. C. Gossard, U. Bhattacharya, M. J. W. Rodwell, *Phys. Rev. Lett.* **1995**, 75, 4102.
- [40] V. V. Ivanov, A. Alberti, M. Schioppa, G. Ferrari, M. Artoni, M. L. Chiofalo, G. M. Tino, *Phys. Rev. Lett.* **2008**, 100, 043602.
- [41] A. R. Kolovsky, *Phys. Rev. A* **2010**, 82, 11601.
- [42] E. Díaz, A. G. Mena, K. Asakura, C. Gaul, *Phys. Rev. A* **2013**, 87, 15601.
- [43] E. Haller, R. Hart, M. J. Mark, J. G. Danzl, L. Reichsöllner, H.-C. Nägerl, *Phys. Rev. Lett.* **2010**, 104, 200403.
- [44] A. R. Kolovsky, H. J. Korsch, *J. Sib. Fed. Univ. Math. Phys.* **2010**, 3, 311.
- [45] Q. Thommen, J. C. Garreau, V. Zehnle, *Phys. Rev. A* **2002**, 65, 53406.
- [46] H. J. Korsch, S. Mossmann, *Phys. Lett. A* **2003**, 317, 54.
- [47] R. A. Caetano, M. L. Lyra, *Phys. Lett. A* **2011**, 375, 2770.
- [48] K. K. Thornber, R. P. Feynman, *Phys. Rev. B* **1970**, 1, 4099.
- [49] R. Kümmel, H. Rauh, E. Bangert, *Phys. Status Solidi* **1978**, 87, 99.
- [50] D. Emin, C. F. Hart, *Phys. Rev. B* **1987**, 36, 2530.
- [51] M. Holthaus, G. H. Ristow, D. W. Hone, *Phys. Rev. Lett.* **1995**, 75, 3914.
- [52] S. Longhi, G. D. Valle, *Phys. Rev. B* **2012**, 86, 75143.
- [53] L. Vidmar, J. Bonča, M. Mierzejewski, P. Prelovšek, S. A. Trugman, *Phys. Rev. B* **2011**, 83, 134301.
- [54] A. Johansson, S. Stafström, *Phys. Rev. Lett.* **2001**, 86, 3602.
- [55] D. M. Basko, E. M. Conwell, *Phys. Rev. Lett.* **2002**, 88, 056401.
- [56] S. Komineas, G. Kalosakas, A. R. Bishop, *Phys. Rev. E* **2002**, 65, 61905.
- [57] M. Mierzejewski, J. Bonča, P. Prelovšek, *Phys. Rev. Lett.* **2011**, 107, 126601.
- [58] D. Golež, J. Bonča, L. Vidmar, *Phys. Rev. B* **2012**, 85, 144304.
- [59] M. Mierzejewski, J. Bonča, J. Dajka, *Phys. Rev. A* **2015**, 91, 52112.
- [60] J. Zak, *Phys. Rev. Lett.* **1968**, 20, 1477.
- [61] J. B. Kreger, G. J. Iafrate, *Phys. Rev. B* **1986**, 33, 5494.
- [62] C. Kittel, *Quantum Theory of Solids*, Wiley, New York **1987**.
- [63] J. Bonča, S. A. Trugman, *Phys. Rev. Lett.* **1997**, 79, 4874.
- [64] N. Zhou, Z. Huang, J. Zhu, V. Chernyak, Y. Zhao, *J. Chem. Phys.* **2015**, 143, 014113.
- [65] N. Zhou, L. Chen, Z. Huang, K. Sun, Y. Tanimura, Y. Zhao, *J. Phys. Chem. A* **2016**, 120, 1562.
- [66] M. Werther, F. Grossmann, *Phys. Scr.* **2018**, 93, 74001.
- [67] L. Chen, M. F. Gelin, W. Domcke, Y. Zhao, *J. Phys. Chem. Lett.* **2018**, 9, 4488.
- [68] L. Wang, Y. Fujihashi, L. Chen, Y. Zhao, *J. Chem. Phys.* **2017**, 146, 124127.
- [69] Y. Fujihashi, L. Wang, Y. Zhao, *J. Chem. Phys.* **2017**, 147, 234107.
- [70] Z. Huang, L. Wang, C. Wu, L. Chen, F. Grossmann, Y. Zhao, *Phys. Chem. Chem. Phys.* **2017**, 19, 1655.
- [71] Z. Huang, Y. Fujihashi, Y. Zhao, *J. Phys. Chem. Lett.* **2017**, 8, 3306.
- [72] S. Bandyopadhyay, Z. Huang, K. Sun, Y. Zhao, *Chem. Phys.* **2018**, <https://doi.org/10.1016/j.chemphys.2018.05.019>.
- [73] Z. Huang, Y. Zhao, *Phys. Rev. A* **2018**, 97, 13803.
- [74] D. V. Shalashilin, *J. Chem. Phys.* **2009**, 130, 244101.
- [75] D. V. Makhov, C. Symonds, S. Fernandez-Alberti, D. V. Shalashilin, *Chem. Phys.* **2017**, 493, 200.
- [76] C. Symonds, J. A. Kattirtzi, D. V. Shalashilin, *J. Chem. Phys.* **2018**, 148, 184113.
- [77] E. E. Mendez, G. Bastard, *Phys. Today* **1993**, 46, 34.
- [78] W. P. Su, J. R. Schrieffer, A. J. Heeger, *Phys. Rev. Lett.* **1979**, 42, 1698.
- [79] M. Dignam, J. E. Sipe, J. Shah, *Phys. Rev. B* **1994**, 49, 10502.
- [80] F. Domínguez-Adame, *Eur. J. Phys.* **2010**, 31, 639.
- [81] B. M. Reid, D. Witthaut, H. J. Korsch, *New J. Phys.* **2006**, 8, 110.
- [82] F. Dreisow, A. Szameit, M. Heinrich, T. Pertsch, S. Nolte, A. Tlznernmann, S. Longhi, *Phys. Rev. Lett.* **2009**, 102, 76802.





## Dynamics of dissipative Landau-Zener transitions

Zhongkai Huang and Yang Zhao\*

Division of Materials Science, Nanyang Technological University, Singapore 639798, Singapore

(Received 29 September 2017; published 3 January 2018)

A nonperturbative treatment, the Dirac-Frenkel time-dependent variation is employed to examine dynamics of the Landau-Zener model with both diagonal and off-diagonal qubit-bath coupling using the multiple Davydov trial states. It is shown that steady-state transition probabilities agree with analytical predictions at long times. Landau-Zener dynamics at intermediate times is little affected by diagonal coupling, and is found to be determined by off-diagonal coupling and tunneling between two diabatic states. We investigate effects of bath spectral densities, coupling strengths, and interaction angles on Landau-Zener dynamics. Thanks to the multiple Davydov trial states, detailed boson dynamics can also be analyzed in Landau-Zener transitions. The results presented here may help provide guiding principles to manipulate the Landau-Zener transitions in circuit QED architectures by tuning off-diagonal coupling and tunneling strength.

DOI: 10.1103/PhysRevA.97.013803

## I. INTRODUCTION

The Landau-Zener (LZ) transition comes into play when the energy difference between two diabatic states is swept through an avoided level crossing. Its final transition probability was calculated by Landau and Zener in 1932 [1,2]. As one of the most fundamental phenomena in quantum dynamics, the LZ transition plays an important role in a variety of fields, including atomic and molecular physics [3–5], quantum optics [6], solid-state physics [7], chemical physics [8], and quantum information science [9]. The list of physical systems dominated by the LZ transition grows and interest in the LZ transition has been renewed recently due to its various new applications [10,11], such as a nitrogen-vacancy center spin in isotopically purified diamond [12], a microwave-driven superconducting qubit coupled to a two-level system, [13] and a spin-orbit-coupled Bose-Einstein condensate [14].

In particular, advances in circuit quantum electrodynamics (QED) devices make them promising candidates for exploration of the LZ transitions due to their potential scalability and tunable parameters over a broad range [15–17]. Circuit QED is the realization of cavity QED in superconducting quantum circuits. A superconducting flux qubit coupled to a quantum interference device [18] has been fabricated by Chiorescu *et al.*, and a charge qubit coupled to a transmission line resonator by Wallraff *et al.* [19]. These developments have paved the way to study the LZ transitions because the energy difference between the two diabatic states has been allowed to be tuned by external fields [20]. Recent measurements of the LZ transitions have been reported on an individual flux qubit within a multiqubit superconducting chip, in which qubits are set up in the compound Josephson-junction radio-frequency superconducting quantum interference device (SQUID) [21].

In any physical realization, a quantum two-state system will be affected by its environment, which may alter the effective

interaction between the two energy levels of the system. For a realistic study of a qubit manipulation via the LZ transitions, the influence of its environment is an important issue because a qubit is never completely isolated. The effects of dissipation have been studied in 1989 by Ao *et al.*, using time-dependent perturbation theory, yielding only the LZ transition probabilities at long times in the fast and slow sweeping limit [22]. Hänggi and co-workers have studied the LZ transitions and dynamics in a qubit coupled to a bath at zero temperature [23]. Temperature effects on the LZ transitions have been explored in a dissipative environment using the quasiadiabatic propagator path-integral method and the nonequilibrium Bloch equations, by which dependence of the transition probability on sweeping velocities is obtained at long times [24–27]. Nalbach *et al.* have further studied the influence of a thermal environment on a harmonically driven quantum two-state system through avoided crossings and proposed a novel rocking ratchet based on electronic double quantum dots [28]. So far most attention has been paid to the transition probabilities in the steady states, where the energy difference of the two diabatic states is much larger than the bandwidth of the bosonic bath [29]. However, understanding of LZ dynamics at intermediate times is needed. This is a time range in which the transitions have not fully taken place and the energy difference of the two diabatic states is still within the bath's bandwidth [30]. Specifically, the dependence of LZ dynamics on the bath frequency and the types of bath spectral densities is still not well-understood.

Recently, high-quality fabrication techniques and physically large shunt capacitors have been developed to reduce densities and electric participation of defects at various metal and substrate interfaces, leading to rapid progress in the performance and manipulation of the flux qubit and its environment [31]. An ohmic-type spectral density can be used to describe the qubit-bath coupling in various devices such as a superconducting circuit consisting of a transmon qubit suspended on top of a microwave guide [32], a superconducting qubit interacting with an array of coupled transmission line resonators [33], and a fabricated circuit QED architecture that

\*yzhao@ntu.edu.sg



contains a capacitively shunted flux qubit coupled capacitively to a planar transmission line resonator [34]. Egger *et al.* showed that a sub-ohmic-type spectral density can characterize the qubit-bath coupling in a multimode circuit QED setup with hybrid metamaterial transmission lines [35]. Super-ohmic-type spectral densities have been applied to characterize the flux noise on multiple flux qubits, especially when scaling up to large numbers of qubits, as was stated by Storcz *et al.* [36,37]. Nalbach *et al.* have uncovered that super-ohmic fluctuations are the main relaxation channel for a detuned double quantum dot which is driven by external voltage pulses [38]. When a superconducting persistent-current qubit is exposed to an underdamped SQUID environment, Lorentzian spectral densities have usually been found [39,40].

The dynamics of the LZ transitions at the intermediate times is influenced by the dissipative environment. Roles of the environment include fluctuations of energies of diabatic states, denoted by diagonal coupling, and environment-induced transitions between diabatic states, expressed by off-diagonal coupling. In the presence of only diagonal coupling, the dynamics of the LZ transitions have been studied by Orth *et al.*, using a stochastic Schrödinger equation [30,41]. Off-diagonal coupling has been demonstrated to exist in a number of experiments, such as in a superconducting charge qubit coupled to an on-chip microwave resonator in the strong-coupling regime [19], in a three-dimensional circuit QED architecture [31], a circuit QED device with seven qubits [42], and in a circuit QED implementation with a time-dependent transverse magnetic field [43]. However, the effects of off-diagonal coupling on LZ dynamics have not been well investigated. Recently, the multiple Davydov  $D_2$  ansatz has been developed to accurately treat the dynamics of the generalized Holstein model with simultaneous diagonal and off-diagonal coupling [44,45]. Influences of off-diagonal coupling have also been probed in the intramolecular singlet fission model using our variational approach [46].

In this work, we investigate the impacts of diagonal and off-diagonal qubit-bath coupling on the standard LZ model using the multi- $D_2$  ansatz with the Dirac-Frenkel variational principle. The converged results by the employed method agree with those from other methods. In addition, calculated probabilities in the steady states concur with analytical predictions at zero temperature, further justifying the validity of our method.

The remainder of the paper is structured as follows. In Sec. II, we present the Hamiltonian and our trial wave function, the multi- $D_2$  ansatz. In Sec. III A, a qubit coupled to a circuit oscillator is studied. In Sec. III B, the influence of bath spectral densities on the LZ transitions is investigated. Finally, the effects of coupling strengths and interaction angles on LZ dynamics are examined in Sec. III C. Conclusions are drawn in Sec. IV.

## II. METHODOLOGY

### A. Model

The total Hamiltonian of a driven two-level system interacting with a bosonic bath is given by

$$\hat{H} = \hat{H}_S + \hat{H}_B + \hat{H}_{SB}, \quad (1)$$

where the system Hamiltonian is the standard LZ Hamiltonian for an isolated two-level system, i.e.,  $\hat{H}_S = \hat{H}_{LZ}$ , with

$$\hat{H}_{LZ} = \frac{vI}{2} \sigma_z + \frac{\Delta}{2} \sigma_x, \quad (2)$$

where  $\sigma_x$  and  $\sigma_z$  are the Pauli matrices. The states,  $|\uparrow\rangle$  and  $|\downarrow\rangle$ , are eigenstates of the qubit Hamiltonian  $\frac{vI}{2} \sigma_z$ . The energy difference between the diabatic states *et* varies linearly with time (with level-crossing speed  $v > 0$ ). Tunneling strength  $\Delta$  represents intrinsic interactions between the two diabatic states and induces the transitions.

To consider the Landau-Zener transition in the presence of an environment, we model a bosonic bath of  $N$  quantum harmonic oscillators by the Hamiltonian  $\hat{H}_B$  and the qubit-bath coupling by the Hamiltonian  $\hat{H}_{SB}$  [20],

$$\begin{aligned} \hat{H}_B &= \sum_{q=1}^N \hbar \omega_q \hat{b}_q^\dagger \hat{b}_q, \\ \hat{H}_{SB} &= \sum_{q=1}^N \frac{\gamma_q}{2} (\cos \theta_q \sigma_z + \sin \theta_q \sigma_x) (\hat{b}_q^\dagger + \hat{b}_q), \end{aligned} \quad (3)$$

where  $\hbar = 1$  is assumed throughout, and  $\omega_q$  indicates the frequency of the  $q$ th mode of the bath with creation (annihilation) operator  $\hat{b}_q^\dagger$  ( $\hat{b}_q$ ).  $\gamma_q$  and  $\theta_q$  are the qubit-oscillator coupling and the interaction angle, respectively. The effect of the bosonic bath is to change the energies of the qubit via the diagonal coupling ( $\sigma_z$ ) and to induce transitions between the levels of the qubit via the off-diagonal coupling ( $\sigma_x$ ).

The environment and its coupling to the system are characterized by a spectral density function,

$$J(\omega) = \sum_q \gamma_q^2 \delta(\omega - \omega_q) = 2\alpha \omega_c^{1-s} \omega^s e^{-\omega/\omega_c}, \quad (4)$$

where  $\alpha$  is the dimensionless coupling strength,  $\omega_c$  denotes the cutoff frequency, and  $s$  determines the dependence of  $J(\omega)$  on the bath frequency  $\omega$ . The bosonic ohmic bath is specified by  $s = 1$ , and  $s < 1$  ( $s > 1$ ) denotes the sub-ohmic (super-ohmic) bath [37]. The effect of spectral density of the Lorentzian line shape on LZ dynamics will be studied in a future work.

### B. The multi- $D_2$ state

The multiple Davydov trial states with multiplicity  $M$  are essentially  $M$  copies of the corresponding single Davydov ansatz [47,48]. They were developed to investigate the polaron model [44,45,49] and the spin-boson model [46] following the Dirac-Frenkel variational principle. In the two-level system, one of the multiple Davydov trial states, i.e., the multi- $D_2$  ansatz with multiplicity  $M$ , can be constructed as

$$\begin{aligned} |D_2^M\rangle &= \sum_{i=1}^M \left\{ A_i(t) |\uparrow\rangle \exp \left[ \sum_{q=1}^N f_{iq}(t) \hat{b}_q^\dagger - \text{H.c.} \right] |0\rangle \right\} \\ &+ \sum_{i=1}^M \left\{ B_i(t) |\downarrow\rangle \exp \left[ \sum_{q=1}^N f_{iq}(t) \hat{b}_q^\dagger - \text{H.c.} \right] |0\rangle \right\}, \end{aligned} \quad (5)$$

where H.c. denotes the Hermitian conjugate, and  $|0\rangle$  is the vacuum state of the bosonic bath.  $A_i$  and  $B_i$  are time-dependent



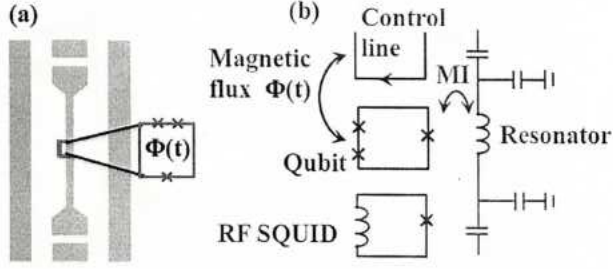


FIG. 1. (a) Schematic diagram of a typical coplanar waveguide resonator with a qubit placed between the center conductor and the ground plane of the waveguide. (b) Sketch of the superconducting qubit coupled to the coplanar transmission line resonator. MI denotes the mutual inductance between the qubit and resonator. The control line supplies the time-dependent magnetic flux  $\Phi(t)$  threading the qubit loop.

variational parameters for the amplitudes in states  $|\uparrow\rangle$  and  $|\downarrow\rangle$ , respectively, and  $f_{iq}(t)$  are the bosonic displacements, where  $i$  and  $q$  label the  $i$ th coherent superposition state and  $q$ th effective bath mode, respectively. If  $M = 1$ , the multi- $D_2$  ansatz is restored to the usual Davydov  $D_2$  trial state.

Equations of motion of the variational parameters  $u_i = A_i, B_i$  and  $f_{iq}$  are then derived by adopting the Dirac-Frenkel variational principle,

$$\frac{d}{dt} \left( \frac{\partial L}{\partial \dot{u}_i} \right) - \frac{\partial L}{\partial u_i} = 0. \quad (6)$$

For the multi- $D_2$  ansatz, the Lagrangian  $L_2$  is formulated as

$$\begin{aligned} L_2 &= \langle D_2^M(t) | \frac{i\hbar}{2} \frac{\overleftrightarrow{\partial}}{\partial t} - \hat{H} | D_2^M(t) \rangle \\ &= \frac{i\hbar}{2} \left[ \langle D_2^M(t) | \frac{\overrightarrow{\partial}}{\partial t} | D_2^M(t) \rangle - \langle D_2^M(t) | \frac{\overleftarrow{\partial}}{\partial t} | D_2^M(t) \rangle \right] \\ &\quad - \langle D_2^M(t) | \hat{H} | D_2^M(t) \rangle. \end{aligned} \quad (7)$$

Details of the Lagrangian, equations of motion, and initial conditions are given in Appendix A.

### III. RESULTS AND DISCUSSION

#### A. A qubit coupled to a single mode

The LZ transitions can occur in a qubit that is coupled to a circuit oscillator in a QED device [18,19]. Figure 1 displays the schematic diagram of a superconducting qubit coupled to a coplanar transmission line resonator. The control line in Fig. 1(b) supplies the time-dependent magnetic flux  $\Phi(t)$  threading a persistent current qubit loop, which contains three junctions. After manipulations of the qubit, the state is detected by a SQUID, which consists of a single Josephson junction in a superconducting loop [50]. By tuning the external magnetic flux  $\Phi(t)$  threading the qubit loop, the energy-level separation can vary linearly with a level-crossing speed  $v$ . The resonator

can represent a harmonic oscillator and is coupled to the qubit. Then this qubit-oscillator setup can simply be modeled by a Hamiltonian,

$$\hat{H} = \frac{vt}{2} \sigma_z + \frac{\Delta}{2} \sigma_x + \hbar\omega \hat{b}^\dagger \hat{b} + \frac{\gamma}{2} \sigma_x (\hat{b}^\dagger + \hat{b}), \quad (8)$$

which can be obtained from the Hamiltonian (1) if the number of modes is set to one ( $N = 1$ ). When the first term in Eq. (8) is replaced by a time-independent energy bias, the Hamiltonian is reduced to be the Rabi model, a paradigmatic construct of a two-level system coupled to a single bosonic mode derived from an atom in an applied electric field. A conventional rotating-wave approximation has often been adopted to treat the Rabi model [51].

Transitions between two diabatic states can result from direct tunneling or indirect off-diagonal coupling to the oscillator. The physical quantity of interest includes the probability that the qubit flipped from the initial state  $|\uparrow\rangle$  to  $|\downarrow\rangle$ , i.e.,  $P_{\uparrow \rightarrow \downarrow}(\infty) = 1 - P_{\uparrow \rightarrow \uparrow}(\infty)$ . Concerning the tunneling between the two diabatic states, the final transition probability through the avoided level-crossing point is given by the familiar Landau-Zener formula  $P_{LZ} = 1 - \exp(-\frac{\pi\Delta^2}{2\hbar|v|})$  [1,2,52–54]. With respect to the indirect off-diagonal coupling to the single-bath mode, the transition probability is proposed as  $P_{\uparrow \rightarrow \downarrow}(\infty) = 1 - \exp(-\frac{\pi\gamma^2}{2\hbar|v|})$  at zero temperature [15,20]. In this work, we have studied the combined effect of the direct tunneling between the two diabatic states and indirect off-diagonal coupling to the single-bath mode. Niemczyk *et al.* [17] using a recently developed circuit QED device showed the breakdown of the widely used rotating-wave approximation and the master-equation method due to the existence of strong qubit-bath coupling [55].

Using the time-perturbation theory [23], we obtain

$$P_{\uparrow \rightarrow \downarrow}(\infty) = 1 - \exp \left[ \frac{-\pi(\Delta^2 + \gamma^2)}{2\hbar|v|} \right]. \quad (9)$$

It has been shown that this formula can provide exact final transition probabilities for the whole parameter regime at zero temperature [15,20]. As shown in Fig. 2,  $P_{\uparrow \rightarrow \downarrow}(\infty)$  calculated

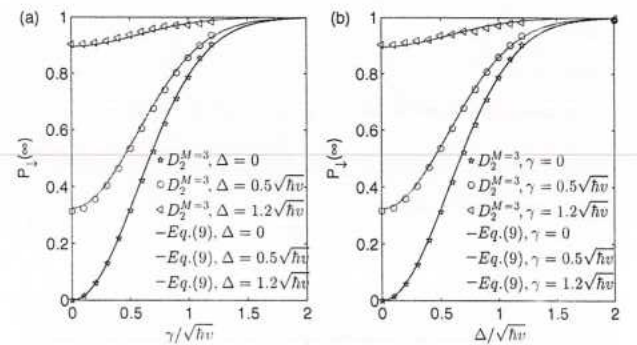


FIG. 2. (a) Final transition probability  $P_{\uparrow \rightarrow \downarrow}(\infty)$  as a function of the off-diagonal coupling strength  $\gamma/\sqrt{\hbar v}$  with fixed tunneling strengths  $\Delta = 0, 0.5\sqrt{\hbar v}$ , and  $1.2\sqrt{\hbar v}$ . (b)  $P_{\uparrow \rightarrow \downarrow}(\infty)$  as a function of the tunneling strength  $\Delta/\sqrt{\hbar v}$  for different off-diagonal coupling strengths  $\gamma = 0, 0.5\sqrt{\hbar v}$ , and  $1.2\sqrt{\hbar v}$ . The oscillator frequency  $\omega$  is set to  $10\sqrt{v/\hbar}$ .



from the multi- $D_2$  ansatz with a sufficiently large multiplicity  $M$  agree with the analytical predictions of Eq. (9) for various off-diagonal coupling strengths  $\gamma$  and tunneling strengths  $\Delta$ . This demonstrates the accuracy of our multi- $D_2$  ansatz and we can numerically provide accurate final transition probabilities.

Here we further justify the validity of the variational method by a comparison with the master-equation method that yields exact results in the weak-coupling regime. It is known that the multi- $D_2$  ansatz, a superposition of coherent states, can easily treat exciton dynamics in the strong-coupling regime [44,45,49]. To reach an accurate description in the weak-coupling cases, we have used a variety of multiplicities  $M$  of the multi- $D_2$  ansatz in the corresponding dynamical calculations. Figures 3(a)–3(c) display the time evolution of the transition probability with oscillator frequencies of  $\omega = 0.1\sqrt{v/\hbar}$ ,  $\sqrt{v/\hbar}$ , and  $10\sqrt{v/\hbar}$ , respectively. The multiplicity of the multi- $D_2$  ansatz needed for convergence, as expected, decreases as the oscillator frequency increases if the coupling strength  $\gamma$  stays constant. The converged results in each scenario concur with those extracted from Ref. [15] (black line with stars) using the master-equation method, demonstrating that the multi- $D_2$  ansatz can well describe the LZ dynamics at intermediate times when the qubit is coupled to a harmonic oscillator of a wide range of frequencies.

In order to gain insight into LZ dynamics at intermediate times, we also perform convergence tests for oscillator frequencies of  $\omega = 0.5\sqrt{v/\hbar}$  and  $20\sqrt{v/\hbar}$ , and the results are shown

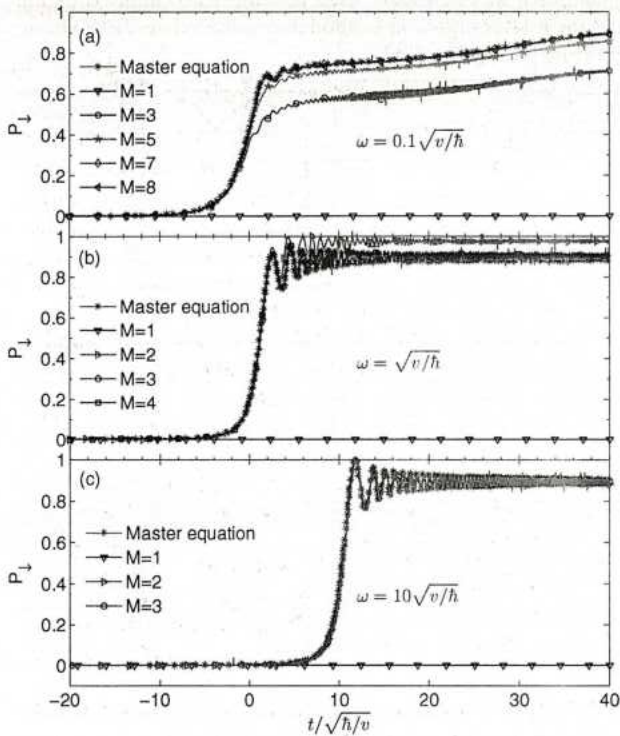


FIG. 3. Time evolution of the transition probability calculated by the master-equation method and the multi- $D_2$  ansatz. Oscillator frequencies used are (a)  $\omega = 0.1\sqrt{v/\hbar}$ , (b)  $\omega = \sqrt{v/\hbar}$ , and (c)  $\omega = 10\sqrt{v/\hbar}$ . Other parameters are  $\Delta = 0$  and  $\gamma = 1.2\sqrt{\hbar v}$ .

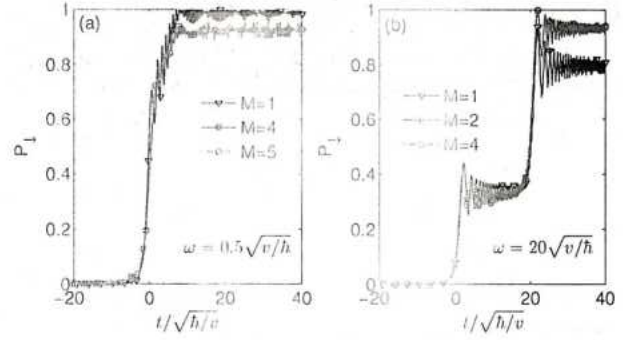


FIG. 4. LZ dynamics with a tunneling strength  $\Delta = 0.5\sqrt{\hbar v}$  and an off-diagonal coupling strength  $\gamma = 1.2\sqrt{\hbar v}$  for two oscillator frequencies (a)  $\omega = 0.5\sqrt{v/\hbar}$  and (b)  $\omega = 20\sqrt{v/\hbar}$ .

in Figs. 4(a) and 4(b), respectively. In the absence (Fig. 3) and the presence (Fig. 4) of tunneling, it can be found that LZ dynamics at intermediate times strongly depends on the oscillator frequency  $\omega$ , while the steady-state population in  $|\downarrow\rangle$ ,  $P_1(\infty)$ , is independent of  $\omega$ . In particular, the transition is temporally shifted from  $t = 0$  to  $t = \hbar\omega/v$  due to the indirect off-diagonal coupling [15]. Therefore, the time shift for the case of  $\omega = 0.5\sqrt{v/\hbar}$  is minor compared to the time scale that is concerned, leading to the LZ transition of only one stage in Fig. 4(a). In contrast,  $P_1(t)$  undergoes two stages in the LZ transitions in Fig. 4(b). The first transition stage is induced by direct tunneling between the two levels  $\Delta = 0.5\sqrt{\hbar v}$ , named after the standard LZ transition, while the second transition stage results from the indirect off-diagonal coupling to the single-oscillator mode with the frequency of  $\omega = 20\sqrt{v/\hbar}$ .

Next, we have investigated the dependence of LZ dynamics on the direct tunneling between the two diabatic states and indirect off-diagonal coupling to the single-oscillator mode. For this simulation, the oscillator frequency of  $\omega = 10\sqrt{v/\hbar}$  has been used. As shown in Fig. 5(a), by evenly changing the tunneling strength, the first plateau between the two stages of transitions can be tuned nonlinearly from zero to almost one,

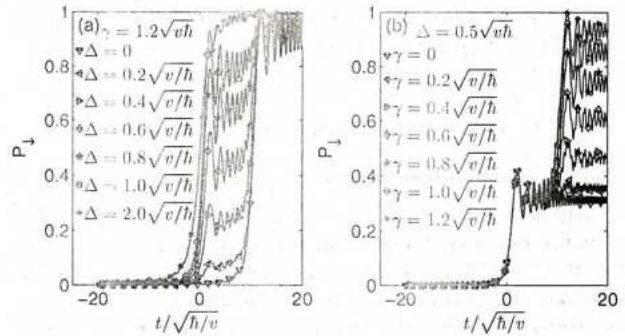


FIG. 5. LZ dynamics (a) for seven tunneling strengths  $\Delta = 0, 0.2\sqrt{\hbar v}, 0.4\sqrt{\hbar v}, 0.6\sqrt{\hbar v}, 0.8\sqrt{\hbar v}, 1.0\sqrt{\hbar v}$ , and  $2.0\sqrt{\hbar v}$  with fixed  $\gamma = 1.2\sqrt{\hbar v}$ , and (b) for different off-diagonal coupling strengths  $\gamma = 0, 0.2\sqrt{\hbar v}, 0.4\sqrt{\hbar v}, 0.6\sqrt{\hbar v}, 0.8\sqrt{\hbar v}, 1.0\sqrt{\hbar v}$ , and  $1.2\sqrt{\hbar v}$  with certain  $\Delta = 0.5\sqrt{\hbar v}$ . The oscillator frequency  $\omega$  is set to  $10\sqrt{v/\hbar}$ .



and the height of the second plateau varies from 0.89 to 1. As presented in Fig. 5(b), the first plateau is kept around 0.32 and the second plateau increases toward 1 as the off-diagonal coupling strength increases. Results in this section offer the possibility to manipulate the quantum states of the qubit that is coupled to only one circuit oscillator in the circuit QED.

### B. Effect of the bath spectral density

Recent developments in circuit QED setups have shown that qubits can couple to a bath of quantum harmonic oscillators [32–34]. The qubit-bath coupling can be characterized by spectral densities of the ohmic type in a superconducting circuit consisting of a transmon qubit suspended on top of a microwave guide [34]. Many theoretical efforts have also been devoted to study LZ transitions at long times in a dissipative environment using ohmic fluctuations [56]. Spectrum densities of the sub-ohmic and the super-ohmic type can be realized in a multimode circuit QED setup with hybrid metamaterial transmission lines [35] and in certain circuit QED setups with multiple flux qubits [36], respectively. Thus, the effects of spectral densities and coupling strengths on LZ dynamics of these systems need to be addressed.

In this section, we have studied LZ dynamics using the spectral density of Eq. (4). We have assumed that all bath oscillators couple to the qubit with identical coupling angles  $\theta_q = \theta$ . We have calculated the Huang-Rhys factor  $S = \sum_q \gamma_q^2 = \frac{\hbar^2}{4\pi} \int_0^\infty d\omega J(\omega) = \frac{\hbar^2}{2\pi} \alpha \omega_c^{s+1} \Gamma(s+1)$  and the total reorganization energy  $E_0 = \frac{\hbar}{4\pi} \int_0^\infty d\omega \frac{J(\omega)}{\omega} = \frac{\hbar}{2\pi} \alpha \omega_c^s \Gamma(s)$ , where  $\Gamma(x)$  is the Euler gamma function. Thus the final transition probability at zero temperature [23] can be given as

$$P_{\uparrow \rightarrow \downarrow}(\infty) = 1 - \exp \left\{ \frac{-\pi \left[ \left| \Delta - \frac{1}{2} E_0 \sin(2\theta) \right|^2 + S \sin^2 \theta \right]}{2\hbar v} \right\}. \quad (10)$$

When the first term in Eq. (2) is replaced by the time-independent term of  $\frac{\epsilon}{2} \sigma_z$ , the Hamiltonian (1) becomes a spin-boson Hamiltonian. When the system-bath coupling increases, a delocalization-localization transition can be found within the framework of the spin-boson model [57]. For LZ problems, however, the system always reaches a steady state with a certain final transition probability because the energy difference between the two diabatic states will be so large that transitions between the two states are unlikely at long times.

As shown in Fig. 6, we compare the LZ dynamics of the sub-ohmic, ohmic, and super-ohmic bath with the same coupling strength  $\alpha = 0.002$ . We have calculated the converged results of LZ dynamics for a qubit coupled to baths using the variational method. Spectral densities of the sub-ohmic bath are computed using logarithmic discretization. For an ohmic and super-ohmic bath, we have used linear discretization [57]. The cutoff frequency is given by  $\omega_c = 10\sqrt{v/\hbar}$ . The roughness of the curves can be significantly reduced by using a large number of frequency modes ( $N = 80$  or greater). Details of the convergence tests are presented in Appendix B.

In Figs. 6(a) and 6(b), we have presented the LZ dynamics for the sub-ohmic bath ( $s = 0.5$ ) and the ohmic bath ( $s = 1$ ), respectively. Figures 6(c) and 6(d) depict the time evolution

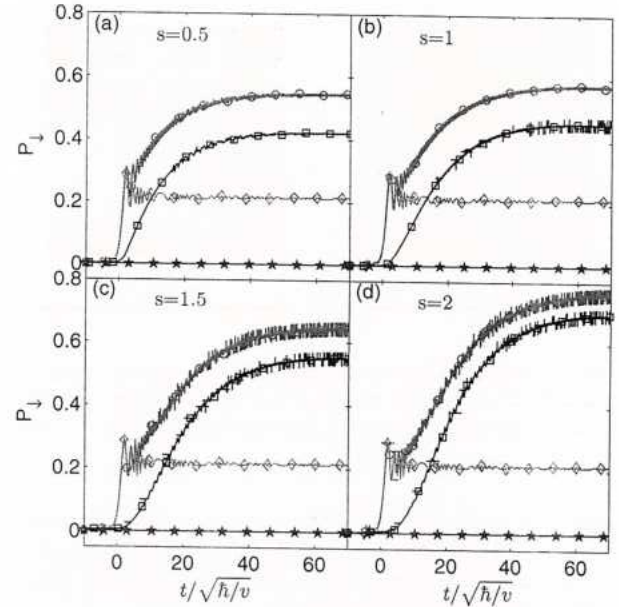


FIG. 6. Time evolution of the transition probability for (a) a sub-ohmic bath of  $s = 0.5$ , (b) an ohmic bath of  $s = 1$ , and a super-ohmic bath of (c)  $s = 1.5$  and (d)  $s = 2$  is obtained from the  $D_2^{M=3}$  ansatz with an identical coupling strength  $\alpha = 0.002$ . For each of the four  $s$  values, four cases are shown:  $\Delta = 0.4\sqrt{\hbar v}$ ,  $\theta = \pi/2$  (red line, circles),  $\Delta = 0.4\sqrt{\hbar v}$ ,  $\theta = 0$  (magenta line, diamonds),  $\Delta = 0$ ,  $\theta = \pi/2$  (black line, squares), and  $\Delta = 0$ ,  $\theta = 0$  (blue line, pentagrams).

of transition probabilities using the super-ohmic bath with  $s = 1.5$  and 2, respectively. When  $\theta = 0$ , there exists only one stage in the LZ transition near  $t = 0$  for nonzero tunneling strengths. That is, in the presence of only diagonal coupling, the LZ dynamics of  $\Delta = 0.4\sqrt{\hbar v}$  (magenta lines, diamonds) are almost identical in the four subplots, irrespective of the spectral densities. Further calculations with finite tunneling strengths have shown that there exists a one-stage LZ transition in general in the presence of diagonal coupling only.

When  $\theta = \pi/2$ , the time evolution of the transition probability for  $\Delta = 0$  has a single stage of slow growth until it reaches its steady state. The converged probabilities and the convergence times are dependent on the spectral densities. This occurs because the LZ dynamics is strongly dependent on the oscillator frequency  $\omega$  for a qubit off-diagonally coupled to a single harmonic oscillator, as has been shown in Sec. III A. Figure 6 also depicts that the convergence time for a large  $s$  is significantly longer than that for a smaller  $s$ , since spectral densities of a large  $s$  involve a prominent contribution from high-frequency oscillators, and the convergence time in the single harmonic oscillator scenario is proportional to the oscillator frequency  $\omega$ . When  $\Delta = 0.4\sqrt{\hbar v}$ , there are two stages in the LZ transitions in the presence of off-diagonal coupling. In the first stage, the transition probability jumps up at  $t = 0$ . In the second stage, it gradually reaches the steady state at the same convergence time as that of  $\Delta = 0$ . Further calculations have shown that there exist the two-stage LZ transitions in general for all nonzero tunneling strengths in the



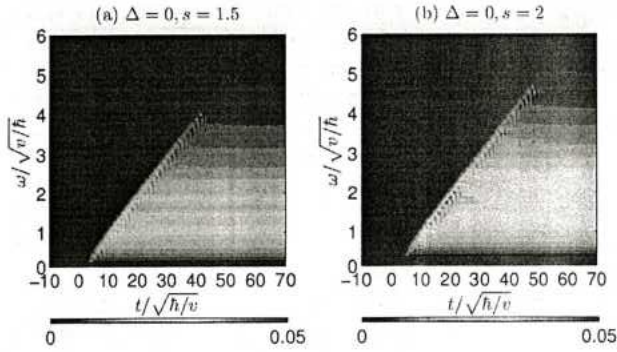


FIG. 7. Time evolution of the boson number used for a superohmic bath of (a)  $s = 1.5$  and (b)  $s = 2$ , in the presence of off-diagonal coupling only ( $\theta = \pi/2$ ). Other parameters are  $\Delta = 0$  and  $\alpha = 0.002$ .

presence of off-diagonal coupling. In addition, as expected, the converged transition probabilities obtained from our dynamics calculations agree with the corresponding steady-state transition probabilities from Eq. (10).

To investigate the role of bosons in the LZ transitions, we have calculated the time evolution of the boson number ( $\hat{b}_q^\dagger \hat{b}_q$ ), which is shown in Fig. 7. The initial boson number is set to be zero in our calculations. The bosons will be created after the transition takes place. If the qubit is only off-diagonally coupled to a single harmonic oscillator, the LZ transition will be temporally shifted from  $t = 0$  to  $t = \hbar\omega/v$ , independent of the coupling strength [15]. If the qubit is off-diagonally coupled to multiple harmonic oscillators, the transition will then occur mainly after  $t = 0$  as there is a temporal shift of each frequency mode, as shown in Fig. 7. Because the energy difference between the diabatic states varies linearly with time, the frequencies of the bosons created via qubit-bath coupling also have the same time dependence, resulting in the left edge of the triangle starting from  $t = 0$  in the  $\omega - t$  plots. It can be found that very few bosons will be created for  $t < 0$ , regardless of  $s$  and coupling strengths. When a larger value of  $s$  is used, more high-frequency bosons are created and this results in a larger steady-state probability for identical coupling strength. Also the time taken to create high-frequency mode bosons increases, which can be seen in the comparison of Figs. 7(b) and 7(a). This is expected from the convergence time taken to reach the steady states in Figs. 6(d) and 6(c).

If the energies corresponding to frequencies of the bath modes  $\omega$  are high in comparison with the thermal energy  $k_B T$ , the oscillators are thermally inactive, and thus the LZ dynamics driven by the bath modes is temperature independent in a wide temperature range [18,19]. Therefore, the temperature can be set to be  $T = 0$  to reduce the numerical cost, although the inclusion of the temperature effect in the multiple Davydov ansatz is straightforward by applying Monte Carlo importance sampling [58].

### C. Effects of coupling strength and interaction angle

Even though effects of various spectral densities have been discussed in Sec. III B, we will focus on the ohmic type in

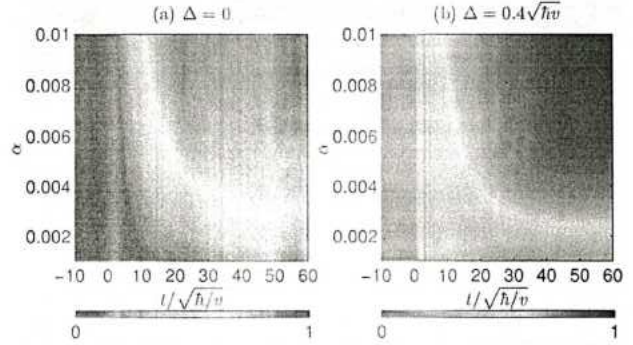


FIG. 8. Time evolution of transition probability for (a)  $\Delta = 0$  and (b)  $\Delta = 0.4\sqrt{\hbar v}$  using an ohmic bath with various coupling strengths  $\alpha$ , in the presence of off-diagonal coupling only ( $\theta = \pi/2$ ).

this section because of the recent progress in nanotechnology [59–62] which allows for feasible control of how ohmic environments are coupled to the superconducting qubit [63,64]. Figures 8(a) and 8(b) present the time evolution of the transition probability as a function of coupling strength  $\alpha$  for two values of tunneling strength,  $\Delta = 0$  and  $0.4\sqrt{\hbar v}$ , respectively. In this section, we have considered the case for off-diagonal coupling ( $\theta = \pi/2$ ) only. Calculated steady-state probabilities agree with Eq. (10), which predicts increases of the probabilities

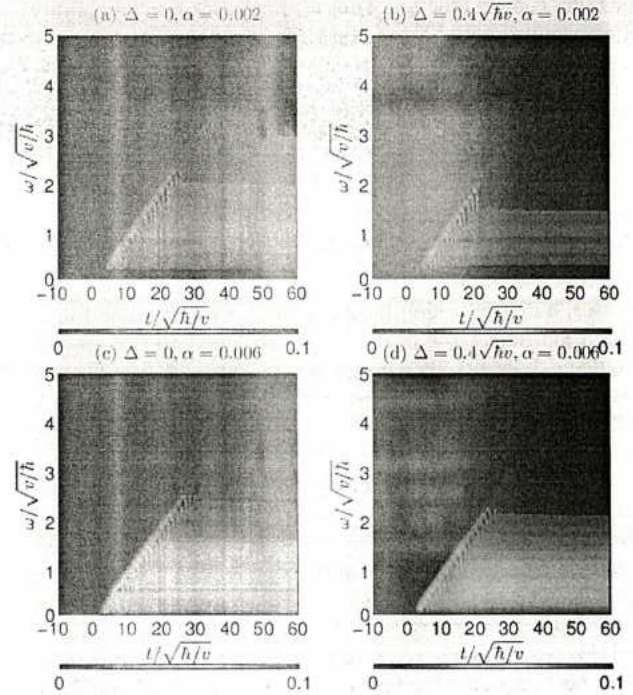


FIG. 9. Time evolution of the boson number using an ohmic bath, in the presence of off-diagonal coupling only ( $\theta = \pi/2$ ). The left column corresponds to  $\Delta = 0$ , while the right column is for  $\Delta = 0.4\sqrt{\hbar v}$ . The upper and lower panels correspond to coupling strength of  $\alpha = 0.002$  and  $\alpha = 0.006$ , respectively.



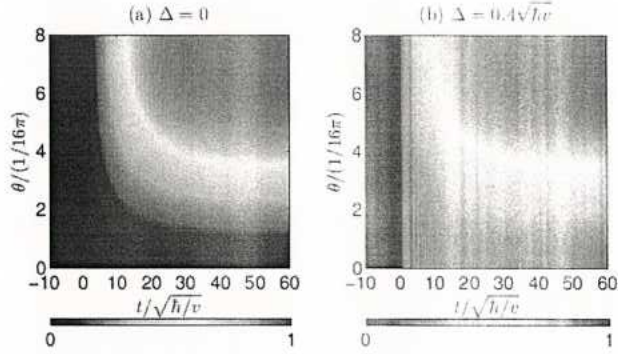


FIG. 10. Time evolution of transition probability for (a)  $\Delta = 0$  and (b)  $\Delta = 0.4\sqrt{\hbar v}$  using an ohmic bath with various interaction angles  $\theta$ . The coupling strength  $\alpha = 0.008$  is set.

with the coupling strength. While the coupling strengths for the left and right panels in Fig. 8 are the same, the steady-state probabilities of Fig. 8(b) are larger than those of Fig. 8(a) because the nonzero tunneling strength  $\Delta = 0.4\sqrt{\hbar v}$  gives rise to one more transition stage at  $t = 0$  compared to that of  $\Delta = 0$ .

The interplay between the circuit qubit and the bosons is characterized by boson dynamics as a function of  $\omega$ , as is shown in Fig. 9. The boson number is initialized to zero. The upper and lower panels correspond to coupling strengths of  $\alpha = 0.002$  and  $\alpha = 0.006$ , respectively. It was found that boson number becomes larger with stronger off-diagonal coupling. We then make a comparison between the left and right panels, in which the left column corresponds to the zero tunneling strength scenarios ( $\Delta = 0$ ) and the right column is for  $\Delta = 0.4\sqrt{\hbar v}$ . If the off-diagonal coupling strength is the same, more bosons are created for weaker tunneling scenarios, though we have larger steady-state transition probabilities for larger tunneling strength cases.

Figures 10(a) and 10(b) present the time evolution of the transition probability as a function of the interaction angle  $\theta$  for  $\Delta = 0$  and  $\Delta = 0.4\sqrt{\hbar v}$ , respectively. The interaction angle  $\theta$  of interest ranges from 0 to  $\pi/2$ . We have only considered coupling strength of  $\alpha = 0.008$  in this section.

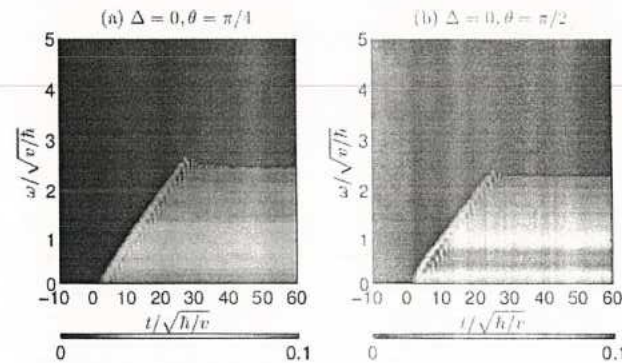


FIG. 11. Time evolution of the boson number using an ohmic bath for interaction angles of (a)  $\theta = \pi/4$  and (b)  $\theta = \pi/2$ . The tunneling strength  $\Delta = 0$  and coupling strength  $\alpha = 0.008$  are set.

In the absence and the presence of tunneling, the transition probabilities undergo the LZ transitions of one stage and two stages, respectively. The transition probabilities  $P_i(t)$  for  $t > 0$  increase with the interaction angle  $\theta$  since a larger interaction angle ( $0 \leq \theta \leq \pi/2$ ) corresponds to stronger off-diagonal coupling. The steady-state probabilities also increase with interaction angles, as expected from Eq. (10). Figure 11 displays the time evolution of the boson number for two interaction angles: (a)  $\theta = \pi/4$  and (b)  $\theta = \pi/2$ . We found that larger interaction angles ( $0 \leq \theta \leq \pi/2$ ) lead to more bosons being created during the transition stage, via stronger off-diagonal coupling.

#### IV. CONCLUSION

In this work, we have studied the intriguing role played by the dissipative environment in LZ dynamics. Following the Dirac-Frenkel time-dependent variational principle, the dynamics of the LZ model with diagonal and off-diagonal qubit-bath coupling is probed by employing the multi- $D_2$  ansatz, also known as a linear combination of the usual Davydov  $D_2$  trial states. Convergence has been ensured in the LZ dynamics calculation by monitoring the multiplicity of the multi- $D_2$  ansatz, and results agree with those of other methods. The final transition probabilities in the steady states obtained from our numerical calculations concur with the analytical predictions. It is revealed in our systematic investigations that larger interaction angles ( $0 \leq \theta \leq \pi/2$ ) and spectral densities with larger exponents and coupling strengths lead to longer transition times and greater steady-state probabilities. Finally, our boson dynamics analysis based on the multi- $D_2$  ansatz has successfully identified the contribution of specific boson modes to the LZ transitions. A detailed understanding of the mechanism using the Lorentz-type spectral density in flux qubit and multilevel transitions is of great interest and awaits further investigations.

#### ACKNOWLEDGMENTS

The authors would like to thank Qinghu Chen, Nengji Zhou, Kewei Sun, and Lipeng Chen for useful discussion. Support from the Singapore National Research Foundation through the Competitive Research Programme (CRP) under Project No. NRF-CRP5-2009-04 and from the Singapore Ministry of Education Academic Research Fund Tier 1 (Grant No. RG106/15) is gratefully acknowledged.

#### APPENDIX A: THE TIME-DEPENDENT VARIATIONAL APPROACH FOR THE DISSIPATIVE LANDAU-ZENER MODEL

In order to apply the Dirac-Frenkel time-dependent variational principle, we first need to calculate the

Lagrangian  $L_2$ ,

$$L_2 = \frac{i}{2} \sum_{i,j} (A_j^* \dot{A}_i - \dot{A}_j^* A_i + B_j^* \dot{B}_i - \dot{B}_j^* B_i) S_{ji} + \frac{i}{2} \sum_{i,j} (A_j^* A_i + B_j^* B_i) \sum_q \left[ \frac{\dot{f}_{jq}^* f_{jq} + f_{jq}^* \dot{f}_{jq}}{2} - \frac{\dot{f}_{iq} f_{iq}^* + f_{iq} \dot{f}_{iq}^*}{2} + f_{jq}^* \dot{f}_{iq} - f_{iq} \dot{f}_{jq}^* \right] S_{ji} - \langle D_2^M(t) | \hat{H} | D_2^M(t) \rangle, \quad (\text{A1})$$

where the Debye-Waller factor is  $S_{ji} = \exp \sum_q \{-(|f_{jq}|^2 + |f_{iq}|^2)/2 + f_{jq}^* f_{iq}\}$ , and the last term in Eq. (A1) can be obtained as

$$\begin{aligned} \langle D_2^M(t) | \hat{H} | D_2^M(t) \rangle &= \frac{vt}{2} \sum_{i,j} (A_j^* A_i - B_j^* B_i) S_{ji} + \frac{\Delta}{2} \sum_{i,j} (A_j^* B_i + B_j^* A_i) S_{ji} + \sum_{i,j} (A_j^* A_i + B_j^* B_i) \sum_q \omega_q f_{jq}^* f_{iq} S_{ji} \\ &+ \frac{1}{2} \sum_{i,j} (A_j^* A_i - B_j^* B_i) \sum_q \gamma_q \cos \theta_q (f_{iq} + f_{jq}^*) S_{ji} + \frac{1}{2} \sum_{i,j} (A_j^* B_i + B_j^* A_i) \sum_q \gamma_q \cos \theta_q (f_{iq} + f_{jq}^*) S_{ji}. \end{aligned} \quad (\text{A2})$$

The Dirac-Frenkel variational principle results in equations of motion for  $A_i$  and  $B_i$ ,

$$\begin{aligned} -i \sum_i \dot{A}_i S_{ki} - \frac{i}{2} \sum_i A_i \sum_q [-(\dot{f}_{iq} f_{iq}^* + f_{iq} \dot{f}_{iq}^*) + 2 f_{kq}^* \dot{f}_{iq}] S_{ki} \\ = -\frac{vt}{2} \sum_i A_i S_{ki} - \frac{\Delta}{2} \sum_i B_i S_{ki} - \sum_i A_i \sum_q \omega_q f_{kq}^* f_{iq} S_{ki} - \frac{1}{2} \sum_i A_i \sum_q \gamma_q \cos \theta_q (f_{iq} + f_{kq}^*) S_{ki} \\ - \frac{1}{2} \sum_i B_i \sum_q \gamma_q \sin \theta_q (f_{iq} + f_{kq}^*) S_{ki}, \end{aligned} \quad (\text{A3})$$

and

$$\begin{aligned} -i \sum_i \dot{B}_i S_{ki} - \frac{i}{2} \sum_i B_i \sum_q [-(\dot{f}_{iq} f_{iq}^* + f_{iq} \dot{f}_{iq}^*) + 2 f_{kq}^* \dot{f}_{iq}] S_{ki} \\ = +\frac{vt}{2} \sum_i B_i S_{ki} - \frac{\Delta}{2} \sum_i A_i S_{ki} - \sum_i B_i \sum_q \omega_q f_{kq}^* f_{iq} S_{ki} + \frac{1}{2} \sum_i B_i \sum_q \gamma_q \cos \theta_q (f_{iq} + f_{kq}^*) S_{ki} \\ - \frac{1}{2} \sum_i A_i \sum_q \gamma_q \sin \theta_q (f_{iq} + f_{kq}^*) S_{ki}. \end{aligned} \quad (\text{A4})$$

The equations of motion for  $f_{iq}$  are

$$\begin{aligned} -i \sum_i [(A_k^* \dot{A}_i + B_k^* \dot{B}_i) f_{iq} - (A_k^* A_i + B_k^* B_i) \dot{f}_{iq}] S_{ki} - \frac{i}{2} \sum_i (A_k^* A_i + B_k^* B_i) f_{iq} S_{ki} \sum_p (2 f_{kp}^* \dot{f}_{ip} - \dot{f}_{ip} f_{kp}^* - f_{ip} \dot{f}_{kp}^*) \\ = -\frac{vt}{2} \sum_i (A_k^* A_i - B_k^* B_i) f_{iq} S_{ki} - \frac{\Delta}{2} \sum_i (A_k^* B_i + B_k^* A_i) f_{iq} S_{ki} - \sum_i (A_k^* A_i + B_k^* B_i) \left( \omega_q + \sum_p \omega_p f_{kp}^* f_{ip} \right) f_{iq} S_{ki} \\ - \frac{1}{2} \sum_i (A_k^* A_i - B_k^* B_i) \gamma_q \cos \theta_q S_{ki} - \frac{1}{2} \sum_i (A_k^* A_i - B_k^* B_i) f_{iq} \sum_p \gamma_p \cos \theta_p (f_{ip} + f_{kp}^*) S_{ki} \\ - \frac{1}{2} \sum_i (A_k^* B_i + B_k^* A_i) \gamma_q \sin \theta_q S_{ki} - \frac{1}{2} \sum_i (A_k^* B_i + B_k^* A_i) f_{iq} \sum_p \gamma_p \sin \theta_p (f_{ip} + f_{kp}^*) S_{ki}. \end{aligned} \quad (\text{A5})$$

It should be noted that the main results of this work are calculated from the above equations of motion. The equations of motion are solved numerically by means of the fourth-order Runge-Kutta method. In this work, the qubit is assumed to initially occupy the state  $|\uparrow\rangle$ , i.e.,  $A_1(0) = 1$ ,  $B_1(0) = 0$ , and  $A_i(0) = B_i(0) = 0$  ( $i \neq 1$ ). The initial bosonic displacement is set to zero [ $f_{iq}(t \rightarrow -\infty) = 0$ ], though the LZ transitions have been demonstrated to depend also on various types of initial coherent superposition states [55,65].

## APPENDIX B: CONVERGENCE TEST OF LANDAU-ZENER DYNAMICS FOR THE QUBIT COUPLED TO A BATH OF QUANTUM HARMONIC OSCILLATORS

We have performed convergence tests using the multi- $D_2$  ansatz for the qubit that is coupled to a bath of harmonic oscillators. As shown in Figs. 12(a)–12(c), we have studied the effects of the multiplicity  $M$ , maximum cutoff frequency  $\omega_{\max}$ , and number of modes  $N$  on numerical calculations,



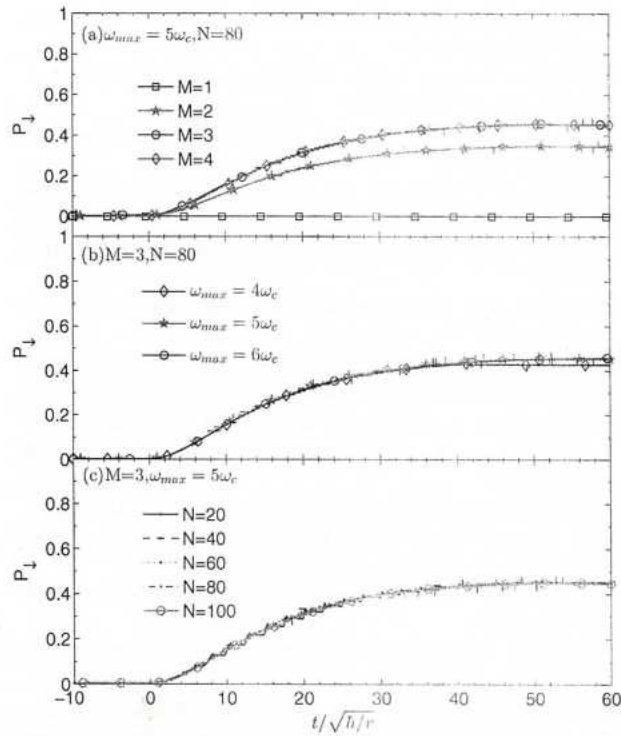


FIG. 12. Time evolution of the transition probability calculated by the multi- $D_2$  ansatz. Tested parameters are (a) number of multiplicity  $M$ , (b) maximum spectrum band frequencies  $\omega_{\max}$ , and (c) number of oscillator modes  $N$ . Other parameters are  $\Delta = 0$ ,  $\alpha = 0.002$ ,  $s = 1$ , and  $\omega_c = 10\sqrt{v/\hbar}$ .

respectively. As shown in Fig. 12(a), multiplicity  $M$  of 1, 2, 3, and 4 are adopted in the calculations. It is found that converged results can be obtained using  $M = 3$  for the studied multiple-mode scenario, which also contains low-frequency bath oscillators. In contrast, for the single low-frequency-mode case, a much larger multiplicity of  $M = 7$  is required for the convergence, as shown in Fig. 3(a). In the following, we briefly explain why a large multiplicity is not necessary in the presence of multiple low-frequency modes. As for Fig. 3, the convergence test is performed for a single-oscillator case. Before  $t = \sqrt{\hbar/v}$ , we have already obtained converged results using  $M = 3$  in the case of  $\omega = 0.1\sqrt{v/\hbar}$ . Around  $t = \sqrt{\hbar/v}$ , the LZ transition of  $\omega = \sqrt{v/\hbar}$  appears much faster than that of  $\omega = 0.1\sqrt{v/\hbar}$  before the onset of the steady state. This indicates that a small multiplicity of  $M = 3$  is sufficient to get accurate results if both frequencies of  $\omega = 0.1\sqrt{v/\hbar}$  and  $\omega = \sqrt{v/\hbar}$  are included. As for Fig. 12(a), the convergence test is performed with respect to multiple harmonic oscillators, which contain both frequencies of  $\omega = 0.1\sqrt{v/\hbar}$  and  $\omega = \sqrt{v/\hbar}$ . Therefore, the multiplicity of  $M = 3$  is satisfactory to provide accurate LZ dynamics. Meanwhile, the steady-state probability of  $M = 3$  also agrees with the analytical prediction [23]. As presented in Fig. 12(b), the maximum cutoff frequencies  $\omega_{\max}$  of  $4\omega_c$ ,  $5\omega_c$ , and  $6\omega_c$  are used with  $\omega_c = 10\sqrt{v/\hbar}$ . It can be found that  $\omega_{\max} = 5\omega_c$  is sufficient to get converged results. Figure 12(c) presents the LZ dynamics using the number of oscillator modes  $N$  of 20, 40, 60, 80, and 100. The roughness of the curves is found to be smaller as the number of modes becomes larger. After the careful convergence tests, the well-tested parameters have been applied in the numerical calculations in this work.

- [1] C. Zener, Proc. R. Soc. London A **137**, 696 (1932).
- [2] L. D. Landau, Phys. Z. Sowjetunion **2**, 46 (1932).
- [3] A. Thiel, J. Phys. G Nucl. Part. Phys. **16**, 867 (1990).
- [4] R. J. Lipert, G. Bermudez, and S. D. Colson, J. Phys. Chem. **92**, 3801 (1988).
- [5] W. Xie and W. Domcke, J. Chem. Phys. **147**, 184114 (2017).
- [6] D. Bouwmeester, N. H. Dekker, F. E. v. Dorsselaer, C. A. Schrama, P. M. Visser, and J. P. Woerdman, Phys. Rev. A **51**, 646 (1995).
- [7] W. Wernsdorfer, R. Sessoli, A. Caneschi, D. Gatteschi, and A. Cornia, Europhys. Lett. **50**, 552 (2000).
- [8] L. Zhu, A. Widom, and P. M. Champion, J. Chem. Phys. **107**, 2859 (1997).
- [9] G. D. Fuchs, G. Burkard, P. V. Klimov, and D. D. Awschalom, Nat. Phys. **7**, 789 (2011).
- [10] J. N. Onuchic and P. G. Wolynes, J. Phys. Chem. **92**, 6495 (1988).
- [11] J. R. Petta, H. Lu, and A. C. Gossard, Science **327**, 669 (2010).
- [12] J. Zhou, P. Huang, Q. Zhang, Z. Wang, T. Tan, X. Xu, F. Shi, X. Rong, S. Ashhab, and J. Du, Phys. Rev. Lett. **112**, 010503 (2014).
- [13] G. Sun, X. Wen, M. Gong, D.-W. Zhang, Y. Yu, S.-L. Zhu, J. Chen, P. Wu, and S. Han, Sci. Rep. **5**, 8463 (2015).
- [14] A. J. Olson, S.-J. Wang, R. J. Niffenegger, C.-H. Li, C. H. Greene, and Y. P. Chen, Phys. Rev. A **90**, 013616 (2014).
- [15] K. Saito, M. Wubs, S. Kohler, P. Hänggi, and Y. Kayanuma, Europhys. Lett. **76**, 22 (2006).
- [16] W. D. Oliver, Y. Yu, J. C. Lee, K. K. Berggren, L. S. Levitov, and T. P. Orlando, Science **310**, 1653 (2005).
- [17] T. Niemczyk, F. Deppe, H. Huebl, E. P. Menzel, F. Hocke, M. J. Schwarz, J. J. Garcia-Ripoll, D. Zueco, T. Hummer, E. Solano, A. Marx, and R. Gross, Nat. Phys. **6**, 772 (2010).
- [18] I. Chiorescu, P. Bertet, K. Semba, Y. Nakamura, C. J. P. M. Harmans, and J. E. Mooij, Nature (London) **431**, 159 (2004).
- [19] A. Wallraff, D. I. Schuster, A. Blais, L. Frunzio, R.-S. Huang, J. Majer, S. Kumar, S. M. Girvin, and R. J. Schoelkopf, Nature (London) **431**, 162 (2004).
- [20] M. Wubs, K. Saito, S. Kohler, P. Hänggi, and Y. Kayanuma, Phys. Rev. Lett. **97**, 200404 (2006).
- [21] J. Johansson, M. H. S. Amin, A. J. Berkley, P. Bunyk, V. Choi, R. Harris, M. W. Johnson, T. M. Lanting, S. Lloyd, and G. Rose, Phys. Rev. B **80**, 012507 (2009).
- [22] P. Ao and J. Rammer, Phys. Rev. Lett. **62**, 3004 (1989).
- [23] K. Saito, M. Wubs, S. Kohler, Y. Kayanuma, and P. Hänggi, Phys. Rev. B **75**, 214308 (2007).
- [24] P. Nalbach and M. Thorwart, Phys. Rev. Lett. **103**, 220401 (2009).

- [25] P. Nalbach, *Phys. Rev. A* **90**, 042112 (2014).
- [26] S. Javanbakht, P. Nalbach, and M. Thorwart, *Phys. Rev. A* **91**, 052103 (2015).
- [27] A. Dodin, S. Garmon, L. Simine, and D. Segal, *J. Chem. Phys.* **140**, 124709 (2014).
- [28] P. Nalbach, N. Klinkenberg, T. Palm, and N. Müller, *Phys. Rev. E* **96**, 042134 (2017).
- [29] S. Ashhab, *Phys. Rev. A* **90**, 062120 (2014).
- [30] P. P. Orth, A. Imambekov, and K. Le Hur, *Phys. Rev. B* **87**, 014305 (2013).
- [31] H. Paik, D. I. Schuster, L. S. Bishop, G. Kirchmair, G. Catelani, A. P. Sears, B. R. Johnson, M. J. Reagor, L. Frunzio, L. I. Glazman, S. M. Girvin, M. H. Devoret, and R. J. Schoelkopf, *Phys. Rev. Lett.* **107**, 240501 (2011).
- [32] J. J. García-Ripoll, B. Peropadre, and S. De Liberato, *Sci. Rep.* **5**, 16055 (2015).
- [33] H.-B. Liu, W. L. Yang, J.-H. An, and Z.-Y. Xu, *Phys. Rev. A* **93**, 020105 (2016).
- [34] F. Yan, S. Gustavsson, A. Kamal, J. Birenbaum, A. P. Sears, D. Hover, T. J. Gudmundsen, D. Rosenberg, G. Samach, S. Weber, J. L. Yoder, T. P. Orlando, J. Clarke, A. J. Kerman, and W. D. Oliver, *Nat. Commun.* **7**, 12964 (2016).
- [35] D. J. Egger and F. K. Wilhelm, *Phys. Rev. Lett.* **111**, 163601 (2013).
- [36] M. J. Storz, J. Vala, K. R. Brown, J. Kempe, F. K. Wilhelm, and K. B. Whaley, *Phys. Rev. B* **72**, 064511 (2005).
- [37] R. S. Whitney, M. Clusel, and T. Ziman, *Phys. Rev. Lett.* **107**, 210402 (2011).
- [38] P. Nalbach, J. Knörzer, and S. Ludwig, *Phys. Rev. B* **87**, 165425 (2013).
- [39] L. Tian, S. Lloyd, and T. P. Orlando, *Phys. Rev. B* **65**, 144516 (2002).
- [40] Z. Sun, L. Zhou, G. Xiao, D. Poletti, and J. Gong, *Phys. Rev. A* **93**, 012121 (2016).
- [41] P. P. Orth, A. Imambekov, and K. Le Hur, *Phys. Rev. A* **82**, 032118 (2010).
- [42] A. A. Houck, J. A. Schreier, B. R. Johnson, J. M. Chow, J. Koch, J. M. Gambetta, D. I. Schuster, L. Frunzio, M. H. Devoret, S. M. Girvin, and R. J. Schoelkopf, *Phys. Rev. Lett.* **101**, 080502 (2008).
- [43] O. Viehmann, J. von Delft, and F. Marquardt, *Phys. Rev. Lett.* **110**, 030601 (2013).
- [44] N. Zhou, Z. Huang, J. Zhu, V. Chernyak, and Y. Zhao, *J. Chem. Phys.* **143**, 014113 (2015).
- [45] Z. Huang, L. Chen, N. Zhou, and Y. Zhao, *Ann. Phys.* **529**, 1600367 (2017).
- [46] Z. Huang, Y. Fujihashi, and Y. Zhao, *J. Phys. Chem. Lett.* **8**, 3306 (2017).
- [47] Y. Zhao, B. Luo, Y. Zhang, and J. Ye, *J. Chem. Phys.* **137**, 084113 (2012).
- [48] Y. Zhao, D. W. Brown, and K. Lindenberg, *J. Chem. Phys.* **107**, 3159 (1997); **107**, 3179 (1997).
- [49] Z. Huang, L. Wang, C. Wu, L. Chen, F. Grossmann, and Y. Zhao, *Phys. Chem. Chem. Phys.* **19**, 1655 (2017).
- [50] T. Lindström, C. H. Webster, J. E. Healey, M. S. Colclough, C. M. Muirhead, and A. Y. Tzalenchuk, *Supercond. Sci. Technol.* **20**, 814 (2007).
- [51] Y.-Y. Zhang and Q.-H. Chen, *Phys. Rev. A* **91**, 013814 (2015).
- [52] C. Wittig, *J. Phys. Chem. B* **109**, 8428 (2005).
- [53] A. I. Chichinin, *J. Phys. Chem. B* **117**, 6018 (2013).
- [54] L. T. A. Ho and L. F. Chibotaru, *Phys. Chem. Chem. Phys.* **16**, 6942 (2014).
- [55] Z. Sun, J. Ma, X. Wang, and F. Nori, *Phys. Rev. A* **86**, 012107 (2012).
- [56] P. Nalbach and M. Thorwart, *Chem. Phys.* **375**, 234 (2010).
- [57] L. Wang, L. Chen, N. Zhou, and Y. Zhao, *J. Chem. Phys.*, **144**, 024101 (2016).
- [58] L. Wang, Y. Fujihashi, L. Chen, and Y. Zhao, *J. Chem. Phys.* **146**, 124127 (2017).
- [59] M. A. Castellanos-Beltrán and K. W. Lehnert, *Appl. Phys. Lett.* **91**, 83509 (2007).
- [60] V. E. Manucharyan, J. Koch, L. I. Glazman, and M. H. Devoret, *Science* **326**, 113 (2009).
- [61] C.-H. Chung, K. Le Hur, M. Vojta, and P. Wölfe, *Phys. Rev. Lett.* **102**, 216803 (2009).
- [62] I. M. Pop, I. Protopopov, F. Lecocq, Z. Peng, B. Pannetier, O. Buisson, and W. Guichard, *Nat. Phys.* **6**, 589 (2010).
- [63] P. Cedraschi, V. V. Ponomarenko, and M. Büttiker, *Phys. Rev. Lett.* **84**, 346 (2000).
- [64] A. Kopp and K. Le Hur, *Phys. Rev. Lett.* **98**, 220401 (2007).
- [65] J. Keeling and V. Gurarie, *Phys. Rev. Lett.* **101**, 033001 (2008).





Letter

pubs.acs.org/JPCLE

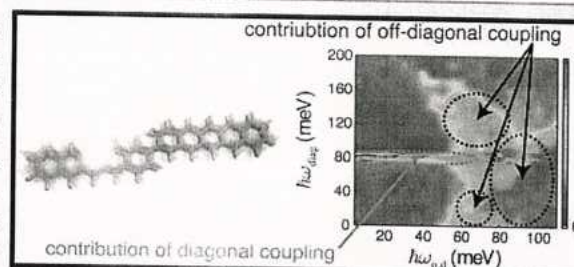
与原件相符

## Effect of Off-Diagonal Exciton–Phonon Coupling on Intramolecular Singlet Fission

Zhongkai Huang,<sup>†</sup> Yuta Fujihashi,<sup>†</sup> and Yang Zhao\*,<sup>†,‡</sup><sup>†</sup>Division of Materials Science, Nanyang Technological University, Singapore 639798, Singapore

Supporting Information

**ABSTRACT:** Intramolecular singlet fission (iSF) materials provide remarkable advantages in terms of tunable electronic structures, and quantum chemistry studies have indicated strong electronic coupling modulation by high frequency phonon modes. In this work, we formulate a microscopic model of iSF with simultaneous diagonal and off-diagonal coupling to high-frequency modes. A nonperturbative treatment, the Dirac-Frenkel time-dependent variational approach is adopted using the multiple Davydov trial states. It is shown that both diagonal and off-diagonal coupling can aid efficient singlet fission if excitonic coupling is weak, and fission is only facilitated by diagonal coupling if excitonic coupling is strong. In the presence of off-diagonal coupling, it is found that high frequency modes create additional fission channels for rapid iSF. Results presented here may help provide guiding principles for design of efficient singlet fission materials by directly tuning singlet–triplet interstate coupling.



Singlet fission (SF) is a multielectron process in which a singlet exciton generated by light irradiation is converted to two triplet excitons.<sup>1–3</sup> In 1965, SF was first coined to explain photophysics in anthracene crystals.<sup>4</sup> In recent years, interest in SF has been renewed because of its potential to increase maximum efficiency of organic solar cells.<sup>5–7</sup> As a result, SF has been studied in various organic materials of polyacenes,<sup>8</sup> polyenes,<sup>9</sup> and other chromophores, such as perylene-3,4,9,10-tetracarboxylic diimide and *tert*-butyl-substituted terrylenes.<sup>10,11</sup>

To date, most efforts have been dedicated to understanding intermolecular singlet fission (xSF), in which a singlet state on one molecule couples with the ground-state of neighboring molecules to form an intermolecular correlated triplet pair. The xSF mainly involves conventional SF materials, such as crystalline solids of pentacene,<sup>12,13</sup> tetracene,<sup>14,15</sup> and other organic materials.<sup>10,16</sup> Mechanisms of xSF have been the focus of many ultrafast spectroscopic measurements<sup>3,12–15</sup> and extensive theoretical studies based on dynamics simulations<sup>17–26</sup> and electronic structures calculations.<sup>27–31</sup> However, due to the intermolecular nature of xSF, the efficiency of this process is highly sensitive to geometric stacking, crystal environment, side-group, and other factors.<sup>24,32–34</sup> Devices based on xSF that manipulate crystal packing are limited by the lack of high throughput processing strategies of developing highly ordered molecular structures. Difficulties in engineering molecular packing morphology have promoted the development of intramolecular singlet fission (iSF), in which the two long-lived triplets are located on the same molecule.<sup>35</sup> Achieved in 2015,<sup>36</sup> iSF materials offer great advantages in terms of tunable molecular and electronic structures, and have included a series of chromophore dimers with a conjugated linker,<sup>37–41</sup> such as covalently coupled pentacenes,<sup>42,43</sup> and a covalent tetracene dimer.<sup>37</sup> Recent transient absorption measurements

for diphenyl-dicyano-oligoene groups (DPDC<sub>n</sub>) molecules have shown that xSF occurs in DPDC<sub>n</sub> in acetonitrile solution, while in DPDC<sub>n</sub> solid films, iSF dominates.<sup>44,45</sup> Based on these findings, Trinh et al. suggested that efficient SF can be achieved by independent tuning of singlet–triplet pair coupling and triplet pair splitting.<sup>45</sup> However, a limited understanding of detailed xSF and iSF mechanisms hinders the design of versatile SF materials. In particular, a unified treatment of phonon effects remains elusive.<sup>19,20,40,42,46</sup>

In organic crystals, fluctuations in electronic energies are induced by intramolecular vibrations.<sup>19,20</sup> (Note that this type of exciton–phonon coupling is often called diagonal coupling.) Recently, ultrafast spectroscopic measurements in xSF materials have shown that phonon modes coupled to electronic excitations play a crucial role in the xSF process.<sup>47–49</sup> In particular, high-frequency modes of pentacene derivatives<sup>46,50,51</sup> and crystalline tetracene<sup>52,53</sup> are found to facilitate efficient fission by resonances between vibrational modes and energy splittings of electronic states. On the other hand, intermolecular vibrations of the crystals induce off-diagonal exciton–phonon coupling, which modulates electronic coupling between the singlet and triplet pair state. Berckelbach et al. have considered off-diagonal coupling in acene crystals and demonstrated that it plays a minor role because frequencies of the intermolecular vibrations are significantly lower than the energy difference between the singlet and triplet pair state.<sup>20</sup> Effects of those forms of exciton–phonon coupling on xSF are usually restricted to particular materials such as perylene-3,4,9,10-tetracarboxylic diimide

Received: May 18, 2017

Accepted: July 3, 2017

Published: July 3, 2017



crystals.<sup>54</sup> By contrast, in the context of iSF, the transition between the singlet state and the triplet pair state occurs within a covalently linked dimer, and thus intramolecular vibrations of the linker part may induce fluctuations in the electronic coupling. Indeed, quantum chemical calculations of the covalent tetracene dimer demonstrated that high frequency intramolecular vibrations induce nonnegligible off-diagonal coupling as well as diagonal coupling.<sup>37</sup> The two kinds of coupling have been found to be tunable in a typical iSF molecule by changing linker types and by engineering dihedral angles between the chromophore units and the linker.<sup>36,42,43</sup> The corresponding iSF dynamics has been obtained by treating the exciton states quantum mechanically and phonons classically, indicating that SF time scales vary with the linker types.<sup>40,41</sup> Those investigations on exciton-phonon coupling are believed to have helped understand fast iSF observed in a broad range of organic molecules. However, detailed iSF mechanisms under the influence of simultaneous diagonal and off-diagonal exciton-phonon coupling remain ill understood, and thus a full quantum dynamical investigation is required for the elucidation of this issue.

Impacts of off-diagonal coupling on exciton dynamics in organic crystals have been investigated previously by the Munn-Silbey theory<sup>55</sup> and a variational method using the Davydov D<sub>2</sub> Ansatz.<sup>56,57</sup> Recently, Zhao and co-workers have developed a refined trial state, the multiple Davydov D<sub>2</sub> Ansatz, to accurately treat dynamics of the generalized Holstein model with simultaneous diagonal and off-diagonal coupling.<sup>58,59</sup> Within the framework of the Dirac-Frenkel time-dependent variation, accuracy of the method can be carefully monitored by quantifying how faithfully our result follows the time-dependent Schrödinger equation. In this work, this variational method will be employed to explore effects of off-diagonal coupling on iSF dynamics, and to demonstrate that high frequency phonon modes may open up additional fission channels for rapid iSF in the presence of off-diagonal coupling.

In this Letter, we focus on a dimer model of iSF dynamics on the basis of the four-electron four-orbital basis.<sup>1,35</sup> A simple scheme is considered for the iSF process,  $|g\rangle \rightarrow |S_1\rangle \rightarrow |TT\rangle$ , where  $|g\rangle$  denotes the electronic ground state,  $|S_1\rangle$  is the singlet state, and  $|TT\rangle$  represents the correlated triplet pair state. In some organic materials, the iSF and xSF processes may be accelerated by a mediated pathway, in which the singlet state converts to a triplet pair state via the charge transfer (CT) state. Quantum chemistry calculations of acene derivatives have demonstrated that the energy of the CT state is significantly higher than that of the singlet excited states,<sup>28,31</sup> and CT states have been found not to participate in the xSF process as actual intermediates between  $S_1$  and  $TT$ .<sup>20,22–26</sup> Moreover, using electronic structures calculations and transient absorption spectroscopy, iSF has been demonstrated to occur via a direct coupling mechanism that is independent of the CT states in the covalent pentacene dimer<sup>42</sup> and tetracene dimer.<sup>37</sup> Therefore, we assume that the sole effect of the CT states is to effectively couple the  $S_1$  and  $TT$  states. We employ a system-bath Hamiltonian describing the both diagonal and off-diagonal coupling,

$$\hat{H} = \hat{H}_{\text{sys}} + \hat{H}_{\text{bath}} + \hat{H}_{\text{sys-bath}} \quad (1)$$

The first term of  $\hat{H}$  is the system Hamiltonian, and is chosen to be that of an electronically diabatic Hamiltonian for  $|g\rangle$ ,  $|S_1\rangle$ , and  $|TT\rangle$

$$\hat{H}_{\text{sys}} = \sum_{n=S_1, TT} \epsilon_n |n\rangle\langle n| + \sum_{m=S_1, TT} \sum_{n \neq m} J_{mn} |m\rangle\langle n| \quad (2)$$

where  $\epsilon_n$  is the Franck-Condon energy associated with electronic transition from  $|g\rangle$  to  $|n\rangle$ , and  $J_{mn}$  is the strength of the interstate coupling between  $S_1$  and  $TT$ .  $J_{S_1, TT}$  includes the contribution of the direct coupling between  $S_1$  and  $TT$  based on the two electron integrals<sup>1,19</sup> as well as that of the effective coupling created by quantum mixing of CT and electronic states. Second term of  $\hat{H}$  represents the bath Hamiltonian  $\hat{H}_{\text{bath}}$  and is given by

$$\hat{H}_{\text{bath}} = \sum_q \hbar \omega_q \hat{b}_q^\dagger \hat{b}_q \quad (3)$$

where  $\omega_q$  indicates the frequency of the  $q$ th mode of the bath with creation operator,  $\hat{b}_q^\dagger$ , and annihilation operator,  $\hat{b}_q$ . The third term of  $\hat{H}$  represents the system-bath coupling,  $\hat{H}_{\text{sys-bath}}$  and is given by

$$\begin{aligned} \hat{H}_{\text{sys-bath}} = & \sum_{n=S_1, TT} |n\rangle\langle n| \sqrt{\lambda_{n,g}} \hat{E}_x \\ & + \sum_{m=S_1, TT} \sum_{n \neq m} |m\rangle\langle n| \sqrt{\lambda_{mn}^{\text{o.d.}}} \hat{E}_y \end{aligned} \quad (4)$$

where we have defined operators  $\hat{E}_x = \hbar \omega_q g_q (\hat{b}_q^\dagger + \hat{b}_q)$  and  $\hat{E}_y = \hbar \omega_q c_q (\hat{b}_q^\dagger - \hat{b}_q)$ .  $g_q$  and  $c_q$  are the diagonal and off-diagonal exciton-phonon coupling strengths between the system and  $q$ th mode, respectively.  $\lambda_{mn}$  represents the reorganization energy associated with the transition from  $|m\rangle$  to  $|n\rangle$ , and  $\lambda_{mn}^{\text{o.d.}}$  is the amplitude of fluctuations in interstate coupling between  $|m\rangle$  and  $|n\rangle$ . Details of both types of coupling are given in the Supporting Information (SI). The diagonal coupling term describes fluctuations in the electronic energies induced by intramolecular vibrations, whereas the term of off-diagonal coupling is attributed to the fluctuations in electronic coupling induced by intramolecular and intermolecular vibrations, as mentioned above. The spectral density  $J_\alpha(\omega)$  ( $\alpha = x, y$ ) is a useful measure for characterizing various forms of exciton-phonon coupling, and can be evaluated in terms of  $g_q$  ( $c_q$ ) as

$$J_x(\omega) = \frac{\pi}{2} \sum_q \hbar \omega_q^2 g_q^2 \delta(\omega - \omega_q) \quad (5)$$

$$J_y(\omega) = \frac{\pi}{2} \sum_q \hbar \omega_q^2 c_q^2 \delta(\omega - \omega_q) \quad (6)$$

In this study, we model the diagonal-coupling spectral densities using underdamped Brownian oscillators with Huang-Rhys factor,  $S_m = \lambda_{mg}/(\hbar \omega_{\text{diag}})$ , such that

$$J_x(\omega) = \frac{4\gamma_{\text{diag}} \omega_{\text{diag}}^2 \omega}{(\omega^2 - \omega_{\text{diag}}^2)^2 + 4\gamma_{\text{diag}}^2 \omega^2} \quad (7)$$

where  $\omega_{\text{diag}}$  is the vibrational frequency and  $\gamma_{\text{diag}}$  is the vibrational relaxation rate. In the iSF materials, the dominant contributions to off-diagonal coupling are from the intramolecular vibrations. Similarly, we model the off-diagonal-coupling spectral densities as



$$J_y(\omega) = \frac{4\gamma_{o,d}\omega_{o,d}^2\omega}{(\omega^2 - \omega_{o,d}^2)^2 + 4\gamma_{o,d}^2\omega^2} \quad (8)$$

where  $\omega_{o,d}$  is the vibrational frequency and  $\gamma_{o,d}$  is the vibrational relaxation rate.

The multiple Davydov trial states with multiplicity  $M$ , which are essentially  $M$  copies of the corresponding single Davydov Ansatz,<sup>58–62</sup> have been developed for the Holstein model and the spin-boson model. In the two level system description of the iSF process, one of the multiple Davydov trial states, the multi- $D_2$  Ansatz with multiplicity  $M$ , can be constructed as<sup>58,59,63,64</sup>

$$|D_2^M\rangle = \sum_{i=1}^M \sum_{n=S_1,TT} c_{in}(t) |n\rangle e^{(\sum_q f_{iq}(t) b_q^\dagger - \text{H.c.})} |0\rangle_{\text{vib}} \quad (9)$$

where H.c. denotes the Hermitian conjugate, and  $|0\rangle_{\text{vib}}$  is the vacuum state of the bosonic bath.  $c_{in}(t)$  is the time-dependent variational parameter for the amplitudes in states  $|n\rangle$ , and  $f_{iq}(t)$  denotes the phonon displacements, where  $i$  and  $q$  denote the  $i$ th coherent superposition state and  $q$ th effective bath mode, respectively. If  $M = 1$ , the multi- $D_2$  Ansatz is reduced to the usual Davydov  $D_2$  trial state. The time-dependent variational parameters  $c_{in}(t)$  and  $f_{iq}(t)$  are determined by adopting the Dirac-Frenkel variational principle. Detailed derivation of equations of motion for variational parameters are given in references elsewhere<sup>58,59,62,63</sup> and the SI.

To obtain numerical solutions to the equations of motion for the variational parameters, the continuum spectral densities  $J_x(\omega)$  and  $J_y(\omega)$  need to be discretized. In this study, the method of linear discretization is employed. The displacement  $g_q$  for each  $\omega_q$  is given by  $g_q^2 = 2J_x(\omega_q)\Delta\omega/(\pi\hbar\omega_q^2)$ . With respect to off-diagonal coupling, the displacement  $c_q$  for each  $\omega_q$  is given by  $c_q^2 = 2J_y(\omega_q)\Delta\omega/(\pi\hbar\omega_q^2)$ . The validity of our variational method for SF dynamics is carefully examined by quantifying how faithfully our result follows the Schrödinger equation in balance with the computational efficiency, as details are given in the SI.

Below we present and discuss numerical results regarding iSF dynamics in the dimer model. A simple dimer model including two excitonic states  $S_1$  and TT is adopted, and our focus is on the effect of two intramolecular vibration modes, one of which is diagonally coupled ( $\hbar\omega_{\text{diag}}$ ) to the exciton states, and the other, off-diagonally coupled ( $\hbar\omega_{o,d}$ ). A Huang–Rhys factor of 0.7 is chosen for  $S_1$ , which is estimated from fitting measured absorption spectra of acene derivatives with a theoretical spectroscopic model.<sup>65–67</sup> It is found that the reorganization energy of TT is several times larger than that of  $S_1$  in pentacene derivatives and tetracenes, and the off-diagonal coupling strength is 1 order of magnitude smaller than the diagonal coupling strength,<sup>24,68</sup> such that the Huang–Rhys factor of TT is set at  $S_{TT} = 2S_{S_1}$  throughout this work, and the off-diagonal coupling Huang–Rhys factor  $S_{S_1,TT}^{o,d} = \lambda_{S_1,TT}^{o,d}/(\hbar\omega_{o,d})$  is chosen to be 0.1. To be in line with the beating lifetime due to vibrational coherence in 2D electronic spectra of pentacene derivatives,<sup>48</sup> the vibrational relaxation rates are set to  $\gamma_{\text{diag}}^{-1} = \gamma_{o,d}^{-1} = 1$  ps. As the initial condition for our numerics, only the singlet state is excited according to the Franck–Condon principle. It has been suggested that efficient SF can be achieved by tuning the  $S_1$ –TT interstate coupling and triplet pair splitting independently.<sup>45</sup> As shown in our Hamiltonian (2), excitonic coupling  $J_{S_1,TT}$  determines the direct  $S_1$ –TT

coupling. If the frequencies of the vibrational modes  $\omega_{\text{diag}}$  and  $\omega_{o,d}$  are high compared with the thermal energy  $k_B T$ , the intramolecular vibrations are thermally inactivated, and the fission dynamics driven by the high frequency modes is temperature independent in a wide temperature range.<sup>46</sup> Thus, in this study, temperature is set to be  $T = 0$  to reduce the numerical cost, although the inclusion of the temperature effect in the multiple Davydov Ansatz is straightforward by applying Monte Carlo importance sampling.<sup>62</sup>

We first look into a scenario with weak excitonic coupling  $J_{S_1,TT} = 20$  meV and the transition energy  $\epsilon_{S_1,g} - \epsilon_{TT,g} = 100$  meV, both of which are typical values for the SF process in pentacene derivatives.<sup>20,24,48</sup> As shown in Figure 1a, the

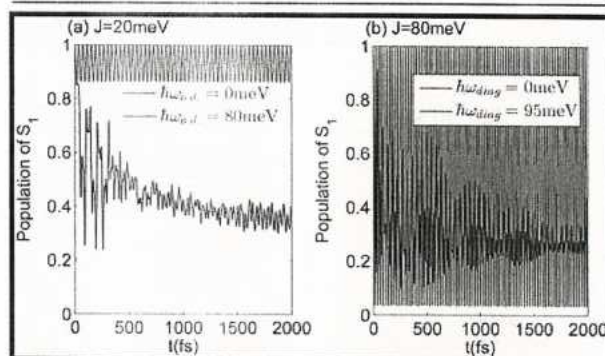


**Figure 1.** Time evolution of the singlet population for (a) the case of weak excitonic coupling  $J_{S_1,TT} = 20$  meV,  $\epsilon_{S_1,g} - \epsilon_{TT,g} = 100$  meV,  $\hbar\omega_{\text{diag}} = 0$  meV, and  $\hbar\omega_{o,d} = 80$  meV, and (b) the case of strong excitonic coupling  $J_{S_1,TT} = 80$  meV,  $\epsilon_{S_1,g} - \epsilon_{TT,g} = 30$  meV,  $\hbar\omega_{\text{diag}} = 95$  meV, and  $\hbar\omega_{o,d} = 0$  meV. The green lines correspond to cases in the absence of exciton–phonon coupling.

oscillation amplitude of population of  $S_1$  is 0.13 in the absence of exciton–phonon coupling (green line). Despite weak direct coupling, it is suggested that strong mixing between  $S_1$  and TT can be allowed with the assistance of exciton–phonon coupling.<sup>19,42</sup> In the presence of diagonal exciton–phonon coupling, the high-frequency phonon modes have been shown to facilitate the efficient SF if excitonic coupling is weak.<sup>46</sup> Here we study the impact of off-diagonal coupling on SF dynamics. As shown in Figure 1a, the population of  $S_1$  for  $\hbar\omega_{o,d} = 80$  meV, calculated by the  $D_2^{M=3}$  Ansatz, decays to 0.4 at long times, signaling an efficient SF process. For this scenario, the emission of a single off-diagonally coupled phonon can relax the initial singlet excitation to a double triplet state.<sup>54</sup> Consequently, the presence of off-diagonal coupling changes the SF process substantially if excitonic coupling is weak.

Next we turn to a case with strong excitonic coupling  $J_{S_1,TT} = 80$  meV and transition energy  $\epsilon_{S_1,g} - \epsilon_{TT,g} = 30$  meV, as strong excitonic coupling has been achieved experimentally via interchromophore bridge control in covalently linked tetracene dimers.<sup>69</sup> As shown in Figure 1b, in the absence of exciton–phonon coupling, the  $S_1$  population exhibits purely Rabi oscillations (green line), due to strong excitonic coupling. If only diagonal exciton–phonon coupling is added, the picture is changed drastically (blue line), and the system becomes trapped in the TT state. This rapid, irreversible decay of the Rabi oscillation in the SF process is owing to dissipation induced by diagonal exciton–phonon coupling, in agreement with decay dynamics in the ultrafast charge transfer process at



an oligothiophene-fullerene heterojunction.<sup>70,71</sup> However, efficient SF is not found under the influence of off-diagonal exciton–phonon coupling if excitonic coupling is strong (see the SI).

In particular, for recently developed iSF materials, such as covalent pentacene and diazadiborane dimers,<sup>37,40,42</sup> excitonic coupling strength is often smaller than the transition energy, so we choose  $J_{S_1,TT} = 20$  meV and  $\epsilon_{S_1,g} - \epsilon_{TT,g} = 100$  meV in our iSF dynamics study. Off-diagonal coupling has been found for low frequency phonon modes in teracene<sup>24,54,68</sup> and high frequency phonon modes in covalent chromophore dimers.<sup>37,40,42</sup> In order to further explore the effects of off-diagonal coupling on iSF, we examine time evolution of singlet population as functions of  $\hbar\omega_{diag}$  and  $\hbar\omega_{o.d.}$ . Figure 2 shows

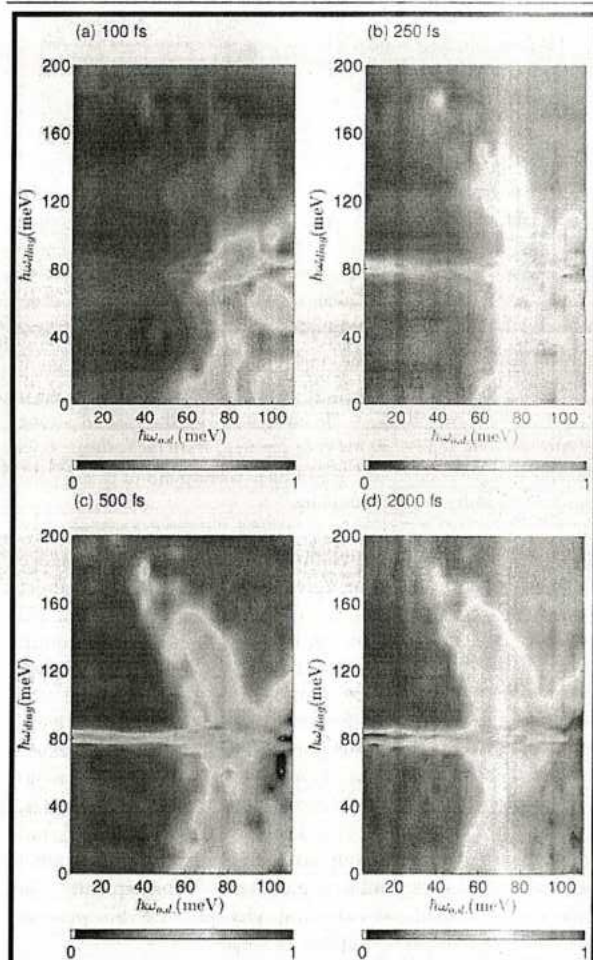


Figure 2. Snapshots of singlet population as functions of  $\hbar\omega_{diag}$  and  $\hbar\omega_{o.d.}$  at the time of (a) 100 fs, (b) 250 fs, (c) 500 fs, and (d) 2000 fs. The other parameters are  $J_{S_1,TT} = 20$  meV and  $\epsilon_{S_1,g} - \epsilon_{TT,g} = 100$  meV.

snapshots of singlet population at  $t = 100, 250, 500$ , and  $2000$  fs. On one hand, a single phonon mode of  $\hbar\omega_{diag} = 80$  meV brings about a single efficient channel for SF dynamics in the absence of off-diagonal coupling.<sup>46</sup> On the other hand, Figure 2 clearly exhibits some channels for rapid SF dynamics due to the presence of off-diagonal coupling, despite a complex dependence of efficient SF on  $\hbar\omega_{o.d.}$ . In order to better interpret this dependence, we divide the phase space into three regions,  $5 \leq$

$\hbar\omega_{o.d.} \leq 50$  meV,  $50 < \hbar\omega_{o.d.} \leq 80$  meV, and  $80 < \hbar\omega_{o.d.} \leq 110$  meV.

If  $5 \leq \hbar\omega_{o.d.} \leq 50$  meV, the SF dynamics in Figure 2c,d is driven by the phonon modes around  $\hbar\omega_{diag} = 80$  meV. Figure 3

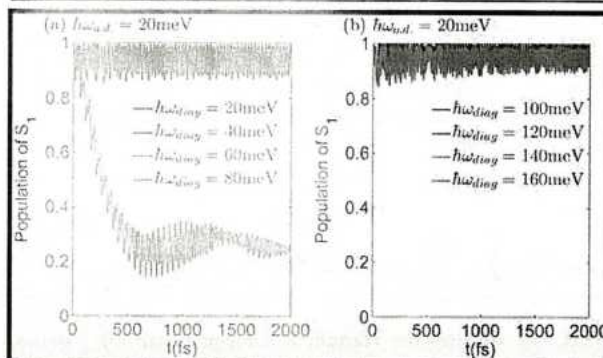


Figure 3. Time evolution of singlet population for the phonon mode  $\hbar\omega_{diag} = 20$  meV diagonally coupled to the  $S_1$  and TT states. The phonon modes off-diagonally coupled are (a)  $\hbar\omega_{o.d.} = 20, 40, 60$ , and  $80$  meV and (b)  $\hbar\omega_{o.d.} = 100, 120, 140$ , and  $160$  meV. The other parameters are same as Figure 2.

shows the time evolution of singlet population for  $\hbar\omega_{o.d.} = 20$  meV and four values of  $\hbar\omega_{diag}$ . The dependence of SF on  $\hbar\omega_{diag}$  here is qualitatively similar to that in the only diagonal coupling scenario.<sup>46</sup> Due to the low frequency phonon mode  $\hbar\omega_{o.d.}$ , the value of  $J_{S_1,TT}^{o.d.} = S_{S_1,TT}^{o.d.}\hbar\omega_{o.d.}$  is significantly lower compared with the diagonal reorganization energy, and thus SF is dominated by the resonances between vibrational modes  $\hbar\omega_{diag}$  and electronic splittings.

Concerning the intermediate region of  $50 < \hbar\omega_{o.d.} \leq 80$  meV, efficient SF is found in Figure 2 via several fission channels, including that around  $\hbar\omega_{diag} = 80$  meV. Figure 4

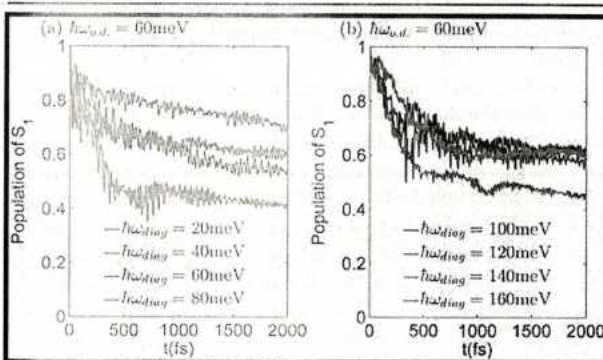


Figure 4. Time evolution of singlet population for the phonon mode  $\hbar\omega_{diag} = 60$  meV diagonally coupled to the  $S_1$  and TT states. The phonon modes off-diagonally coupled are (a)  $\hbar\omega_{o.d.} = 20, 40, 60$ , and  $80$  meV and (b)  $\hbar\omega_{o.d.} = 100, 120, 140$ , and  $160$  meV. The other parameters are same as Figure 2.

shows the time evolution of singlet population for  $\hbar\omega_{o.d.} = 60$  meV and various values of  $\hbar\omega_{diag}$ . The magenta line of  $\hbar\omega_{diag} = 80$  meV in Figure 4a and the green line of  $\hbar\omega_{diag} = 140$  meV in Figure 4b exhibit fast decay dynamics. However, SF dynamics for both cases is much slower than that in Figure 3a, because the interplay between fission dynamics and the mode  $\hbar\omega_{diag} = 80$  meV is drastically affected by the introduction of the mode  $\hbar\omega_{o.d.} = 60$  meV. What is shown in Figure 4 is compatible with



the SF mechanism with two diagonal coupled phonon modes,<sup>46</sup> in which inclusion of a second phonon mode creates a new SF channel, and if there is only diagonal coupling, shifts the optimal phonon frequency that promotes SF dynamics. However, in the presence of off-diagonal coupling, the SF channel around  $\hbar\omega_{\text{diag}} = 80$  meV is found unchanged.

As for the third region, SF dynamics is mainly facilitated by the high frequency phonon mode ( $\hbar\omega_{\text{o.d.}}$ ), as shown in Figure 2. Comparing to the first and second region, efficient SF in this region is found to be dependent on a larger number of phonon modes, in qualitative agreement with the dependence of SF on multiple phonon modes in covalent tetracene dimers.<sup>37</sup> Figure 5 presents the time evolution of singlet population for  $\hbar\omega_{\text{o.d.}} =$

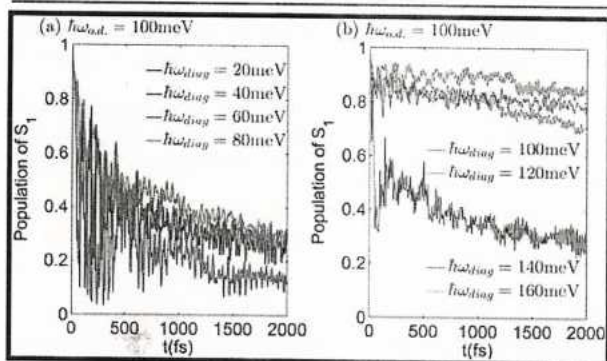


**Figure 5.** Time evolution of singlet population for the phonon mode  $\hbar\omega_{\text{diag}} = 60$  meV diagonally coupled to the  $S_1$  and TT states. The phonon modes off-diagonally coupled are (a)  $\hbar\omega_{\text{o.d.}} = 20, 40, 60,$  and  $80$  meV and (b)  $\hbar\omega_{\text{o.d.}} = 100, 120, 140,$  and  $160$  meV. The other parameters are same as Figure 2.

100 meV and different values of  $\hbar\omega_{\text{diag}}$ . Due to the high frequency phonon mode  $\hbar\omega_{\text{o.d.}}$ , the initial oscillation amplitude is much larger than 0.13, which is the oscillation amplitude in the absence of exciton–phonon coupling. The envelope of fast oscillations is found to decrease gradually owing to dissipation induced by exciton–phonon coupling. Moreover, the SF time increases with increasing  $\hbar\omega_{\text{diag}}$ .

In conclusion, we have developed a model of iSF dynamics including simultaneous diagonal and off-diagonal exciton–phonon coupling. Following the Dirac–Frenkel time-dependent variational principle, we provide an accurate description for iSF using the multi- $D_2$  Ansatz, a superposition of the usual Davydov  $D_2$  states. To our knowledge, diagonal coupling has been reported to aid efficient SF if excitonic coupling is weak,<sup>19,46</sup> and it has also been shown in this work to facilitate efficient fission if excitonic coupling is strong. Furthermore, we have demonstrated for the first time that off-diagonal coupling plays a crucial role in the fission process only if excitonic coupling is weak. It is determined that iSF dynamics strongly depends on the frequency of phonon modes in the presence of off-diagonal coupling, and high frequency phonon modes result in efficient iSF, even if the off-diagonal coupling strength is weak. Multiple SF channels can be created by the simultaneous presence of diagonal and off-diagonal coupling. Thus, a unified framework has been provided to capture the effects of diagonal and off-diagonal coupling on SF dynamics. Results presented here may help provide guiding principles for design of efficient singlet fission materials by directly tuning singlet–triplet interstate coupling.

## ■ ASSOCIATED CONTENT

### Supporting Information

The Supporting Information is available free of charge on the ACS Publications website at DOI: 10.1021/acs.jpclett.7b01247.

Details regarding the modeling intramolecular vibration, the validity of the variational method, the multi- $D_2$  Davydov trial state, and the equations of motion (PDF)

## ■ AUTHOR INFORMATION

### Corresponding Author

\*Electronic mail: YZhao@ntu.edu.sg.

### ORCID

Yang Zhao: 0000-0002-7916-8687

### Notes

The authors declare no competing financial interest.

## ■ ACKNOWLEDGMENTS

Support from the Singapore National Research Foundation through the Competitive Research Programme (CRP) under Project No. NRF-CRP5-2009-04 is gratefully acknowledged.

## ■ REFERENCES

- (1) Smith, M. B.; Michl, J. Singlet Fission. *Chem. Rev.* **2010**, *110* (11), 6891–6936.
- (2) Smith, M. B.; Michl, J. Recent Advances in Singlet Fission. *Annu. Rev. Phys. Chem.* **2013**, *64*, 361–86.
- (3) Chan, W.-L.; Berkelbach, T. C.; Provorse, M. R.; Monahan, N. R.; Tritsch, J. R.; Hybertsen, M. S.; Reichman, D. R.; Gao, J.; Zhu, X.-Y. The Quantum Coherent Mechanism for Singlet Fission: Experiment and Theory. *Acc. Chem. Res.* **2013**, *46* (6), 1321–1329.
- (4) Singh, S.; Jones, W. J.; Siebrand, W.; Stoicheff, B. P.; Schneider, W. G. Laser Generation of Excitons and Fluorescence in Anthracene Crystals. *J. Chem. Phys.* **1965**, *42* (1), 330–342.
- (5) Hanna, M. C.; Nozik, A. J. Solar Conversion Efficiency of Photovoltaic and Photoelectrolysis Cells with Carrier Multiplication Absorbers. *J. Appl. Phys.* **2006**, *100* (7), 074510.
- (6) Congreve, D. N.; Lee, J.; Thompson, N. J.; Hontz, E.; Yost, S. R.; Reuswig, P. D.; Bahlke, M. E.; Reineke, S.; Van Voorhis, T.; Baldo, M. A. External Quantum Efficiency Above 100% in a Singlet-Exciton-Fission-Based Organic Photovoltaic Cell. *Science* **2013**, *340* (6130), 334–337.
- (7) Piland, G. B.; Burdett, J. J.; Dillon, R. J.; Bardeen, C. J. Singlet Fission: From Coherences to Kinetics. *J. Phys. Chem. Lett.* **2014**, *5* (13), 2312–2319.
- (8) Ramanan, C.; Smeigh, A. L.; Anthony, J. E.; Marks, T. J.; Wasielewski, M. R. Competition between Singlet Fission and Charge Separation in Solution-Processed Blend Films of 6,13-Bis-(triisopropylsilyl)ethynyl)pentacene with Sterically-Encumbered Perylene-3,4,9,10-Bis(dicarboximide)s. *J. Am. Chem. Soc.* **2012**, *134* (1), 386–397.
- (9) Dillon, R. J.; Piland, G. B.; Bardeen, C. J. Different Rates of Singlet Fission in Monoclinic versus Orthorhombic Crystal Forms of Diphenylhexatriene. *J. Am. Chem. Soc.* **2013**, *135* (46), 17278–17281.
- (10) Eaton, S. W.; Shoer, L. E.; Karlen, S. D.; Dyar, S. M.; Margulies, E. A.; Veldkamp, B. S.; Ramanan, C.; Hartzler, D. A.; Savikhin, S.; Marks, T. J.; et al. Singlet Exciton Fission in Polycrystalline Thin Films of a Slip-Stacked Perylene-3,4,9,10-Bis(dicarboximide)s. *J. Am. Chem. Soc.* **2013**, *135* (39), 14701–14712.
- (11) Eaton, S. W.; Miller, S. A.; Margulies, E. A.; Shoer, L. E.; Schaller, R. D.; Wasielewski, M. R. Singlet Exciton Fission in Thin Films of Tert-Butyl-Substituted Terrylenes. *J. Phys. Chem. A* **2015**, *119* (18), 4151–4161.
- (12) Wilson, M. W. B.; Rao, A.; Clark, J.; Kumar, R. S. S.; Brida, D.; Cerullo, G.; Friend, R. H. Ultrafast Dynamics of Exciton Fission in



Polycrystalline Pentacene. *J. Am. Chem. Soc.* **2011**, *133* (31), 11830–11833.

(13) Chan, W.-L.; Ligges, M.; Jailaubekov, A.; Kaake, L.; Miaja-Avila, L.; Zhu, X.-Y. Observing the Multiexciton State in Singlet Fission and Ensuing Ultrafast Multielectron Transfer. *Science* **2011**, *334* (6062), 1541–1545.

(14) Chan, W.-L.; Ligges, M.; Zhu, X.-Y. The Energy Barrier in Singlet Fission Can Be Overcome through Coherent Coupling and Entropic Gain. *Nat. Chem.* **2012**, *4* (10), 840–845.

(15) Wilson, M. W. B.; Rao, A.; Johnson, K.; Glinas, S.; di Pietro, R.; Clark, J.; Friend, R. H. Temperature-Independent Singlet Exciton Fission in Tetracene. *J. Am. Chem. Soc.* **2013**, *135* (44), 16680–16688.

(16) Ma, L.; Zhang, K.; Kloc, C.; Sun, H.; Michel-Beyerle, M. E.; Gurzadyan, G. G. Singlet Fission in Rubrene Single Crystal: Direct Observation by Femtosecond Pump-Probe Spectroscopy. *Phys. Chem. Chem. Phys.* **2012**, *14* (23), 8307–8312.

(17) Greyson, E. C.; Vura-Weis, J.; Michl, J.; Ratner, M. A. Maximizing Singlet Fission in Organic Dimers: Theoretical Investigation of Triplet Yield in the Regime of Localized Excitation and Fast Coherent Electron Transfer. *J. Phys. Chem. B* **2010**, *114* (45), 14168–14177.

(18) Teichen, P. E.; Eaves, J. D. A Microscopic Model of Singlet Fission. *J. Phys. Chem. B* **2012**, *116* (37), 11473–11481.

(19) Berkelbach, T. C.; Hybertsen, M. S.; Reichman, D. R. Microscopic Theory of Singlet Exciton Fission. I. General Formulation. *J. Chem. Phys.* **2013**, *138* (11), 114102.

(20) Berkelbach, T. C.; Hybertsen, M. S.; Reichman, D. R. Microscopic Theory of Singlet Exciton Fission. II. Application to Pentacene Dimers and the Role of Superexchange. *J. Chem. Phys.* **2013**, *138* (11), 114103.

(21) Berkelbach, T. C.; Hybertsen, M. S.; Reichman, D. R. Microscopic Theory of Singlet Exciton Fission. III. Crystalline Pentacene. *J. Chem. Phys.* **2014**, *141* (7), 074705.

(22) Mirjani, F.; Renaud, N.; Gorczak, N.; Grozema, F. C. Theoretical Investigation of Singlet Fission in Molecular Dimers: The Role of Charge Transfer States and Quantum Interference. *J. Phys. Chem. C* **2014**, *118* (26), 14192–14199.

(23) Tao, G. Electronically Nonadiabatic Dynamics in Singlet Fission: A Quasi-Classical Trajectory Simulation. *J. Phys. Chem. C* **2014**, *118* (31), 17299–17305.

(24) Tamura, H.; Huix-Rotlant, M.; Burghardt, I.; Olivier, Y.; Beljonne, D. First-Principles Quantum Dynamics of Singlet Fission: Coherent versus Thermally Activated Mechanisms Governed by Molecular  $\pi$  Stacking. *Phys. Rev. Lett.* **2015**, *115* (10), 107401.

(25) Fujihashi, Y.; Ishizaki, A. Fluctuations in Electronic Energy Affecting Singlet Fission Dynamics and Mixing with Charge-Transfer State: Quantum Dynamics Study. *J. Phys. Chem. Lett.* **2016**, *7* (3), 363–369.

(26) Yao, Y. Coherent Dynamics of Singlet Fission Controlled by Nonlocal Electron-Phonon Coupling. *Phys. Rev. B: Condens. Matter Mater. Phys.* **2016**, *93* (11), 115426.

(27) Zimmerman, P. M.; Zhang, Z.; Musgrave, C. B. Singlet Fission in Pentacene through Multi-Exciton Quantum States. *Nat. Chem.* **2010**, *2* (8), 648–652.

(28) Zimmerman, P. M.; Bell, F.; Casanova, D.; Head-Gordon, M. Mechanism for Singlet Fission in Pentacene and Tetracene: From Single Exciton to Two Triplets. *J. Am. Chem. Soc.* **2011**, *133* (49), 19944–19952.

(29) Feng, X.; Luzanov, A. V.; Krylov, A. I. Fission of Entangled Spins: An Electronic Structure Perspective. *J. Phys. Chem. Lett.* **2013**, *4* (22), 3845–3852.

(30) Yost, S. R.; Lee, J.; Wilson, M. W. B.; Wu, T.; McMahon, D. P.; Parkhurst, R. R.; Thompson, N. J.; Congreve, D. N.; Rao, A.; Johnson, K.; et al. A Transferable Model for Singlet-Fission Kinetics. *Nat. Chem.* **2014**, *6* (6), 492–497.

(31) Casanova, D. Electronic Structure Study of Singlet Fission in Tetracene Derivatives. *J. Chem. Theory Comput.* **2014**, *10* (1), 324–334.

(32) Renaud, N.; Sherratt, P. A.; Ratner, M. A. Mapping the Relation between Stacking Geometries and Singlet Fission Yield in a Class of Organic Crystals. *J. Phys. Chem. Lett.* **2013**, *4* (7), 1065–1069.

(33) Wang, L.; Olivier, Y.; Prezhd, O. V.; Beljonne, D. Maximizing Singlet Fission by Intermolecular Packing. *J. Phys. Chem. Lett.* **2014**, *5* (19), 3345–3353.

(34) Lukman, S.; Chen, K.; Hodgkiss, J. M.; Turban, D. H. P.; Hine, N. D. M.; Dong, S.; Wu, J.; Greenham, N. C.; Musser, A. J. Tuning the Role of Charge-Transfer States in Intramolecular Singlet Exciton Fission through Side-Group Engineering. *Nat. Commun.* **2016**, *7*, 13622.

(35) Monahan, N.; Zhu, X.-Y. Charge Transfer-Mediated Singlet Fission. *Annu. Rev. Phys. Chem.* **2015**, *66* (1), 601–618.

(36) Busby, E.; Xia, J.; Wu, Q.; Low, J. Z.; Song, R.; Miller, J. R.; Zhu, X.-Y.; Campos, L. M.; Sfeir, M. Y. A Design Strategy for Intramolecular Singlet Fission Mediated by Charge-Transfer States in Donor-Acceptor Organic Materials. *Nat. Mater.* **2015**, *14* (4), 426–433.

(37) Alguire, E. C.; Subotnik, J. E.; Damrauer, N. H. Exploring Non-Condon Effects in a Covalent Tetracene Dimer: How Important Are Vibrations in Determining the Electronic Coupling for Singlet Fission? *J. Phys. Chem. A* **2015**, *119* (2), 299–311.

(38) Sanders, S. N.; Kumarasamy, E.; Pun, A. B.; Appavoo, K.; Steigerwald, M. L.; Campos, L. M.; Sfeir, M. Y. Exciton Correlations in Intramolecular Singlet Fission. *J. Am. Chem. Soc.* **2016**, *138* (23), 7289–7297.

(39) Varnavski, O.; Abeyasinghe, N.; Aragón, J.; Serrano-Pérez, J. J.; Ortí, E.; López Navarrete, J. T.; Takimiya, K.; Casanova, D.; Casado, J.; Goodson, T. High Yield Ultrafast Intramolecular Singlet Exciton Fission in a Quinoidal Bithiophene. *J. Phys. Chem. Lett.* **2015**, *6* (8), 1375–1384.

(40) Zeng, T. Through-Linker Intramolecular Singlet Fission: General Mechanism and Designing Small Chromophores. *J. Phys. Chem. Lett.* **2016**, *7* (21), 4405–4412.

(41) Zeng, T.; Goel, P. Design of Small Intramolecular Singlet Fission Chromophores: An Azaborine Candidate and General Small Size Effects. *J. Phys. Chem. Lett.* **2016**, *7* (7), 1351–1358.

(42) Fuemmeler, E. G.; Sanders, S. N.; Pun, A. B.; Kumarasamy, E.; Zeng, T.; Miyata, K.; Steigerwald, M. L.; Zhu, X.-Y.; Sfeir, M. Y.; Campos, L. M.; et al. A Direct Mechanism of Ultrafast Intramolecular Singlet Fission in Pentacene Dimers. *ACS Cent. Sci.* **2016**, *2* (5), 316–324.

(43) Ito, S.; Nagami, T.; Nakano, M. Design Principles of Electronic Couplings for Intramolecular Singlet Fission in Covalently-Linked Systems. *J. Phys. Chem. A* **2016**, *120* (31), 6236–6241.

(44) Meisner, J. S.; Sedbrook, D. F.; Krikorian, M.; Chen, J.; Sattler, A.; Carnes, M. E.; Murray, C. B.; Steigerwald, M.; Nuckolls, C. Functionalizing Molecular Wires: A Tunable Class of  $\alpha,\omega$ -Diphenyl- $\mu,\nu$ -Dicyano-Oligoethenes. *Chem. Sci.* **2012**, *3* (4), 1007–1014.

(45) Trinh, M. T.; Zhong, Y.; Chen, Q.; Schiros, T.; Jockusch, S.; Sfeir, M. Y.; Steigerwald, M.; Nuckolls, C.; Zhu, X. Intra- to Intermolecular Singlet Fission. *J. Phys. Chem. C* **2015**, *119* (3), 1312–1319.

(46) Fujihashi, Y.; Chen, L.; Ishizaki, A.; Wang, J.; Zhao, Y. Effect of High-Frequency Modes on Singlet Fission Dynamics. *J. Chem. Phys.* **2017**, *146* (4), 044101.

(47) Musser, A. J.; Liebel, M.; Schnedermann, C.; Wende, T.; Kehoe, T. B.; Rao, A.; Kukura, P. Evidence for Conical Intersection Dynamics Mediating Ultrafast Singlet Exciton Fission. *Nat. Phys.* **2015**, *11* (4), 352–357.

(48) Bakulin, A. A.; Morgan, S. E.; Kehoe, T. B.; Wilson, M. W. B.; Chin, A. W.; Zigmantas, D.; Egorova, D.; Rao, A. Real-Time Observation of Multiexcitonic States in Ultrafast Singlet Fission Using Coherent 2D Electronic Spectroscopy. *Nat. Chem.* **2016**, *8* (1), 16–23.

(49) Monahan, N. R.; Sun, D.; Tamura, H.; Williams, K. W.; Xu, B.; Zhong, Y.; Kumar, B.; Nuckolls, C.; Harutyunyan, A. R.; Chen, G.; et al. Dynamics of the Triplet-Pair State Reveals the Likely



Coexistence of Coherent and Incoherent Singlet Fission in Crystalline Hexacene. *Nat. Chem.* **2017**, *9* (4), 341–346.

(50) Tempelaar, R.; Reichman, D. R. Vibronic Exciton Theory of Singlet Fission. I. Linear Absorption and the Anatomy of the Correlated Triplet Pair State. *J. Chem. Phys.* **2017**, *146* (17), 174703.

(51) Tempelaar, R.; Reichman, D. R. Vibronic Exciton Theory of Singlet Fission. II. Two-Dimensional Spectroscopic Detection of the Correlated Triplet Pair State. *J. Chem. Phys.* **2017**, *146* (17), 174704.

(52) Morrison, A. F.; Herbert, J. M. Evidence for Singlet Fission Driven by Vibronic Coherence in Crystalline Tetracene. *J. Phys. Chem. Lett.* **2017**, *8*, 1442–1448.

(53) Elenewski, J. E.; Cubeta, U. S.; Ko, E.; Chen, H. Functional Mode Singlet Fission Theory. *J. Phys. Chem. C* **2017**, *121* (8), 4130–4138.

(54) Renaud, N.; Grozema, F. C. Intermolecular Vibrational Modes Speed Up Singlet Fission in Perylenediimide Crystals. *J. Phys. Chem. Lett.* **2015**, *6* (3), 360–365.

(55) Munn, R. W.; Silbey, R. Theory of Electronic Transport in Molecular Crystals. II. Zeroth Order States Incorporating Nonlocal Linear Electron-phonon Coupling. *J. Chem. Phys.* **1985**, *83* (4), 1843.

(56) Zhao, Y.; Luo, B.; Zhang, Y.; Ye, J. Dynamics of a Holstein polaron with off-diagonal coupling. *J. Chem. Phys.* **2012**, *137*, 084113.

(57) (a) Zhao, Y.; Brown, D. W.; Lindenberg, K. Variational Energy Band Theory for Polarons: Mapping Polaron Structure with the Toyozawa Method Variational Energy Band Theory for Polarons: Mapping Polaron Structure with the Toyozawa Method. *J. Chem. Phys.* **1997**, *107* (8), 3159. (b) Brown, D. W.; Lindenberg, K.; Zhao, Y. Variational Energy Band Theory for Polarons: Mapping Polaron Structure with the Global-Local Method Variational Energy Band Theory for Polarons: Mapping Polaron Structure with the Global-Local Method. *J. Chem. Phys.* **1997**, *107* (8), 3179.

(58) Zhou, N.; Huang, Z.; Zhu, J.; Chernyak, V.; Zhao, Y. Polaron dynamics with a multitude of Davydov  $D_2$  trial states. *J. Chem. Phys.* **2015**, *143*, 014113.

(59) Zhou, N.; Chen, L.; Huang, Z.; Sun, K.; Tanimura, Y.; Zhao, Y. Fast, Accurate Simulation of Polaron Dynamics and Multidimensional Spectroscopy by Multiple Davydov Trial States. *J. Phys. Chem. A* **2016**, *120*, 1562–1576.

(60) Bera, S.; Florens, S.; Baranger, H. U.; Roch, N.; Nazir, A.; Chin, A. W. Stabilizing Spin Coherence through Environmental Entanglement in Strongly Dissipative Quantum Systems. *Phys. Rev. B: Condens. Matter Mater. Phys.* **2014**, *89* (12), 121108.

(61) Zhou, N.; Chen, L.; Zhao, Y.; Mozyrsky, D.; Chernyak, V.; Zhao, Y. Ground-State Properties of Sub-Ohmic Spin-Boson Model with Simultaneous Diagonal and off-Diagonal Coupling. *Phys. Rev. B: Condens. Matter Mater. Phys.* **2014**, *90* (15), 155135.

(62) Wang, L.; Fujihashi, Y.; Chen, L.; Zhao, Y. Finite-Temperature Time-Dependent Variation with Multiple Davydov States. *J. Chem. Phys.* **2017**, *146* (12), 124127.

(63) Huang, Z.; Wang, L.; Wu, C.-Q.; Chen, L.; Grossmann, F.; Zhao, Y. Polaron Dynamics with off-Diagonal Coupling: Beyond the Ehrenfest Approximation. *Phys. Chem. Chem. Phys.* **2017**, *19* (2), 1655–1668.

(64) Huang, Z.; Chen, L.; Zhou, N.; Zhao, Y. Transient Dynamics of a One-Dimensional Holstein Polaron under the Influence of an External Electric Field. *Ann. Phys.* **2017**, *529* (3), 1600367.

(65) Yamagata, H.; Norton, J.; Hontz, E.; Olivier, Y.; Beljonne, D.; Brédas, J. L.; Silbey, R. J.; Spano, F. C. The Nature of Singlet Excitons in Oligoacene Molecular Crystals. *J. Chem. Phys.* **2011**, *134* (20), 204703.

(66) Beljonne, D.; Yamagata, H.; Brédas, J. L.; Spano, F. C.; Olivier, Y. Charge-Transfer Excitations Steer the Davydov Splitting and Mediate Singlet Exciton Fission in Pentacene. *Phys. Rev. Lett.* **2013**, *110* (22), 226402.

(67) Chen, L.; Lu, J.; Long, G.; Zheng, F.; Zhang, J.; Zhao, Y. Optical and Transport Properties of Single Crystal Rubrene: A Theoretical Study. *Chem. Phys.* **2016**, *481*, 198–205.

(68) Ito, S.; Nagami, T.; Nakano, M. Density Analysis of Intra- and Intermolecular Vibronic Couplings toward Bath Engineering for Singlet Fission. *J. Phys. Chem. Lett.* **2015**, *6* (24), 4972–4977.

(69) Vallett, P. J.; Snyder, J. L.; Damrauer, N. H. Tunable Electronic Coupling and Driving Force in Structurally Well-Defined Tetracene Dimers for Molecular Singlet Fission: A Computational Exploration Using Density Functional Theory. *J. Phys. Chem. A* **2013**, *117* (42), 10824–10838.

(70) Tamura, H.; Burghardt, I.; Tsukada, M. Exciton Dissociation at Thiophene/Fullerene Interfaces: The Electronic Structures and Quantum Dynamics. *J. Phys. Chem. C* **2011**, *115* (20), 10205–10210.

(71) Tamura, H.; Martinazzo, R.; Ruckebauer, M.; Burghardt, I. Quantum Dynamics of Ultrafast Charge Transfer at an Oligothiophene-Fullerene Heterojunction. *J. Chem. Phys.* **2012**, *137* (22), 22A540.







# Transient dynamics of a one-dimensional Holstein polaron under the influence of an external electric field

Zhongkai Huang, Lipeng Chen, Nengji Zhou, and Yang Zhao\*

与原件相符

Received 14 November 2016, revised 16 January 2017, accepted 27 January 2017  
Published online 3 March 2017

Following the Dirac-Frenkel time-dependent variational principle, transient dynamics of a one-dimensional Holstein polaron with diagonal and off-diagonal exciton-phonon coupling in an external electric field is studied by employing the multi- $D_2$  Ansatz, also known as a superposition of the usual Davydov  $D_2$  trial states. Resultant polaron dynamics has significantly enhanced accuracy, and is in perfect agreement with that derived from the hierarchy equations of motion method. Starting from an initial broad wave packet, the exciton undergoes typical Bloch oscillations. Adding weak exciton-phonon coupling leads to a broadened exciton wave packet and a reduced current amplitude. Using a narrow wave packet as the initial state, the bare exciton oscillates in a symmetric breathing mode, but the symmetry is easily broken by weak coupling to phonons, resulting in a non-zero exciton current. For both scenarios, temporal periodicity is unchanged by exciton-phonon coupling. In particular, at variance with the case of an infinite linear chain, no steady state is found in a finite-sized ring within the anti-adiabatic regime. For strong diagonal coupling, the multi- $D_2$  Ansatz is found to be highly accurate, and the phonon confinement gives rise to exciton localization and decay of the Bloch oscillations.

hibit BOs and Wannier-Stark ladders [11, 12], in accordance with theoretical predictions [13–15]. Further experimental evidence of BOs was found in atomic Bose-Einstein condensates (BEC) in optical lattices [16–18], in a semiconductor waveguide [19], and in a thermo-optic polymer array subjected to a temperature gradient [20]. It was also suggested that waveguide arrays with a changeable effective index of individual guides would be an optimal system to detect optical BOs in the space domain [21]. In addition, BOs have received much attention in the past decades for its potential application in THz generation and negative differential conductance [3]. Investigations of BOs have been carried out in THz emission [22], electro-optic detection [23], and DFWM experiments [1]. Recently, a new mesoscopic amplifier by the name of Bloch Oscillating Transistor has been proposed based on BOs [24].

Following the remarkable experimental progress, recent theoretical work explores the presence of BOs in a variety of contexts. For example, formation of photonic BOs was investigated in an exponentially chirped one-dimensional Bragg grating using Hamiltonian optics, where paths of geometrical rays are determined from Hamilton's equations [25]. BOs were also theoretically predicted to exist in magnetic systems, such as soliton-like domain walls in anisotropic spin 1/2 chains under magnetic fields [26]. Furthermore, BOs in interacting quantum few body systems have been modeled with the Bose-Hubbard model [27].

One important issue for BOs dynamics is the effect of carrier-phonon interactions, which is of essential importance for systems such as semiconductor superlattices [28, 29], organic materials [30–36] and quantum dots [37, 38]. The phonon bath is treated classically and the associated carrier-phonon coupling semi-classically in the Su-Schrieffer-Heeger model for polymers [30–33] and in the Peyrard-Bishop-Holstein model for DNA [34,

## 1 Introduction

Early evidence of time-domain Bloch oscillations (BOs) in superlattices was revealed by transient degenerate four-wave mixing (DFWM) [1, 2], yielding results in agreement with the work of Esaki and Tsu [3]. BOs emerge when an electron subject to a perfectly periodic lattice potential executes periodic motion in the presence of an external electric field [4–10]. In recent decades, BOs were found in various physical systems. For example, with the progress of laser cooling and manipulation, cold atoms in an optical lattice were found to ex-

\* Corresponding author E-mail: YZhao@ntu.edu.sg  
Division of Materials Science, Nanyang Technological University,  
Singapore 639798, Singapore



35]. More than forty years ago, Thornber and Feynman studied the motion of an electron in a polar crystal in a strong electric field using Fröhlich's polaron model, and found that the electron acquires a constant velocity due to the emission of phonons [39]. Much theoretical work based on the rate equations or the Boltzmann equation later focused on calculating transition rate probabilities, rather than complex quantum amplitudes [40, 41]. However, full quantum coherence was revealed to be retained in an inelastic quantum transport process and a steady state was found to be reached subject to an infinite lattice, leaving the dispersionless optical phonon absorbing the excess energy from the external field [42, 43].

Despite dedicated studies of BOs dynamics, the effect of complex interplay between the electron and its accompanying phonon cloud in a one-dimensional lattice remains an open question [44, 45]. Spatial dynamics influenced by exciton-phonon coupling is also inadequately studied given initial broad and narrow exciton wave packets [46, 47]. Moreover, a unified treatment on various types of exciton-phonon coupling remains elusive.

The intramolecular (diagonal) and intermolecular (off-diagonal) exciton-phonon coupling has been demonstrated to coexist in organic materials [48], and it is shown that off-diagonal coupling plays a crucial role in polaronic diffusion [49]. In the presence of an external electric field, polaron motion with off-diagonal coupling in polymer chains has been simulated with a semiclassical method [36, 50], neglecting the quantum nature of phonons and exciton-phonon coupling. Fully quantum mechanical treatments are few in the literature with little attention paid to Hamiltonians with off-diagonal exciton-phonon coupling and an external field due to inherent difficulties to obtain reliable solutions [43].

Based on the Holstein molecular crystal model, which describes the motion of an exciton enveloped by a cloud of phonons [51], we include both diagonal and off-diagonal exciton-phonon coupling. Despite apparent simplicity of its Hamiltonian, the Holstein model never ceases to surprise us with rich physics related to exciton-phonon correlations. The off-diagonal coupling was investigated earlier by the Munn-Silbey theory [52] and a variational method using the Davydov  $D_2$  Ansatz [53] and the global-local Ansatz [54]. Recently, Zhao *et al.* developed a refined trial state, the multiple Davydov  $D_2$  Ansatz, to accurately treat the dynamics of the Holstein model with simultaneous diagonal and off-diagonal coupling [55, 56]. In this work we will apply this method to polaron dynamics in an external field.

In addition, only interactions between the exciton and optical phonons were considered previously

[39, 43, 55]. Quantum-mechanical calculations indicated that excitons are coupled to both acoustic and optical phonons [59, 60]. Discussions on the role played by acoustic modes are inadequate in the literature, especially in the simultaneous presence of acoustic and optical phonons accompanied by an external field [61, 62].

In this work, we investigate the impact of diagonal and off-diagonal exciton-phonon coupling on polaron dynamics in a ring system in the presence of a constant electric field using the multiple Davydov  $D_2$  trial state with the Dirac-Frenkel variational principle. Accuracy of the method is verified by the comparison with benchmark calculations obtained from the numerically exact hierarchical equations of motion (HEOM) method [63, 64], which is also firstly used in this work to deal with field-driven cases to the best of our knowledge. The validity of our variational method is also carefully examined by quantifying how faithfully our result follows the Schrödinger equation in balance with the computational efficiency. For weak exciton-phonon coupling in the anti-adiabatic regime, we consider both acoustic and optical phonons, and calculate the time evolution of various quantities with special attention paid to the effect of weak dissipation on the spatial amplitudes of BOs using different initial conditions. Treating strong diagonal coupling is a formidable challenge for the HEOM method, but our variational method using the multi- $D_2$  Ansatz remains numerically affordable (in fact, with a higher precision with stronger coupling).

The rest of the paper is structured as follows. In Sec. 2, we present the Hamiltonian in the gauge transformed form and our trial wave function, the multi- $D_2$  Ansatz. In Sec. 3.1, our variational results are compared to those of the benchmark HEOM calculations. In Sec. 3.2, the influence of weak diagonal coupling in the anti-adiabatic regime on the exciton wave packet is investigated using initial Gaussian wave packets with varying widths with particular attention paid to the possible existence of a steady state. Finally, polaron dynamics is examined in the strong diagonal coupling regime in Sec. 3.3. Conclusions are drawn in Sec. 4.

## 2 Methodology

### 2.1 Model

The Hamiltonian of the one-dimensional Holstein polaron reads

$$\hat{H} = \hat{H}_{\text{ex}} + \hat{H}_{\text{ph}} + \hat{H}_{\text{ex-ph}}^{\text{diag}} + \hat{H}_{\text{ex-ph}}^{\text{o.d.}} \quad (1)$$



where  $\hat{H}_{\text{ex}}$ ,  $\hat{H}_{\text{ph}}$ ,  $\hat{H}_{\text{ex-ph}}^{\text{diag}}$  and  $\hat{H}_{\text{ex-ph}}^{\text{o.d.}}$  denote the exciton Hamiltonian, the bath (phonon) Hamiltonian, the diagonal and off-diagonal exciton-phonon coupling Hamiltonian, respectively. An extra term  $F \sum_n n a_n^\dagger a_n$  is added to represent the scalar potential induced by a constant external electric field  $F$ . After bending a linear chain of atoms into a ring, however, potential of the field would become discontinuous at end points, leaving the use of periodic boundary conditions questionable [65]. A later treatment [66] using a gauge transformed vector potential [67] avoids this problem and is thus suitable for ring systems. We will use the gauge transformed Hamiltonian for the ring system under a constant electric field (see Supporting Information for details), which can be defined as

$$\begin{aligned}\hat{H}_{\text{ex}} &= -J \sum_n a_n^\dagger (e^{-iFt} a_{n+1} + e^{iFt} a_{n-1}), \\ \hat{H}_{\text{ph}} &= \omega_0 \sum_n b_n^\dagger b_n, \\ \hat{H}_{\text{ex-ph}}^{\text{diag}} &= -g\omega_0 \sum_n a_n^\dagger a_n (b_n + b_n^\dagger), \\ \hat{H}_{\text{ex-ph}}^{\text{o.d.}} &= \frac{1}{2} \phi \omega_0 \sum_{n,l} \left[ a_n^\dagger a_{n+1} (b_l + b_l^\dagger) (\delta_{n+1,l} - \delta_{n,l}) \right. \\ &\quad \left. + a_n^\dagger a_{n-1} (b_l + b_l^\dagger) (\delta_{n,l} - \delta_{n-1,l}) \right]\end{aligned}\quad (2)$$

where  $\hat{a}_n^\dagger$  ( $\hat{a}_n$ ) and  $\hat{b}_n^\dagger$  ( $\hat{b}_n$ ) are the exciton and phonon creation (annihilation) operators for the  $n$ -th site, respectively. Written in the phonon momentum space,

$$\begin{aligned}\hat{H}_{\text{ph}} &= \sum_q \omega_q \hat{b}_q^\dagger \hat{b}_q, \\ \hat{H}_{\text{ex-ph}}^{\text{diag}} &= -N^{-1/2} g \sum_{n,q} \omega_q \hat{a}_n^\dagger \hat{a}_n (e^{iqn} \hat{b}_q + e^{-iqn} \hat{b}_q^\dagger), \\ \hat{H}_{\text{ex-ph}}^{\text{o.d.}} &= \frac{1}{2} N^{-1/2} \phi \sum_{n,q} \omega_q \{ \hat{a}_n^\dagger \hat{a}_{n+1} [e^{iqn} (e^{iq} - 1) \hat{b}_q + \text{H.c.}] \\ &\quad + \hat{a}_n^\dagger \hat{a}_{n-1} [e^{iqn} (1 - e^{-iq}) \hat{b}_q + \text{H.c.}] \},\end{aligned}\quad (3)$$

where  $\omega_q$  is the phonon frequency with momentum  $q$ , and  $\hat{b}_q^\dagger$  ( $\hat{b}_q$ ) is the creation (annihilation) operator of a phonon with momentum  $q$ ,

$$\hat{b}_q^\dagger = N^{-1/2} \sum_n e^{iqn} \hat{b}_n^\dagger, \quad \hat{b}_n^\dagger = N^{-1/2} \sum_q e^{-iqn} \hat{b}_q^\dagger. \quad (4)$$

The parameters  $J$ ,  $g$  and  $\phi$  represent the transfer integral, the diagonal coupling strength and off-diagonal coupling strength, respectively. In this work, we take  $\omega_q = \omega_0 |\sin(q/2)|$  as the dispersion relation for acoustic phonons, where  $q = 2\pi l/N$  represents the momen-

tum index with  $l = -\frac{N}{2} + 1, \dots, \frac{N}{2}$ ; in the case of optical phonons, we consider the Einstein dispersionless model, i.e.,  $\omega_q = \omega_0$ . For simplicity, the Debye frequency is taken to be equal to the Einstein frequency  $\omega_0$ . In the remainder of the paper,  $\omega_0$  is set to unity as the energy unit.

## 2.2 Multiple Davydov trial states

The multiple Davydov trial states with multiplicity  $M$ , which are essentially  $M$  copies of the corresponding single Davydov *Ansatz*, have been developed to investigate the time evolution of the Holstein polaron following the Dirac-Frenkel variational principle. The multi- $D_2$  *Ansatz* has less variational variables than the multi- $D_1$  *Ansatz* when same  $M$  is used, nonetheless it can more accurately describe polaron dynamics in the presence of off-diagonal coupling [55]. In this work, we employ the multi- $D_2$  *Ansatz*. It can be constructed as

$$\begin{aligned}|\mathcal{D}_2^M(t)\rangle &= \sum_i^M \sum_n^N \psi_{in} |n\rangle |\lambda_i\rangle, \\ &= \sum_i^M \sum_n^N \psi_{in} \hat{a}_n^\dagger |0\rangle_{\text{ex}} \exp \left\{ \sum_q [\lambda_{iq} \hat{b}_q^\dagger - \lambda_{iq}^* \hat{b}_q] \right\} |0\rangle_{\text{ph}},\end{aligned}\quad (5)$$

where  $\psi_{in}$  and  $\lambda_{iq}$  are time-dependent variational parameters for the exciton probability and phonon displacement, respectively,  $n$  represents the site number, and  $i$  labels the coherent superposition state. If  $M = 1$ , the  $|\mathcal{D}_2^M(t)\rangle$  *Ansatz* is restored to the usual Davydov  $D_2$  trial state. The equations of motion of the variational parameters  $\psi_{in}$  and  $\lambda_{iq}$  are then derived by adopting the Dirac-Frenkel variational principle,

$$\begin{aligned}\frac{d}{dt} \left( \frac{\partial L_2}{\partial \psi_{in}^*} \right) - \frac{\partial L_2}{\partial \psi_{in}} &= 0, \\ \frac{d}{dt} \left( \frac{\partial L_2}{\partial \lambda_{iq}^*} \right) - \frac{\partial L_2}{\partial \lambda_{iq}} &= 0.\end{aligned}\quad (6)$$

for the multi- $D_2$  *Ansatz*, and the Lagrangian  $L_2$  is formulated as

$$\begin{aligned}L_2 &= \langle \mathcal{D}_2^M(t) | \frac{i}{2} \frac{\overleftrightarrow{\partial}}{\partial t} - \hat{H} | \mathcal{D}_2^M(t) \rangle \\ &= \frac{i}{2} \left[ \langle \mathcal{D}_2^M(t) | \frac{\overrightarrow{\partial}}{\partial t} | \mathcal{D}_2^M(t) \rangle - \langle \mathcal{D}_2^M(t) | \frac{\overleftarrow{\partial}}{\partial t} | \mathcal{D}_2^M(t) \rangle \right] \\ &\quad - \langle \mathcal{D}_2^M(t) | \hat{H} | \mathcal{D}_2^M(t) \rangle.\end{aligned}\quad (7)$$

where the first term yields

$$\begin{aligned} & \frac{i}{2} \left[ \langle D_2^M(t) | \frac{\partial}{\partial t} | D_2^M(t) \rangle - \langle D_2^M(t) | \frac{\partial}{\partial t} | D_2^M(t) \rangle \right] \\ &= \frac{i}{2} \sum_{i,j} \sum_n (\psi_{jn}^* \psi_{in} - \psi_{jn}^* \psi_{in}) S_{ji} \\ &+ \frac{i}{2} \sum_{i,j} \sum_n \psi_{jn}^* \psi_{in} S_{ji} \sum_q \left[ \frac{\dot{\lambda}_{jq}^* \lambda_{jq} + \lambda_{jq}^* \dot{\lambda}_{jq}}{2} \right. \\ &\quad \left. - \frac{\dot{\lambda}_{iq}^* \lambda_{iq} + \lambda_{iq}^* \dot{\lambda}_{iq}}{2} + \lambda_{jq}^* \dot{\lambda}_{iq} - \lambda_{iq}^* \dot{\lambda}_{jq} \right], \end{aligned} \quad (8)$$

and the second term takes the form

$$\begin{aligned} & \langle D_2^M(t) | \hat{H} | D_2^M(t) \rangle \\ &= \langle D_2^M(t) | \hat{H}_{\text{ex}} | D_2^M(t) \rangle + \langle D_2^M(t) | \hat{H}_{\text{ex}} | D_2^M(t) \rangle \\ &+ \langle D_2^M(t) | \hat{H}_{\text{ex-ph}}^{\text{diag}} | D_2^M(t) \rangle + \langle D_2^M(t) | \hat{H}_{\text{ex-ph}}^{\text{o.d.}} | D_2^M(t) \rangle, \end{aligned} \quad (9)$$

where the Debye-Waller factor is formulated as

$$S_{ij} = \exp \left\{ \sum_q \lambda_{iq}^* \lambda_{jq} - \frac{1}{2} (|\lambda_{iq}|^2 + |\lambda_{jq}|^2) \right\}. \quad (10)$$

Detailed derivations of the equations of motion for the variational parameters are given in Supporting Information. In the numerical calculations, the fourth-order Runge-Kutta method is used to integrate the equations of motion.

With the wave function  $|D_2^M(t)\rangle$  available, the total energy  $E_{\text{total}} = E_{\text{ex}} + E_{\text{ph}} + E_{\text{diag}} + E_{\text{off}}$  is calculated, where  $E_{\text{ex}} = \langle D_2^M | \hat{H}_{\text{ex}} | D_2^M \rangle$ ,  $E_{\text{ph}} = \langle D_2^M | \hat{H}_{\text{ph}} | D_2^M \rangle$ ,  $E_{\text{diag}} = \langle D_2^M | \hat{H}_{\text{ex-ph}}^{\text{diag}} | D_2^M \rangle$ , and  $E_{\text{off}} = \langle D_2^M | \hat{H}_{\text{ex-ph}}^{\text{o.d.}} | D_2^M \rangle$ . Additionally, time evolution of the exciton probability  $P_{\text{ex}}(t, n)$  and the phonon displacement  $X_{\text{ph}}(t, n)$  is also calculated

$$\begin{aligned} P_{\text{ex}}(t, n) &= \langle D_2^M | \hat{a}_n^\dagger \hat{a}_n | D_2^M \rangle, \\ X_{\text{ph}}(t, n) &= \langle D_2^M | \hat{b}_n + \hat{b}_n^\dagger | D_2^M \rangle. \end{aligned} \quad (11)$$

We further use a standard deviation  $\sigma(t)$  and a mean value  $c(t)$  of the exciton wave packet to characterize the motion of the exciton wave, which are defined as follows

$$\begin{aligned} c(t) &= \sum_i^n n P_{\text{ex}}(t, n) \\ \sigma(t)^2 &= \sum_i^n (n - c(t))^2 P_{\text{ex}}(t, n) \end{aligned} \quad (12)$$

where the mean value  $c(t)$  describes the centroid of the exciton wave packet, and the standard deviation is used to measure how far the exciton wave spreads out from the mean position. It is noted that the standard deviation  $\sigma(t)$  and the mean value  $c(t)$  are sensitive to the initial standard deviation  $\sigma_0$  of the exciton wave packet.

## 3 Numerical results and discussions

### 3.1 Validity of variation for transient dynamics

In this subsection, we show that the multi- $D_2$  Ansatz with sufficiently large multiplicity  $M$  yields quantitatively accurate solutions to the dynamics of the Holstein polaron with both diagonal and off-diagonal coupling, in perfect agreement with the benchmark calculations of the numerically exact HOEM method (see Sec. 4 of Supporting Information) [63, 64]. For simplicity, only optical phonons are used in this subsection.

#### 3.1.1 Diagonal Coupling

First, we study the case of diagonal exciton-phonon coupling. Dynamics of the Holstein polaron under a constant external field is investigated by using the multi- $D_2$  Ansatz, in comparison with those obtained with the single Davydov  $D_2$  Ansatz and the HEOM method. Using these approaches, the time evolution of the exciton probability  $P_{\text{ex}}(t, n)$  as shown in Fig. 1 is simulated in the case of  $J = 0.1$ ,  $g = 0.28$  and  $F = 0.1$  in a small ring with  $N = 8$  sites for simplicity. The exciton is created on two nearest neighboring sites  $\psi_n = (\delta_{n, N/2} + \delta_{n, N/2+1})/\sqrt{2}$ , and the phonon displacement  $\lambda_{i,q}(t=0) = 0$  is set. As depicted in Figs. 1(a) and (b), distinguishable deviations in  $P_{\text{ex}}(t, n)$  can be found between the variational results from the  $D_2^{M=1}$  and  $D_2^{M=16}$  Ansätze. Interestingly,  $P_{\text{ex}}(t, n)$  obtained from the HEOM method in Fig. 1(c) is almost identical to that by the  $D_2^{M=16}$  Ansatz in Fig. 1(b). Furthermore, the difference in the time evolution of the exciton probability between the variational and HEOM methods,  $\Delta P_{\text{ex}}(t, n)$ , as displayed in Fig. 1(d), is two orders of magnitude smaller than the value of  $P_{\text{ex}}(t, n)$ , indicating that the variational dynamics of the Holstein polaron under the external field can be numerically exact if the multiplicity  $M$  of the multi- $D_2$  Ansatz is sufficiently large.

It should be noted that the HEOM method is numerically expensive and thus impractical when the system size is large, while time dependent variational approaches are still valid to treat the polaron dynamics



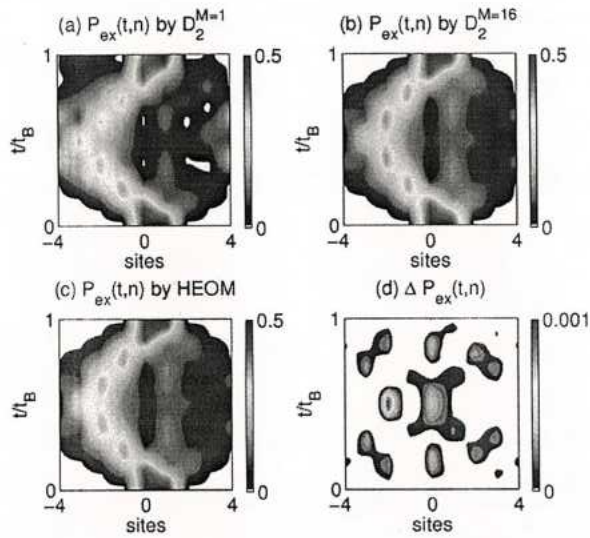


**Figure 1** Time evolution of the exciton probability  $P_{\text{ex}}(t, n)$  for a diagonal coupling case of  $J = 0.1$ ,  $g = 0.28$  and  $F = 0.1$  is obtained from (a) the single  $D_2^{M=1}$  Ansatz, (b) the  $D_2^{M=16}$  Ansatz, and (c) the HEOM method. The difference  $\Delta P_{\text{ex}}(t, n)$  between the HEOM and the  $D_2^{M=16}$  trial state is displayed in (d). The time unit  $t_B$  denotes the time period of BOs.  $N = 8$  is used in the calculations.

for large systems once a proper trial wave function is adopted.

### 3.1.2 Off-diagonal Coupling

We extend our discussion to the off-diagonal coupling, which is a formidable problem due to intrinsic difficulties in achieving reliable results. The off-diagonal coupling was emphasized as modulations of electron-electron interactions by ion vibrations in Mahan's celebrated textbook on many-particle physics [68]. Due to a lack of dependable solutions, a complete understanding of out-of-equilibrium dynamics for off-diagonal coupling remains elusive. Below we start with a validity check of our variational method.

Dynamics of the Holstein polaron with off-diagonal coupling under a constant external field is examined by using the multi- $D_2$  Ansatz with different multiplicity  $M$ . As shown in Figs. 2(a)–(c) and (e), the time evolution of the exciton probability  $P_{\text{ex}}(t, n)$  is obtained by the  $D_2^{M=1}$ ,  $D_2^{M=8}$ ,  $D_2^{M=20}$  Ansätze and the HEOM method, respectively. Figs. 2(b), (c) and (e) display quite similar patterns and all three are largely different from Fig. 2(a). Difference between  $P_{\text{ex}}(t, n)$  obtained by the  $D_2^{M=8}$  and  $D_2^{M=20}$  Ansatz as shown in Fig. 2(d) is two orders of magnitude smaller than the value of  $P_{\text{ex}}(t, n)$ , pointing to the nearly

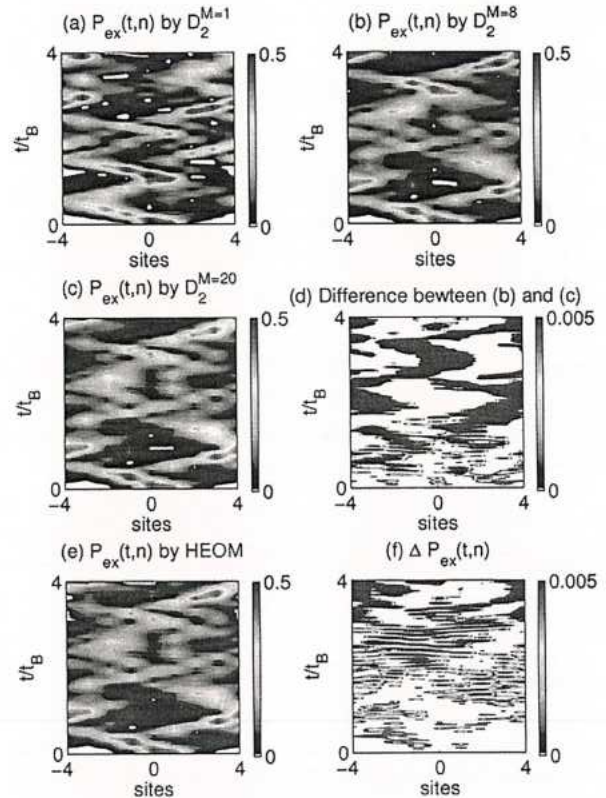


**Figure 2** Time evolution of the exciton probability  $P_{\text{ex}}(t, n)$  for an off-diagonal coupling case of  $J = 0.1$ ,  $\phi = 0.28$  and  $F = 0.1$  is obtained from (a) the  $D_2^{M=1}$  Ansatz, (b) the  $D_2^{M=8}$  Ansatz, (c) the  $D_2^{M=20}$  Ansatz, and (e) the HEOM method. (d) The difference between the  $D_2^{M=8}$  and  $D_2^{M=20}$  Ansätze and (f)  $\Delta P_{\text{ex}}(t, n)$  between the HEOM and the  $D_2^{M=20}$  Ansatz are displayed.

converged results already obtained by  $M = 8$ . Moreover, the difference in  $P_{\text{ex}}(t, n)$  between the  $D_2^{M=20}$  Ansatz and the HEOM method,  $\Delta P_{\text{ex}}(t, n)$ , as depicted in Fig. 1(f), is also two orders of magnitude smaller than the value of  $P_{\text{ex}}(t, n)$ , showing the superior accuracy of the multi- $D_2$  Ansatz.

In addition, a quantity named the relative deviation  $\Sigma$  (see Supporting Information) is also used to test the validity of our time-dependent variational approach by quantifying how closely the trial state follows the Schrödinger equation, as depicted in Fig. 3. As the multiplicity  $M$  increases, the relative deviation  $\Sigma$  decreases and approaches zero as  $M$  goes to infinity. This is supported by the relationship  $\Sigma \sim M^{-\mu}$  with an exponent of  $\mu = 3.15(1)$  in the inset of Fig. 3. Therefore, in the limit of large  $M$ , our variational method using the multi- $D_2$  Ansatz provides a numerically exact solution to the



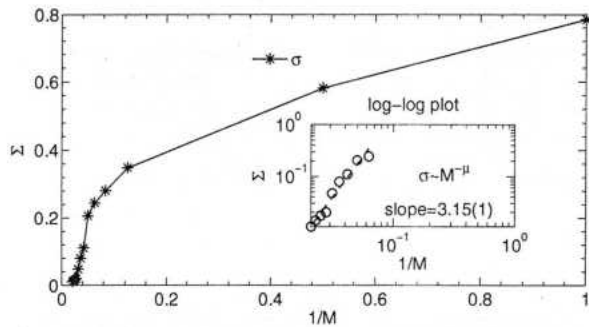


**Figure 3** Relative deviation  $\Sigma$  from the multi- $D_2$  Ansatz is displayed as a function of  $1/M$  with parameters  $J = 0.1$ ,  $\phi = 0.28$  and  $F = 0.1$ . The inset reveals the relationship  $\Sigma \sim M^\mu$  on a log-log scale, where the dashed line represents a power-law fit.

Schrödinger equation in the presence of the external field.

### 3.2 Anti-adiabatic regime

The effect of a bosonic environment on BOs, i.e., BOs in a polaron framework, is further investigated in this subsection. As usually envisioned for electronic transport in crystals, motion of electrons is occasionally scattered by lattice vibrations [39]. Pronounced modulations of the four-wave mixing signal with characteristics of the temporal periodicity of BOs has been detected experimentally in an optical investigation of BOs in a semiconductor superlattice, and can be attributed to lattice scattering [1]. Bouchard *et al.* excluded interband transitions from being responsible for the signal modulations and confirmed the single-band model as an appropriate approximation [69]. Several pioneering theoretical studies also demonstrated the modulations of BOs by the electron-phonon interaction [39, 43, 70]. Despite tremendous experimental and theoretical efforts dedicated to the phonon modulated BOs, the underlying mechanisms are still not well understood.

To be specific, both the acoustic and optical phonons have been experimentally revealed to coexist in the semiconductor superlattice [71], and amplitudes of exciton wave packets has been confirmed to be very sensitive to the precise excitation conditions in a weak external field [46]. However, there is a lack of investigation on BOs dynamics influenced by the two phonon branches when the exciton starts from a Gaussian wave packet with varying widths.

In this subsection we will focus on dynamic properties of the Holstein polaron including the time evo-

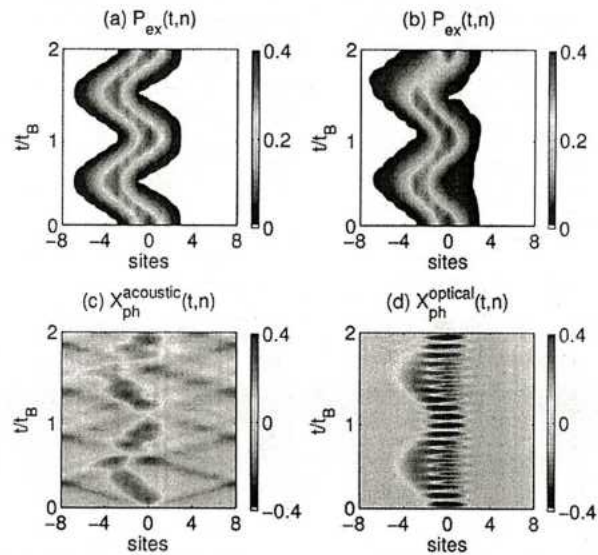


**Figure 4** Time evolution of the exciton probability  $P_{\text{ex}}(t, n)$  obtained from the  $D_2^{M=16}$  Ansatz in the case of  $J = 0.1$  and  $F = 0.1$  and an initial broad Gaussian wave packet of  $\sigma_0 = 1$  is displayed in (a) ( $g = 0$ ) and (b) ( $g = 0.4$ ). In the presence of weak diagonal coupling ( $g = 0.4$ ), the phonon displacement  $X_{\text{ph}}(t, n)$  is shown for (c) acoustic phonons and (d) optical phonons.

lution of the exciton probability and the phonon displacement for weak exciton-phonon coupling subject to a constant external electric field. Two typical scenarios are discussed by considering initial Gaussian wave packets with initial widths  $\sigma_0 = 1$  and  $0.2$ , as shown in Fig. 4 and Fig. 5, respectively. The initial Gaussian distribution [72] is described as follows

$$\rho(n, t=0) = [(2\pi)^{1/2} \sigma_0]^{-1} \exp(-n^2/2\sigma_0^2) \quad (13)$$

which is centered at site  $n=0$ , and the associated initial wave function is taken as the square root of the distribution:

$$\psi(n, t=0) = [(2\pi)^{1/2} \sigma_0]^{-1/2} \exp(-n^2/4\sigma_0^2) \quad (14)$$

In particular, the roles played by the acoustic and optical phonons on the exciton transport are explicitly compared under the same external field. It is difficult to partition these branches rigorously [59], and in order to avoid the complexity induced by partitioning these branches, we include only one phonon branch in each separate calculation and then compare the results of two calculations.

We start from using an initial broad Gaussian wave packet of  $\sigma_0 = 1$ . Transfer integral  $J = 0.1$  and an



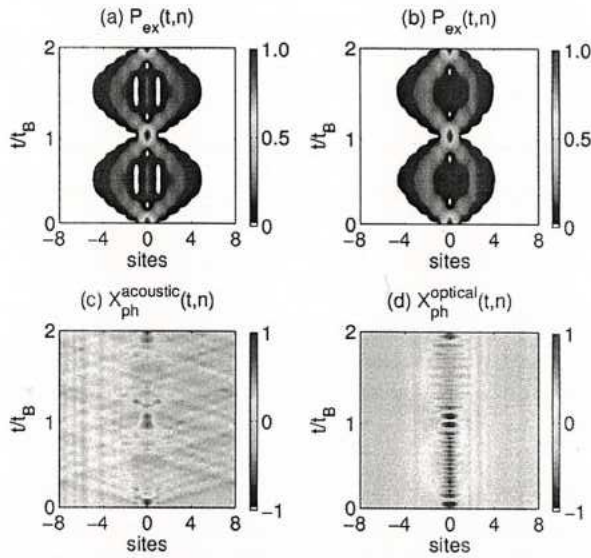


**Figure 5** Time evolution of the exciton probability  $P_{\text{ex}}(t, n)$  obtained from the  $D_2^{M=16}$  Ansatz in the case of  $J = 0.1$  and  $F = 0.1$  and an initial narrow Gaussian wave packet of  $\sigma_0 = 0.2$  is shown in (a) ( $g = 0$ ) and (b) ( $g = 0.4$ ). The phonon displacement  $X_{\text{ph}}(t, n)$  is shown for (c) the acoustic phonons and (d) optical phonons respectively in the presence of  $g = 0.4$ .

external field of  $F = 0.1$  is set in the calculations of this subsection. In the absence of exciton-phonon coupling, as shown in Fig. 4(a), the exciton exhibits typical BOs, with the center of mass of the wave packet oscillates while its shape is essentially unchanged, in agreement with earlier theoretical work based on an ideal GaAs/Al<sub>x</sub>Ga<sub>1-x</sub>As superlattice in a uniform electric field as described by a conventional flat-band picture [69, 72]. In the presence of the weak diagonal coupling ( $g = 0.4$ ), we focus on the anti-adiabatic regime where the phonon frequencies are larger than the transfer integral  $J$ . Only  $P_{\text{ex}}(t, n)$  of optical phonons is shown in Fig. 4(b) because the effect of the two phonon branches turned out to be similar. By comparing Figs. 4(a) and (b), the time periods of the exciton transport are the same because the temporal periodicity is determined by the external field. This agrees with the experimental observation that the detected signal is found to be modulated over time but the time period of the signal is found to be equal to the temporal periodicity of BOs [1]. The largest oscillation amplitude of the center of mass of the exciton wave packet in Fig. 4(a) is in accordance with the theoretical value of  $4J/F$  [73].

Even though the temporal periodicity is preserved after the exciton-phonon coupling is turned on, the

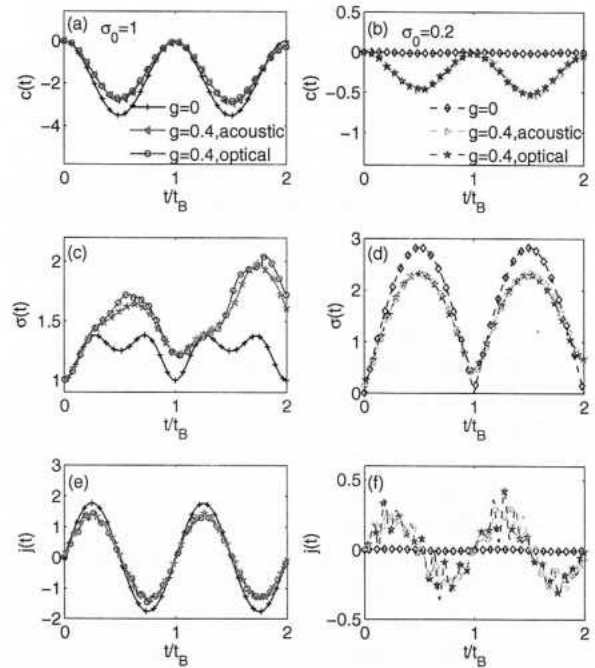


**Figure 6** (a) Mean value  $c(t)$ , (c) standard deviation  $\sigma(t)$  and (e) current  $j(t)$  as functions of the time  $t$  in the case of  $J = 0.1$  are displayed using the initial standard deviation  $\sigma_0 = 1$  and (b), (d), (f) using  $\sigma_0 = 0.2$ , respectively. In each panel, the results with  $g = 0$  and  $g = 0.4$  are compared.

spatial periodicity is changed over time. The addition of the exciton-phonon coupling moves the center of mass of the exciton wave packet of  $g = 0$  closer to the initial location, which is in line with the contrast in the mean value  $c(t)$  between  $g = 0$  and  $0.4$  in Fig. 6(a). Not only the motion of the center of mass of the exciton wave packet is changed, but also the width of the wave packet is enlarged as an effect of the weak coupling, giving rise to a broadened wave packet. The width  $\sigma(t)$  in Fig. 6(c) is increased due to smearing of the wave packet.

The phonon displacement  $X_{\text{ph}}(t, n)$  is shown in Figs. 4(c) and (d) for the acoustic and optical phonons, respectively. Before the exciton creation at  $t = 0$ , the phonons are in their vacuum states for both scenarios. By comparing the two figures, parts of  $X_{\text{ph}}(t, n)$  (red and yellow) are found to propagate with BOs frequency  $\omega_B$  because they are generated by the moving exciton wave packet and would in turn smear out the exciton wave fronts. As for the remainder of  $X_{\text{ph}}(t, n)$  (blue), a V-shaped feature and an oscillatory component with the phonon frequency  $\omega_0$  are respectively found in Figs. 4(c) and (d). Moreover, the existence of ten peaks in one Bloch period  $t_B$  can be attributed to the ratio  $\omega_0/\omega_B$  (phonon



frequency  $\omega_0$  over BOs frequency). In the presented cases,  $\omega_0$  is ten times of  $\omega_B = de|F|/\hbar$ , where  $d$  is the lattice constant,  $e$  is the charge of the exciton, and  $d = e = \hbar = 1$  is set. Meanwhile, the weak coupling affects the transport and the exciton current in Fig. 6(e). At zero coupling, the exciton current  $j(t)$  (see Supporting Information) in the case of an initial broad Gaussian wave packet is  $j(t) = 2 \sin Ft$  with the largest amplitude among all cases studied. The amplitude of the exciton current is decreased after the coupling is switched on, mitigating unidirectional exciton transport.

Next, we consider the effect the weak exciton-phonon coupling on the dynamics with an initial narrow Gaussian wave packet of  $\sigma_0 = 0.2$ . As shown in Fig. 5(a), the exciton undergoes a symmetric breathing mode at zero coupling. The exciton wave packet propagates with its center of mass fixed at the original location and its width oscillates with the Bloch period, in accord with previous studies on the breathing mode [46, 69, 74]. After the addition of the weak diagonal coupling  $g = 0.4$ , the exciton amplitude becomes larger in the left branch than that in the right branch (Fig. 5(b)) and the center of mass of the wave packet is moved away from the original location. These features of the exciton indicate that the symmetry of the breathing mode is broken by even minute exciton-phonon interactions, and are further reflected by the mean value  $c(t)$  plotted in Fig. 6(b), which oscillates for the weak coupling case of  $g = 0.4$  in contrast to being zero at all times for  $g = 0$ . Recently, the breakdown of the breathing mode has been confirmed in semiconductor superlattices [75] and cold atoms trapped in optical lattice [76–78], making our results here highly relevant in the study of breathing modes in those systems. Furthermore, the width of the exciton wave packet for the weak coupling case of  $g = 0.4$  is reduced in comparison to that for  $g = 0$ , as depicted in Fig. 6(d). A comparison between Figs. 6(c) and (d) reveals that weak diagonal coupling has opposite influences on the width of the exciton wave packet: the exciton wave packet is broadened in the case of  $\sigma_0 = 1$  while that in the case of  $\sigma_0 = 0.2$  is suppressed after the exciton-phonon coupling is switched on.

Similar to the scenario of  $\sigma_0 = 1$ , the phonon displacement  $X_{ph}(t, n)$  of  $\sigma_0 = 0.2$  propagates along with the movement of the exciton. As shown in Fig. 5(c),  $X_{ph}(t, n)$  maintains its V-shaped feature in the case of acoustic phonons. As for Fig. 5(d), characteristic oscillations with frequency  $\omega_0$  is found in the case of optical phonons. Reciprocally, the generated  $X_{ph}(t, n)$  induces smearing of the exciton in its center. A brief comparison between Fig. 4 and Fig. 5 reveals that the exciton triggered phonon displacement leads to the weakening of the exciton wave packet in its center and edge, respectively. As shown in

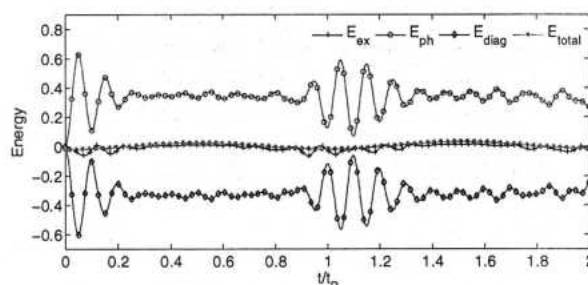


**Figure 7**  $E_{ex}(t)$ ,  $E_{ph}(t)$ ,  $E_{diag}(t)$  and  $E_{diag}(t)$  obtained by the  $D_2^{M=16}$  Ansatz in the case of  $J = 0.1$ ,  $F = 0.1$  and  $\sigma_0 = 0.1$  in the presence of weak diagonal coupling ( $g = 0.4$ ) with the optical phonons.

Fig. 6(f), the current in the zero coupling case is zero due to the spatial symmetry of the exciton wave packet. The exciton current in the weak coupling exhibits fast beating with the characteristic frequency  $\omega_0$  superimposed by slower BOs.

So far, we have focused on the impact of weak exciton-phonon coupling on the quantum transport with respect to the two typical scenarios. In general, BOs are very sensitive to any kind of dephasing generated by the electron-hole Coulomb interaction effects or lattice imperfections, since they rely on the coherent reflection of waves [78]. The electron-hole Coulomb interaction is pointed out to destroy the breathing mode by Dignam *et al.* after they examined the nature of the exciton wave packets in undoped semiconductor superlattices in a uniform along-axis electric field [75]. The effects of atom-atom interactions in the dilute BEC trapped in a periodic potential were actively studied using a discrete nonlinear Schrödinger equation (DNLS), and the atom-atom interactions can result in the decoherence of atomic BOs [17, 76, 79] and enhancement or suppression of the breathing width [77, 78]. To the best of our knowledge, ours is the first investigation on the influence of the exciton-phonon interaction on both the typical BOs and the breathing mode.

Finally, we analyze the characteristics of the nonequilibrium dynamics of the ring system, including a comparison with the steady state of an infinite linear chain. First of all, in the absence of an external electric field, in the anti-adiabatic limit of  $\omega_0 \gg J$ , exciton dynamics in both weak and strong coupling regimes is dominated by coherent oscillations and negligible energy transfer, leaving a conserved total energy [80]. After an external field is applied, the total energy is not conserved as plotted in Fig. 7 because of the addition of the extra energy acquired from the external field. Secondly, a steady state with a saturated current can be obtained



in a linear chain that extends to infinity in both directions, where the exciton acquires kinetic energy from the applied field while dissipating its energy by a net emission of optical phonons [39]. Being a steady state situation, the expectation value of the rate of change of electron momentum is zero, and the steady state is left with an equation which balances the applied field, or rate of increase of electron momentum, against the rate of loss of momentum due to the lattice scattering. This result is an explicit field dependence of the steady-state velocity of the electron. The key feature of the steady state is also explored in Ref. [43, 81, 82]. Equivalently, the condition of the steady state can be that there exist linear regimes of the total energy and phonon energy following the equality of  $dE_{\text{total}}/dt = dE_{\text{ph}}/dt$  [43], meaning that the total energy gain is entirely absorbed by the lattice. Specifically, with increasing time  $t$ , the total energy vs time approaches a straight line, and the phonon energy has a linear time dependence as well. But in our ring system, the condition of the steady state can not be met as this equation can not be satisfied from the curves of  $E_{\text{total}}$  and  $E_{\text{ph}}$  as shown in Fig. 7. For example, the value of  $dE_{\text{ph}}/dt$  at  $t = 2t_B$  is not equal to but 9 times of the value of  $dE_{\text{total}}/dt$ . The energy imported by the external field can not cancel out the energy emitted to the phonons, leaving the exciton energy oscillates over time. Thus, the electron's acceleration in the ring can no longer be balanced out by the lattice's deceleration and the electron can not drift with a saturated velocity. Consequently, no saturated constant current is found in the anti-adiabatic regime for the small ring systems, and steady states in the adiabatic regime will be investigated elsewhere.

To sum up, weak exciton-phonon coupling in the anti-adiabatic regime breaks the spatial periodicity but retains the temporal periodicity of both the typical BOs and the breathing mode. The exciton movement shows similar features in spite of the difference between the acoustic and optical phonon branches. In fact, in a weak external field, when diagonal coupling is strong between the exciton and both the acoustic and optical phonons, the exciton become localized, leading to the diminishing of the typical BOs and the breathing mode. The localization is similar to that in the moderate external field cases in the next subsection, therefore the details are not shown.

### 3.3 Strong diagonal coupling

In this subsection we seek to present a general picture of the exciton wave packet evolution in the regime of

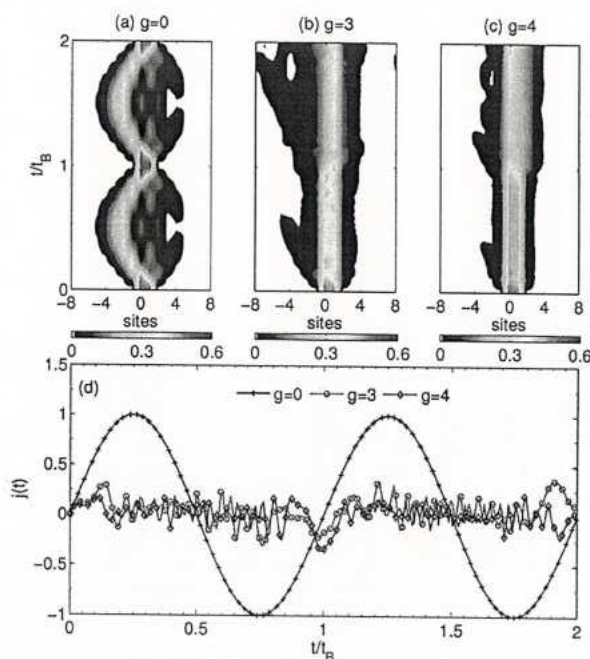


**Figure 8** Time evolution of the exciton probability  $P_{\text{ex}}(t, n)$  obtained from the  $D_2^{M=16}$  Ansatz in the case of  $J = 1$ ,  $N = 16$  and a moderate external field of  $F = 1$  is displayed for different diagonal coupling strengths: (a)  $g = 0$ , (b)  $g = 3$  and (c)  $g = 4$ . Corresponding currents  $j(t)$  are shown in (d).

strong diagonal coupling. We first investigate the exciton wave packets as well as the exciton currents under a moderate external field of  $F = 1$ . The time evolution of the exciton probability  $P_{\text{ex}}(t, n)$  for different diagonal coupling strengths  $g = 0, 3$  and  $4$  is illustrated in Figs. 8(a), (b) and (c), respectively. The exciton is created on two nearest neighbouring sites. We set  $J = 1$  and  $N = 16$ . As shown in Figs. 8(a)–(c), the bare exciton exhibits a partially BOs pattern, while the strong exciton-phonon coupling is found to localize the exciton to the initial excitation sites. BOs are largely quenched due to strong exciton-phonon coupling [83]. This behaviour is also demonstrated in Fig. 8(d), which shows that the amplitude of the exciton current decreases with increasing exciton-phonon coupling and fluctuates around zero.

We then discuss the case of a strong external field. Using the same parameters as the case of  $F = 1$ , the time evolution of the exciton probability  $P_{\text{ex}}(t, n)$  and exciton current  $j(t)$  under a strong field of  $F = 70$  are presented in Figs. 9(a)–(c) and Fig. 9(d), respectively. Due to the strong external field, the exciton is found to be localized at the initial site of excitation irrespective of the exciton-phonon coupling strength. A bare exciton



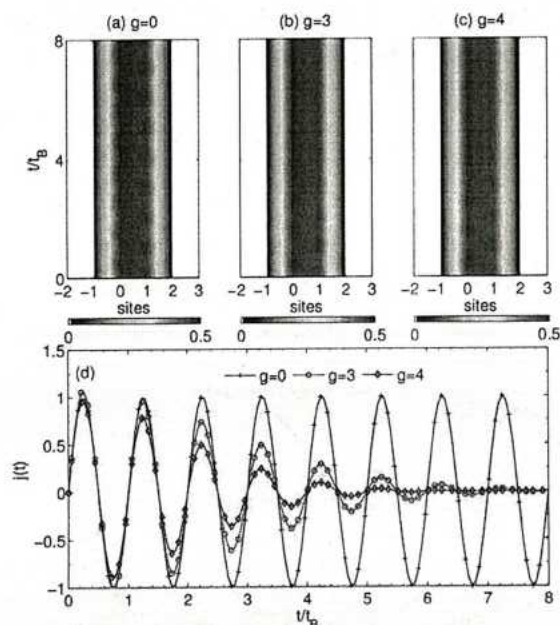


**Figure 9** Time evolution of the exciton probability  $P_{ex}(t, n)$  obtained from the  $D_2^{M=16}$  Ansatz in the case of  $J = 1$ ,  $N = 16$  and a strong external field of  $F = 70$  is displayed for different diagonal coupling strengths: (a)  $g = 0$ , (b)  $g = 3$  and (c)  $g = 4$ . Corresponding currents  $j(t)$  are shown in (d).

case is shown in Fig. 9(a) for comparison. The localization of the exciton wave packet can be rationalized in terms of Wannier-Stark states [7]. In the Wannier representation, the Wannier-Stark states are denoted as  $|\Psi_n\rangle = \sum_m J_{m-n}(\gamma) |m\rangle$ , where  $J_{m-n}(\gamma)$  is the Bessel function of order  $m - n$  with  $\gamma = 2J/Fd$  [73]. Due to properties of the Bessel functions, the Wannier-Stark states extend over the interval  $L \simeq 2J/F$ , which leads to well localized states in the limit of a strong external field [41]. As shown in Figs. 9(b) and (c), strong exciton-phonon coupling leads to the decay of BOs. The exciton currents in the presence of strong exciton-phonon coupling exhibits damped oscillations with a time scale of  $8t_B$  ( $6t_B$ ) for  $g = 3$  (4).

## 4 Conclusion

We have studied transient dynamics of the Holstein polaron in a one-dimensional ring under a constant external field using the Dirac-Frenkel time-dependent variational principle and the novel multi- $D_2$  Ansatz, which is a linear combination of the usual Davydov  $D_2$  trial states. In both the diagonal and off-diagonal coupling cases, our efficient variational calculations are in perfect

agreement with those obtained from the numerically exact HEOM method. Moreover, the relative deviation is found to decay with the increasing multiplicity of the multi- $D_2$  Ansatz, which vanishes in the limit of  $M \rightarrow \infty$ , inferring that our approach is numerically exact in that limit.

Firstly, the influence of the initial condition is studied in the absence of exciton-phonon coupling. For an initial broad Gaussian wave packet, typical BOs are found with the center of the wave packet oscillating but its shape essentially unchanged. Starting from an initial narrow Gaussian wave packet, the exciton wave exhibits a symmetric breathing mode with its width oscillating with the Bloch period and its center of mass fixed at the original location.

The effect of the exciton-phonon coupling is the focus of our investigation. In general, weak diagonal coupling breaks the spatial periodicity while keeping the temporal periodicity of the exciton wave. For an initial broad Gaussian wave packet, the application of weak diagonal coupling modifies BOs with the exciton wave packet broadened and the exciton current reduced. For an initial narrow Gaussian wave packet, after the addition of weak coupling, the spatial symmetry of the exciton wave is broken and the center of mass of the exciton wave packet oscillates away from the original position, leading to a non-zero exciton current. In particular, a saturated current which exists in an infinite linear lattice is not found in a finite-sized ring within the anti-adiabatic regime, since the energy imported by the external field is not entirely absorbed by the lattice, leaving the steady state unreachable.

For strong exciton-phonon coupling, the variational method using the multi- $D_2$  Ansatz is found to be highly accurate while it is prohibitively expensive for the HEOM method to tackle higher phonon excited states. The exciton wave packet is found to be localized due to either strong diagonal coupling or a strong external field. Finally, strong diagonal coupling gives rise to the decay of BOs under a strong external field, leading to damped oscillations of the exciton current.

## Acknowledgments

Support from the Singapore National Research Foundation through the Competitive Research Programme (CRP) under Project No. NRF-CRP5-2009-04 is gratefully acknowledged.

**Key words.** Bloch oscillations, polaron dynamics, Davydov Ansatz, exciton-phonon coupling, electric field.



## References

- [1] J. Feldmann, K. Leo, J. Shah, D. A. B. Miller, J. E. Cunningham, T. Meier, G. von Plessen, A. Schulze, P. Thomas and S. Schmitt Rink, *Phys. Rev. B* **46**, 7252 (1992).
- [2] E. E. Mendez and G. Bastard, *Phys. Today* **46**, 34 (1993).
- [3] L. Esaki and R. Tsu, *IBM J. Res. Dev.* **14**, 61 (1970).
- [4] F. Bloch, *Zeitschrift Für Phys.* **52**, 555 (1928).
- [5] C. Zener, *Proc. R. Soc. A* **145**, 523 (1934).
- [6] J. N. Churchill and F. E. Holmstrom, *Phys. Scr.* **27**, 91-98 (1983).
- [7] G. H. Wannier, *Phys. Rev.* **117**, 432 (1960).
- [8] W. V. Houston, *Phys. Rev.* **57**, 184 (1940).
- [9] M. Holthaus and D. W. Hone, *Phil. Mag. B.* **74**, 105 (1996).
- [10] H. Fukuyama, R. A. Bari, and H. C. Fogedby, *Phys. Rev. B* **8**, 5579 (1973).
- [11] C. Cohen-Tannoudji, *AIP Conf. Proc.* **160**, 318 (1987).
- [12] S. Chu, *Science* **253**, 861 (1991).
- [13] M. B. Dahan, E. Peik, J. Reichel, Y. Castin, and C. Salomon, *Phys. Rev. Lett.* **76**, 4508 (1996).
- [14] S. R. Wilkinson, C. F. Bharucha, K. W. Madison, Q. Niu, and M. G. Raizen, *Phys. Rev. Lett.* **76**, 4512 (1996).
- [15] O. Morsch, J. H. Müller, M. Cristiani, D. Ciampini, and E. Arimondo, *Phys. Rev. Lett.* **87**, 140402 (2001).
- [16] B. P. Anderson and M. A. Kasevich, *Science* **282**, 1686 (1998).
- [17] A. R. Kolovsky, E. A. Gomez, and H. J. Korsch, *Phys. Rev. A* **81**, 025603 (2010).
- [18] M. Cristiani, O. Morsch, J. H. Müller, D. Ciampini, and E. Arimondo, *Phys. Rev. A* **65**, 063612 (2002).
- [19] R. Morandotti, U. Peschel, J. S. Aitchinson, H. S. Eisenberg, and Y. Silberberg, *Phys. Rev. Lett.* **83**, 4756 (1999).
- [20] T. Pertsch, P. Dannberg, W. Elfle, and A. Bräuer, *Phys. Rev. Lett.* **83**, 4752 (1999).
- [21] U. Peschel, T. Pertsch, and F. Lederer, *Opt. Lett.* **23**, 1701 (1998).
- [22] C. Waschke, H. G. Roskos, R. Schwedler, K. Leo, H. Kurz, and K. Köhler, *Phys. Rev. Lett.* **70**, 3319 (1993).
- [23] M. Först, G. Segschneider, T. Dekorsy, H. Kurz, and K. Köhler, *Phys. Rev. B* **61**, R10563 (2000).
- [24] J. Delahaye, J. Hassel, R. Lindell, M. Sillanpää, M. Paalanen, H. Seppä, and P. Hakonen, *Phys. E Low-Dimensional Syst. Nanostructures* **18**, 15 (2003).
- [25] P. B. Wilkinson, *Phys. Rev. E* **65**, 056616 (2002).
- [26] J. Kyriakidis and D. Loss, *Phys. Rev. B* **58**, 5568 (1998).
- [27] A. Buchleitner and A. R. Kolovsky, *Phys. Rev. Lett.* **91**, 253002 (2003).
- [28] T. Dekorsy, A. Bartels, H. Kurz, K. Köhler, R. Hey, and K. Ploog, *Phys. Rev. Lett.* **85**, 1080 (2000).
- [29] A. W. Ghosh, L. Jönsson, and J. W. Wilkins, *Phys. Rev. Lett.* **85**, 1084 (2000).
- [30] A. Johansson and S. Stafström, *Phys. Rev. Lett.* **86**, 3602 (2001).
- [31] D. M. Basko and E. M. Conwell, *Phys. Rev. Lett.* **88**, 056401 (2002).
- [32] A. A. Johansson and S. Stafström, *Phys. Rev. B* **69**, 235205 (2004).
- [33] Y. Qui and L.-P. Zhu, *J. Chem. Phys.* **131**, 134903 (2009).
- [34] M. Peyrard and A. R. Bishop, *Phys. Rev. Lett.* **62**, 2755 (1989).
- [35] E. Díaz, R. P. A. Lima, and F. Domínguez-Adame, *Phys. Rev. B* **78**, 134303 (2008).
- [36] S. V. Rakhmanova and E. M. Conwell, *Appl. Phys. Lett.* **75**, 1518 (1999).
- [37] I. A. Dmitriev and R. A. Suris, *Semiconductors* **35**, 212 (2001).
- [38] P. M. Petroff, A. Lorke, and A. Imamoglu, *Phys. Today* **54**, 46 (2001).
- [39] K. K. Thornber and R. P. Feynman, *Phys. Rev. B* **1**, 4099 (1970).
- [40] R. Kümmel, H. Rauh, and E. Bangert, *Phys. Status Solidi* **87**, 99 (1978).
- [41] D. Emin and C. F. Hart, *Phys. Rev. B* **36**, 2530 (1987).
- [42] J. Bonca and S. A. Trugman, *Phys. Rev. Lett.* **79**, 4874 (1997).
- [43] L. Vidmar, J. Bonca, M. Mierzejewski, and P. Prelovsek, and S. A. Trugman, *Phys. Rev. B* **83**, 134301 (2011).
- [44] W. Zhang, A. O. Govorov, and S. E. Ulloa, *Phys. Rev. B* **66**, 134302 (2002).
- [45] A. K. C. Cheung and M. Berciu, *Phys. Rev. B* **88**, 35132 (2013).
- [46] V. G. Lyssenko, G. Valusis, F. Löser, T. Hasche, K. Leo, M. M. Dignam, and K. Köhler, *Phys. Rev. Lett.* **79**, 301 (1997).
- [47] M. Sudzius, V. G. Lyssenko, F. Löser, K. Leo, M. M. Dignam, and K. Köhler, *Phys. Rev. B* **57**, R12693 (1998).
- [48] V. Coropceanu, J. Cornil, D. S. Filho, Y. Olivier, R. Silbey, and J. Bredas, *Chem. Rev.* **107**, 926 (2007).
- [49] H. Tamura, M. Tsukada, H. Ishii, N. Kobayashi, and K. Hirose, *Phys. Rev. B* **86**, 35208 (2012).
- [50] Å. Johansson and S. Stafström, *Phys. Rev. B* **65**, 045207 (2002).
- [51] T. Holstein, *Ann. Phys. (N.Y.)* **8**, 325 (1959); **8**, 343 (1959).
- [52] R. W. Munn and R. Silbey, *J. Chem. Phys.* **83**, 1843 (1985).
- [53] Y. Zhao, B. Luo, Y. Zhang, and J. Ye, *J. Chem. Phys.* **137**, 084113 (2012).
- [54] Y. Zhao, D. W. Brown, and K. Lindenberg, *J. Chem. Phys.* **107**, 3159 (1997); **107**, 3179 (1997).
- [55] N. J. Zhou, Z. K. Huang, J. F. Zhu, V. Chernyak, and Y. Zhao, *J. Chem. Phys.* **143**, 014113 (2015).
- [56] N. Zhou, L. Chen, Z. Huang, K. Sun, Y. Tanimura, and Y. Zhao, *J. Phys. Chem. A* **120**, 1562 (2016).
- [57] L. Wang, L. Chen, N. Zhou, and Y. Zhao, *J. Chem. Phys.* **144**, 024101 (2016).
- [58] P. A. M. Dirac, *Proc. Cambridge Philos. Soc.* **26**, 376 (1930); J. Frenkel, *Wave Mechanics* (Oxford University Press, 1934).
- [59] Y. Yi, V. Coropceanu, and J.-L. Bredas, *J. Chem. Phys.* **137**, 164303 (2012).

- [60] Y. Li, V. Coropceanu, and J.-L. Bredas, *J. Chem. Phys.* **138**, 204713 (2013).
- [61] A. S. Davydov, *Phys. Status Solidi* **20**, 143 (1967).
- [62] A. La Magna and R. Pucci, *Phys. Rev. B* **55**, 6296 (1997).
- [63] Y. Tanimura and R. Kubo, *J. Phys. Soc. Jpn* **58**, 101 (1989).
- [64] L. Chen, Y. Zhao, and Y. Tanimura, *J. Phys. Chem. Lett.* **6**, 3110 (2015).
- [65] J. Zak, *Phys. Rev. Lett.* **20**, 1477 (1968).
- [66] J. B. Kreger and G. J. Iafrate, *Phys. Rev. B* **33**, 5494 (1986).
- [67] C. Kittel, *Quantum Theory of Solids* (Wiley, New York, 1987).
- [68] G. D. Mahan, *Many-Particle Physics* (Kluwer Academic/Plenum, New York, 2000).
- [69] A. M. Bouchard and M. Luban, *Phys. Rev. B* **52**, 5105 (1995).
- [70] V. D. L. N. S. Fialko, *JETP Lett.* **79**, 575 (2004).
- [71] E. Molinari and A. Fasolino, *Superlattices Microstruct.* **4**, 449 (1988).
- [72] J. Stockhofe and P. Schmelcher, *Phys. Rev. A* **91**, 023606 (2015).
- [73] T. Hartmann, F. Keck, H. J. Korsch, and S. Mossmann, *New J. Phys.* **6**, 2 (2004).
- [74] F. Domínguez-Adame, *Eur. J. Phys.* **31**, 639 (2010).
- [75] M. Dignam, J. E. Sipe, and J. Shah, *Phys. Rev. B* **49**, 10502 (1994).
- [76] A. Trombettoni and A. Smerzi, *Phys. Rev. Lett.* **86**, 2353 (2001).
- [77] C. Gaul, R. P. A. Lima, E. Diaz, C. A. Müller, and F. Domínguez-Adame, *Phys. Rev. Lett.* **102**, 255303 (2009).
- [78] C. Gaul, E. Diaz, R. P. A. Lima, F. Domínguez-Adame, and C. A. Müller, *Phys. Rev. A* **84**, 053627 (2011).
- [79] A. R. Kolovsky, H. J. Korsch, and E.-M. Graefe, *Phys. Rev. A* **80**, 023617 (2009).
- [80] F. Dorfner, L. Vidmar, C. Brockt, E. Jeckelmann, and E. Heidrich-Meisner, *Phys. Rev. B* **91**, 104302 (2015).
- [81] V. D. Lakhno, *Int. J. Quantum Chem.* **110**, 127 (2010).
- [82] V. D. Lakhno and A. N. Korshunova, *Eur. Phys. J. B* **79**, 147 (2011).
- [83] V. D. Lakhno and A. N. Korshunova, *Eur. Phys. J. B* **55**, 85 (2007).

### Supporting Information

Additional supporting information may be found in the online version of this article at the publisher's website.





Cite this: *Phys. Chem. Chem. Phys.*,  
2017, 19, 1655

## Polaron dynamics with off-diagonal coupling: beyond the Ehrenfest approximation

Zhongkai Huang,<sup>a</sup> Lu Wang,<sup>ab</sup> Changqin Wu,<sup>c</sup> Lipeng Chen,<sup>a</sup> Frank Grossmann<sup>d</sup> and Yang Zhao<sup>\*a</sup>

Treated traditionally by the Ehrenfest approximation, the dynamics of a one-dimensional molecular crystal model with off-diagonal exciton-phonon coupling is investigated in this work using the Dirac-Frenkel time-dependent variational principle with the multi- $D_2$  Ansatz. It is shown that the Ehrenfest method is equivalent to our variational method with the single  $D_2$  Ansatz, and with the multi- $D_2$  Ansatz, the accuracy of our simulated dynamics is significantly enhanced in comparison with the semi-classical Ehrenfest dynamics. The multi- $D_2$  Ansatz is able to capture numerically accurate exciton momentum probability and help clarify the relation between the exciton momentum redistribution and the exciton energy relaxation. The results demonstrate that the exciton momentum distributions in the steady state are determined by a combination of the transfer integral and the off-diagonal coupling strength, independent of the excitonic initial conditions. We also probe the effect of the transfer integral and the off-diagonal coupling on exciton transport in both real and reciprocal space representations. Finally, the variational method with importance sampling is employed to investigate temperature effects on exciton transport using the multi- $D_2$  Ansatz, and it is demonstrated that the variational approach is valid in both low and high temperature regimes.

Received 17th October 2016,  
Accepted 28th November 2016

DOI: 10.1039/c6cp07107d

www.rsc.org/pccp

## 1 Introduction

Conducting polymers (CPs) are a special class of organic materials with electronic and ionic conductivity, advanced processability and extraordinary wettability.<sup>1,2</sup> In 1977, Heeger *et al.* reported oxidized iodine-doped polyacetylene as a forerunner of CPs.<sup>3,4</sup> Various experimental strategies have been developed to produce CPs by techniques such as monomer oxidation using chemical oxidative polymerization in solution,<sup>5</sup> electrochemical polymerization on conductive substrates,<sup>6</sup> and vapor-phase polymerization.<sup>7</sup> Electrical properties of CPs can be tuned by oxidation and reduction, giving rise to rapid growth of applications. Based on their good charge transport property and high luminescence quantum efficiency, important utilizations of CPs are found in large scale organic light-emitting diodes<sup>8</sup> and electronic devices such as field-effect transistors.<sup>9</sup> CPs have also been used as electrode materials for supercapacitors.<sup>10,11</sup> As a logical alternative to conventional inorganic electrode materials, a composite architecture of various CPs has been developed as a

cathode for ultrafast rechargeable batteries.<sup>12</sup> In comparison with non-conducting polymers, there are many advantages of CPs with regard to their electronic properties. CPs have also been used for other purposes.<sup>13</sup> For example, because of easy processability in microstructuring processes,<sup>14</sup> CPs have been considered for a wide range of biomedical and bioengineering applications: artificial muscles,<sup>15</sup> controlled drug release,<sup>16</sup> and neural recording.<sup>17,18</sup> Surface wettability based on CPs can switch between superhydrophilicity and superoleophobicity by surface morphology control at the nanoscale,<sup>5</sup> implying the usage of CPs in intelligent orthopedic and dental implants.<sup>19</sup>

In the aforementioned applications, the efficiency of charge carrier transport and exciton transport significantly impacts the overall device performance.<sup>13</sup> The carrier or exciton transport in CPs is well described by the Su-Schrieffer-Heeger (SSH) model in which the  $\pi$  electrons are treated in a tight-binding approximation and the  $\sigma$  electrons are assumed to move adiabatically with the nuclei.<sup>20</sup> Su *et al.* convincingly demonstrated that solitons play a critical role in the carrier transport doping mechanism.<sup>21</sup> Troisi *et al.* applied the SSH model to investigate charge carrier dynamics in crystalline organic semiconductors by solving the time-dependent Schrödinger equation for the charge wave function and using the Ehrenfest theorem for classical accelerations of nuclear positions.<sup>22,23</sup> Improvements have been made in this semi-classical method to study charge transport in organic materials in recent years.<sup>24–26</sup> Temperature dependent

<sup>a</sup> Division of Materials Science, Nanyang Technological University, Singapore, Singapore. E-mail: yzhao@ntu.edu.sg; Fax: +65 6790 9081; Tel: +65 6513 7990

<sup>b</sup> Department of Physics, Zhejiang University, Hangzhou 310027, China

<sup>c</sup> State Key Laboratory of Surface Physics and Department of Physics, Fudan University, Shanghai 200433, China

<sup>d</sup> Institute for Theoretical Physics, Technische Universität Dresden, D-01062 Dresden, Germany



charge carrier mobility has also been considered.<sup>22,26</sup> It is believed that for short times (comparable to the phonon period) the evolution of the system is dominated by semi-classical dynamics. The traditional Ehrenfest dynamics did not well treat the decoherence effect, which is incorporated by an instantaneous decoherence correction (IDC) approach in the framework of the semi-classical method.<sup>26,27</sup>

Even though the semi-classical dynamics in the SSH model can capture certain features of charge transport, enormous challenges still remain to accurately describe fully quantum dynamical correlations between the electronic and vibrational subsystems.<sup>28</sup> In realistic polymer chains, charge transport processes occur on the nano scale and the carriers interact with the environment including the dominant phonon degrees of freedom.<sup>29</sup> The SSH model includes off-diagonal exciton-phonon coupling as a nontrivial dependence of the exciton transfer integral on lattice coordinates.<sup>21,30</sup> Due to inherent difficulties, the off-diagonal coupling is often inadequately treated in theoretical studies. Early treatments of the off-diagonal coupling include the Munn-Silbey theory.<sup>31</sup> Recently, the Davydov  $D_2$  Ansatz<sup>32</sup> and the multiple Davydov trial states<sup>33</sup> have been developed to study the polaron dynamics in the presence of the off-diagonal coupling. However, much awaits to be studied on polaron dynamics with off-diagonal coupling with regard to exciton momentum redistribution and energy relaxations.<sup>34</sup>

In this work, in order to offer an accurate description of polaron dynamics including off-diagonal coupling, the Dirac-Frenkel time-dependent variational approach with the multiple Davydov trial states will be employed. We also aim to examine the accuracy of the Ehrenfest dynamics in the SSH model. We first demonstrate that the semi-classical method and the variational method using the single  $D_2$  Ansatz are equivalent. Then, we check the validity of the semi-classical method (the variational method with the single  $D_2$  Ansatz) by examining its from the exact quantum dynamics. The underlying physics is revealed in the real and reciprocal space representations, including the exciton transport, the exciton momentum redistribution and the exciton energy dissipation. At the end of the paper, we show that the fully quantum mechanical method using our multiple Davydov trial states is also applicable at finite temperatures.

The remainder of the paper is structured as follows. In Section 2, we present the model Hamiltonian and the variational wave function, the multi- $D_2$  Ansatz used for describing the exciton transport. In Section 3.1, the accuracy of the variational method using the multi- $D_2$  Ansatz is examined by the ansatz deviation, which quantifies how faithfully the trial state follows the Schrödinger equation, and it is shown that a large enhancement over that of the semi-classical method has been achieved. Numerical results of polaron dynamics by the variational method using the multi- $D_2$  Ansatz are discussed in Section 3.2. Impacts of the transfer integral and the off-diagonal coupling on the exciton transport are studied in Section 3.3. Effects of temperature on polaron dynamics is investigated in Section 3.4. Conclusions are drawn in Section 4.

## 2 Methodology

### 2.1 Model

In the presence of only off-diagonal coupling, the Hamiltonian of the one-dimensional Holstein molecular crystal model takes the form

$$\hat{H} = \hat{H}_{\text{ex}} + \hat{H}_{\text{ph}} + \hat{H}_{\text{ex-ph}}^{\text{o.d.}}, \quad (1)$$

where  $\hat{H}_{\text{ex}}$ ,  $\hat{H}_{\text{ph}}$  and  $\hat{H}_{\text{ex-ph}}^{\text{o.d.}}$  denote the exciton Hamiltonian, the bath (phonon) Hamiltonian, and the off-diagonal exciton-phonon coupling Hamiltonian, respectively. In the site representation,

$$\begin{aligned} \hat{H}_{\text{ex}} &= -J \sum_n a_n^\dagger (a_{n+1} + a_{n-1}), \\ \hat{H}_{\text{ph}} &= \omega_0 \sum_n b_n^\dagger b_n, \\ \hat{H}_{\text{ex-ph}}^{\text{o.d.}} &= \frac{1}{2} \phi \omega_0 \sum_{n,l} \left[ a_n^\dagger a_{n+1} (b_l + b_l^\dagger) (\delta_{n+1,l} - \delta_{n,l}) \right. \\ &\quad \left. + a_n^\dagger a_{n-1} (b_l + b_l^\dagger) (\delta_{n,l} - \delta_{n-1,l}) \right], \end{aligned} \quad (2)$$

where  $\hat{a}_n^\dagger$  ( $\hat{a}_n$ ) and  $\hat{b}_n^\dagger$  ( $\hat{b}_n$ ) are the exciton and phonon creation (annihilation) operators for the  $n$ -th site, respectively. In this work, only the anti-symmetric exciton-phonon coupling is considered in eqn (2). In the phonon momentum space, we can rewrite  $\hat{H}_{\text{ph}}$  and  $\hat{H}_{\text{ex-ph}}^{\text{o.d.}}$  as,

$$\begin{aligned} \hat{H}_{\text{ph}} &= \sum_q \omega_q \hat{b}_q^\dagger \hat{b}_q, \\ \hat{H}_{\text{ex-ph}}^{\text{o.d.}} &= \frac{1}{2} N^{-1/2} \phi \sum_{n,q} \omega_q \left\{ \hat{a}_n^\dagger \hat{a}_{n+1} \left[ e^{iqn} (e^{iq} - 1) \hat{b}_q + \text{H.c.} \right] \right. \\ &\quad \left. + \hat{a}_n^\dagger \hat{a}_{n-1} \left[ e^{iqn} (1 - e^{-iq}) \hat{b}_q + \text{H.c.} \right] \right\}, \end{aligned} \quad (3)$$

where  $\omega_q$  is the phonon frequency at the phonon momentum  $q$ , and  $\hat{b}_q^\dagger$  ( $\hat{b}_q$ ) is the creation (annihilation) operator of a phonon with the momentum  $q$ ,

$$\hat{b}_q^\dagger = N^{-1/2} \sum_n e^{iqn} \hat{b}_n^\dagger, \quad \hat{b}_n^\dagger = N^{-1/2} \sum_q e^{-iqn} \hat{b}_q^\dagger. \quad (4)$$

The parameters  $J$  and  $\phi$  represent the transfer integral and the off-diagonal coupling strength, respectively. A linear phonon dispersion is assumed,

$$\omega_q = \omega_0 \left[ 1 + \left( \frac{2|q|}{\pi} - 1 \right) W \right], \quad (5)$$

where  $\omega_0$  denotes the central phonon frequency,  $W$  is a constant between 0 and 1, the bandwidth of the phonon frequency is  $2W\omega_0$ , and  $q = 2\pi l/N$  represents the momentum index with  $l = \frac{N}{2} - 1, \dots, \frac{N}{2}$ . In the rest of the paper,  $\omega_0$  is set to unity as the energy unit, and a dispersionless optical phonon band with  $W = 0$  is used.

### 2.2 Multiple Davydov trial states

In this work, we employ the Dirac-Frenkel variational principle to obtain quantum dynamics. We use the multiple Davydov



trial states with multiplicity  $M$ , which are essentially  $M$  copies of the corresponding single Davydov *Ansatz*. The multi- $D_2$  *Ansatz* has less variational variables than the multi- $D_1$  *Ansatz* when the same  $M$  is used, but performs better in illuminating the polaron dynamics with the off-diagonal coupling.<sup>33</sup> The multi- $D_2$  *Ansatz* with the multiplicity  $M$ , can be written as

$$\begin{aligned} |D_2^M(t)\rangle &= \sum_i^M \sum_n^N \psi_{in} |n\rangle |\lambda_i\rangle, \\ &= \sum_i^M \sum_n^N \psi_{in} \hat{a}_n^\dagger |0\rangle_{\text{ex}} \exp \left\{ \sum_q \left[ \lambda_{iq} \hat{b}_q^\dagger - \lambda_{iq}^* \hat{b}_q \right] \right\} |0\rangle_{\text{ph}}, \end{aligned} \quad (6)$$

where  $\psi_{in}$  and  $\lambda_{iq}$  are the exciton amplitudes and the phonon displacements, respectively,  $n$  is the site index of the molecular ring, and  $i$  denotes the  $i$ -th  $D_2$  state in the coherent superposition. If  $M = 1$ , the multi- $D_2$  *Ansatz* reduces to the original single Davydov  $D_2$  trial state. Equations of motion for the variational parameters  $\psi_{in}$  and  $\lambda_{iq}$  are then derived by adopting the Dirac-Frenkel variational principle,

$$\begin{aligned} \frac{d}{dt} \left( \frac{\partial L}{\partial \dot{\psi}_{in}^*} \right) - \frac{\partial L}{\partial \psi_{in}^*} &= 0, \\ \frac{d}{dt} \left( \frac{\partial L}{\partial \dot{\lambda}_{iq}^*} \right) - \frac{\partial L}{\partial \lambda_{iq}^*} &= 0. \end{aligned} \quad (7)$$

For the multi- $D_2$  *Ansatz*, the Lagrangian  $L$  is given as

$$\begin{aligned} L &= \langle D_2^M(t) | \frac{i}{2} \frac{\partial}{\partial t} - \hat{H} | D_2^M(t) \rangle \\ &= \frac{i}{2} \left[ \langle D_2^M(t) | \frac{\partial}{\partial t} | D_2^M(t) \rangle - \langle D_2^M(t) | \frac{\partial}{\partial t} | D_2^M(t) \rangle \right] \\ &\quad - \langle D_2^M(t) | \hat{H} | D_2^M(t) \rangle, \end{aligned} \quad (8)$$

where the first term yields

$$\begin{aligned} &\frac{i}{2} \left[ \langle D_2^M(t) | \frac{\partial}{\partial t} | D_2^M(t) \rangle - \langle D_2^M(t) | \frac{\partial}{\partial t} | D_2^M(t) \rangle \right] \\ &= \frac{i}{2} \sum_{ij}^M \sum_n^N \left( \psi_{jn}^* \dot{\psi}_{in} - \dot{\psi}_{jn}^* \psi_{in} \right) S_{ji} \\ &\quad \times \sum_{ij}^M \sum_n^N \psi_{jn}^* \psi_{in} S_{ji} \sum_q \left[ \frac{\dot{\lambda}_{jq}^* \lambda_{jq} + \lambda_{jq}^* \dot{\lambda}_{jq}}{2} \right. \\ &\quad \left. - \frac{\dot{\lambda}_{iq} \lambda_{iq}^* + \lambda_{iq} \dot{\lambda}_{iq}^*}{2} + \lambda_{jq}^* \dot{\lambda}_{iq} - \dot{\lambda}_{iq} \lambda_{jq}^* \right], \end{aligned} \quad (9)$$

and the second term is

$$\begin{aligned} \langle D_2^M(t) | \hat{H} | D_2^M(t) \rangle &= \langle D_2^M(t) | \hat{H}_{\text{ex}} | D_2^M(t) \rangle \\ &\quad + \langle D_2^M(t) | \hat{H}_{\text{ph}} | D_2^M(t) \rangle \\ &\quad + \langle D_2^M(t) | \hat{H}_{\text{ex-ph}}^{\text{o.d.}} | D_2^M(t) \rangle. \end{aligned} \quad (10)$$

Detailed derivations of the equations of motion for the variational parameters are given in Appendix C, together with discussions on the initial conditions and numerical details.

To quantify the accuracy of the variational dynamics based on the multiple Davydov trial states, we introduce a deviation vector  $\vec{\delta}(t)$  defined as

$$\begin{aligned} \vec{\delta}(t) &= \vec{\chi}(t) - \vec{\gamma}(t) \\ &= \frac{\partial}{\partial t} |\Psi(t)\rangle - \frac{\partial}{\partial t} |D_2^M(t)\rangle, \end{aligned} \quad (11)$$

where the vectors  $\vec{\chi}(t)$  and  $\vec{\gamma}(t)$  obey the Schrödinger equation  $\vec{\chi}(t) = \partial |\Psi(t)\rangle / \partial t = -i\hat{H} |\Psi(t)\rangle$  and the Dirac-Frenkel variational dynamics  $\vec{\gamma}(t) = \partial |D_2^M(t)\rangle / \partial t$  in eqn (7), respectively. The deviation vector  $\vec{\delta}(t)$  can be calculated as

$$\vec{\delta}(t) = -i\hat{H} |D_2^M(t)\rangle - \frac{\partial}{\partial t} |D_2^M(t)\rangle. \quad (12)$$

Thus, the accuracy of the trial state is indicated by the amplitude of the deviation vector  $\Delta(t) = \|\vec{\delta}(t)\|$ . In order to view the deviation in the parameter space  $(W, J, \phi)$ , a dimensionless relative deviation  $\sigma$  is calculated as

$$\sigma = \frac{\max\{\Delta(t)\}}{\text{mean}\{N_{\text{err}}(t)\}}, \quad t \in [0, t_{\text{max}}], \quad (13)$$

where  $N_{\text{err}}(t) = \|\vec{\gamma}(t)\|$  is the amplitude of the time derivative of the wave function,

$$\begin{aligned} N_{\text{err}}(t) &= \sqrt{-\left\langle \frac{\partial}{\partial t} \Psi(t) \left| \frac{\partial}{\partial t} \Psi(t) \right. \right\rangle} \\ &= \sqrt{\langle D_2^M(t) | \hat{H}^2 | D_2^M(t) \rangle}. \end{aligned} \quad (14)$$

With the wave function  $|D_2^M(t)\rangle$  obtained, the total energy  $E_{\text{total}} = E_{\text{ex}} + E_{\text{ph}} + E_{\text{ex-ph}}$  is calculated, where  $E_{\text{ex}} = \langle D_2^M(t) | \hat{H}_{\text{ex}} | D_2^M(t) \rangle$ ,  $E_{\text{ph}} = \langle D_2^M(t) | \hat{H}_{\text{ph}} | D_2^M(t) \rangle$ , and  $E_{\text{ex-ph}} = \langle D_2^M(t) | \hat{H}_{\text{ex-ph}}^{\text{o.d.}} | D_2^M(t) \rangle$  (see eqn (32)). In addition, the exciton probability  $P_{\text{ex}}(t, n)$  and the exciton momentum probability  $P_{\text{ex}}(t, k)$  are also calculated

$$\begin{aligned} P_{\text{ex}}(t, n) &= \langle D_2^M(t) | \hat{a}_n^\dagger \hat{a}_n | D_2^M(t) \rangle, \\ P_{\text{ex}}(t, k) &= \langle D_2^M(t) | \hat{a}_k^\dagger \hat{a}_k | D_2^M(t) \rangle, \end{aligned} \quad (15)$$

where  $\hat{a}_k^\dagger$  ( $\hat{a}_k$ ) is the creation (annihilation) operator of the exciton with the exciton momentum  $k$ ,

$$\hat{a}_k^\dagger = N^{-1/2} \sum_n e^{-ikn} \hat{a}_n^\dagger, \quad \hat{a}_k = N^{-1/2} \sum_n e^{ikn} \hat{a}_n. \quad (16)$$

We then calculate the mean square displacement  $\text{MSD}(t)$  of the exciton probability  $P_{\text{ex}}(t, n)$  as a function of time  $t$ ,

$$\begin{aligned} c(t) &= \sum_n^n n P_{\text{ex}}(t, n), \\ \text{MSD}(t) &= \sum_n^n [n - c(t)]^2 P_{\text{ex}}(t, n), \end{aligned} \quad (17)$$



where  $c(t)$  describes the centroid motion of the exciton probability. In the exciton momentum representation, the counterpart,  $k$ -MSD( $t$ ) denotes the degree of deviation of the state at the time  $t$  from the initial state, as shown in the following equations,

$$c_k(t) = \sum_{k=-\pi}^{\pi} k P_{\text{ex}}(t, k),$$

$$k\text{-MSD}(t) = \sum_{k=-\pi}^{\pi} [k - c_k(t)]^2 P_{\text{ex}}(t, k), \quad (18)$$

where  $c_k(t)$  illustrates the centroid motion of the exciton momentum probability.

## 3 Results and discussions

### 3.1 The multi- $D_2$ Davydov Ansatz

In this subsection, the dynamics of Hamiltonian (1) is described fully quantum mechanically using the multi- $D_2$  Ansatz with sufficiently large multiplicity  $M$ , yielding numerically accurate quantum dynamics at zero temperature.<sup>33</sup>

We first test the accuracy of our multi- $D_2$  Ansatz with parameters extracted from ref. 22 and 26 (this parameter set was extensively used to study realistic models of pentacene molecules). As shown in Fig. 1, the relative deviation  $\sigma$  goes to zero as the multiplicity  $M$  approaches infinity. A log-log plot of  $(\sigma, 1/M)$  (inset) indicates a power-law relationship with an exponent of  $\mu = 0.29(1)$ , further inferring a numerically exact solution in the limit of  $M \rightarrow \infty$ . The largest relative deviation  $\sigma$  is found for the single  $D_2$  Ansatz. As presented in Appendix A, the SSH Hamiltonian is equivalent to the Holstein Hamiltonian with off-diagonal coupling only. The equivalence between the semiclassical method and the variational method using the single  $D_2$  Ansatz is shown in Appendix B. Therefore, this implies that the accuracy of the semi-classical Ehrenfest dynamics can be quantified by the relative deviation of the single  $D_2$  Ansatz. The variational method with sufficiently large  $M$  fully takes into account the quantum effects, yielding a much more accurate result than that with the single  $D_2$  Ansatz, which is equivalent to the semi-classical method. For example, the  $\sigma$  of the  $D_2^{M=16}$  Ansatz in Fig. 1 is smaller than 0.1, thus the multiplicity of  $M = 16$  is

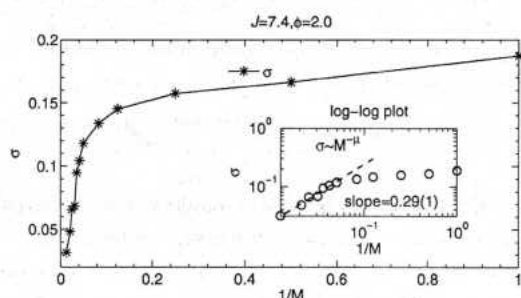


Fig. 1 The relative deviation  $\sigma$  of the multi- $D_2$  Ansatz is displayed as a function of  $1/M$  for a commonly used set of parameters with off-diagonal coupling  $\phi = 2.0$  and large transfer integral  $J = 7.4$ . In the inset, the relationship  $\sigma \sim M^\mu$  is displayed on a log-log scale and the dashed line represents a power-law fit.

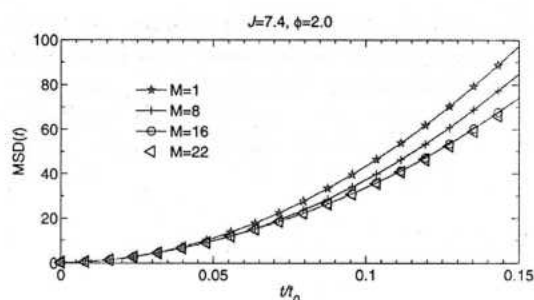


Fig. 2 MSD( $t$ ) of the exciton for the case of  $J = 7.4$  and  $\phi = 2.0$  is obtained from the single  $D_2^{M=1}$ , the  $D_2^{M=8}$ , the  $D_2^{M=16}$ , and the  $D_2^{M=22}$  Ansatz, respectively.

employed to explore polaron dynamics in following subsections, unless otherwise specified.

In order to further compare the performance of our variational method using the multi- $D_2$  Ansatz and that of the semi-classical method, the exciton movement is studied by calculating the mean square displacement MSD( $t$ ). As shown in Fig. 2, the amplitudes of MSD( $t$ ) from the fully quantum variational method using the  $D_2^{M=8}$ , the  $D_2^{M=16}$ , and the  $D_2^{M=22}$  Ansatz are smaller than that from the semi-classical Ehrenfest method (equivalent to the single  $D_2$  Ansatz), and MSD( $t$ ) shows apparent convergence as the multiplicity  $M$  exceeds 16. This result is in agreement with that obtained by the IDC approach, in which the carrier is found to be less mobile in comparison with that of the original Ehrenfest method.<sup>27,35</sup> In this case, the transfer integral is much larger than the exciton-phonon coupling and makes more contribution to the movement of the wave front in the carrier propagation. Consequently, the exciton-phonon coupling leads to localization of the wave front. The Ehrenfest method treats the phonons semi-classically and underestimates the confinement effect of the exciton-phonon coupling on the wave function. Therefore, the reduction of the mobility is attributed to the quantum mechanical description of the phonons and the electron-phonon coupling. We note, however, the change in MSD( $t$ ) depends on parameter regimes. In some other cases (e.g.,  $J = 0$  and  $\phi = 1.0$ ), phonon assisted transport dominates the exciton movement as discussed in ref. 33.

### 3.2 Polaron dynamics in exciton momentum representation

In this subsection, we explore the impacts of off-diagonal coupling on the exciton movement in the exciton momentum representation by using the multi- $D_2$  Ansatz. Without the exciton-phonon coupling, the Hamiltonian of the bare exciton can be described by the first term of Hamiltonian (1),  $\hat{H}_{\text{ex}}$ , and the energy band is  $E(k) = -2J \cos(k)$ . The exciton energy and the exciton momentum are constants of motion. However, in the presence of the exciton-phonon coupling, the exciton momentum may move away from the initial values and the exciton energy would be dissipated.

The left and the right column of Fig. 3(a)–(d) present the time evolution of the exciton momentum probability  $P_{\text{ex}}(t, k)$ , starting from the initial conditions  $P_{\text{ex}}(0, k) = 1$  at  $k = 0$  and  $\pi$ , respectively.  $P_{\text{ex}}(t, k)$  redistributes toward a quasi stationary state, where no net energy transfer takes place between the exciton and the phonons, as shown in Fig. 3(e) and (f).



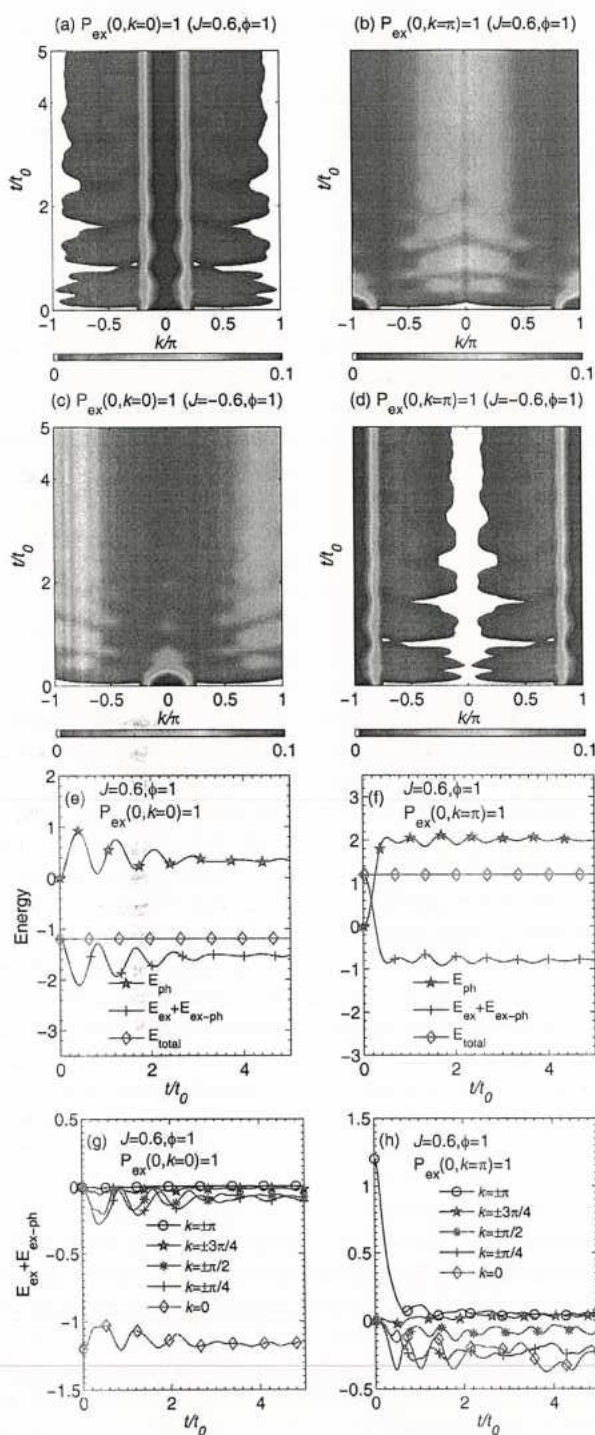


Fig. 3 (a–d) Time evolution of the exciton momentum probability  $P_{\text{ex}}(t, k)$  is obtained using two excitonic initial conditions:  $P_{\text{ex}}(0, k = 0) = 1$  (left column) and  $P_{\text{ex}}(0, k = \pi) = 1$  (right column). Two transfer integrals,  $J = 0.6$  and  $-0.6$ , are used together with the same off-diagonal coupling strength  $\phi = 1$ . Energies for the case of  $J = 0.6$  and  $\phi = 1$  are plotted for (e)  $P_{\text{ex}}(0, k = 0) = 1$  and (f)  $P_{\text{ex}}(0, k = \pi) = 1$ . Energies of the exciton and the exciton-phonon coupling are displayed for each exciton momentum  $k$  using the initial conditions of (g)  $P_{\text{ex}}(0, k = 0) = 1$  and (h)  $P_{\text{ex}}(0, k = \pi) = 1$ . The number of sites  $N = 8$  is fixed in these calculations.

Notwithstanding the difference in the initial excitonic conditions,  $P_{\text{ex}}(t, k)$  in the case of Fig. 3(a) and (b) still relaxes to the same stationary regime, where the final  $P_{\text{ex}}(t, k)$  is centered around  $k = 0$ . As for  $J = -0.6$ ,  $P_{\text{ex}}(t, k)$  is centered around  $k = \pm\pi$ , as shown in Fig. 3(c) and (d). Moreover, the exciton momentum pattern in Fig. 3(a) is shifted by  $\pi$  compared to that in Fig. 3(d) because the Brillouin zone of the former is shifted by  $\pi$  from that of the latter, and the shift also occurs for  $P_{\text{ex}}(t, k)$  in Fig. 3(b) and (c).

The energy relaxation process is known to be accompanied by a redistribution of the exciton momentum probability.<sup>34</sup> With regard to the Holstein model with diagonal coupling, the exciton kinetic energy is transferred to the phonons, ending up with a constant value of  $E_{\text{ex}} + E_{\text{ex-ph}}$ .<sup>36</sup> However, energy relaxation in the Holstein model with off-diagonal coupling is still not well understood. In order to clarify this issue, we consider time evolution of the exciton and the phonon energy. Fig. 3(e) and (f) show the time evolution of energies in the case of  $J = 0.6$  and  $\phi = 1$  for  $P_{\text{ex}}(0, k = 0) = 1$  and  $P_{\text{ex}}(0, k = \pi) = 1$ , respectively. Under this parameter set, the initial exciton energy of  $P_{\text{ex}}(0, k = 0) = 1$  is the lowest, that of  $P_{\text{ex}}(0, k = \pi) = 1$  is the highest, and those of the other initial conditions fall in between. After the transfer integral is changed to  $J = -0.6$ , due to a phase shift of the Brillouin zone in the exciton momentum space, the initial exciton energy of  $P_{\text{ex}}(0, k = 0) = 1$  becomes maximal, while that of  $P_{\text{ex}}(0, k = \pi) = 1$  turns to minimal under all initial excitonic conditions. As a result, identical energy relaxation processes occur despite that transfer integrals have opposite signs. Thus, only the case of  $J = 0.6$  and  $\phi = 1$  is displayed for simplicity. At  $t = 0$ , the phonons are in their vacuum states. Later, the incident exciton wave fronts generate phonons via the exciton-phonon coupling. As a consequence, the exciton energy is transferred to the phonon degrees of freedom. After a fast relaxation process, both the energies of the exciton and the phonons reach steady values.  $E_{\text{ex}} + E_{\text{ex-ph}}$  in the steady state settles around  $-2|J|$ , which corresponds to the energy minimum of the exciton in the absence of the exciton-phonon coupling. In order to identify the energy contribution of each exciton momentum, we also investigate  $E_{\text{ex}} + E_{\text{ex-ph}}$  in the exciton momentum representation. As plotted in Fig. 3(g) and (h), the initial  $E_{\text{ex}} + E_{\text{ex-ph}}$  is  $-1.2$  and  $1.2$ , respectively. After relaxation, the momentum of  $k = 0$  becomes the main contributor of  $E_{\text{ex}} + E_{\text{ex-ph}}$  for both cases, and also determines the locations of the quasi stationary regime after the exciton momentum redistribution.

Fig. 4 presents the time evolution of the exciton momentum probability in the absence of the transfer integral. We set the initial excitonic conditions  $P_{\text{ex}}(0, k) = 1$  of  $k = 0$  and  $\pi$  in the left ((a), (c) and (e)) and the right ((b), (d) and (f)) column of Fig. 4, respectively. Akin to the cases of  $J = 0.6$  and  $\phi = 1$  in Fig. 3, by comparing  $P_{\text{ex}}(t, k)$  with two types of initial conditions, it is found that the exciton momentum probabilities redistribute and become centered around the same regimes, as shown in Fig. 4(a) and (b). Even in the absence of the transfer integral, the exciton can still be transported by the off-diagonal coupling. Fig. 4(c) and (d) plot the time evolution of the phonon energy and the exciton-phonon interaction energy. As also shown in



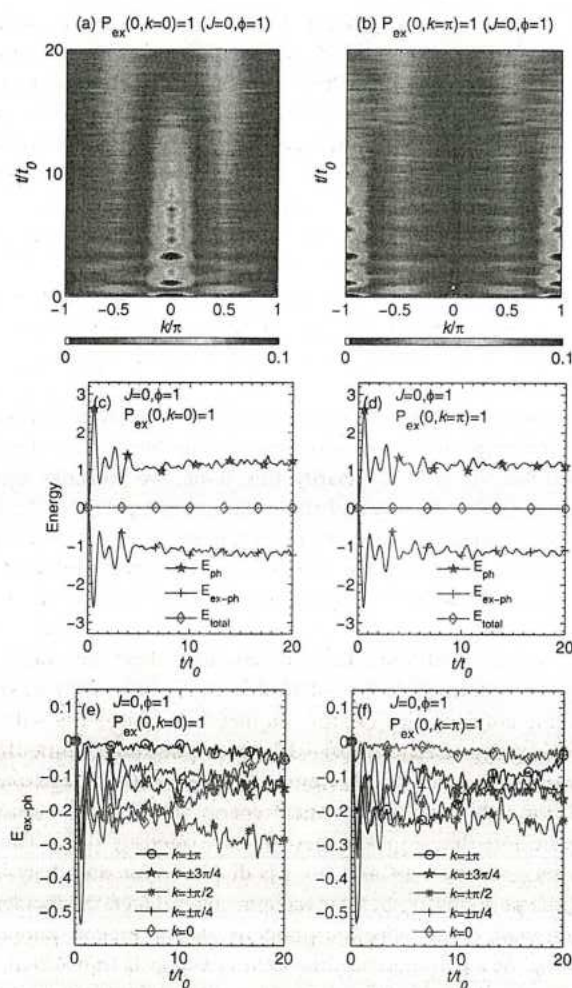


Fig. 4 Time evolution of the exciton momentum probability  $P_{\text{ex}}(t, k)$  for  $J = 0$  and  $\phi = 1$  is obtained using two initial conditions: (a)  $P_{\text{ex}}(0, k = 0) = 1$  (left column) and (b)  $P_{\text{ex}}(0, k = \pi) = 1$  (right column). Corresponding energies are displayed in (c) and (d). The contributions to the exciton-phonon interaction energy from each exciton momentum are shown in (e) and (f).

Fig. 4(c) and (d), for  $0 < t < t_0$ , the amplitudes of both  $E_{\text{ph}}$  and  $E_{\text{ex-ph}}$  reach their peaks and fluctuate until the exciton and the phonons cease to exchange energy at  $t = 10t_0$ . The energy relaxation process only involves  $E_{\text{ex-ph}}$  because  $E_{\text{ex}}$  is always zero. As presented in Fig. 4(e),  $E_{\text{ex-ph}}$  of each exciton momentum undergoes three stages during the energy relaxation process. During  $0 < t \leq t_0$ , they all show strong oscillations with the largest amplitudes. At the intermediate stage  $t_0 < t \leq 10t_0$ , the energies of  $k = \pm\pi/2$  compete with that of  $k = 0$ . At  $t > 10t_0$ , the contribution of the energy of  $k = 0$  to  $E_{\text{ex-ph}}$  reduces to almost zero, leaving the energy of  $k = \pm\pi/2$  to be the dominant energy contributor. As for the case of the initial condition  $P_{\text{ex}}(0, k = \pi) = 1$  as shown in Fig. 4(f), the competition at the second stage  $t_0 < t \leq 10t_0$  occurs between the energies of  $k = \pm\pi$  and  $\pm\pi/2$  instead, and the energy of  $k = \pm\pi/2$  also turns out to be the prominent contributor to  $E_{\text{ex-ph}}$ . Consequently, the exciton momentum probability finally becomes centered around  $k = \pm\pi/2$  as shown in Fig. 4(a) and (b).

### 3.3 Effect of transfer integral and off-diagonal coupling on exciton transport

In this subsection, we investigate the influence of the transfer integral and the off-diagonal coupling on exciton transport of Hamiltonian (1).

By tuning the transfer integral, contributions of the transfer integral and the off-diagonal coupling to the exciton movement are examined, as shown in Fig. 5. It can be shown in the site representation that the off-diagonal exciton-phonon coupling plays a crucial role in polaron transport.<sup>37,38</sup> As shown in Fig. 5(b), the off-diagonal coupling is the only agent for exciton movement in the absence of the transfer integral, also known as phonon-assisted transport.<sup>39</sup> When both the off-diagonal coupling and the direct, phonon-free exchange transfer are present, because of the competition between them, the exciton transport may be inhibited, as shown in Fig. 5(a). The self-trapping phenomenon is expected due to the competition between the off-diagonal coupling and the transfer integral when the energy bands are flattened at the Brillouin zone center.<sup>30</sup> In this work, the Toyozawa Ansatz is adopted to study the ground state energy bands of the Holstein model using the variational method. As presented in Fig. 5(i), the lowest energy band of  $J = 0.5$  and  $\phi = 1.0$  meets the self-trapping condition, and we can thereby take this case as an example to study the self-trapped exciton from the perspective of dynamics. In agreement with our expectation,  $P_{\text{ex}}(t, n)$  turns out to be localized in Fig. 5(a). By directly flipping the sign of the transfer integral to  $J = -0.5$ , the exciton wave fronts are found to move considerably, as shown in Fig. 5(c). Using  $\text{MSD}(t)$  as defined in eqn (17), the expansion of the exciton wave packets is further investigated for  $J = -0.6, -0.5, 0, 0.5$  and  $0.6$ . As plotted in Fig. 5(g), the amplitude of  $\text{MSD}(t)$  for  $J = 0$  and  $\phi = 1$  is smaller than those in other cases with non-zero transfer integrals, except for the self-trapped case of  $J = 0.5$  and  $\phi = 1.0$ .

In the crystal momentum representation, the underlying physics of the ground states can be elucidated, where the crystal momentum is denoted as  $K$  (see eqn (38)). The Toyozawa Ansatz is a time independent translationally invariant trial state, viewed as a superposition of the replicas of the  $D_2$  Ansatz displaced to every lattice site, weighed by a phase factor of the total momentum.<sup>30</sup> We analyzed the energy bands of the ground states obtained from the Toyozawa Ansatz (see Appendix D). In the off-diagonal coupling only case ( $J = 0$ ), the minima of the band are located at  $K = \pm\pi/2$ . The addition of positive (negative) transfer integrals moves the minima towards the center (boundary). In particular, as mentioned above, in the case of  $J = 0.5$  the band flattens at the center of the Brillouin zone, leading to the largest effective mass among all the studied cases, in accord with the self-trapping of  $P_{\text{ex}}(t, n)$  in Fig. 5(a).

The effect of the transfer integrals on the exciton movement in the presence of the off-diagonal coupling is further examined in the exciton momentum representation in Fig. 5(d)–(f) and (h). The exciton is created in the profile of  $(2 + \cos k)/2N$  in the momentum space as we excite two nearest neighboring sites initially (see Appendix C). In the subsequent relaxation process,



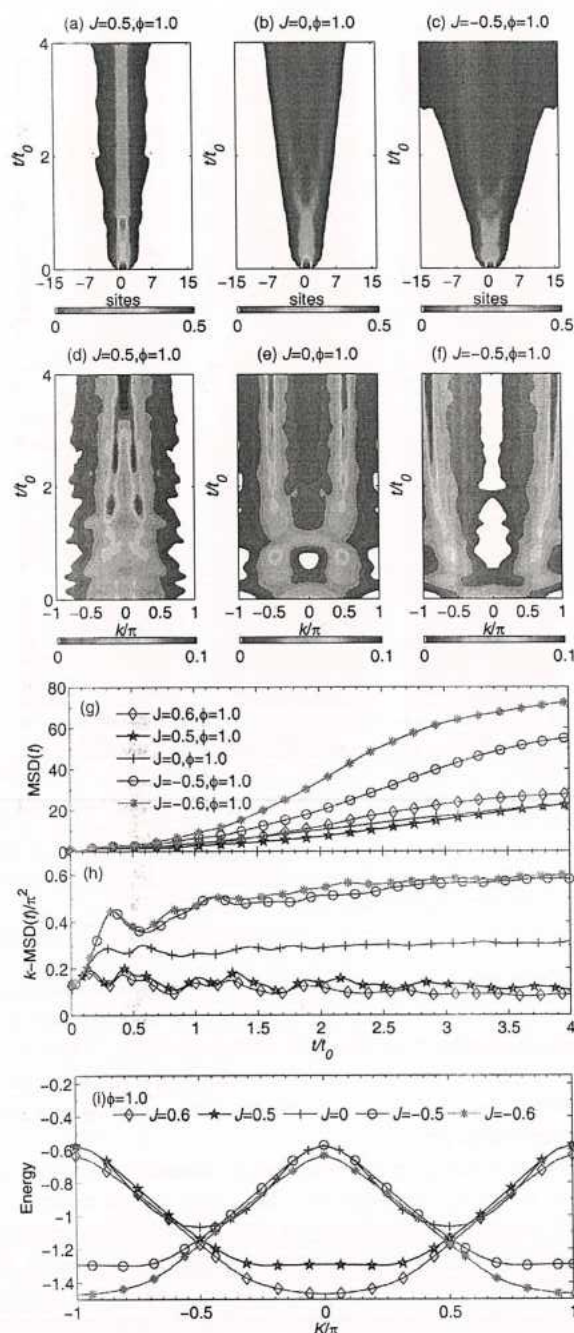


Fig. 5 Time evolution of the exciton probability  $P_{\text{ex}}(t, n)$  for the case of the off-diagonal coupling ( $\phi = 1.0$ ) is obtained with transfer integrals (a)  $J = 0.5$ , (b) 0, and (c)  $-0.5$ ; the related time evolution of the exciton momentum probability  $P_{\text{ex}}(t, k)$  is shown in (d)–(f); (g)  $\text{MSD}(t)$  of  $J = 0.6, 0.5, 0, -0.5$  and  $-0.6$  together with  $\phi = 1.0$  is plotted in the site representation; (h)  $k\text{-MSD}(t)$  is displayed in the exciton momentum representation; (i) energy bands of the ground state are obtained from the Toyozawa Ansatz. The number of sites  $N = 32$  is fixed in these calculations.

$P_{\text{ex}}(t, k)$  redistributes and becomes localized in a quasi stationary region, and the mean square displacement of the exciton momentum  $k\text{-MSD}(t)$  approaches a plateau, as shown in Fig. 5(h).

After the relaxation process, the final  $P_{\text{ex}}(t, k)$  is found to be determined by a combination of the transfer integral and the off-diagonal coupling strength. For the off-diagonal coupling only case,  $P_{\text{ex}}(t, k)$  progressively becomes localized around  $k = \pm\pi/2$  (Fig. 5(e)). In the case of  $J = 0.5$  and  $0.6$ ,  $P_{\text{ex}}(t, k)$  aggregates toward  $k = 0$ , as seen in Fig. 5(d). Similarly, the  $P_{\text{ex}}(t, k)$  of both  $J = -0.5$  and  $-0.6$  correspond to  $\pm\pi$  in Fig. 5(f). In addition,  $k\text{-MSD}(t)$  of the extreme cases of  $P_{\text{ex}}(t, k) = \delta_{k,0}$  and  $\delta_{k,\pm\pi}$  are 0 and  $2\pi^2$ , respectively. As shown in Fig. 5(h),  $k\text{-MSD}(t)$  of  $J = 0.6$  is closer to the analytical value of 0 than that of  $J = 0.5$ , indicating that the  $P_{\text{ex}}(t, k)$  of  $J = 0.6$  is more localized around the zone center than that of  $J = 0.5$ . Likewise,  $k\text{-MSD}(t)$  of  $J = -0.6$  is nearer to the limited value of  $2\pi^2$  than that of  $J = -0.5$ , illustrating that the  $P_{\text{ex}}(t, k)$  of the former case is more localized around  $k = \pm\pi$ .

In the site representation, the off-diagonal coupling is known to play the role of assisting the transport of the exciton.<sup>38,39</sup> In Fig. 6(a), in the absence of the transfer integral ( $J = 0$ ), we study the dependence of  $\text{MSD}(t)$  on the off-diagonal coupling strength. It is found that the exciton propagation is facilitated by the off-diagonal coupling, as shown by the site-space  $\text{MSD}(t)$  in Fig. 6(a). However, the off-diagonal coupling can be simultaneously an agent for exciton localization. The localization effect of  $\phi$  gradually increases with the coupling strength  $\phi$  if  $\phi$  is greater than a critical value  $\phi_c$ .<sup>32</sup> As shown in Fig. 6(a), the amplitude of  $\text{MSD}(t)$  decreases with the off-diagonal coupling strength  $\phi$  for  $\phi > \phi_c = 1.0$ .

In the exciton momentum representation,  $P_{\text{ex}}(t, k)$  all end up around  $k = \pm\pi/2$  for a variety of off-diagonal coupling strengths, and the corresponding  $k\text{-MSD}(t)$  approaches the same narrow regime around  $0.25\pi^2$ , which is the theoretical value of  $k\text{-MSD}(t)$  for  $P_{\text{ex}}(t, k) = (\delta_{k,\pi/2} + \delta_{k,-\pi/2})/2$ , as shown in Fig. 6(b). However, the relaxation time diverges due to the variance of the off-diagonal coupling. The time for the exciton momentum to reach the stationary regime is inversely related to the off-diagonal coupling

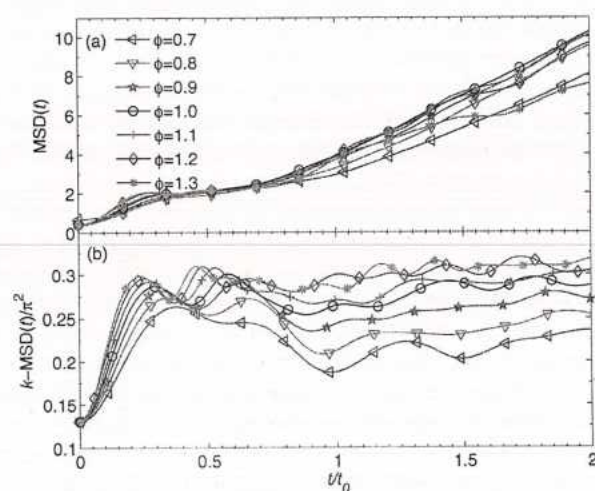


Fig. 6 (a)  $\text{MSD}(t)$  of the exciton in the site representation is shown for  $J = 0$  and  $\phi = 0.7, 0.8, 0.9, 1.0, 1.1, 1.2$  and  $1.3$ ; the related  $k\text{-MSD}(t)$  in the exciton momentum representation is displayed in (b).



## Paper

strength, because the first stage of the time evolution ( $t < 0.5t_0$ ) is accompanied by a fast exciton movement in the case of large off-diagonal coupling as presented in Fig. 6. In addition, the energy bands of various off-diagonal coupling strengths imply that the band width and effective mass are largest for  $\phi_c^{\text{static}} = 1.4$  and get smaller as  $\phi$  moves away from  $\phi_c^{\text{static}}$ .<sup>32</sup> The localization feature is found both in static and dynamic calculations although the value of  $\phi_c$  differs slightly. The off-diagonal exciton-phonon coupling leads to exciton energy dissipation and redistribution of exciton momentum in three typical scenarios corresponding to completely distinguishable band structures (this conclusion is independent of the system size), which may be formed due to a variety of compositions and geometrical structures of the organic materials, defects, doping mechanisms and deformations of CPs.<sup>40,41</sup>

### 3.4 Temperature effects

In this subsection, we extend the work to study the effect of finite temperatures on polaron dynamics. The conductivity of polymers has been measured by many researchers as a function of temperature.<sup>20,42,43</sup> The temperature effects have been in contention from a theoretical point of view. For example, Cruzeiro *et al.* claims that the Davydov soliton is stable at  $T = 310$  K.<sup>44</sup> Later, a quantum Monte Carlo treatment has shown that the Davydov soliton is unstable above 7 K.<sup>45</sup> In this work, several approaches are used to study the temperature effects: a variational method with importance sampling (see Appendix E.2), the hierarchical equations of motion (HEOM) method,<sup>46,47</sup> and the averaged Hamiltonian method (see Appendix E.1). The variational method with importance sampling developed by Wang *et al.* simulates the thermal fluctuation of phonon modes by sampling the initial phonon displacements based on the Bose distribution, and thus it can deal with Holstein polaron dynamics at both low and high temperatures.<sup>48</sup> The HEOM method is numerically exact and is capable of treating any finite temperature, serving as a benchmark here. However, the HEOM method is also numerically expensive and thus impractical when the system size is large. The variational approach can treat large systems once a suitable trial wave function is adopted. In order to compare with previous attempts in the literature, the averaged Hamiltonian method has also been used, and we found that this approach is not even suitable for the spin-boson model (*i.e.*,  $N = 2$ ) as shown in Appendix E.

Fig. 7 shows polaron dynamics calculated by the multi- $D_2$  Ansatz with importance sampling and the HEOM method at two temperatures. The calculations are carried out for  $J = 0.8$  and  $\phi = 0.3$  in a ring of  $N = 8$  sites.  $P_{\text{ex}}(t, n)$  outputs obtained from the  $D_2^{M=16}$  Ansatz and the HEOM method at  $T = 0$  are shown and compared in Fig. 7(a) and (b), respectively. As revealed in Fig. 7(c),  $\Delta P_{\text{ex}}(t, n)$ , *i.e.*, the difference between the two methods, is two orders of magnitude smaller than the value of  $P_{\text{ex}}(t, n)$ , indicating that the variational method can be numerically exact at low temperatures with sufficient multiplicity  $M$  of the multi- $D_2$  Ansatz. The phonon displacement  $\lambda_{i,q}(t = 0)$  is set to zero at  $T = 0$ , while importance sampling is used at  $T = 2/k_B$  ( $\beta = 0.5$ ) to simulate the finite temperature effects with the results displayed

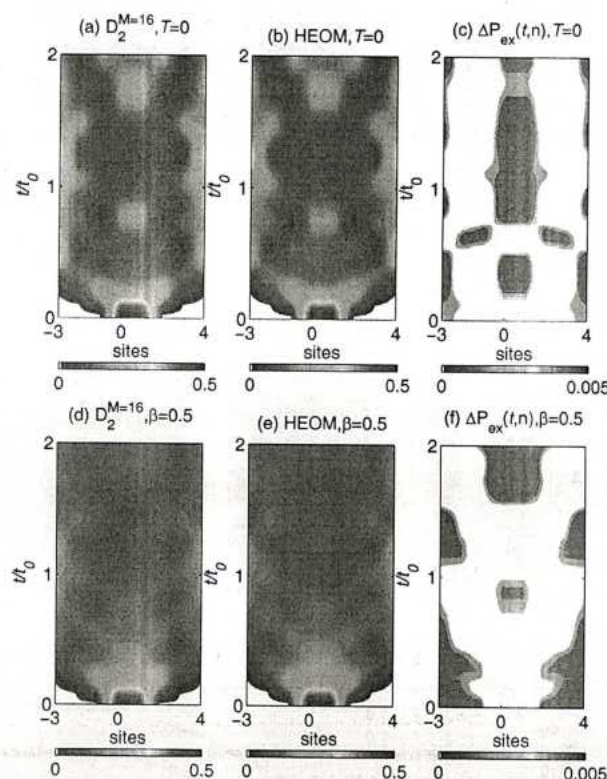


Fig. 7 Time evolution of the exciton probability  $P_{\text{ex}}(t, n)$  obtained at  $T = 0$  and  $2/k_B$ .  $P_{\text{ex}}(t, n)$  at  $T = 0$  obtained from (a) the  $D_2^{M=16}$  Ansatz, (b) the HEOM method, and (c)  $\Delta P_{\text{ex}}(t, n)$  between the  $D_2^{M=16}$  Ansatz and the HEOM method;  $P_{\text{ex}}(t, n)$  obtained from (d) the  $D_2^{M=16}$  Ansatz, (e) the HEOM method, and (f) the related  $\Delta P_{\text{ex}}(t, n)$  at  $T = 2/k_B$  ( $\beta = 0.5$ ).

in Fig. 7(d). Similarly, as shown in Fig. 7(f), differences between the results obtained from the two methods are two orders of magnitude smaller than the value of  $P_{\text{ex}}(t, n)$  in Fig. 7(d) and (e), inferring that the variational method with importance sampling provides numerically exact results at high temperatures with sufficiently large  $M$ .

Next, we investigate the influence of thermal fluctuations on exciton transport. At both low and high temperatures, the exciton wave fronts depart from the site of exciton creation and propagate in opposing directions until they meet at the opposite side of the ring. During the time evolution, distinct features observed at zero temperature (Fig. 7(a) and (b)) are now significantly smeared due to the thermal fluctuations (Fig. 7(d) and (e)). As shown in Fig. 7(d) and (e), during  $0.2t_0 < t < t_0$  the exciton probability is more centered around the site of creation than those of Fig. 7(a) and (b). At  $t \geq t_0$ , the bright spots shown in Fig. 7(a) and (b) are significantly quenched in Fig. 7(d) and (e). These results indicate that the exciton transport is weakened when the temperature is increased, in line with ref. 22 and 49.

## 4 Conclusion

In this work, we have studied the dynamics of the Holstein molecular crystal model with off-diagonal coupling using the



Dirac–Frenkel time-dependent variational principle and the novel multi- $D_2$  Ansatz, which is a linear combination of the usual Davydov  $D_2$  trial state from the soliton literature. The semi-classical Ehrenfest method, traditionally used to simulate such dynamics, has been shown to be equivalent to our time-dependent variational method with the single  $D_2$  Ansatz. The calculation of the relative deviation, which quantifies the Ansatz accuracy, demonstrates that the variational method with the multi- $D_2$  Ansatz presents much more accurate results than the semi-classical Ehrenfest dynamics. With a sufficiently large multiplicity, our variational method using the multi- $D_2$  Ansatz can offer numerically exact solutions. We further compare MSD( $t$ ) obtained from the semi-classical method with that from the multi- $D_2$  Ansatz, and find that the mobility is overestimated by the semi-classical method. These results indicate that the description beyond the semi-classical method is essential to quantitatively capture the dynamics of the SSH model.

Secondly, we have explored the underlying physics from the accurate dynamics data for the Holstein model with the off-diagonal coupling. The energy and the momentum of the bare exciton are constants of motion. However, in the presence of the exciton–phonon coupling, the exciton momentum probability is found to redistribute and become centered in stationary regions. We reveal that the momentum redistribution is only determined by the combination of the transfer integral and the off-diagonal coupling strength, and is independent of the initial excitonic conditions used. In addition, in order to study the competition between the transfer integral and the off-diagonal coupling, we investigate the exciton transport within the exciton site and the exciton momentum representation, and the crystal momentum representation. The results show that the combination of the transfer integral and the off-diagonal coupling does not necessarily play a role in enhancing the exciton transport. Moreover, the off-diagonal coupling is demonstrated to be the simultaneous agent of transport and localization in dynamical calculations.

Lastly, the temperature effects are studied using the variational method with importance sampling by employing the multi- $D_2$  Ansatz. In both the low and high temperature regimes, the time evolution of the exciton probability calculated from the variational method with importance sampling agrees well with that from the numerically exact HEOM method, and can be obtained much more efficiently. The results at finite temperatures show that fast delocalization of the exciton wave is quenched due to thermal fluctuations, indicating the weakening of the exciton transport by increasing the temperature.

## Appendix A. Fully quantum description of the semiclassical Hamiltonian

The semi-classical Hamiltonian is composed of the electronic and the phonon part  $H = H_{\text{el}} + H_{\text{ph}}$ , the electronic part is

$$H_{\text{el}} = \sum_n [-J + \alpha(u_{n+1} - u_n)](\hat{a}_n^\dagger \hat{a}_{n+1} + \text{H.c.}), \quad (19)$$

where  $J$  is the transfer integral,  $\alpha$  the electron–phonon coupling constant,  $u_n$  the displacement of phonon on the  $n$ -th site, and  $\hat{a}_n^\dagger$  ( $\hat{a}_n$ ) are the creation (annihilation) operators of the electron. The phonon part is

$$H_{\text{ph}} = \frac{K}{2} \sum_n (u_{n+1} - u_n)^2 + \frac{M}{2} \sum_n \dot{u}_n^2, \quad (20)$$

in which,  $K$  denotes the force constant originating from the  $\sigma$  bond between carbon atoms,  $K = M\omega_0^2$  and  $M$  is the total mass of a CH-unit for *trans*-polyacetylene. The combination of the two parts mentioned above is identical to the Su–Schrieffer–Heeger (SSH) model used for conductive polymers.<sup>20</sup>

Using the quantum mechanical creation and annihilation operators to describe the displacement of the phonon bath,

$$u_n = \sqrt{\frac{1}{2M\omega}}(\hat{b}_n^\dagger + \hat{b}_n) \\ \gamma = \sqrt{\frac{1}{2M\omega}}\alpha \quad (21)$$

we get  $\hat{H} = \hat{H}_{\text{ex}} + \hat{H}_{\text{ph}} + \hat{H}_{\text{int}}$ , with the electronic part

$$\hat{H}_{\text{ex}} = -J \sum_n (\hat{a}_n^\dagger \hat{a}_{n+1} + \text{H.c.}), \quad (22)$$

the phonon part

$$\hat{H}_{\text{ph}} = \sum_n \omega_0 \hat{b}_n^\dagger \hat{b}_n, \quad (23)$$

and the electron–phonon interaction part

$$\hat{H}_{\text{int}} = \gamma \sum_{n,l} [\hat{a}_n^\dagger \hat{a}_{n+1} (\hat{b}_l + \hat{b}_l^\dagger) (\delta_{n+1,l} - \delta_{n,l}) \\ + \hat{a}_n^\dagger \hat{a}_{n-1} (\hat{b}_l + \hat{b}_l^\dagger) (\delta_{n,l} - \delta_{n-1,l})]. \quad (24)$$

By Fourier transforming the phonon operators into momentum space,

$$\hat{b}_n^\dagger = N^{-1/2} \sum_q e^{-iqn} \hat{b}_q^\dagger, \\ \hat{b}_n = N^{-1/2} \sum_q e^{iqn} \hat{b}_q, \quad (25)$$

we get

$$\hat{H}_{\text{ex}} = -J \sum_n (\hat{a}_n^\dagger \hat{a}_{n+1} + \text{H.c.}), \\ \hat{H}_{\text{ph}} = \omega_0 \sum_q \hat{b}_q^\dagger \hat{b}_q, \\ \hat{H}_{\text{ex-ph}}^{\text{o.d.}} = \gamma N^{-1/2} \sum_{n,q} \left\{ \hat{a}_n^\dagger \hat{a}_{n+1} [e^{iqn} (e^{iq} - 1) \hat{b}_q + \text{H.c.}] \right. \\ \left. + \hat{a}_n^\dagger \hat{a}_{n-1} [e^{iqn} (1 - e^{-iq}) \hat{b}_q + \text{H.c.}] \right\}, \quad (26)$$

just being the off-diagonal Holstein polaron model.

## Appendix B. Comparison between the variational method using the single $D_2$ Ansatz and the semi-classical method

In this part, it is shown that the dynamics obtained from the semi-classical method and the variational method using only the single  $D_2$  Ansatz are equivalent for the spin-boson model ( $N = 2$ ).

### B.1 The variational method

The Hamiltonian of the spin-boson model is

$$\hat{H} = \frac{\varepsilon}{2}\sigma_z + V\sigma_x + \omega\hat{a}^\dagger\hat{a} + \frac{\lambda}{2}\sigma_z(\hat{a}^\dagger + \hat{a}) + \frac{\phi}{2}\sigma_x(\hat{a}^\dagger + \hat{a}), \quad (27)$$

where  $\varepsilon$  and  $V$  are the spin bias and the tunneling constant, respectively.  $\lambda(\phi)$  is the diagonal(off-diagonal) coupling strength.  $\sigma_x$  and  $\sigma_z$  are the Pauli matrices,  $\hat{a}^\dagger(\hat{a})$  is the boson creation (annihilation) operator for the phonon of frequency  $\omega_0$ .

Using the variational principle and the  $D_2$  Ansatz,  $|D_2\rangle = A(t)|+\rangle e^{i\int(t)\hat{a}^\dagger - f^*(t)\hat{a}}|0\rangle + B(t)|-\rangle e^{i\int(t)\hat{a}^\dagger - f(t)\hat{a}}|0\rangle$ , the equations of motion can be obtained,

$$\begin{aligned} 0 &= i\dot{A} - \frac{\varepsilon}{2}A - VB - \frac{\lambda}{2}A(f + f^*) - \frac{\phi}{2}B(f^* + f), \\ 0 &= i\dot{B} + \frac{\varepsilon}{2}B - VA + \frac{\lambda}{2}B(f + f^*) - \frac{\phi}{2}A(f^* + f), \\ 0 &= i\dot{f} - \omega f - \frac{\lambda}{2}(|A|^2 - |B|^2) - \frac{\phi}{2}(A^*B + AB^*). \end{aligned} \quad (28)$$

### B.2 The semi-classical method

The semi-classical Hamiltonian can also be written as

$$\begin{aligned} \hat{H} &= \frac{\varepsilon}{2}\sigma_z + V\sigma_x + \frac{p^2}{2m} + \frac{1}{2}m\omega^2x^2 \\ &+ \lambda\sqrt{\frac{m\omega}{2}}\sigma_zx + \phi\sqrt{\frac{m\omega}{2}}\sigma_xx, \end{aligned} \quad (29)$$

the electronic state is described by the wave function  $|\psi\rangle = A(t)|+\rangle + B(t)|-\rangle$ ,  $m$  is the effective mass of the phonon. The equations of motion from the semi-classical formalism are

$$\begin{aligned} i\dot{A} &= \left(\frac{\varepsilon}{2} + \sqrt{\frac{m\omega}{2}}\lambda x\right)A + VB + \phi\sqrt{\frac{m\omega}{2}}xB, \\ i\dot{B} &= -\left(\frac{\varepsilon}{2} + \sqrt{\frac{m\omega}{2}}\lambda x\right)B + VA + \phi\sqrt{\frac{m\omega}{2}}xA, \\ \dot{x} &= v, \end{aligned} \quad (30)$$

$$\dot{v} = -\omega^2x - \lambda\sqrt{\frac{\omega}{2m}}(|A|^2 - |B|^2) - \phi\sqrt{\frac{\omega}{2m}}(A^*B + AB^*).$$

### B.3 Comparison

We now compare the equations of motion obtained from the variational method and the semi-classical method. From eqn (A7)

of ref. 50, we get  $f = \frac{1}{\sqrt{2m\omega}}(m\omega x + ip)$  and  $f + f^* = \sqrt{2m\omega}x$ . After we put this into the last equation of eqn (28), we get

$$\begin{aligned} 0 &= i\frac{1}{\sqrt{2m\omega}}(m\omega\dot{x} + i\dot{p}) - \omega\frac{1}{\sqrt{2m\omega}}(m\omega x + ip) \\ &- \frac{\lambda}{2}(|A|^2 - |B|^2) - \frac{\phi}{2}(A^*B + AB^*) \end{aligned} \quad (31)$$

The real part of eqn (31) agrees with the fourth equation of eqn (30), and imaginary part of eqn (31) is equal to the third equation of eqn (30), proving the equivalence of the semi-classical method and variational method using only the single  $D_2$  Ansatz.

In conclusion, the expectation value of position  $x$  and momentum  $p$  obtained from the semi-classical method agree with the ones from the variational method using the single  $D_2$  Ansatz.

## C. The multi- $D_2$ trial states

The energies of the system are given by the following equations,

$$\begin{aligned} \langle D_2^M(t) | H_{\text{ex}} | D_2^M(t) \rangle &= -J \sum_{ij} \sum_n \psi_{jn}^* (\psi_{i,n+1} + \psi_{i,n-1}) S_{ji}, \\ \langle D_2^M(t) | H_{\text{ph}} | D_2^M(t) \rangle &= \omega_0 \sum_{ij} \sum_n \psi_{jn}^* \psi_{in} \sum_q \lambda_{jq}^* \lambda_{iq} S_{ji}, \\ \langle D_2^M(t) | H_{\text{ex-ph}}^{\text{o.d.}} | D_2^M(t) \rangle &= \frac{1}{2}N^{-1/2}\phi \sum_{n,q} \sum_{ij} \omega_q S_{ji} \\ &\times \left\{ \psi_{jn}^* \psi_{i,n+1} [e^{iqn}(e^{iq} - 1)\lambda_{iq} + e^{-iqn}(e^{-iq} - 1)\lambda_{jq}^*] \right. \\ &\left. + \psi_{jn}^* \psi_{i,n-1} [e^{iqn}(1 - e^{-iq})\lambda_{iq} + e^{-iqn}(1 - e^{iq})\lambda_{jq}^*] \right\}, \end{aligned} \quad (32)$$

where the Debye-Waller factor is formulated as

$$\begin{aligned} S_{ij} &= \langle \lambda_i | \lambda_j \rangle, \\ &= \exp \left\{ \sum_q \lambda_{jq}^* \lambda_{iq} - \frac{1}{2}(|\lambda_{iq}|^2 + |\lambda_{jq}|^2) \right\}. \end{aligned} \quad (33)$$

In addition, the energies can be converted to the exciton momentum representation by using

$$\begin{aligned} \psi_{in} &= N^{-1/2} \sum_k e^{-ikn} \psi_{ik}, \\ \psi_{in}^* &= N^{-1/2} \sum_k e^{ikn} \psi_{ik}^*. \end{aligned} \quad (34)$$



The Dirac-Frenkel variational principle results in equations of motion including

$$\begin{aligned}
 & -i \sum_i \dot{\psi}_{in} S_{ki} \\
 & = +\frac{i}{2} \sum_i \psi_{in} \sum_q \left( 2\lambda_{kq}^* \dot{\lambda}_{iq} - \dot{\lambda}_{iq} \lambda_{iq}^* - \lambda_{iq} \dot{\lambda}_{iq}^* \right) S_{ki} \\
 & + J \sum_i (\psi_{i,n+1} + \psi_{i,n-1}) S_{ki} \\
 & - \omega_0 \sum_i \psi_{in} \sum_q \lambda_{kq}^* \lambda_{iq} S_{ki} \\
 & - \frac{1}{2} N^{-1/2} \phi \sum_i \sum_q \omega_q \psi_{i,n-1} [e^{iqn} (1 - e^{-iq}) \lambda_{iq} \\
 & + e^{-iqn} (1 - e^{iq}) \lambda_{kq}^*] S_{ki},
 \end{aligned} \quad (35)$$

and

$$\begin{aligned}
 & -i \sum_i \sum_n \psi_{kn}^* \dot{\psi}_{in} \lambda_{iq} S_{ki} - i \sum_i \sum_n \psi_{kn}^* \dot{\psi}_{in} \dot{\lambda}_{iq} S_{ki} \\
 & - \frac{i}{2} \sum_i \sum_n \psi_{kn}^* \dot{\psi}_{in} \lambda_{iq} S_{ki} \\
 & \times \sum_p \left( 2\lambda_{kp}^* \dot{\lambda}_{ip} - \dot{\lambda}_{ip} \lambda_{ip}^* - \lambda_{ip} \dot{\lambda}_{ip}^* \right) \\
 & = J \sum_i \sum_n \psi_{kn}^* (\psi_{i,n+1} + \psi_{i,n-1}) \lambda_{iq} S_{ki} \\
 & - \sum_i \sum_n \psi_{kn}^* \psi_{in} \left( \omega_0 + \omega_0 \sum_p \lambda_{kp}^* \lambda_{ip} \right) \lambda_{iq} S_{ki} \\
 & - \frac{1}{2} N^{-1/2} \phi \sum_i \sum_n \omega_q \psi_{kn}^* [\psi_{i,n+1} e^{-iqn} (e^{-iq} - 1) \\
 & + \psi_{i,n-1} e^{-iqn} (1 - e^{iq})] S_{ki} \\
 & - \frac{1}{2} N^{-1/2} \phi \sum_i \sum_n (\psi_{k,n+1}^* \psi_{i,n} + \psi_{kn}^* \psi_{i,n+1}) \lambda_{iq} \\
 & \times \sum_p \omega_p [e^{ipn} (e^{ip} - 1) \lambda_{ip} + e^{-ipn} (e^{-ip} - 1) \lambda_{kp}^*] S_{ki}.
 \end{aligned} \quad (36)$$

It should be noted that the main results of this work are calculated from the above equations of motion. The equations of motion are solved numerically by means of the fourth-order Runge-Kutta method. The exciton initially sits on two nearest-neighboring sites, i.e.  $\psi_n = (\delta_{n,N/2} + \delta_{n,N/2+1})/\sqrt{2}$ . At  $T = 0$ , the phonon is in the vacuum state, i.e.  $\lambda_{iq} = 0$ . In order to avoid singularity, the uniformly distributed noise  $[-10^{-5}, 10^{-5}]$  is added to the initial variational parameters  $\psi_{in}$  and  $\lambda_{iq}$  at  $t = 0$ . More than one hundred samples are averaged to get rid of the influence of the noise and reach convergent results in the simulations.

## Appendix D. The Toyozawa Ansatz

Our interest here is the polaron ground-state energy band, computed as

$$E(K) = \langle \Psi(K) | \hat{H} | \Psi(K) \rangle, \quad (37)$$

where  $|\Psi(K)\rangle$  is an appropriately normalized, delocalized trial state, and  $\hat{H}$  is the system Hamiltonian. The joint crystal momentum is indicated by  $K$ . It should be noted that the crystal momentum operator commutes with the system Hamiltonian, and energy eigenstates are also eigenfunctions of the crystal momentum. Therefore, variations for distinct  $K$  are independent. The set of  $E(K)$  constitutes a variational estimate (an upper bound) for the polaron energy band. The relaxation iteration technique, viewed as an efficient method for identifying the energy minima of a complex variational system, is adopted to obtain numerical solutions to a set of self-consistency equations derived from the variational principle. To achieve efficient and stable iterations toward the variational ground state, one may take advantage of the continuity of the ground state with respect to small changes in system parameters over most of the phase diagram and may initialize the iteration using a reliable ground state already determined at some nearby points in parameter space. Starting from those limits where exact solutions can be obtained analytically and executing a sequence of variations along the well-chosen paths through the parameter space using solutions from one step to initialize the next, the whole parameter space can be explored.

As the  $D_2$  Ansatz is a localized state from the soliton theory. It can be delocalized into the Toyozawa Ansatz, which is the Bloch state with the designated crystal momentum, via a projection operator  $\hat{P}_K$ .

$$\hat{P}_K = N^{-1} \sum_n e^{i(K-\hat{P})n} = \delta(K - \hat{P}), \quad (38)$$

where

$$\hat{P} = \sum_k k a_k^\dagger a_k + \sum_q q b_q^\dagger b_q. \quad (39)$$

After the delocalization onto the usual  $D_2$  Ansatz, the Toyozawa Ansatz is given by

$$|\Psi_2(K')\rangle = |K'\rangle \langle K' | K' \rangle^{-1/2}, \quad (40)$$

$$\begin{aligned}
 |K'\rangle &= \sum_n e^{iK'n} \sum_{n_1} \psi_{n_1-n}^{K'} a_{n_1}^\dagger \\
 &\times \exp \left[ - \sum_{n_2} \left( \lambda_{n_2-n}^{K'} b_{n_2}^\dagger - \text{H.c.} \right) \right] |0\rangle,
 \end{aligned} \quad (41)$$

where  $\psi_{n_1-n}^{K'}$  is the exciton amplitude and  $\lambda_{n_2-n}^{K'}$  is the phonon displacement.

## Appendix E. Alternative approaches to temperature effects

We aim to investigate the effect of temperature by comparing the following approaches: the averaged Hamiltonian (see Appendix E.1),

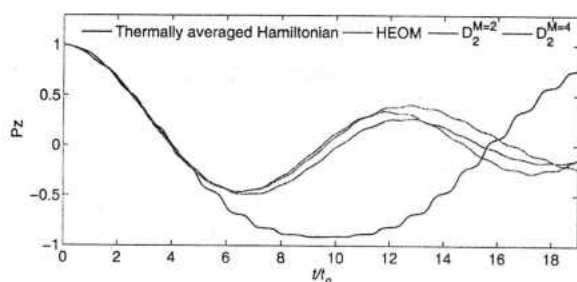


Fig. 8  $P_z(t)$  obtained from averaged Hamiltonian, HEOM method, the  $D_2^{M=2}$  Ansatz, and the  $D_2^{M=4}$  Ansatz. The parameters are  $V = -0.05$ ,  $\lambda = 0.5$ , and  $\beta = 0.5$ .

the variational method with importance sampling (see Appendix E.2), and the numerically exact HEOM method. The spin-boson model, *i.e.*, a Holstein model with  $N = 2$ , is taken as the simplest example.

The variational method with importance sampling is simulated by initially employing random number generators to investigate the temperature effects using the multiple Davydov trial wave states. The influence of the temperature on the dynamical behavior is also studied using the method of averaged Hamiltonian with the Davydov  $D_1$  Ansatz developed here (see eqn (42)) and the HEOM method. The population differences  $P_z(t)$  (see eqn (51)) obtained from the  $D_2^{M=2}$  Ansatz, the  $D_2^{M=4}$  Ansatz, and the other two methods are plotted in Fig. 8 using parameters  $V = -0.05$ ,  $\lambda = 0.5$ ,  $\beta = 0.5$ . Unfortunately, the more complex  $D_1$  Ansatz does not show an improvement over the multi- $D_2$  Ansatz and the HEOM method, at finite  $T$  the distinct damping out of the oscillations is not observed, in contrast to the case of the variational method with importance sampling and the HEOM method. Moreover, with more  $D_2$  states used, the results obtained from the variational method with importance sampling come closer to those from the HEOM method.

### E.1 Averaged Hamiltonian

According to the papers by Cruzeiro *et al.*<sup>44</sup> and by Förner,<sup>51</sup> which are based on earlier work by Davydov and coworkers, the temperature effects can be taken into account approximately, by using a generalized Davydov Ansatz

$$|\psi_\nu(t)\rangle = A(t)|+\rangle e^{[f(t)\hat{a}^\dagger - f^*(t)\hat{a}]}|\nu\rangle + B(t)|-\rangle e^{[g(t)\hat{a}^\dagger - g^*(t)\hat{a}]}|\nu\rangle, \quad (42)$$

with the normalized excited states

$$|\nu\rangle = \frac{1}{\sqrt{\nu!}}(\hat{a}^\dagger)^\nu|0\rangle. \quad (43)$$

In this way, one can view the 'thermally averaged state' as a linear combination of all states with a fixed phonon distribution in the lattice, where the weight factors of the individual states follow Bose-Einstein statistics. Then, we can get a thermally averaged Hamiltonian

$$H_T = \sum_\nu \rho_\nu H_{\nu\nu}, \quad (44)$$

with

$$\rho_\nu = \frac{\langle \nu | e^{-\beta\omega\hat{a}^\dagger\hat{a}} | \nu \rangle}{\sum_\nu \langle \nu | e^{-\beta\omega\hat{a}^\dagger\hat{a}} | \nu \rangle} = \frac{e^{-\beta\omega\nu}}{Q}, \quad (45)$$

where  $\beta = 1/kT$  is proportional to the inverse temperature and

$$H_{\nu\nu} = \langle \psi_\nu(t) | \hat{H} | \psi_\nu(t) \rangle, \quad (46)$$

in which  $\hat{H}$  is given in eqn (27). Thus,

$$\begin{aligned} H_T = & \frac{\varepsilon}{2}(|A|^2 - |B|^2) + V(AB^*D_{21} + A^*BD_{12}) \\ & + \omega[|A|^2(\bar{\nu} + |f|^2) + |B|^2(\bar{\nu} + |g|^2)] \\ & - \frac{\lambda}{2}[|A|^2(f + f^*) - |B|^2(g + g^*)] \\ & + \frac{\phi}{2}[AB^*(g^* + f)D_{21} + A^*B(f^* + g)D_{12}], \end{aligned} \quad (47)$$

where the average phonon number is  $\bar{\nu} = 1/(e^{\beta\omega} - 1)$  and

$$\begin{aligned} D_{12} = & e^{(\bar{\nu}+1)f^*g + \bar{\nu}g^*f - \left(\bar{\nu} + \frac{1}{2}\right)(|f|^2 + |g|^2)}, \\ D_{21} = & e^{(\bar{\nu}+1)g^*f + \bar{\nu}f^*g - \left(\bar{\nu} + \frac{1}{2}\right)(|f|^2 + |g|^2)}. \end{aligned} \quad (48)$$

From the Dirac-Frenkel variational principle, we get the equations of motion

$$\begin{aligned} 0 = & i\dot{A} + \frac{i}{2}A(f^*f - f^*f) - \frac{\varepsilon}{2}A - \omega A(\bar{\nu} + |f|^2) \\ & - VBD_{12} - \frac{\lambda}{2}A(f + f^*) - \frac{\phi}{2}B(f^* + g)D_{12}, \\ 0 = & i\dot{B} + \frac{i}{2}B(g^*g - g^*g) + \frac{\varepsilon}{2}B - \omega B(\bar{\nu} + |g|^2) \\ & - VAD_{21} + \frac{\lambda}{2}B(g + g^*) - \frac{\phi}{2}A(g^* + f)D_{21}, \\ 0 = & i|A|^2\dot{f} - \omega|A|^2f - \frac{\lambda}{2}|A|^2 \\ & - VAB^*\bar{\nu}(g - f)D_{21} - VA^*B[(\bar{\nu} + 1)(g - f)]D_{12} \\ & - \frac{\phi}{2}A^*BD_{12} - \frac{\phi}{2}AB^*(g^* + f)\bar{\nu}(g - f)D_{21} \\ & - \frac{\phi}{2}A^*B(f^* + g)(\bar{\nu} + 1)(g - f)D_{12}, \\ 0 = & i|B|^2\dot{g} - \omega|B|^2g + \frac{\lambda}{2}|B|^2 \\ & - VAB^*(\bar{\nu} + 1)(f - g)D_{21} - VA^*B\bar{\nu}(f - g)D_{12} \\ & - \frac{\phi}{2}AB^*D_{21} - \frac{\phi}{2}AB^*(g^* + f)(\bar{\nu} + 1)(f - g)D_{21} \\ & - \frac{\phi}{2}A^*B(f^* + g)\bar{\nu}(f - g)D_{12}. \end{aligned} \quad (49)$$

In the spin-boson model, physical variables of interest are

$$P_i(t) \equiv \langle \sigma_i \rangle = \langle D_s | \sigma_i | D_s \rangle, \quad i = x, y, z \quad (50)$$



Here,  $P_z(t)$  describes the population difference. With the above trial state, we obtain

$$P_z(t) = |A|^2 - |B|^2. \quad (51)$$

## E.2 Variational method with importance sampling

The variational method with importance sampling is used to obtain the dynamics of the Holstein model with the off-diagonal coupling, where initial phonon displacements are chosen according to the Bose distribution. Using only two sites for simplicity, the Holstein model with the off-diagonal coupling can be reduced to a spin-boson Hamiltonian (eqn (27)). We solve the dynamics by the variational method using the multi-D<sub>2</sub> Ansatz

$$|D_2^M(t)\rangle = \sum_i^M A_i(t)|+\rangle e^{[f_i(t)\hat{a}^\dagger - f_i^*(t)\hat{a}]}|0\rangle + \sum_i^M B_i(t)|-\rangle e^{[f_i(t)\hat{a}^\dagger - f_i^*(t)\hat{a}]}|0\rangle. \quad (52)$$

The temperature effects are included by considering the initial displacements based on the Bose distribution.<sup>52</sup> The initial bath can be expressed as

$$\frac{1}{Z_B} e^{-\beta\omega\hat{a}^\dagger\hat{a}} = \int d\alpha^2 P(\alpha)|\alpha\rangle\langle\alpha|, \quad (53)$$

where  $|\alpha\rangle \equiv e^{\alpha\hat{a} - \alpha^*\hat{a}}|0\rangle$  and the distribution  $P(\alpha)$  is

$$P(\alpha) = \frac{1}{\pi} (e^{\beta\omega} - 1) \exp(-|\alpha|^2(e^{\beta\omega} - 1)), \quad (54)$$

it is shown to be a well-behaved Gaussian function and has no singularity. Numerically, let  $2\sigma^2 = 1/(e^{\beta\omega} - 1)$  and  $\alpha = x + iy$ ,

$$P(\alpha) = \frac{1}{\pi} \frac{1}{2\sigma^2} e^{-\frac{x^2+y^2}{2\sigma^2}} = \frac{1}{\sqrt{2\pi}\sigma} e^{-\frac{x^2}{2\sigma^2}} \frac{1}{\sqrt{2\pi}\sigma} e^{-\frac{y^2}{2\sigma^2}}. \quad (55)$$

Then, we can generate the configuration  $\alpha$  for the bath according to  $P(\alpha)$  by the Monte Carlo method. The initial displacements in the trial states are determined by setting  $f_i(t=0) = \alpha + \varepsilon_0$ , where a small noise  $\varepsilon_0 \in [-10^{-2}, 10^{-2}]$  is added to increase the numerical stability. According to the equations of motion obtained from the Dirac-Frenkel variational principle, the dynamics of the system can be obtained. The final result is averaged over enough realizations (more than 50 000) to ensure the convergence of relevant quantities. In the same way, initial displacements are also chosen according to the temperature in the fully quantum description of the SSH model.

The following are the corresponding equations of motion

$$-i \sum_i \dot{A}_i S_{ki} - \frac{i}{2} \sum_i A_i \left[ -(\dot{f}_i f_i^* + f_i \dot{f}_i^*) + 2f_k^* \dot{f}_i \right] S_{ki} \\ = -\frac{\varepsilon}{2} \sum_i A_i S_{ki} - V \sum_i B_i S_{ki} - \sum_i A_i \omega_0 f_k^* f_i S_{ki} \quad (56)$$

$$-\frac{\lambda}{2} \sum_i A_i (f_i + f_k^*) S_{ki} - \frac{1}{2} \phi \sum_i B_i (f_i + f_k^*) S_{ki}, \\ -i \sum_i \dot{B}_i S_{ki} - \frac{i}{2} \sum_i B_i \left[ -(\dot{f}_i f_i^* + f_i \dot{f}_i^*) + 2f_k^* \dot{f}_i \right] S_{ki} \\ = +\frac{\varepsilon}{2} \sum_i B_i S_{ki} - V \sum_i A_i S_{ki} - \sum_i B_i \omega_0 f_k^* f_i S_{ki} \quad (57) \\ +\frac{\lambda}{2} \sum_i B_i (f_i + f_k^*) S_{ki} - \frac{1}{2} \phi \sum_i A_i (f_i + f_k^*) S_{ki},$$

and

$$-i \sum_i (A_k^* \dot{A}_i + B_k^* \dot{B}_i) f_i S_{ki} - i \sum_i (A_k^* A_i + B_k^* B_i) \dot{f}_i S_{ki} \\ -\frac{i}{2} \sum_i (A_k^* A_i + B_k^* B_i) f_i S_{ki} (2f_k^* \dot{f}_i - \dot{f}_i f_k^* - f_i \dot{f}_i^*) \\ = -\frac{\varepsilon}{2} \sum_i (A_k^* A_i - B_k^* B_i) f_i S_{ki} \\ -V \sum_i (A_k^* B_i + B_k^* A_i) f_i S_{ki} \\ -\sum_i (A_k^* A_i + B_k^* B_i) (\omega_0 + \omega_0 f_k^* f_i) f_i S_{ki} \quad (58) \\ -\frac{\lambda}{2} \sum_i (A_k^* A_i - B_k^* B_i) S_{ki} \\ -\frac{\lambda}{2} \sum_i (A_k^* A_i - B_k^* B_i) f_i (f_i + f_k^*) S_{ki} \\ -\frac{1}{2} \phi \sum_i (A_k^* B_i + B_k^* A_i) S_{ki} \\ -\frac{1}{2} \phi \sum_i (A_k^* B_i + B_k^* A_i) (f_i + f_k^*) f_i S_{ki},$$

where  $S_{ki} = e^{-\frac{1}{2}(f_k^* f_k + f_i^* f_i) + f_k^* f_i}$ .

## Acknowledgements

We thank Yuta Fujihashi and Zheng Fulu for helpful discussion. Support from the Singapore National Research Foundation through the Competitive Research Programme (CRP) under Project No. NRF-CRP5-2009-04 is gratefully acknowledged.

## References

1. L. Xu, W. Chen, A. Mulchandani and Y. Yan, *Angew. Chem., Int. Ed.*, 2005, **44**, 6009.

- 2 T. K. Das and S. Prusty, *Polym.-Plast. Technol. Eng.*, 2012, **51**, 1487.
- 3 H. Shirakawa, E. J. Louis, A. G. MacDiarmid, C. K. Chiang and A. J. Heeger, *J. Chem. Soc., Chem. Commun.*, 1977, **16**, 578.
- 4 E. J. Heller, Y. Yang and L. Kocia, *ACS Cent. Sci.*, 2015, **1**, 40.
- 5 T. Darmanin and F. Guittard, *Prog. Polym. Sci.*, 2014, **39**, 656.
- 6 T. Darmanin, F. Guittard, S. Amigoni, E. de Givenchy, X. Noblin, R. Kofman and F. Celestini, *Soft Matter*, 2011, **7**, 1053.
- 7 S. G. Im, D. Kusters, W. Choi, S. H. Baxamusa, M. C. M. van de Sanden and K. K. Gleason, *ACS Nano*, 2008, **2**, 1959.
- 8 J. H. Burroughes, D. D. C. Bradley, A. R. Brown, R. N. Marks, K. Mackay, R. H. Friend, P. L. Burns and A. B. Holmes, *Nature*, 1990, **347**, 539.
- 9 L. Torsi, A. Dodabalapur, L. Sabbatini and P. G. Zamboni, *Sens. Actuators, B*, 2000, **67**, 312.
- 10 F. Fusalba, P. Gouérec, D. Villers and D. Bélanger, *J. Electrochem. Soc.*, 2001, **148**, A1.
- 11 B. N. Reddy, M. Deepa and A. G. Joshi, *Phys. Chem. Chem. Phys.*, 2014, **16**, 2062.
- 12 J. Kim, H.-S. Park, T.-H. Kim, S. Yeol Kim and H.-K. Song, *Phys. Chem. Chem. Phys.*, 2014, **16**, 5295.
- 13 M. Ates, T. Karazehir and A. Sezai Sarac, *Curr. Phys. Chem.*, 2012, **2**, 224.
- 14 J. W. Schultze and H. Karabulut, *Electrochim. Acta*, 2005, **50**, 1739.
- 15 T. F. Otero and J. M. Sansiena, *Adv. Mater.*, 1998, **10**, 491.
- 16 M. R. Abidian, D.-H. Kim and D. C. Martin, *Adv. Mater.*, 2006, **18**, 405.
- 17 M. R. Abidian, K. A. Ludwig, T. C. Marzullo, D. C. Martin and D. R. Kipke, *Adv. Mater.*, 2009, **21**, 3764.
- 18 R. Ravichandran, S. Sundarajan, J. R. Venugopal, S. Mukherjee and S. Ramakrishna, *J. R. Soc., Interface*, 2010, **7**, S559.
- 19 J. Liao, C. Ning, Z. Yin, G. Tan, S. Huang, Z. Zhou, J. Chen and H. Pan, *ChemPhysChem*, 2013, **14**, 3891.
- 20 A. J. Heeger, S. Kivelson, J. R. Schrieffer and W. P. Su, *Rev. Mod. Phys.*, 1988, **60**, 781–850.
- 21 W. P. Su, J. R. Schrieffer and A. J. Heeger, *Phys. Rev. Lett.*, 1979, **42**, 1698.
- 22 A. Troisi and G. Orlandi, *Phys. Rev. Lett.*, 2006, **96**, 86601.
- 23 P. Ehrenfest, *Zeitschrift Für Phys.*, 1927, **45**, 455.
- 24 M. Hultell and S. Stafström, *Chem. Phys. Lett.*, 2006, **428**, 446.
- 25 A. Troisi, D. L. Cheung and D. Andrienko, *Phys. Rev. Lett.*, 2009, **102**, 116602.
- 26 W. Si and C.-Q. Wu, *J. Chem. Phys.*, 2015, **143**, 024103.
- 27 J. Dong, W. Si and C.-Q. Wu, *J. Chem. Phys.*, 2016, **144**, 144905.
- 28 G. Li, B. Movaghar, A. Nitzan and M. A. Ratner, *J. Chem. Phys.*, 2013, **138**, 044112.
- 29 P. Szymanski, S. Garrett-Roe and C. B. Harris, *Prog. Surf. Sci.*, 2005, **78**, 1–39.
- 30 Y. Zhao, D. W. Brown and K. Lindenberg, *J. Chem. Phys.*, 1997, **107**, 3159; Y. Zhao, D. W. Brown and K. Lindenberg, *J. Chem. Phys.*, 1997, **107**, 3179.
- 31 R. W. Munn and R. Silbey, *J. Chem. Phys.*, 1985, **83**, 1843.
- 32 Y. Zhao, B. Luo, Y. Zhang and J. Ye, *J. Chem. Phys.*, 2012, **137**, 084113.
- 33 N. J. Zhou, Z. K. Huang, J. F. Zhu, V. Chernyak and Y. Zhao, *J. Chem. Phys.*, 2015, **143**, 014113.
- 34 F. Dorfner, L. Vidmar, C. Brockett, E. Jeckelmann and F. Heidrich-Meisner, *Phys. Rev. B: Condens. Matter Mater. Phys.*, 2015, **91**, 104302.
- 35 Y. Yao, W. Si, X. Hou and C.-Q. Wu, *J. Chem. Phys.*, 2012, **136**, 234106.
- 36 D. Golez, J. Bonca, L. Vidmar and S. A. Trugman, *Phys. Rev. Lett.*, 2012, **109**, 236402.
- 37 H. Tamura and M. Tsukada, *Phys. Rev. B: Condens. Matter Mater. Phys.*, 2012, **85**, 54301.
- 38 H. Tamura, M. Tsukada, H. Ishii, N. Kobayashi and K. Hirose, *Phys. Rev. B: Condens. Matter Mater. Phys.*, 2012, **86**, 35208.
- 39 Y. Zhao, D. W. Brown and K. Lindenberg, *J. Chem. Phys.*, 1994, **100**, 2335.
- 40 J. L. Brédas, B. Thémans, J. G. Fripiat, J. M. André and R. R. Chance, *Phys. Rev. B: Condens. Matter Mater. Phys.*, 1984, **29**, 6761.
- 41 M. M. Kukulja and S. N. Rashkeev, *Phys. Rev. B: Condens. Matter Mater. Phys.*, 2007, **75**, 104111.
- 42 T. Ishiguro, H. Kaneko, Y. Nogami, H. Ishimoto, H. Nishiyama, J. Tsukamoto, A. Takahashi, M. Yamaura, T. Hagiwara and K. Sato, *Phys. Rev. Lett.*, 1992, **69**, 660.
- 43 X. B. Chen, J.-P. Issi, M. Cassart, J. Devaux and D. Billaud, *Polymer (Guildf.)*, 1994, **35**, 5256.
- 44 L. Cruzeiro, J. Halding, P. L. Christiansen, O. Skovgaard and A. C. Scott, *Phys. Rev. A*, 1988, **37**, 880.
- 45 X. Wang, D. W. Brown and K. Lindenberg, *Phys. Rev. Lett.*, 1989, **62**, 1796.
- 46 Y. Tanimura and R. Kubo, *J. Phys. Soc. Jpn.*, 1989, **58**, 101.
- 47 L. Chen, Y. Zhao and Y. Tanimura, *J. Phys. Chem. Lett.*, 2015, **6**, 3110.
- 48 L. Wang, Y. Fujihashi, L. Chen and Y. Zhao, to be published.
- 49 J.-F. Chang, T. Sakanoue, Y. Olivier, T. Uemura, M.-B. Dufourg-Madec, S. G. Yeates, J. Cornil, J. Takeya, A. Troisi and H. Sirringhaus, *Phys. Rev. Lett.*, 2011, **107**, 66601.
- 50 F. Grossmann, M. Werther, L. Chen and Y. Zhao, *Chem. Phys.*, 2016, **481**, 99–107.
- 51 W. Förner, *J. Phys.: Condens. Matter*, 1992, **4**, 1915.
- 52 M. Hillery, R. F. O. onnell, M. O. Scully and E. P. Wigner, *Phys. Rep.*, 1984, **106**, 121.



附件 1

## 项目研究开发合同

项目名称：新型智能开关系统集成设计与材料研发

委托方（甲方）：三门峡市宏达电器有限公司

受托方（乙方）：长江师范学院

签订时间：2025 年 9 月 22 日

起止时间：2025 年 9 月 22 日-2027 年 12 月 31 日

与原件相符



A handwritten signature in black ink, appearing to be 'Jing Li' or similar, written over a horizontal line.





# 项目研究开发合同

委托方（甲方）：三门峡市宏达电器有限公司

项目联系人：翟梦阳 电话：15039858546

通讯地址：河南省三门峡市黄河西路陕州公园南大街东排东侧3号

受托方（乙方）：长江师范学院

项目负责人：黄忠凯 电话：15292291686

通讯地址：重庆市涪陵区聚贤大道16号

甲方委托乙方研究开发新型智能开关系统集成设计与材料研发项目，并支付研究开发经费和报酬，乙方接受委托并进行此项研究开发工作。根据《中华人民共和国民法典》的规定，经双方平等协商，达成如下协议。

## 第一条 项目研究开发的要求如下：

1. 研究开发目标：本项目旨在通过产学研合作，运用先进计算模拟与创新设计方法，进行面向未来的智能开关系统集成设计与新材料应用研究。项目专注于理论层面的前瞻性探索，旨在形成具有指导意义的产品概念设计方案、材料计算数据集与技术研究报告，为甲方的长期产品战略规划提供创新方向与理论支持。

2. 研究开发内容：(1) 市场趋势、技术路线与用户需求前瞻性研究：宏观行业态势分析：深入研究全球及国内智能家居与电气附件行业的政策导向、市场规模、竞争格局及产业链分布，识别潜在的增长机会与技术突破口。技术发展路线梳理：系统梳理智能开关在智能化、可持续性等方面的技术演进路径，并对未来数年的技术发展趋势做出研判。竞争产品标杆分析：对国内外市场主流及创新型竞品进行多维度解构分析，包括其设计语言、技术应用、材料选择与商业模式，以期汲取经验并定位





差异化创新方向。社会文化与美学趋势研究：探索当代及未来的社会文化、生活方式及设计美学潮流对家居产品设计的影响，确保设计理念的前瞻性与文化契合度。(2) 基于 DFT 计算的新材料多尺度模拟与性能预测研究：计算模型与方法论构建：采用密度泛函理论 (DFT)、分子动力学 (MD) 模拟等多尺度计算模拟方法，建立适用于高分子复合材料、无机非金属材料等候选体系的精准原子/分子模型。电子结构与基础物性计算：从量子力学层面系统计算候选材料的电子能带结构等基础物理化学性质，从根本上理解其性能成因。(3) 基于多源输入的系统创新与概念设计集成：设计策略与理念定义：综合市场研究、用户洞察与计算模拟的结论，凝练出项目的核心设计策略与创新理念，明确设计的方向、原则与价值主张。多轮概念创意与发散：组织跨学科脑力激荡，运用多种创意设计方法，生成多组不同风格、不同技术实现路径的前瞻性概念方案，并进行可视化表达。高保真方案表达与交付：运用二维效果图等多种媒介，对最终确定的系统化概念设计方案进行可视化的呈现，并形成完整的设计说明报告。

第二条 乙方应在本合同生效后按下列进度完成研发工作：

1. 研究开发起止时间：2025 年 9 月 22 日——2027 年 12 月 31 日；
2. \_\_\_\_\_；

第三条 甲方应向乙方提供的技术资料及协作事项如下：

1. 技术资料清单：用户需求反馈调研报告、产品测试结果。
2. 提供时间和方式：2026 年 12 月 31 日之前提供不少于五次需求反馈；合同结束前对材料及设计方案提供合理的反馈。
3. 其他协作事项：提供专业培训，提升团队的设计能力与研发能力。

第四条 甲方支付乙方研究开发经费和报酬总额为 壹佰 万元，采取分期支付方式，具体支付方式和时间如下：





一次性付款：合同签订之日起40个工作日内，甲方支付全部经费和报酬。

乙方银行帐户信息如下：

户名：长江师范学院

开户银行：中国农业银行重庆涪陵城区支行

银行帐号：31620101040009181

行号：103669062014

用途：材料科学与工程学院黄忠凯科研经费

第五条 本合同的变更必须由双方协商一致，并以书面形式确定。未经甲方同意，乙方不得将本合同项目部分或全部研究开发工作转让第三方承担。

第六条 乙方应按以下方式向甲方交付研究开发成果及结题验收：

1. 成果形式及数量：需求报告1份，新材料模拟报告1份，产品设计方案1份。

2. 验收标准及方法：双方均认可的方式。

第七条 双方确定，履行本合同所产生的研究开发成果及其相关知识产权归双（甲、乙、双）方所有，乙方不得在向甲方交付研究开发成果之前，自行将研究开发成果转让给第三方。

第八条 乙方完成本项目的研究开发人员享有在有关技术成果文件上写明技术成果完成者的权利和取得有关荣誉证书、奖励的权利。

第九条 双方确定：任何一方违反本合同约定，造成研究开发工作停滞、延误或失败的，按以下约定承担违约责任：

1. 甲方违反本合同第四条约定，应当支付违约金（或损失赔偿额）一万元。

2. 乙方违反本合同第五条约定，应当支付违约金（或





损失赔偿额) 一万元。

第十条 双方确定,因发生不可抗力或技术风险或双方一致认可的意外情况,致使本合同履行成为不必要或不可能的,一方可通知另一方解除合同。

第十一条:本合同未尽事宜或双方因履行合同而发生的争议,应协商、调解解决。协商、调解不成的,提交仲裁委员会仲裁。

第十二条 本合同一式四份,其中甲方持壹份、乙方持三份,具有同等法律效力,经双方签字盖章后生效。

甲方: 三门峡市宏达电器有限公司 (盖章)

法定代表人/委托代理人 程转阳 (签名)

乙方: 长江师范学院 (盖章)

法定代表人/委托代理人: 黄忠凯 (签名)

项目负责人: 黄忠凯 (签名)

2025 年 9 月 22 日







# 长江师范学院来款认领单

来款信息					
流水号:	202510130006		凭证编号:	[25年10月](01)00313	
付款单位:	三门峡市宏达电器有限公司		银行:	农行重庆涪陵城区支行	
来款金额:	1,000,000.00	本次认领金额:	1,000,000.00	未认领金额:	0.00
来款日期:	2025-10-11	来款类型:	单位	银行流水号:	
收入代码:	未确认收入类型	资金来源:	其他收入	来款状态:	认领完毕
对冲号:	20251000060100313				
备注:	来款				
认领信息					
流水号:	202510130006	认领序号:	1	认领金额:	1,000,000.00
部门编号:		部门名称:			
项目编号:		项目名称:			
科研项目编号:		科研项目名称:			
认领人信息					
认领人:	(20190011)黄忠凯		认领时间:	2025-10-14	
认领人签字:					



与原件相符





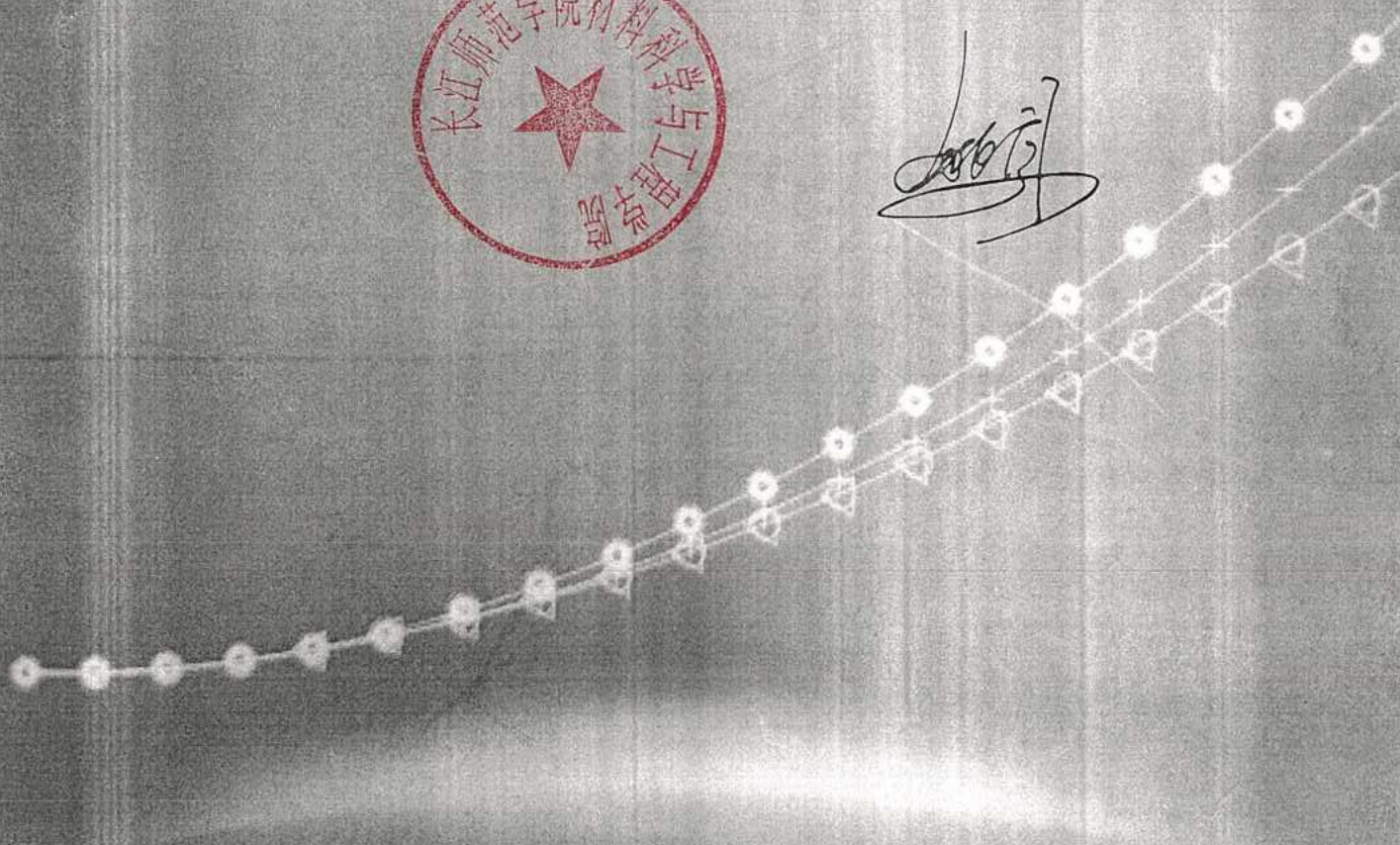
# Davydov Wavefunction Theory in Open Quantum Systems

量子开放系统中的  
达维多夫波函数理论

英文版

与原件相符

黄忠凯 刘松利 著



中国科学技术大学出版社





## 内 容 简 介

本书系统介绍基于多维达维多夫波函数理论的开放量子体系理论框架,为解决量子动力学中系统-环境相互作用这一关键难题提供兼具数值精确度与计算效率的解决方案。通过几类典型量子体系的应用示范,表明该方案有助于揭示激子-声子关联系统的物理本质,并能为量子材料和器件设计提供有益的理论指导。

本书主要面向量子物理、理论化学和材料科学领域的研究人员,也供高年级本科生和研究生学习开放量子体系动力学的波函数研究方法。

## 图书在版编目(CIP)数据

量子开放系统中的达维多夫波函数理论:英文/黄忠凯、刘松利著. — 合肥:中国科学技术大学出版社, 2025. 10. — ISBN 978-7-312-06480-7

I. 0413.1

中国国家版本馆 CIP 数据核字第 2025EN6650 号

## 量子开放系统中的达维多夫波函数理论(英文版)

LIANGZI KAIFANG XITONG ZHONG DE DAWEIDUOFU BOHANSHU LILUN (YINGWENBAN)

出版 中国科学技术大学出版社

安徽省合肥市金寨路 96 号, 230026

<http://press.ustc.edu.cn>

<https://zgkxjcsdx.cbs.tmall.com>

印刷 安徽省瑞隆印务有限公司

发行 中国科学技术大学出版社

开本 787 mm×1092 mm 1/16

印张 14

字数 415 千

版次 2025 年 10 月第 1 版

印次 2025 年 10 月第 1 次印刷

定价 65.00 元





# Contents

<b>Preface</b> .....	<b>i</b>
<b>Abbreviations</b> .....	<b>viii</b>
<b>Chapter 1 Introduction</b> .....	<b>1</b>
1.1 Background .....	1
1.2 Objectives and Scope .....	4
1.3 Book Overview .....	8
<b>Chapter 2 Scholarly Review</b> .....	<b>15</b>
2.1 Theoretical Foundations of the Davydov Trial States .....	15
2.2 Implementation and Applications of the Multiple Davydov $D_2$ Trial State ..	21
2.2.1 Charge Transport Mechanisms in Conducting Polymers .....	21
2.2.2 Dynamics of Bloch Oscillations in Condensed Matter Systems .....	22
2.2.3 Dynamics of Super Bloch Oscillations .....	24
2.2.4 Singlet Fission Dynamics and Mechanisms .....	26
2.2.5 Landau-Zener Transitions in Quantum Electrodynamical Systems ....	27
2.2.6 Bloch-Zener Oscillations in Tunable-Gap Systems .....	29
2.2.7 Polaronic Effects in Bloch-Zener Oscillations: An Extended Holstein Model Approach .....	31
<b>Chapter 3 Theoretical Framework and Methodological Approaches</b> .....	<b>47</b>
3.1 Variational Dynamics: The Dirac-Frenkel Approach .....	47
3.2 Variational Wave Functions: The Davydov Ansatz .....	49
3.3 Application Domains of the Multiple Davydov $D_2$ Ansatz .....	51

3.3.1	Exciton-Phonon Dynamics in One-Dimensional Molecular Crystals ..	52
3.3.2	Field-Driven Polaron Transport in Holstein Chains .....	54
3.3.3	AC-Field Effects on Holstein Polarons .....	55
3.3.4	Intramolecular Singlet Fission in Molecular Dimers .....	57
3.3.5	Quantum Dissipation in Landau-Zener Transitions .....	59
3.3.6	Gap-Tuning Bloch-Zener Oscillations Model .....	60
3.3.7	An Extended Holstein Model of Polaron Dynamics of Bloch-Zener Oscillations .....	65
<b>Chapter 4</b>	<b>Quantum Dynamics of Polaron with Off-Diagonal Coupling .....</b>	<b>71</b>
4.1	Introduction .....	71
4.2	The Multi-D <sub>2</sub> Davydov Ansatz .....	72
4.3	Polaron Dynamics in Exciton Momentum Representation .....	74
4.4	Effect of Transfer Integral and Off-diagonal Coupling on Exciton Transport	78
4.5	Temperature Effects .....	82
<b>Chapter 5</b>	<b>Field-Driven Polaron Dynamics in One-Dimensional Systems .....</b>	<b>86</b>
5.1	Introduction .....	86
5.2	Validity of Variation for Transient Dynamics .....	87
5.2.1	Diagonal Coupling .....	87
5.2.2	Off-Diagonal Coupling .....	89
5.3	Anti-Adiabatic Regime .....	89
5.4	Strong Diagonal Coupling .....	98
<b>Chapter 6</b>	<b>AC-Field Induced Polaron Dynamics in One-Dimensional Systems .....</b>	<b>103</b>
6.1	Introduction .....	103
6.2	Detuned and Resonant Cases .....	105
6.3	AC Phase Modulation .....	110
<b>Chapter 7</b>	<b>Quantum Dynamics of Intramolecular Singlet Fission Processes .....</b>	<b>116</b>
7.1	Introduction .....	116
7.2	Validity of Variational Dynamics for the Singlet Fission Process .....	117



7.3	Population Dynamics .....	119
7.3.1	Effect of Excitonic Coupling on Fission Dynamic .....	119
7.3.2	Effect of Exciton-Phonon Coupling on Fission Dynamics .....	120
<b>Chapter 8</b>	<b>Quantum Dynamics of Dissipative Landau-Zener Transitions .....</b>	<b>126</b>
8.1	Introduction .....	126
8.2	A Qubit Coupled to a Single Mode .....	127
8.3	Effect of the Bath Spectral Density .....	131
8.4	Effects of Coupling Strength and Interaction Angle .....	135
<b>Chapter 9</b>	<b>Dynamics of Bloch-Zener Oscillations with Tuning Gap .....</b>	<b>141</b>
9.1	Introduction .....	141
9.2	BZO with Fine Tuned Constant Gap .....	142
9.3	Linearly Time-Dependent Tuning of Gaps .....	145
9.4	Dissipative BZ Dynamics .....	146
<b>Chapter 10</b>	<b>Dynamics of Bloch-Zener Oscillations in an Extended Holstein Model .....</b>	<b>150</b>
10.1	Introduction .....	150
10.2	Spectral Properties of BZO Phenomenon .....	151
10.2.1	BZO Dynamics of a Free Excitation .....	153
10.2.2	Effects of the Optical Phonon .....	156
10.2.3	Dissipative Dynamics of BZO in an Ohmic Environment .....	164
<b>Chapter 11</b>	<b>The Journey So Far: A Summary .....</b>	<b>168</b>
<b>Chapter 12</b>	<b>Future Perspectives and Research Directions .....</b>	<b>174</b>
12.1	Neural Network Approaches for Open Quantum System Dynamics .....	174
12.2	Controlling Photon Delocalization in Rabi Dimer Systems .....	175
<b>Appendix</b>	<b>.....</b>	<b>179</b>
Appendix A	For Quantum Dynamics of Polaron with Off-Diagonal Coupling .....	179
Appendix B	For Field-Driven Polaron Dynamics in One-Dimensional Systems .....	187

Appendix C	For AC-Field Induced Polaron Dynamics in One-Dimensional Systems .....	193
Appendix D	For Quantum Dynamics of Intramolecular Singlet Fission Processes .....	194
Appendix E	For Quantum Dynamics of Dissipative Landau-Zener Transitions ..	196
Appendix F	For Dynamics of Bloch-Zener Oscillations with Tuning Gap .....	198
Appendix G	For Dynamics of Bloch-Zener Oscillations in an Extended Holstein Model .....	202



选题编辑 韩继伟  
责任编辑 吴金华  
封面设计 刘苏锐



定价：65.00 元

ISBN 978-7-312-06480-7



9 787312 064807